GRI–91/0072

GEOLOGIC AND HYDROLOGIC CONTROLS ON THE OCCURRENCE AND PRODUCIBILITY OF COALBED METHANE, FRUITLAND FORMATION, SAN JUAN BASIN

TOPICAL REPORT

(AUGUST 1987–JULY 1990)

Prepared by

W. B. Ayers, Jr., W. R. Kaiser, S. E. Laubach, W. A. Ambrose, R. W. Baumgardner, Jr., A. R. Scott, Roger Tyler, Joseph Yeh, G. J. Hawkins, T. E. Swartz, D. D. Schultz-Ela, and S. D. Zellers

Bureau of Economic Geology
W. L. Fisher, Director
The University of Texas at Austin
Austin, Texas 78713-7508

C. M. Tremain

Colorado Geological Survey

N. H. Whitehead III

New Mexico Bureau of Mines and Mineral Resources

For

GAS RESEARCH INSTITUTE
Contract No. 5087-214-1544
Richard C. Klem, Project Manager
Coalbed Methane Technology

March 1991

QAe7643

Disclaimer

LEGAL NOTICE This report was prepared by the Bureau of Economic Geology as an account of work sponsored by the Gas Research Institute (GRI). Neither GRI, members of GRI, nor any person acting on behalf of either:

a. Makes any warranty or representation, expressed or implied, with respect to the accuracy, completeness, or usefulness of the information contained in this report, or that the use of any apparatus, method, or process disclosed in this report may not infringe privately owned rights; or

b. Assumes any liability with respect to the use of, or for damages resulting from the use of, any information, apparatus, method, or process disclosed in this report.

50272-101

REPORT DOCUMENTATION PAGE	1. REPORT NO.	2.	3. Recipient's Accession No.

4. Title and Subtitle
Geologic and Hydrologic Controls on the Occurrence and Producibility of Coalbed Methane, Fruitland Formation, San Juan Basin

5. Report Date
March 1991

6.

7. Author(s) W. B. Ayers, Jr., W. R. Kaiser, S. E. Laubach, W. A. Ambrose, R. W. Baumgardner, Jr., A. R. Scott, Roger Tyler, Joseph Yeh, G. J. Hawkins, T. E. Swartz, D. D. Schultz-Ela, S. D. Zellers, C. M. Tremain, and N. H. Whitehead III

8. Performing Organization Rept. No.

9. Performing Organization Name and Address
Bureau of Economic Geology
The University of Texas at Austin
University Station, Box X
Austin, Texas 78713-7508

10. Project/Task/Work Unit No.

11. Contract(C) or Grant(G) No.
(C) 5087-214-1544
(G)

12. Sponsoring Organization Name and Address
Gas Research Institute
8600 West Bryn Mawr Avenue
Chicago, IL 60631 Project Manager: Richard C. Klem

13. Type of Report & Period Covered
Topical Report
August 1, 1987 - July 31, 1990

14.

15. Supplementary Notes

16. Abstract (Limit: 200 words)

Coalbed methane resources in the Fruitland Formation in the San Juan Basin are estimated to be 43 to 49 trillion cubic feet at depths between 400 and 4,200 ft. The San Juan Basin leads the United States in coalbed methane production; in 1989, the basin produced approximately 65 billion cubic feet of coalbed methane. In the past 5 years, more than 1,000 coalbed methane wells have been drilled in the basin.

The thickest Fruitland coal seams occur in the northern part of the basin and trend northwestward, paralleling Pictured Cliffs barrier/strandplain sandstones; in the southern part of the basin, anomalously thick coal seams trend northeastward and occur between Fruitland fluvial sandstone complexes. Fruitland coal seams commonly are extensive, overriding sandstones.

Coal beds are fractured reservoirs, and commonly, permeability is greatest in the direction of the dominant fracture set (face cleat). Face-cleat strikes in Fruitland coal beds delineate two principal domains. In the southern part of the basin, face cleats strike northward or northeastward, whereas in the northern part of the basin, face-cleat strike is predominantly northwestward.

Coal seams, major aquifers in the Fruitland Formation, are overpressured in the northern part of the basin due to artesian conditions. These overpressured coal seams commonly are water-productive. In the southern part of the basin, the Fruitland Formation is underpressured, and coalbed methane wells produce little or no water. The composition of Fruitland coalbed gas varies regionally and predictably; both dry and wet Fruitland gases are present, and carbon dioxide content ranges up to 13 percent. On the basis of geologic and hydrologic studies, the San Juan Basin was divided into regions in which Fruitland coal beds have similar reservoir characteristics.

17. Document Analysis a. Descriptors
Coalbed methane; Fruitland Formation; Pictured Cliffs Sandstone; depositional systems; structural geology; cleat; coal occurrence; coal resources; gas in place; coalbed methane production; hydrology; hydrochemistry; pressure regime; gas composition; San Juan Basin; Colorado; New Mexico

b. Identifiers/Open-Ended Terms
Methane from coal seams; occurrence and producibility

c. COSATI Field/Group

18. Availability Statement	19. Security Class (This Report)	21. No. of Pages
	20. Security Class (This Page)	22. Price

RESEARCH SUMMARY

Title

Geologic and Hydrologic Controls on the Occurrence and Producibility of Coalbed Methane, Fruitland Formation, San Juan Basin

Contractor

Bureau of Economic Geology, The University of Texas at Austin; Colorado Geological Survey; New Mexico Bureau of Mines and Mineral Resources. GRI Contract No. 5087-214-1544.

Principal Investigator

W. B. Ayers, Jr.

Report Period

August 1, 1987 – July 31, 1990

Objectives

To identify geologic controls on the occurrence of coalbed methane in the Fruitland Formation; to document the distribution and continuity of Fruitland coal seams; to delineate structures that may form conventional traps and enhance coalbed permeability; to identify cleat and fracture trends and the regional stress regime; to define the regional hydrodynamics of the Fruitland Formation; to map Fruitland coalbed methane production; to relate coalbed methane producibility to geologic and hydrologic factors; and to estimate the resources of coalbed methane in the Fruitland Formation.

Technical Perspective

Coalbed methane resources in the Fruitland Formation of the San Juan Basin are estimated to be between 43 and 49 trillion cubic feet (Tcf). The technology required to exploit this resource is in the developmental stage; the goal of this study was to relate coalbed methane occurrence and producibility to geologic and hydrologic settings, leading to models for exploration and production. The models developed in this study should reduce the cost of exploration, optimize production of this large unconventional energy resource, and ensure a supply of natural gas at a reasonable cost.

Results

To evaluate coalbed methane in the Fruitland Formation, we studied depositional setting, structure, hydrology, and production. The thickest coal seams (individual seams thicker than 20 ft [6 m] and net coal thickness more than 50 ft [15 m]) occur in the northern part of the basin, in northwest-trending deposits parallel to ancient shoreline deposits of the Pictured Cliffs Sandstone. In the southern part of the basin, thick coal seams, which trend northeastward, formed in a floodplain setting. Fruitland coal seams commonly are extensive, overriding sandstones. Gas in place in Fruitland Formation coal beds was calculated to be 43 to 49 Tcf at depths between 400 and 4,200 ft (120 and 1,280 m). Fruitland coal resources in the same interval are 245 billion short tons.

Cleats (fractures) in Fruitland coal beds and joints in adjacent rocks are extensional fractures. Face (primary) and butt (secondary) cleats in Fruitland coal seams are well developed. Face-cleat strikes delineate two principal domains that are separated by a boundary of variable orientation near the Colorado–New Mexico border. South of the boundary, face cleats strike predominantly north-

ward or northeastward; north of the boundary, they strike predominantly northwestward. Prevalence of two strongly developed fracture sets along the boundary may increase coal friability. Fractures are inferred to be more abundant in major and minor tectonic folds at the periphery of the basin floor. Lineaments mapped in Landsat Thematic Mapper images of the San Juan Basin show little relation to the gas or water production parameters tested. Wells on lineaments do not have consistently higher production values than those not on lineaments. There is no significant correlation between production data and length of or distance to the nearest lineament.

Permeability is the most critical parameter for the producibility of coalbed methane. Fruitland coal beds are more permeable than Fruitland or Pictured Cliffs sandstones in the northern San Juan Basin; the coal beds are the major aquifer elements. Artesian overpressuring explains the need to dewater northern San Juan Basin coalbed methane wells. In the south, the Fruitland behaves as an aquitard, which accounts for water-free gas production. Waters produced from overpressured Fruitland coal seams have high alkalinities and low chlorinities. Stimulation of coalbed wells and disposal (injection) of these waters will require knowledge of their chemical compatibility with completion fluids and host formation waters, respectively.

In 1989, the San Juan Basin led the United States in coalbed methane production; more than 65 billion cubic feet (Bcf) of coalbed gas was produced from the Fruitland Formation. Coalbed methane production is log-normally distributed. The most productive wells occur in thick coal beds near hydrologic and geologic transition zones (potentiometric, pressure, chemical, structural, and depositional) in the ovepressured, northern part of the basin. Because it is necessary to dewater coal beds in this area, gas production may be greater from a single thick coal bed than from several thin beds. Significant volumes of coalbed methane may be conventionally trapped. Production-decline behavior of coalbed wells differs from that of sandstone wells. Sandstone wells that exhibit coal-decline behavior are probably producing coalbed methane indirectly from adjacent coal seams.

Reservoir characteristics of Fruitland coal beds and the composition of Fruitland coalbed gas vary regionally and predictably. On the basis of integrated studies of geology, hydrology, gas composition, and production, the San Juan Basin was divided into three regions and several subregions. Wells in the overpressured, northern part of the basin (Area 1) have the greatest coalbed gas production (up to 20,000,000 cubic feet per day [20,000 Mcf/d]) and produce predominantly dry gas with 3 to 13 percent carbon dioxide, which must be stripped or diluted by mixing with low-carbon dioxide gas; these wells commonly are water productive. Wells in the underpressured, regional discharge area (Area 2) generally are less productive than those in Area 1, but production values from the two areas overlap. Coalbed methane wells in Area 2 commonly produce wet gas with less than 1 percent carbon dioxide. These wells are shallower than those in Area 1, and they produce little or no water. Area 3 is the regionally underpressured eastern part of the basin where data are too sparse for adequate characterization of reservoirs.

Technical Approach

As many as 2,500 geophysical well logs were used in the geologic study covering 7,000 mi² in the San Juan Basin. A grid of interlocking cross sections was made with closely spaced well logs, and the remaining logs were correlated with the cross sections. Stratigraphic units defined by 18 marker beds in the Upper Cretaceous and lower Tertiary section were correlated in these cross sections. Structure, isopach, lithofacies, and coal-occurrence maps were evaluated individually and were compared with one another to interpret geologic controls on the occurrence and producibility of coalbed methane.

To evaluate cleat patterns in the Fruitland Formation, fractures were studied in coal beds and adjacent sandstones in 11 cores and at 90 outcrop stations along the basin margin, and fractures were mapped in selected areas of the San Juan Basin. To quantify the relations between lineaments and coalbed methane production and to determine the utility of these relations for predicting coalbed methane production, lineaments were mapped on 1:250,000-scale Landsat Thematic Mapper images and compared with lineaments from previous studies. Lineament length, azimuth, and distance from wells were compared with production data. Linear regression was applied to determine the significance of the relationship between lineament attributes and production data.

Fruitland hydrodynamics were evaluated on the basis of hydraulic head, pressure gradients, hydrochemistry, and cross-sectional modeling. Bottom-hole pressures calculated from wellhead shut-in pressures were used to map hydraulic head and pressure regime and to estimate vertical and lateral pressure gradients. A chlorinity map and Stiff ionic-ratio diagrams were made to characterize ground-water flow and hydrochemical facies. Cross-sectional modeling was done to elucidate cross-formational flow and to conceptualize ground-water flow in the basin.

Production-decline curves and Q plots were used to evaluate decline behavior of Fruitland coalbed wells. Initial potential and maximum annual production were mapped to compare productivity among wells with varying production histories. Data from more than 550 Fruitland wells were analyzed. Gas and water production maps were compared with coal-occurrence, structure, potentiometric-surface, pressure-gradient, and hydrochemical maps to establish correlations between geohydrology and coalbed methane occurrence and producibility. On the basis of these comparisons, the San Juan Basin was divided into regions in which Fruitland coal beds have similar reservoir characteristics.

Implications

This report describes coalbed methane occurrence and resources, coal rank, coal-gas composition, fracture patterns, and regional hydrodynamics in the Fruiltand Formation in the San Juan Basin. Comprehensive investigation of the coal seams integrates the preceding information with an analysis of coalbed methane production to divide the San Juan Basin into three regions and several subregions in which Fruiltand coal beds have similar reservoir characteristics. The report significantly advances our understanding of controls on the occurrence and producibility of Fruitland coalbed methane in the San Juan Basin. In addition, the report provides a rationale for directing coalbed methane exploration, as well as a framework for interpreting the results obtained. Finally, this research provides technical insights and approaches that are transferable to other western coal basins.

Richard C. Klem
GRI Project Manager

CONTENTS

FIGURES

Geologic Controls on Coalbed Occurrence, Thickness, and Continuity, Cedar Hill Field and the COAL Site

FIGURES

Geologic Controls on Fruitland Coal Occurrence, Thickness, and Continuity, Navajo Lake Area, San Juan Basin

FIGURES

FRACTURE PATTERNS

Coal Fracture (Cleat) Patterns in Upper Cretaceous Fruitland Formation, San Juan Basin, Colorado and New Mexico: Implications for Coalbed Methane Exploration and Development

FIGURES

TABLES

Fracture Swarms in Upper Cretaceous Sandstone and Coal, Northern San Juan Basin, Colorado: Potential Targets for Methane Exploration

FIGURES

TABLES

Effects of Compaction on Cleat Characteristics: Preliminary Observations

FIGURES

Comparative Lineament Analysis of the San Juan Basin: Relationships between Lineament Attributes and Coalbed Methane Production

FIGURES

TABLES

Predicting Fracture Permeability from Bed Curvature

FIGURES

TABLE

HYDROLOGY, THERMAL MATURITY, AND GAS COMPOSITION

Hydrology of the Fruitland Formation, San Juan Basin

FIGURES

TABLES

Thermal Maturity of Fruitland Coal and Composition and Distribution of Fruitland Formation and Pictured Cliffs Sandstone Gases

FIGURES

TABLE

INTEGRATION OF GEOLOGIC AND HYDROLOGIC STUDIES

Geologic and Hydrologic Characterization of Coalbed Methane Production, Fruitland Formation, San Juan Basin

FIGURES

Preface

Coal beds in the Fruitland Formation contain an estimated 43 to 49 Tcf of methane. With more than 500 producing coalbed methane wells and approximately 1,000 wells scheduled to be drilled in 1990, this basin is one of the most active areas of coalbed methane exploration and production in the United States. Coalbed methane production from the Fruitland Formation was approximately 65 Bcf in 1989 and was predicted to exceed nearly 130 Bcf in 1990.

For the past three years, the Bureau of Economic Geology has evaluated geologic and hydrologic controls on the occurrence and producibility of coalbed methane in the Fruitland Formation. Research results from the each of the first two years were summarized in Annual Reports to the Gas Research Institute (GRI-88/0332.1 and GRI-90/0014.1, respectively). This topical report on Fruitland coalbed methane supersedes those reports, integrating their contents with research results from the third year of this study.

Sections in this report are grouped in five topical areas, with each topic relating to factors that control the occurrence or producibility of coalbed methane. The first topic, the ***Tectonic Setting*** of the San Juan Basin, reviews regional tectonic controls on depositional systems and coalbed attitude. Among the most important geologic factors affecting the occurrence and producibility of coalbed methane is the ***Depositional Setting***, the second topic of this report; a paper on the regional depositional setting of Fruitland coalbed methane is followed by two papers describing local studies. The ***Fracture Patterns*** in Fruitland coal beds and adjacent strata are discussed in five papers that deal with such diverse subjects as regional cleat trends, tectonic- and compaction-related fractures, and lineament and curvature analysis. Studies of ***Hydrology, Thermal History, and Gas Composition*** are essential to understanding and predicting regional hydrodynamics and coalbed gas content and quality; these considerations are the subject of two papers. Finally, the last topic is ***Integration of Geologic and Hydrologic Studies***. In this section we summarize gas and water production from Fruitland coal beds, and on the basis of the relations among production, geologic setting, and hydrodynamics, we divide the San Juan Basin into regions in which Fruitland coal beds have similar reservoir characteristics.

Tectonic Setting

Regional Tectonic Setting of the San Juan Basin

S. E. Laubach and C. M. Tremain

Abstract

Tectonic history influenced Mesozoic and Cenozoic depositional patterns, coal occurrence, and gas generation in the San Juan Basin of New Mexico and Colorado. Tectonic events also affected or controlled the distribution and orientation of folds and fractures in coals and adjacent rocks. This section reviews basin origin and evolution in order to provide a framework for studies of depositional patterns and fracture occurrence in Cretaceous and Tertiary rocks in the San Juan Basin. An understanding of the overall tectonic setting of this basin, combined with the studies in the following chapters, provides a basis for predicting coalbed methane occurrence and producibility in this and other western coal basins.

Location and Structure of the Basin

The San Juan Basin occupies the east-central part of the Colorado Plateau in northwestern New Mexico and southwestern Colorado. It is a roughly circular, asymmetrical, structural basin of Late Cretaceous to early Tertiary age (fig. 1). The structures that bound the basin include the Hogback Monocline on the west and northwest, the San Juan–Archuleta Uplift on the north, the Nacimiento Uplift to the southeast, and the Chaco Slope and Zuni Uplift to the south and southwest. The depocenter and the synclinal axis of the basin on Upper Cretaceous strata occur near, and parallel, the northern and the northeastern margins of the basin.

Rocks in the basin range in age from Precambrian through Cenozoic. In the deepest part of the basin, Precambrian crystalline basement rocks are more than 14,000 ft (4,270 m) beneath the surface. Coal is present throughout the Cretaceous System, but the largest coal and coalbed methane resources are in the Fruitland Formation, which is the focus of this study. The area of Fruitland Formation outcrop occurrence encompasses approximately 6,700 mi^2 (17,350 km^2). Fruitland coal seams occur from outcrop to depths as great as 4,200 ft (1,280 m).

Evolution of the Basin

During the Cretaceous, the area of the present San Juan Basin was on the western margin of the Western Interior Seaway, a rapidly subsiding, elongate, asymmetric trough. At that time, the basin was occupied by a shallow sea (fig. 2) that extended from north to south across much of the Midcontinent (Kauffman, 1977; Merewether and Cobban, 1986; Weimer, 1986). The Western Interior Basin was bounded on the west by the Cordilleran orogenic belt, a fold and thrust belt that is exposed west of the San Juan Basin in Utah and Nevada (Armstrong, 1968; Burchfiel and Davis, 1975; Royse and others, 1975) and southwest of the Colorado Plateau in western Arizona and southeastern California (Burchfiel and Davis, 1975; Laubach and others, 1989). The western margin of the Western Interior Basin was the site of the greatest subsidence, which was controlled by tectonism in the orogenic belt. The eastern part of the basin was shallow and adjacent to a broad, stable platform (Hattin, 1965; Kauffman, 1977).

A major episode of subsidence in the Western Interior Basin during mid-Cretaceous (Aptian–Cenomanian) time is interpreted as recording the initiation of thrust-loading deformation in the adjacent overthrust belt (Heller and others, 1986). The correlation of transgressions and regressions of the Upper Cretaceous shoreline with episodic thrust faulting and uplift of the orogenic belt shows that basin subsidence was accelerated by thrust-loading deformation (Jordan, 1981). The structure of the Western Interior Basin is complicated by spatial and temporal variability of thrusting and subsidence and by intermittent uplift of broad, gentle arches in the foreland resulting from flexure.

The San Juan structural basin in the east-central Colorado Plateau formed as a result of the Laramide orogeny, which began in the Late Cretaceous, peaked in the Paleocene, and waned in the Eocene (approximately 80 to 40 mya). The Colorado Plateau was translated east-northeast to northeast relative to the North American craton (Hamilton, 1978). The San Juan Basin and other Rocky Mountain intermontane basins and Precambrian-cored uplifts formed in this compressional regime (Chapin and Cather, 1981; Dickinson and others, 1988). The San Jose Formation (Eocene) is the oldest rock unit for which isopachs clearly indicate a depocenter for the San Juan Basin (Stone and others, 1983, their figs. 18, 21, and 27; Fassett, 1985). Reactivation

In Ayers, W. B., Jr., and others, 1991, Geologic and hydrologic controls on the occurrence and producibility of coalbed methane, Fruitland Formation, San Juan Basin: The University of Texas at Austin, Bureau of Economic Geology, topical report prepared for the Gas Research Institute under contract no. 5087-214-1544 (GRI-91/0072), p. 3–5.

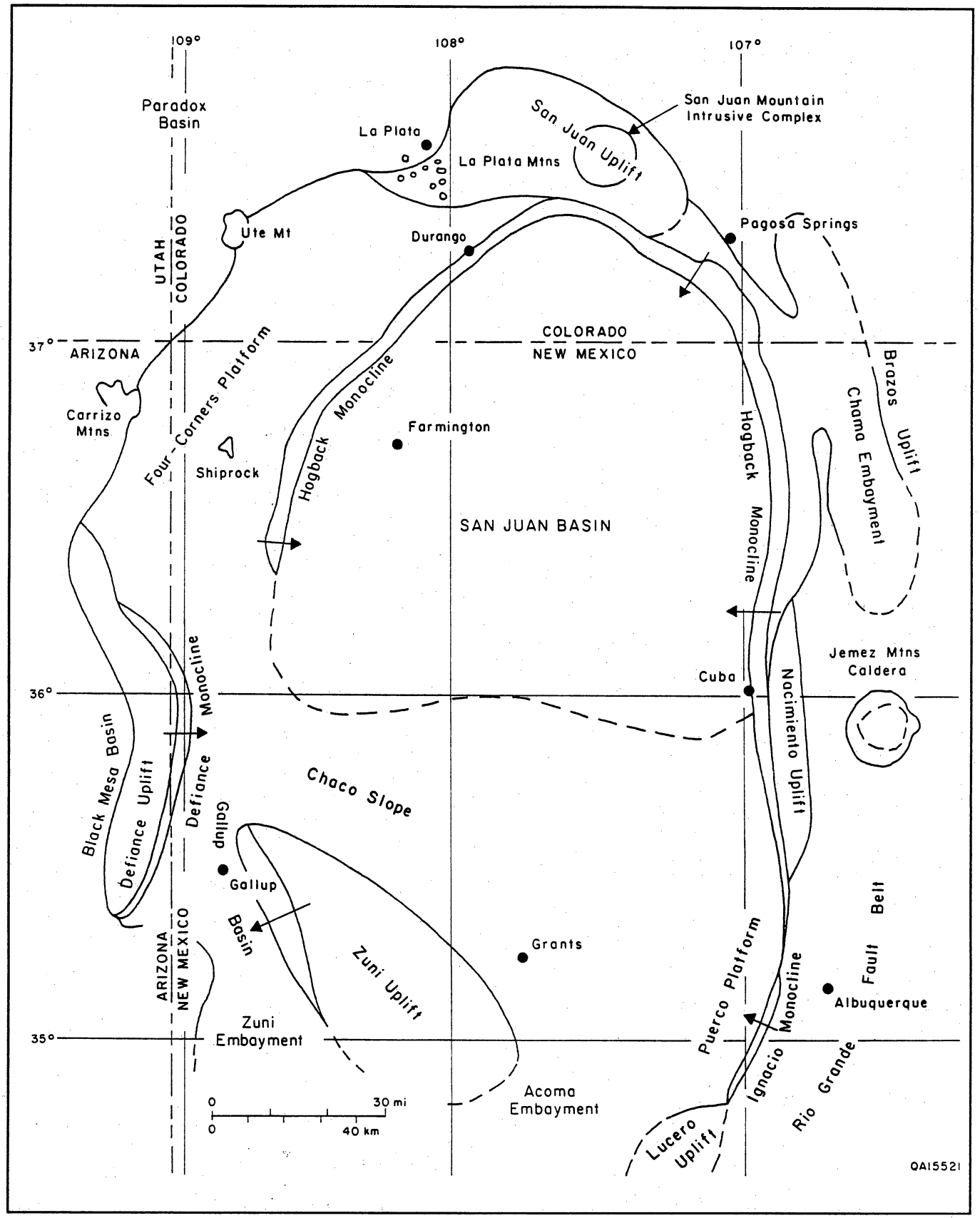

Figure 1. Regional tectonic setting of the San Juan Basin. Steeply dipping strata form the Hogback Monocline that rims the northern half of the basin. Modified from Fassett and Hinds (1971) after Kelley (1951, p. 125).

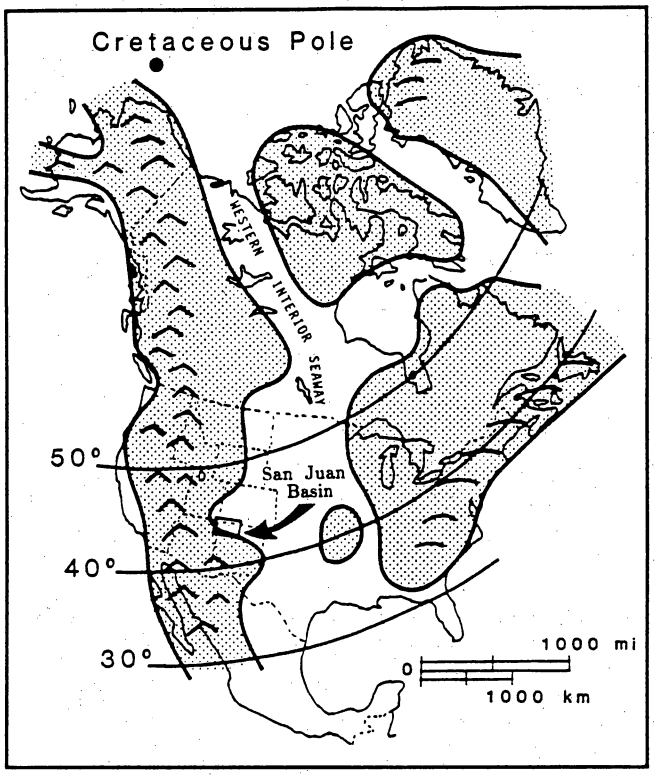

Figure 2. Location of the San Juan Basin relative to the Western Interior Seaway. Modified from Palmer and Scott (1984) after Williams and Stelck (1975) and Irving (1979).

of basement anisotropy (Cordell and Grauch, 1985; Huffman and Taylor, in press) and Paleozoic structures (Kluth and Coney, 1981; Ross and Ross, 1986) may have localized Mesozoic and Cenozoic deformation or controlled structural trends.

Northwest- and northeast-striking faults in the basin were intermittently active during the Mesozoic and early Cenozoic (Taylor and Huffman, 1988; Huffman and Taylor, in press). The eruption of voluminous Oligocene volcanic rocks to form the San Juan volcanic field and the emplacement of igneous intrusives beneath the volcanic pile along the northern side of the San Juan Basin marked this time of extensional stress (Steven, 1975; Lipman and others, 1978). This late Oligocene thermal event was a heat source for hydrocarbon generation in the San Juan Basin (Choate and Rightmire, 1982; Bond, 1984; Meissner, 1984; Clarkson and Reiter, 1988). In the northeastern San Juan Basin, the north-trending Dulce dike swarm gives radiometric ages of 28 to 22 mya. These dikes indicate east-west least principal horizontal stress when the Rio Grande Rift–Colorado Plateau boundary was being delineated (Aldrich and others, 1986). The Dulce dikes had only a local heating effect on the basin, as indicated by the lack of deflection of coal rank contours across the dike swarm (Meissner, 1984, his fig. 18; Kelso and others, 1988, their fig. 19; Kaiser and others, this vol.).

The Colorado Plateau is a coherent, uplifted crustal block surrounded by the extended terrain of the Basin and Range and Rio Grande Rift provinces (Thompson and Zoback 1979). It began to decouple from the Basin and Range province and the Rio Grande Rift about 32 mya (Aldrich and others, 1986, their fig. 3). The plateau has not had major crustal deformation since the Laramide orogeny, but it was affected by mild Cenozoic extension and volcanism.

Regional uplift of the Colorado Plateau began in the Miocene and has continued to the present (Epis and Chapin, 1975). Erosion of basin fill from the San Juan Basin has contributed to the post-Oligocene cooling of the basin (Meissner, 1984). Especially important from the standpoint of this report is the erosion of Oligocene volcanic and volcaniclastic rocks over the upturned outcrop of the Fruitland Formation along the northern flank of the basin, which allowed meteoric recharge of elevated sandstones and coal seams to cause artesian conditions and overpressuring in the Fruitland Formation in the northwestern part of the basin (Kaiser and Swartz, 1988; 1989; Kaiser and others, this vol.).

Minor Structures and Stress Regime

A structural map of the San Juan Basin shows only minor anticlinal and synclinal noses superimposed on large areas of homoclinal dip (Ayers and others, this vol.). These minor folds, which may cause fracture-enhanced permeability in coal seams (Tyler and others, this vol.), have structural relief of less than 200 ft (61 m).

Natural fractures (joints and cleats) are widespread in Cretaceous and Tertiary rocks in the San Juan Basin. Within the Fruitland Formation and adjacent rocks, opening mode (extensional) fractures are predominant (Laubach and others, this vol.; Tremain and others, this vol.). Face and butt cleats that intersect at approximately 90 degrees are well developed within the Fruitland coal seams.

The present stress regime of the Colorado Plateau is extensional, the minimum horizontal stress being oriented east-northeast. This stress direction is rotated approximately 70 degrees counterclockwise from the west-northwest direction of the surrounding Rio Grande Rift–Basin and Range extensional province (Zoback and Zoback, 1980; 1990; Wong and Humphrey, 1989).

Acknowledgments

We thank N. H. Whitehead III for his contributions to this overview.

Depositional Systems

Depositional and Structural Controls on Coalbed Methane Occurrence and Resources in the Fruitland Formation, San Juan Basin

W. B. Ayers, Jr., W. A. Ambrose, and Joseph Yeh

Abstract

The San Juan Basin is the leading producer of coalbed methane in United States; production from the Upper Cretaceous Fruitland Formation was more than 65 Bcf in 1989 and was predicted to exceed 130 Bcf in 1990. To evaluate depositional systems controls on the occurrence and producibility of Fruitland coalbed methane, we used data from 2,500 geophysical well logs to make structure, isopach, and coal-occurrence maps, and to calculate coal and coalbed methane resources. Fruitland coal accumulated southwest of the Pictured Cliffs wave-dominated shoreline, which prograded northeastward. The shoreline crossed an inferred northwest-striking structural hingeline; sporadic faulting down-dropped the basin floor north of the hingeline, which created accommodation space and caused shoreline stillstands and transgressions, recorded in upper Pictured Cliffs tongues. These stillstands allowed extensive peat deposits to form and to overspread abandoned shoreline- and fluvial-sandstone complexes. The thickest Fruitland coal occurs in northwest-trending belts parallel to, and landward of, associated Pictured Cliffs tongues. Net coal thickness in these belts locally exceeds 100 ft (30 m), and individual coal seams can be more than 30 ft (9 m) thick. Northeast-trending coal deposits are common in the southwestern part of the basin, where they occur between dip-elongate fluvial-sandstone complexes. Coal resources of the Fruitland Formation are calculated to be 245 billion short tons; this coal contains an estimated 43 to 49 Tcf of coalbed methane.

Introduction

Depositional systems and structural features (fractures and faults in coal beds) are the primary geologic controls on coalbed methane resources and recoverability. The depositional system controls the occurrence, geometry, and thickness of coal seams by building platforms for peat (coal) accumulation and by bounding the seams. Additionally, the framework sandstones of the depositional system commonly are conduits for fluid flow. Although coal seams are the primary aquifers in the Fruitland Formation, Fruitland coal beds and associated sandstones perform as a single regional aquifer in the San Juan Basin (Kaiser, Swartz, and Hawkins, this vol.). However, fluid migration within coal seams and, hence, producibility of coalbed methane, is locally enhanced or impeded by faults and fractures. Therefore, this section integrates sedimentology, coal occurrence, and structure of the Fruitland Formation and the Pictured Cliffs Sandstone to clarify geologic controls on coalbed methane occurrence and producibility.

In Ayers, W. B., Jr., and others, 1991, Geologic and hydrologic controls on the occurrence and producibility of coalbed methane, Fruitland Formation, San Juan Basin: The University of Texas at Austin, Bureau of Economic Geology, topical report prepared for the Gas Research Institute under contract no. 5087-214-1544 (GRI-91/0072), p. 9–46.

Regional Geologic Setting and Stratigraphy

During the Late Cretaceous (Campanian), the region of the present San Juan Basin was on the west margin of the Western Interior Seaway (Laubach and Tremain, this vol., their fig. 2). The coastline migrated to the northeast, depositing a vertical succession of shelf through coal-bearing continental sediments. The Pictured Cliffs Sandstone is a coastal facies that was deposited as the Late Cretaceous shoreline prograded northeastward into the Western Interior Seaway. In geophysical well logs (fig. 1) and at outcrop, the Pictured Cliffs Sandstone is divisible into genetically related upper and lower units. The lower unit is composed of a series of upward-coarsening subunits and is interpreted as shelf and shoreface mudstone and sandstone interbeds (fig. 1). The upper unit has a blocky well-log response and is composed of amalgamated sandstone bodies having a composite thickness of 40 to 120 ft (12 to 36 m); it is inferred to be the framework facies of prograding barrier-strandplain or wave-dominated delta depositional systems (fig. 1).

Conventionally, the base of the Pictured Cliffs Sandstone is placed at the base of the upward-coarsening units (fig. 1). However, that boundary is time-transgressive because the Pictured Cliffs Sandstone intertongues with the Lewis Shale (figs. 2 and 3). The

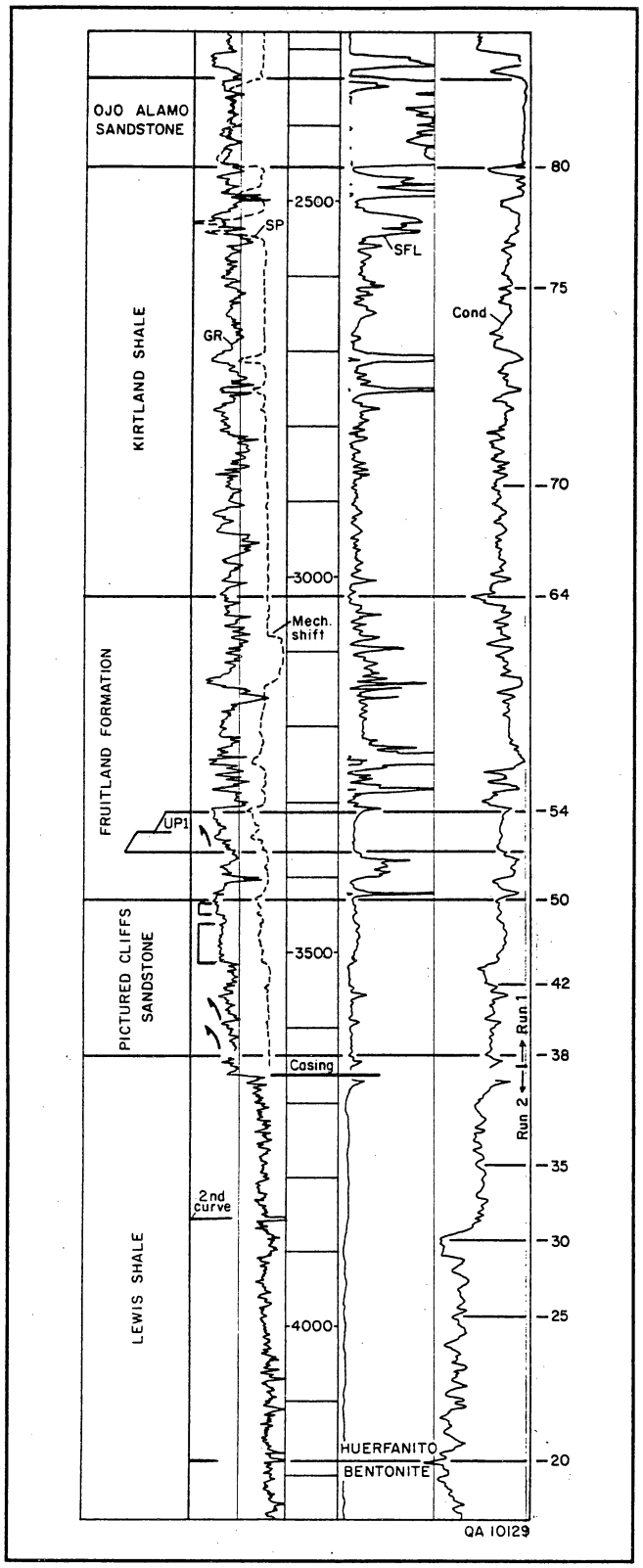

Figure 1. Type log showing Upper Cretaceous stratigraphy in the San Juan Basin. See figure 5 for well location and figure 19 for identification of Fruitland coal seams. Two-digit numbers on the right margin of the conductivity curve refer to marker beds used in this study (from Ayers and Ambrose, 1990).

marine Lewis Shale (figs. 1 through 3) contains several bentonite beds that are excellent marker beds for correlation. However, only the Huerfanito Bentonite Bed has been correlated throughout the San Juan Basin (Fassett and Hinds, 1971). Contemporaneity of the coastal (blocky) and shoreface and shelf (upward-coarsening) units is documented by marker beds, representing time lines, that cross the proximal shelf and shoreface to intersect and terminate in the Pictured Cliffs coastal sandstones (fig. 2). The Pictured Cliffs Sandstone and equivalent marine units thicken basinward above the Huerfanito Bentonite Bed partly because of differential subsidence in the northern part of the basin. Progradation of the Pictured Cliffs shoreline resulted in basinward offset of the landward pinch-outs of these marker beds.

In subsurface studies, the contact between the Pictured Cliffs Sandstone and the Fruitland Formation (fig. 1) is "placed at the top of the massive sandstone below the lowermost coal of the Fruitland except in those areas where the Fruitland and Pictured Cliffs intertongue" (Fassett and Hinds, 1971, p. 8). Pictured Cliffs sandstones are the depositional platforms upon which Fruitland peat (coal) accumulated, and ultimately, Pictured Cliffs shoreline sandstones bound coal seams in the basinward direction. Progradation of the Pictured Cliffs shoreline, dependent on complex interactions of sediment supply, basin subsidence, and eustasy, was intermittent, resulting in shoreline stillstands. Intertonguing of the Pictured Cliffs and the Fruitland Formation resulted from temporary landward shifts of the shoreline during overall regression of the Late Cretaceous shoreline. In this study, the Pictured Cliffs sandstones that intertongue with the Fruitland Formation are called "upper Pictured Cliffs sandstones," or "upper Pictured Cliffs tongues." There are three upper Pictured Cliffs tongues in the basin; individually, they are called "UP1," "UP2," or "UP3" in this volume (fig. 2). Together, they account for approximately 270 ft (82 m) of stratigraphic rise of the Pictured Cliffs over a 25-mi (40-km) distance in the northern third of the San Juan Basin (fig. 2). The upper Pictured Cliffs tongues are upward-coarsening sequences on geophysical logs (fig. 1), and each is composed of wave-dominated deltaic or northwest-trending, amalgamated barrier-strandplain sandstones up to 100 ft (30 m) thick.

The Fruitland Formation (fig. 1), the primary coal-bearing formation in the San Juan Basin and the focus of this study, is the continental facies deposited landward of the Pictured Cliffs Sandstone shoreline and is composed of sandstone, mudstone, and coal interbeds. In past regional subsurface studies, the contact between the Fruitland Formation (Campanian) and the overlying Kirtland Shale (Campanian and Maestrichtian) was placed at the top of the highest coal bed or carbonaceous shale bed; for the most part, the Kirtland lacks

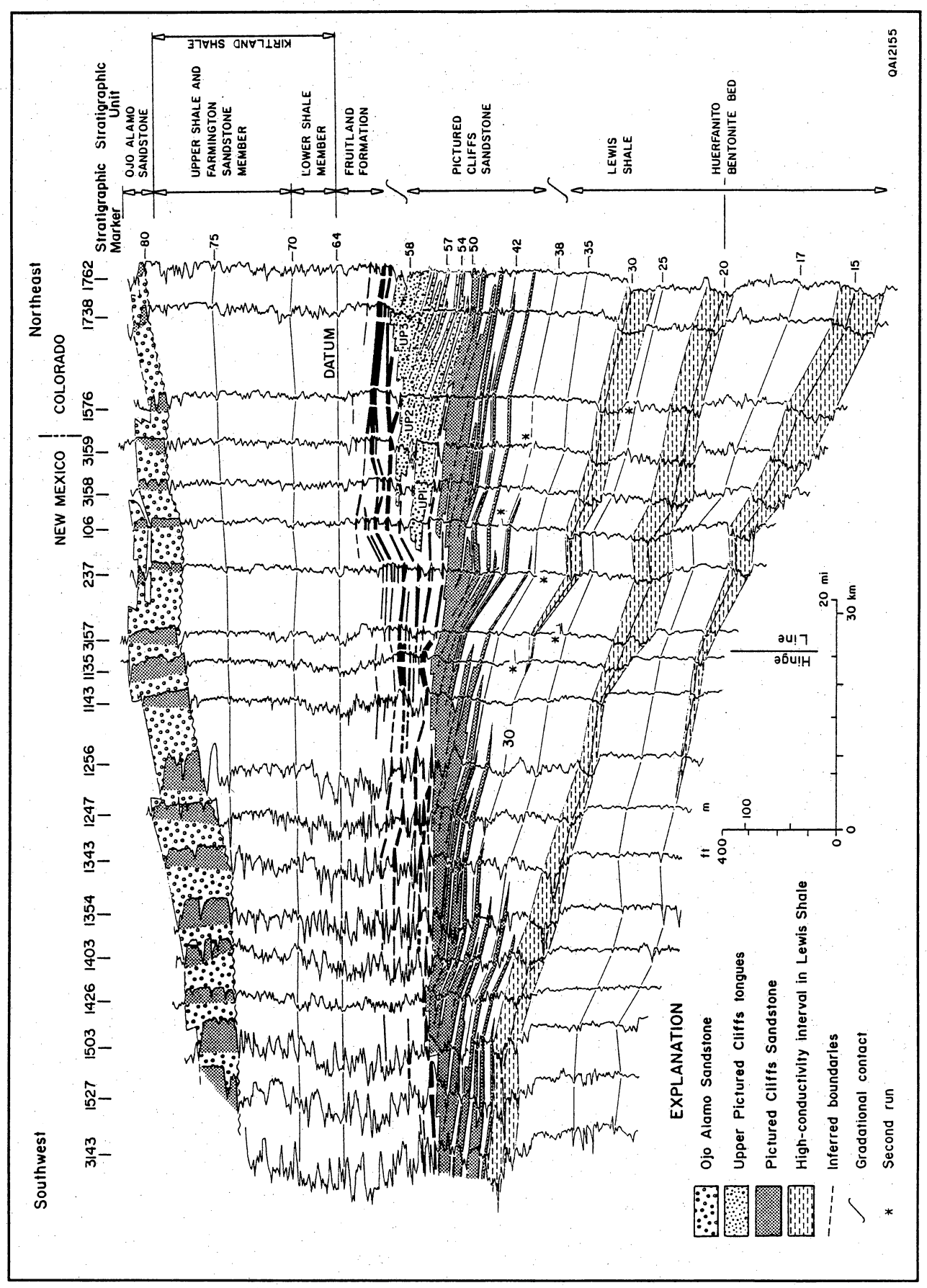

Figure 2. Stratigraphic dip section D20, located in figure 9. Traces of conductivity curves are shown for wells in this section; datum is the base of the Kirtland Shale, defined as a high-conductivity zone at the top of an upward-fining sequence in the upper Fruitland Formation. Log 106 ties with cross section S10 (fig. 3) (from Ayers and Ambrose, 1990).

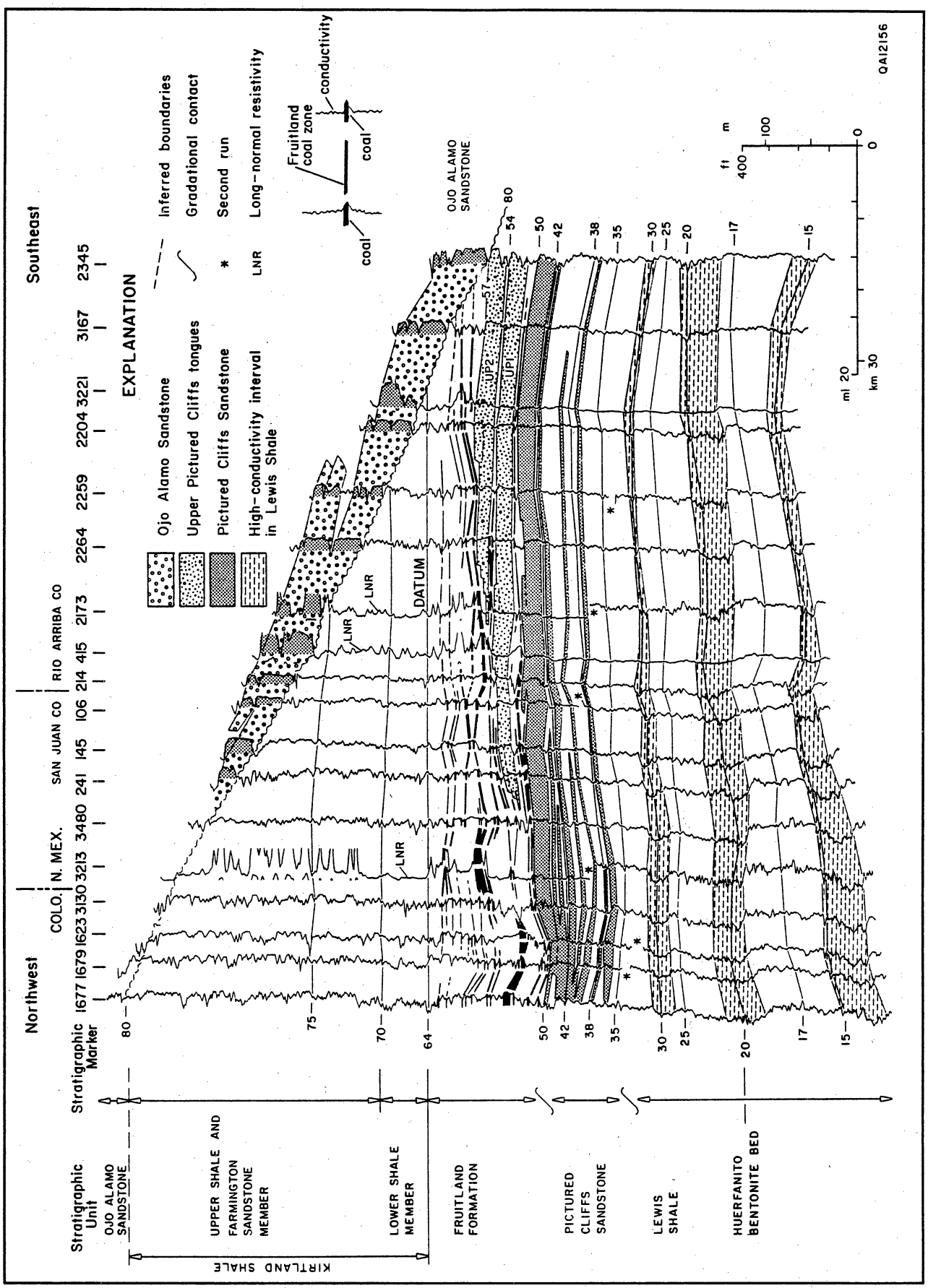

Figure 3. Stratigraphic strike section S10, located in figure 9. Log traces not labeled as log-normal resistivity are traces of conductivity logs. Datum is the high-conductivity, low-resistivity marker also used in cross section D20 (fig. 2). Log 106 ties with cross section D20 (fig. 2) (from Ayers and Ambrose, 1990).

coal and carbonaceous shale (Fassett and Hinds, 1971). However, because coal and carbonaceous shale occur locally in the Kirtland, that boundary is erratic. Therefore, in this study the Fruitland–Kirtland contact was placed at a high-conductivity peak that occurs at the top of an upward-fining sequence (figs. 1 through 4). This high-conductivity peak corresponds to the base of a regionally extensive shale (lower Kirtland shale) that may have formed as a consequence of a short-lived marine transgression over the Fruitland coastal plain. Foraminifera have been reported in this interval (Dilworth, 1960). This marker is at approximately the same stratigraphic position as the boundary chosen by earlier workers (Fassett and Hinds, 1971; Molenaar and Baird, 1989), and it has more genetic significance and less variability than the previously selected boundary.

The Kirtland Shale, which overlies the Fruitland Formation, is composed of the lower shale member, the Farmington sandstone, and the upper shale member (fig. 1). The basal contact of the Paleocene Ojo Alamo Sandstone (fig. 1) is unconformable with the Kirtland Shale and Fruitland Formation (figs. 2 and 3); a hiatus of approximately 11 million years (m.y.) is reported at the southern margin of the basin (Fassett, 1985), but this hiatus diminishes in magnitude northwestward. Near the eastern margin of the basin, the fluvial Ojo Alamo Sandstone truncates the Kirtland Shale and Fruitland Formation, and in the southeastern part of the basin, the Kirtland Shale and Fruitland Formation are truncated by a pre–Ojo Alamo unconformity that merges westward with the Ojo Alamo unconformity (fig. 4). This pre–Ojo Alamo unconformity is at the base of an upward-fining unit inferred to be a fluvial sandstone, and it beveled a planar, tilted surface, as is apparent from the relation between this unconformity and the Huerfanito Bentonite Bed (fig. 4). Although some earlier workers recognized that this sandstone differed in character from adjacent sandstones, they generally assumed that it was a facies variation of either the Fruitland Formation (Fassett and Hinds, 1971, p. 17) or the Ojo Alamo Sandstone (Sikkink, 1987, p. 89-90). However, a pre–Ojo Alamo unconformity at the southeastern margin of the basin was suggested from an earlier outcrop study, on the basis of thickness variations in the Fruitland Formation and Kirtland Shale and lithologic differences in pre–Ojo Alamo and Ojo Alamo sandstones (Baltz, 1967, p. 34).

Previous Studies

Fassett and Hinds (1971) described the regional geology and energy resources of the Fruitland Formation in the San Juan Basin. They used measured sections and data from approximately 325 well logs to calculate 200 billion short tons of Fruitland coal in the basin, but they did not report coalbed methane resources. Choate and others (1984) summarized previous work in which TRW, Inc., working under contracts with the U.S. Department of Energy, estimated 31 Tcf of methane in Fruitland coal seams. This estimate was made by multiplying Fassett and Hinds' (1971) coal-tonnage estimate by gas-content values for Fruitland coal seams. The gas-content estimates were based on limited data. Kelso and others (1988) reevaluated coal and coalbed methane resources in the Fruitland Formation. For their estimate, they used coal-thickness data from 549 geophysical well logs to calculate coal volume and desorbed-gas values from 28 coal samples to calculate gas content; Kelso and others (1988) estimated 219 billion short tons of coal and 50 Tcf of coalbed methane in Fruitland coal seams thicker than 2 ft (0.6 m). Although the previous regional studies defined regional coalbed methane resources of the Fruitland Formation, they did not address geologic and hydrologic controls on the occurrence and producibility of the methane.

In a study of the Navajo Lake area, Ayers and Zellers (1988, and this vol.) used closely spaced well control (approximately 400 well logs in a 215-mi² [557-km²] area) to show that geologic conditions that affect the occurrence and producibility of coalbed methane are more complex than inferred from regional studies conducted with sparse data. Using a datum above rather than below the coal-bearing Fruitland Formation, as had been done by previous researchers, they showed that basin subsidence indirectly controlled the occurrence of thick coal seams by causing reversals in the direction of shoreline migration and deposition of interfingering upper Pictured Cliffs sandstones. They also concluded that, although lower Fruitland coal seams pinch out behind Pictured Cliffs shoreline sandstones, upper Fruitland seams may override abandoned-shoreline sandstones, thereby forming extensive coalbed methane reservoirs.

Objectives

Goals of this study were to (1) evaluate the structural evolution of the San Juan Basin as it applies to the distribution and maturation of Fruitland coal, (2) define depositional systems, (3) delineate the regional occurrence and continuity of coal seams and evaluate geologic controls on coal occurrence, geometry, and trends, and (4) identify structural features that may enhance coal permeability or affect coalbed continuity. Results from this study of the geologic framework will be integrated with other results from studies of structure, gas composition, and hydrology to interpret controls on coalbed methane occurrence and producibility (Kaiser, Ayers, and others, this vol.).

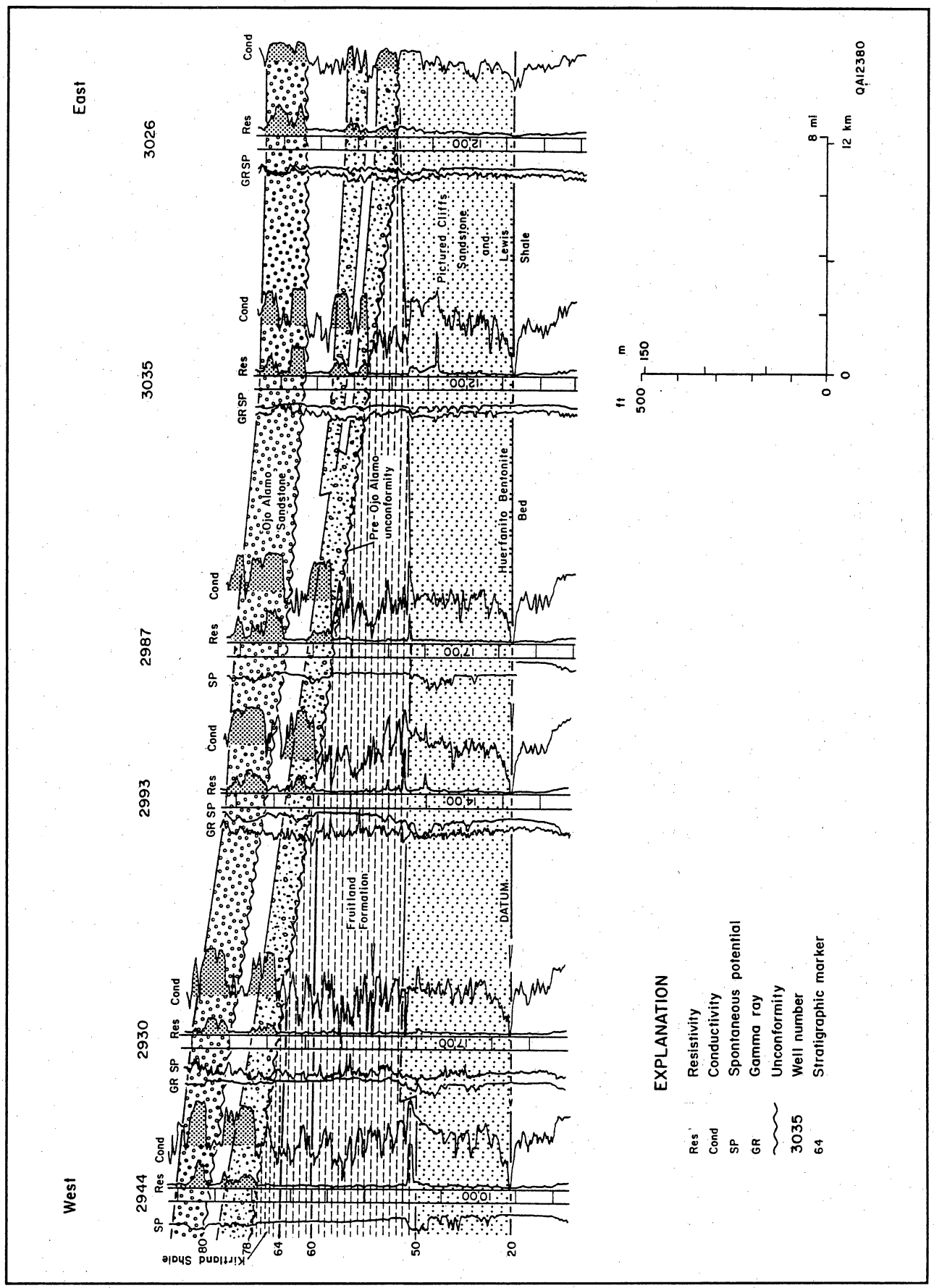

Figure 4. Stratigraphic strike section in the southeastern part of the San Juan Basin, illustrating truncation of the Kirtland Shale, Fruitland Formation, and Pictured Cliffs Sandstone by a pre–Ojo Alamo unconformity. Cross section is shown in figures 14, 15, and 17 (from Ayers and Ambrose, 1990).

Methods

In the San Juan Basin, which covers approximately 6,700 mi² (17,350 km²) encompassed by the Fruitland Formation outcrop, more than 17,000 oil and gas wells have been drilled and logged, providing an excellent data base for a subsurface study of Fruitland coalbed methane. In this study we used approximately 2,500 geophysical logs from these wells. Well logs were used to make interlocking cross sections, and stratigraphic units, defined by 18 marker beds in the Upper Cretaceous and lower Tertiary section, were correlated in these cross sections. All remaining logs were correlated to these sections. Structure, isopach, lithofacies, and coal data from the logs were tabulated in computer files; these data were used to make computer-contoured maps, or they were posted by the computer for hand contouring. The cross sections and maps were then evaluated individually and compared to interpret evolution of the San Juan Basin and geologic controls on the occurrence and producibility of coalbed methane. Geologic interpretation from subsurface data were verified in studies of outcrops and cores.

Structural Evolution of the San Juan Basin

Structure affected the availability and producibility of Fruitland coalbed methane in four ways. First, increased subsidence north of an inferred hingeline affected a shoreline stillstand and allowed thick peat to accumulate. Second, the timing of structural development of the San Juan Basin affected the burial depth and, hence, thermal maturity of Fruitland coal seams. Third, structural deformation caused fractures that may enhance coalbed permeability or offset the coal beds and impede flow. Finally, structural folding uplifted and exposed Fruitland strata at the basin margin, thereby greatly affecting the water movement by exposing truncated beds (especially coal beds) for recharge or expulsion of fluids and by providing potential energy for fluid movement.

Structure of Huerfanito Bentonite Bed

The structure map of the Huerfanito Bentonite Bed (fig. 5a) was made using data from approximately 2,500 well logs (fig. 5b). Structural relief on the Huerfanito Bentonite Bed in the basin exceeds 4,500 ft (1,370 m). The steeply dipping Hogback Monocline is apparent around the northern, northwestern, and eastern margins of the basin. In the southern half of the basin, dip is 1 degree (92 ft/mi [17m/km]) to the northeast. The structural axis of the basin is complex and is strongly displaced to the northeastern side. The basin floor is the conspicuously flat area below 2,600 ft (790 m) (fig. 5a) that trends northwestward and measures about 20 × 30 mi² (50 × 75 km²). Dip on the floor is approximately 0.1 degree (10 ft/mi [2 m/km]). An inferred structural hingeline coincides with the 2,600-ft (790-m) contour at the southwestern margin of the basin floor.

This structural hingeline is interpreted to be a zone of complex, northwest-trending, en echelon normal faults, with net downdrop to the north; width of the zone is 6 to 10 mi (10 to 16 km). Its presence is inferred from coincidence of geologic anomalies that are apparent in many regional maps and cross sections. Among these are (1) change in structural attitude from northeast-dipping beds on the southwest to flat-lying but folded and faulted beds on the northeast (fig. 5a); (2) faults identified in well logs in this area (Ambrose and Ayers, this vol., their fig. 3); (3) marked thickening of the interval from the Huerfanito Bentonite to the top of the uppermost Pictured Cliffs sandstone (fig. 2); (4) southwestward pinch-out of marine marker beds in the Lewis Shale (fig. 2); (5) highly organized gravity values that trend northwestward, parallel to the hingeline, and are closely spaced (Scott and others, this vol., their fig. 4); (6) closely spaced contours in maps of vitrinite reflectance (Scott and others this vol., their fig. 3), potentiometric surface, and pressure gradient (Kaiser, Swartz and Hawkins, this vol., their fig. 1); (7) marked changes in coalbed-gas composition (Scott and others, this vol., their figs. 9 and 10); (8) increased net coal thickness on the northeast; and (9) permeability contrasts in the Fruitland Formation (Kaiser, Swartz, and Hawkins, this vol.) and the Pictured Cliffs Sandstone. Additionally, northwest-trending normal faults, having as much as 70 ft (21 m) of displacement (Roberts and Uptegrove, 1991), are present where the hingeline projects to outcrop along the western margin of the basin, and from studies of reflection seismic data, the U.S. Geological Survey reports northwest-trending faults affecting basement rock in this area (Curtis Huffman, personal communication, 1990). The significance of this hingeline to Pictured Cliffs shoreline trends and Fruitland coal and coalbed methane occurrences will be developed further in subsequent discussions.

Coal seams may have fracture-enhanced permeability in major folds like the Hogback Monocline and Ignacio Anticline (fig. 5a). From the northern margin of the basin, a complex structural promontory consisting of several folds extends southward approximately 25 mi (40 km). The most prominent of these folds is the Ignacio Anticline in Colorado that plunges southeastward. In New Mexico, the distal nose of the Ignacio Anticline turns eastward. Maximum structural relief on the anticline is approximately 250 ft (75 km).

Minor folds with structural relief less than 100 ft (30 m) may also form structural traps and contribute

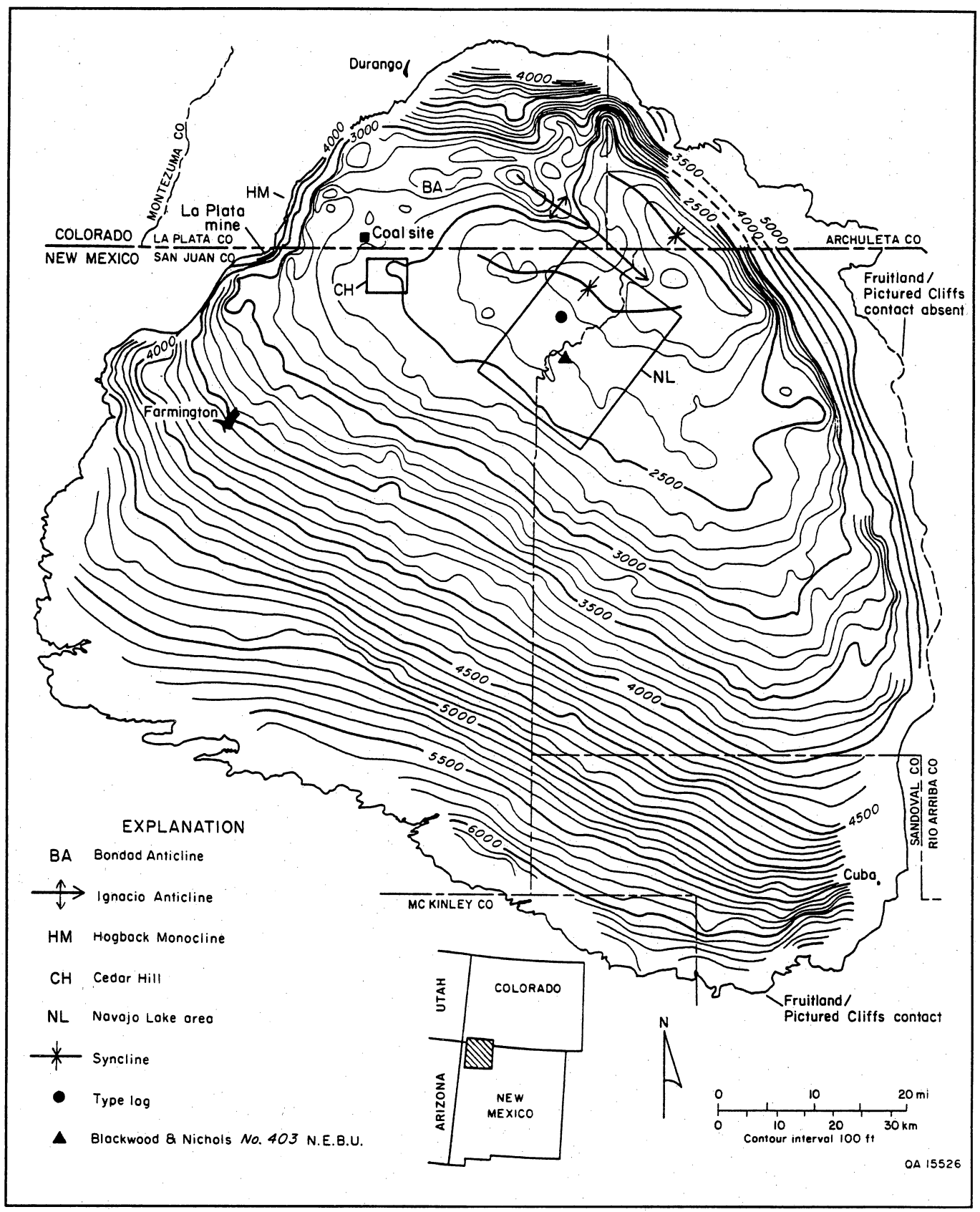

Figure 5a. Structure map of the San Juan Basin, contoured on the Huerfanito Bentonite Bed, location of type log (fig. 1) and Blackwood and Nichols NEBU No. 403 (Ayers and Zellers, this vol., their fig. 5). The basin displays gentle dips on the southern margin and steep dips on the northern margin along the Hogback Monocline (modified from Ayers and Ambrose, 1990).

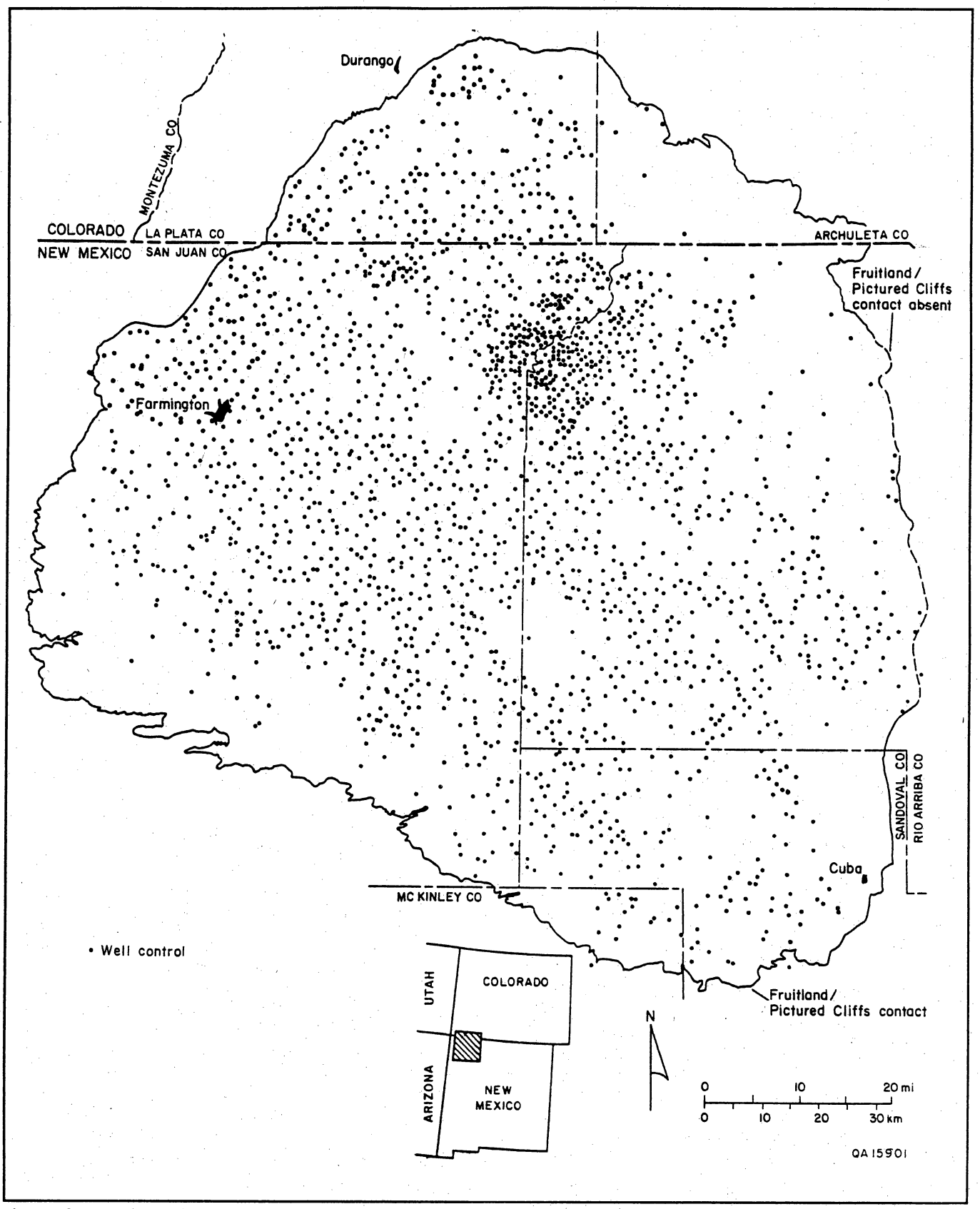

Figure 5b. Locations of wells used in this study. Not shown are locations of approximately 100 additional boreholes (from Roybal and others, 1985) that were used to evaluate coal beds near the southern margin of the basin.

fracture-enhanced permeability to coal seams. These minor folds occur throughout the basin and are especially apparent where the regional dip changes, such as near the Hogback Monocline and at the periphery of the basin floor. Northwest-plunging folds occur in the Navajo Lake area (Ayers and Zellers, this vol.), and a tightly folded, east-plunging syncline bisects Cedar Hill field (fig. 5a; Ambrose and Ayers, this vol., their figs. 4 and 5). These minor folds were not apparent in an earlier regional structural map of the Huerfanito Bentonite Bed that was made using a data density of one to two well logs per township and a contour interval of 400 ft (122 m) (Fassett and Hinds, 1971, their fig. 15).

Elevation of Pictured Cliffs Sandstone

The elevation of the top of the Pictured Cliffs Sandstone (fig. 6) was mapped because it is subjacent to the thick lower Fruitland coal beds in the southern two-thirds of the basin, whereas the Huerfanito Bentonite Bed is as much as 700 ft (215 m) below the Fruitland Formation in that area. This is not a true structure map because the Pictured Cliffs Sandstone is time-transgressive (fig. 2). Relief on top of the Pictured Cliff Sandstone is approximately 3,500 ft (1,065 m), which is considerably less than structural relief on the Huerfanito Bentonite Bed (more than 4,500 ft [1,370 m]); this difference is due to northward thickening of the Huerfanito to Pictured Cliffs interval (see "Huerfanito Bentonite Bed to Top of Pictured Cliffs Sandstone" section). The map shows, with minor differences, the structural features delineated on the Huerfanito Bentonite map (fig. 5a), confirming that formation of the structural basin mostly postdates deposition of the Pictured Cliffs Sandstone.

Elevation of the Base of the Ojo Alamo Sandstone

Having demonstrated that most basin structure postdates Pictured Cliffs deposition, we mapped the elevation of the base of the Ojo Alamo Sandstone (fig. 7) to constrain the timing of deformation. This map also is not a structure map because the basal Ojo Alamo contact is unconformable and significant basin tilting predated Ojo Alamo deposition. However, post–Ojo Alamo deformation is indicated by a structural axis that trends north-northwestward in the east-central part of the basin. As a result of the southeast-dipping unconformity at the base of the Ojo Alamo Sandstone (fig. 3), relief on the base of the Ojo Alamo Sandstone is 1,500 ft (457 m) in the northwest-southeast direction—compared with only 1,000 ft (305 m) of relief on Huerfanito Bentonite Bed and 500 ft (150 m) on the Pictured Cliffs Sandstone (fig. 6) across the same region.

Depositional Framework of the Pictured Cliffs Sandstone and the Fruitland Formation

The thickness, continuity, and extent of Fruitland coal seams were controlled by their depositional setting, which in turn was controlled by syndepositional tectonic activity. To interpret the tectonic and depositional controls on coal seam occurrence, we made cross sections and isopach, lithofacies, and coal-occurrence maps. Formation-thickness, or isopach, maps are useful in defining the regional paleoslope, basin evolution, and local syndepositional structural features. The intervals mapped in this study are shown in figures 2 and 3. They are identified either by stratigraphic name or by bounding marker beds that were numbered consecutively, beginning with the lowest (oldest) marker bed. These two-digit numbers were used to facilitate computer manipulation of data in this study and are not suggested as official names or as replacements for existing stratigraphic nomenclature. In this study isopach maps were made of the (1) top of the Huerfanito Bentonite Bed to the top of the Pictured Cliffs Sandstone (marker 20 to 50), (2) Huerfanito Bentonite Bed to the top of the upper Pictured Cliffs tongues (marker 20 to 58), (3) Pictured Cliffs Sandstone to the top of the Fruitland Formation (marker 50 to 64), (4) Huerfanito Bentonite Bed to the base of the Ojo Alamo Sandstone (marker 20 to 80), and (5) top of the Fruitland Formation to the base of the Ojo Alamo Sandstone (Kirtland Shale; marker 64 to 80). Other maps in this report are isopach, isopleth, and lithofacies maps of the upper Pictured Cliffs tongues (marker 50 to 58).

Huerfanito Bentonite Bed to Top of Pictured Cliffs Sandstone (Marker 20 to 50)

This interval, which does not include the Pictured Cliffs tongues, thickens from less than 100 ft (30 m) on the south to more than 950 ft (290 m) on the north (fig. 8), consistent with a paleoslope to the north or northeast; basinward thickening of the interval (900 ft over 90 mi [275 m over 145 km]) averages 10 ft/mi (2 m/km) but is less in the northern third of the basin, north of the 750-ft isopach. The area north of the 750-ft isopach nearly coincides with the basin floor described in the Huerfanito structure map (fig. 5a). Throughout the basin, isopach trends are oblique to updip (southwest) pinch-out lines of marker beds in Lewis Shale, demonstrating that isopach trends—although useful in evaluating paleoslopes—do not necessarily parallel depositional strike.

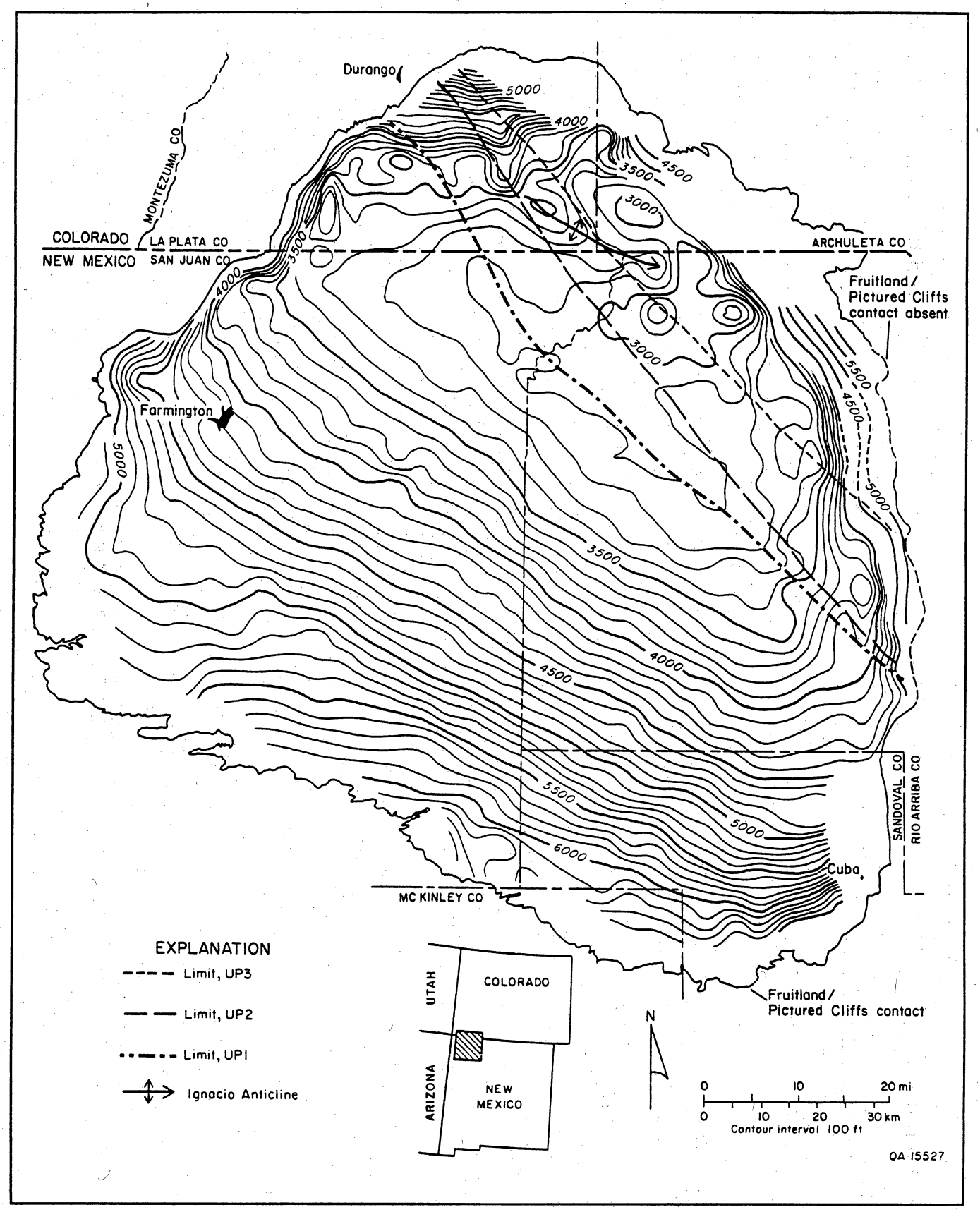

Figure 6. Elevation of the top of the Pictured Cliffs Sandstone, showing structural features similar to those in the structure map contoured on the Huerfanito Bentonite Bed (see fig. 5) (from Ayers and Ambrose, 1990).

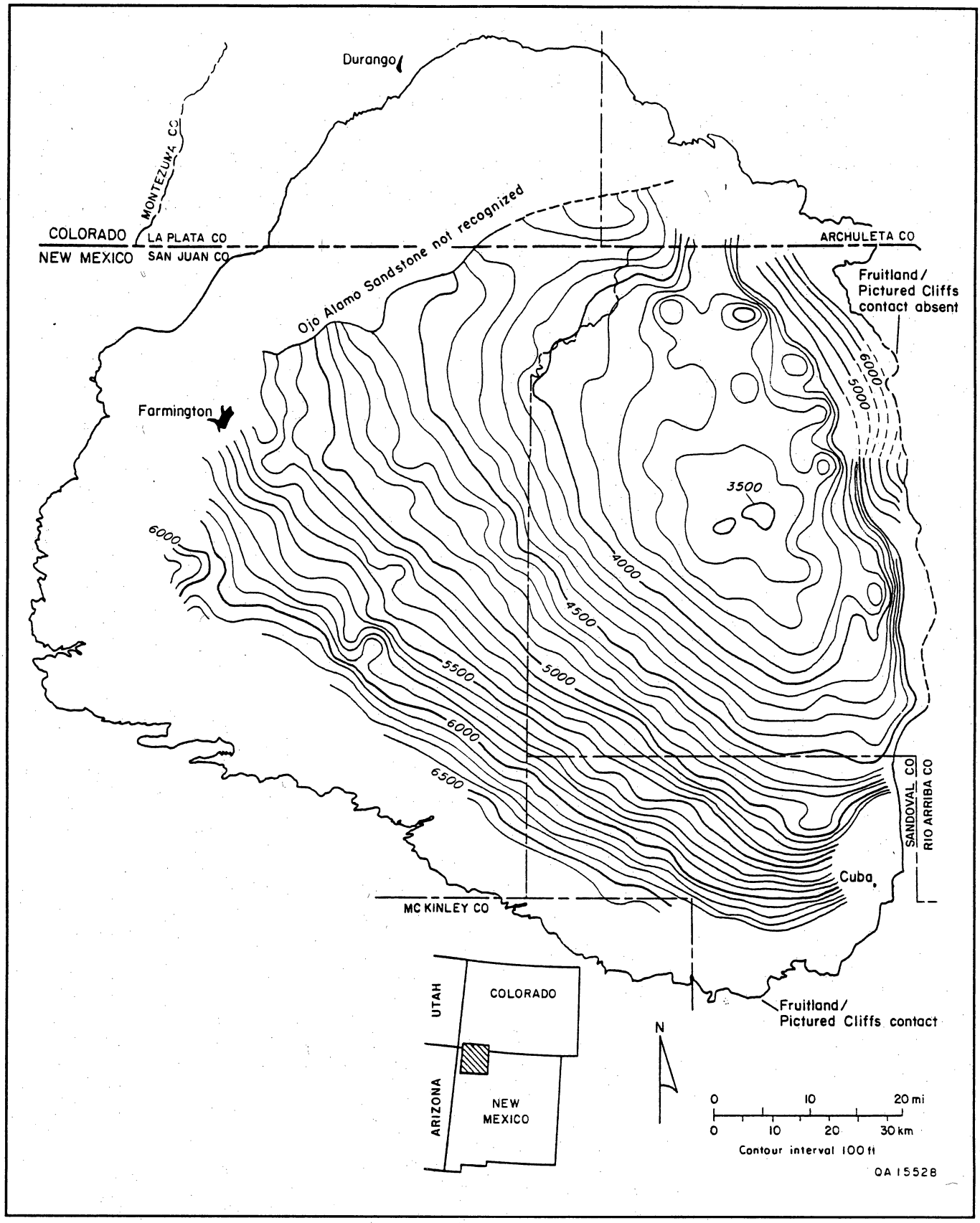

Figure 7. Elevation of the base of the Ojo Alamo Sandstone, which is an erosional surface (from Ayers and Ambrose, 1990).

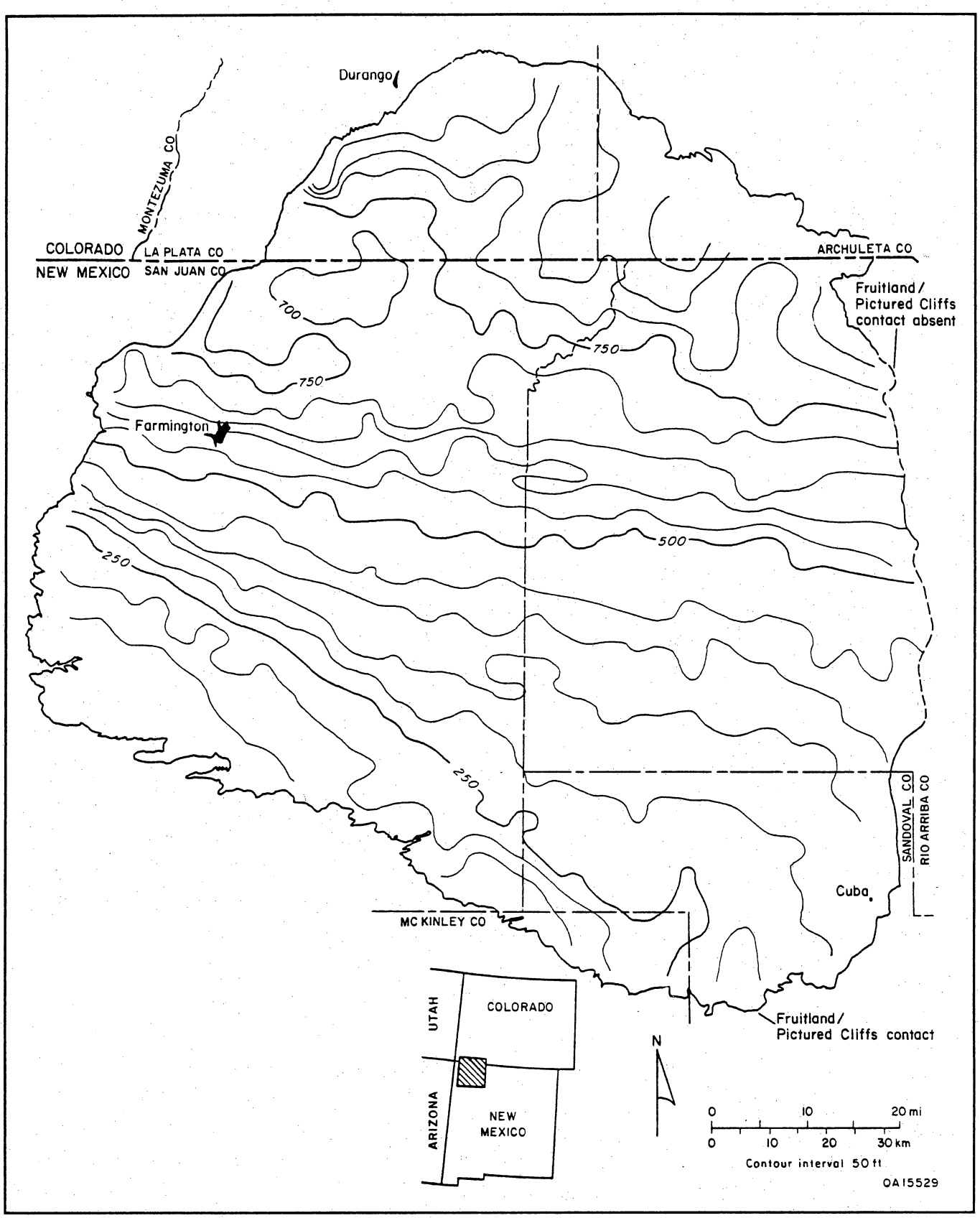

Figure 8. Isopach map of the Huerfanito Bentonite Bed to the top of the Pictured Cliffs Sandstone. The interval thickens basinward from less than 100 ft (30 m) to more than 900 ft (275 m) near the northern rim of the basin. Greatest thickening, or stratigraphic rise, occurs near the western rim of the basin (from Ayers and Ambrose, 1990).

The 500- to 750-ft isopachs cut across the structural axis (fig. 5a) on the eastern side of the basin, indicating that basin axis was not subsiding during deposition. Furthermore, there is no evidence of thinning over the Ignacio Anticline or Bondad Anticline (fig. 5a). However, the northern 750-ft isopach is subparallel to many of the fold axes in the basin floor.

Huerfanito Bentonite Bed to Top of Upper Pictured Cliffs Tongues (Marker 20 to 58)

This map (fig. 9) is equivalent to the Huerfanito to Pictured Cliffs Sandstone isopach of Fassett and Hinds (1971, their fig. 7); the interval includes lower Fruitland tongues and is bounded by the top of the uppermost Pictured Cliffs tongue. Southwest of the updip pinch-out line of UP1, the map is identical to the isopach map of the Huerfanito Bentonite Bed to the top of the Pictured Cliffs Sandstone (fig. 8).

This interval thickens from less than 100 ft (30 m) on the southwest to more than 1,200 ft (365 m) on the northeast. The rate of thickening northeast of the 800-ft isopach is approximately 15 ft/mi (3 m/km). The 800-ft contour nearly coincides with the UP1 pinch-out line (fig. 9). In the northern part of the basin, isopach trends are discordant (rotated about 30° clockwise) with the underlying Huerfanito–Pictured Cliffs Sandstone (marker 20 to 50) isopach trends (fig. 8), suggesting initiation of differential subsidence across the hingeline at the southwest floor of the basin and realignment of the upper Pictured Cliffs shoreline parallel to that hinge. Contours are closely spaced north of the 800-ft contour (for example, the 900- to 1,000-ft contour) where UP2 and UP3 pinch out, particularly in the northwestern part of the basin. The interval thins at minor anticlines in northwestern Rio Arriba County and at Bondad Anticline, suggesting that these structures were active during deposition of upper Pictured Cliffs tongues. Thinning across the Ignacio Anticline indicates minor syndepositional structural activity, as suggested by Sandberg (1988).

Upper Pictured Cliffs Tongues (Marker 50 to 58)

In the northeastern half of the San Juan Basin, thick lower Fruitland coal seams occur landward (southwest) of shoreline deposits of the upper Pictured Cliffs tongues. To evaluate controls on Fruitland coal occurrence, we mapped the number and net thickness of major sandstones (figs. 10 and 11, respectively), the maximum sandstone thickness (fig. 12), and the thickness of the undivided upper Pictured Cliffs tongues (fig. 13) (see fig. 2, marker 50 to 58). Maps of the major sandstones (here defined as those more than 20 ft [6 m] thick) and maximum sandstone (thickest individual sandstone) delineate the depositional framework facies that bound thick Fruitland coal beds in the northeastern part of the basin.

Lithofacies

The upper Pictured Cliffs sandstone interval is composed of 1 to 3 tongues (UP1, UP2, and UP3) (fig. 10). The updip (southwest) limits of these tongues are defined by contours in the major-sandstone isopleth map (fig. 10, contours 1, 2, and 3), and they coincide with the 20-ft, 60-ft, and 140-ft contours, respectively, on the net-major-sandstone map (fig. 11). Sand-body geometries of upper Pictured Cliffs tongues (figs. 11 and 12) are consistent with deposition in a wave-dominated shoreline setting. Both dip-elongate and strike-elongate (northeast- and northwest-trending, respectively) sandstone bodies occur northwest of the Rio Arriba county line, where a wave-dominated delta system (Cedar Hill delta system) is inferred to have prograded the Pictured Cliffs shoreline (figs. 11 and 12). Dip-elongate sandstone bodies (distributaries) in the upper Pictured Cliffs tongues northwest of Rio Arriba County project landward (southwestward) to tie with fluvial/distributary channel-fill sandstones in the Fruitland Formation in the Cedar Hill area (Ambrose and Ayers, this vol.; Ayers, unpublished map, 1991). In Rio Arriba County, dominance of strike-elongate sand-body trends in the upper Pictured Cliffs tongues suggests a strandplain-barrier system whose sediments primarily were derived from the Cedar Hill deltaic complex by longshore drift. Convergence of the UP2 and UP1 pinch-out lines (fig. 10) and lower values of net major sandstone thickness (fig. 11) in this area suggest lower rates of sediment input. Subordinate dip-elongate sand-body trends in Rio Arriba County suggest sediment input from minor Fruitland fluvial systems.

Isopach

The isopach map (fig. 13) of the combined upper Pictured Cliffs tongues (marker 50 to 58) and the interbedded Fruitland tongues shows strike-elongate (northwest-trending) contours that parallel the structural grain of the basin. The northwest-trending pinch-out line of UP1 parallels the southern margin of the structural floor (hingeline) and nearly coincides with structural axes of the basin as mapped on the Pictured Cliffs Sandstone (fig. 6), suggesting that transgression was initiated by subsidence of the basin floor and that landward pinch-out of UP1 was against this hingeline.

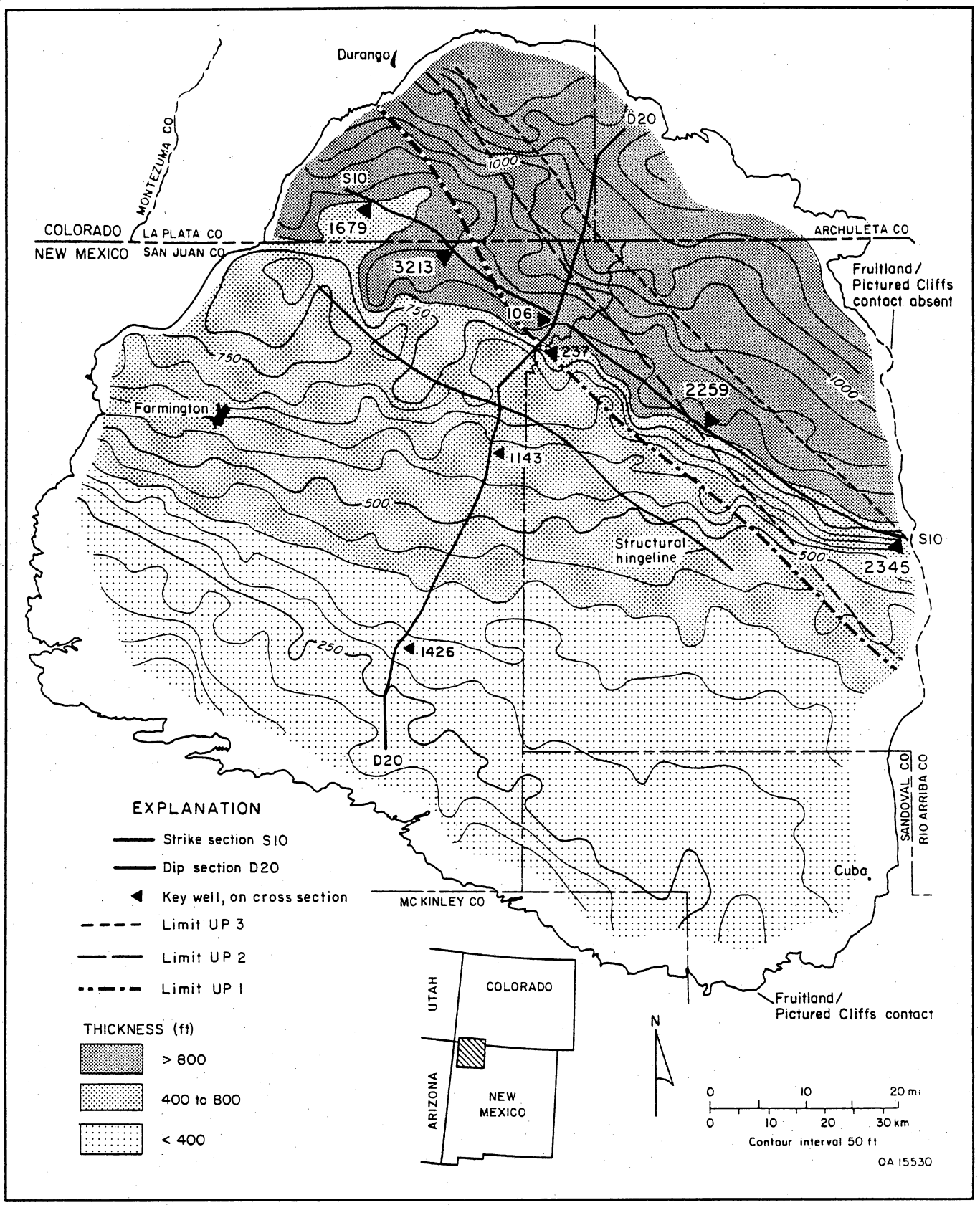

Figure 9. Isopach map of the Huerfanito Bentonite Bed to the uppermost upper Pictured Cliffs sandstone. Closely spaced contours show abrupt thickening across the updip (southwest) limit of UP1, UP2, and UP3. Cross sections D20 and S10 are shown on figures 2 and 3, respectively (from Ayers and Ambrose, 1990).

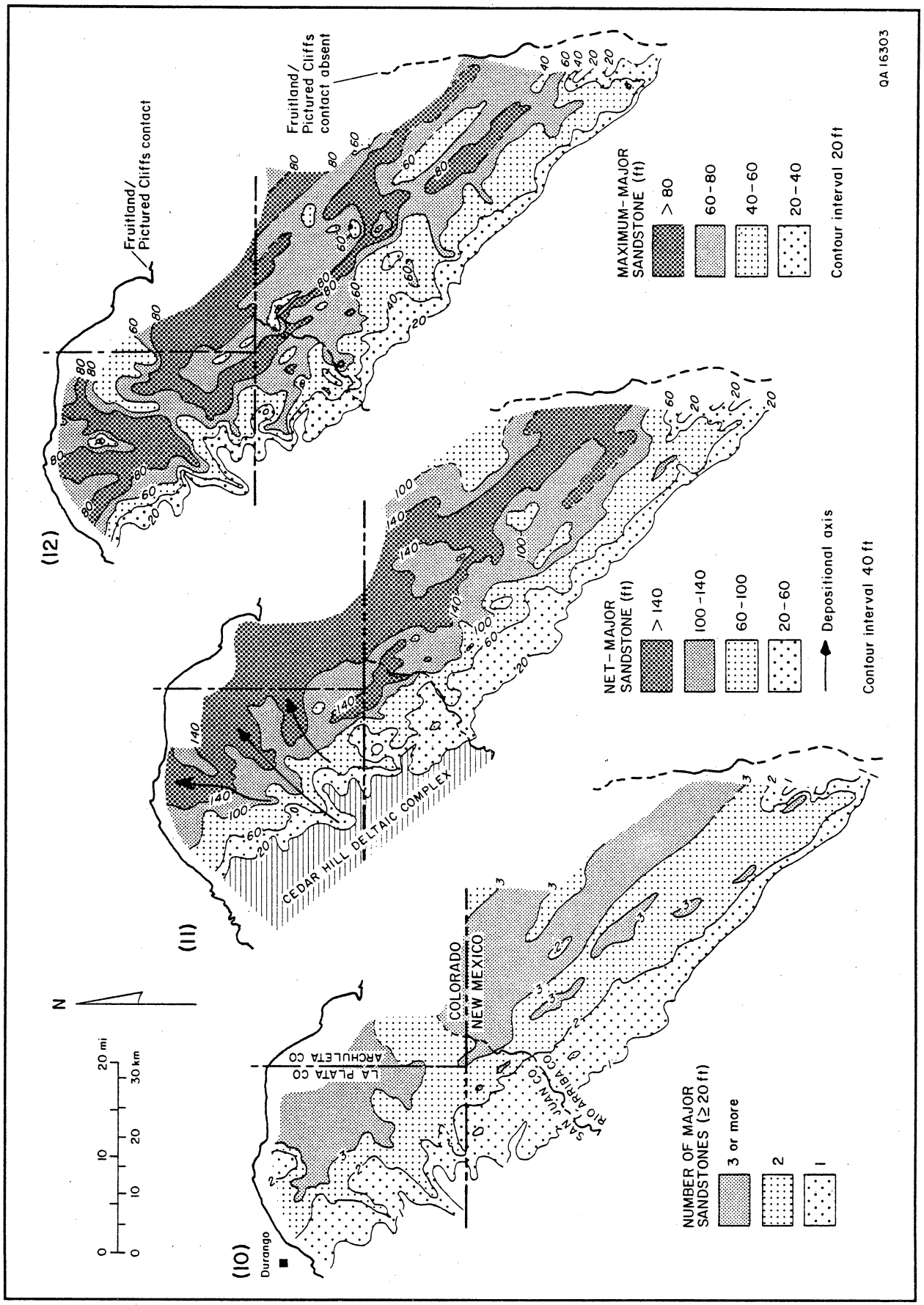

Figure 10. Map of number of major sandstones in the upper Pictured Cliffs tongues.

Figure 11. Map of net thickness of major sandstones in the upper Pictured Cliffs tongues.

Figure 12. Map of maximum sandstone thickness in the upper Pictured Cliffs tongues.

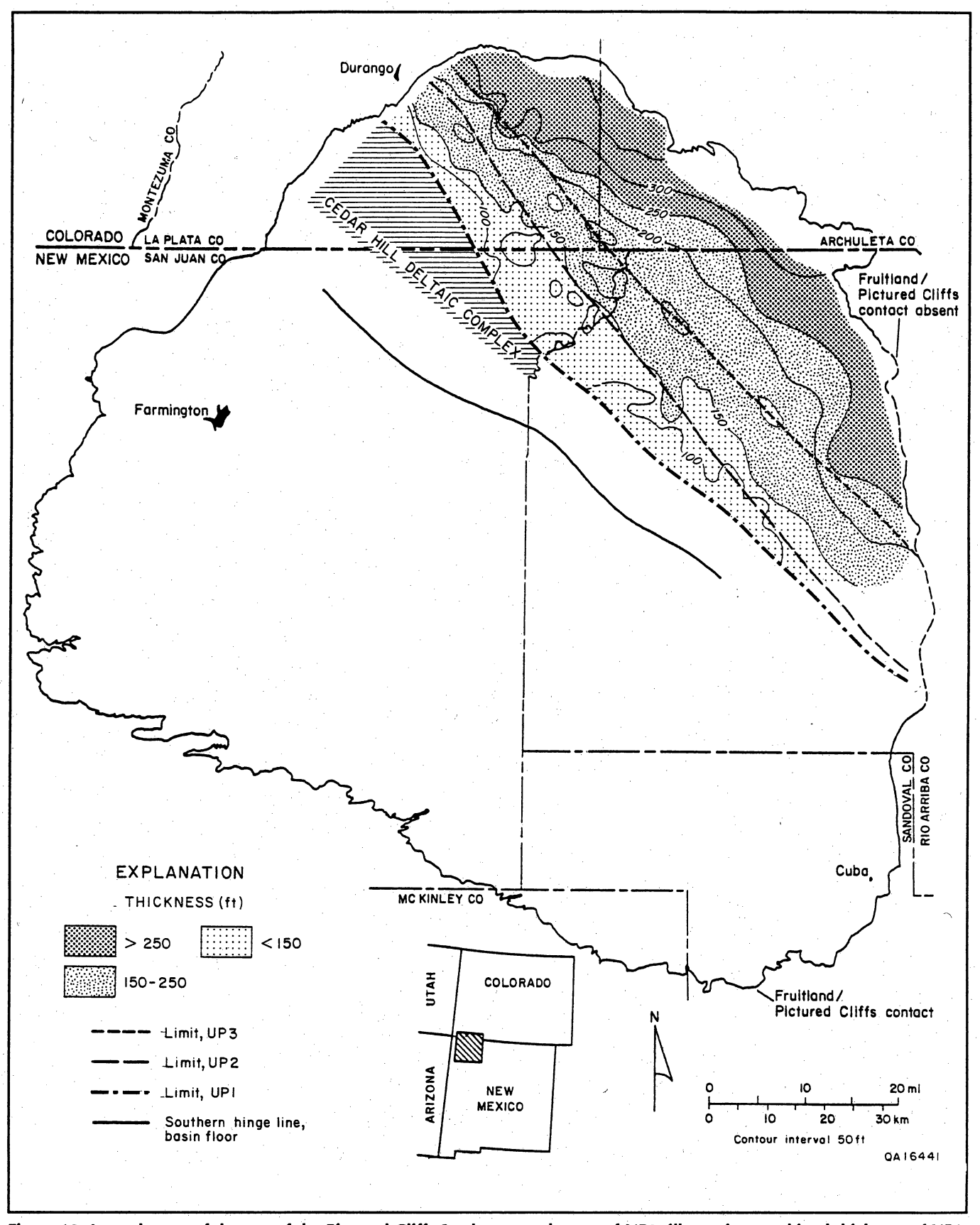

Figure 13. Isopach map of the top of the Pictured Cliffs Sandstone to the top of UP3, illustrating combined thickness of UP1, UP2, and UP3 (from Ayers and Ambrose, 1990).

The depocenter is near the northern margin of the basin, where interval thickness locally exceeds 350 ft (105 m) (fig. 13). Thickness of the composite interval (60 to 350 ft [18 to 105 m]) is less than the sum of the maximum thicknesses of component sandstones (UP1 through UP3) because of a basinward offset (fig. 2, shingled or imbricated relation) of sucessive depocenters. Rates of thickening are greatest north of the pinch-out lines of individual Pictured Cliffs tongues. For example, the greatest rate of thickening (30 to 60 ft/mi [6 to 12 m/km]) is north of the UP3 pinch-out line.

Fruitland Formation Isopach (Marker 50 to 64)

The interval from the top of the Pictured Cliffs Sandstone to the top of the Fruitland Formation (marker 50 to 64) includes the Pictured Cliffs tongues and the coal-bearing Fruitland Formation (fig. 2). Two isopach maps of this interval were made—one that includes the Pictured Cliffs tongues (fig. 14) and one without the tongues (fig. 15). Marked eastward thinning and truncation of the Fruitland Formation resulted from erosional beveling by the pre–Ojo Alamo unconformity.

The isopach map of the combined Fruitland and Pictured Cliffs tongues (fig. 14) shows that this interval thickens to more than 650 ft (200 m) in the northern half of the basin from a rather uniform thickness of 300 to 350 ft (90 to 110 m) in the southern half. By contrast, the isopach map of only the coal-bearing Fruitland (fig. 15) indicates a basinward-thinning trend in the northeastern and north-central parts of the basin. Both of these maps show local thickening in the northwestern San Juan Basin near the Colorado–New Mexico state line. This area may be the Fruitland depocenter that was described for the Fruitland Formation by earlier workers (Silver, 1951; 1957). If so, then southeastward thinning of the Huerfanito–Ojo Alamo interval (fig. 16) may not be due entirely to postdepositional erosion of the Kirtland Shale, as concluded by Fassett and Hinds (1971), and uplift of the southeast rim of the basin may have started during Pictured Cliffs–Fruitland deposition.

Eastward and southeastward thinning of the Kirtland Shale in the southern and southeastern parts of the basin also was attributed to deposition rather than exclusively to the effects of erosion (Dane, 1936, p. 120–121). During deposition of the Fruitland Formation and Kirtland Shale, local uplift occurred at the southeastern margin of the basin (Baltz, 1967, p. 34). Therefore, lower subsidence rates and reduced basin accommodation (thus, more oxidizing conditions) may have existed along the eastern margin even before Kirtland time and may partly explain the absence of thick coal seams in the eastern part of the basin.

Huerfanito Bentonite Bed to Base of Ojo Alamo Sandstone (Marker 20 to 80)

Northeast-trending contours on the isopach map of this interval (fig. 16) are the result of truncation of Upper Cretaceous strata by the southeastward-dipping unconformity at the base of the Ojo Alamo Sandstone. This interval is not mapped in the northwestern part of the basin where the Ojo Alamo Sandstone is unrecognized, owing either to facies change or to erosional truncation of the Ojo Alamo. Fassett (1985) suggested that the pre–Ojo Alamo strata were eroded by a northwestward-flowing fluvial system that predated the southward-flowing Ojo Alamo fluvial system that was deposited above the unconformity. The second-order, northwest-trending bands of isopach thinning were present in an earlier map and were inferred to be paleovalleys (Fassett and Hinds, 1971; Fassett, 1985). However, we have identified and mapped an unconformable surface 50 to 200 ft (15 to 61 m) below and discordant with the Ojo Alamo unconformity in the southeastern part of the basin (fig. 4).

Because of erosional truncation, Upper Cretaceous strata thin southeastward from more than 2,200 ft (670 m) thick in the northwest to less than 500 ft (150 m) thick in the southeastern part of the basin (figs. 3 and 16). Closer spacing of contours in the northwestern part of the basin indicates that the surface of the unconformity is steeper there, suggesting that there was relatively little tilting in the southeastern part, which was uplifted as a platform and was bounded to the northwest by a poorly defined, northeast-trending hingeline. Rate of thinning in the platform area is 35 ft/mi (6.6 m/km) northwest and 15 ft/mi (3 m/km) southeast of the 1,000-ft contour.

Kirtland Shale Isopach (Marker 64 to 80)

The Kirtland Shale thins southeastward because it has been beveled by erosion (figs. 3 and 17). In the southeastern part of the basin, the pre–Ojo Alamo unconformity (fig. 4) truncates the Kirtland Shale east of the zero contour (fig. 17) in Rio Arriba and Sandoval Counties.

Tertiary Fill of the San Juan Basin (Depth to Base of Ojo Alamo Sandstone)

The map of Tertiary fill of the San Juan Basin, or depth to base of the Ojo Alamo Sandstone (fig. 18), indicates post-Cretaceous basin fill. This map reflects

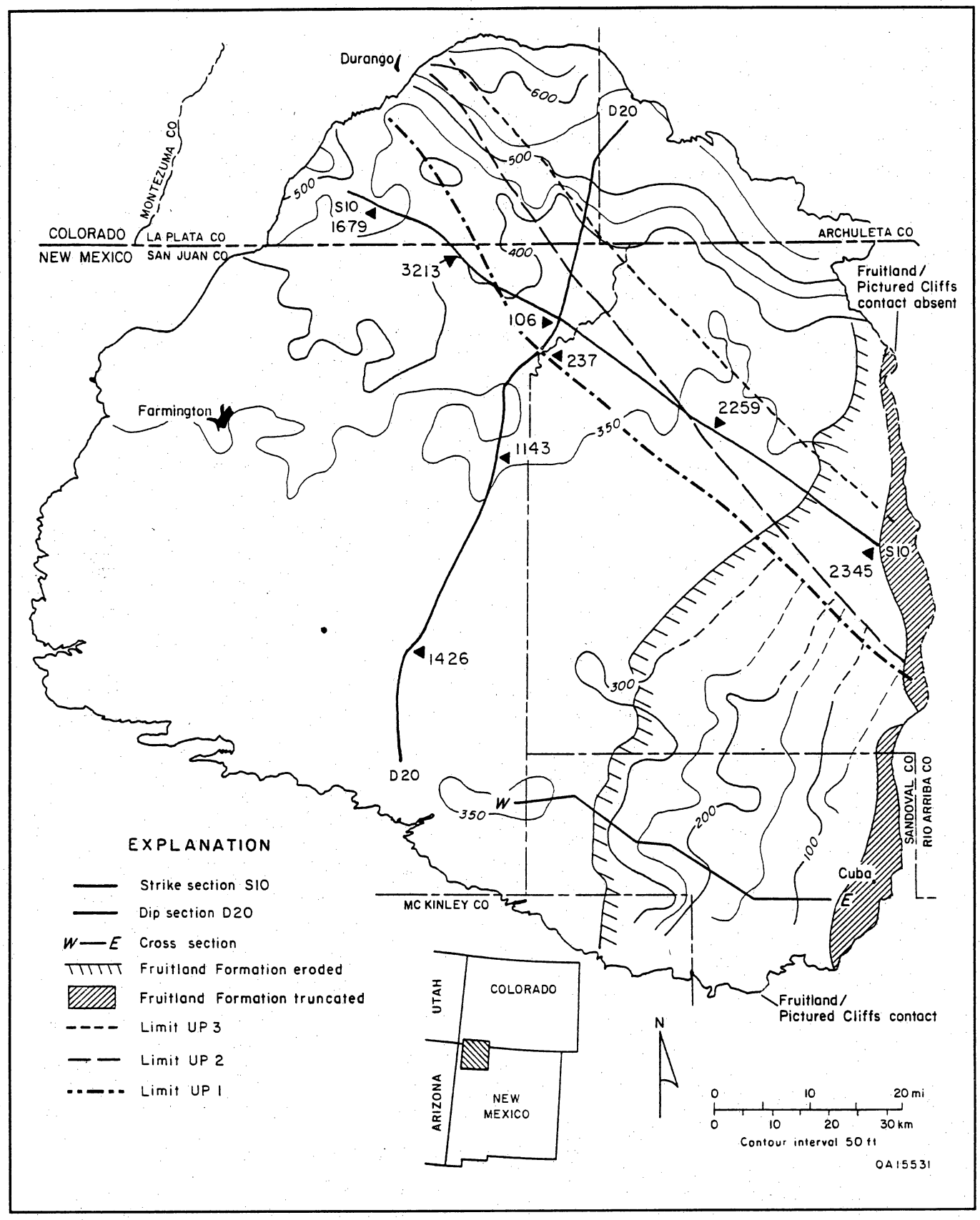

Figure 14. Isopach map of the Fruitland Formation, including upper Pictured Cliffs tongues UP1, UP2, and UP3. Cross sections D20 and S10 are shown in figures 2 and 3, respectively (from Ayers and Ambrose, 1990).

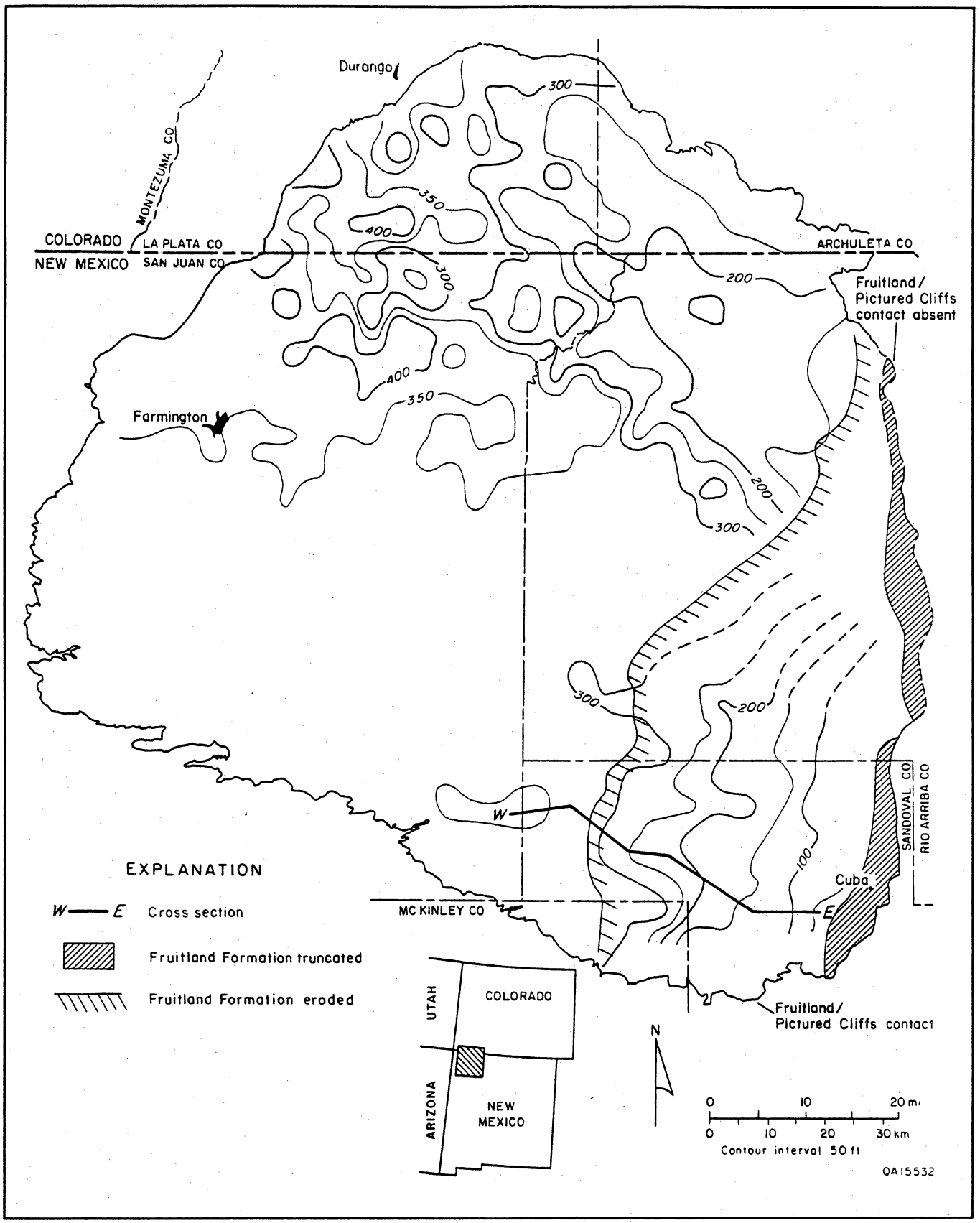

Figure 15. Isopach map of the Fruitland Formation without upper Pictured Cliffs tongues (from Ayers and Ambrose, 1990).

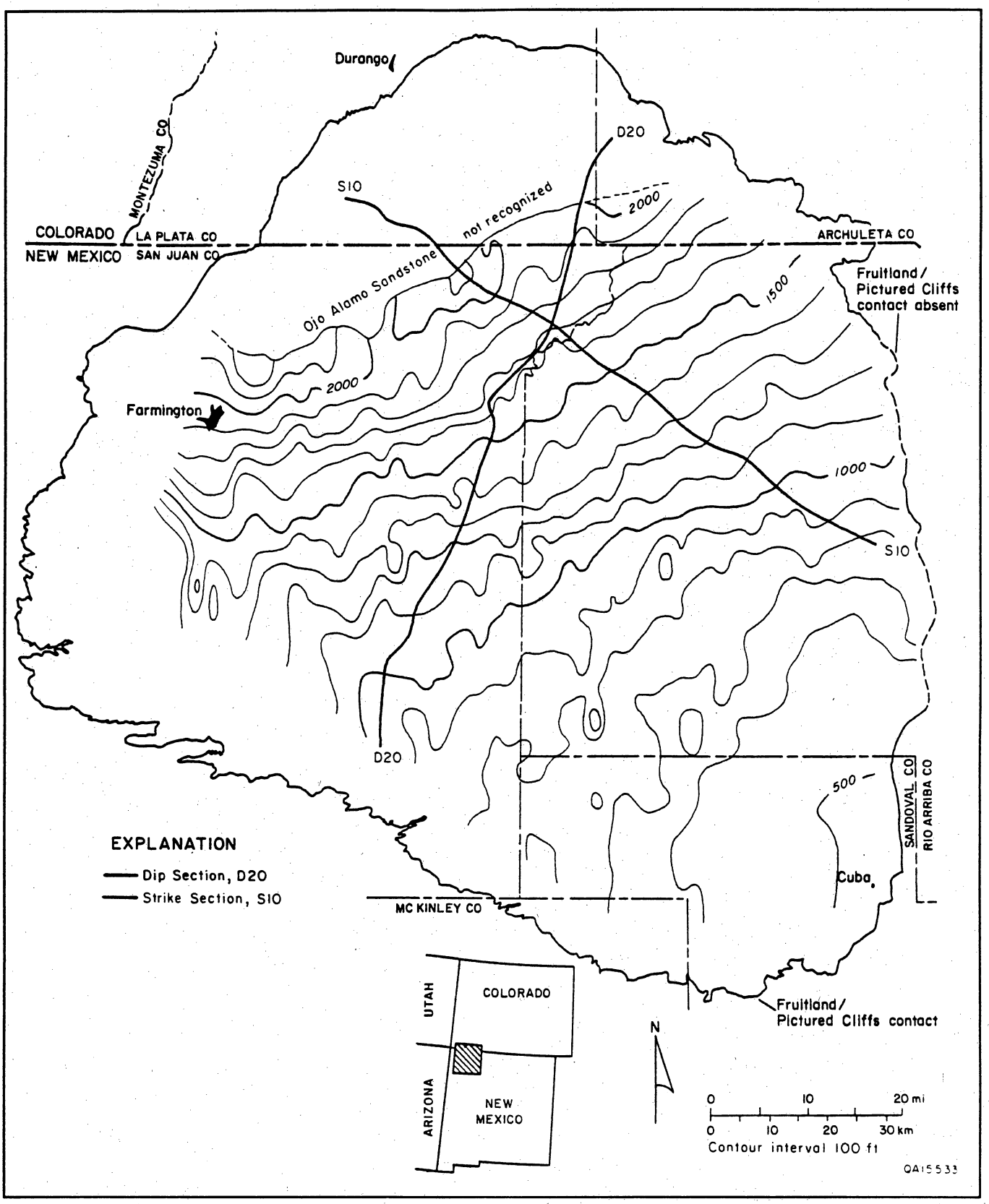

Figure 16. Isopach map of the Huerfanito Bentonite Bed to the base of the Ojo Alamo Sandstone. East-northeast orientation of contours results from combination of eastward-dipping erosional surface of the Ojo Alamo unconformity and basinward thickening of the Pictured Cliffs Sandstone. Cross sections D20 and S10 are shown in figures 2 and 3, respectively (from Ayers and Ambrose, 1990).

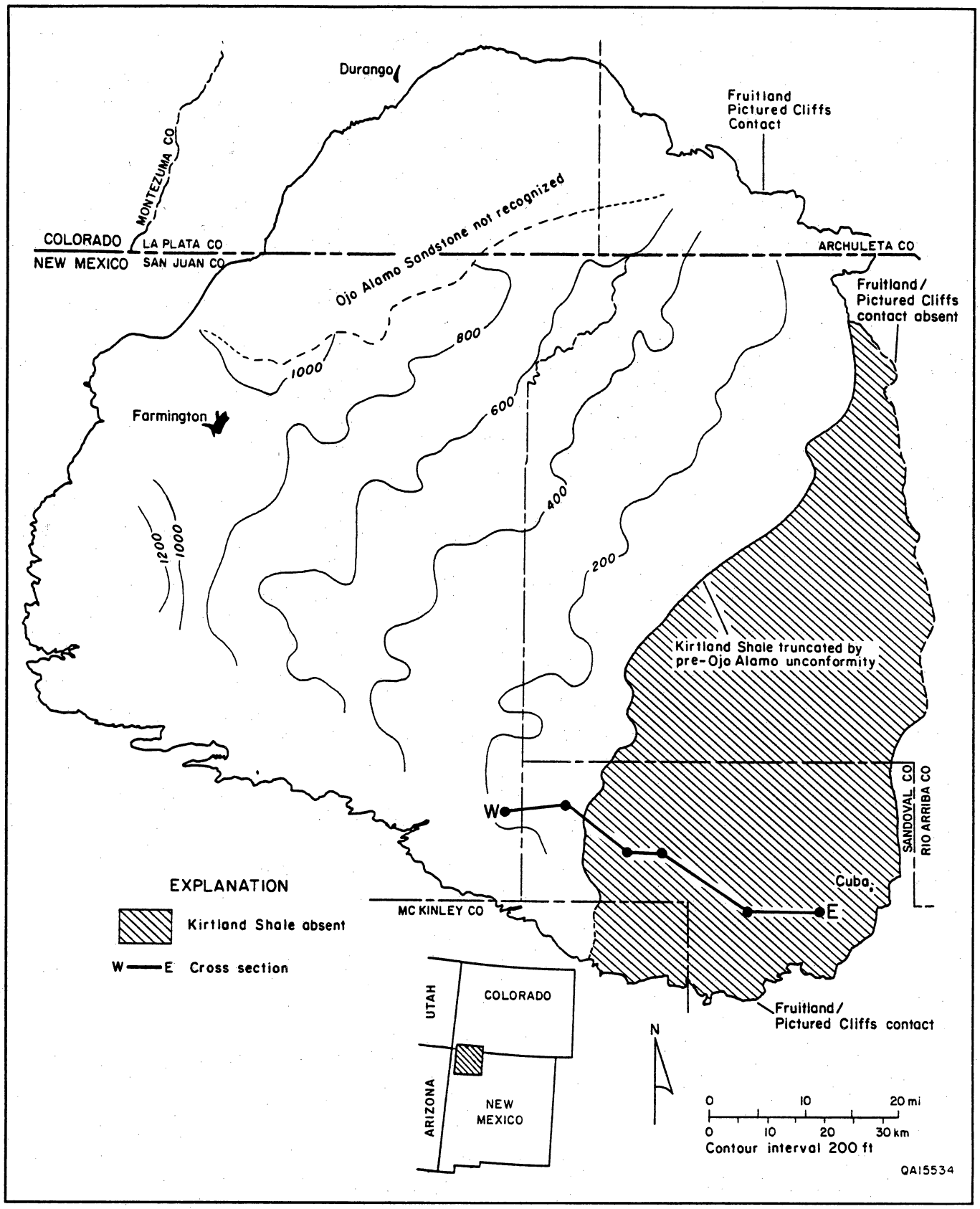

Figure 17. Isopach map of the Kirtland Shale. North-northeast-oriented contours reflect gradual eastward beveling of the Kirtland Shale below the Ojo Alamo unconformity (from Ayers and Ambrose, 1990).

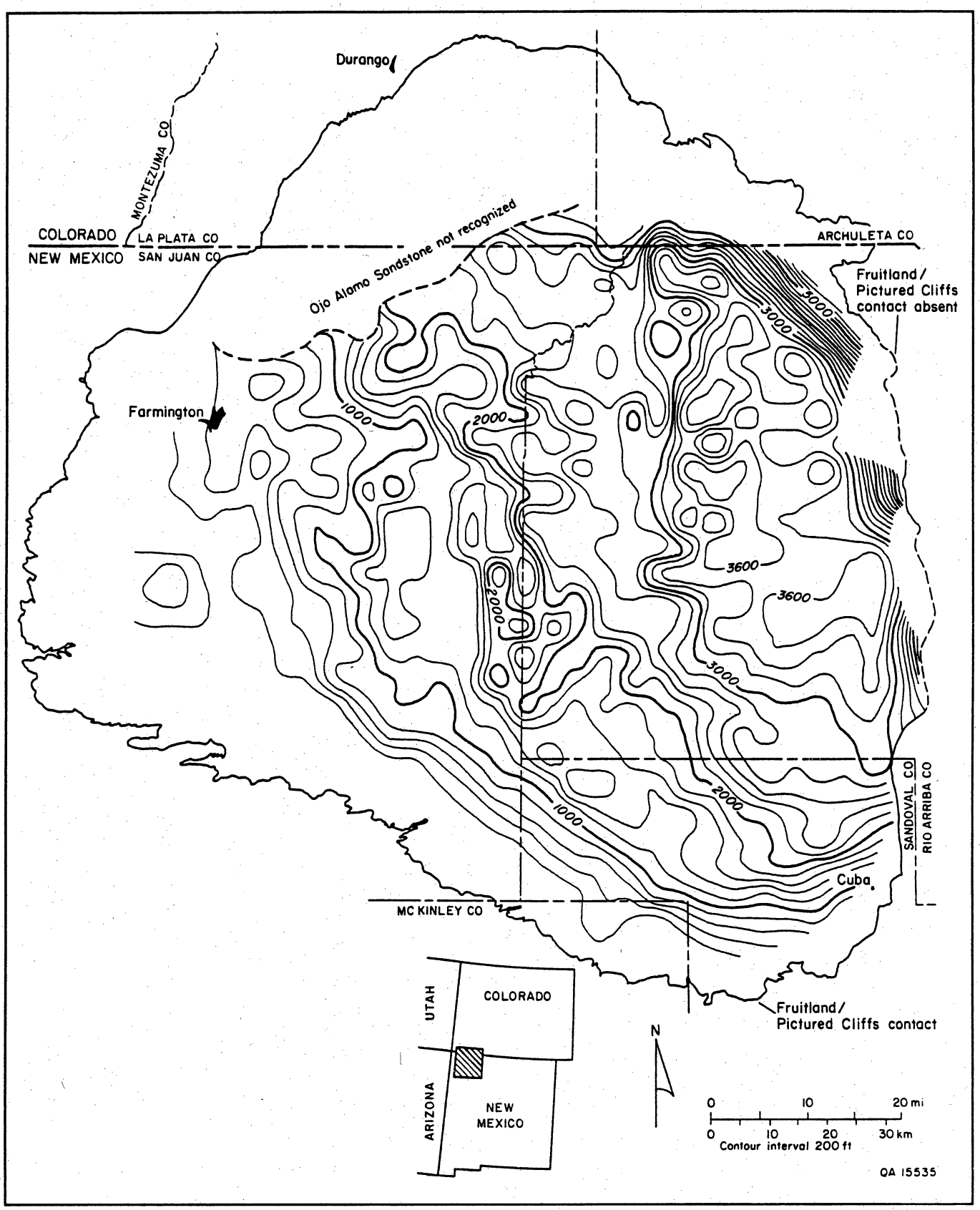

Figure 18. Isopach map of Tertiary fill in the San Juan Basin, defined as depth to the base of the Ojo Alamo Sandstone (from Ayers and Ambrose, 1990).

several factors, including (1) slope of the unconformable surface, (2) basin structure, and (3) topography. More than 3,500 ft (1,065 m) of Tertiary sediments occur in the east-central part of the basin, where the base of the Ojo Alamo Sandstone is structurally low (fig. 7) and topographic relief is great along the Continental Divide. To date, no regional marker bed has been recognized in the Tertiary strata that will allow further analysis of the structural development of the basin.

Fruitland Coal

Fruitland coal rank is subbituminous B to high-volatile A bituminous around much of the southern and western margins of the San Juan Basin; rank increases into the basin to low-volatile bituminous in T34N, R8W (Scott and others, this vol., fig. 3). However, the area of highest coal rank does not coincide with present depth of burial or basin structure (Kaiser and Swartz, 1988). Ash content ranges from 10 to 30 percent and commonly is greater than 20 percent; sulfur averages less than 1 percent, and moisture averages 10 percent in New Mexico and approximately 2 percent in Colorado (Keystone, 1986; Fassett, 1987).

Coal Identification

On geophysical well logs, coal was identified by low density, high neutron and density porosities, low sonic velocity, and/or low neutron count (fig. 19). Low natural-gamma response can be used to reliably identify coal seams in some basins. However, gamma response in Fruitland coal seams is variable, probably because of high and variable ash content of the coal. In figure 19, the thick coal at 3,225 to 3,255 ft is split by a parting at 3,240 ft. Coal above the parting is more radioactive (higher gamma count) than coal below the parting; response in the upper coal is similar to that in the overlying sandstone (3,180 to 3,215 ft). The upper coal has a higher bulk density than coal below the parting, implying greater ash content in the upper coal. The gamma-ray curve is useful for correlation locally; high-gamma counts (peaks) in coal seams and associated Fruitland deposits (fig. 19) can be correlated for several miles. These natural-gamma peaks are attributed to thin clastic beds that are interpreted as volcanic ash layers (tonsteins) in the coal or attributed to organically bound radioactive elements in adjacent sediments. Volcanic ash beds are described in Fruitland coal seams from the southern margin of the basin (Fassett and Hinds, 1971), and bentonite beds are common in the Lewis Shale. The abundant tonstein layers most likely contribute to the high-ash content of Fruitland coal seams. Formation resistivity is of limited use for coal identification in the northern San Juan Basin. However, it can be used to reliably identify coal in the southern part because there are no other highly resistive beds in the Fruitland Formation in this area (Fassett and Hinds, 1971).

On geophysical logs, the thickness of a bed is commonly measured halfway between the shale baseline and the peak corresponding to that bed. On the bulk density log (fig. 19), coal-seam thickness was measured at a density of approximately 1.80 g/cm^3, which is a slightly conservative measurement. We recorded the thickness of coal seams thicker than 2 ft (0.6 m); partings thinner than 2 ft (0.6 m) within thick coal seams were included as coal because of the limits of resolution of the geophysical logs. High-ash coal also is a source and reservoir rock for coalbed methane, and inclusion of minor thicknesses of high-ash coal does not conflict with our goals of delineating the distribution and depositional setting of the coal seams. A 3-ft (0.9-m) parting cutoff in thick coal seams was used by Fassett and Hinds (1971) in mapping the thickest individual (maximum) coal in the Fruitland Formation. However, Fassett and Hinds (1971) excluded partings thicker than 1 ft (0.3 m) when mapping total coal thickness. Kelso and others (1987, 1988) did not state the maximum thickness of partings included in coal-seam measurements for their resource calculations.

Coal Stratigraphy

In the southern San Juan Basin, thick coal seams occur in the lower half (150 to 200 ft [45 to 60 m]) of the Fruitland Formation; seams in the upper Fruitland Formation are thin (fig. 2). In the northern part of the basin, some thick, lower Fruitland coal beds pinch out against the Pictured Cliffs Sandstone, and the thickest coal seams are stratigraphically equivalent to other seams in the upper Fruitland in the south. The lower Fruitland Formation and coal seams of the southern part of the basin are absent in the north owing to pinching out between Pictured Cliffs tongues UP1, UP2, and UP3 (fig. 2). Thick coal seams in the north either pinch out against or override upper Pictured Cliffs tongues. However, because they are immediately above UP1, UP2, or UP3, these coal seams are commonly referred to as lower Fruitland seams, even though they are stratigraphically higher than thick coal seams in the south. As pointed out by Fassett (1987), the terms "upper and lower" Fruitland have little validity in regional discussions.

Coal Overburden

The depth to Pictured Cliffs Sandstone or the uppermost Pictured Cliffs tongue, where present (fig. 20; overburden map), indicates thickness of the overburden for sealing Fruitland coal seams and the

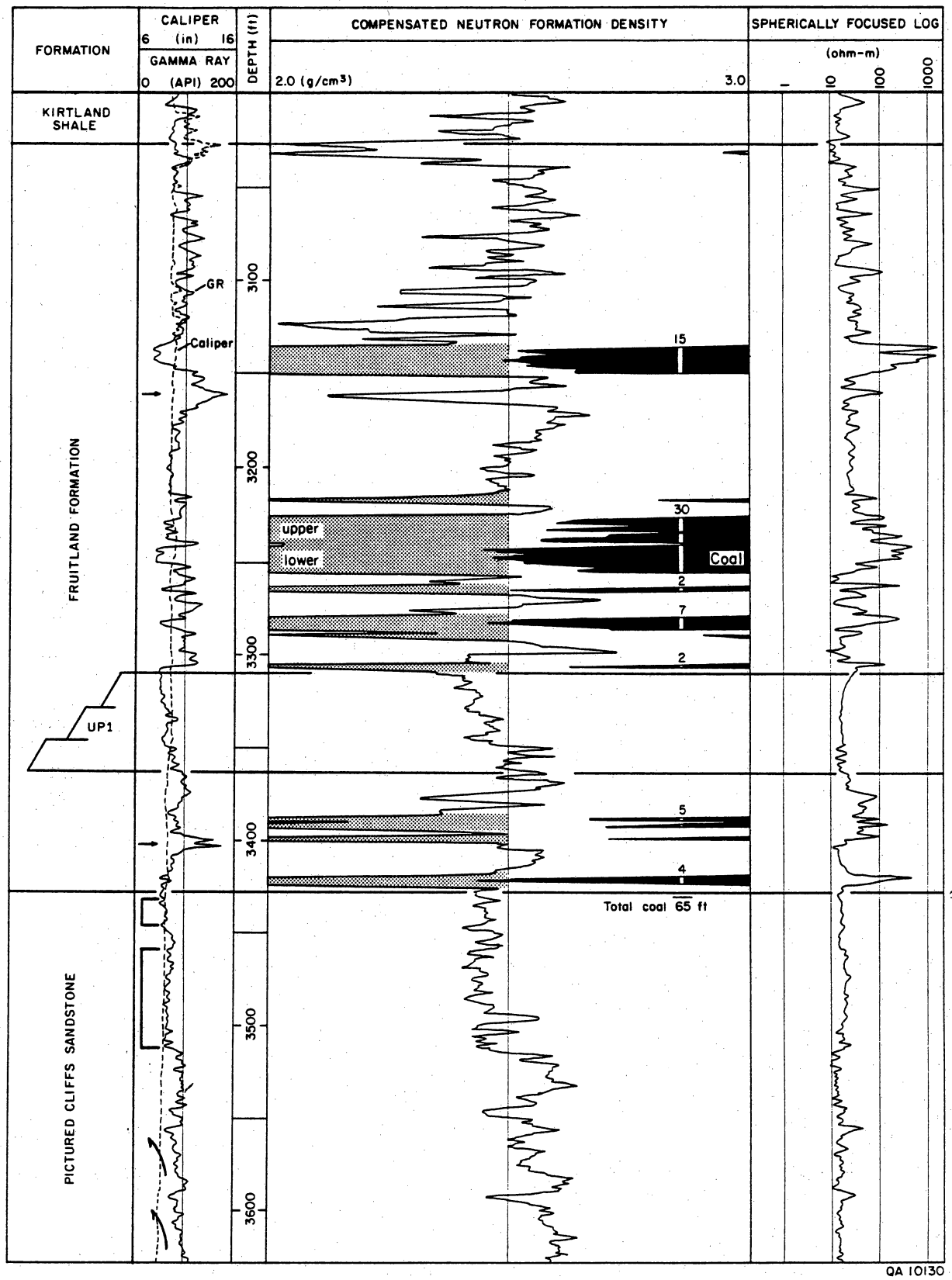

Figure 19. Identification and measurement of Fruitland coal in type log in figure 1. High natural gamma-ray responses, indicated by arrows, are attributed to volcanic ash beds and to organically bound radioactive elements in coal seams (from Ayers and Ambrose, 1990).

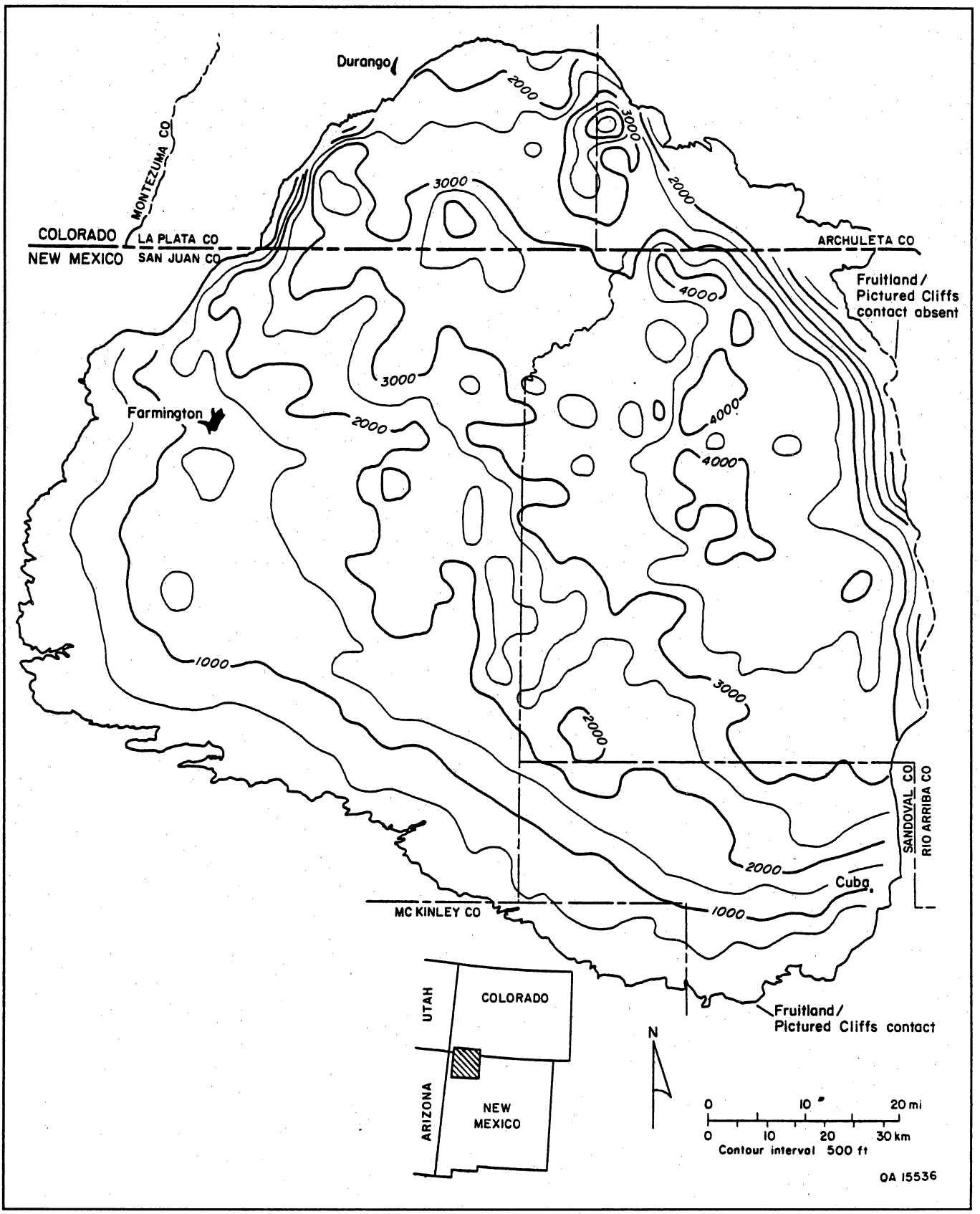

Figure 20. Coal-overburden map, defined as the depth to the top of the Pictured Cliffs Sandstone or to the top of the uppermost Pictured Cliffs tongue (from Ayers and Ambrose, 1990).

drilling depth required to evaluate all Fruitland coal seams. Depth to the top of the Pictured Cliffs reflects present topographic relief, basin structure, and stratigraphic rise of Pictured Cliffs tongues. Overburden is thickest in the eastern part of the basin, in a north-northwest trending area. Fruitland coal seams in the San Juan Basin are as deep as 4,200 ft (1,280 m). However, overburden thickness (present burial depth) does not relate to greatest coal rank (Kelso and others, 1988). Eastward thinning of the Huerfanito Bentonite Bed–Ojo Alamo Sandstone interval (fig. 16) suggests lesser burial depths in the eastern part of the basin. Thus, Fruitland coal seams there are inferred to be lower rank. Coal seams are absent near the eastern margin of the basin because the Fruitland Formation is truncated.

Coal Distribution

To evaluate the occurrence of coal and coalbed methane, we mapped net, maximum, and average coal thickness as well as the number of coal seams in the Fruitland Formation. These maps were compared to identify trends of persistent coal occurrence. These trends are summarized in figure 21. Thick Fruitland coal seams occur in several major northwest-trending, strike-parallel belts (fig. 21, belts A through G) and in minor northeast-trending, dip-elongate belts (fig. 21, belts 1 through 3). Fruitland coal and coalbed methane are concentrated northeast of the hingeline, as discussed in a later section ("Geologic Controls on Coal Occurrence").

Net Coal Thickness

The greatest Fruitland net coal thickness occurs in a northwest-trending belt in the northeastern half of the basin where net coal thickness exceeds 50 ft (15 m) and is locally as much as 110 ft (33 m) (fig. 22); this complex belt, which encompasses belts E and F in figure 21, is about 50 mi (80 km) wide in the northwest and narrows southeastward, terminating about 12 mi (19 km) from the eastern margin of the basin. Narrowing of this belt is due to erosional beveling of the Fruitland Formation and truncation of coal seams by the post-Cretaceous unconformity (figs. 3 and 22).

The major northwest-trending region of thick coal was described in earlier regional maps (Fassett and Hinds, 1971; Kelso and others, 1987). However, these earlier studies used less data and showed fewer secondary coal trends. For example, these studies did not show the presence of numerous dip-elongate belts of coal, 1 to 8 mi (1.6 to 13 km) wide and 30 to 70 ft thick (9 to 21 m), that extend southwestward from the main northwest-trending belt of 50 to 100 ft (15 to 30 m) of net coal to the Fruitland outcrop at the southwestern margin of the basin (fig. 22).

Maximum Coal Thickness

The maximum coal map (fig. 23) was made by contouring the thickest Fruitland coal seam recorded in each well, regardless of its stratigraphic position. Therefore, it does not record an individual seam across the basin. However, individual thick seams are mapped locally, where a persistent thick seam occurs.

Maximum Fruitland coal-seam thickness is as much as 40 ft (12 m). Coal seams greater than 20 ft (6 m) thick occur primarily in northwest-trending belts (fig. 23) that coincide with trends of greatest net coal thickness (fig. 22). Within these strike-elongate belts, the thickest individual coal seams (1) are more than 30 ft (9 m) thick, (2) have podlike geometries, and (3) are 2 to 8 mi (3.2 to 13 km) across. A northwest-trending belt of coal more than 30 ft (9 m) thick occurs in the northern third of the basin (fig. 23; belts E and F in fig. 21). A second northwest-trending belt of thick coal occurs near the northeastern margin of the basin (fig. 23; belt G in fig. 21). Less prominent, northwest-trending belts of thick coal occur at the southwestern margin of the basin (fig. 23; belts A and B in fig. 21). Northeast-trending, dip-elongate belts, in which the maximum coal thickness is greater than 10 ft (3 m), intersect the northwest-trending coal belts (fig. 23; belts 1, 2, and 3 in fig. 21). An earlier regional maximum coal map (Fassett and Hinds, 1971, their fig. 22), which was made with fewer data, shows the major northwest-trending belts of maximum coal but little evidence of the secondary northeast-trending coal deposits.

Number of Coal Seams

Fruitland coal occurs in as many as 16 seams in the San Juan Basin (fig. 24); these coal seams are most abundant in a 40-mi-wide (64-km), northwest-trending belt of six or more coal seams that bisects the basin; seams are most numerous in the northwestern half of this trend. Areas with the greatest numbers of coal seams (more than nine) coincide with areas of greatest net coal thickness (more than 70 ft [21 m], fig. 22) and with the thickest individual seams (more than 30 ft [9 m] thick, fig. 23).

Average Coal Thickness

The map of average coal thickness (fig. 25) clearly delineates coal occurrences and geometries. In the northern half of the San Juan Basin, three distinct belts of northwest-trending, thick coal are defined by areas where average coal thickness exceeds 9 ft (2.7 m) (fig. 25; belts E, F, and G in fig. 21). The northernmost belt (fig. 21, belt G) of thick coal is better defined in this map than in other coal maps; although there are few coal seams in this area (fig. 25), individual seams are commonly greater than 30 ft (9 m) thick (fig. 24).

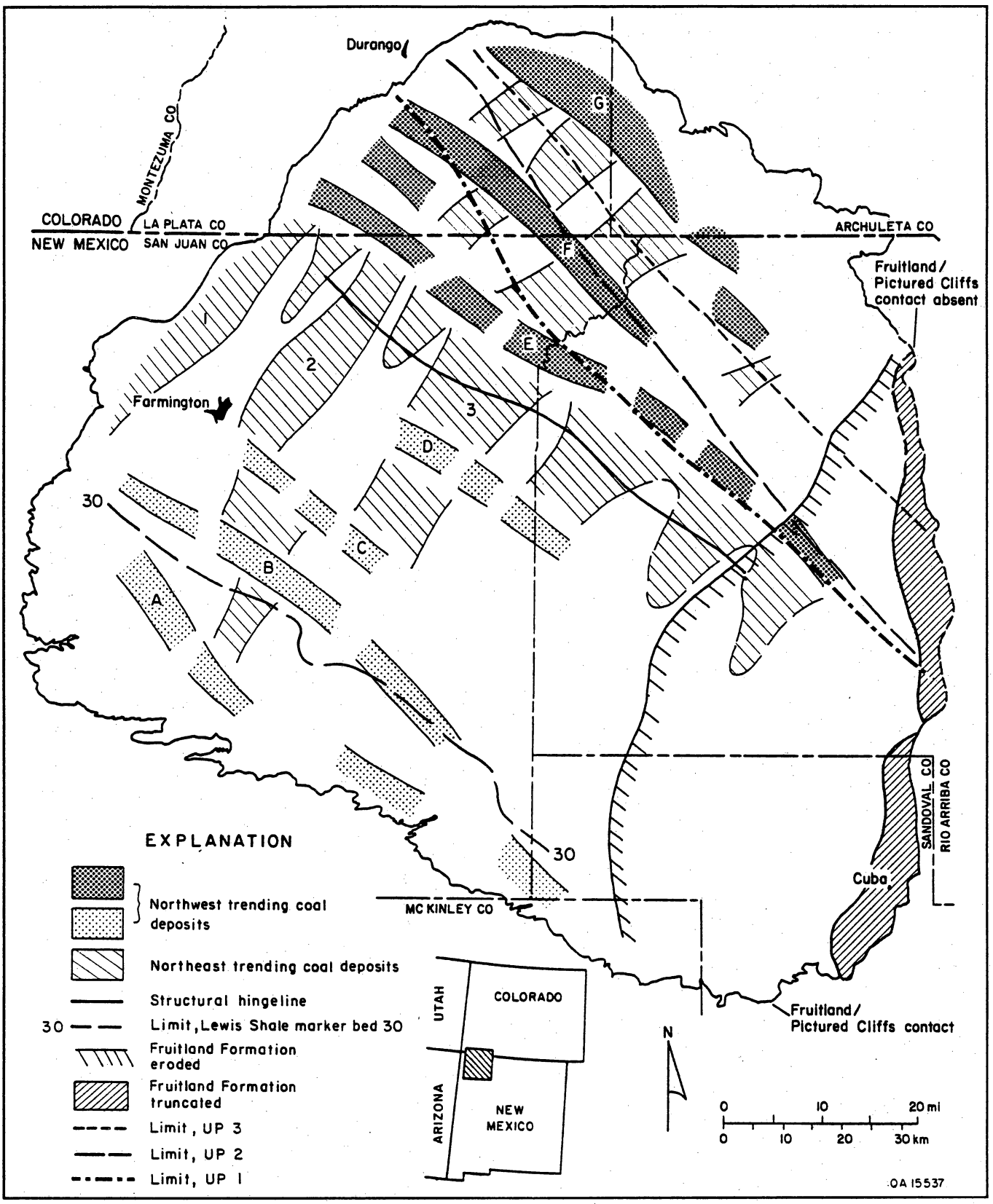

Figure 21. Major coal-occurrence trends in the Fruitland Formation, summarizing figures 22 through 25. Thickest coal seams occur northeast of the structural hingeline, and they parallel northwest-trending upper Pictured Cliffs tongues UP1, UP2, and UP3. Southwest of the hingeline, anomalously thick coal either strikes northwest and parallels minor Pictured Cliffs shoreline buildups or trends northeast and lies between Fruitland fluvial systems (from Ayers and Ambrose, 1990).

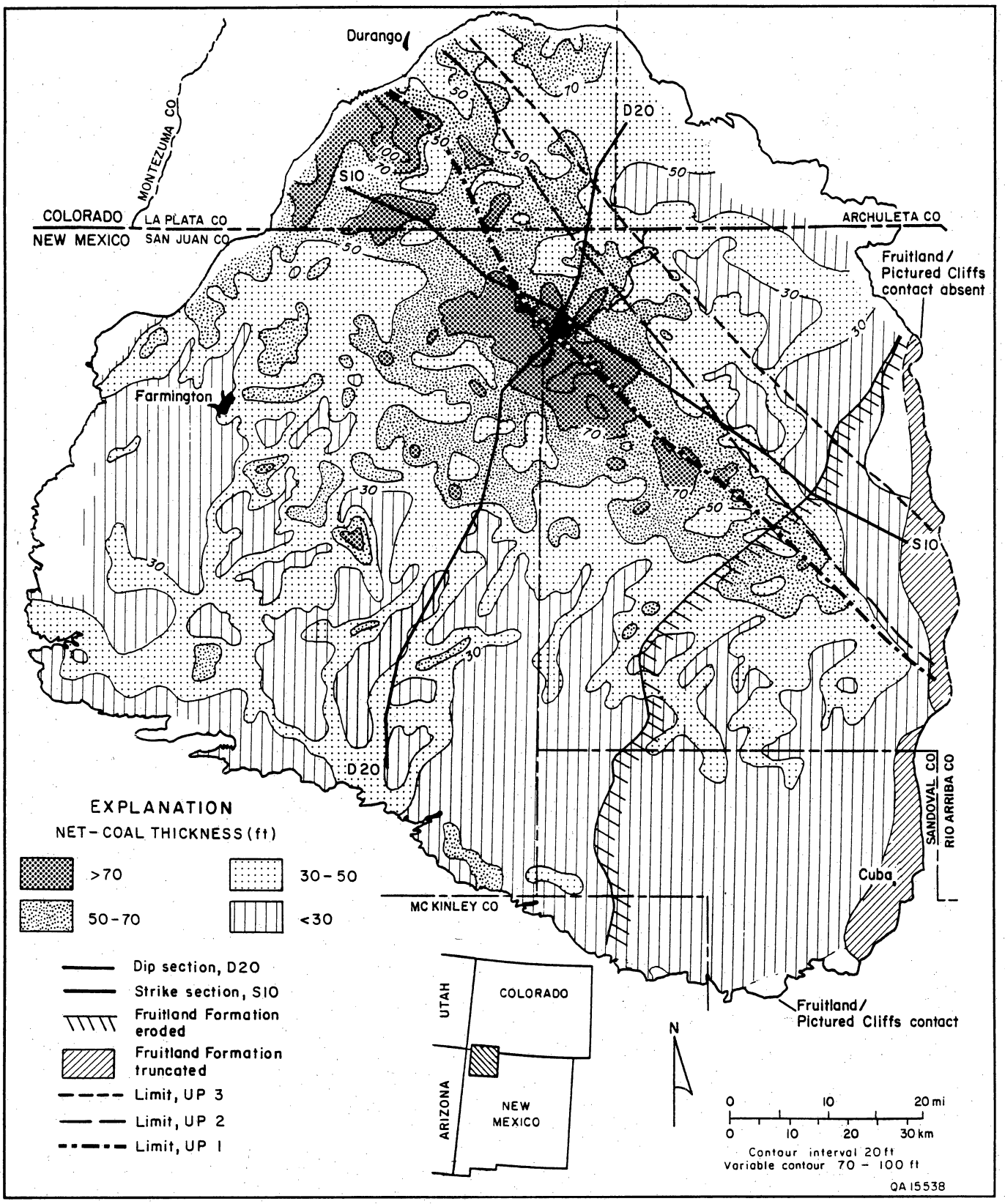

Figure 22. Fruitland net coal map. Greatest net coal thickness occurs in a northwest-trending belt in the north-central part of the basin. Narrow, dip-oriented net coal deposits trend southwestward from this belt and are inferred to have formed in a floodplain setting. Cross sections D20 and S10 are shown in figures 2 and 3, respectively (from Ayers and Ambrose, 1990).

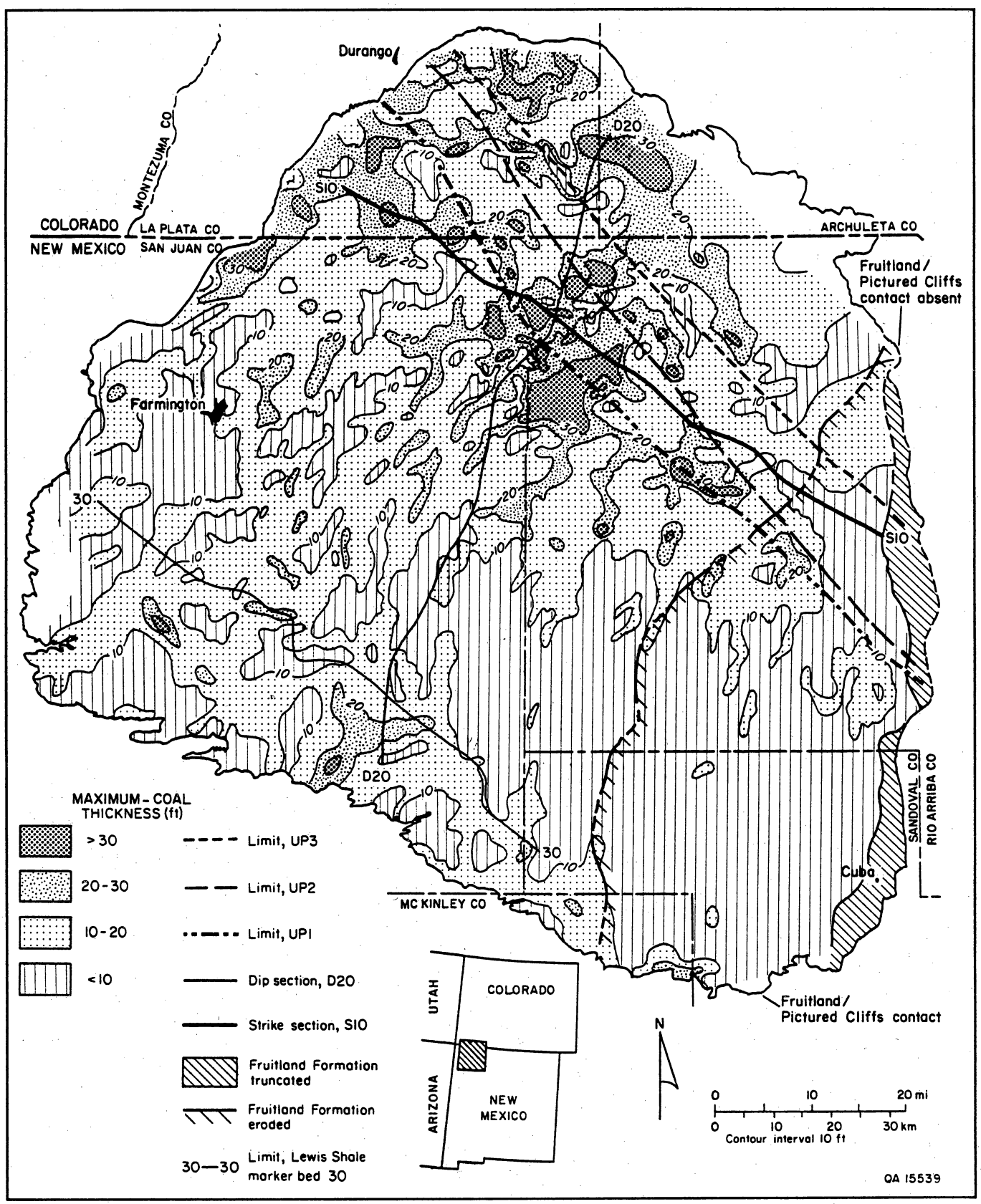

Figure 23. Fruitland maximum coal map. The thickest coal beds occur in the northern part of the basin. Strike-elongate coal deposits in the southwestern part of the basin are genetically related to the 30 marker bed (see figs. 1 through 3). Cross sections D20 and S10 are shown in figures 2 and 3, respectively (from Ayers and Ambrose, 1990).

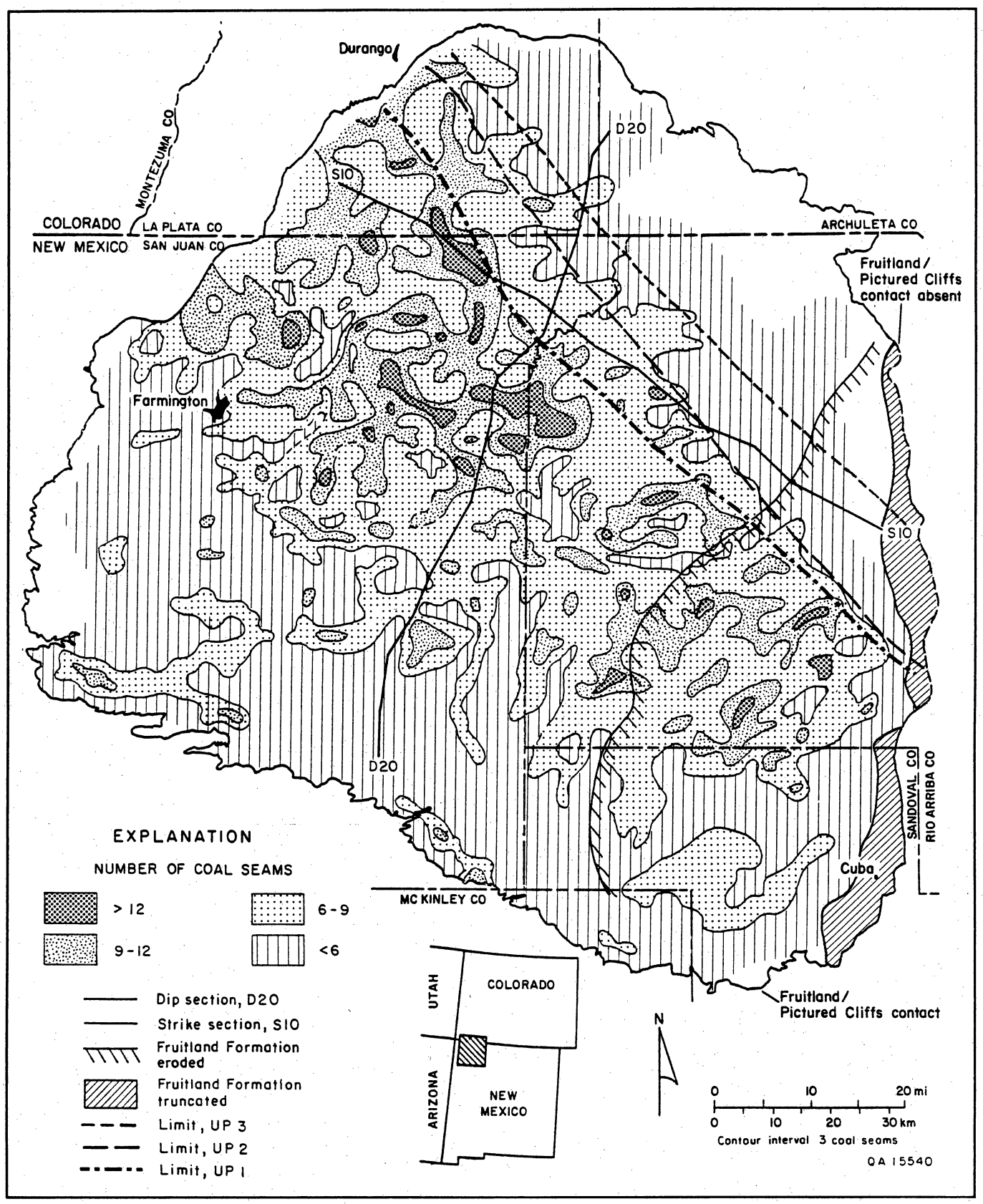

Figure 24. Fruitland coal isopleth map. Coal seams are most numerous in a broad, strike-elongate belt in the central part of the basin; this belt is landward (southwest) of UP1, UP2, and UP3 shorelines. Cross sections D20 and S10 are shown in figures 2 and 3, respectively (from Ayers and Ambrose, 1990).

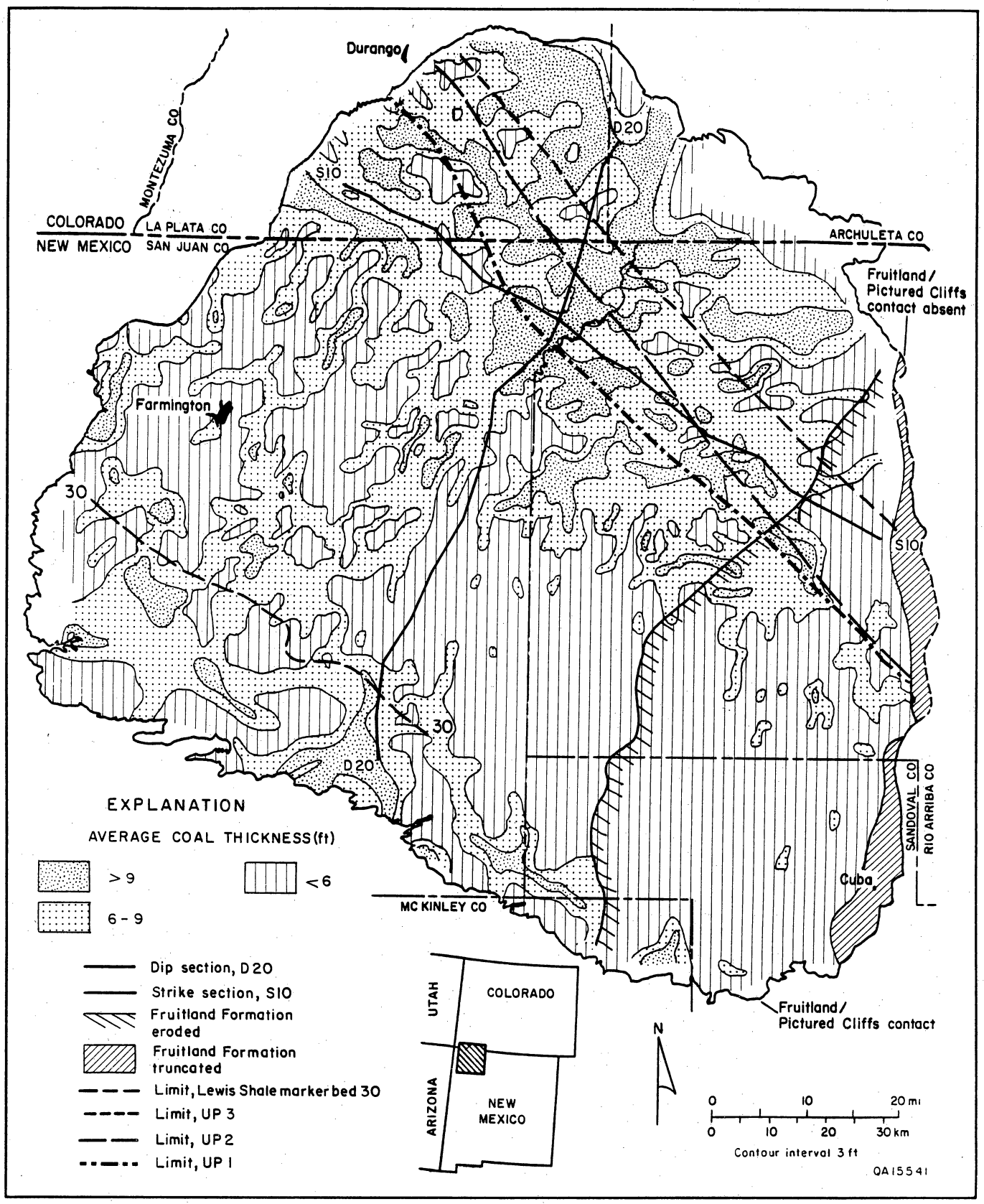

Figure 25. Fruitland average-coal-thickness map. Trends of coal occurrence are similar to those in other Fruitland coal maps. Strike-elongate trends are well developed landward (southwest) of UP1, UP2, and UP3. Cross sections D20 and S10 are shown in figures 2 and 3, respectively (from Ayers and Ambrose, 1990).

Belts A and B coincide with the northeast-trending belts of high values of net coal thickness (fig. 22). In the southwestern part of the basin, there are three strike-elongate belts in which the average coal seam is more than 6 ft (1.8 m) thick (fig. 25; belts A, B, and C in fig. 21). Several dip-oriented belts occur in which the coal seam thickness is greater than 6 ft (1.8 m) (fig. 25; belts 1, 2, and 3 in fig. 21). These northeast-trending belts are common in the southwestern part of the basin.

Geologic Controls on Occurrence of Coal Seams

Previous Studies

Coal seams are facies or subsets of genetically related sedimentary units called depositional systems (Fisher and others, 1969). The depositional system controls the occurrence, trend, and thickness and greatly influences the quality of coal (McGowen, 1968; Horne and others, 1978; Kaiser and others, 1978; Donaldson and others, 1979; Houseknecht and Iannacchione, 1982). Therefore, the relations between depositional systems and coal occurrence, determined from maps and cross sections, are predictive and are a useful tool in coalbed methane exploration.

Pictured Cliffs and Fruitland sandstones are the depositional framework facies that control the occurrence, trend, and thickness of Fruitland coal seams. Previous studies of the depositional setting of the Pictured Cliffs Sandstone and of the Fruitland Formation and other coal-bearing and coal-bounding strata in the San Juan Basin (Sears and others, 1941; Scruton, 1961; Fassett and Hinds, 1971; Erpenbeck, 1979; Flores and Erpenbeck, 1981; Devine, 1980; Kelso and others, 1980; Cumella, 1981; Palmer and Scott, 1984; Wright, 1986) were reviewed in Ayers and Zellers (1988). Wave-dominated coastal processes and resulting wave-dominated deltas and barrier-strandplain systems have long been suggested for the Pictured Cliffs and earlier coastal units in the basin. However, "fluvial-influenced" deltas flanked by barrier-strandplains were described for the Pictured Cliffs in the southwestern quarter of the basin by Flores and Erpenbeck (1981, p. 33) and Erpenbeck (1979, p. 67), who suggested that Fruitland coal seams occur in two depositional settings. These workers concluded that the thickest coal seams are in the lower Fruitland and are dip-elongate seams flanked by distributary channel-fill sandstones and that Fruitland back-barrier coal seams are thinner and contain abundant carbonaceous shale.

The thinness of Fruitland fluvial sandstone complexes and their poor definition on lithofacies maps (Ayers and Zellers, this vol.) suggest that fluvial systems within the north-central part of the basin (Navajo Lake area) were minor and of insufficient size to form fluvially dominated deltas where they debouched into the Western Interior Seaway. This conclusion is supported by linear geometry of the Pictured Cliffs shoreline sandstone tongues that suggest a wave-dominated coastline.

The depositional setting of Fruitland coal seams in the Navajo Lake area (Ayers and Zellers, this vol.) was established from coal-seam geometry and distribution and from the relations between the coal seams and the Pictured Cliffs and Fruitland depositional framework facies. Coal seams are thickest and most numerous landward of upper Pictured Cliffs tongues (fig. 26). These relationships suggest that thick coal formed in persistent and recurring swamp environments landward of the upper Pictured Cliffs barrier shorelines. At Cedar Hill field, coal beds are dip elongate and formed in upper delta-plain to lower alluvial-plain settings (Ambrose and Ayers, this vol.). Palynologic studies (Manfrino, 1984) and the low sulfur content of Fruitland coal seams indicate peat accumulation in a fresh-water setting that was isolated from marine influence, suggesting that peat accumulation occurred inland behind abandoned and foundering shoreline deposits. From cross sections and maps made in this regional study and in previous studies, we conclude that syndepositional tectonic activity controlled the depositional system and, indirectly, the occurrence of thick Fruitland coal (fig. 26). Pulsatory differential subsidence across the hingeline at the southwestern margin of the basin floor (figs. 2 and 9) caused a relative sea-level rise, which resulted in stillstands of the Pictured Cliffs shoreline (UP1, UP2, and UP3). These stillstands allowed ample time for peat (coal) to aggrade and to overspread abandoned shoreline- and fluvial-sandstone complexes. Hence, the greatest concentrations of coal resources occur in northwest-trending belts, north of the hingeline.

Relations between Depositional Systems and Coal Occurrence

Northwest-trending belts of thick Fruitland coal (figs. 21 through 25) are related to Pictured Cliffs shoreline positions. The oldest Fruitland coal in the basin is in belts A and B (fig. 21) and formed behind a shoreline associated with initial Pictured Cliffs shoreline progradation. In contrast, belt G contains the youngest Fruitland coal, formed as the Pictured Cliffs shoreline prograded beyond the northern margin of the present San Juan Basin.

The initial Pictured Cliffs shoreline progradation temporarily reached a limit in the southern part of the basin, marked by the updip pinch-out of the 30 marker bed (figs. 2 and 21). The 30 marker occurs in a high-conductivity shale that was deposited during a minor transgression over an early Pictured Cliffs progradational

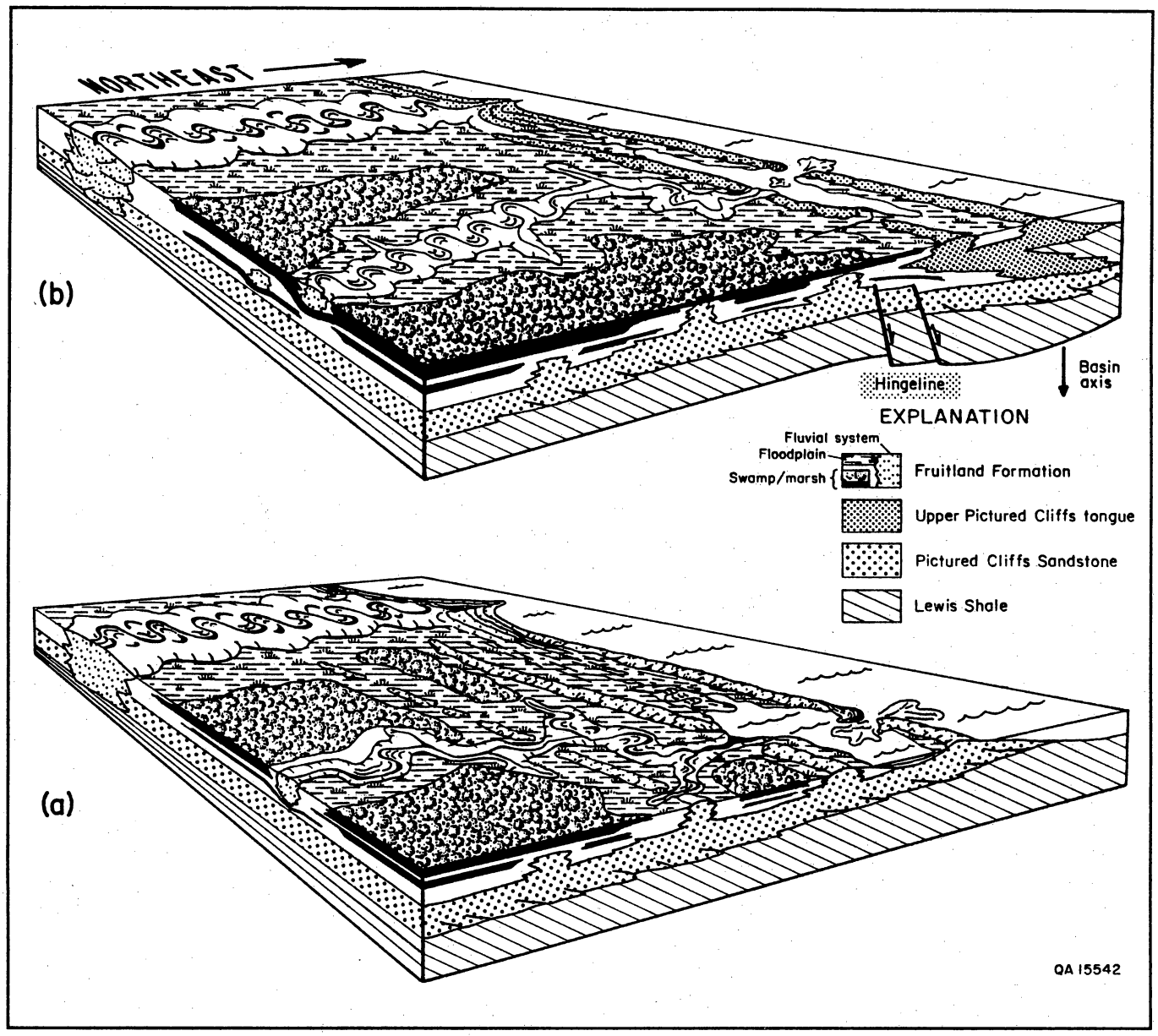

Figure 26. Depositional model of Fruitland coal seams in the Navajo Lake area. (a) Peat is deposited behind, and overrides, abandoned and foundered Pictured Cliffs shoreline sandstones that occur inland and downdrift of a postulated wave-dominated delta. Area is crossed only by minor fluvial feeders that shift periodically. (b) Intermittent subsidence along basin axis temporarily halts regression, causing a shoreline stillstand and allowing accumulation of thick, extensive peat deposits. Not to scale. From Ayers and Zellers (1988).

wedge. Individual coal seams as much as 30 ft (9 m) thick and net coal as much as 50 ft (15 m) thick locally occur at the updip limit of this 30 marker bed (figs. 22 and 23). Following the transgression associated with the 30 marker, the Pictured Cliffs shoreline prograded rapidly to the north-central third of the San Juan Basin. As the Pictured Cliffs shoreline advanced basinward, relatively thin peats (coal seams less than 20 ft [6 m] thick; fig. 23) formed in floodplains between northeast-flowing Fruitland rivers that supplied sediment to the prograding Pictured Cliffs shoreline. This northeast-trending system of interfluvial coal seams was superimposed over older, northwest-trending belts of shoreline-related coal seams as the Pictured Cliffs shoreline prograded toward the northeast. Areas that were occupied by inferred Fruitland rivers correspond to areas of low values of net, maximum, and average coalbed thickness (figs. 22, 23, and 25); in contrast, interfluvial areas correspond to narrow (1- to 8-mi-wide [1.6- to 13-km]), dip-elongate pods of relatively thick coal. In the southwestern part of the basin, a wide band of thick coal (figs. 22, 23, and 25; belts 1, 2, and 3,

fig. 21) formed in a relatively stable part of the coastal plain that was not occupied by major Fruitland fluvial systems.

The thickest and most laterally continuous Fruitland coal seams were deposited in back-barrier settings that correspond to the northwest-trending belts, E, F, and G (fig. 21). These belts of thick coal are landward (southwest) of pinch-out lines of upper Pictured Cliffs tongues that were deposited during periods of shoreline stillstand and/or marine transgression (retrogradation). Two minor, discontinuous belts of northwest-trending coal (fig. 21, belts C and D) also were deposited during short-lived Pictured Cliffs shoreline stillstands associated with deposition of transgressive shales represented by the 35 and 38 marker beds (figs. 2 and 3).

As much as 100 ft (30 m) of coal locally occurs landward of UP1, the oldest upper Pictured Cliffs tongue (fig. 22). This is the thickest belt (fig. 21, belt E) of Fruitland coal in the basin, which suggests a long period of stability of the Pictured Cliffs shoreline. This belt of thick coal encompasses Cedar Hill field and the Navajo Lake area (fig. 5), two of the most productive Fruitland coalbed methane areas in the basin (Kaiser and others, this vol.). Downdip (northeast) of coal belt E in the north-central part of the basin, the number of coal seams (fig. 24) and the net coal thickness (fig. 22) decrease as the Fruitland Formation thins at the expense of Pictured Cliffs tongues UP1 and UP2 (figs. 2 and 15); commonly, net coal thickness is less than 70 ft (21 m) landward of UP2 and 50 ft (15 m) landward of UP3.

Geologic Controls on Producibility of Coalbed Methane

Locally in the San Juan Basin, Fruitland coal seams are folded because of tectonic activity, and structure maps can indicate areas of fracture-enhanced permeability. In other areas, coal seams may be folded over or under Fruitland channel-fill sandstones or Pictured Cliffs shoreline sandstones because of differential compaction. Such compactional folding of brittle coal beds may cause fractures that enhance coalbed permeability. If fracture systems of differential-compaction origin are sufficiently developed, areas of interbedded sandstones and coal seams would be good targets for coalbed methane exploration.

Earlier workers concluded that Fruitland coal seams have limited extent and that they are bounded on their basinward (northeast) margins by Pictured Cliffs shoreline sandstone and along paleostrike (northwest-southeast) by Fruitland fluvial sandstones (Fassett and Hinds, 1971; Fassett, 1986). However, some Fruitland coal seams may be regionally continuous, overriding the Pictured Cliffs Sandstone and Pictured Cliffs tongues with continued progradation. This implies that many Fruitland coal seams are time-transgressive, and it conflicts with the previous interpretation that Fruitland coal beds are "essentially time-equivalent throughout their extent" (Fassett, 1988, p. 35). In at least one area of the San Juan Basin, thick Fruitland coal seams override an upper Pictured Cliffs tongue in the paleodip direction (Ayers and Zellers, this vol., their fig. 16). Along paleostrike, coal seams split and interfinger with fluvial channel-fill sandstone complexes (Ayers and Zellers, this vol., their fig. 17). Areas where Fruitland coal seams drape over upper Pictured Cliffs tongues may be sites of compaction-induced fractures.

The significance of this complex coal-seam geometry is threefold: (1) coal seams, and hence coalbed methane reservoirs, are more extensive than previous workers suggested; (2) compaction-induced fractures, and therefore enhanced coalbed permeability, may occur in areas where coal seams drape over shoreline sandstones or form zig-zag splits with channel-fill sandstone complexes; and (3) the greater lateral extent of coal seams, inferred from this research, is critical to the interpretation of ground-water flow and abnormal pressure in the Fruitland Formation (Kaiser and Swartz, 1988, 1989). The abundance of folds and their potential contribution to enhanced production justify further study. Evaluations of compaction and tectonic folds, in both subsurface and outcrop studies, will be required for clarification of the relations between folding and fracturing (Tyler and others, this vol.).

Coal and Coalbed Methane Resources

In this study, we calculated coal and coalbed methane resources only in Fruitland coal seams deeper than 400 ft (122 m) deep. Coal resources in the Fruitland Formation were calculated to be 245 billion short tons. This estimate is 11 percent greater than that of Kelso and others (1988; 219 billion short tons), and it is 23 percent greater than that of Fassett and Hinds (1971; 200 billion short tons). Coalbed methane in place was calculated to be 43 to 49 Tcf, which is 2 to 14 percent less than that reported by Kelso and others (1988; 50 Tcf) but is 39 to 58 percent greater than the estimate by Choate and others (1984; 31 Tcf).

Approximately 2,500 geophysical well logs were used to make most maps in this study. Of these logs, 1,731 were of sufficiently good quality to be used to evaluate and map Fruitland coal beds. This database was much larger than that used in previous studies, and it resulted in better definition of coal occurrences and trends and in a larger coal resource estimate than in previous studies. Fassett and Hinds (1971) used data from approximately 325 well logs to calculate Fruitland coal resources; the coalbed-methane-resource estimate

of Choate and others (1984) was based on Fassett and Hinds' (1971) coal-resource estimate. Kelso and others (1988) used 549 well logs to calculate coal and coalbed methane resources.

Although coal resources estimated in this study are 11 percent greater than those estimated by Kelso and others (1988), the gas in place in Fruitland coal seams estimated in this study is 2 to 14 percent less than that of Kelso and others (1988). Differences between the coalbed methane estimates stem from differences in the methods of calculation and from assumed ash content of coal seams. Kelso and others (1988) calculated coalbed methane resources on the basis of average coalbed thickness, rank, depth, and gas content in each township; the total resource is the sum of the resources in individual townships. To account for the reduced gas content of the coal because of the presence of inorganic material (commonly referred to as ash) in coal seams, Kelso and others (1988) assumed that the ash values (10 to 36 percent) mapped by Fassett and Hinds (1971, their fig. 24) reflected regional trends common in all Fruitland coal seams (B. Kelso, personal communication, 1989). In the present study, resources were computer calculated on a well-by-well basis using coal thickness and depth data recorded from well logs. Values for gas content and coal density were those used by Kelso and others (1988). Rather than assuming that the ash content of one coal sample was representative of all Fruitland coal seams at that locality, we used average ash contents of 20 percent and 30 percent to calculate 49 Tcf and 43 Tcf, respectively, of methane in Fruitland coal seams.

Gas in place in Fruitland coal seams locally exceeds 35 Bcf/mi² in the north-central part of the basin (fig. 27). Gas in place, although influenced by coal rank and present depth, predominantly is controlled by coal thickness. Gas contents greater than 35 Bcf/mi² (fig. 27) generally coincide with northwest-trending areas where net coal thickness exceeds 70 ft (21 m) (fig. 22) and maximum coal thickness exceeds 20 ft (6 m) (fig. 23); the 10-Bcf/mi² contour (fig. 27) generally coincides with the 50-ft net coal thickness contour (fig. 22).

Conclusions

1. Geologic factors that affected the occurrence and producibility of coalbed methane in the San Juan Basin were tectonic controls on sedimentation, depositional controls on coal occurrence and geometry, and structural controls on the permeability of coal seams.

2. Pictured Cliffs shoreline sandstones accumulated in northwest-trending barrier-strandplains. Retrogradational deposits, upper Pictured Cliffs tongues UP1, UP2, and UP3, were due partly to differential basin subsidence; UP1 pinches out northeast of, and parallel to, a structural hingeline that separates the northeast-dipping monocline of the southern half of the basin from the low-relief basin floor.

3. The thickest and most continuous coal seams in the Fruitland Formation occur in the northwestern part of the basin and are associated with upper Pictured Cliffs tongues. These coal deposits occur in three northwest-trending belts that are updip (southwest) of, and parallel to, these upper Pictured Cliffs shoreline sandstones. Other northwest-trending belts of thick Fruitland coal seams in the southern part of the basin are genetically related to older, minor Pictured Cliffs transgressions.

4. Dip-elongate belts of thick Fruitland coal seams project landward (southwestward) from the northwest-trending belts of thick coal and are inferred to have formed in a floodplain setting. These belts of Fruitland coal were identified and the geometry of the northwest-trending belts of thick coal were better defined in this study than in previous studies because regional maps were made using more data (12 to 15 well logs per township versus 2 to 5 wells per township).

5. The Fruitland Formation thins eastward in the southeastern part of the San Juan Basin because of syndepositional uplift. Coal seams are thinner and fewer in that area. Postdepositional uplift of the southeast part of the basin caused pre–Ojo Alamo erosion that beveled the Fruitland Formation, truncating coal seams near the eastern margin of the basin.

6. The northwest-trending belts of thick coal crop out along the northern and northwestern margins of the basin where they may receive or discharge fluids; hydrologic maps suggest that these Fruitland coal seams are major aquifers that are regionally overpressured because of the elevated recharge area and coal-seam pinch-out (Kaiser and Swartz, 1988, 1989). These northwest-trending seams are poorly connected to dip-elongate coal seams in the southwestern part of the basin because coal seams pinch out to the southwest, and, possibly, because coal seams are offset by faults along the structural hingeline.

7. Coal and coalbed methane resources in the Fruitland Formation are 245 billion short tons and 43 to 49 Tcf, respectively, at depths of 400 ft (122 m) or more. These resources are most abundant in the northwestern part of the basin, where Fruitland gas in place may exceed 35 Bcf/mi².

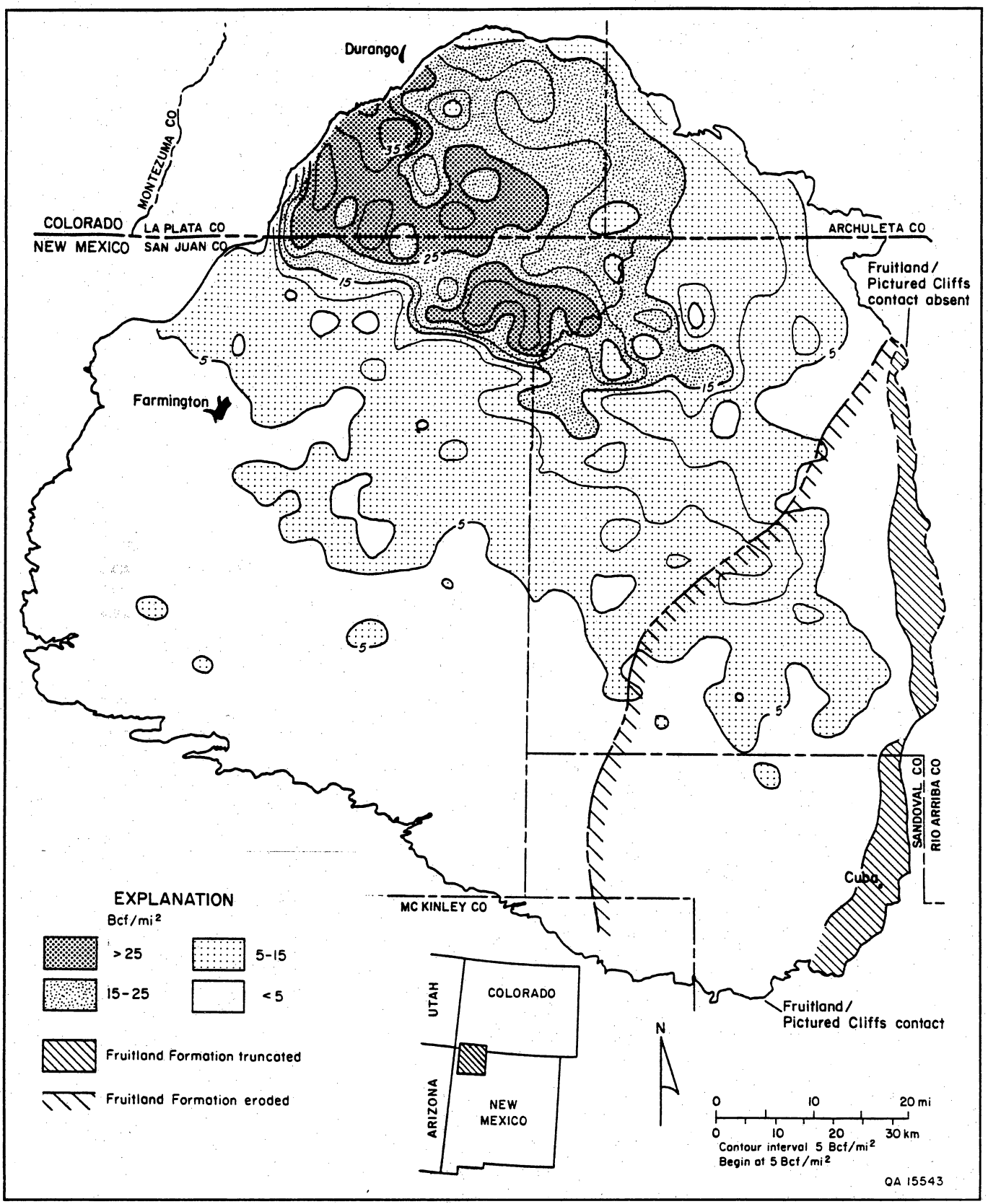

Figure 27. Gas-in-place map for Fruitland Formation coal seams, calculated on the basis of 20 percent average ash content in coal. High values of gas in place occur in the west-central part of the San Juan Basin and reflect the presence of thick coal seams, high coal rank, and high formation pressure (from Ayers and Ambrose, 1990).

8. Targets for increased coalbed methane production because of fracture-enhanced permeability may exist along minor tectonic folds such as those developed along the Hogback Monocline or at the margin of the basin floor. Coal seams commonly override sandstones to extend tens of miles in either the paleodip or the paleostrike direction. Potential targets for enhanced permeability caused by compaction-induced fractures occur where Fruitland coal seams drape Pictured Cliffs and Fruitland sandstones.

Acknowledgments

This study benefited from discussions with W. B. Hanson, W. F. Hoppe, A. C. Huffman, Jr., W. R. Kaiser, B. S. Kelso, and Robert Kemp. C. M. Tremain and N. H. Whitehead III contributed data and geologic insights and assisted with field work. Data from Roybal and others (1985) were used to map coal in the shallow subsurface near the southern margin of the basin. D. R. Grote, Areef Ahamad, J. D. Beckman, P. S. Reiss, G. A. Warren, W. J. Garey, M. M. Newton, R. G. McMurry, and J. N. Ashton assisted with data collection and processing. We gratefully acknowledge review comments by J. C. Close and W. R. Kaiser.

Geologic Controls on Coalbed Occurrence, Thickness, and Continuity, Cedar Hill Field and the COAL Site

William A. Ambrose and Walter B. Ayers, Jr.

Abstract

Fruitland coal seams are complex reservoirs at Cedar Hill field and the Completion Optimization and Assessment Laboratory (COAL) site because of coalbed-sandstone relations and minor structural deformation. Coal formed in fluvial and deltaic settings; compactional folding is present where coal beds underlie or override Fruitland channel-fill sandstones. Northwest-trending (?) faults along the basin hingeline and a syncline that bisects Cedar Hill field contribute to coal seam complexity. Coal beds may be more intensely fractured, and thus more permeable, where folded. Faults at the hingeline offset coal beds and may hinder fluid flow, thus causing the boundary between overpressured and underpressured strata.

Introduction

Cedar Hill field, in the north-central San Juan Basin, has the longest history of coalbed methane production in the basin (fig. 1). Developed by Amoco Production Company in 1977, Cedar Hill field produces from basal Fruitland Formation coal seams at a depth of approximately 2,800 ft (850 m). There coal seams contain an estimated 313 million tons of coal and 89 billion cubic feet (Bcf) of gas in place (Decker and others, 1988). Approximately 17.2 Bcf of coalbed methane and 737,000 bbl of water were produced in Cedar Hill field from 1977 through 1989 (Petzet, 1990).

The COAL site, located approximately 2.5 mi (4.5 km) northwest of Cedar Hill field (fig. 1) in Colorado, has a coalbed methane field research laboratory operated jointly by Amoco Production Company and the Gas Research Institute (GRI). Research at the COAL site is designed to compare the effectiveness of open-hole cavity completions with cased-hole, hydraulically fractured completions, and to determine the parameters that favor open-hole cavity completions. At both Cedar Hill field and the COAL site, the Fruitland Formation is overpressured. Because overpressuring is due to artesian conditions, most coalbed methane wells in the area produce water.

Objectives

The objectives of this study were to (1) identify Fruitland coal groups and depositional units, (2) define geologic control on the thickness, continuity, and structural attitude of major coal seams (reservoirs) that occur in each coal group, and (3) characterize the boundary between overpressured and underpressured Fruitland strata. The geologic characteristics defined in this study will be compared with coalbed methane production trends to determine geologic and hydrologic controls on coalbed methane producibility (Kaiser, Ayers, and others, this vol.). This area was selected because (1) Cedar Hill field has the longest history of coalbed methane production in the basin, and (2) geologic characterization of the COAL site is critical in the interpretation of coalbed methane research results.

Methods

Data from 260 geophysical logs, including 22 from shallow (less than 600 ft [180 m] deep) boreholes near the Fruitland outcrop, were used in this study. Outcrops were described to document relationships between Fruitland and Pictured Cliffs stratigraphic units, to evaluate coalbed continuity, and to support depositional systems interpretations.

Stratigraphic units below and above the Fruitland Formation were correlated on eight structural and stratigraphic cross sections as a framework for determining the lateral extent of Fruitland coal seams and sandstones. Marker beds that were correlated included the Huerfanito Bentonite Bed, five shale marker beds in the Lewis Shale and Pictured Cliffs Sandstone, tonsteins in Fruitland coal seams, carbonaceous shales in the Fruitland Formation, and a high-conductivity shale at the Fruitland–Kirtland contact (see Ayers and others, this vol.).

The Fruitland Formation was divided into three depositional subunits, each bounded by continuous coal beds or locally by shale and sandstone beds. Depositional models of each subunit were based on comparisons of net coal thickness, net sandstone thickness, isopach, and structure maps. Sandstone thickness was determined from resistivity and natural-gamma curves; lithologic identification was confirmed with bulk-density logs. Coal identification and thickness were determined from bulk-density logs, and coal thickness

In Ayers, W. B., Jr., and others, 1991, Geologic and hydrologic controls on the occurrence and producibility of coalbed methane, Fruitland Formation, San Juan Basin: The University of Texas at Austin, Bureau of Economic Geology, topical report prepared for the Gas Research Institute under contract no. 5087-214-1544 (GRI–91/0072), p. 47–68.

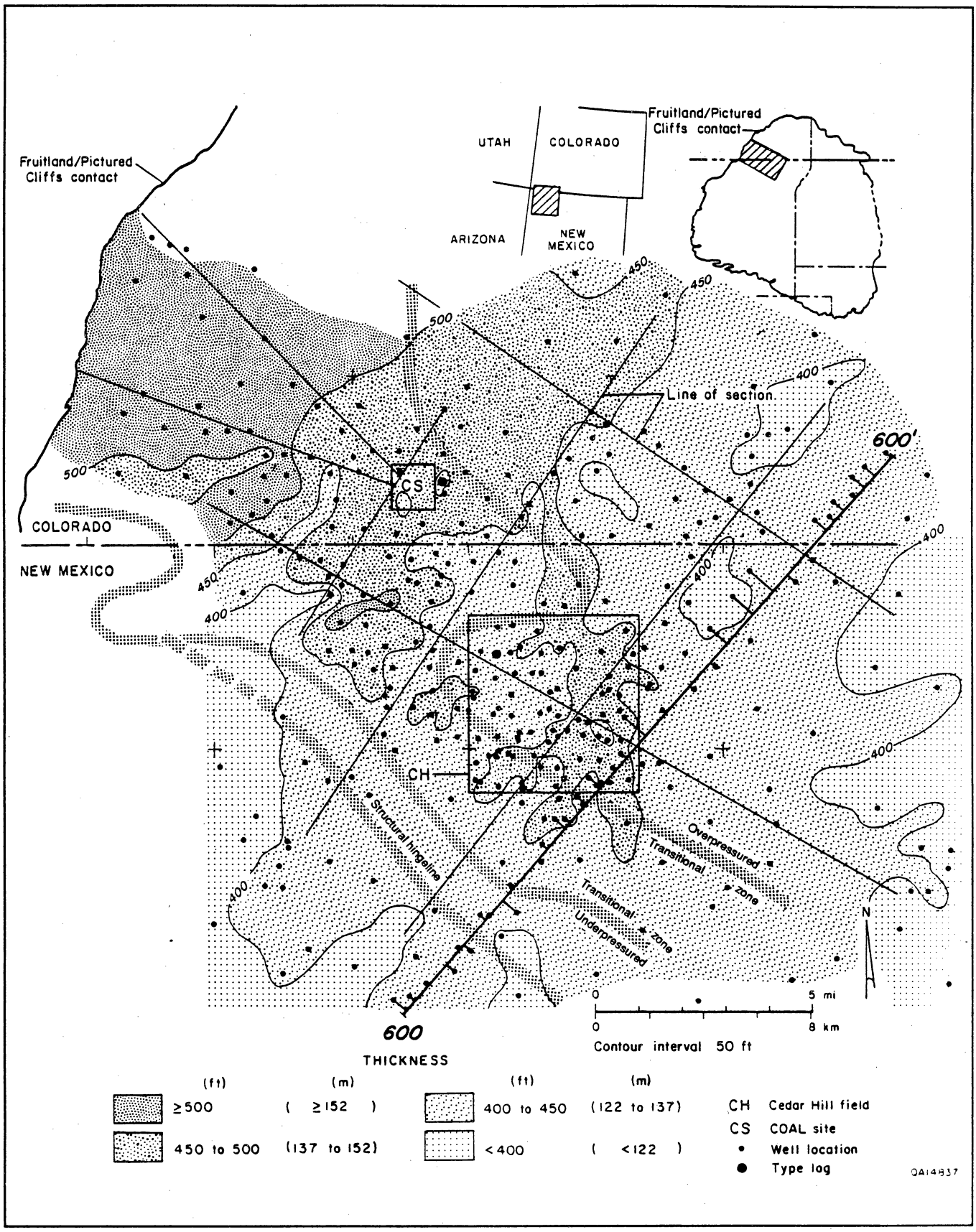

Figure 1. Isopach map of the Fruitland Formation at Cedar Hill field and the COAL site. The Fruitland Formation thickens northwestward.

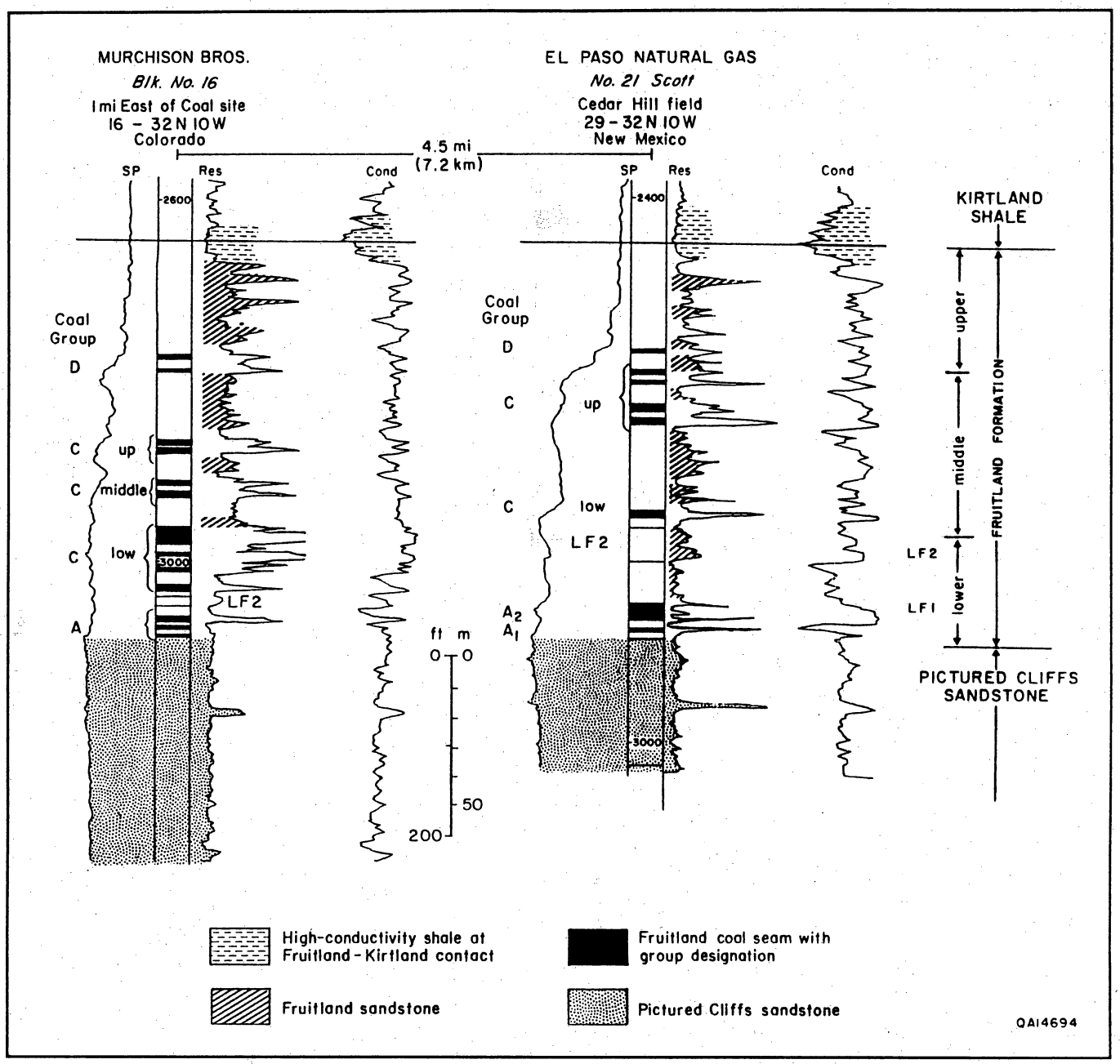

Figure 2. Type logs (located in fig. 1) showing Fruitland stratigraphic units in Cedar Hill field and in the area of the COAL site. Group B coal seams (shown in fig. 3) are absent in Cedar Hill field and in the COAL site.

was measured at a density of approximately 1.80 g/cm^3. We recorded coal seams thicker than 2 ft (0.6 m); partings thinner than 2 ft (0.6 m) were included as coal because of the limits of resolution of the geophysical logs. For logs without a density curve, other curves including natural gamma, neutron, and resistivity were used; coal seams in these logs were identified by correlation with coal seams in nearby logs having bulk-density curves.

Stratigraphic and Structural Setting

At Cedar Hill field and the COAL site, the Fruitland Formation is 430 to 470 ft (130 to 143 m) thick; it thickens northwest toward the Fruitland outcrop, where it is more than 570 ft (174 m) thick (fig. 1). The Fruitland Formation was divided into three depositional subunits (lower, middle, and upper) that contain four coal groups (A, B, C, and D) (figs. 2 and 3).

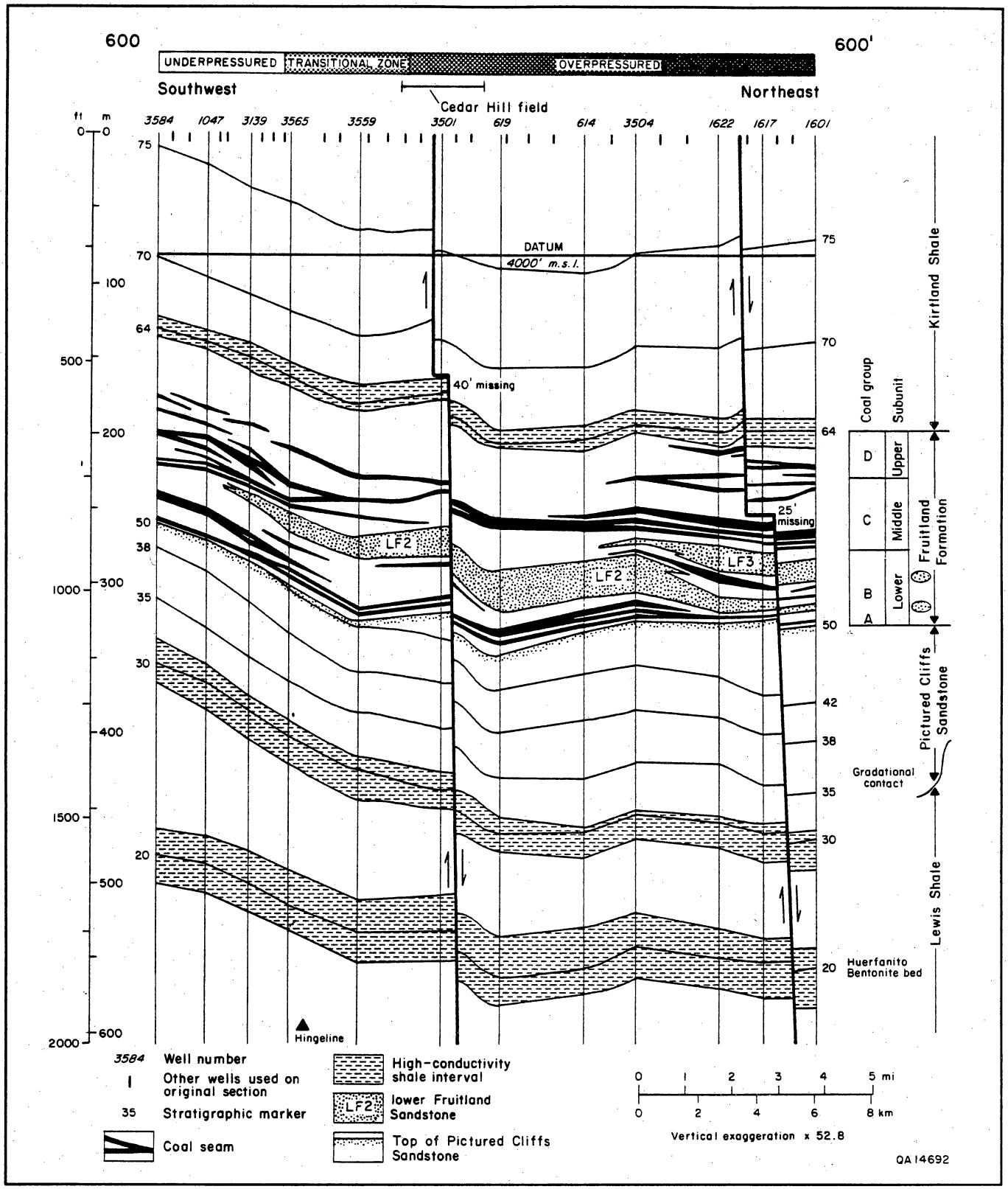

Figure 3. Structural dip section in the northwestern San Juan Basin (see figure 1 for location). A transition from gently northeast-dipping to nearly flat-lying but folded and faulted strata occurs at the hingeline and the southwestern margin of regional overpressuring.

Fruitland subunits are bounded by coal groups. In areas where the bounding coal groups pinch out, subunit boundaries are locally occuring shale (or sandstone) beds at the stratigraphic horizon of the coal group. For example, the middle subunit is defined as all strata between the base and the top of coal group C (fig. 2). However, the basal coal seam in group C, which directly overlies the LF2 sandstone, is absent in the eastern half of Cedar Hill field. Therefore, the base of the middle subunit is locally defined in eastern Cedar Hill field as the top of LF2. Although coal seams that bound Fruitland subunits pinch out locally in the Cedar Hill–COAL site area, they are present in most areas.

The lower Fruitland subunit, which overlies the Pictured Cliffs Sandstone (figs. 2 and 3), is further divided into three parts, LF1, LF2, and LF3. LF1 consists of thin sandstones, mudstones, and basal Fruitland coal seams (coal group A). LF2, a sandstone that varies greatly in thickness, is separated from LF1 by carbonaceous shales or thin, discontinuous coal seams at the top of coal group A (fig. 2). Northeast of Cedar Hill field, LF2 is separated from LF3 by one or two thin (less than 5 ft [1.5 m] thick) seams of coal group B (fig. 3). LF3 is a lenticular sandstone that overlies coal group B northeast of Cedar Hill field (fig. 3).

The middle and upper Fruitland subunits compose most of the Fruitland Formation and contain coal groups C and D, respectively. Group C coal seams overlie LF2 sandstones in Cedar Hill field but override LF3 sandstones northeast of the field (fig. 3). Group C coal seams are thicker and more continuous than group D seams, which occur between thick channel-fill sandstones in the upper Fruitland subunit.

The Fruitland–Kirtland contact is a regionally extensive, high-conductivity shale (fig. 2). This shale interval is inferred to be a condensed marine section deposited over older Fruitland coastal plain deposits (Ayers and others, this vol.). Foraminifera have been reported in this shale (Dilworth, 1960), which has a geophysical-log response (high natural gamma, high conductivity) and regional continuity similar to that described for other shallow-water condensed sections in the Western Interior Seaway (Leckie and others, 1990).

Cedar Hill field is bisected by an east-plunging syncline (fig. 4). In the syncline, Fruitland strata are more tightly folded (fig. 4a) than the underlying Huerfanito Bentonite Bed (fig. 4b). Structural relief on the base of Fruitland coal group A across Cedar Hill field is 70 ft (21 m) (fig. 4a). Up to 40 ft (12 m) of structural relief occurs across faults and where coal seams override sandstones (fig. 3).

Depositional Systems

Pictured Cliffs Sandstone

The Pictured Cliffs Sandstone, which is the platform underlying the Fruitland Formation, consists of northwest-trending, strike-elongate shoreline deposits of barrier-island and wave-dominated delta systems (Ayers and others, this vol.). North of the study area, upper Pictured Cliffs tongues bound Fruitland coal beds. The Pictured Cliffs Sandstone intertongues with the Lewis Shale and is 175 ft (53 m) thick, 2 mi (3.2 km) updip (southwest) of the basin hingeline (fig. 3). However, it is 250 ft (76 m) thick in Cedar Hill field, and 4 mi (6.4 km) northeast of the field it thickens basinward to more than 350 ft (107 m). Marker beds in the Lewis Shale, used to correlate well logs in this study, are isochronous units that cross the proximal shelf and shoreface to intersect and terminate in Pictured Cliffs coastal sandstones (Ayers and others, this vol.). Similar stratigraphic marker beds have been described in prograding coastline deposits in the Upper Cretaceous Point Lookout Sandstone in the southern San Juan Basin (Wright, 1986).

Fruitland Formation

The Fruitland Formation, the primary coal-bearing formation in the San Juan Basin, is the continental facies deposited landward of the coastal (barrier-island and deltaic) facies of the Pictured Cliffs Sandstone; it is composed of sandstone, mudstone, and coal interbeds (fig. 3). Within the Fruitland Formation, dip-elongate (northeast-trending), fluvial-deltaic sandstone bodies form the depositional framework. Net sandstone thickness in the Fruitland Formation ranges from 110 to 230 ft (33.5 to 70 m) (fig. 5).

Lower Fruitland Subunit

LF1, the basal part of the lower Fruitland subunit, is bounded below by the Pictured Cliffs Sandstone and above by the LF2 sandstone; it consists of coal group A, mudstones, and sandstones (fig. 2). The sandstones are dip-elongate (northeast-trending) and are locally more than 40 ft (12 m) thick, but they thin to only 10 ft (3 m) downdip (fig. 6a). LF1 consists of lower delta plain (distributary-channel and floodplain) sediments deposited landward (southwest) of the Pictured Cliffs shoreline. The Pictured Cliffs delta front, inferred from pinch-outs of distributary-channel sandstones, was 3 to 6 mi (4.8 to 9.6 km) northeast of Cedar Hill field and the COAL site.

At Cedar Hill field and the COAL site, lower Fruitland sandstone, LF2, overlies group A coal beds in

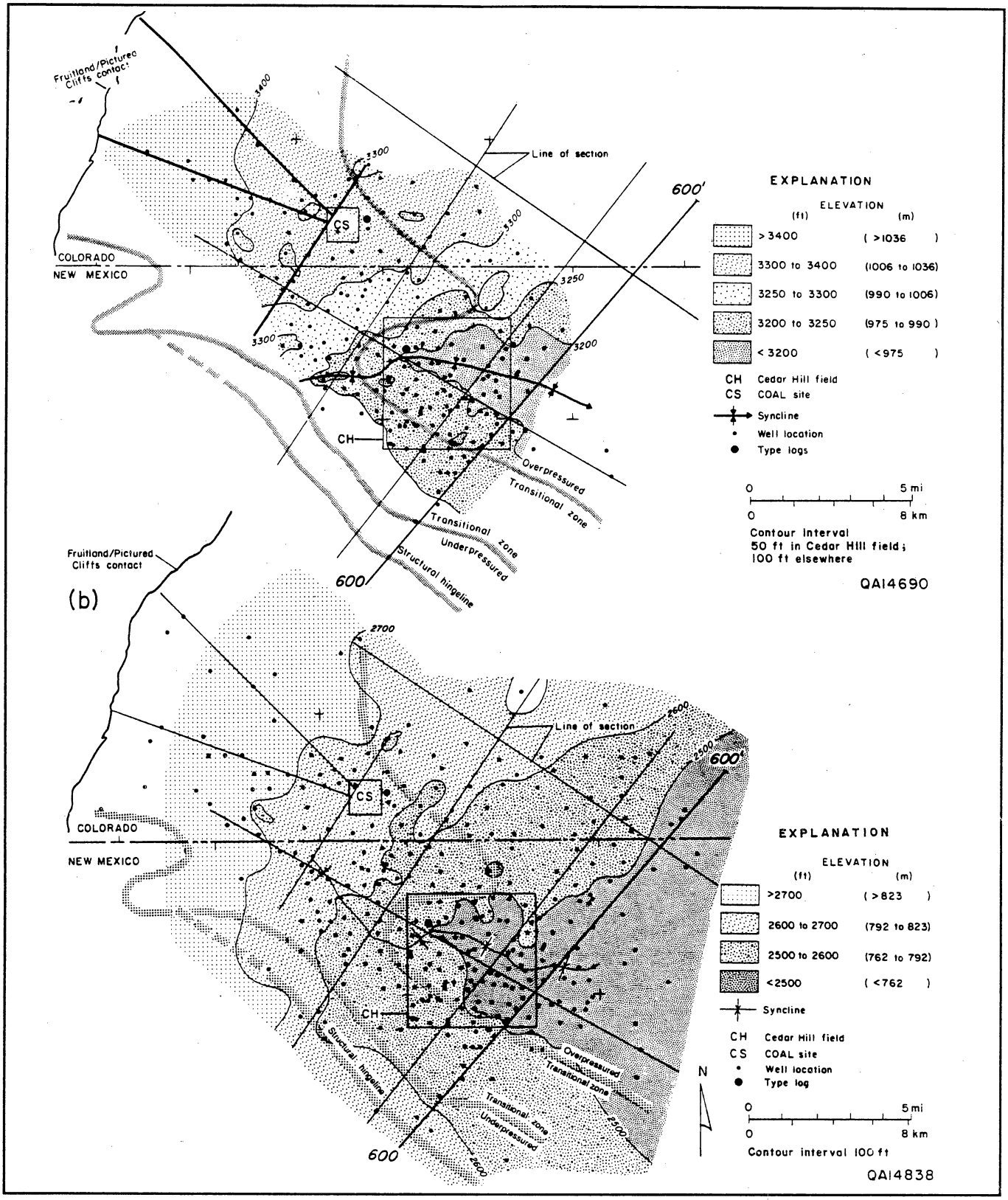

Figure 4. (a) Structure map of the base of Fruitland coal group A at Cedar Hill field and the COAL site. An east-plunging syncline bisects Cedar Hill field. (b) Structure map of the Huerfanito Bentonite Bed. The synclinal fold at Cedar Hill field is more open in this map than in the structure map of Fruitland coal group A.

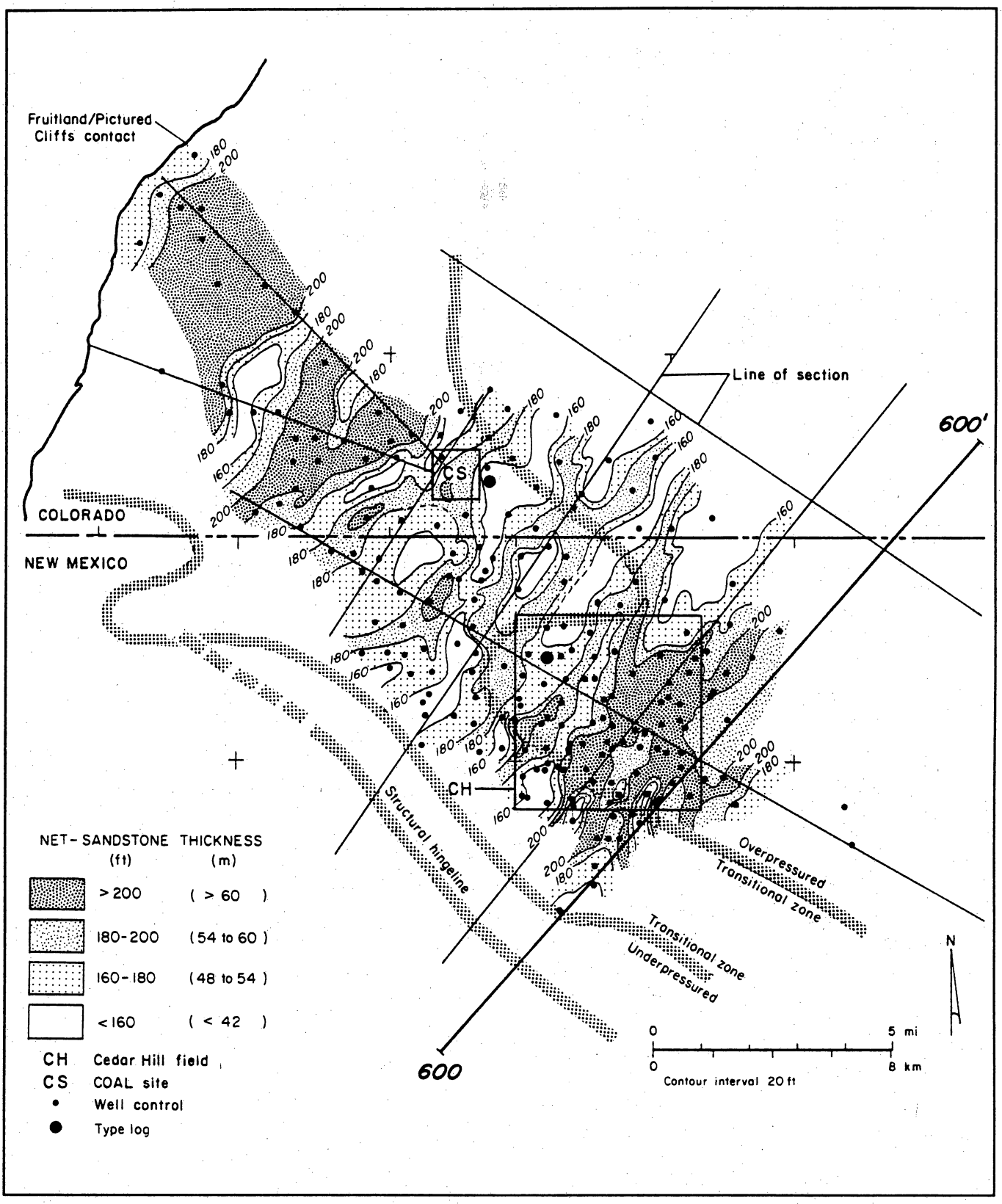

Figure 5. Sandstone isolith map of the Fruitland Formation. Net thickness of dip-elongate, northeast-trending sandstone bodies exceeds 200 ft (60 m) near the Fruitland outcrop.

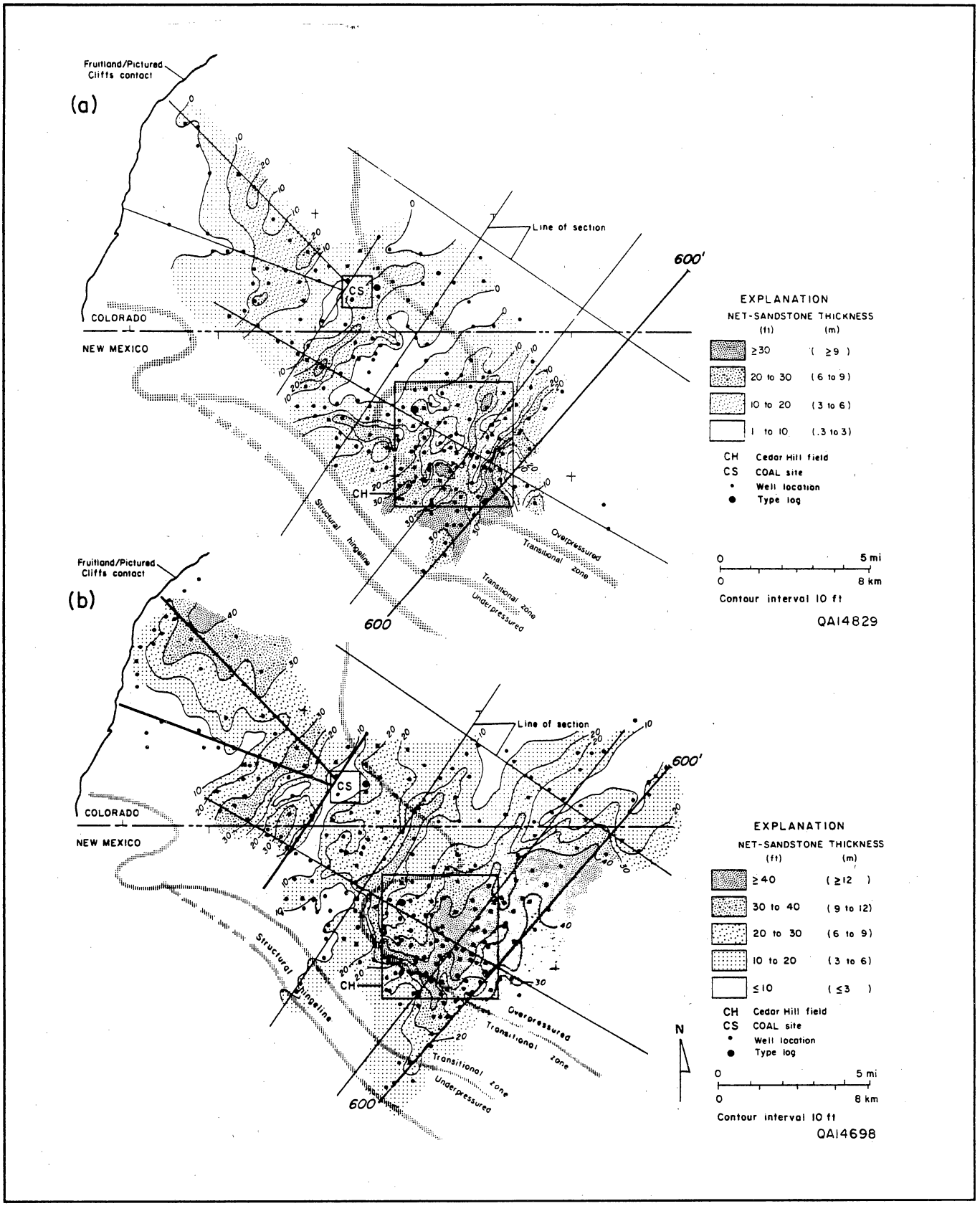

Figure 6. (a) Sandstone isolith map of LF1 in the lower Fruitland subunit. A depocenter at Cedar Hill field is defined by dip-elongate sandstone bodies that are locally more than 40 ft (12 m) thick. (b) Sandstone isolith map of lower Fruitland sandstone LF2. Multiple, dip-elongate sandstone bodies are more than 30 ft (9 m) thick.

LF1 and is in turn overlain by coal group C (fig. 2). Because LF1 pinches out near the Fruitland outcrop belt, LF2 directly overlies and merges with the Pictured Cliffs Sandstone along the northwestern margin of the basin. LF2 depositional axes are defined by multiple, northeast-trending sandstone bodies more than 30 ft (9 m) thick (fig. 6b). A major LF2 depocenter in the eastern half of Cedar Hill field is defined by northeast-trending sandstones more than 40 ft (12 m) thick. In contrast, the COAL site is located between LF2 depositional axes, where net sandstone thickness is less than 10 ft (3 m). Because LF2 sandstone thickness varies along depositional strike, the structural attitude of coal seams above and below this unit varies.

LF3 is a lenticular sandstone less than 20 ft (6 m) thick. It was not mapped because it occurs only locally at the northeastern margin of Cedar Hill field and the COAL site (fig. 3). However, northeast of Cedar Hill field, lower C coal seams override LF3 (fig. 3), which affects the attitude of these seams.

Middle Fruitland Subunit

The middle Fruitland subunit consists of strata from the base to the top of coal group C (figs. 2 and 3). Sandstone bodies in the middle Fruitland subunit are strongly dip elongate. Net sandstone thickness is 40 to 60 ft (12 to 18 m) in Cedar Hill field and more than 80 ft (24 m) near the northwestern margin of the basin (fig. 7a).

The inferred depositional setting of the middle Fruitland subunit is a transition between upper coastal plain and lower alluvial plain. As the Pictured Cliffs shoreline prograded northeastward, there was a corresponding landward shift in depositional environments of overlying, younger Fruitland strata. The Pictured Cliffs shoreline at this time was located farther basinward than it was during deposition of LF1 because of net shoreline progradation.

Upper Fruitland Subunit

The upper Fruitland subunit consists of all Fruitland strata above coal group C (fig. 2). Sandstones of this subunit occur in dip-elongate (northeast-trending) belts; in Cedar Hill field, these belts are less than 2,000 ft (600 m) wide (fig. 7b). The upper Fruitland subunit contains the thickest Fruitland sandstones, with thickness of individual sandstone bodies up to 50 ft (15 m) and net sandstone thickness up to 130 ft (40 m). The upper Fruitland subunit is interpreted to be the most proximal part of the Fruitland fluvial system that supplied sand to the Pictured Cliffs shoreline. At Cedar Hill field and the COAL site, sandstone belts that merge downdip (northeastward) represent tributary streams that joined to form alluvial trunk streams.

Fruitland Coal Groups

The four Fruitland coal groups (A, B, C, and D) consist of one or more individual coal seams (figs. 2 and 3). Coal seams in these groups vary in thickness and continuity because of deposition of peat in different settings. Coal group B occurs only locally and pinches out approximately 1 mi (1.6 km) northeast of Cedar Hill field (fig. 3); therefore, it was not evaluated in this study. In this section we describe coal groups A, C, and D, and relate coal characteristics to depositional setting.

Net coal thickness of coal in the undivided Fruitland Formation at Cedar Hill field and the COAL site ranges from less than 40 ft (12 m) to as much as 100 ft (30 m) (fig. 8a). Coal deposits commonly are dip parallel (northeast-trending) in Cedar Hill field and south of the COAL site. Dip-elongate bands of 60 to 80 ft (18 to 24 m) of coal merge downdip (northeastward) to form a strike-elongate (northwest-trending) sheet of more than 80 ft (24 m) of net coal, approximately 3 mi (5 km) northeast of Cedar Hill field. The dip-elongate coal deposits in the Fruitland Formation formed in floodplain and interdistributary environments, whereas the strike-elongate coal deposits accumulated in swamps landward (southwest) of Pictured Cliffs shoreline sandstones.

Coal Group A

Coal group A consists of as many as three coal seams. In the northwestern San Juan Basin, the greatest net thickness (35 ft [11 m]) of coal in group A occurs in northeast-trending bands in Cedar Hill field (fig. 8b), where this group is the main target for coalbed methane production. Coal seams in group A pinch out 1 to 3 mi (1.6 to 4.8 km) from the northwestern margin of the basin.

Coal group A is genetically associated with sandstones in LF1 (fig. 6a). The thickest coal in group A coincides with a 3-mi-wide (5-km) area centered on Cedar Hill field, where net sandstone thickness in LF1 exceeds 20 ft (6 m). This relation suggests that peat in coal group A accumulated on a crevasse-splay or small deltaic platform (LF1). However, within Cedar Hill field, net coal thickness in group A is greatest (more than 30 ft [9 m] thick) in sand-poor (net sandstone less than 20 ft [6 m] thick) areas in the underlying LF1 sandstone.

The depositional setting of coal group A is similar to that described by Levey (1985) for lower delta plain coal seams in the Upper Cretaceous Rock Springs Formation in southwestern Wyoming. Thick Rock Springs coal seams formed as peats overspreading abandoned delta lobes, with greatest accumulation between distributaries.

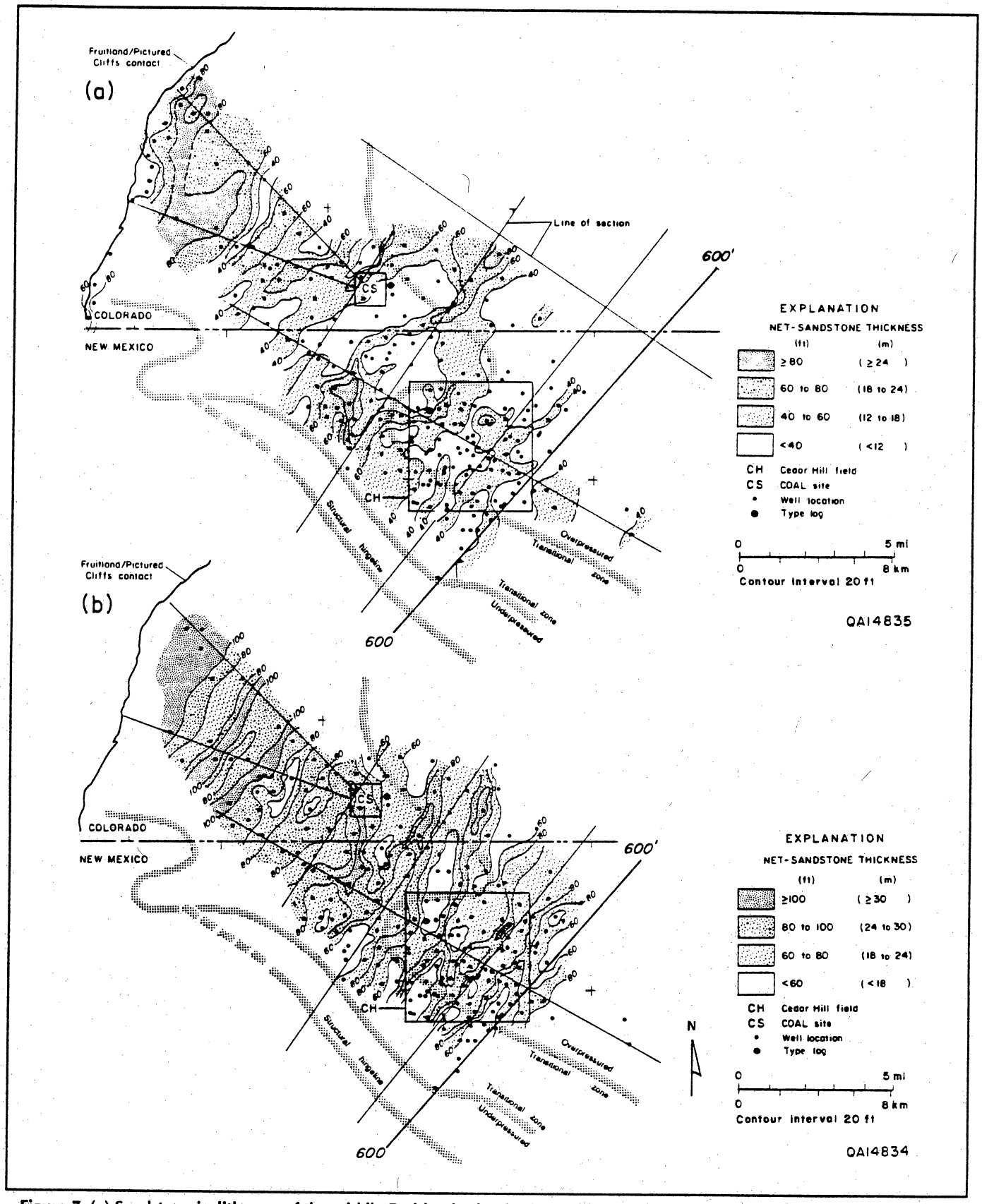

Figure 7. (a) Sandstone isolith map of the middle Fruitland subunit. (b) Sandstone isolith map of the upper Fruitland subunit.

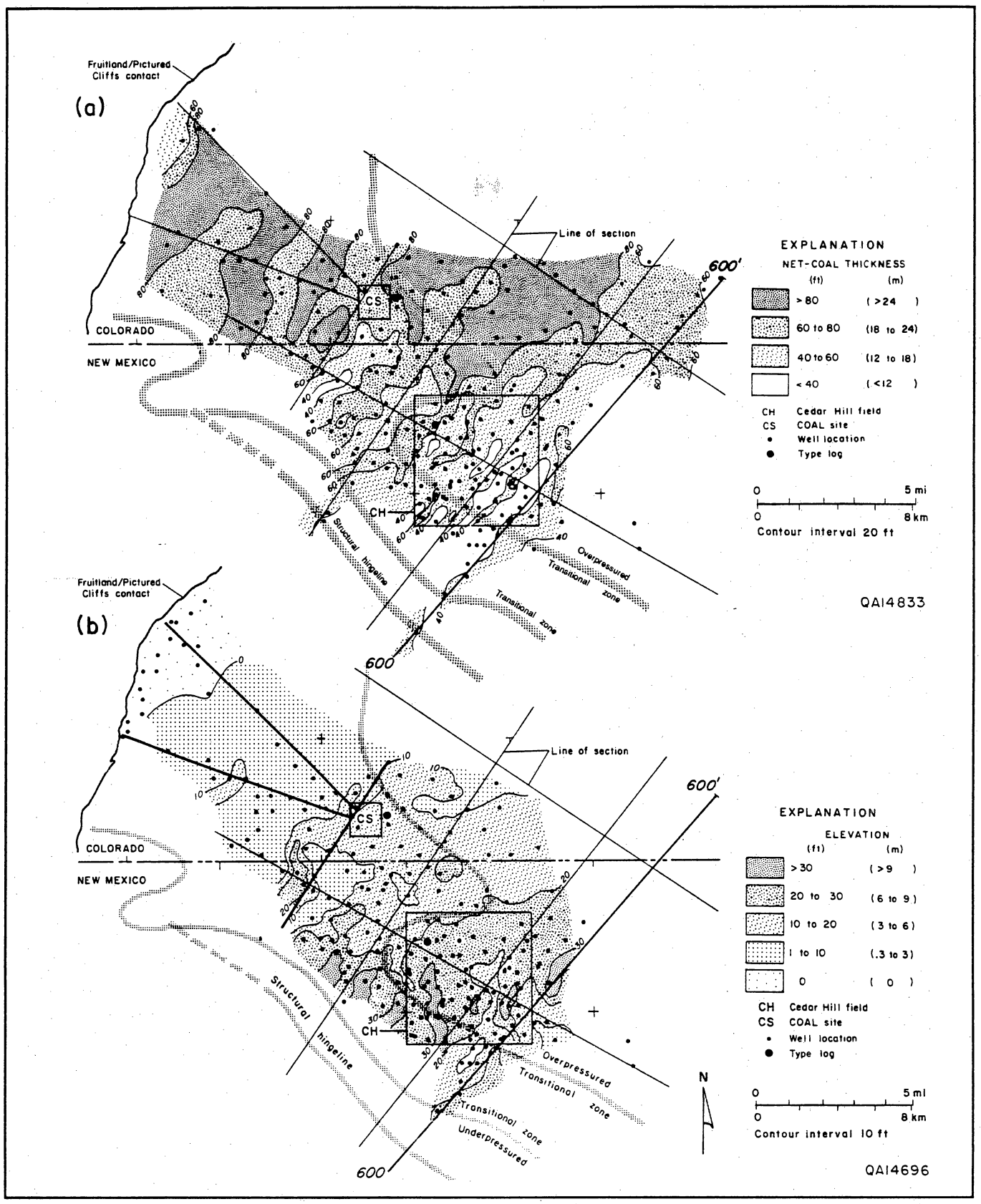

Figure 8. (a) Coal isolith map of the undivided Fruitland Formation. Dip-parallel deposits of more than 80 ft (24 m) of coal broaden and merge downdip of Cedar Hill field and the COAL site. (b) Coal isolith map of Fruitland coal group A, which contains the greatest thickness of coal at Cedar Hill field.

Coal Group C

Coal group C occurs in the middle Fruitland subunit (figs. 2 and 3). Net coal thickness in group C is greatest northwest of Cedar Hill field, where thickness exceeds 60 ft (18 m) (fig. 9). Coal occurs in dip-elongate deposits that merge downdip (northeastward) to form a strike-elongate sheet north of Cedar Hill field. Net coal thickness is generally less than 40 ft (12 m) in Cedar Hill field, where coal group C overlies thick LF2 sandstones (fig. 6b). Coal group C is divided into lower, middle, and upper subgroups that will be described separately.

Lower C Coal Seams

Lower C coal seams are the thickest seams in group C. They overlie LF2 sandstones at Cedar Hill field and at the COAL site (fig. 2). Two net coal thickness trends (more than 30 ft [9 m] of net coal) are present in lower C coal seams (fig. 10a). Dip-elongate (northeast-trending) belts occur south of the COAL site. These belts merge downdip (northeastward) into a strike-elongate sheet.

Lower C coal seams overlie LF2 sandstones over much of the area, but at Cedar Hill field they pinch out against thick LF2 distributary sandstones. These sandstones vary from 20 to 100 ft (6 to 30 m) thick in Cedar Hill field (fig. 6b), resulting in considerable structural relief on lower C coal seams. Dip-elongate pods of lower C coal south of the COAL site accumulated between distributary channel-fill sandstone deposits, whereas widespread lower C coal seams north of the site formed in a lower delta plain setting.

Middle and Upper C Coal Seams

Middle and upper C coal seams (fig. 2) are thin and discontinuous; because of similarities in these two subgroups, only middle C coal seams will be described. Like the lower C seams, middle C seams are absent in the eastern part of Cedar Hill field (fig. 10b). However, there are notable differences in net coal thickness (hence, reservoir continuity) of middle and lower C coal seams: at the COAL site, middle C coal seams are thin (less than 10 ft [3 m] thick) and lower C coal seams are thick (more than 30 ft [9 m]). Near the Fruitland outcrop at the northwestern margin of the basin, middle C coal seams are more than 40 ft (12 m) thick and are the thickest coal seams in the Fruitland Formation.

Coal Group D

Coal seams in group D are associated with the upper Fruitland subunit (figs. 2 and 3). These seams are the thinnest and least continuous coal seams in the Fruitland Formation. They occur in discontinuous, dip-elongate pods having net coal thickness of more than 5 ft (1.5 m) at Cedar Hill field and the COAL site (fig. 11a). Net coal thickness of group D coal seams is greatest (more than 15 ft [4.6 m] thick) near the Fruitland outcrop.

Group D coal seams are thin and discontinuous because they formed in an unstable floodplain setting between upper Fruitland fluvial meanderbelts (fig. 7b). Aggradation of the coastal plain resulted in stacked channel-fill sandstones that locally exceed 130 ft (40 m) thick. Channel avulsion and lateral migration resulted in termination of short-lived peat swamps on unstable floodplains.

Depositional Controls on Coalbed Continuity and Structural Attitude

The thickness and original continuity of coal seams were controlled by depositional environment. In the southwestern part of the study area, thick Fruitland coal seams occur in northeast-trending belts between channel-fill sandstone complexes, whereas in the northeastern part, they occur in northwest-trending sheet deposits that formed landward of Pictured Cliffs barrier-strandplain deposits.

Depocenters for Fruitland coal beds (reservoirs) shifted northwestward with time (fig. 11b). Thick coal beds in group A are the main coalbed reservoirs in Cedar Hill field, but these coal beds are thin at the COAL site (fig. 8b), where thick lower C coal beds are the primary coalbed methane target (fig. 10a). Fruitland coal beds vary considerably in thickness across the basin, and although they act as an integrated, regional reservoir, locally individual beds may be in poor hydraulic communication. Stratigraphic studies of these coal beds are required to (1) delineate limits of individual reservoirs and (2) evaluate well spacing and location.

The relationship between sandstone LF2 and lower C coal seams is an example of sandstone-body control on the extent and thickness of coal seams. Lower C coal seams have an inverse thickness relation to underlying LF2 sandstones. At Cedar Hill field, these seams thin and pinch out over thick (more than 40 ft [12 m]) LF2 sandstones. Conversely, at the COAL site, where lower C coal seams are thick (locally more than 30 ft [9 m]), LF2 sandstones are thin (less than 5 ft [1.5 m]).

Coal seams overlying channel-fill sandstones are the result of peat having accumulated over abandoned-channel complexes, whereas coal seams that underlie channel-fill sandstones result from avulsion that redirected streams into swamps. Where they overlie and underlie lenticular sandstone bodies, coal seams commonly are folded because of differential compaction of sandstones and adjacent mudstones and coal beds. Such compactional folding of coal beds may cause fractures (Donaldson, 1979; Houseknecht and Iannacchione, 1982) that enhance coalbed permeability.

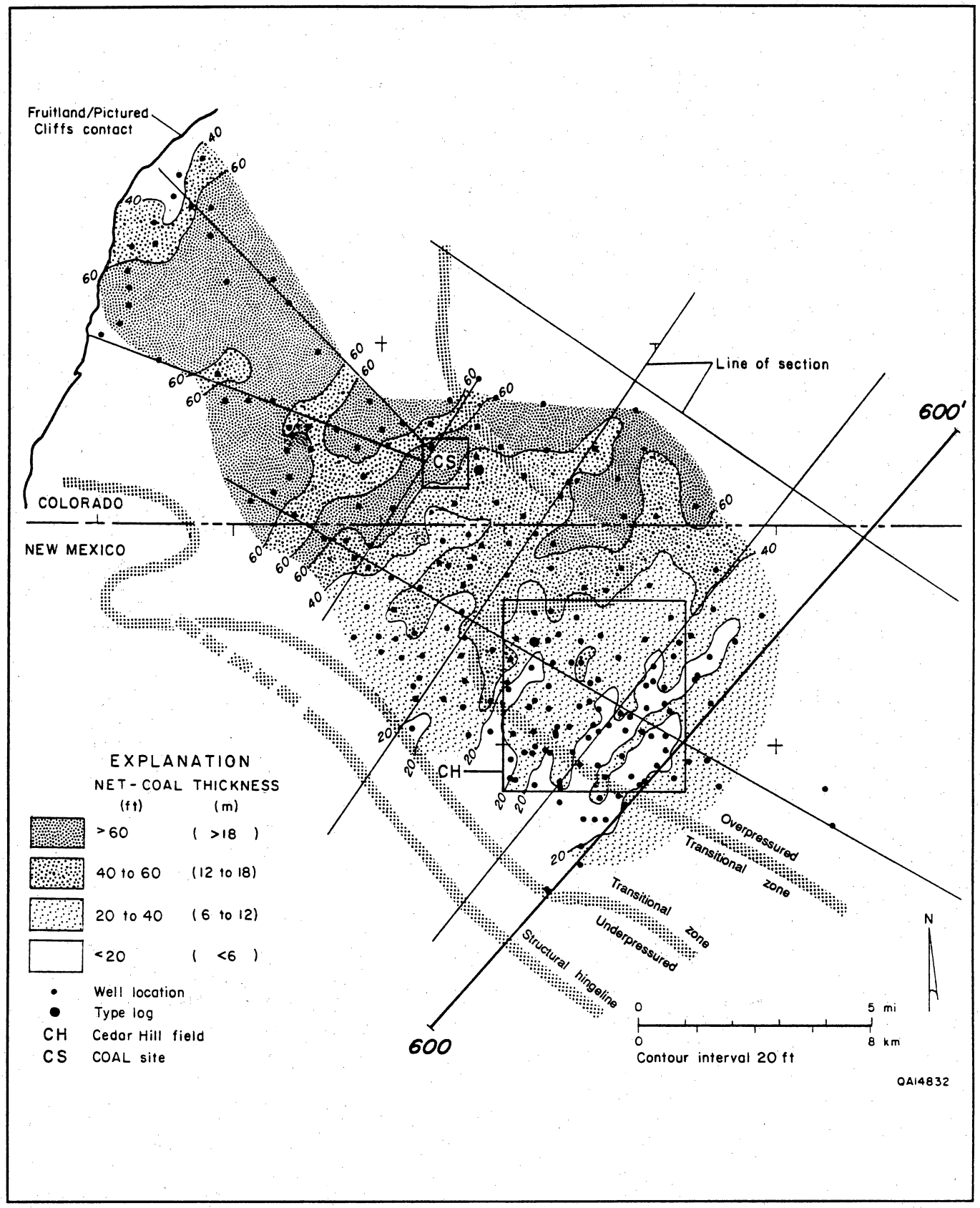

Figure 9. Coal isolith map of the undivided coal group C, which overlies LF2 (lower Fruitland sandstone) at Cedar Hill field and the COAL site.

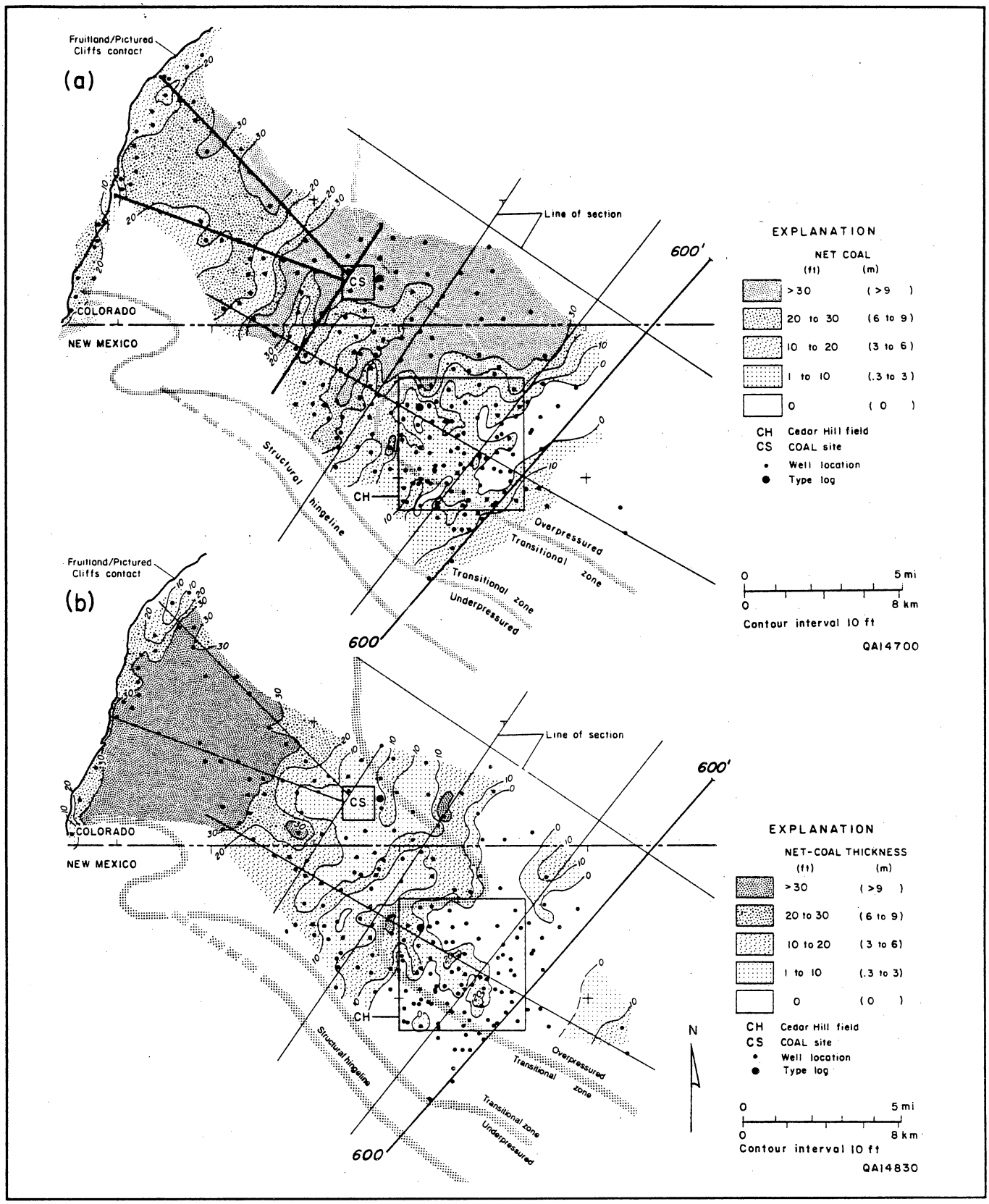

Figure 10. (a) Coal isolith map of lower C coal seams at Cedar Hill field and the COAL site. Lower C coal seams are absent over thick LF2 sandstones (fig. 6a) in the eastern part of Cedar Hill field. (b) Coal isolith map of middle C coal seams. Net coal thickness of middle C coal seams is less than that of lower C coal seams at the COAL site. However, middle C coal seams thicken northwestward toward the Fruitland outcrop.

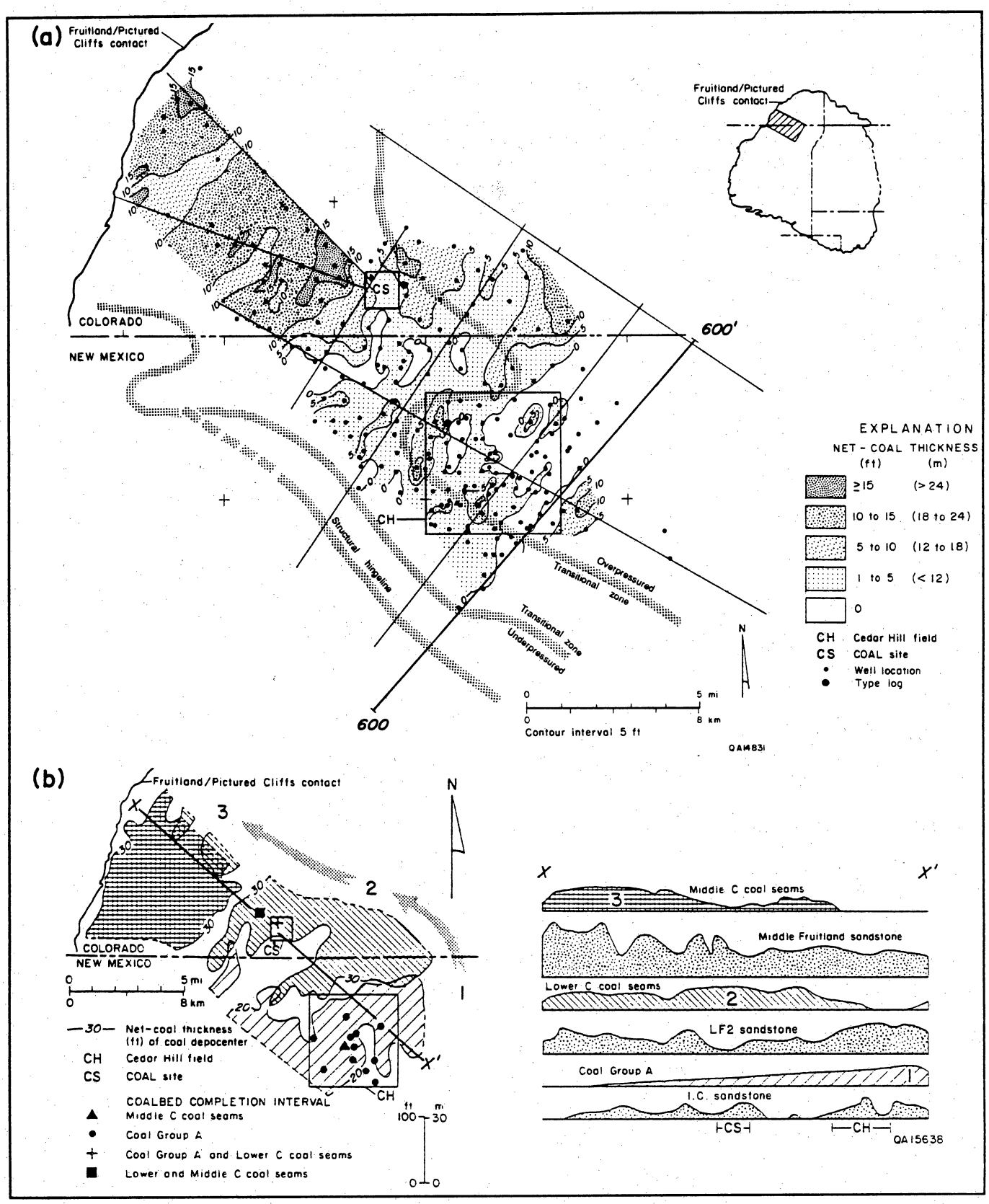

Figure 11. (a) Coal isolith map of coal group D in the upper Fruitland subunit. (b) Fruitland coal depocenters (A, lower C, and middle C) and well distribution by coalbed completion interval at Cedar Hill field and the COAL site. Coal depocenter, defined by area of greatest net coal thickness, shifted northwestward with time. Net thickness of lower C coal beds is inversely related to thickness of underlying Fruitland sandstone, LF2.

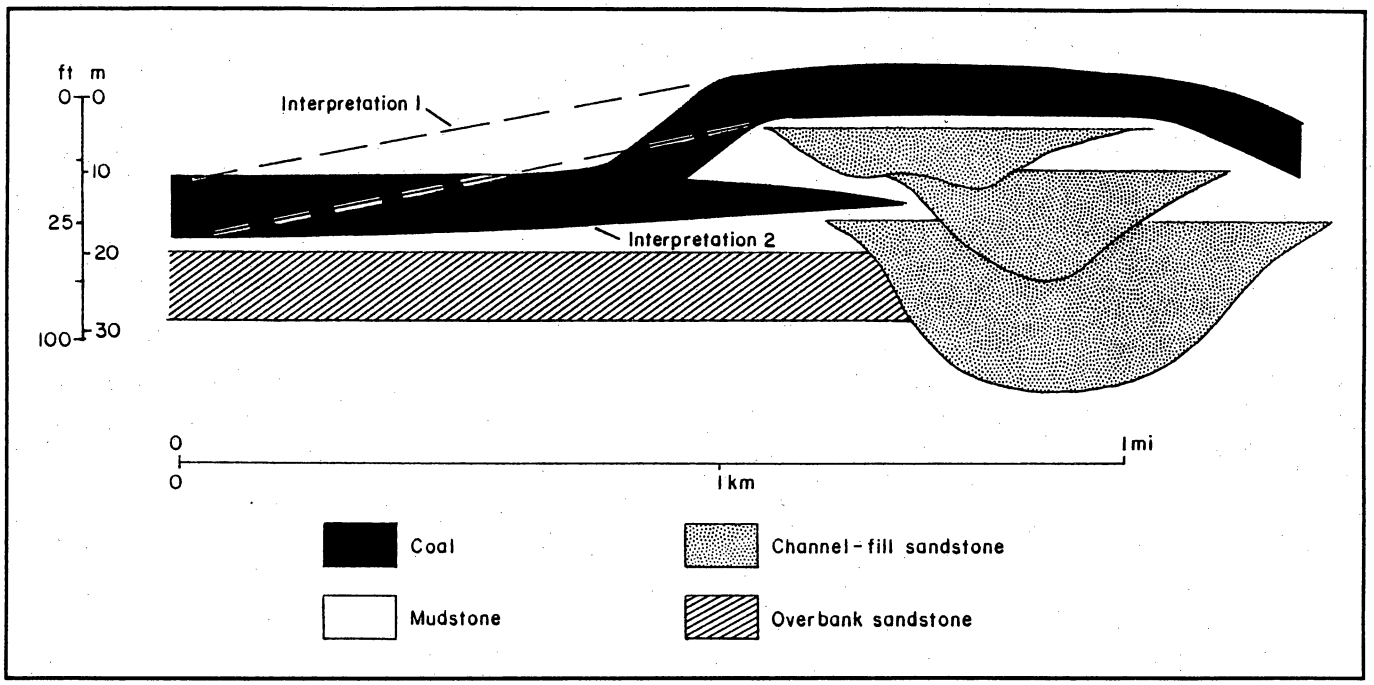

Figure 12. Either abrupt or gradual changes in structural attitude of coal seams may be interpreted where seams override lenticular channel-sandstone bodies, which are less compactable than the coal seams and mudstones.

At Cedar Hill field and the COAL site, coal seams occur above or below channel-fill sandstones complexes that are less than 2,000 ft (600 m) wide. Therefore, changes in structural attitude of overriding coal seams are inferred to be abrupt (occurring over distances of hundreds of feet) rather than gradual (occurring over distances of several thousands of feet) (fig. 12). In a cross section located near the northwestern margin of the basin, stratigraphic relief on Fruitland coal seams is as great as 60 ft (18 m) where coal seams underlie or override thick (up to 80 ft [24 m]) channel sandstones (fig. 13).

The COAL site is located in a northeast-trending structural trough (fig. 14). At the site, structural relief on the lower C coal seam is 50 ft (15 m) (fig. 15). This structural relief is due to tectonic deformation and the relation of the coal seam to Fruitland channel-fill sandstones above and below the seam. The sandstone above this coal seam in the Amoco No. I-1 So. Ute well trends northeastward (fig. 16) and coincides with the structural trough mapped on the lower C coal seam (figs. 14 and 15). This channel-fill sandstone complex is 30 ft (9 m) thick and is less than 2,000 ft (600 m) wide.

The significance of continuous coal seams that override and underlie sandstones but are sharply folded at facies boundaries is twofold: (1) coal seams (methane reservoirs) are more extensive than inferred by previous workers, and (2) folding-induced fractures, and therefore enhanced coalbed permeability, may occur where coal seams are associated with sandstone complexes.

Fruitland Reservoir Characteristics and Production

Reservoir characteristics of coal beds vary regionally and locally. Assessment of coalbed reservoirs requires knowledge of (1) gas occurrence and resources, (2) gas composition, (3) coalbed permeability, and (4) pressure regime and fracture-filling fluids (Kaiser and others, this vol.). These parameters, in turn, are controlled by the structural setting, regional cleat trends, and coalbed occurrence, thickness, depth, and rank.

Coal Occurrence, Trends, and Thickness

Greatest thickness of Fruitland coal beds occurs in the northern San Juan Basin in northwest-trending belts of back-barrier and coastal plain coal, where net thickness exceeds 50 ft (15 m) (Ayers and others, this vol.). Extending southeastward from these northwest-trending belts are northeast-trending, dip-elongate belts of floodplain coal deposits, 1 to 8 mi (1.6 to 12.8 km) wide where net coal thickness is 30 to 70 ft (9 to 21 m). Cedar Hill field and the COAL site are located at the intersection of these two major coal trends. Discontinuous coal beds (reservoirs) in this area occur where coastal plain coal beds split or pinch out landward (southwestward) into muddy floodplain deposits or along strike (northwest-southeast), where they interfinger with fluvial complexes.

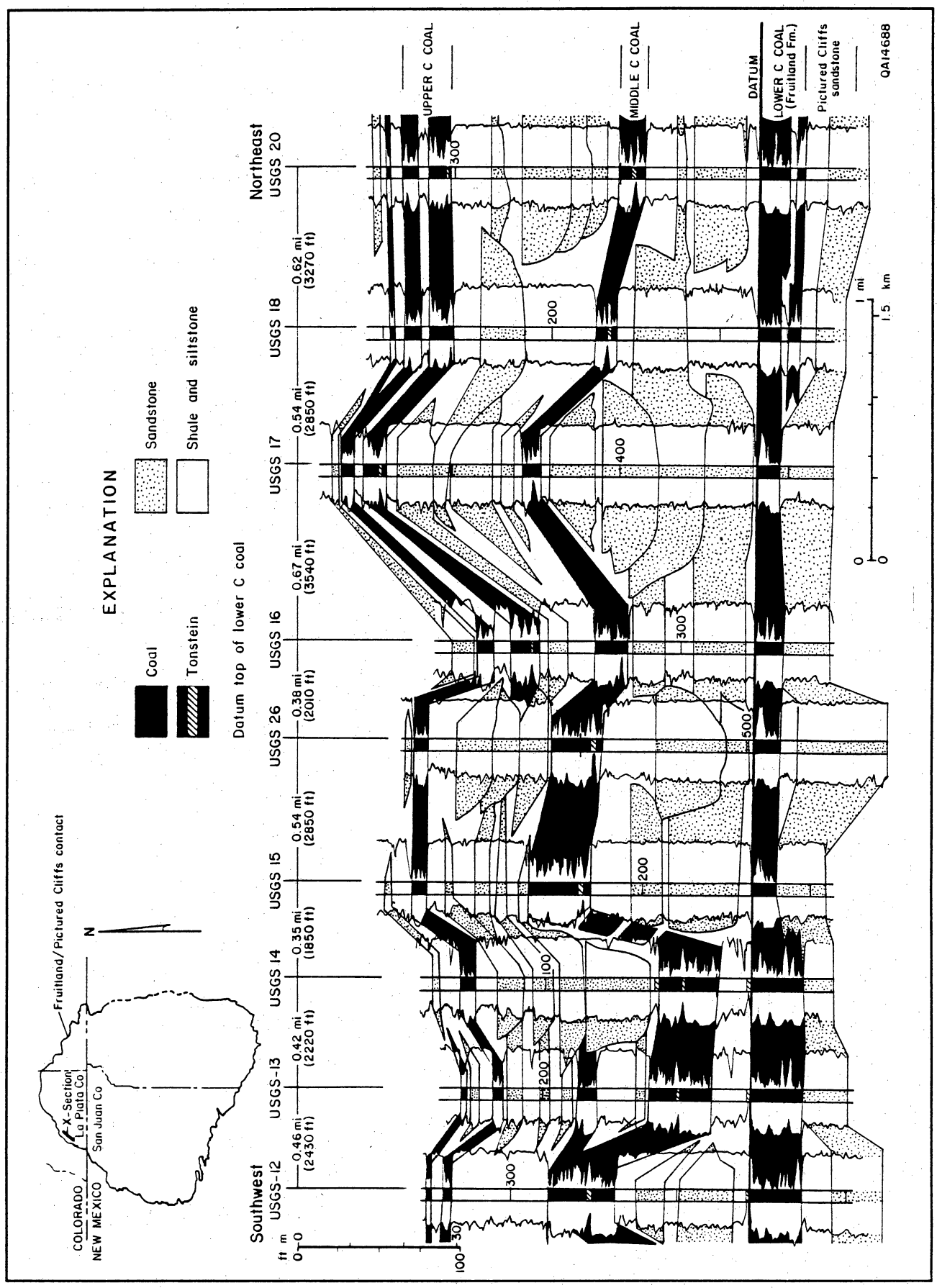

Figure 13. Fruitland coal and sandstone architecture, northwestern San Juan Basin. Coal seams are complex reservoirs where they overlie, underlie, or pinch out between channel-fill sandstones. Cross section is near the Fruitland outcrop. Data from Roberts (1989).

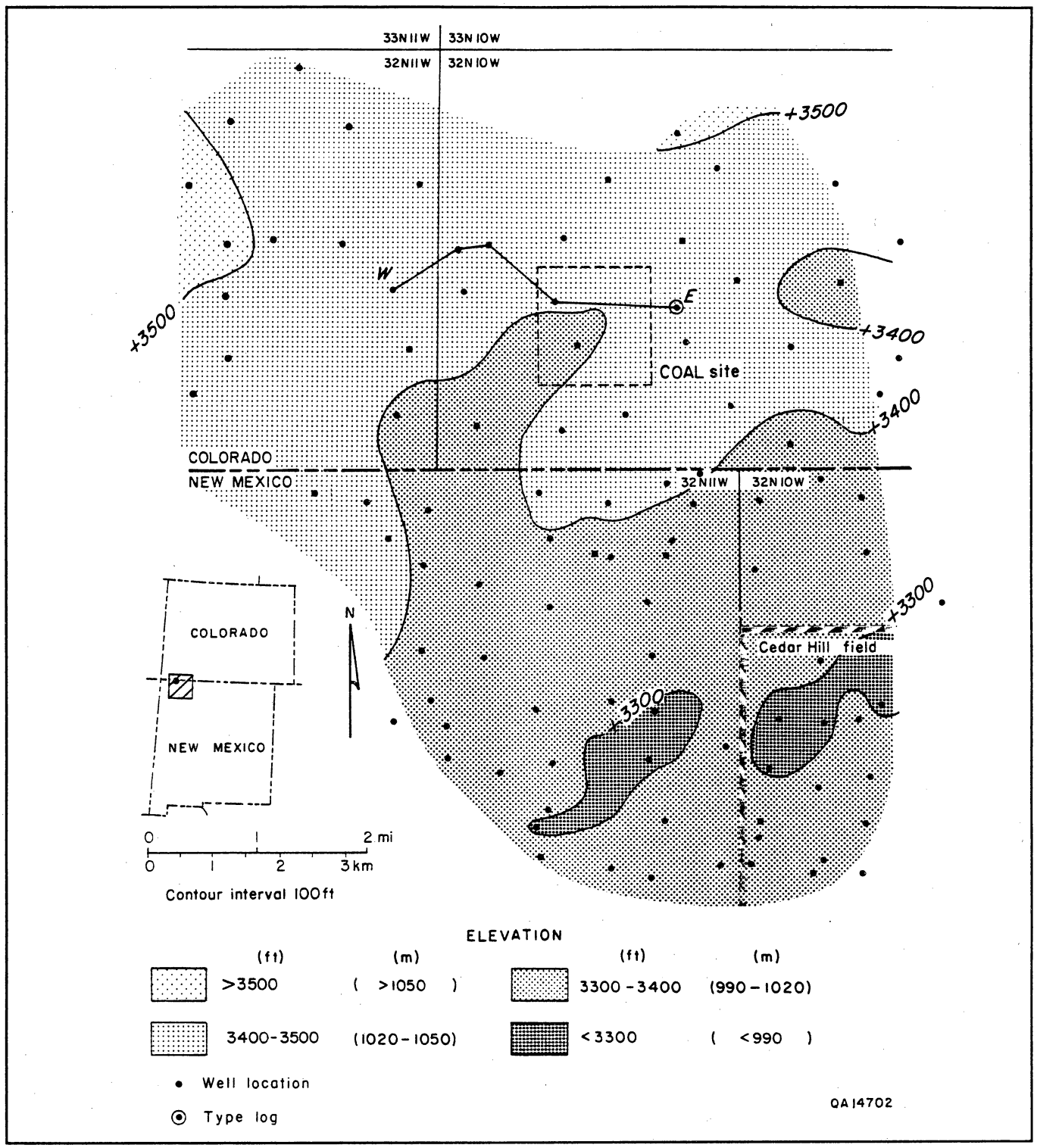

Figure 14. Structure map of the base of the lower C coal seam at the COAL site. Cross section W–E is shown in figure 15.

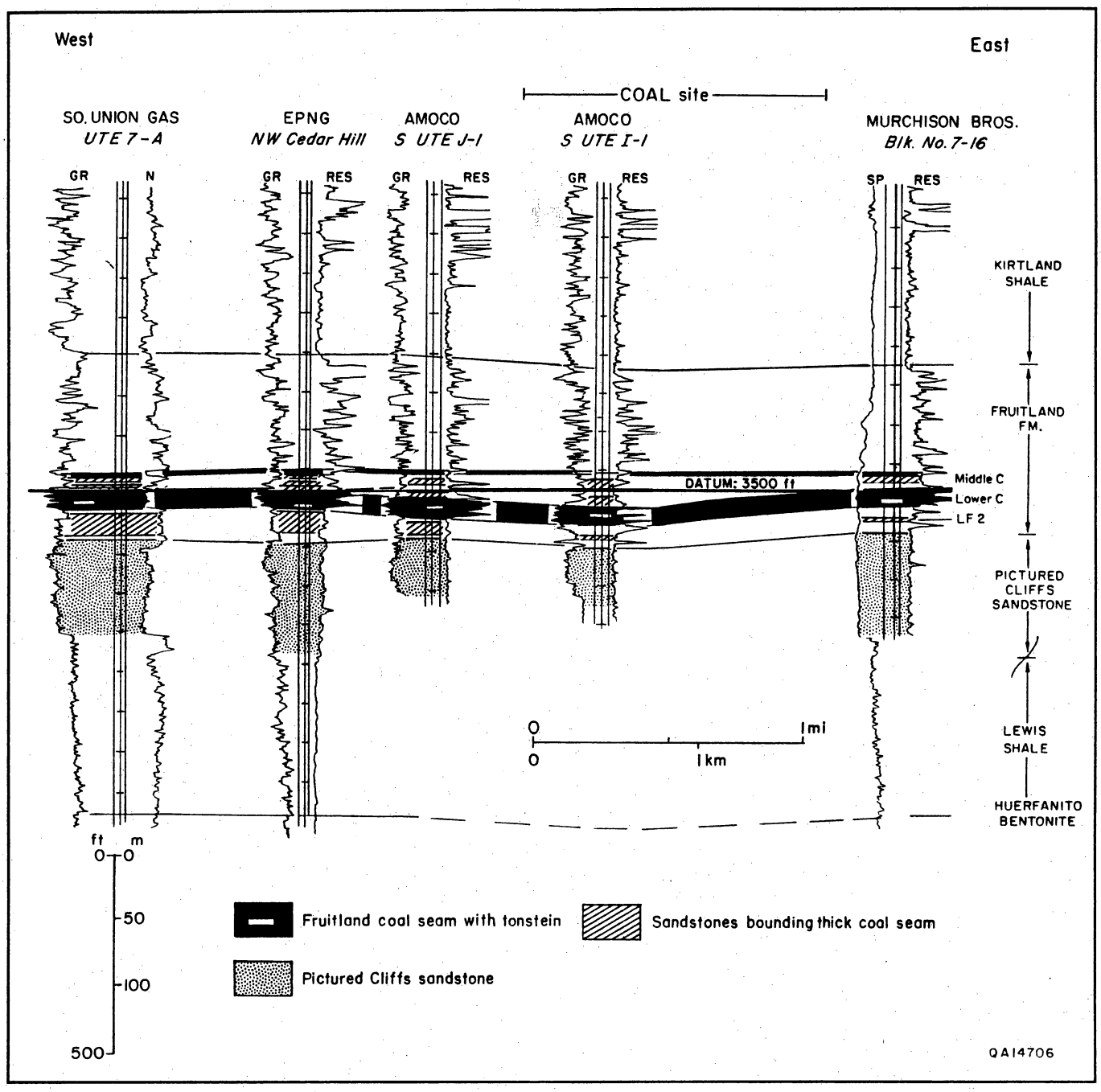

Figure 15. Structural strike section W–E. As much as 50 ft (15 m) of structural relief exists on the lower C coal seam because of tectonic and compactional deformation. See figure 14 for location.

Coal Rank

The quantity of methane generated and stored by coal beds varies directly with rank, or thermal maturity, of the coal. Cedar Hill field is located at the transition between high-volatile B and A bituminous coal (vitrinite reflectance 0.78 percent) (Scott and others, this vol.). Southwest of Cedar Hill field is a rather abrupt decrease in vitrinite reflectance values coincident with the structural hingeline (Ayers and others, this vol.). Offset of coal beds along the hingeline, coupled with southwestward pinch-out of floodplain coal beds, may have inhibited the southwestward migration of fluids derived from the thermally mature northern part of the basin.

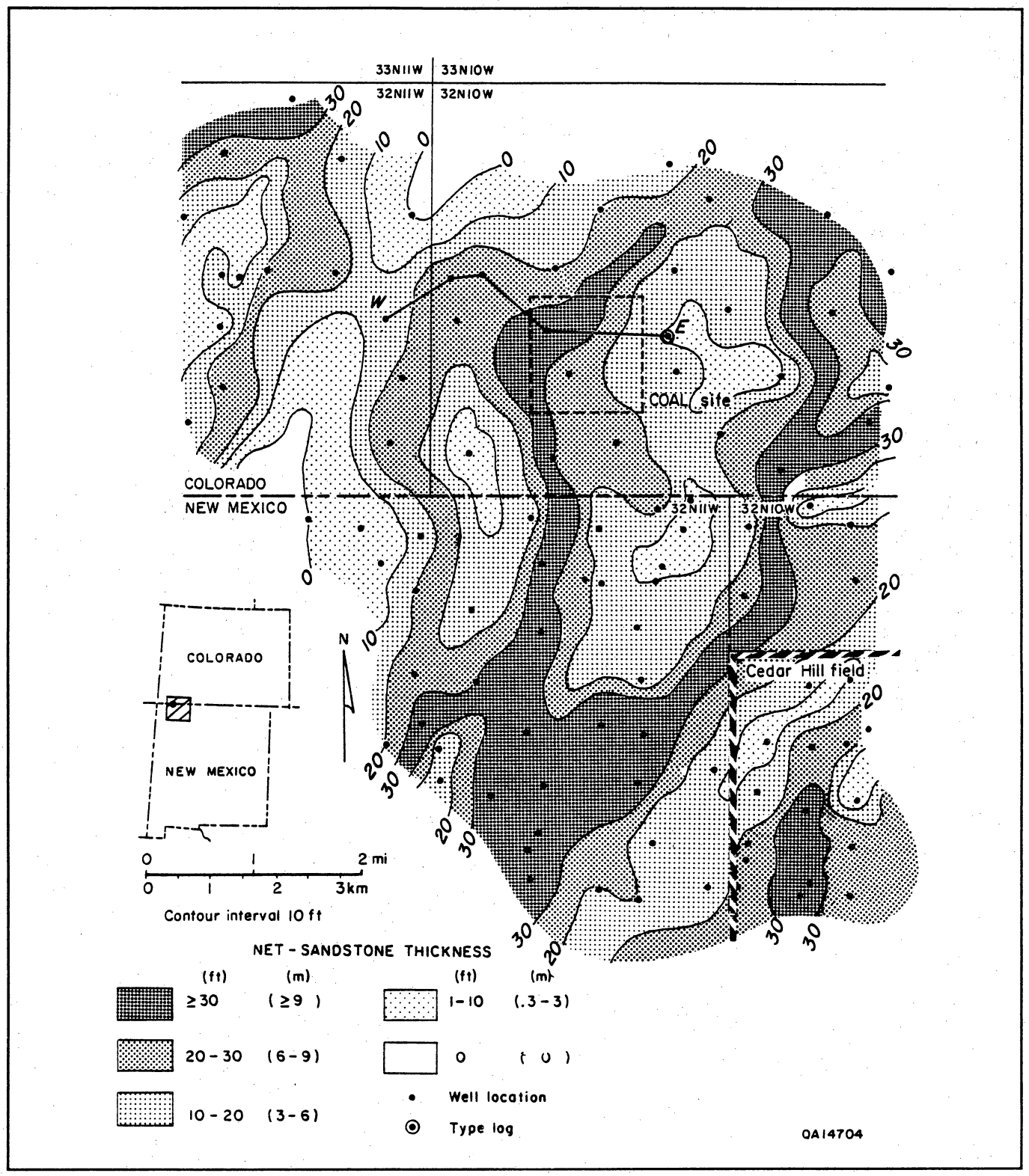

Figure 16. Sandstone isolith map of the Fruitland fluvial complex directly overlying the lower C coal seam at the COAL site. Cross section W–E is shown in figure 15.

Formation Pressure

Methane storage capacity of coal is also pressure dependent. In the San Juan Basin, the Fruitland Formation is abnormally pressured relative to the freshwater hydrostatic gradient (0.433 psi/ft). The north-central part of the basin is overpressured, whereas much of the rest of the basin is underpressured (Kaiser and others, this vol.). Because Fruitland overpressuring is due to hydrodynamics, most overpressured coalbed methane wells are water productive. The pressure gradient at Cedar Hill field, which is located near the southwestern margin of regional Fruitland overpressuring, is approximately 0.50 psi/ft. At Cedar Hill field, the southwest boundary of overpressured Fruitland strata conforms to a synclinal fold (fig. 4). The transition between overpressured and underpressured Fruitland strata is marked by pronounced steepening of the potentiometric surface and potential for upward flow (Kaiser and others, this vol.). High productivity from overpressured Fruitland coal beds near the transition zone may reflect potential for upward flow and free gas in conventional stratigraphic traps along the southwestward pinch-out of aquifer coal beds.

Coalbed Methane Resources

The Cedar Hill field area includes some of the highest values for Fruitland gas in place (more than 25 Bcf/mi^2) in the San Juan Basin. This high gas resource reflects the presence of thick coal beds, high coal rank, and high formation pressure (Ayers and others, this vol.). Cedar Hill field is in a transitional area where gas-in-place values range from 15 to 25 Bcf/mi^2. This range reflects the change from the locally thick, northeast-trending floodplain coal deposits in the southern part of the basin to the extensive, thick, northwest-trending delta plain and back-barrier coal deposits in the northern part of the basin.

Controls on Coalbed Permeability

Permeability in coal beds is controlled by the intensity and interconnectedness of fractures. The orientation of coalbed cleats (fractures) is determined by regional stresses present during coalification. At Cedar Hill field, face cleats (dominant fracture) trend northeastward (Tremain and others, this vol.). Also, Cedar Hill field is bisected by a synclinal axis (Ayers and others, this vol.). Coal beds in this east-plunging syncline (fig. 4) are folded, and therefore may have high fracture intensity and enhanced permeability. Coalbed continuity in the Cedar Hill field area is partly controlled by the structural hingeline of the basin, which is inferred to comprise a complex of northwest-trending normal faults. Individual faults in this complex offset coal beds by as much as 50 ft (15 m).

Gas Production Trends

The most productive coalbed methane wells in the San Juan Basin are completed in overpressured Fruitland coal beds along the southwestern margin of the overpressured region (Kaiser and others, this vol.). This highly productive trend occurs in thick Fruitland coal beds of delta plain and back-barrier origin and includes Cedar Hill field. In this northwest-trending belt, highest production (more than 1,000 Mcf/d) is in locally occurring, northeast-trending patterns that reflect the presence of thick, interdistributary coal beds.

Production at Cedar Hill field reflects geologic controls; coal beds, channel-fill sandstones, and production trends (fig. 17) all trend northeastward. Individual coalbed methane wells in the field typically produce 300 to more than 1,000 Mcf/d. In 1980 the average coalbed gas production per well at Cedar Hill field was approximately 600 Mcf/d; by 1990, average well production had increased to 1,000 Mcf/d. Northeast-trending belts of high production (maximum production more than 1,500 Mcf/d) in the southwestern part of the field coincide with thick (locally more than 30 ft [9 m]) basal Fruitland coal beds (coal group A; fig. 8b). In contrast, low production (maximum production less than 500 Mcf/d) in the southeastern part of Cedar Hill field coincides with thin coal beds in coal groups A and C (figs. 8b and 9). The most productive wells (maximum production more than 1,800 Mcf/d) are on the southern flank of the synclinal axis in the eastern part of Cedar Hill field (fig. 10), where folding may have caused fracture-enhanced permeability.

Additional Reservoir Characteristics

Gas Composition

At Cedar Hill field and throughout the overpressured, northern part of the basin, Fruitland coalbed gases are chemically dry (C_1/C_{1-5} values greater than 0.94) (Scott and others, this vol.). However, the COAL site is 3 mi (4.8 km) southwest of the transitional zone of overpressured Fruitland strata, and Fruitland coalbed gases are chemically wet (C_1/C_{1-5} values less than 0.94) in this area. Carbon dioxide content of Fruitland coal beds also changes abruptly across the northwest-trending pressure transition, between Cedar Hill field and the COAL site. At Cedar Hill field, carbon dioxide content ranges from less than 3 percent to more than 6 percent, whereas at the COAL site it is less than 1 percent (Scott and others, this vol.). Both gas wetness and carbon dioxide content mimic the pressure and structural contours, consistent with interpretation of structural control on formation pressure, fluid migration, and gas composition. Further geologic control on Fruitland coalbed gas composition is suggested by tongues of high carbon dioxide gas that extend southwestward

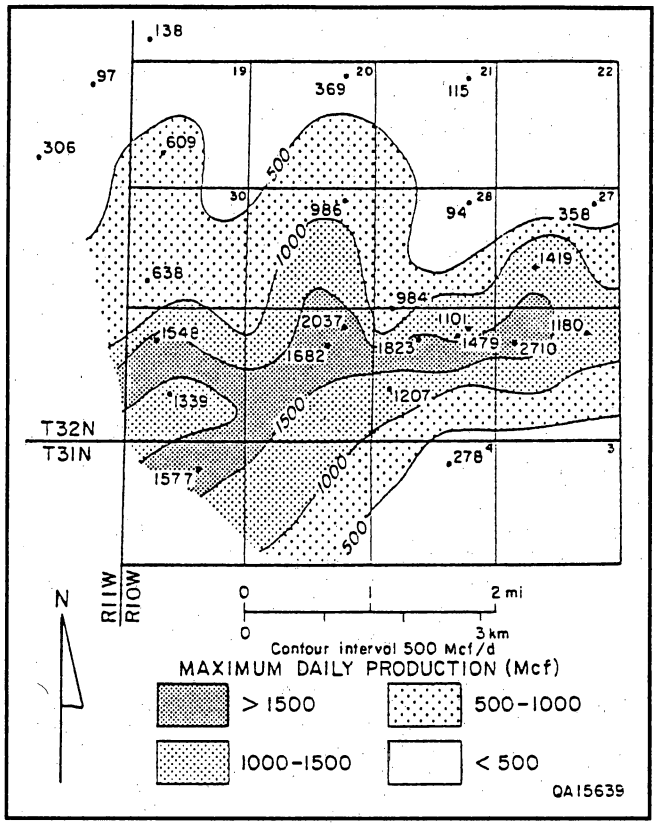

Figure 17. Fruitland coalbed methane production at Cedar Hill field. Values are average daily production (Mcf/d) in the well's most productive year.

from the overpressured area and coincide with thick Fruitland floodplain coals south of Cedar Hill field (Scott and others, this vol.).

Produced Water

Overpressured wells in Cedar Hill field commonly produce water, requiring disposal of brines and adding to operation costs. Areas of greatest water production (20 to 152 bwpd) in Cedar Hill field occur in central and eastern areas along the syncline that bisects the field. Wells in Cedar Hill field are still dewatering; in 1980 the average water production per well was approximately 200 bwpd. By 1990, average water production had declined to 20 bwpd per well.

Conclusions

1. At Cedar Hill field and the COAL site, four Fruitland coal groups occur in three Fruitland depositional subunits. The characteristics of coal seams in these groups were determined by depositional setting. The thickest, most continuous coal seams occur in the lower and middle Fruitland subunits; these seams (coal groups A and C), which formed in a delta plain setting, are of subregional extent and commonly continue over or under channel-fill sandstone bodies. In contrast, upper Fruitland coal beds (coal group D) are thin and discontinuous; they formed in a floodplain setting and are bounded by channel-fill sandstone bodies.

2. Although lower and middle Fruitland coal groups (groups A and C) are extensive, they are not present, or equally well developed, throughout the area. At Cedar Hill field, the thickest and most extensive coal seams occur in group A, but these seams pinch out near the northwestern margin of the basin. At the COAL site, seams are best developed in coal group C, which is thin or absent to the southeast, at Cedar Hill field.

3. Increased fracture intensity, and therefore enhanced coalbed permeability, may occur where coal seams are folded. Tectonic folding has formed synclines at Cedar Hill field and the COAL site. Also, many lower and middle Fruitland coal seams are folded where they underlie and overlie northeast-trending channel-fill sandstone complexes. At the COAL site, structural relief on the thickest Fruitland seam is 50 ft (15 m).

4. Cedar Hill field is located at the southwestern margin of regionally overpressured Fruitland strata. The northwest-trending structural hingeline south of Cedar Hill field nearly coincides with the overpressure/underpressure boundary. The hingeline may result from a northwest-trending fault complex that offsets overpressured, water-saturated coal beds in the northern part of the basin from underpressured, predominantly gas-saturated coal beds in the southern part of the basin. Existence of this fault complex remains to be proven, but if present, it should be detectable on seismic sections.

5. Coalbed gas occurrence and producibility in Cedar Hill field are primarily controlled by the depositional setting; productivity trends are dominantly northeast-trending in the field and coincide with thick, northeast-trending coal beds that formed in interdistributary areas on a crevasse-splay platform. Other coalbed methane production trends in the area are controlled by structure; a high-productivity trend occurs along a syncline that bisects Cedar Hill field. Coalbed permeability may also be enhanced where coal beds are locally fractured because of differential compaction.

Acknowledgments

This manuscript benefited from reviews by Jay C. Close, Richard C. Klem, Tucker F. Hentz, and Andrew Scott. Amoco Production Company and Dwight's Energydata Company provided data on gas and water production.

Geologic Controls on Fruitland Coal Occurrence, Thickness, and Continuity, Navajo Lake Area, San Juan Basin

Walter B. Ayers, Jr., and Sarah D. Zellers

Abstract

The most productive coalbed methane wells in the United States, with production commonly greater than 250 Mcf/d per well, occur in the Navajo Lake area. Coal-occurrence, lithofacies, structure, and isopach maps were made to clarify geologic controls on coalbed methane resources and producibility in this area. Structural activity and depositional systems controlled coal occurrence. The thickest coal deposits trend northwestward and occur in a back-barrier setting; increased subsidence north of a structural hingeline created accommodation space and initiated a shoreline stillstand, allowing thick, strike-elongate peat deposits to form. Individual coal beds are dip elongate but laterally continuous, pinching and swelling in the paleostrike direction. Coal beds are the major aquifers in the Fruitland; they are more permeable than adjacent Fruitland and Pictured Cliffs sandstones. Therefore, coalbed geometry and extent control hydrologic and reservoir conditions in the Fruitland Formation. Structural features in Fruitland coal beds are both tectonic and compactional in origin; minor folds are common. Structural attitude of coal beds is unique to each coal bed. High productivity from coalbed methane wells in the Navajo Lake area is attributed to presence of thick coal beds (reservoir rock), Fruitland hydrodynamics, and enhanced coalbed permeability, possibly because of folding-induced fractures.

Introduction

Geologic controls on coalbed methane occurrence and producibility commonly are more complex than is apparent from regional studies. Therefore, we used closely spaced data to study these controls in the Fruitland Formation at Navajo Lake in northern San Juan and Rio Arriba Counties, New Mexico (Ayers and others, this vol., their fig. 5). This area, encompassing 215 mi² (557 km²) and including the Northeast Blanco Unit and the Meridian 400 coalbed methane wells, was selected because it (1) contains some of the thickest Fruitland coal beds in the San Juan Basin, (2) contains two upper Pictured Cliffs sandstone tongues that bound the thick coal, causing a major stratigraphic rise of the Pictured Cliffs, (3) has the most productive coalbed methane wells in the basin and a history of coalbed methane production extending from the early 1950's, and (4) has no major structural features in the area that might contribute to the high productivity.

Objectives

The objectives of this study were to (1) evaluate the structural evolution of the San Juan Basin as it applies to the distribution and maturation of Fruitland coal, (2) define depositional systems and evaluate the interconnectedness of depositional framework (sandstone) facies, (3) define the occurrence and continuity of coal seams and evaluate framework facies control on coal occurrence, geometry, and trends, (4) identify structural features that may enhance coal permeability or affect coalbed continuity, and (5) relate coalbed methane reservoir conditions to the geologic and hydrologic settings.

Methods

The primary data used for this study were approximately 400 geophysical well logs from oil and gas tests. Geophysical logs were used to make 10 interlocking cross sections, and all remaining logs were correlated to those sections. Structure, isopach, lithofacies, and coal data from the logs were tabulated in computer files and were used to make computer-contoured maps and to post data for hand contouring. The cross sections and maps were then evaluated to interpret geologic controls on the occurrence and producibility of coalbed methane.

Regional Geologic Setting and Stratigraphy

During the Late Cretaceous, the region of the present San Juan Basin was on the western margin of the Western Interior Seaway (Tremain and others, this vol., their fig. 2). In the Late Cretaceous (Campanian), the coastline migrated northeastward, resulting in deposition of

***In* Ayers, W. B., Jr., and others, 1991, Geologic and hydrologic controls on the occurrence and producibility of coalbed methane, Fruitland Formation, San Juan Basin: The University of Texas at Austin, Bureau of Economic Geology, topical report prepared for the Gas Research Institute under contract no. 5087-214-1544 (GRI–91/0072), p. 69–94.**

a vertical succession of shelf (Lewis Shale) through coastal (Pictured Cliffs Sandstone) to coal-bearing continental sediments (Fruitland Formation) (fig. 1).

The contact between the Pictured Cliffs Sandstone and the Fruitland Formation (fig. 1) was placed at the top of the massive coastal sandstone complex below the lowermost Fruitland coal; because the shoreline migrated basinward, this boundary is time-transgressive. The Fruitland–Kirtland contact was placed at a high-conductivity peak that occurs in a shale at the top of an upward-fining Fruitland sequence (fig. 1). This shale is inferred to be the base of the regionally extensive lower Kirtland shale, which may have formed as a consequence of a short-lived marine transgression over the Fruitland coastal plain. The Kirtland Shale (Campanian/Maestrichtian) conformably overlies the Fruitland Formation and is unconformably overlain by the fluvial Ojo Alamo Sandstone (Paleocene). For a more detailed stratigraphic review, see Ayers and others, this volume.

Structural Evaluation

Structural activity has impacted the availability and producibility of coalbed methane in four ways: (1) syndepositional structural activity influenced depositional systems and, hence, coal occurrence; (2) the structural development of the San Juan Basin affected the burial depth and thermal maturity of Fruitland coal seams; (3) structural deformation caused fractures that may offset the coal beds (reservoirs); and (4) minor folds form structural traps, and fractures that formed during folding may enhance coalbed permeability.

Structure of Huerfanito Bentonite Bed

The Huerfanito Bentonite Bed, present in the Lewis Shale throughout much of the basin (Fassett and Hinds, 1971), was used as a structural horizon and as a boundary for isopach maps. To delineate the presence of structural features that may affect the continuity of Fruitland coal seams, we made a computer-contoured structure map of the Huerfanito Bentonite. In the Navajo Lake area, structural relief on the Huerfanito Bentonite is 450 ft (135 m) (fig. 2). A major synclinal axis in the San Juan Basin crosses the northeast quarter of the area, approximately 7 mi (11 km) north of the Meridian wells. South of the synclinal axis, an anticline, centered in T30N and T31N, R7W, has 75 to 100 ft (22 to 30 m) of structural relief and plunges northward toward the syncline. It is flanked on the west by a northward-plunging syncline with similar amplitude, and on the east by a series of lower amplitude, northeast-plunging folds. Minor faults (displacements less than 50 ft [15 m]) are inferred in some areas where structural relief changes abruptly, and faults are documented in some well logs. The northwest-trending structural hingeline of the basin (Ayers and others, this vol.) crosses the southern part of the area, 1 to 5 mi (1.6 to 8 km) south of the Meridian wells (fig. 2). This hingeline is inferred to be a diffuse, complex zone of northwest-trending faults.

Elevation of Pictured Cliffs Sandstone

Throughout the San Juan Basin, the most prospective coalbed methane reservoirs are thick lower Fruitland coal seams. The elevation of the top of the Pictured Cliffs Sandstone (fig. 3) was mapped because it immediately underlies these thick coal beds, whereas the Huerfanito Bentonite Bed is 675 to 850 ft (205 to 260 m) below the Fruitland in the study area. Although this is not a true structure map because the Pictured Cliffs Sandstone is time-transgressive, the map shows, with minor differences, the structural features delineated in the Huerfanito Bentonite map (fig. 2), confirming that most structural features in the Navajo Lake area postdate deposition of the Pictured Cliffs Sandstone.

Elevation of Fruitland Formation

A structure map of the top of the Fruitland Formation (Ayers, unpublished map) also has several major features in common with the Huerfanito structure map (fig. 2). For example, in the south area of both maps, regional dip is to the north and the structural axis of the basin crosses the northern third of the maps. However, the morphology of minor structural features (in figs. 2 and 3) differs from that of the Huerfanito map, and a minor northeast-plunging anticline with less than 50 ft (15 m) of relief is located just south of the Phillips No. 6-17 well (fig. 2). There is further evidence from structure maps of coal seams that pre-Fruitland structural features may not reflect present structural attitude of Fruitland coal seams (see section on "Structural Controls on Producibility of Coalbed Methane").

Isopachous Trends

Huerfanito Bentonite–Pictured Cliffs Sandstone Isopach

Thickness variations are useful indicators of paleoslope and syndepositional structural activity. Sedimentary units commonly (but not always) thicken in the paleoslope direction and pinch and swell over uplifted and downdropped areas, respectively. The Huerfanito Bentonite–Pictured Cliffs Sandstone interval thickens from 675 ft (205 m) at the south to 850 ft (260 m) at the north end of the Navajo Lake area (fig. 4), consistent with a paleoslope to the north or northeast; basinward thickening of the interval, 175 ft over 17 mi (52 m over 27 km), averages 10 ft/mi (1.9 m/km). Slight thinning

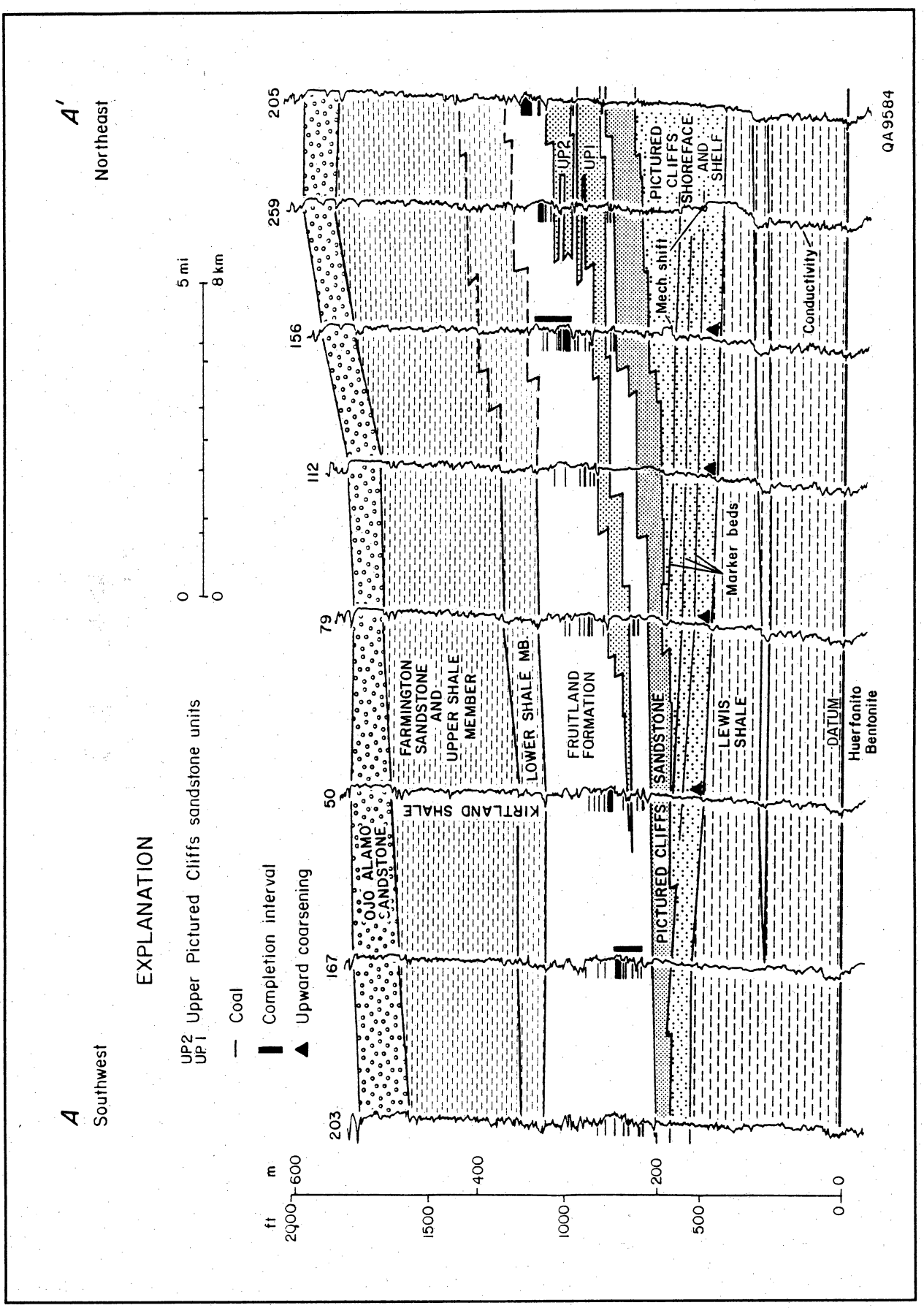

Figure 1. Stratigraphic cross section A–A'. The coal-bearing Fruitland Formation is a coastal plain unit deposited landward (southwest) of the regressive Pictured Cliffs Sandstone that prograded into the Western Interior Seaway. Thick coal seams in the northeast that overlie upper Pictured Cliffs sandstones (UP1 and UP2) are stratigraphically higher than thick seams in the southwest. See figure 2 for location.

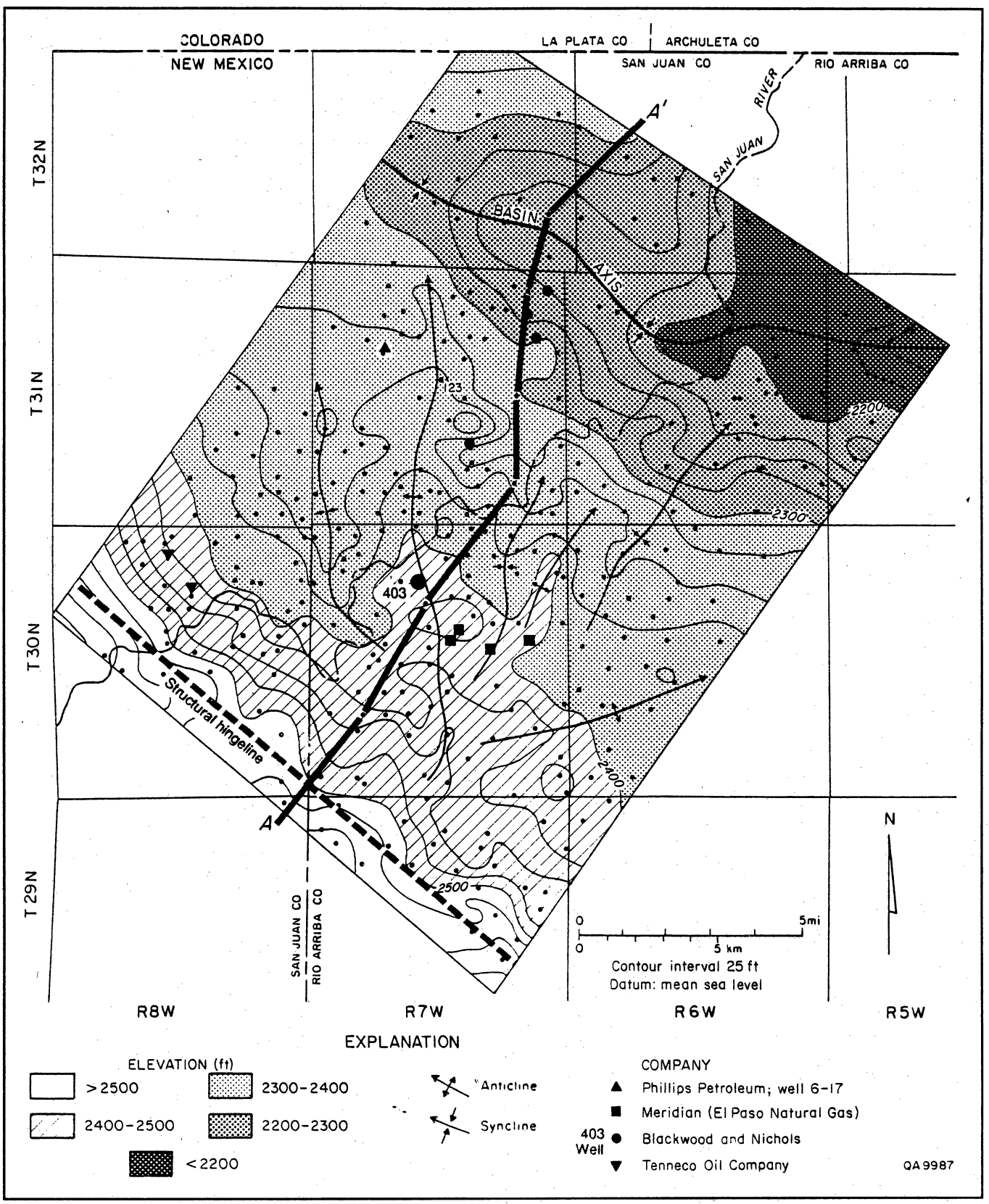

Figure 2. Structure map of the Huerfanito Bentonite Bed showing location of cross section A–A' (fig. 1). A major synclinal axis crosses the northern quarter of the area, and the structural hingeline crosses the southwest part of the map. Minor folds may form conventional traps and contribute fracture permeability to Fruitland coal seams. See Ayers and others, this volume, figure 5, for location of Navajo Lake area.

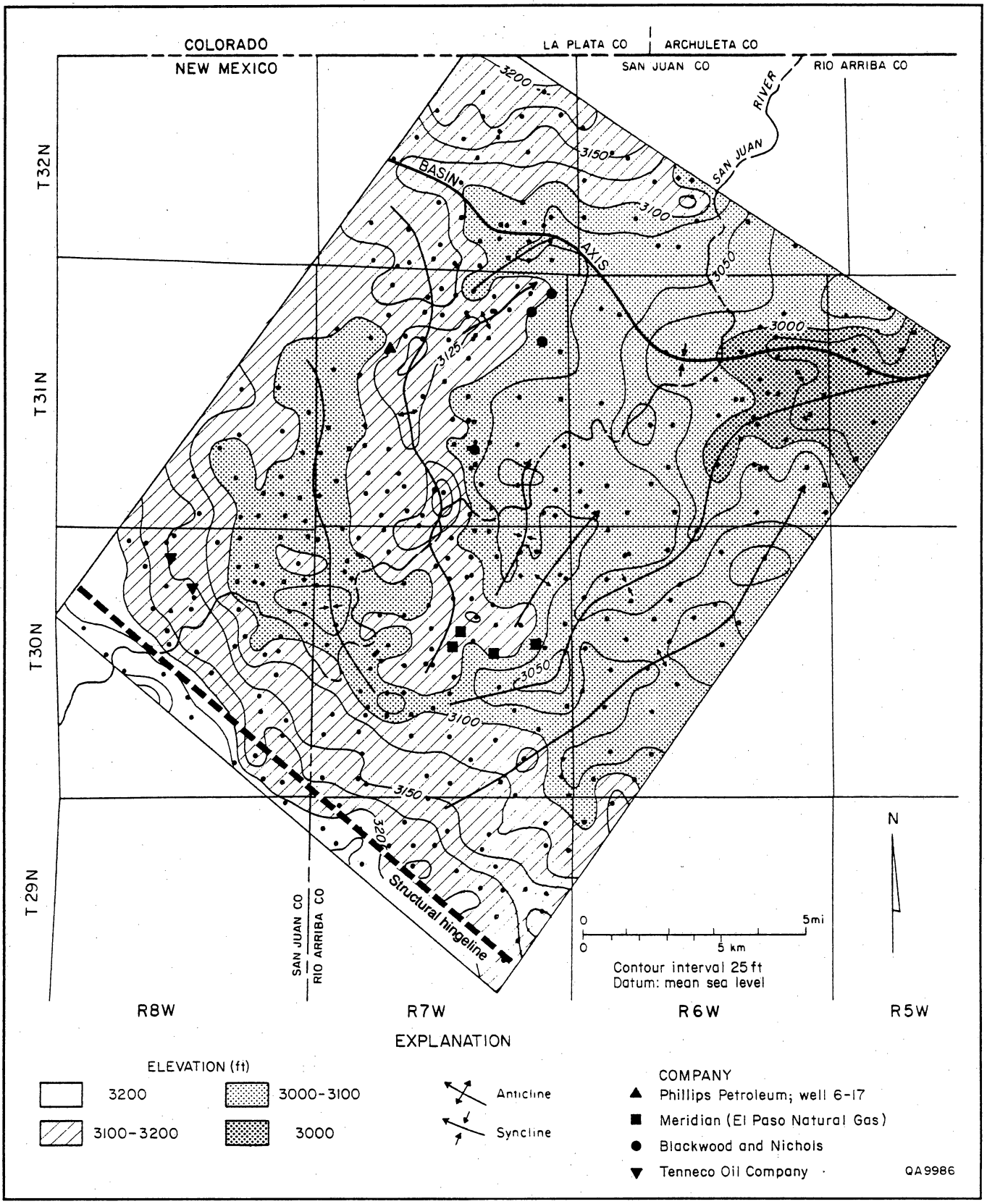

Figure 3. Elevation of the top of the Pictured Cliffs Sandstone results primarily from structural features (compare with figure 2) and secondarily from sedimentary facies changes.

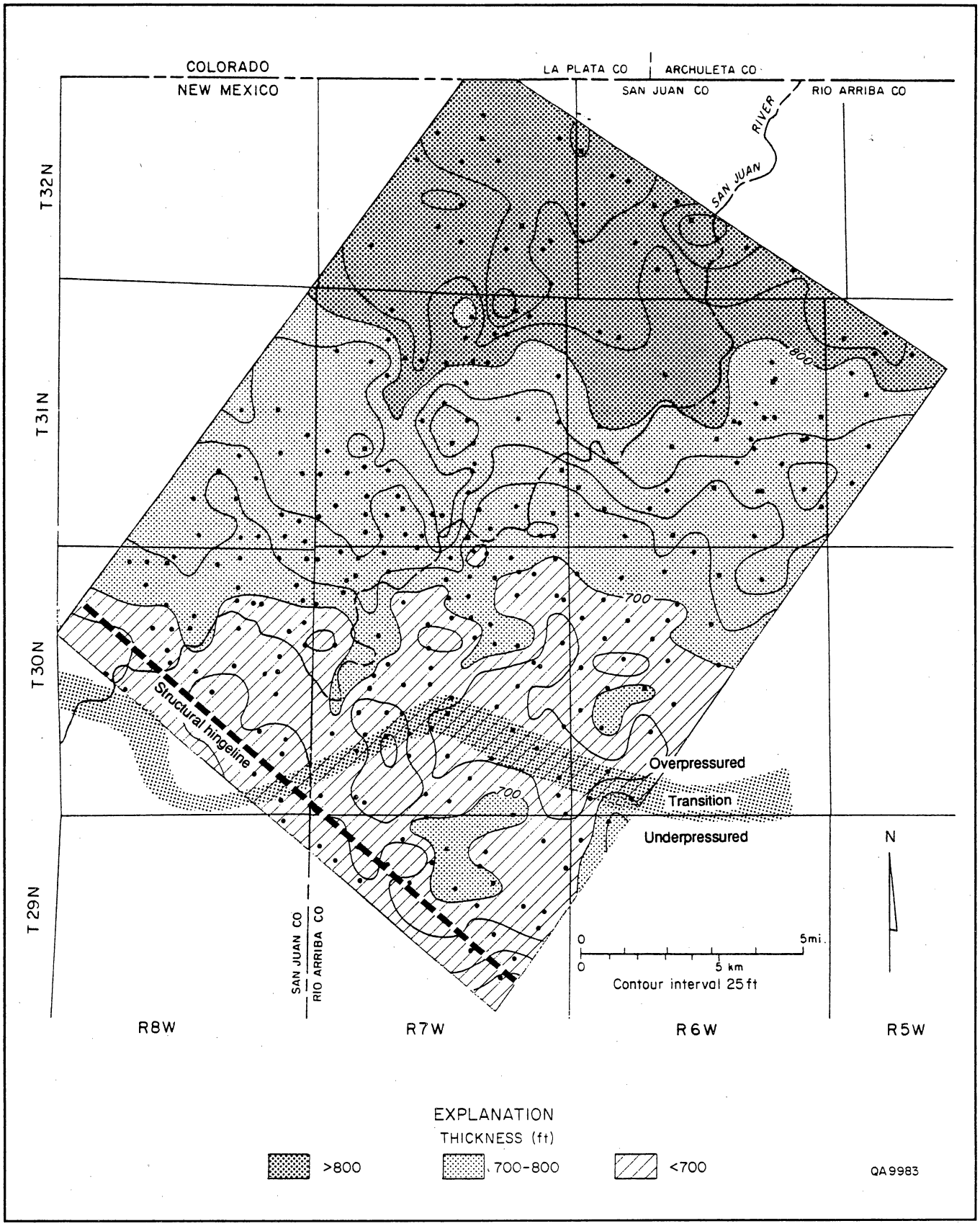

Figure 4. Isopach map from Huerfanito Bentonite Bed to top of Pictured Cliffs Sandstone. The interval thickens northward. Boundary between overpressured and underpressured Fruitland strata is from Kaiser, Swartz, and Hawkins (this vol.).

and thickening at the axes of the minor anticlines and synclines, respectively, and greater increases of thickness coincident with structural steepening on the south side of the basin axis suggest syndepositional folding (compare figs. 2 and 4). Minor increase in thickness (25 ft [7.5 m]) along the structural hingeline indicates possible syndepositional faulting.

Fruitland Formation Isopach

The Fruitland Formation thickens from 350 ft (105 m) on the east side of the area to 450 ft (135 m) on the west side of the Navajo Lake area (Ayers, unpublished map), which may reflect a depocenter in the northwestern San Juan Basin (Silver, 1951, 1957). If so, then southeastward thinning of the Huerfanito Bentonite–Ojo Alamo interval (Ayers and Zellers, 1988, their fig. 13) may not be due entirely to postdepositional erosion of the Kirtland Shale, as concluded by Fassett and Hinds (1971); uplift of the southeastern rim of the basin may have started during Pictured Cliffs–Fruitland deposition.

Sedimentary Facies

Depositional framework facies are composed of the coarsest sediment and are deposited by the highest energy processes operating within a depositional system; they are the skeletons of the depositional systems. In the Pictured Cliffs Sandstone, framework facies are barrier-strandplain, delta-front, and distributary/tidal channel-fill sandstones, and in the Fruitland Formation, framework facies are fluvial channel-fill sandstones deposited by rivers that carried sediments to the Pictured Cliffs shoreline.

Sediments marginal to the framework facies, representing deposition by lower energy processes acting in many environments, collectively are called nonframework facies. Nonframework facies of Pictured Cliffs barrier-strandplain and deltaic systems are washover fan, tidal flat, lagoon, back-barrier marsh, and delta plain; common nonframework facies in Fruitland Formation are natural levee, floodplain, lacustrine, and swamp (coal) facies. To determine controls on coal occurrence, thickness, and trends, we mapped depositional framework facies in the coal-bearing Fruitland Formation and in the Pictured Cliffs Sandstone, which bounds Fruitland coal beds on their basinward side.

Pictured Cliffs Lithofacies

Pictured Cliffs Sandstone

Pictured Cliffs shoreline sandstones are the depositional platforms upon which Fruitland peats (coals) accumulated; ultimately these sandstones bound coal seams in the basinward (northeast) direction. In geophysical logs, the Pictured Cliffs is divisible into upper and lower units. The lower unit is composed of a series of upward-coarsening sequences that are interpreted as upward-shoaling, shelf and shoreface mudstone and sandstone interbeds (fig. 1; Ayers and others, this vol., their fig. 1). The upper unit of the Pictured Cliffs Sandstone has a blocky log signature and is interpreted to be amalgamated barrier-strandplain and/or wave-dominated deltaic sandstones. In a core from the Blackwood and Nichols NEBU No. 403, the upper unit of the Pictured Cliffs contains well-sorted and crossbedded sandstone (figs. 5 and 6). Grain size increases slightly upward to medium sand near the top of the unit, but the upper 2 to 4 ft (0.5 to 1.2 m) of the Pictured Cliffs consists of fine sand. This upper part of the unit contains planar and contorted laminae; plant fragments are common, and the interval is organic stained. In the Navajo Lake area, two successive Pictured Cliffs amalgamated sandstone units range from 40 to 120 ft (12 to 36 m) in thickness and strike northwest (fig. 7, shorelines 1 and 2), oblique to thickness trends defined in the Huerfanito Bentonite–Pictured Cliffs isopach map (fig. 4).

Upper Pictured Cliffs Sandstones (UP1 and UP2)

The Pictured Cliffs Sandstone and equivalent marine units thicken basinward above the Huerfanito Bentonite Bed of the Lewis Shale because of progradation into a subsiding basin. Note the basinward shift of the updip limits of marker beds (time lines), which originate in the shelf facies and terminate in the shoreline facies (fig. 1). Progradation of the Pictured Cliffs shoreline, dependent on complex interactions of sediment supply, basin subsidence, and eustasy, was intermittent, resulting in shoreline stillstands. Periodically, shoreline movement reversed direction, and the Pictured Cliffs shoreline migrated (transgressed) southwestward over the Fruitland Formation, resulting in intertonguing of upper Pictured Cliffs transgressive-regressive sandstone beds with the Fruitland Formation. Two upper Pictured Cliffs tongues (UP1 and UP2) are present in the Navajo Lake area (fig. 1).

Upper Pictured Cliffs tongues typically consist of crossbedded, burrowed, fine sandstone that overlies a coal-bearing lower Fruitland tongue (figs. 5 and 6). These sandstones grade upward into planar-bedded, medium sandstones that make up the upper two-thirds of the Pictured Cliffs tongue (fig. 6). UP1 and UP2 sandstones trend northwestward and are as much as 100 ft (30 m) thick (figs. 8 and 9). The Pictured Cliffs tongues thin updip (southwestward), and their boundaries were placed where net sandstone thickness is 20 ft (6 m). Together, UP1 and UP2 account for approximately 150 ft (45 m) of stratigraphic rise of the Pictured Cliffs over a 10-mi (16-km) distance from the southern third to the northern border of the study area (fig. 1).

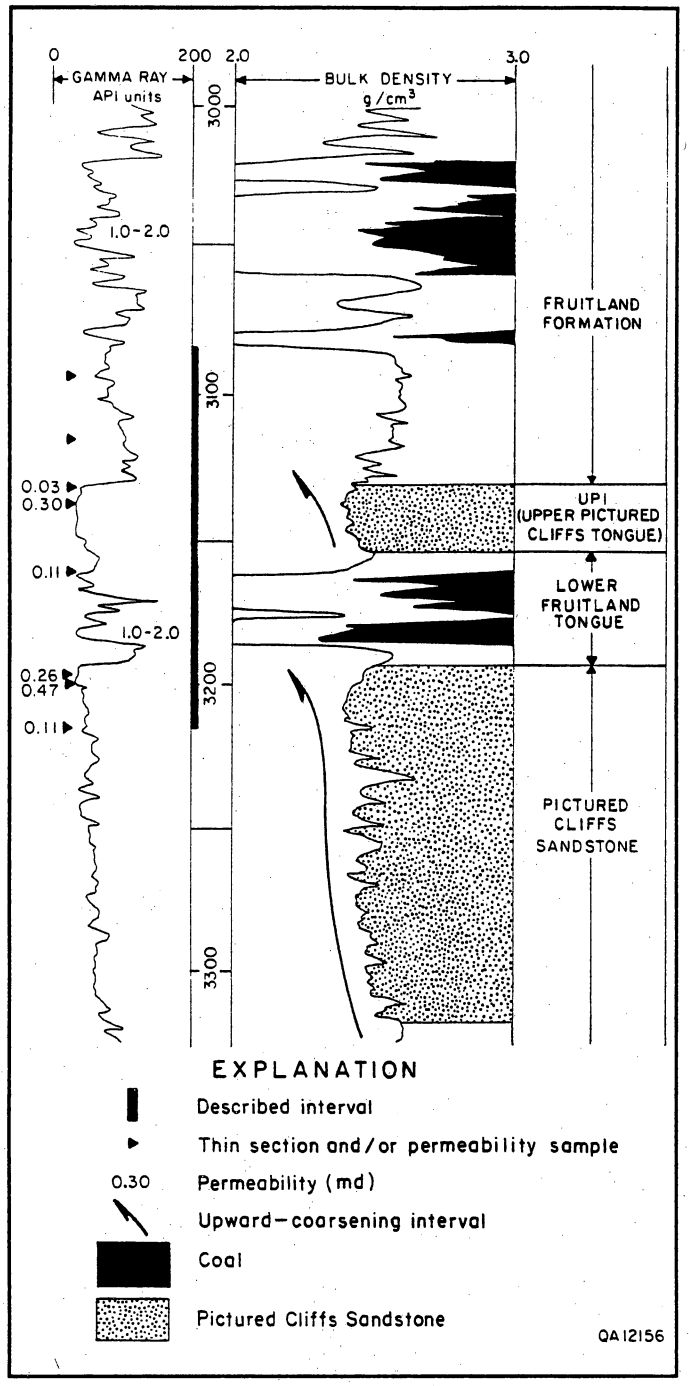

Figure 5. Gamma-density log of Blackwood and Nichols NEBU No. 403, shown in figure 2. Cored interval is described in figure 6. Permeabilities are from core plugs in sandstones and well tests in coal beds.

The depocenter of UP1, defined by the 70-ft (21-m) contour in figure 8, coincides with a depocenter of the underlying Pictured Cliffs Sandstone (fig. 7), suggesting structural or subsidence control of shoreline position. Northeast-oriented fluvial or tidal channel-fill sandstones are inferred where the 60-ft contour projects landward (southwest) from areas of more than 90 ft (27 m) of UP1 sandstone (fig. 8). UP1 pinches out basinward, northeast of the study area. UP2 overlaps UP1, but its depocenter is offset basinward (northeast) of UP1, reflecting net Pictured Cliffs regression (figs. 8 and 9). Lower Fruitland mudstone and coal that separate UP1 and UP2 in the southwest pinch out in the northeast area, where UP2 rests on UP1 (fig. 1).

Fruitland Formation Lithofacies

The coal-bearing Fruitland Formation is a coastal plain unit deposited landward of the Pictured Cliffs shoreline (fig. 1). It is composed of sandstone, mudstone, and coal interbeds. Framework facies of the Fruitland Formation were delineated in the net and percent sandstone maps (figs. 10 and 11). The net thickness of Fruitland sandstone ranges from 30 to 100 ft (9 to 30 m) (fig. 10). Net sandstone thickness is lowest in the northern third of the area where the Fruitland Formation intertongues with the upper Pictured Cliffs sandstones. Sandstone commonly comprises 15 to 30 percent of the Fruitland Formation (fig. 11). In the Navajo Lake area, individual Fruitland framework sandstones are less than 40 ft (12 m) thick and, most commonly, are 20 to 30 ft (6 to 9 m) thick. These sandstone bodies are elongate and trend northeastward (fig. 11), parallel to the inferred paleoslope, and log signatures of Fruitland sandstones are upward-fining, spiky, and serrate, consistent with the fluvial interpretation.

Fruitland rivers flowed northeastward but bypassed Fruitland swamps and supplied sediment to the Pictured Cliffs shoreline. The thinness of Fruitland sandstones suggests that fluvial systems in the Navajo Lake area were minor and of insufficient size to form fluvially dominated deltas. This conclusion is supported by linear geometry of the Pictured Cliffs shoreline sandstone (for example, UP1; fig. 8), which suggests a wave-dominated coastline. The dip-elongate sandstone-body trends described in UP1 (fig. 8) coincide with Fruitland sandbody trends, reinforcing the interpretation of Fruitland sandstones as minor fluvial feeders to the Pictured Cliffs shoreline.

Fruitland nonframework sandstones typically are thin, ranging from a few inches to less than 15 ft (4 m) thick (fig. 6). These sandstones are fine-grained, rich in plant fragments, and commonly interbedded with silty mudstone. They contain poorly defined sedimentary structures that have been distorted by soft-sediment deformation, microfaults, and burrowing. Fruitland

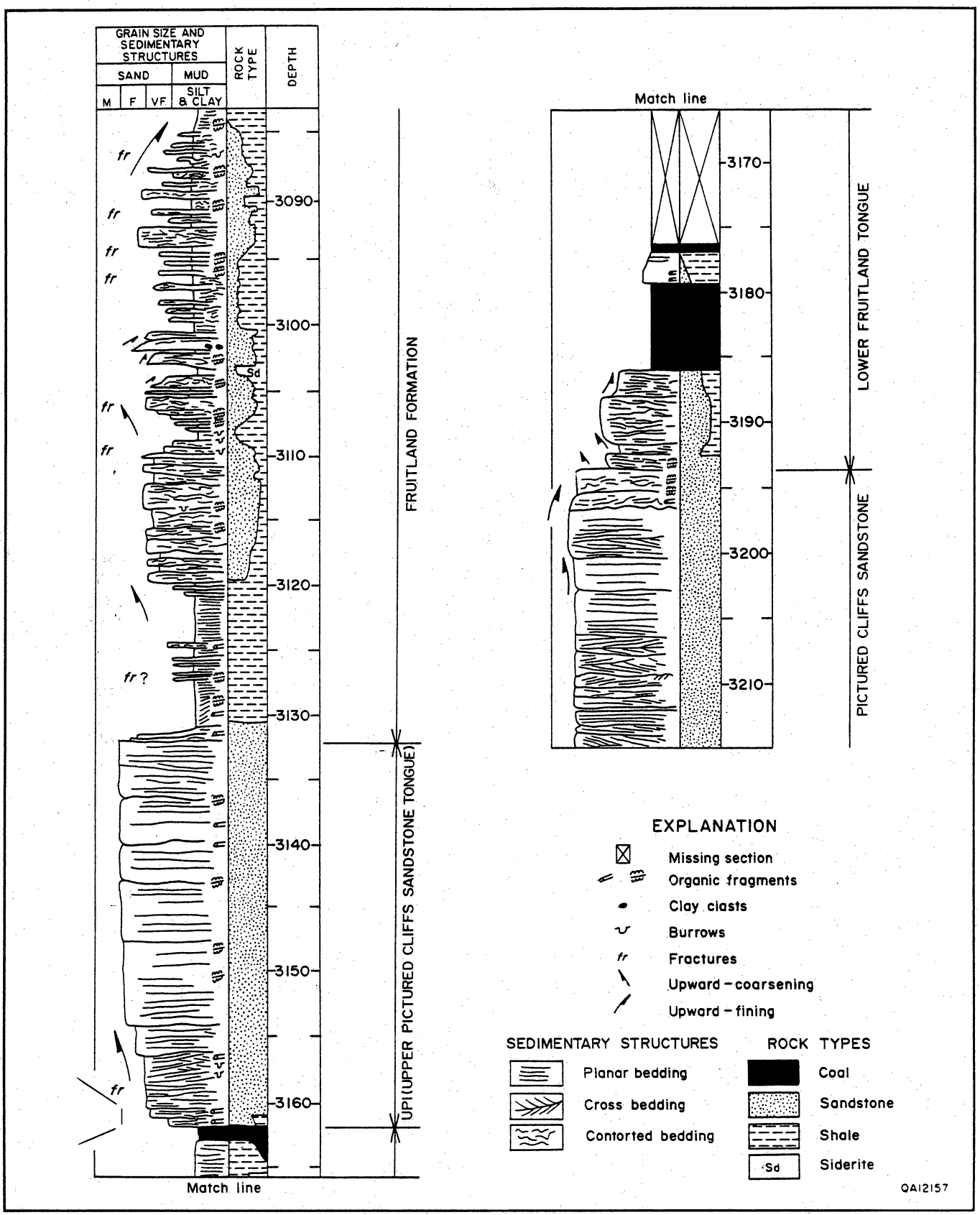

Figure 6. Core description of Pictured Cliffs Sandstone, lower Fruitland tongue, upper Pictured Cliffs tongue (UP1), and Fruitland Formation in Blackwood and Nichols NEBU No. 403 (see fig. 5).

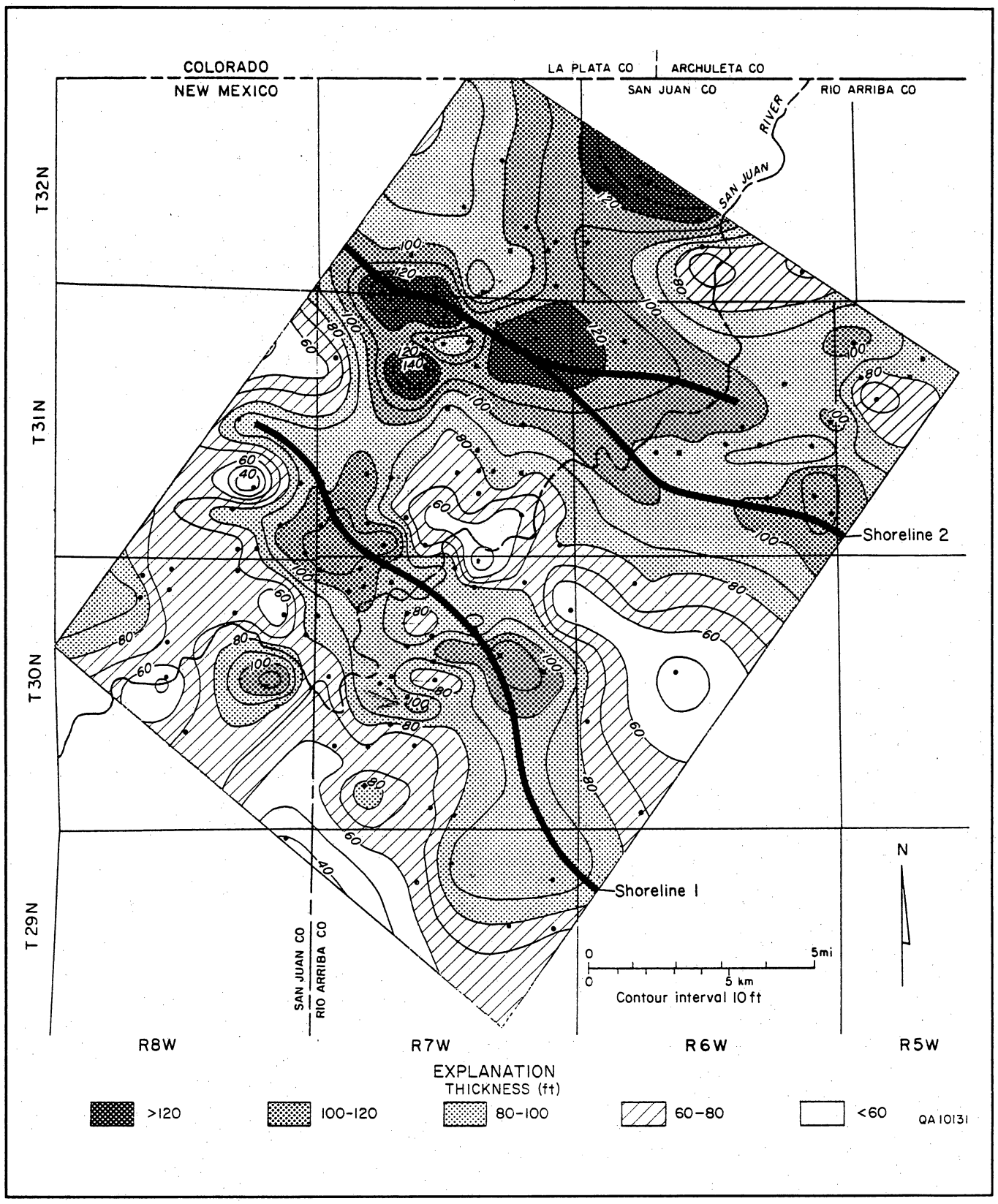

Figure 7. Sandstone isolith map of the Pictured Cliffs Sandstone. Net sandstone thickness trends of the Pictured Cliffs Sandstone suggest two successive, subparallel, northwest-trending shoreline sand bodies.

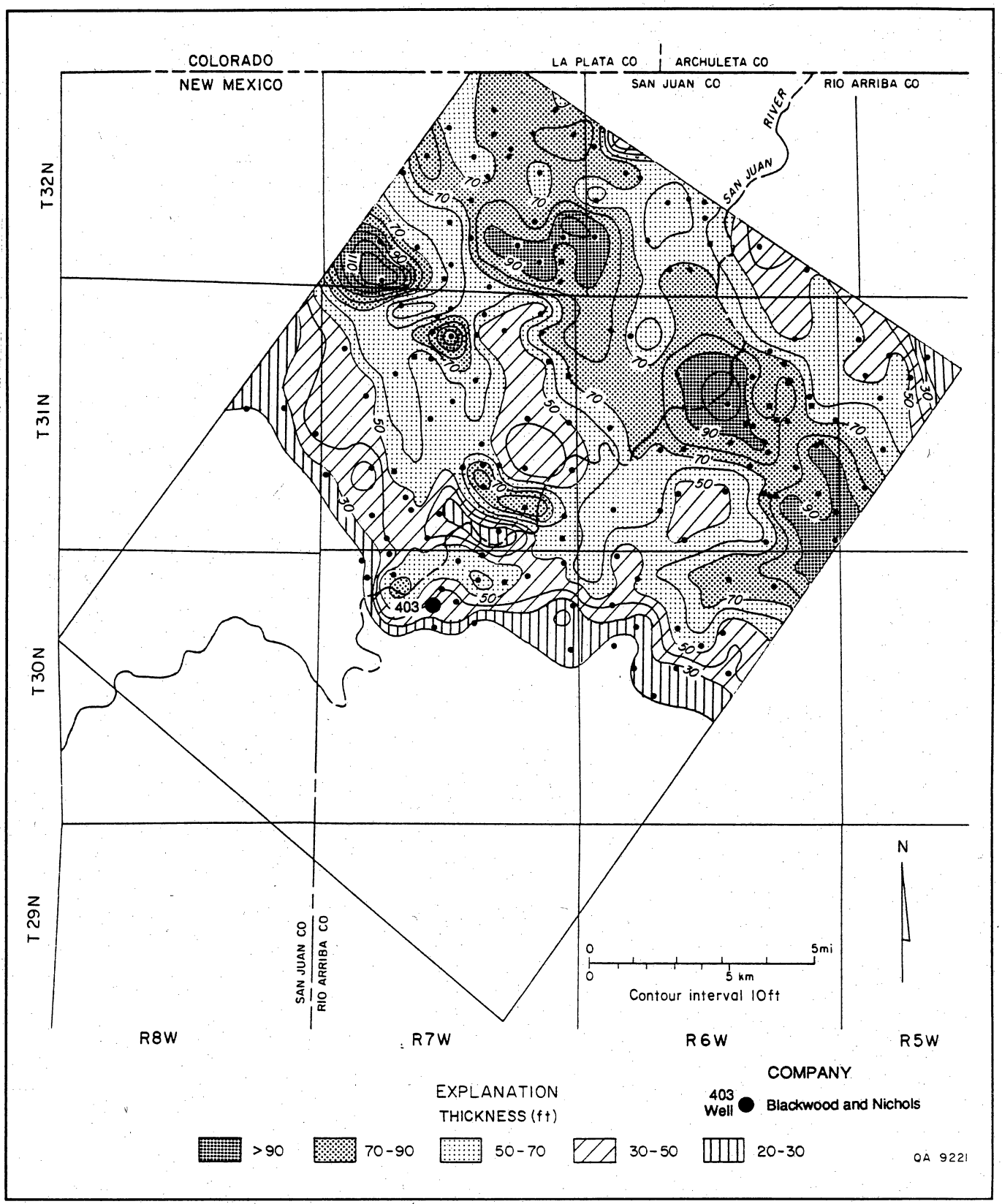

Figure 8. Sandstone isolith map of UP1 (figs. 1, 5, and 6), showing strike-elongate geometry of the barrier-strandplain shoreline. Landward deflections of the 60-ft contour may represent dip-elongate fluvial or tidal channel-fill sandstones. Area mapped is where net sandstone thickness exceeds 20 ft (6 m).

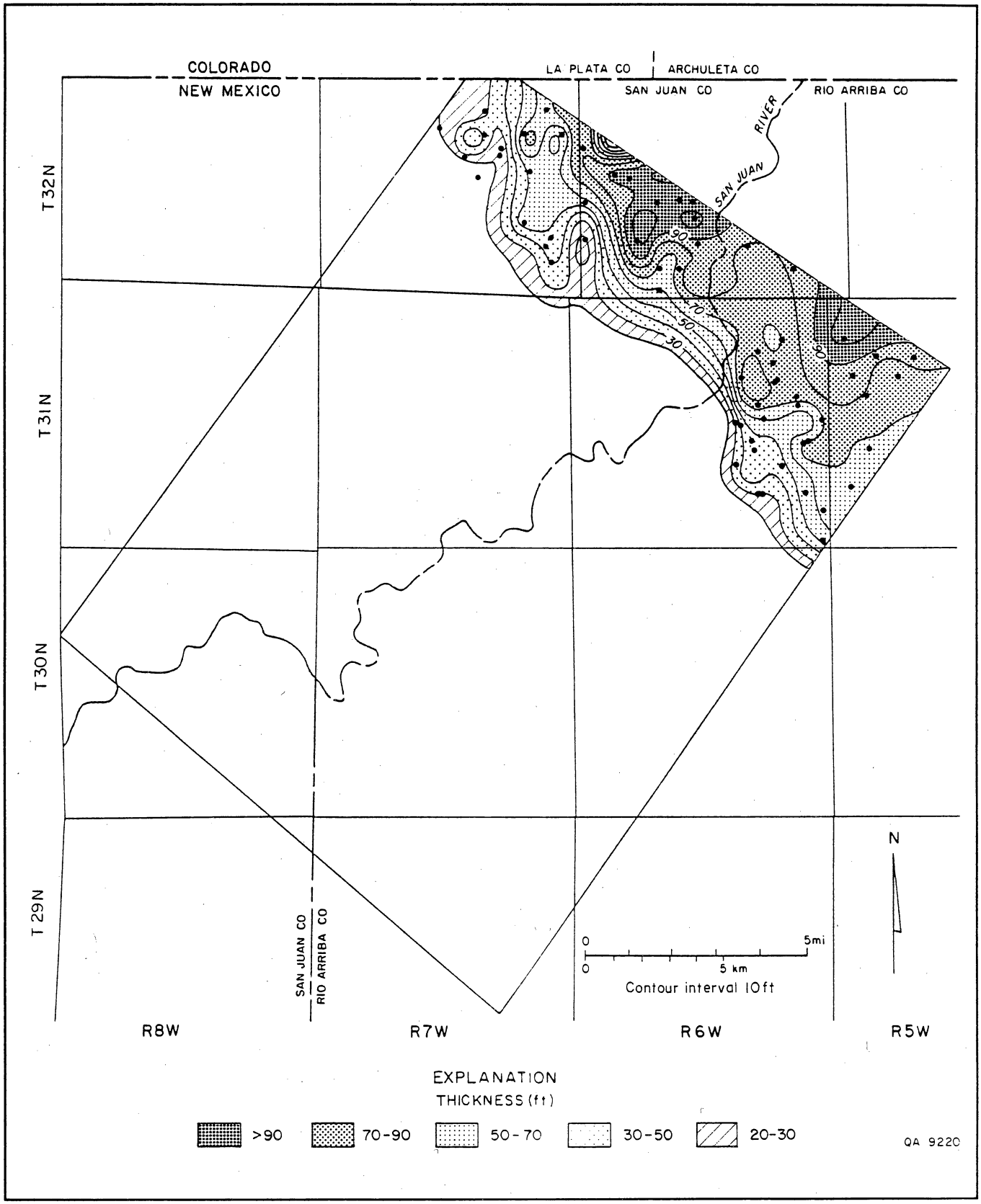

Figure 9. Sandstone isolith map of UP2 (fig. 1). Depocenter of strike-elongate coastal sandstone is offset basinward of UP1 (fig. 8). Area mapped is where net sandstone thickness exceeds 20 ft (6 m).

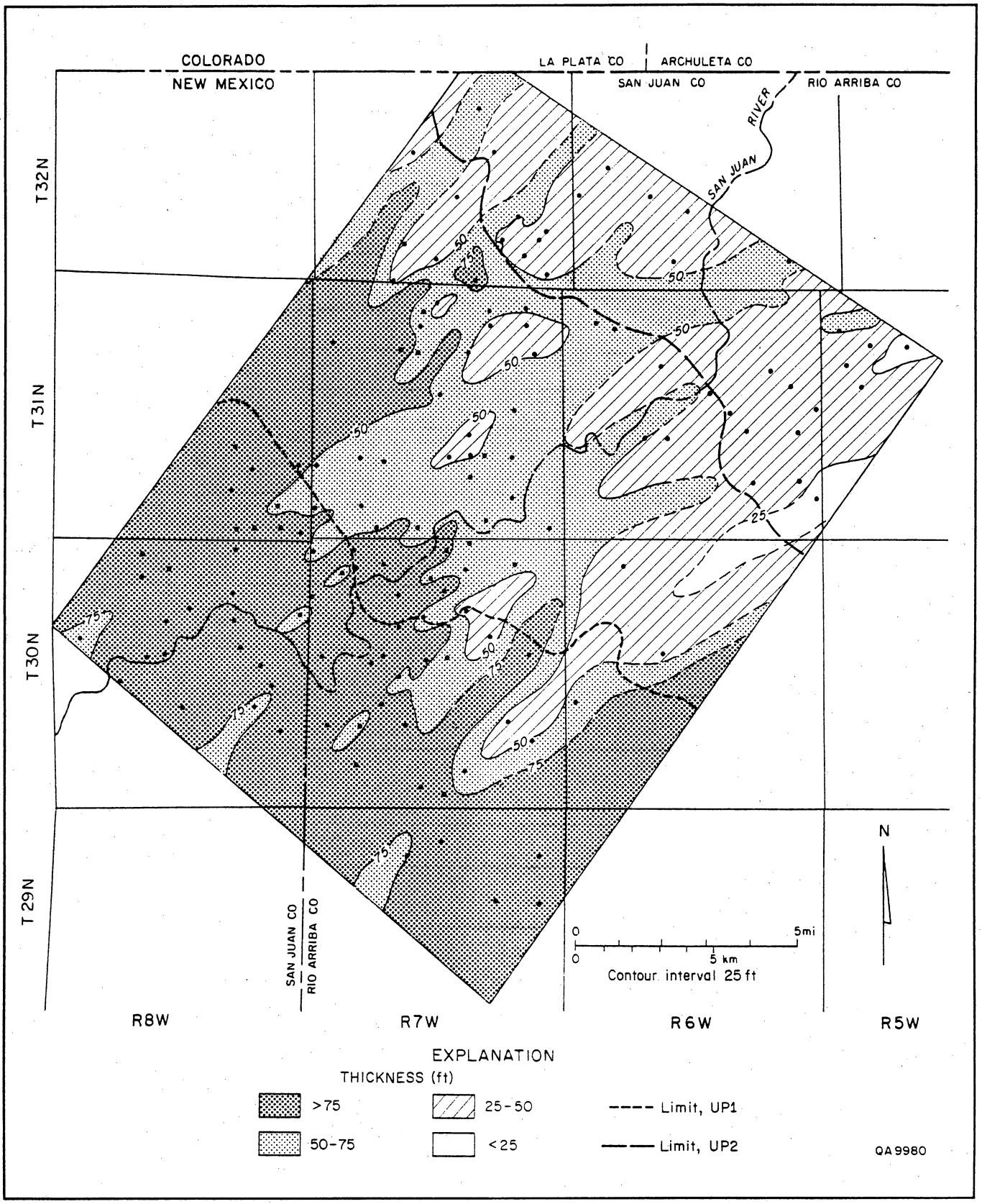

Figure 10. Sandstone isolith map of the Fruitland Formation. Net thickness of Fruitland sandstones is greatest in the southwestern part of the area. Dip-elongate sandstone bodies were deposited by minor Fruitland fluvial systems that supplied sediment to the Pictured Cliffs shoreline.

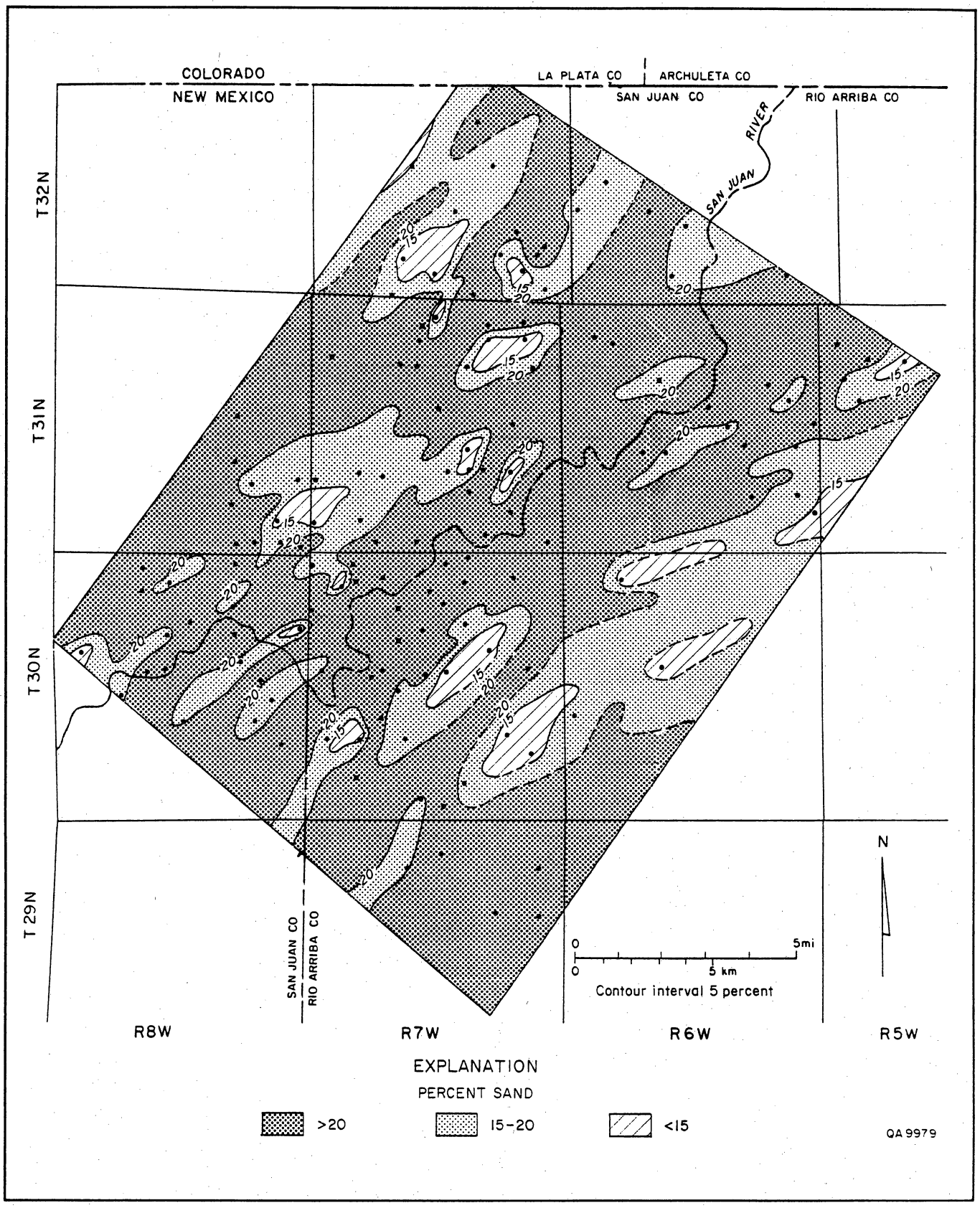

Figure 11. Sandstone percent map of the Fruitland Formation. Dip-elongate sandstone bodies make up 15 to 30 percent of the formation.

nonframework sandstone beds occur in upward-coarsening sequences 3 to 6 ft (1 to 2 m) thick and amalgamated or upward-fining sequences as much as 15 ft (4 m) thick; these nonframework sandstones are interpreted to be crevasse-splay and natural levee deposits.

Coal Occurrence

Net Coal Thickness

The net thickness of Fruitland coal seams in the Navajo Lake area ranges from 40 to 110 ft (12 to 33 m) (fig. 12). The greatest net coal thickness, more than 70 ft (21 m), occurs in the south, and the least net coal thickness is in the northeastern quarter of the area, which has 30 to 50 ft (9 to 15 m) of coal. The local northwest trend in the Navajo Lake area (fig. 12) is also present in regional maps (Fassett and Hinds, 1971; Kelso and others, 1987; Ayers and others, this vol., their fig. 22).

Maximum Coal Thickness

The maximum coal map (fig. 13) was made by the contouring of the thickest Fruitland coal seam recorded in each well, regardless of its stratigraphic position. Therefore, it does not record an individual seam. However, locally, as in the southeast corner of the map, an individual seam is mapped. Maximum coal thickness ranges from 15 to 50 ft (4 to 15 m) (fig. 13). Depocenters for thick coal, where individual coal seams are thicker than 30 ft (9 m), occur in pods 2 to 6 mi (3 to 10 km) in diameter. Coal seams thin radially from those depocenters, but they extend throughout most of the Navajo Lake area. A thick coal seam (thicker than 30 ft [9 m]; T29 and 30N, R7W) in the south coincides with an area of great net coal thickness (fig. 12) and indicates an area of persistent peat-forming conditions. Although a regional maximum coal map shows little internal complexity in northwest-trending belts of thick maximum coal (Ayers and others, this vol., their fig. 23), the maximum coal map of the Navajo Lake area, which was made with closely spaced well control, suggests that geometry of individual coal seams in the northwest-trending belts is podlike or dip elongate.

Number of Fruitland Coal Seams

In the Navajo Lake area, Fruitland coal occurs in 2 to 14 seams, which are most numerous in the southwest and least numerous in the northeast (fig. 14). A northwest strike is also apparent in this coal isopleth map. The greatest number of coal seams (14 seams) coincides with the location of greatest total coal thickness (greater than 90 ft [27 m]; fig. 12) and the thickest individual seam in the south (thicker than 30 ft [9 m]; fig. 13).

Depositional Controls on Coal Occurrence, Trends, and Thickness

The depositional setting of Fruitland coal seams in the Navajo Lake area was determined from coalbed trends and from relations between coal beds and Pictured Cliffs and Fruitland framework sandstones. Principal aspects of these relations are summarized in figure 15, a map of depositional elements, and in the depositional model (Ayers and others, this vol., their fig. 26).

In coal isolith and isopleth maps (figs. 12 and 14), strike-elongate trends are apparent, and coal seams are thickest and most abundant landward of upper Pictured Cliffs tongues. These relations suggest that thick coal formed in persistent, recurring swamps located landward of upper Pictured Cliffs linear shorelines. Although some coal beds terminate behind shoreline sandstones (figs. 15 and 16), other coal beds override them (fig. 16, upper two seams) to form laterally extensive coal beds. In the maximum coal map (fig. 13), coalbed geometry is podlike and dip elongate rather than strike elongate because thick coal seams formed in peat depocenters between dip-elongate, Fruitland channel-fill sandstone complexes (figs. 15 and 17). Palynologic studies (Manfrino, 1984) and the low sulfur content of Fruitland coal seams indicate that peat accumulated in a freshwater setting. Therefore, we conclude that the thickest peats formed inland, behind abandoned and foundering shoreline deposits of the Pictured Cliffs Sandstone (Ayers and others, this vol., their fig. 26).

Structural Controls on Depositional Systems

Fruitland net coal thickness is greatest landward of the greatest Pictured Cliffs stratigraphic rise, and yet, as pointed out by Fassett (1986), analogous thick coals are not associated with stratigraphic rises in subjacent coal-bearing formations. This implies that a process(es), which was lacking during deposition of previous San Juan Basin coal beds, operated during Fruitland deposition. We suggest that structural activity caused a higher rate of subsidence in the northern part of the basin, northeast of the structural hingeline (Ayers and others, this vol.). This greater subsidence created more accommodation space, causing a stillstand of the Pictured Cliffs shoreline and allowing the accumulation of thick Fruitland peats.

Fassett and Hinds (1971) used the Huerfanito Bentonite of the Lewis Shale as a datum for correlating Fruitland coal seams because it is stratigraphically the closest regional marker to the Fruitland Formation. However, the Huerfanito Bentonite is 675 to 850 ft

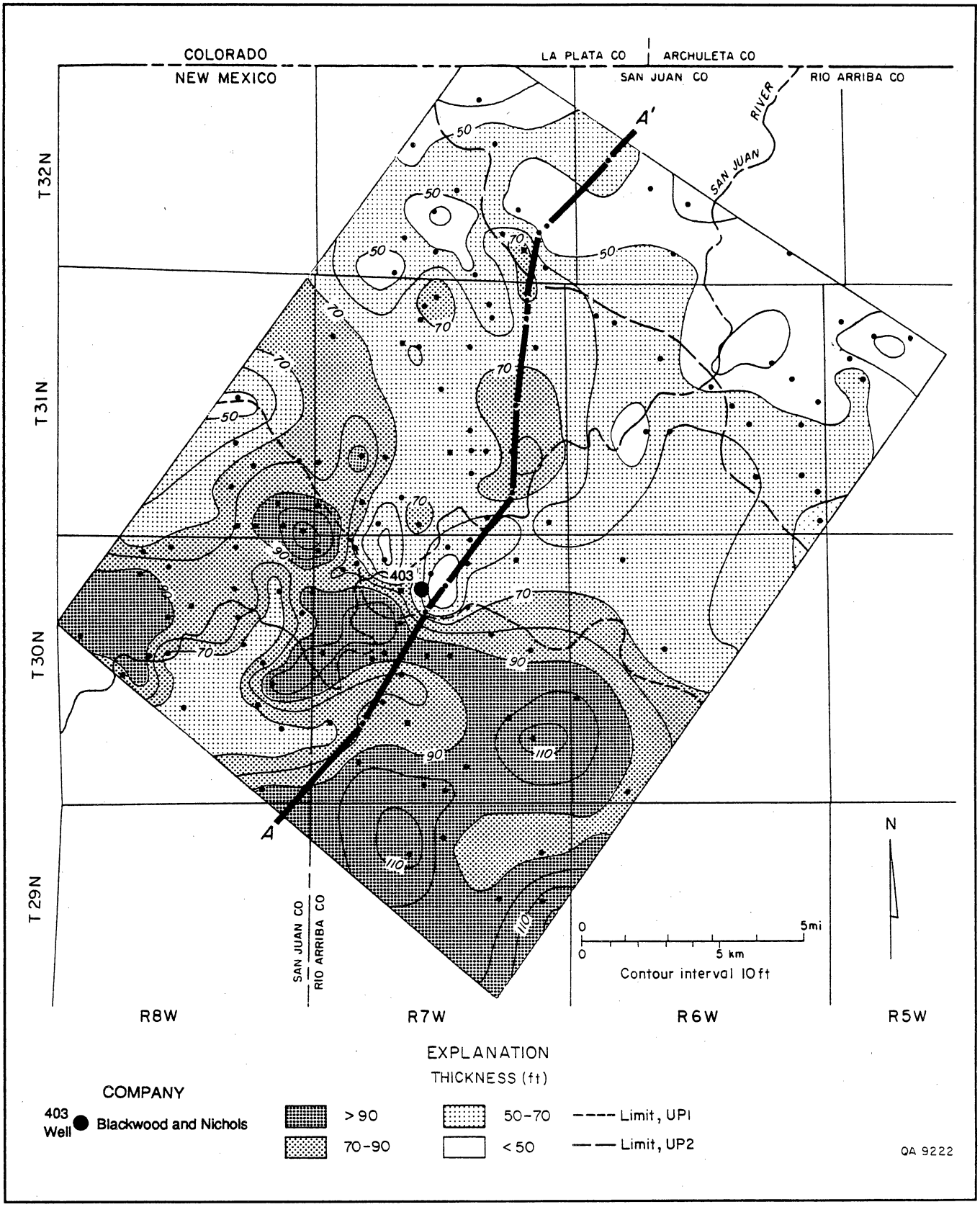

Figure 12. Fruitland coal isolith map. Net coal thickness ranges from 40 to 110 ft (12 to 33 m). Greatest net coal thickness is in the southern third of the area, and thickness trends strike northwestward, parallel to, and landward of the trends of upper Pictured Cliffs shoreline sandstones UP1 and UP2 (figs. 8 and 9).

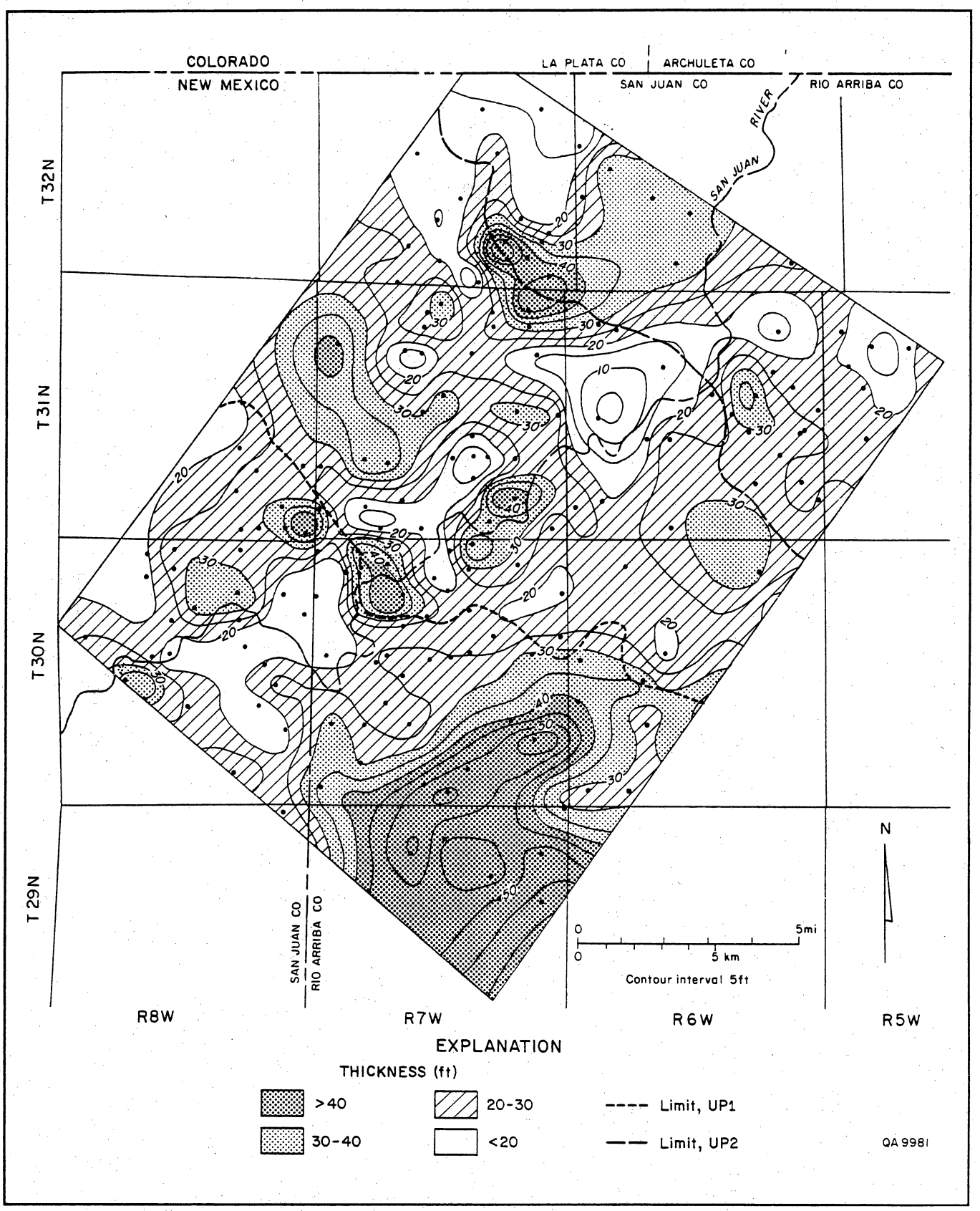

Figure 13. Fruitland maximum coal map. Map of the thickest coal seam at each location shows a thickness range from 15 to 50 ft (4 to 15 m). Thickest coal is in the south, and no preferred orientation is apparent.

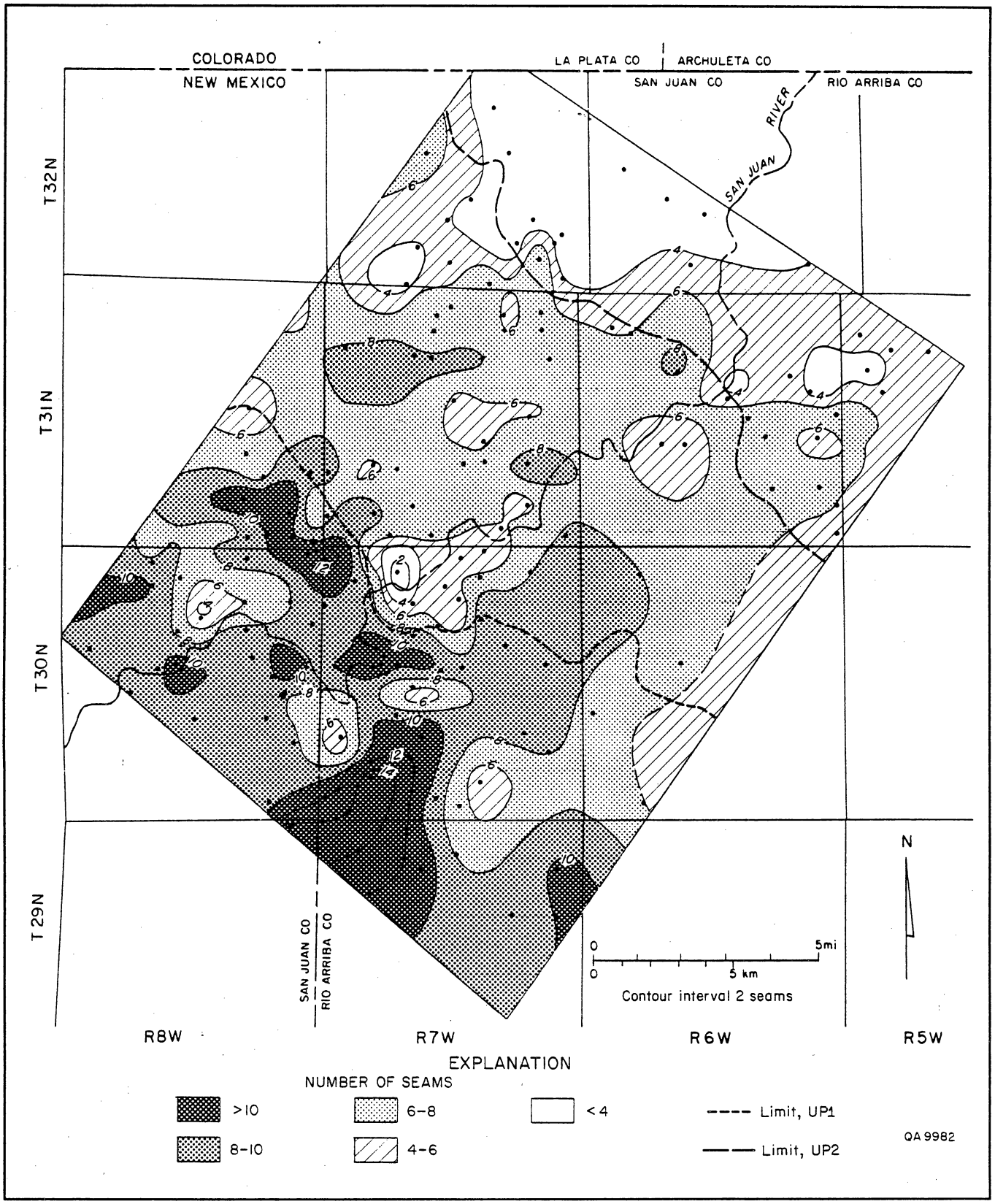

Figure 14. Fruitland coal isopleth map. Fruitland Formation coal occurs in 2 to 14 seams that trend northwestward, parallel to upper Pictured Cliffs sandstones UP1 and UP2 (figs. 8 and 9).

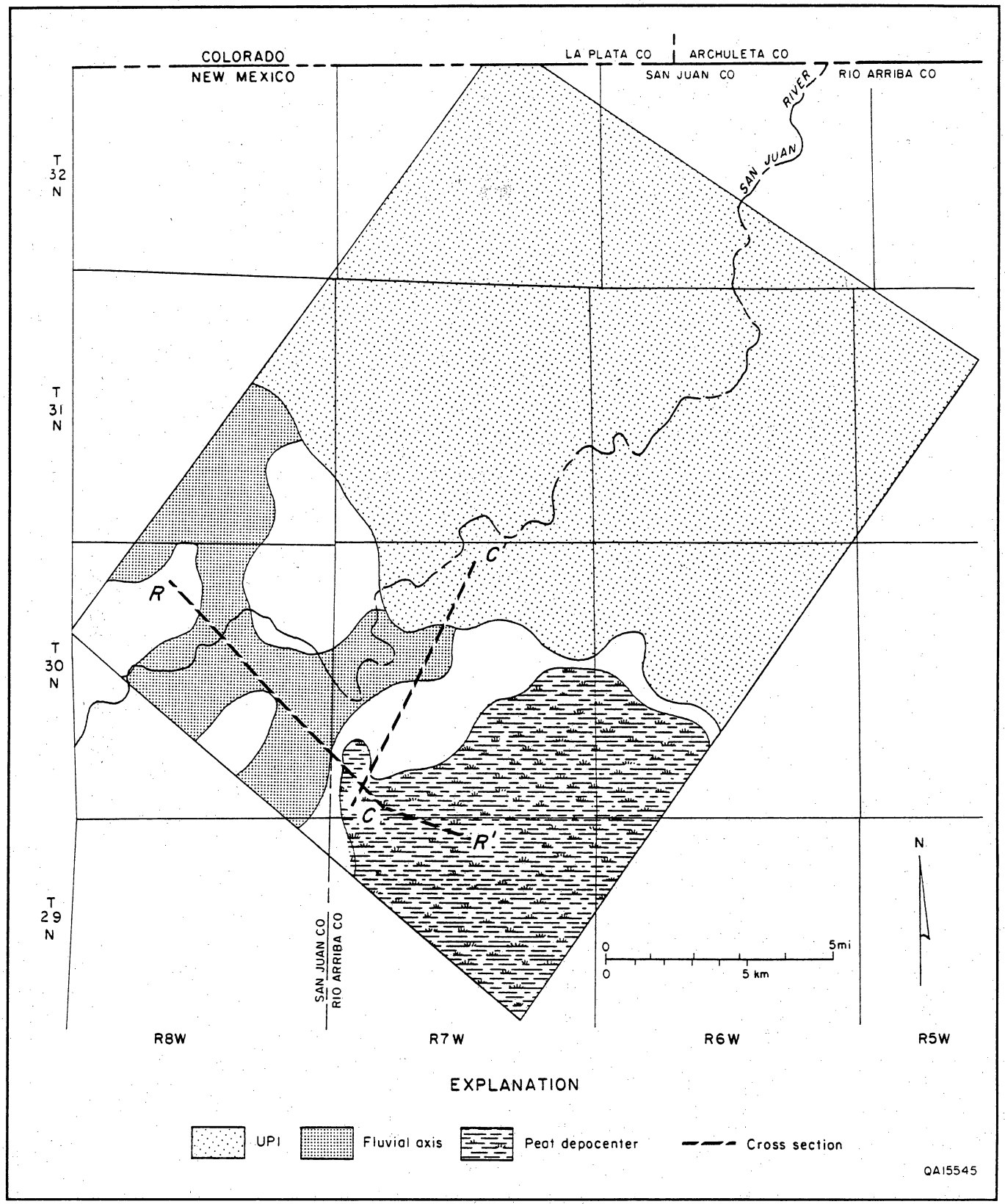

Figure 15. Depositional elements of Fruitland Formation and upper Pictured Cliffs tongue (UP1) in the Navajo Lake area. Peat depocenter persisted southwest of the Pictured Cliffs shoreline and lateral to Fruitland fluvial depositional axes. Cross sections C–C′ and R–R′ are shown in figures 16 and 17.

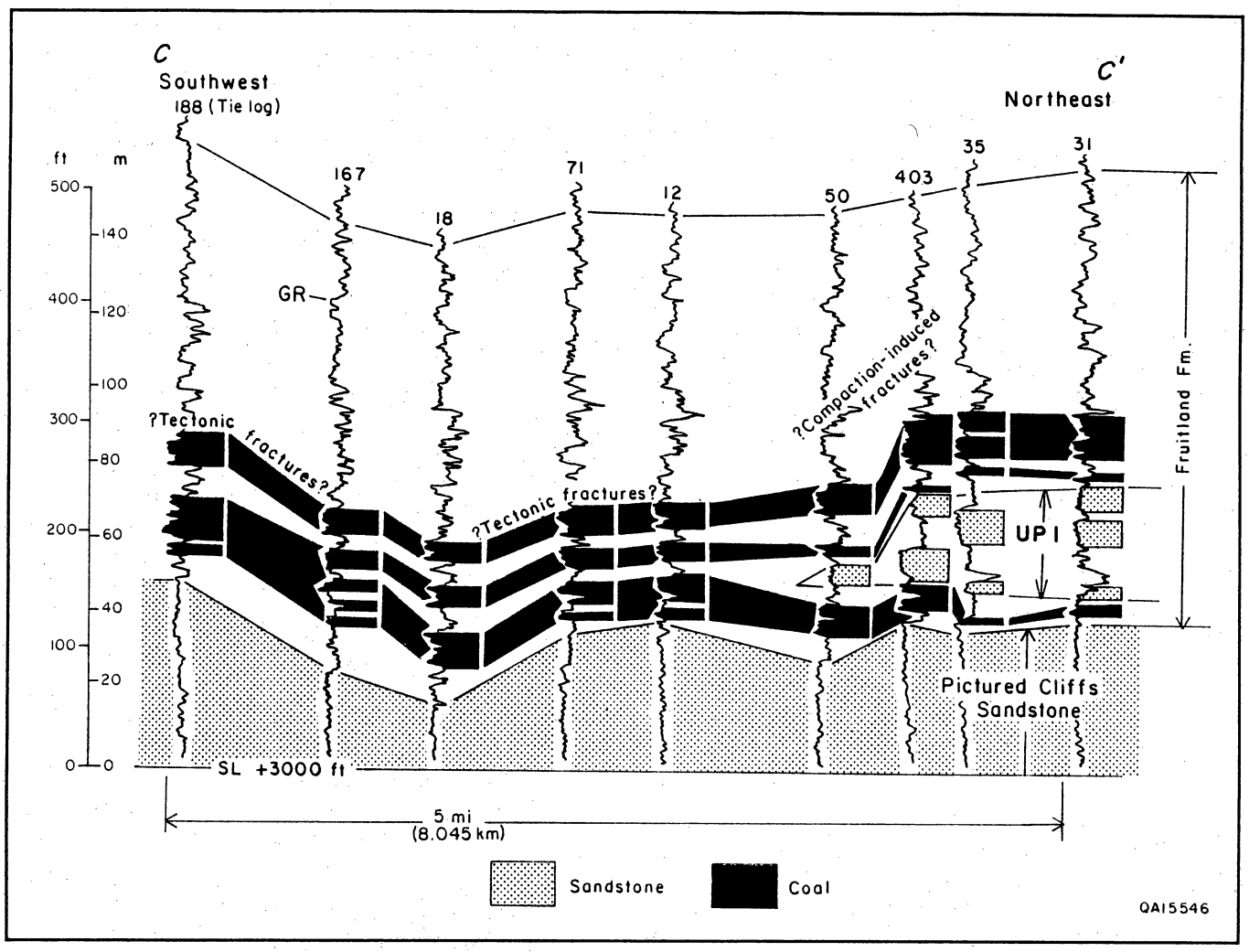

Figure 16. Structural cross section C–C'. Although lower Fruitland coal seams pinch out landward of Pictured Cliffs shoreline sandstones, a thick upper Fruitland coal seam overrides UP1. Fractures may occur in areas of tectonic folding, such as between wells 188 and 71 in all seams, and in areas of compaction-induced folding where coal seams override shoreline sandstones, such as between wells 50 and 403 in the upper two thick seams. Well 188 ties with figure 17. See figure 15 for location.

(205 to 260 m) below the Fruitland in the Navajo Lake area (fig. 4). Although it is an excellent regional marker, the Huerfanito Bentonite has limitations in Fruitland coal evaluations. Fassett (1987) reports that Fruitland coal seams parallel the Huerfanito Bentonite, but Fruitland coal seams can parallel the Huerfanito only if (1) stratigraphic rise of the Pictured Cliffs is due to eustasy (impossible, considering the magnitude of thickening—1,200 ft [365 m] across the basin) or a uniform subsidence rate across the entire basin, which is inconsistent with isopach maps and other findings expanded on below, and (2) there has been no differential compaction of the underlying Pictured Cliffs Sandstone and Lewis Shale. Use of the Huerfanito Bentonite as a datum suggests that all coal seams terminate abruptly against Pictured Cliffs sandstones (fig. 18a). It also requires rapid aggradation of the continental Fruitland facies to keep pace with rapid rise of relative sea level (fig. 18a); however, rapid aggradation of coastal plain sediment is incompatible with persistent peat accumulation.

Use of a datum above the Fruitland Formation (fig. 18b) gives a different perspective of basin-filling processes and suggests structural control of the Pictured Cliffs shoreline and, indirectly, the distribution of thick Fruitland coal seams. Fassett and Hinds (1971, p. 38) state that "the pre-Ojo Alamo surface was probably a relatively flat peneplain." Cross section B–B' is aligned with the present-day strike of that surface (Ayers and Zellers, 1988, their fig. 12), which, in turn, nearly parallels the Pictured Cliffs–Ojo Alamo isopach strike (Ayers, 1988, unpublished map). Therefore, the base of

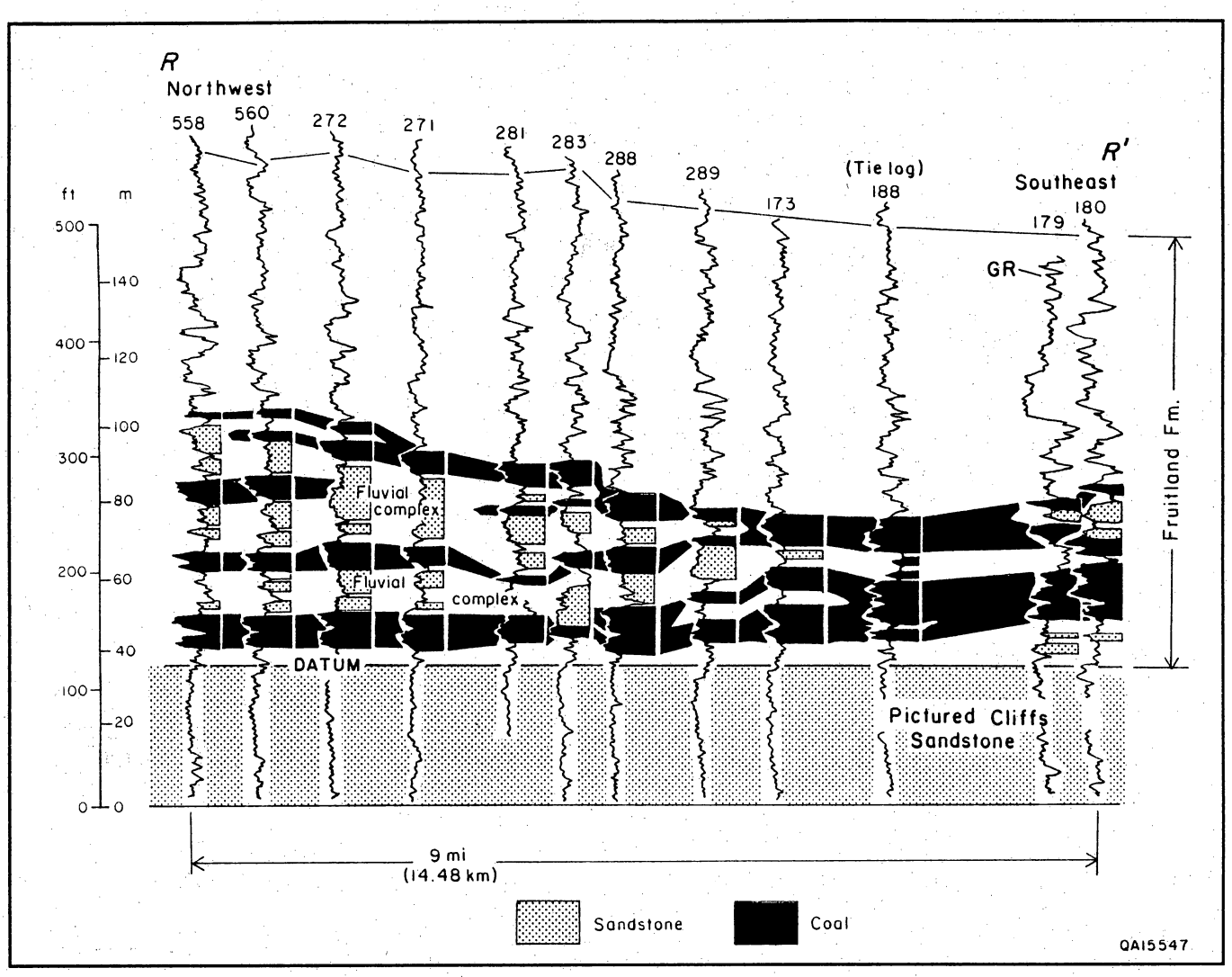

Figure 17. Stratigraphic cross section R–R'. Thick Fruitland coal in well 188 forms zig-zag splits to the northwest where more compactible peat (coal) interfingers with fluvial complexes (sandstones) along paleostrike. These folds may cause fracture-enhanced permeability. Because datum is the top of the Pictured Cliffs Sandstone, true structural attitude of the coal beds is not shown. Well 188 ties with figure 16. See figure 15 for location.

the Ojo Alamo Sandstone was used as a local datum. From figure 18b we surmise that differential subsidence north of a structural hingeline (fig. 2; Ayers and others, this vol., their fig. 26) controlled movement of the Pictured Cliffs shoreline by creating more accommodation space in the northern part of the basin.

In figure 18b, it is apparent that (1) if the increased thickness of Lewis Shale between wells 70 and 213 is due to differential subsidence, then thick coals in well 70 may override UP1 and UP2 in well 213 rather than terminate against them as suggested in figure 18a, and (2) if less rapid aggradation is required at well 70 to keep pace with aggradation in well 213, then more time is available for uninterrupted peat accumulation at well 70, and hence the greater thickness of peat southwest of UP1. Because Upper Cretaceous strata thicken basinward, due in part to increased basin subsidence, coal seams are not parallel to the Huerfanito Bentonite.

Several lines of evidence support a higher rate of subsidence in the northern part of the basin: (1) if basinward thickening of the Huerfanito Bentonite–Pictured Cliffs Sandstone interval is due to eustasy or uniform platform subsidence, the Pictured Cliffs Sandstone should not parallel the unconformable base (Fassett and Hinds, 1971) of the Ojo Alamo Sandstone in figures 1 and 18a; (2) UP1 is stacked on an underlying Pictured Cliffs Sandstone shoreline (figs. 7 and 8), and it pinches out at approximately the same area as a marine marker zone above the Huerfanito (fig. 1) and a

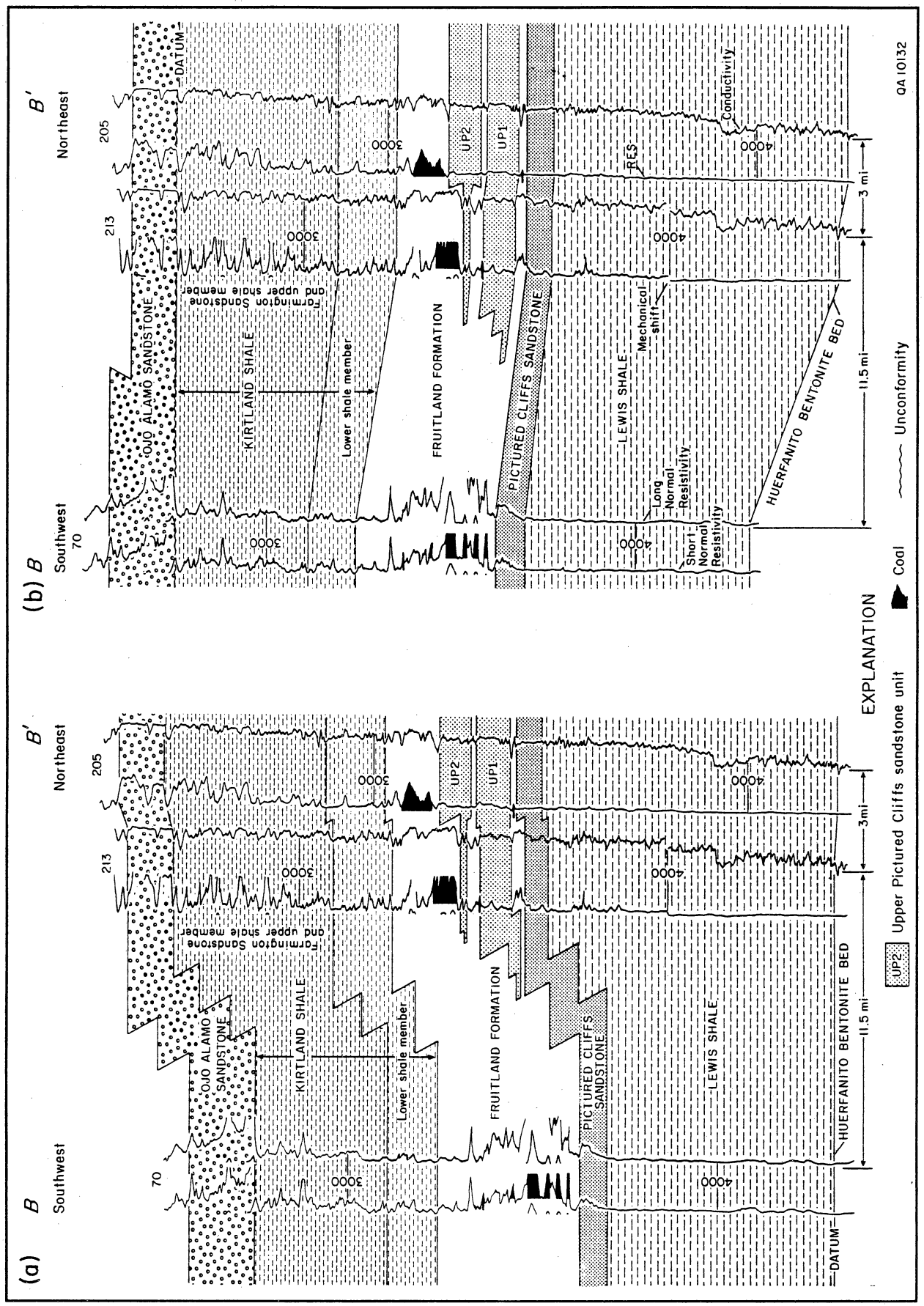

Figure 18. Cross section B–B'. (a) Datum is the Huerfanito Bentonite. Use of this datum suggests that coal seams terminate abruptly against Pictured Cliffs shoreline sandstones. (b) Datum is base of the Ojo Alamo Sandstone. Use of a datum above the Fruitland Formation suggests that swamp facies (coal seams) migrated over abandoned, foundered Pictured Cliffs shoreline sandstones. See figure 19 for location.

similar marker zone (not shown) below the Huerfanito; (3) the inclined marker beds in Pictured Cliffs shelf and shoreface deposits (fig. 1) show notable thickening of these deposits basinward, northeast of well 50, whereas to the southwest of well 50, shelf and shoreface markers are horizontal and the deposits are thin; and finally (4) although stratigraphic rise of the Pictured Cliffs occurs in the southern part of the basin, the greatest stratigraphic rise is northeast of the structural hingeline. The regional Huerfanito Bentonite–upper Pictured Cliffs Sandstone isopach shows a realignment of contours from an east trend in the central part of the basin to a northwest trend in the area of greatest stratigraphic rise (Ayers and others, this vol., their fig. 9).

We suggest that structural activity contributed to relatively greater stratigraphic rise in this area and, indirectly, to the distribution of thick Fruitland coal seams (Ayers and others, this vol., their fig. 26). The Pictured Cliffs shoreline prograded rapidly basinward across the southern half of the basin. After the shoreline crossed the structural hingeline, sporadic structural activity began and the northern part of the basin subsided more rapidly to accommodate a greater thickness of sediment. The changing balance between sediment input and pulsatory subsidence north of the hingeline resulted in oscillation and aggradation of the shoreline, accounting for the most significant stratigraphic rise of the Pictured Cliffs in the basin and allowing time for thick peat accumulation landward of the oscillating shoreline. This model explains why the greatest net thickness of Fruitland coal is in the northern part of the basin, and why coal seams in the Fruitland Formation are thicker than those in subjacent continental strata. Further testing is needed to verify the existence of the structural hingeline; seismic studies would be especially useful. A regional map of structural elements that were identified in regional reflection seismic lines shows northwest-trending faults in the area of this hingeline (Curtis Huffman, Jr., personal communication, 1990).

Structural Controls on Producibility of Coalbed Methane

Earlier studies suggested that Fruitland coal seams have limited extent and that they are bounded on their basinward (northeast) margins by Pictured Cliffs shoreline sandstone and along paleostrike (northwest-southeast) by Fruitland fluvial sandstones (Fassett and Hinds, 1971; Fassett, 1986). However, as we have demonstrated, some Fruitland coal seams may be regionally continuous, overriding and thinning over upper Pictured Cliffs tongues (figs. 16 and 18) in the paleodip direction. Updip pinch-out lines of upper Pictured Cliffs tongues may be areas where Fruitland coal seams drape over shoreline sandstones and have a higher fracture density because of compaction-induced fractures. The structural attitude of an upper Fruitland coal bed (fig. 19) differs markedly from the structural attitude of other strata, such as the Huerfanito Bentonite (fig. 2). Along paleostrike, coal seams split and interfinger with fluvial channel-fill sandstone complexes (fig. 17), and many of these coal benches, rather than terminating against the channel sandstones, override or underlie them, forming zig-zag splits similar to those described in coal-bearing strata in other basins (Britten and others, 1975; Ayers and Kaiser, 1984). Although these coal seams pinch and swell, they are laterally continuous, which contributes to their effectiveness as aquifers. Fractures related to compactional folding of coal beds are well documented (Donaldson, 1979; Houseknecht and Iannacchione, 1982; Tyler and others, this vol.). If such fracture systems are sufficiently developed, areas of interbedded sandstones and coal seams would be good targets for coalbed methane exploration (fig. 20).

This study has shown that Fruitland coal beds are more extensive and complex than previously inferred (figs. 16, 17, and 18). The significance of these findings is threefold. First, coalbed methane reservoirs are larger (more extensive) than previously thought. Second, compaction-induced fractures, and therefore enhanced coalbed permeability, may occur in areas where extensive coal seams drape over shoreline sandstones or form zig-zag splits with channel-fill sandstone complexes. Finally, the greater lateral extent of coal seams, inferred from this research, is critical to the interpretation of ground-water flow and abnormal pressure in the Fruitland Formation (Kaiser, Swartz, and Hawkins, this vol.).

The viability of the hypothesis of increased fracture density where coal beds are folded is uncertain; additional subsurface and outcrop studies are required. However, given the abundance of folds and the potential for folding-induced fractures to contribute to enhanced coalbed methane production, such studies are warranted. Evaluations of coalbed fractures in outcrop and mine exposures are in progress (Tyler and others, this vol.)

Coalbed Methane Activity and Reservoir Conditions

The Navajo Lake area has a long and noteworthy history of coalbed methane production. The Phillips No. 6-17 well (figs. 1 and 2) is often referred to as the discovery well for coalbed methane in the San Juan Basin. This well, which is an open-hole completion in upper Fruitland coal beds and sandstones, is located on the northwest flank of a minor, north-plunging anticline. It has operated for more than 25 yr with little decline in gas production (averaging 160 to 180 Mcf/d)

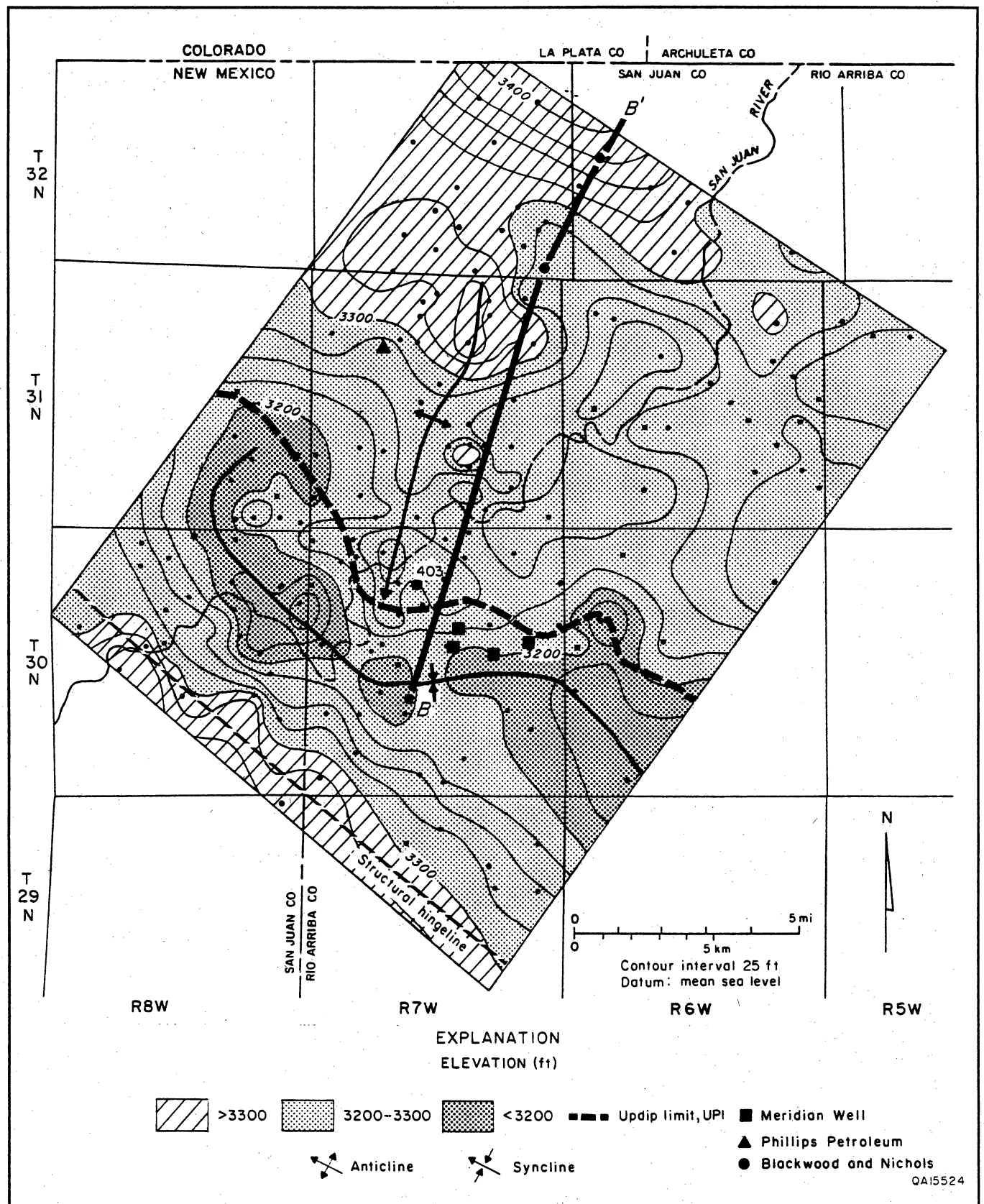

Figure 19. Structure map of upper Fruitland coal seam in figure 16. Attitude of the coal bed differs markedly from that of the Huerfanito Bentonite and the Pictured Cliffs Sandstone (figs. 2 and 4, respectively). Structural trough occurs southwest of the pinch-out of UP1. Cross section B–B' is figure 18.

or pressure (Hale and Firth, 1988). The well produces little or no water, indicating some element of structural and/or stratigraphic trapping. Although Hale and Firth (1988) discount structural trapping, their interpretation was based on a structure map of the Huerfanito Bentonite, which does not accurately reflect the structural attitude of Fruitland coal beds. Since 1985, Meridian Oil has completed several coalbed methane wells in the Navajo Lake area, including the most productive coalbed methane wells in the United States. Some Meridian wells in this area have produced at a rate of 300 to 10,000 Mcf/d (figs. 2, 3, and 19) (see Kaiser, Ayers, and others, this vol., for discussion of production). Meridian 400 wells are completed in lower Fruitland coal beds on the margin of a syncline and near the updip pinch-out of UP1 (fig. 19).

In the Navajo Lake area, Fruitland coal beds are mostly in the area of regional overpressuring and highest Fruitland bottom-hole pressures; overpressuring is attributed to artesian conditions (Kaiser, Swartz, and Hawkins, this vol.). The boundary between overpressured and underpressured strata crosses the southern part of the area (fig. 4); this boundary may be caused by southwestward pinch-out and/or offset of aquifer coal beds across faults that are inferred to make up the structural hingeline (fig. 2). Both gas- and water-saturated coal seams are present in the Navajo Lake area. In this area, Fruitland coal rank increases from high-volatile B bituminous at the south to medium-volatile bituminous at the north (Scott and others, this vol., their fig. 3), and it contains more than 10 Bcf of methane/mi² (Ayers and others, this vol., their fig. 27). Fruitland coalbed gas is dry (C_1/C_{1-5} >95 percent), and it contains a high percentage of carbon dioxide (commonly 3 to 10 percent) (Scott and others, this vol., their fig. 10). Primary fractures (face cleats) in oriented cores from Blackwood and Nichols NEBU No. 403 trend northeastward, consistent with regional cleat trends in the southern part of the basin (Tremain and others, this vol., their fig. 1). Highly productive wells in the Navajo Lake area are reported to have fracture-enhanced permeability that can be predicted from lineament analysis. However, a recent study showed no significant relations between methane production and lineament attributes in the northern San Juan Basin (Baumgardner, this vol.). Geologic and hydrologic controls on producibility of coalbed methane in the Navajo Lake area are further discussed by Kaiser, Ayers, and others (this vol.).

Summary and Conclusions

In summary, we suggest both depositional and structural controls on the occurrence and producibility of Fruitland coalbed methane in the Navajo Lake area. The distribution of thick coal seams is controlled by depositional setting, which in turn was structurally controlled; tectonically induced subsidence north of the hingeline temporarily confined the Pictured Cliffs shoreline to a narrow belt, and this stillstand resulted in thick Fruitland coal seams by allowing thick peat to accumulate. Locally, low-amplitude folds of tectonic or differential-compaction origin may form conventional structural traps. Fractures associated with the folds may enhance permeability of Fruitland coal seams locally, thus improving the producibility of coalbed methane. We conclude the following.

1. In the Navajo Lake area, thick Fruitland coal formed in a back-barrier setting. During the Late Cretaceous, the Pictured Cliffs barrier-strandplain system prograded rapidly northward across the area of the present San Juan Basin. Sporadic subsidence north of a northwest-trending structural hingeline is inferred to have caused two major shoreline reversals and deposition of upper Pictured Cliffs transgressive-regressive sandstones, UP1 and UP2, that interfinger with the continental Fruitland Formation to the southeast.

2. Increased accommodation space north of the hingeline caused the Pictured Cliffs shoreline to aggrade within a narrow belt, favoring the accumulation of thick Fruitland peat; as much as 110 ft (33 m) of coal occurs in as many as 14 seams. Regionally, coal seams show strike-elongate geometry, with both the greatest net coal thickness and greatest number of coal seams occurring landward of the northwest-trending upper Pictured Cliffs shoreline sandstones. Although thin coal seams pinch out behind Pictured Cliffs shoreline sandstones, thick seams appear to override abandoned shoreline sandstones, commonly thinning basinward. Individual coal seams are podlike or dip elongate rather than strike elongate because along paleostrike they interfinger with, or thin and override, dip-elongate Fruitland channel-fill sandstones.

3. In the Navajo Lake area, coal seams may be isolated from, or in contact with, Fruitland and Pictured Cliffs sandstones. Also, upper Pictured Cliffs sandstone tongues and the Pictured Cliffs Sandstone commonly are isolated from each other but are locally in contact. Permeabilities of Fruitland coal beds exceed those of Fruitland and Pictured Cliffs sandstones, but all of these units produce some gas. Because the dominant trend of the most extensive permeable units (Fruitland coal seams and Pictured Cliffs sandstones) is northwest, all other factors being equal, regional fluid movement parallel to that trend is favored.

4. From isopach maps, we conclude that during Fruitland and Kirtland deposition, a depocenter existed in the northwestern San Juan Basin and the Nacimiento

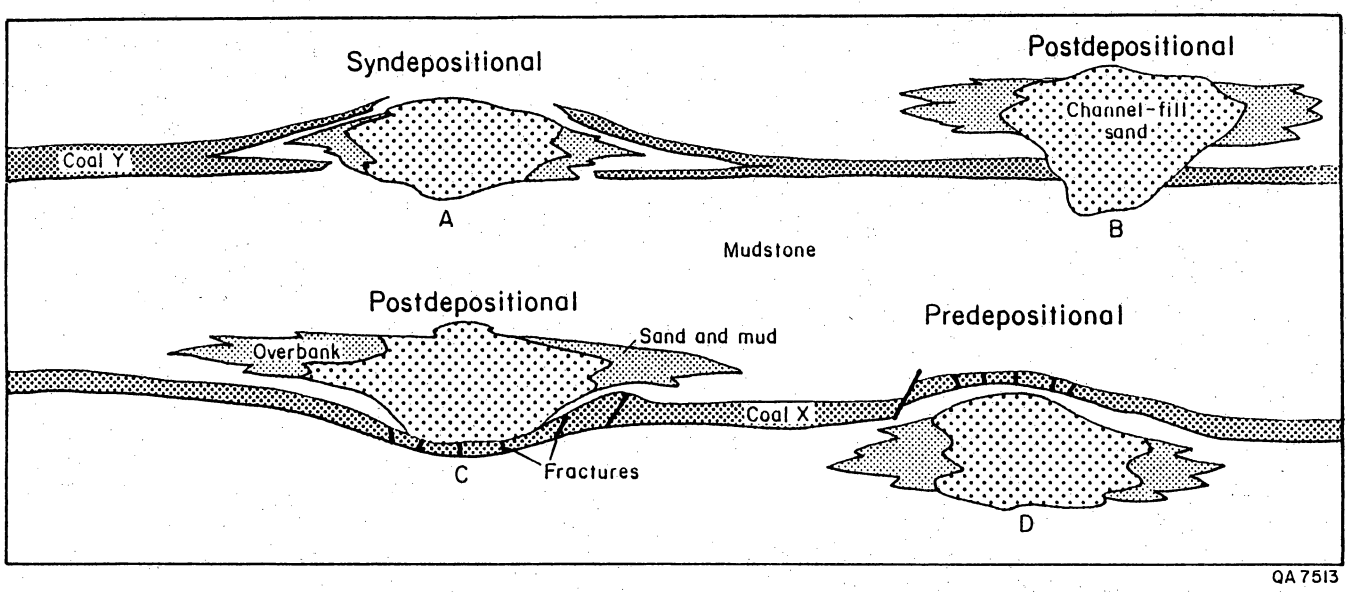

Figure 20. Relationship between depositional framework facies and coal seams. Coal seam Y splits and pinches out at interface with channel-fill sandstone A; seam Y was removed postdepositionally by channel B. Coal seam X is folded and fractured under postdepositional channel-fill sandstone C and over channel-fill sandstone D (from Ayers and Zellers, 1988; concepts from Donaldson, 1979).

uplift was active. The regional distribution of coal supports this conclusion; both the maximum and the net coal thicknesses decrease eastward in the basin, which may reflect deposition under less reducing conditions because of slower rates of subsidence. These conditions suggest lesser burial depths and thermal maturity for coal seams in the southeastern part of the basin.

5. Most structures in the Navajo Lake area formed after deposition of the Pictured Cliffs Sandstone. Minor structures that may cause conventional trapping and fracture-enhanced permeability are common in the San Juan Basin. However, minor structures mapped on the top of the Fruitland Formation may not parallel structures mapped on Fruitland coal seams because of differential compaction of Fruitland sand, mud, and peat.

6. Coalbed methane may be hydrodynamically trapped where thick coal seams pinch out to the southwest and where they are offset at the structural hingeline; the most productive wells in the basin are less than 5 mi (8 km) northeast of the structural hingeline.

Acknowledgments

We thank W. A. Ambrose, T. F. Hentz, and W. R. Kaiser for their review comments. W. A. Ambrose described the Blackwood and Nichols NEBU No. 403 core.

Fracture Patterns

Coal Fracture (Cleat) Patterns in Upper Cretaceous Fruitland Formation, San Juan Basin, Colorado and New Mexico: Implications for Coalbed Methane Exploration and Development

C. M. Tremain, S. E. Laubach, and N. H. Whitehead III

Abstract

Producibility of coalbed methane depends on fracture permeability. To evaluate controls on fracture (cleat) patterns in coal seams in Upper Cretaceous Fruitland Formation in the San Juan Basin, we studied fractures in coal and adjacent sandstones in 11 cores and at 90 outcrop stations along the basin margin and mapped fractures in selected areas. Cleats are planar, perpendicular to bedding, usually uniform in strike within an outcrop or core, and arranged in closely spaced subparallel sets. Because cleats tend to terminate at laterally extensive volcanic ash interbeds, small faults and fracture zones that offset or cut across these layers can significantly increase vertical interconnectedness of fracture networks, and thus reservoir permeability, in coal beds.

Face-cleat strikes delineate two principal domains of regional extent that are separated by a boundary of variable cleat orientation near the Colorado–New Mexico border. South of the boundary, face cleats strike predominantly northward or northeastward; north of the boundary, they strike predominantly northwestward. Prevalence of two directions of strongly developed fractures in the domain boundary region and resulting increased coal friability may enhance the success of well completion by open-hole cavity methods in this area.

Introduction

Coal fractures (cleats) enhance gas and water flow in coal beds. With the increasing importance of coalbed methane as a natural gas source, information on cleat patterns is becoming critical for planning coalbed methane well placement and spacing. Moreover, fracture patterns in coal and adjacent rocks can affect success of completion and stimulation techniques such as horizontal drilling, open-hole cavitation, and hydraulic fracture treatment. More than 1,000 methane wells have been drilled in the Fruitland Formation of the San Juan Basin of Colorado and New Mexico in the past decade, making it one of the most important coalbed-methane-producing areas in the country. The aim of our study is to document cleat characteristics and patterns in the Fruitland Formation in this basin. Results can help guide coalbed methane development in the San Juan Basin and provide a standard of comparison for cleat patterns in other coalbed-methane-producing basins in western North America.

In Ayers, W. B., Jr., and others, 1991, Geologic and hydrologic controls on the occurrence and producibility of coalbed methane, Fruitland Formation, San Juan Basin: The University of Texas at Austin, Bureau of Economic Geology, topical report prepared for the Gas Research Institute under contract no. 5087-214-1544 (GRI-91/0072), p. 97–117.

Previous studies of cleat on the northwestern margin of the San Juan Basin have documented northwest, north, and northeast fracture strikes (Newman and McCord, 1980; Condon, 1988). Newman and McCord reported joint strikes in sandstones at 70 locations in the Colorado part of the San Juan Basin and cleat strikes at approximately a dozen stations. Condon measured cleat and/or joint strikes at 15 locations on the northwest side of the Colorado part of the basin. Our study builds on this previous work with observations of fracture orientations and intensity made from 90 outcrop stations as well as from 6 oriented and 5 unoriented cores from wells in Colorado and New Mexico. Our study involved mapping fracture patterns in coal and adjacent sandstone bedding plane (pavement) outcrops and documentation of cleat orientation, length, spacing, and mineral fill. We discuss our observations in the context of new stratigraphic, structural, and coal-rank maps of the basin.

Setting of Cleat Development, San Juan Basin

The San Juan Basin of the east-central Colorado Plateau, New Mexico and Colorado, is an asymmetrical structural basin of Late Cretaceous to early Tertiary age (fig. 1). The basin contains more than 14,000 ft (4,270 m) of Paleozoic, Mesozoic, and Cenozoic marine and continental rocks. As defined by the Upper Cre-

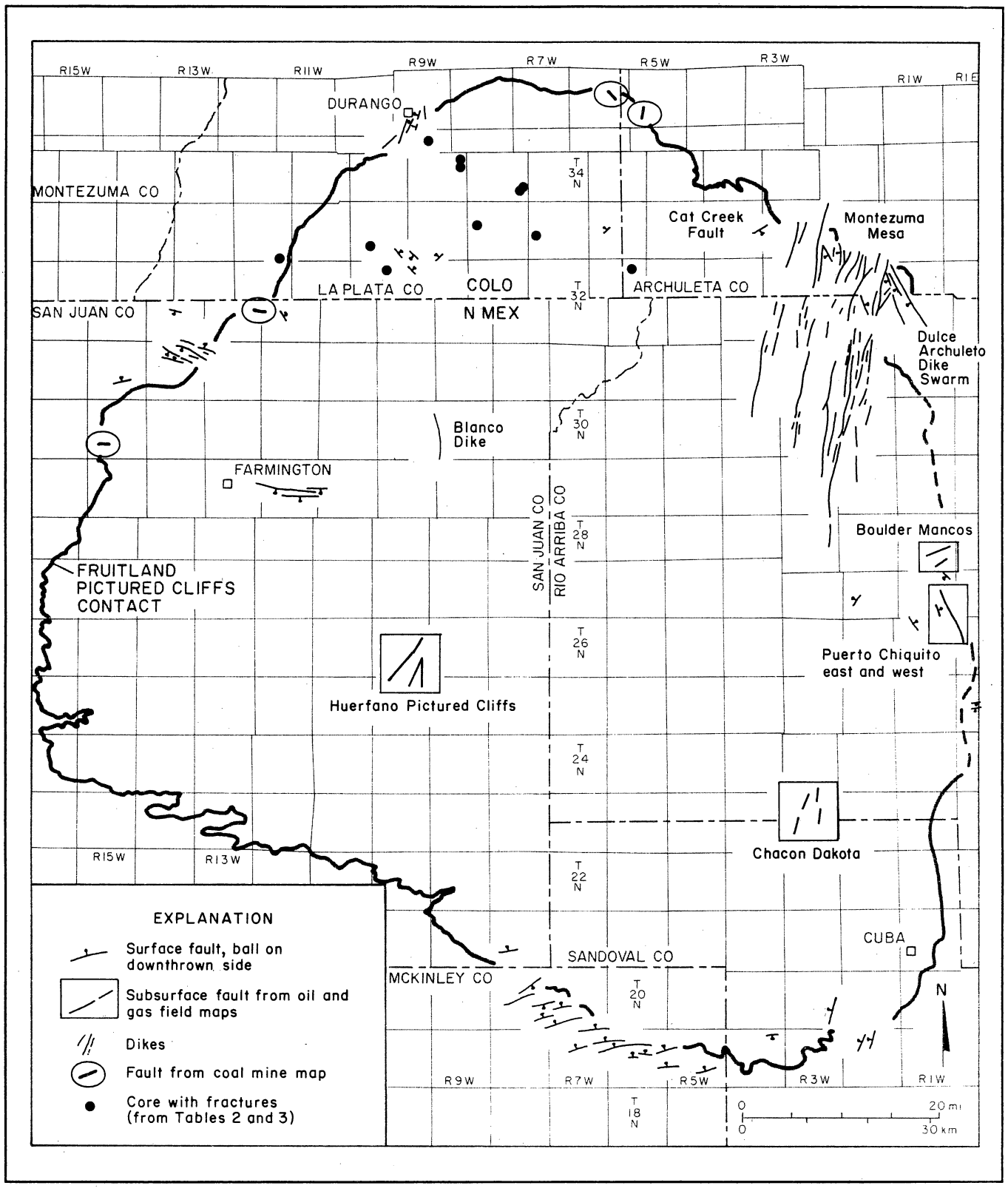

Figure 1. Faults and dikes in the San Juan Basin.

taceous Fruitland Formation outcrop, the basin is roughly circular with an area of approximately 6,700 mi² (17,350 km²). Its margin is delineated by the Chaco Slope and Zuni Uplift to the south, the Hogback Monocline on the west and northwest, the San Juan–Archuleta Uplift on the north, and the Nacimiento Uplift to the southeast. Pattern and timing of movement of faults along the basin margin suggest that it formed by northeast- and southeast-directed shortening during the Late Cretaceous to early Tertiary Laramide Orogeny (Fassett, 1985; Ridgley and Huffman, 1990).

Upper Cretaceous (Campanian) Fruitland Formation is the principal coalbed methane target in the basin. The Fruitland consists of coastal plain deposits composed of sandstone, mudstone, coal, and carbonaceous shale. It is more than 400 ft (120 m) thick in the northwestern part of the basin, but it decreases in thickness and disappears in the eastern part as a result of depositional thinning and erosional truncation. The Fruitland overlies coastal deposits of Pictured Cliffs Sandstone, and it is overlain by shales and sandstones of predominantly continental Kirtland Shale. Individual Fruitland coalbed thicknesses locally are as much as 20 to 40 ft (6 to 12 m), and total net coal thicknesses can reach 110 ft (33 m) (Ayers and others, this vol.). Thick lower Fruitland coal seams parallel northwest-trending strandlines of Pictured Cliffs Sandstone and are southwest (landward) of pinch-outs of marine Pictured Cliffs Sandstone that represent stillstands of the Pictured Cliffs shoreline (Ayers and others, this vol.). Coals stratigraphically higher in the Fruitland Formation parallel northeast-trending fluvial channel sandstones (Ayers and others, this vol.). Where coal directly overlies Pictured Cliffs sandstones, the coal-sandstone contact is generally nearly planar over distances ranging from hundreds to thousands of feet. Geometry of coal interbedded with fluvial sandstone is less uniform because of differential compaction of coal around discontinuous channel-fill sandstone.

Typical Fruitland coal seams are composed of interbedded bright (vitrain-rich), intermediate or semibright (clarain- and clarodurain-rich), and dull (durain-rich) horizons that range in thickness from several feet (1 m) to less than a tenth of an inch (0.25 cm). Ash content of typical Fruitland coal ranges from 8 to 30 percent and is commonly greater than 20 percent, primarily because of the presence of abundant interbedded thin (<5 inches [<13 cm]) volcanic ash layers (tonsteins). Moisture content ranges from 2 to 5 percent, and sulfur content is low, averaging less than 1 percent (Fassett, 1987). Rank of Fruitland coal ranges from subbituminous B in southern outcrops to high-volatile A bituminous around the northern margin of the basin (Scott and others, this vol.). Rank increases to low-volatile bituminous in the north-central part of the basin in T34N, R8W, but highest rank coal does not correlate with greatest structural depth (Rice, 1983), a discrepancy that may result from Cenozoic uplift history of the basin, from coal-rank upgrading caused by heat from the San Juan Mountain volcanic complex to the north (Choate and Rightmire, 1982), or from a deep, localized heat source beneath the northern part of the basin (Law, 1990a). In the deepest part of the basin near the Colorado–New Mexico border, Fruitland coals are at depths of approximately 4,200 ft (1,280 m).

Characteristics of Fruitland Formation Cleat

Cleats are systematic fractures in coal that are equivalent to joints in other sedimentary rocks. Cleats in Fruitland Formation coal beds are opening-mode fractures that are perpendicular to bedding, generally planar, commonly uniform in strike within an outcrop or core, and arranged in subparallel sets (table 1). Crossing or mutually abutting fracture patterns are present locally, but in general relative ages of cleats can be determined on the basis of abutting relations, where a younger fracture terminates against a preexisting fracture. The earliest formed fractures, against which other fractures terminate, are called face cleats (fig. 2). Face cleats are planar, smooth-sided fractures that *usually* make up the most prominent fracture set. They may be as much as several meters long in plan view. Butt cleats formed later and in most cases strike perpendicular to face cleat, with average angles of intersection typically between 80 and 90 degrees. A single face-cleat set and an associated, nearly orthogonal butt-cleat set are present in most exposures. However, butt cleats are locally absent in core and in some outcrops. Butt cleats are much shorter than face cleats, having lengths commonly less than 4 inches (10 cm). Their surfaces are predominantly irregular and hackly, and they are typically less continuous and less well developed than associated face cleats, although in some areas or in particular coal beds both cleat sets are equally developed (locs. 18 and 19, table 1).

Fractures in regional cleat sets in the San Juan Basin coal seams cut across subhorizontal compaction fabrics defined by flattened objects such as coalified wood. Locally, fractures in cleat sets cross rigid concretions. Cleats are perpendicular to bedding planes regardless of bedding plane dip, and consequently, face- and butt-cleat inclinations are locally as low as approximately 30 to 40 degrees in the northern San Juan Basin, where coalbed dips of as much as 50 degrees occur on the Hogback Monocline.

Cleat strikes are generally uniform over wide areas of the basin (fig. 1), but curved cleats are evident in

Table 1. Fruitland coal cleat stations.

Loc. no.	Location	Mean face strike	Primary spacing (inches)	Secondary/ tertiary spacing (inches)	Coal/seam attitude (strike/dip)	Position	Luster & rank	Comments (see below)
1	A + B Mine NWNE 32, 33N, 2W	334	1 1/2	—	356/2	3.3 ft above PC	HVA	2
2	Old Talian Mine SENESW 16, 33N, 3W	336	1/4 1 3/4	1/16	288/33	lower Kf	Bright	1, 6
3	Chimney Rock Strip NE 30, 34N, 4W	329	—	—	310/7	mid Kf	A=HVB B=HVA C=HVA	4
4	East Fosset Gulch Road NWNE 24, 34N, 5W	42	2 3/4	1/32–3/8	318/7	lower Kf	Dull	2, 6, 5, 10
5	West Fosset Gulch Road NENE 15, 34N, 5W	324	1/4	1/32	328/31 290/35	24 ft seam near PC	HVA	3, 5, 11
6	Squaw Creek CNE 9, 34.5N, 5W	326	—	1/16	325/26	lower Kf	HVA	2, 4, 9, 19, 21
7	Beaver Creek Road SESE 13, 35N, 6W (2 seams)	2 314	— 1 1/2	— 1/16 1/4	— 294/30	lower Kf	— Dull HVA	11, 20
8	Los Pinos Mine SWNW 14, 35N, 7W	16	3/4 1 1/2	1/8	295/40	lower Kf	Mod. Bright HVA	5
9	South Fork Texas Creek NWSE 7, 35N, 7W, CW1/2 8, 35N, 7W	345 356	1/2 2 1/4	1/8 1/4	76/21 95/29	lower Kf	Weathered Dull	1, 5, 8, 19
10	Florida River 24, 35N, 9W	325	1/4 2	1/32 1/8	42/40 67/62	lower Kf + Kf tongue	Mod. dull	5, 12, 15
11	La Plata Mine SE 27, 35N, 9W (4 seams)	344	—	—	—	mid Kf	—	1, 6
		338	1 10	1/32	59/41	mid Kf	—	
		330	3/4 2 1/2	1/16 —	40/40	lower Kf	HVA	
		337	—	—	50/35	Kf tongue	—	
12	Carbon Junction Strip SESE 33, 35N, 9W NWNE 53, 34, 5N, 9W	340 —	1/2 6	1/32 1/4	48/26 —	Kf tongue	HVA	13, 20
13	Carbon Junction Roadcut SWNW 4, 34N, 9W	340		1/16	27/24	lower Kf	—	1, 8, 20
14	East Gap NWSW 17, 34N, 10W NE 18, 34N, 10W (2 seams)	356	3/4 1 1/2	1/4 1/8	355/23 330/9	mid-lower Kf	Weathered ?	3, 5, 12

Table 1 (cont.)

Loc. no.	Location	Mean face strike	Primary spacing (inches)	Secondary/ tertiary spacing (inches)	Coal/seam attitude (strike/dip)	Position	Luster & rank	Comments (see below)
15	West Gap SENE 13, 34N, 11W	353	3/4 – 1 1/2	1/4 – 1/8	40/11	lower Kf	Weathered	3, 5, 7
16	Houston well SWSE 9, 33N, 11W	286		1/4	38/31	lower Kf	—	6
17	Fort Lewis Mine NENE 1, 32N, 12W NESE 36, 33N, 12W	NW	1/4 – 12	1/32 – 1/4	25	lower Kf	HVA	2, 3, 6, 14
18	Old Soda Springs Mine CSE 1, 32N, 12W	314	—	1/4–1/2	25/9	lower Kf	HVA-HVB	5, 7, 22
19	Cinder Buttes NENE 14, 32N, 12W	317	1 12	—	17/11 32/12	lower Kf	HVB	1, 5, 7

1 = planar cleat
2 = curved cleat
3 = local curved cleat
4 = variable strike
5 = "third cleat" present
6 = friable
7 = blocky
8 = poor butt-cleat development
9 = striations (slickensides)
10 = "third cleat" abuts face cleat
11 = 2 stations combined
12 = 3 stations combined
13 = 5 stations combined
14 = 27 stations combined
15 = Fruitland ss jnts strike 330–350
16 = Fruitland ss jnts strike 330
17 = Fruitland ss jnts strike 345–350
18 = Fruitland ss jnts strike 347, 285
19 = Fruitland ss jnts strike 016, 355
20 = Fruitland ss jnts strike NW
21 = calcite-filled veins in PC strike 330
22 = gas bleeding from coal

HVA = high-volatile A bituminous
HVB = high-volatile B bituminous
Dashes indicate attribute not determined.

some large exposures and in several mine pit floors (fig. 3a and b). In addition to face and butt cleats, other systematic, generally less closely spaced fracture sets occur in some coal outcrops (table 1). Among these are fractures that are indistinguishable from cleats except for their divergent strike. These fractures occur in association with typical face and butt cleats, and locally in the northern San Juan Basin, abutting relations suggest that some of these fractures predate the main face-cleat set whereas others are younger. Fractures with polygonal patterns occur in some dull (bone) coals where other cleat sets are absent. Faults and associated fractures crosscut cleat in some areas; elsewhere, cleats curve as they approach faults.

Cleat Types and Cleat Spacing

Cleat spacing in Fruitland Formation coal ranges from less than 0.03 inch (0.1 cm) to more than 1 ft (30 cm). To obtain cleat spacing measurements that can be compared from one station to another, we define a hierarchy of cleat (fracture) sizes that can exist within a given bed. These range from primary cleats that extend across one or several coal-type (lithotype) layers, to secondary and tertiary cleats that are vertically discontinuous within coal-type layers (fig. 4). These fractures and associated butt cleat (which also shows a hierarchy of sizes) give coal its blocky appearance. We distinguish three measures of fracture intensity in

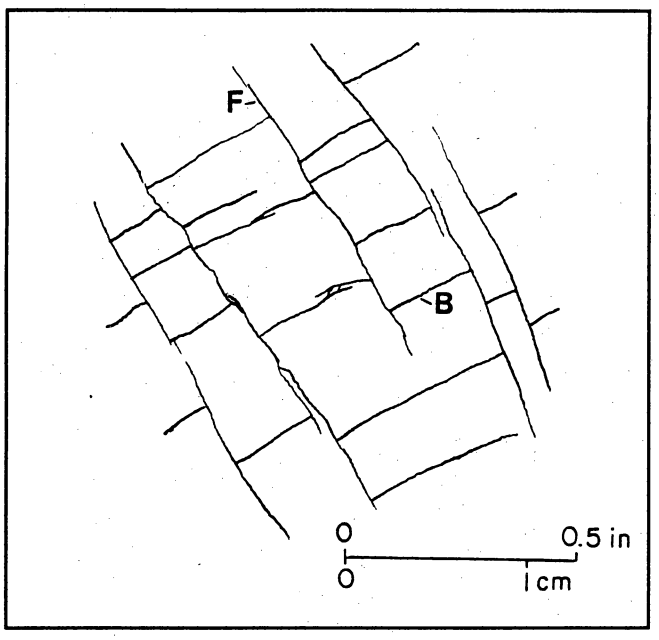

Figure 2. Diagram illustrating abutting relations between face (F) and butt (B) cleats.

Fruitland coal: primary-face-cleat spacing; total fracture intensity, defined as total number of fractures (primary, secondary, and tertiary) along a given distance in a coal seam; and fracture density, defined as total length of all fractures in a given area. In this report we use primary-face-cleat spacing as our standard measure of cleat intensity in outcrop because many of the exposures we studied are too small for fracture density measurements. Such measurements and fracture connectivity indices (Laubach and others, this vol.) may provide a better indication of fluid flow in coal. Total fracture intensity was used in core measurements.

Primary cleats are the most prominent cleat set in most Fruitland exposures. Two scales of primary cleat are evident locally. The most frequent primary cleats in Fruitland coals have average spacing of 1 to 3 inches (2 to 8 cm), are 1 inch to over 3 ft (several centimeters to over a meter) long, and commonly have oxidized surfaces indicating fluid flow. Their height is equal to the thickness of the coal lithotype layer in which they occur, from a foot or more (several tens of centimeters) tall in thick layers to less than half an inch

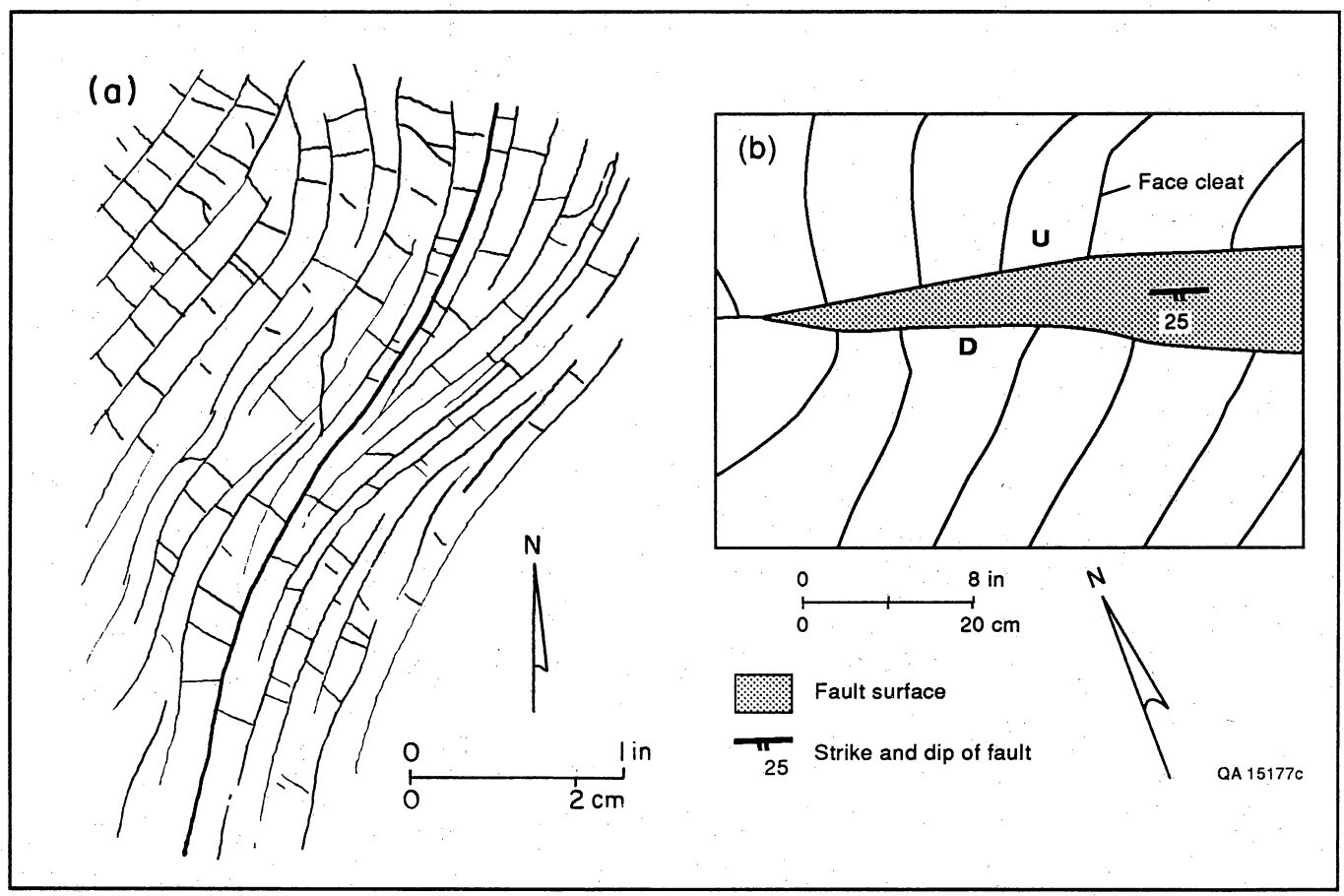

Figure 3. (a) Bundle of curved cleat traces in flat-lying coal, Fossett Gulch. (b) Curved cleats near small normal fault, Navajo mine.

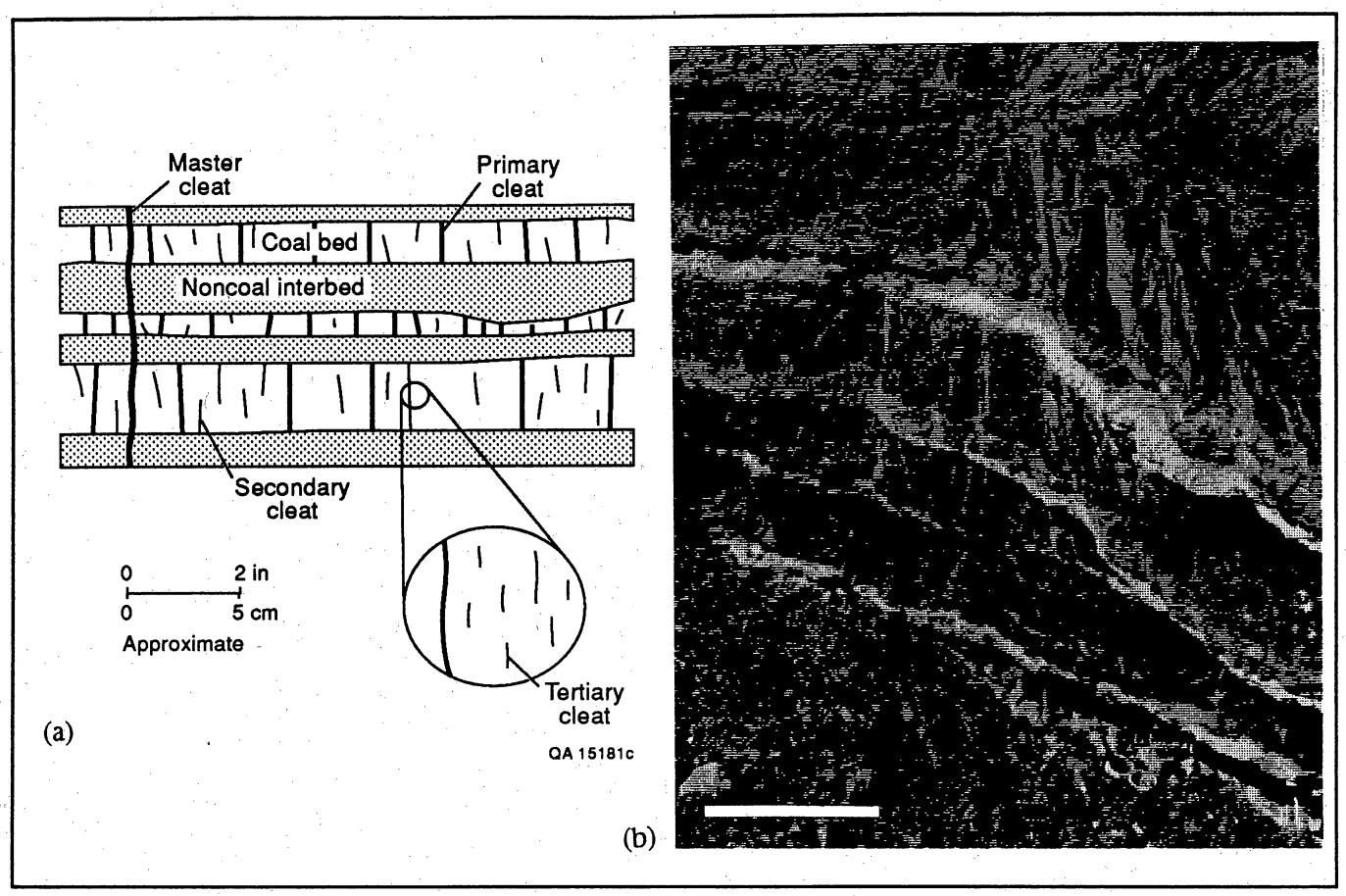

Figure 4. Hierarchy of cleat sizes. (a) Diagram illustrating primary, secondary, and tertiary cleats. (b) Photograph showing primary cleats terminating at interbedded tonsteins and secondary cleats terminating within coal-type layers. This hierarchy of fracture sizes suggests that approaches that account for scaling properties of fracture patterns (fractal geometry) should be applied to coal fractures (see Laubach and Tremain, this vol.). Scale bar is 6 inches (15 cm).

in thin vitrain layers. They rarely cross interbedded tonsteins or thin shale partings, even where interbeds are less than half an inch thick. For example, in one lower Fruitland coal bed in the Pinto pit (Navajo mine), fewer than 20 percent of cleats penetrate or cross interbeds 0.2 inch (0.5 cm) thick or less. Master cleats (Henckle and others, 1977) are primary cleats that cross several coal-type layers. Master cleats are visible in some large Fruitland outcrops and coal pits, where spacing ranges from 1 to 3 ft (30 cm to 1 m). Where coal seams are less than 6.5 ft (2 m) thick, master cleats may cross the entire seam.

Secondary cleats are fractures parallel to primary cleats that are *vertically discontinuous* within a lithotype. Secondary cleat spacing is commonly 1 to 2.5 inches (2.5 to 6.3 cm) in subbituminous to high-volatile C bituminous coals in the southern part of the basin and 0.25 to 0.5 inch (0.6 to 1.2 cm) in high-volatile B bituminous coals in the west. Spacing ranges from 0.12 to 0.25 inch (0.3 to 0.6 cm) in high-volatile A bituminous coals in the northern part of the basin. Length and height of secondary cleats are generally less than 1 inch (2 cm). The distinction between primary and secondary cleats is obvious in outcrop but less so in core.

The hierarchy of fracture sizes applies to butt cleat as well as face cleat. Most butt cleats could be classified as secondary cleats in that they rarely extend completely across coal lithotype layers; they are vertically and laterally less persistent than associated face cleats. Butt-cleat spacing is generally greater than face-cleat spacing in the southern San Juan Basin, but it is commonly similar to or closer than face-cleat spacing in the central and northern San Juan Basin.

Tertiary cleats are very closely spaced fractures and microfractures with spacing and height on the order of 0.03 to 0.12 inch (0.1 to 0.3 cm) or less that occur between primary or secondary cleats. Intensity of tertiary cleats is commonly greater in weathered outcrops, and locally, where fresh coal can be traced into weathered

exposures, tertiary cleats become more prevalent. Lack of mineral infill or staining, greater intensity in weathered outcrops, and terminations at open horizontal unloading fractures suggest that tertiary cleats formed near the Earth's surface and may not have been present at depth.

Cleat spacings in coal cores are similar to those in coal beds at outcrop (tables 1, 2, and 3). In core, cleat spacing ranges from less than 0.03 inch to an inch or more (1 mm to several cm). Core observations do not indicate significant variation in cleat spacing with depth or position in the basin, but cleat intensity appears to be greater in bright coals and thinner coal beds, as is the case in outcrop. In core and in fresh mine exposures, secondary and tertiary cleats are less prevalent and less closely spaced than in natural outcrops.

Spacing of coal fractures in regional cleat sets (total fracture intensity) is uniform over distances of as much as a mile where coal occurs above sandstones with planar upper surfaces. For example, in a single 4-inch (10-cm) thick layer of uniform-composition coal approximately 15 ft (4.6 m) above the Pictured Cliffs Sandstone that is exposed in a highwall over a distance of 2,300 ft (700 m) in Navajo mine, most cleat spacing values fall within one standard deviation of the mean of the entire data set (fig. 5). Where sandstones have irregular contacts, and locally near lateral terminations or beneath thick parts of lenticular fluvial sandstones, cleat intensity increases by as much as 25 percent. Such an increase in fracture intensity could arise from several processes, including fracturing caused by stress concentrations at irregularly shaped lithologic boundaries. Variation in primary regional cleat spacing and localization of other fracture types such as small faults at or near irregular rock-type boundaries occur in some Cretacous coals in the western United States (Tyler and others, this vol.).

Causes of Variation in Cleat Spacing

Previous studies suggest that cleat spacing is controlled by coal rank and lithotype as well as bed thickness (Ammosov and Eremin, 1960). Primary cleat spacing in the San Juan Basin depends on coal rank and type, and to a lesser extent, within areas of equal rank, on stratigraphic and structural position and the thickness of individual coal beds within a seam. In Fruitland coal beds, average primary face cleat is closer in the high rank coals in the northern third of the basin than in the lower rank coals to the south. Mean primary-face-cleat spacing is 1.5 inches (4 cm) in outcrops along the northern and western margins of the basin. In the southern San Juan Basin, where coal rank is lower, spacing ranges from to 0.75 to 6 inches (2 to 15 cm), but typically is between 2.5 and 3.5 inches (6.5 and 9 cm) for medium-brightness coal. Decreased cleat spacing with increased bituminous coal rank has been reported in other basins (Ammosov and Eremin, 1960; Ting, 1977).

Primary cleat spacing depends in part on coal type (Ammosov and Eremin, 1960; Ting, 1977). In Fruitland coals, spacing is closest in bright vitrain-rich layers and widest in dull durain-rich layers. Some primary cleats in 0.1-inch-thick (0.25-cm) vitrain-rich layers or lenses have spacing of less than 0.03 inch (0.1 cm), whereas some thin dull (or bone) coal layers are virtually uncleated. However, these thin lenses of very bright or dull coal are volumetrically insignificant (<10 percent); most Fruitland coals that we examined are of intermediate composition, ranging from medium bright to medium dull. We used a qualitative visual field assessment of coal brightness to distinguish three categories of medium-brightness coal. Within this range of coal composition, no significant trend of cleat spacing with coal type is evident (fig. 6).

Fracture spacing in coal and in many other stratified rocks is commonly inversely proportional to bed thickness, with more closely spaced fractures in thinner beds and spacing somewhat less than bed thickness (Ladeira and Price, 1981; Spears and Caswell, 1986). Thickness of coal beds (those divisions of a coal seam separated by noncoal layers such as shale partings or tonsteins) within medium-brightness coal seams in the northern and western San Juan Basin ranges from less than 0.4 inch (1 cm) to more than 20 inches (50 cm), with a mean thickness of 4 inches (10 cm). Primary-face-cleat spacing in these beds ranges from 0.03 to 12 inches (0.1 cm to 30 cm), with a mean spacing of 1.5 inches (4 cm). Although primary cleat spacing can be as much as 4 inches (10 cm) for a bed 2 inches (5 cm) thick, most beds less than 8 inches (20 cm) thick have cleat spacing of less than 2 inches (5 cm), and several beds that are between 10 and 12 inches (25 and 30 cm) thick have spacing of less than 4 inches (10 cm). No systematic increase in cleat spacing is evident for beds thicker than 4 inches (10 cm). Some variation in cleat spacing for a given bed thickness may be due to compositional effects, since a range of coal compositions has been included in the medium-brightness coal data set. In some exposures, cleats are more widely spaced in thicker coal beds, but observations combined from several localities in the northern third of the basin show a relation between bed thickness and cleat spacing that has marginal statistical significance (figs. 7 and 8), even when brighter and duller varieties of medium-brightness coals are excluded. Variance of cleat spacing increases as beds become thicker.

More closely spaced cleats in thin coal beds result from both the bed-thickness effect and the tendency of thin-bedded coals to be vitrain rich. Coal beds with

Table 2. Mineralization in fractures in coal core.

Well name	Location	Core depth (ft)	Mineralization	References
USGS Core Hole A-15	Sec. 1, T23N, R13W	262–295	Gypsum	Wilson and Jentgen, 1980
USGS Core Hole A-4	Sec. 30, T24N, R13W	276–296	Pyrite, gypsum	Wilson and Jentgen, 1980
El Paso Natural Gas Gasbuggy No. 1	Sec. 36, T29N, R4W	3803–3819, 3880–3910	Calcite, pyrite	Fassett, 1967
Blackwood & Nichols NEBU No. 403	Sec. 9, T30N, R7W	3025–3059	Calcite	Mavor and Close, 1989a
Tenneco Pritchard No. 9	Sec. 1, T30N, R9W	2467–2491, 2621–2651	Calcite, gypsum	CGS files
Western Coal P-70	Sec. 22, T30N, R15W	384–414	Calcite, pyrite	TRW Preliminary Well Test Report, 1978
USGS Core Hole SJ 23-4	Sec. 23, T30N, R15W	461–471, 583–608	Pyrite, gypsum	Beach and Jentgen, 1978
Tiffany Glover No.1	Sec. 2, T32N, R6W	3062–3111	Calcite	Jones, 1985
Mobil Colorado 32-7, No.9	Sec. 4, T32N, R7W	2783–2804	Pyrite	COGCC files
USGS No. 2	Sec. 23, T32N, R12W	61–119	Pyrite	Roberts, 1989
USGS No. 10	Sec. 31, T33N, R11W	337–397, 416–460	Pyrite	Roberts, 1989
Amoco Hott 29-1, No. 2	Sec. 29, T33N, R6W	3021–3031	Calcite	COGCC files
USGS No. 8	Sec. 36, T33N, R12W	75–129	Pyrite	Roberts, 1989
SUTEC Oxford No. 1	Sec. 25, T34N, R8W	2769–2787	Calcite	CGS files
SUTEC Oxford No. 2	Sec. 25, T34N, R8W	2832–2850	Calcite, gypsum, Pyrite	CGS files
Tenneco Fassett 2-13	Sec. 13, T34N, R9W	2468–2482	Calcite	CGS files

CGS = Colorado Geological Society

COGCC = Colorado Oil and Gas Conservation Commission

many vitrain-rich layers and numerous tonsteins or shale partings tend to have more closely spaced cleats, but the cleat system may be poorly interconnected vertically because cleats tend to terminate at noncoal interbeds.

Cleat-Filling Minerals

Many fractures in Fruitland coals are barren and lack macroscopically visible infill minerals, but some cleats have thin mineral veins. Principal cleat-filling minerals,

Table 3. Oriented cores.

Well name and location	Cleat orientation	Cleat frequency (number/cm)	Cleat length	Fruitland coal stratigraphic position	Coal sample depth (ft)	Coal rank	Comments and references
Bowen-Edwards McCulloch 28-1 SWSE Sec. 28, T34N, R10W[1]	Face: 320–340° Butt: 40–70°	—	.4 mm–13.4 cm 75% avg. 1.11 cm 25% over 2.54 cm	Lower	3140.5–3143	?	COGCC[2]
Amoco Southern Ute Tribal H No. 1 NWNW Sec. 18, T32N, R10W	Face: 20–40° Butt: 280–320°	Face: 4.3–17/cm avg. 7.1/cm Butt: 3.3–15/cm avg. 6.1/cm	Face: <.1–4.5 cm avg. 2.3 cm Butt: <.1–3.7 cm avg. 1.8 cm	Lower	3110–3131		(TerraTek, 1990)
Mesa Hamilton No.3 SWSW Sec. 30, T32N, R10W	Face: 30–50° Butt: 300–320° Third: 0–10°	all beds: 1–16/cm Core 2: 1–8/cm	all beds: avg. 4 cm Core 2: max. 9 cm	Upper	1) 2652–2670.6 2) 2673.8–2680.9	HVA	"Cleat frequency, length...inversely proportional to ash content" (Decker and others, 1989)
		Core 3: max. 12/cm	Core 3: .1 mm–18 cm	Lower	3) 2872–2886.8		
Mobil Colorado 32-7 No. 9 SWSW Sec. 4, T32N, R7W	Face: 0–20° Butt: 80–110°	Face: 2–22/cm Butt: 3–18/cm thin vitrain: Face: 28/cm Butt: 20/cm	Face: 1–3 mm and Butt	Lower	2906.6–2911.7	MV	"Some gouge and calcite filled fracs in ss below coals, strike same as cleats" (GRI-90/0043 Mavor and Close, 1989c)
Tiffany Glover No. 1 NESE Sec. 2, T32N, R6W	Face: 294°	Face: 2/cm Butt: 1/cm	—	Lower	3074–3089	MV	"Some calcite on cleats" (Jones, 1985)
Blackwood & Nichols NEBU No. 403 SENE Sec. 9, T30N, R7W	Face: 20–40 Butt: 300–320°			Upper	3025.5–3058.5	HVA	"calcite in joints and cleats, late-stage joints in face cleat direction"; "cleat . . . varies inversely with lithotype thickness"; "cleats terminate at partings" (GRI-90/0041 Mavor and Close, 1989a)
				Lower	3160.6–3186		
McKenzie Methane So. Ute Mobil 36-1 SENE Sec. 36, T34N, R10W	—	avg. 6/cm in thin vitrain: avg. 15/cm max. 40/cm	avg. 6 mm max. 3 cm .5–5 mm (layer thickness)	Mid	2415.2–2453.9	MV	(GRI-90/0042 Mavor and Close, 1989b)

MV = medium-volatile bituminous
HVA = high-volatile A bituminous
[1]Well number on figure 1
[2]Geological well report, Colorado Oil and Gas Conservation Commission
Dash indicates attribute not determined.

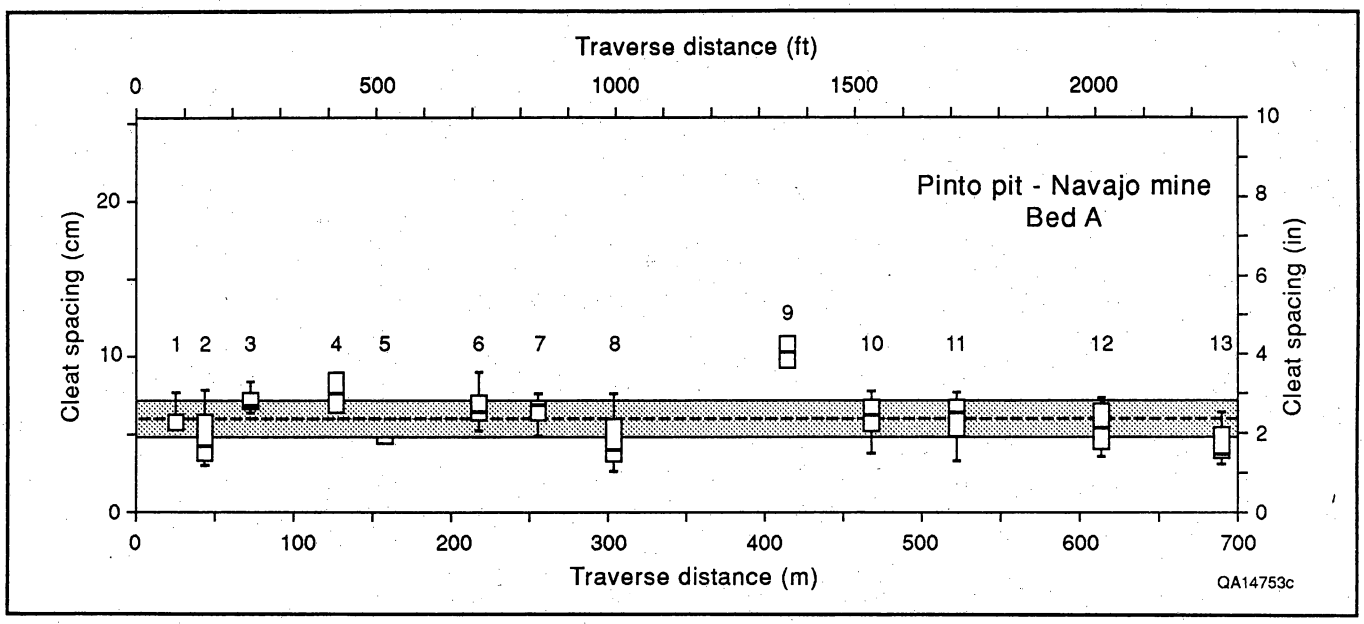

Figure 5. Cleat spacing versus traverse distance in a bed of uniform dip, thickness, and composition, Navajo mine. Center half of the data at each station is represented by a rectangle (box) and median is indicated by a bar. Dashed line and shaded area represent mean and one standard deviation of measurements from all stations.

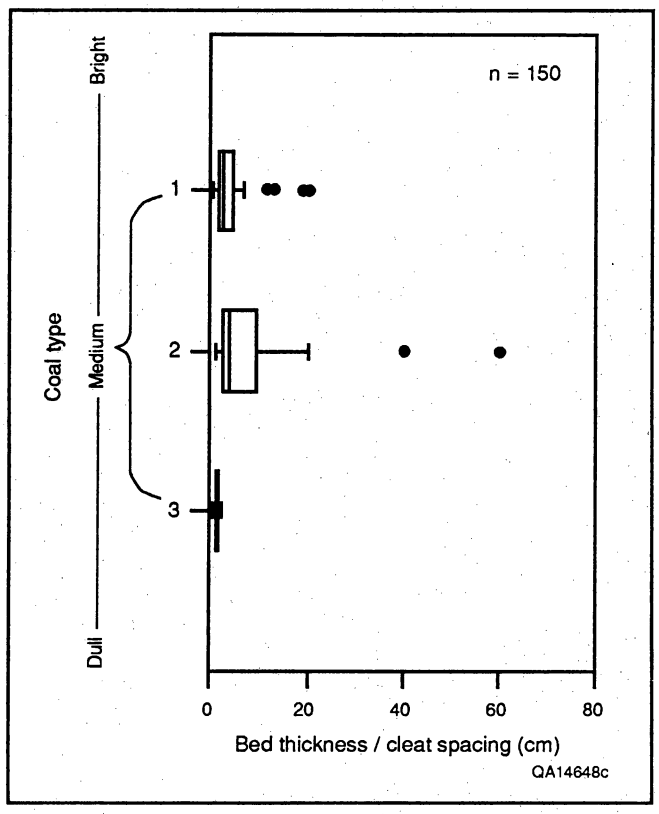

Figure 6. Coal type versus bed thickness/cleat spacing ratio (spacing index) for three classes of medium-brightness coal, Fruitland Formation, San Juan Basin. Center half of data is represented by a rectangle (box) and median is indicated by a bar.

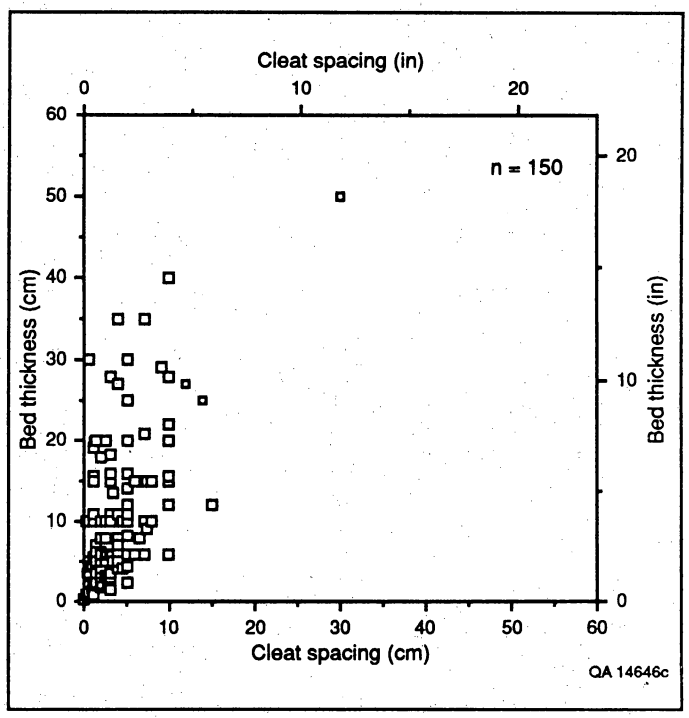

Figure 7. Cleat spacing versus bed thickness for Fruitland coal beds in northern San Juan Basin.

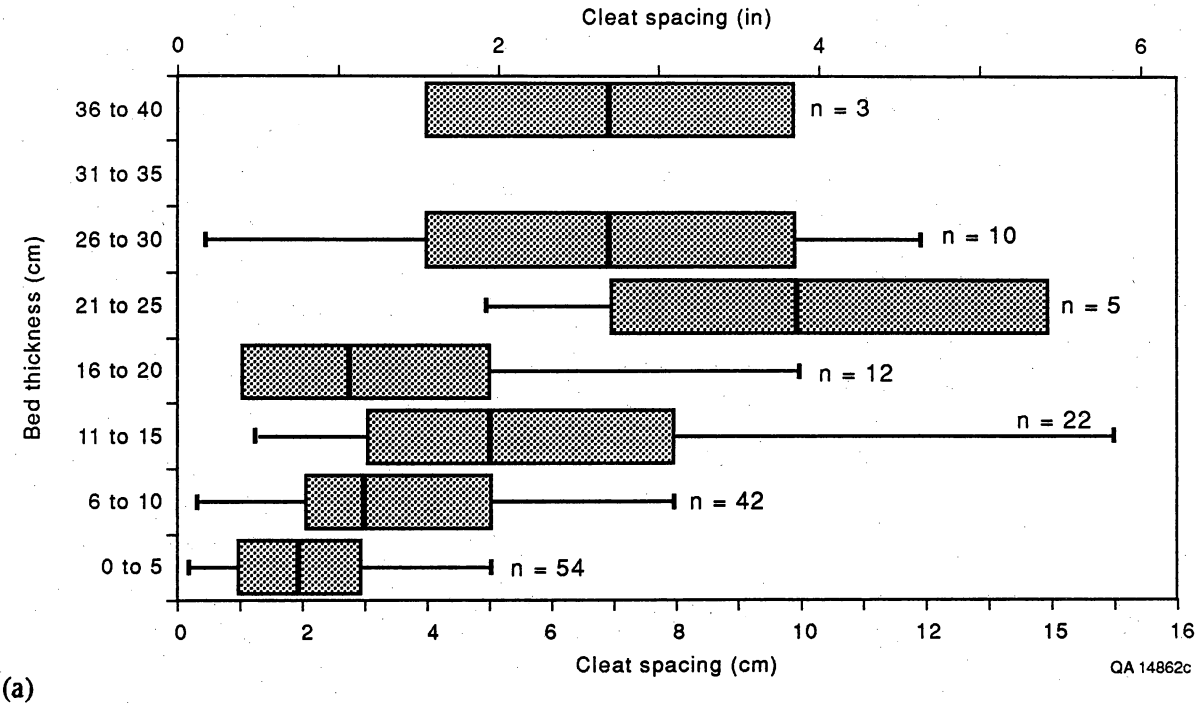

(a)

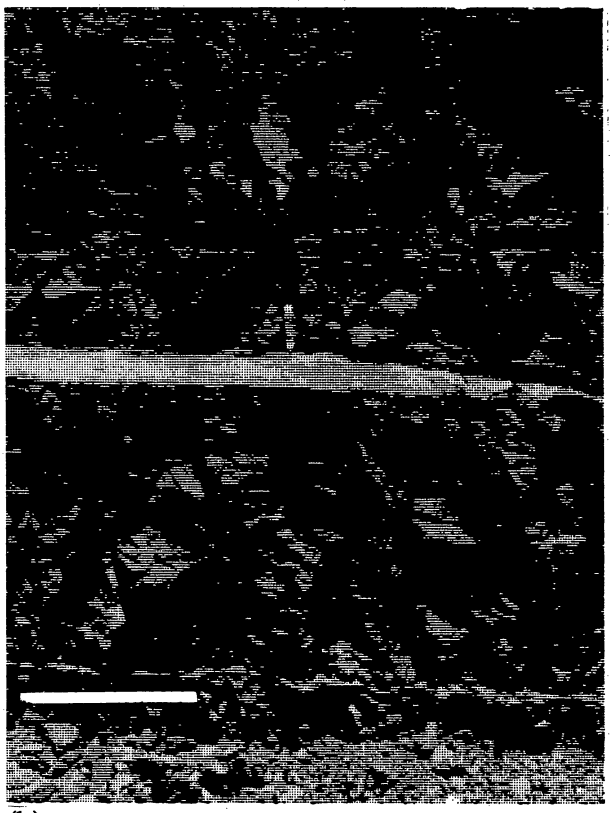

(b)

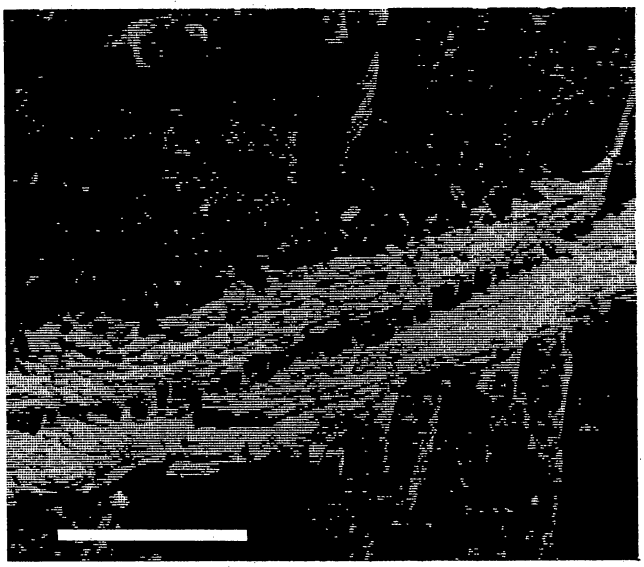

(c)

Figure 8. Illustrations of cleat spacing patterns. (a) Cleat spacing grouped by equal bed-thickness intervals. Center half of data is represented by a rectangle (box) and median is indicated by a bar. (b) Widely spaced primary cleats in thick coal bed, Navajo mine. Scale is 9 inches (23 cm). (c) Close cleat spacing in thin coal bed, Navajo mine. Scale is 4 inches (10 cm).

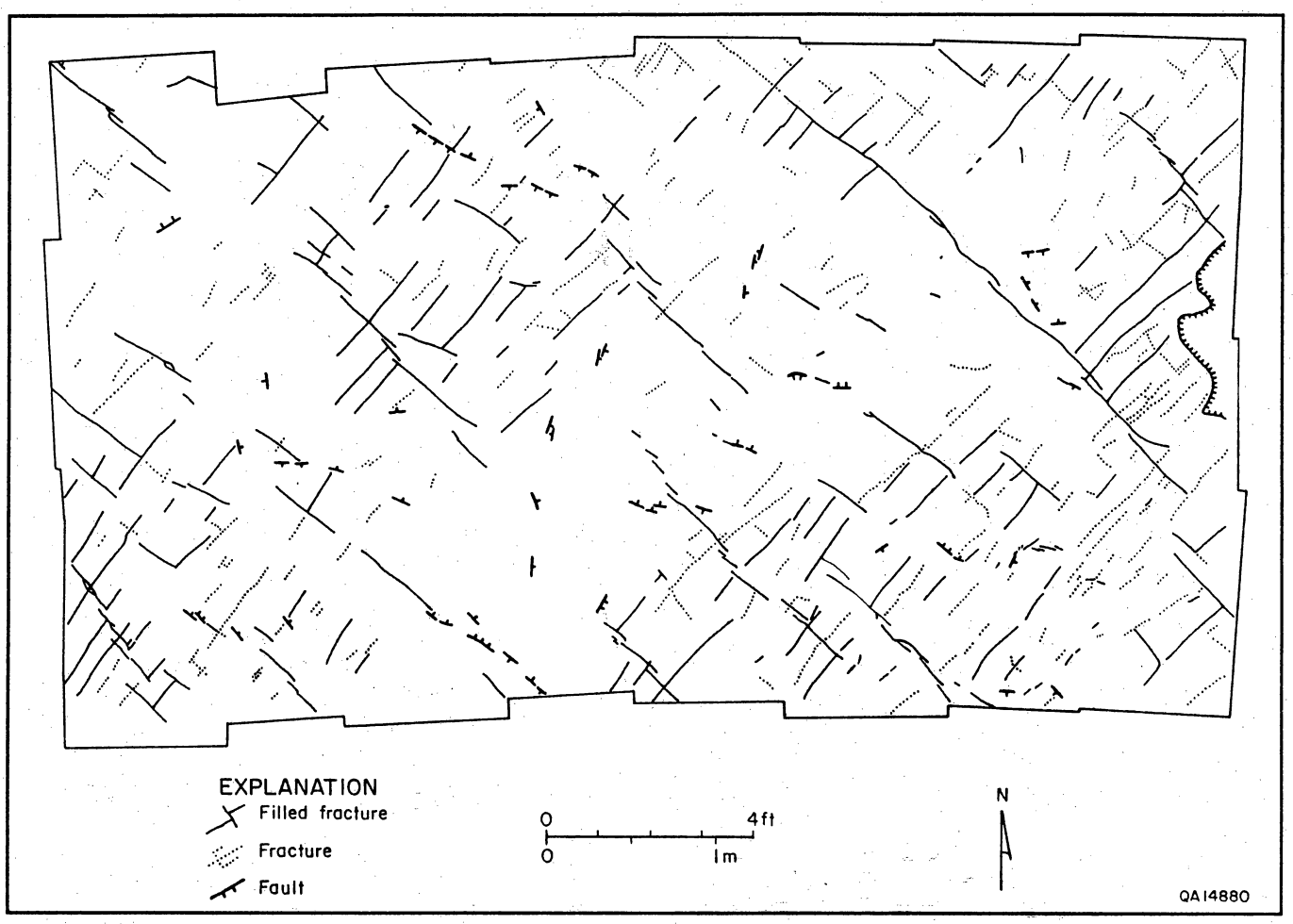

Figure 9. Cleat pavement map showing crisscrossing and mutually abutting face-cleat (fracture) pattern in a single bedding plane at Navajo mine. Natural barren and mineral-filled fractures are shown. Secondary and tertiary cleats not shown.

pyrite, calcite, and gypsum, are present in both outcrop and in core from depths ranging from 0 to 3,900 ft (0 to 1,190 m) in the northern and central basin (table 2). Pyrite occurs in thin films and isolated patches on some cleat surfaces in mines and core. In outcrop, primary face cleats commonly have a reddish-brown to red stain that may represent oxidation products of finely disseminated sulfides formerly present in fractures. Near the Colorado–New Mexico border, isolated pyrite rosettes occur on both face- and butt-cleat surfaces.

Calcite fills some primary face cleat in several mines (locs. 2, 3, and 4, table 1) and in cores from 10 wells (table 2). In sandstone of the SUTEC No. 1 Oxford core, calcite occurs in a vertical extension fracture that is parallel to, and possibly continuous with, adjacent calcite-filled cleats. Calcite-filled cleats and parallel calcite-filled fractures in sandstone also occur in Chimney Rock mine in Colorado, and vein widths are as much as 0.05 to 0.1 inch (1.3 to 2.5 mm) in some New Mexico examples. Calcite typically has a fibrous habit.

Cleat-filling fibrous gypsum is present in several outcrops in New Mexico, in the Navajo mine, in three shallow USGS cores from New Mexico, and in core from Tenneco Pritchard No. 9 and SUTEC Oxford No. 2 wells. In exposures in the northern San Juan Basin, fine-grained clay minerals (kaolinite?) occur on some face-cleat surfaces. Fracture-filling resin is common in outcrop and in core from USGS wells in New Mexico and Colorado, and in Western Coal P-70 core (table 2), but on the basis of abutting relations, most of these resin-filled veins are thought to predate regional cleat. Resin in primary face cleat is rare. Where present, pyrite and calcite mineral fill generally exists in primary face cleats in a given bed, but maps of fractures in coal pavements show that mineral fill is discontinuous along fracture traces (fig. 9). Many butt cleats, and most secondary and tertiary cleats, lack mineral fill or stain.

Wide mineral-filled veins and vein networks occur near some faults and in several outcrops where presence or absence of faults could not be demonstrated. Vein widths are as much as 0.39 inch (1 cm). Veins are filled

with gypsum, calcite, or quartz, and subsidiary pyrite and clay minerals. Infilling gypsum has a fibrous habit, and locally veins have medial lines and coal inclusions.

Cleat Orientation

Cleat strike was measured in 6 cores (table 3) and 90 outcrop stations. Core orientation was by standard downhole orientation techniques (Nelson and others, 1987); strike uncertainty is approximately ±10 degrees. Outcrop stations ranged from selected areas of large, active open-pit mines and abandoned mines to natural exposures and small excavations. Most stations have areas of 100 ft² (9 m²) or less. Fracture measurements in steeply dipping beds were restored to prefolding attitudes stereographically by rotation about strike of bedding. In general, change in cleat strike because of this rotation is less than 10 degrees. In selected areas, cleat measurements were supplemented by maps of cleat patterns on bedding surfaces. Cleat maps were constructed either by mapping with reference to a grid marked on the outcrop or by mapping directly on color photographs.

Face cleats strike predominantly northwest in the northern San Juan Basin, and predominantly north or northeast in the southern part (fig. 1). Cleat strike typically varies by less than 10 degrees in individual cores and in most small (<100 ft² [<9 m²]) outcrops (locs. 9, 14, and 19, table 1). Large, continuous or nearly continuous exposures show that in parts of the basin cleat strikes are nearly constant over large areas. For example, face-cleat strikes vary by less than 5 degrees in a 2,300-ft (700-m) transect in the Pinto pit in the Navajo mine. In a traverse approximately 6 mi (10 km) long in mid- to lower Fruitland coals between the Las Animas and Florida Rivers, mean face-cleat strikes at 15 stations (face n >6 per station) have a maximum variation of 37 degrees (dispersion = 0.85), but typically vary by less than 10 degrees (Laubach and Tremain, this vol.). Cleat strikes are uniform between adjacent coal seams at the old La Plata mine (loc. 11, table 1), where four coal beds in the lower Fruitland have mean face-cleat strikes between 330 and 344 degrees (fig. 10), and at the south fork of Texas Creek and East Gap (locs. 9 and 14, table 1), where cleat strikes in adjacent lower and lower to mid-Fruitland coal seams vary by only 11 and 5 degrees, respectively, between basal and higher Fruitland coal beds.

Great dispersion in face-cleat strike or abrupt strike variations of 20 degrees or more occur locally (for example, locs. 3, 6, and 17, table 1). Variations in face-cleat strike are due to curved cleats, gradual changes in cleat strike over wide areas, and cleats with different strikes in adjacent coal beds. Curved cleats occur at seven stations in the Fort Lewis mine (loc. 17, table 1) and at six widely spaced stations in the northern part of the basin (locs. 1, 4, 5, 6, 14, and 15, table 1). Cleats

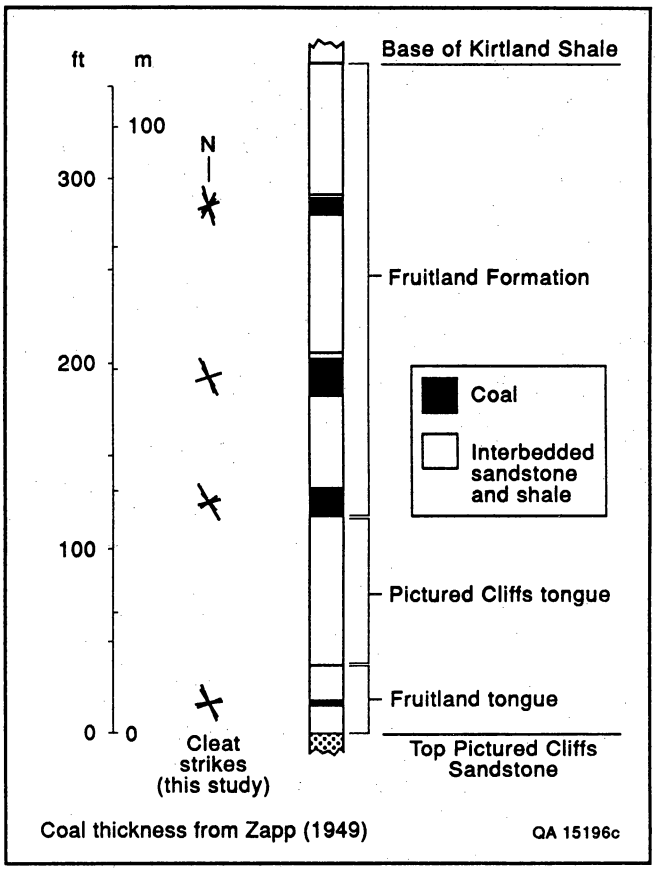

Figure 10. Cleat strikes in several coal seams at La Plata mine.

change strike by between 5 and more than 30 degrees in distances of a few inches to several feet (centimeters to meters). Some curvature results from hooking of cleats into an adjacent fracture, probably caused by interaction between a growing and preexisting fracture (for example, Pollard and Aydin, 1988), but in several cases, the entire array of face cleats curves in unison (loc. 6, table 1). Unlike curved cleats that define some polygonal patterns in coal, such a pattern would not be expected from brittle failure in an isotropically shrinking medium. Wavy or curved cleats have rarely been mentioned in accounts of other coal basins (one example is Ver Steeg, 1942), and since curved cleat arrays typically occur in only a small part of a given outcrop, they may have been overlooked elsewhere.

Greatest variation in cleat strike over short distances is where curved cleats occur near faults (fig. 3). At the Fort Lewis mine, cleats change strike by 35 to 40 degrees near a small graben. Cleat strikes are more nearly parallel to the fault plane within approximately 30 ft (9 m) of the fault. In the Navajo mine, in the hanging wall of a small (6 inches [15 cm] net slip) east-striking normal fault, northeast-striking cleats change strike by 30 degrees over a distance of only 14 inches (35 cm) as they

approach the fault plane. The fault is one of several localized in the hinge of a small anticline, where difference in coalbed dip is between two and five degrees. This fault zone differs from some that crosscut and disrupt regional cleats in that no fracture zone parallels the fault and it has an anomalously gentle dip of 20 to 30 degrees, characteristics that are consistent with fault and cleat-curvature development during a late stage of coal compaction.

Cleat strike can vary greatly between adjacent beds. At West Gap, Beaver Creek, and Fort Lewis mine (loc. 15, 7, and 17, table 1), face-cleat strikes vary by 53, 48, and 71 degrees, respectively, among adjacent beds. These differences have no consistent pattern with stratigraphic position. The area of greatest variability in cleat strike is near the Fort Lewis mine (fig. 11). Some cleat-strike variation may reflect folds, faults, and fracture zones that occur in this area (fig. 11) (Newman and McCord, 1980; Laubach and others, 1990; Laubach and Tremain, this vol.). However, this region is also part of a wider zone, described in the following section, where face-cleat strike shifts by nearly 90 degrees.

Basin-Scale Cleat-Strike Domains

Face-cleat strikes are typically uniform throughout large areas of the San Juan Basin, but they are not the same throughout the entire basin (figs. 1 and 12). Face-cleat strikes delineate two principal domains of regional extent. In the northern part of the basin, northwest-striking face cleats predominate (mean strike, 344 degrees), but south of the New Mexico–Colorado state line, north-northeast- and northeast-striking face cleats predominate (mean strike, 020 degrees). These domains are separated by a boundary domain that extends eastward from the Colorado–New Mexico border, at the western margin of the basin, to T32N, R7W, where it turns southward into New Mexico (fig. 12).

In addition to the difference in polarity of the earliest formed (face) cleat from northeast in the southern part of the basin to northwest in the northern part, face cleats in the northern domain strike approximately 10 to 15 degrees more northerly than butt cleats in the southern domain. Yet within each domain, face and butt cleats are orthogonal. The northern area (domain 1) is further characterized by gentle west- to west-northwest-trending folds, thick sandstones and coal beds with northwest depositional trends (Ayers and others, this vol.), and higher coal rank (high-volatile A bituminous or greater) (Scott and others, this vol.). In contrast, the southern area (domain 2) of north to northeast face-cleat strikes is developed on a gentle northeast-dipping homocline, the Chaco Slope. Fluvial channel-fill sandstone and coal deposits have predominantly northeast or north trends, and coals generally are lower rank (high-volatile B bituminous or lower). Cleat spacing is apparently somewhat wider in the southern domain. Based solely on face-cleat strike, the southern part of the basin can be further subdivided into a domain of northeast-striking cleat in the west and a domain of north-striking cleat in the east (domain 2a and 2b, fig. 12).

The boundary between domain 1 and domain 2 is a wide area of variable face-cleat strike that is exposed in T33N, R11, and 12W near the Colorado–New Mexico border. We interpret the domain 1-2 boundary region to be between 15 and 20 mi (24 and 32 km) wide on the basis of the width of outcrop that has nonuniform or opposed face-cleat strikes. In the subsurface to the east, the boundary is constrained to strike east or northeast by divergent face-cleat strikes in widely spaced wells, suggesting that the boundary is approximately parallel to the east-trending Late Cretaceous basin hingeline and several gentle folds (the Bondad and Ignacio anticlines). The outcrop of the boundary zone is where greatest cleat-strike variability occurs, and northwest- and northeast-striking cleats are typically equally prominent in a given bed. As a result, coal is generally friable. Near Soda Springs, Cinder Buttes, and the Fort Lewis mine, face-cleat strike (defined by abutting relations) is either northeast or northwest in adjacent beds. Beds with mutual abutting cleat relations and crossing cleat patterns are prominent. These patterns suggest two interfering face-cleat trends.

The location and nature of the boundary between domains 2a and 2b is difficult to determine accurately because well information on cleat strike in the central basin is lacking. The transition may be gradual because difference in strike is slight. There is no indication that crosscutting or interfering cleat sets exist along the boundary. Cleats in low-rank domain 2b coal may have a greater tendency to be open in the subsurface because north-striking fractures are normal to modern least horizontal stress (Zoback and Zoback, 1980, 1990).

Faults and Associated Fractures

East-, northeast-, and northwest-striking faults are present in the basin (Wood and others, 1948; Zapp, 1949; Barnes, 1953; Barnes and others, 1954; Newman and McCord, 1980; Condon, 1988; Tremain and Whitehead, 1990, their fig. 41). Faults and associated fractures are superimposed on cleat patterns in some areas, but elsewhere cleats curve near faults, suggesting that faults and cleats formed together. Faults in coal seams are poorly exposed, except where they occur in mines in the west-central part of the basin. West-northwest- to northwest-striking normal faults occur on the western margin of the basin in the La Plata and Fort

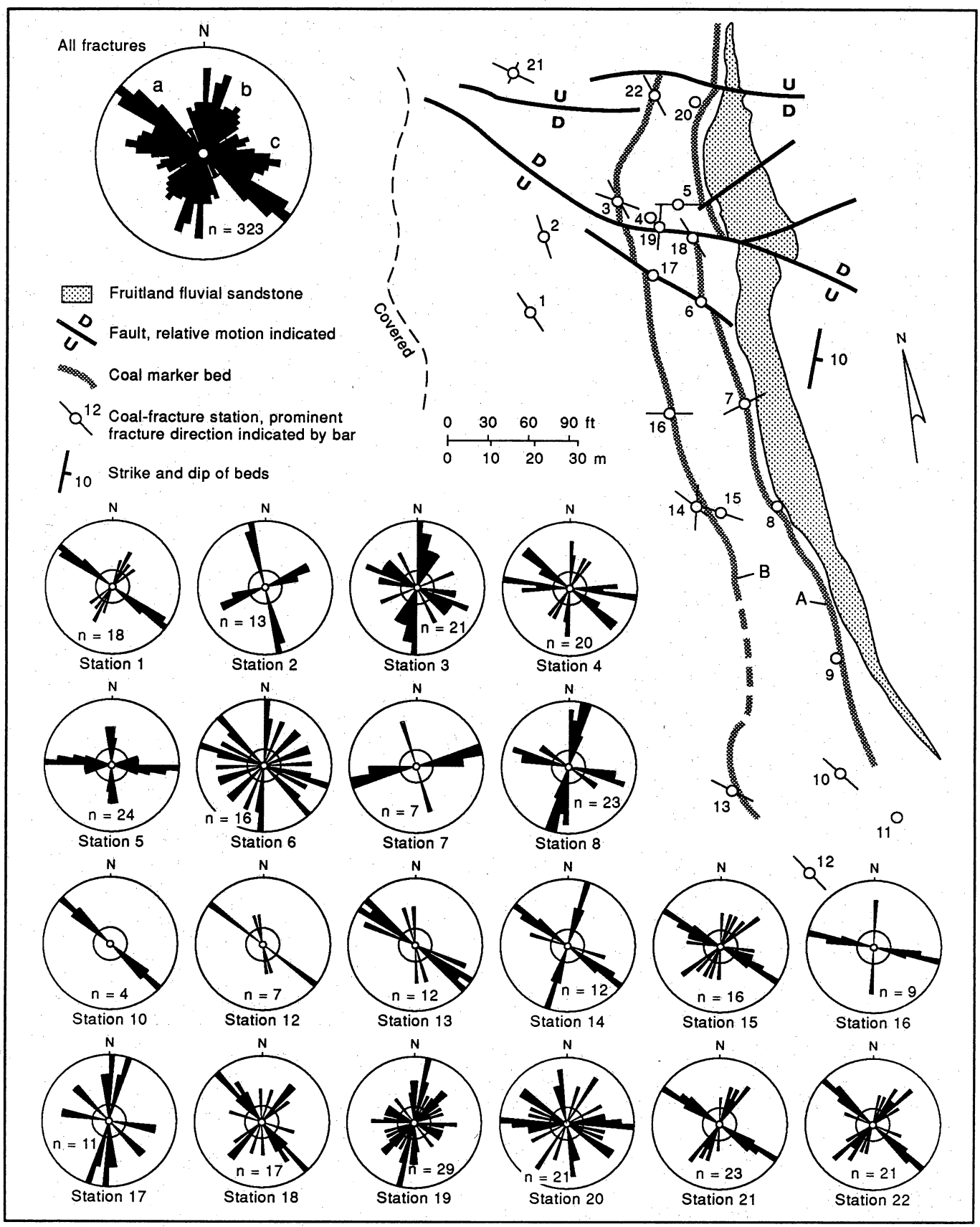

Figure 11. Faults and fracture (cleat) strikes in a part of Fort Lewis mine area.

QA 15037c

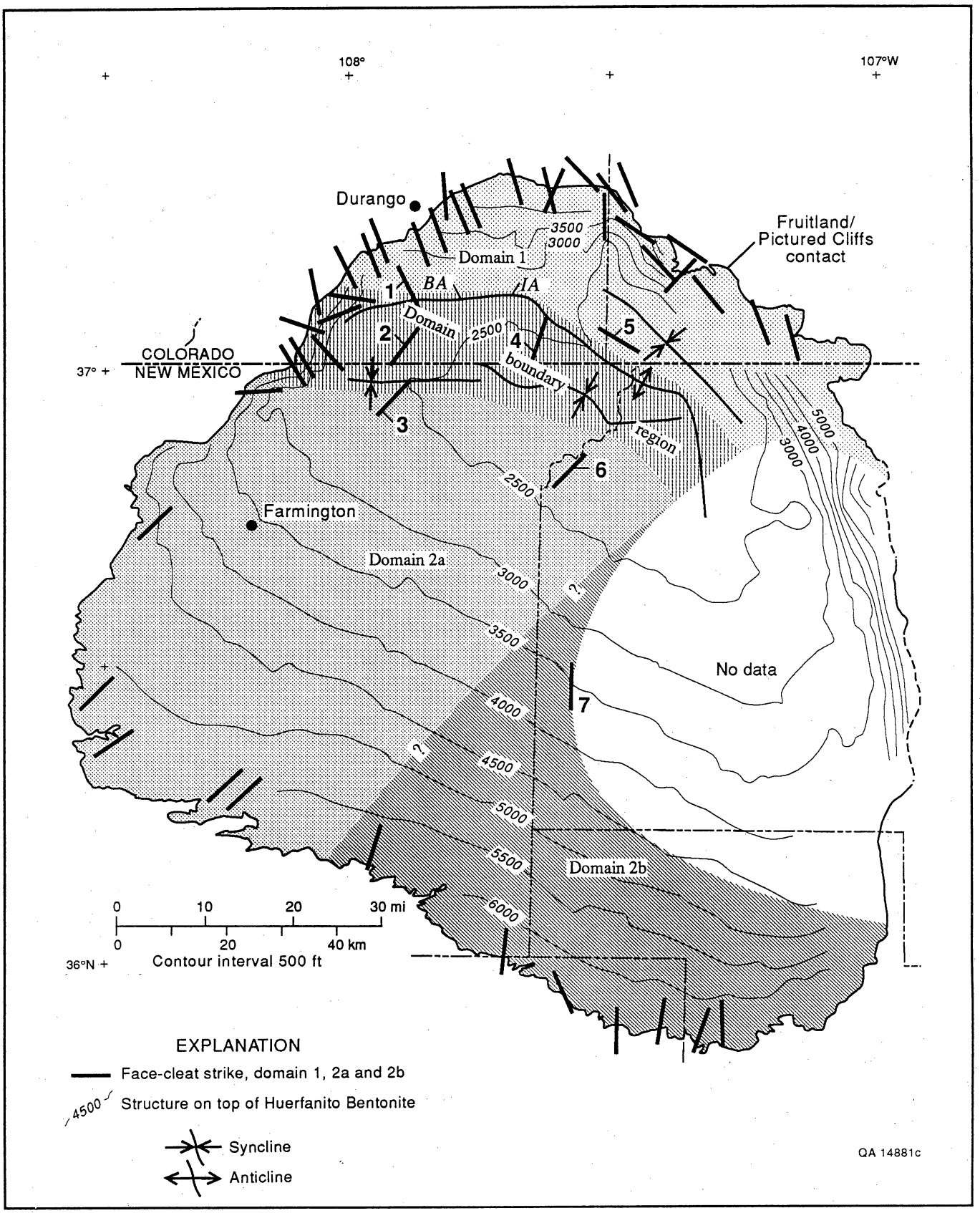

Figure 12. Face-cleat-strike domains, San Juan Basin. Domain boundaries are gradational and approximately located. Numbers indicate wells with core that were used in this study. Structure is contoured on the Huerfanito Bentonite. BA–IA = Bondad-Ignacio Anticline. See table 3.

Lewis mines. Northeast- and northwest-striking faults occur near Bondad, and northeasterly striking faults occur south of Durango. Cat Creek fault in Archuleta County strikes northeast, and faults near the southern boundary of the basin have northeast or east-northeast strikes.

Some large faults are marked by zones that are as much as several tens of feet (several meters) wide composed of intensely fractured rock. Fractures within and adjacent to these zones are taller and more vertically continuous than is typical of primary face cleats, and fractures commonly extend across noncoal interbeds. Cleat strike at stations near some large faults show marked variations (fig. 11), and abrupt cleat curvature occurs near some small faults (fig. 3). Many fault-related fractures are closed, and they may be barriers to, rather than conduits of, fluid flow. Faults large enough to juxtapose coal and noncoal layers could disrupt continuity of regional flow paths in coal seams. Such faults are visible in mines and can be mapped in the subsurface in areas of dense well control in the northwestern and north-central parts of the basin.

Small faults (net slip <3 ft [<1 m]) at the Fort Lewis and Navajo mines and at Squaw Creek are isolated, polished, and striated slip surfaces with little or no variation in cleat spacing adjacent to the fault. Such faults commonly lack associated fracture zones, or the zone may be narrow (fig. 13). As little as 0.4 to 0.8 inch (1 to 2 cm) of slip on such faults can interconnect cleat sets in adjacent coal layers that would otherwise be isolated by unfractured interbedded tonsteins.

Another type of fault zone comprises many small striated, polished slip surfaces in anastomosing arrays. Although these zones are locally as much as 3 to 6 ft (1 to 2 m) wide, net slip on microfault arrays is commonly less than 4 inches (10 cm) (loc. 6, table 1). Because small faults and microfault zones are not open fractures but have polished surfaces consisting of dense, comminuted coal, they may be permeability barriers. Intensity of faulting and proportions of different fault types are unknown, but observations in extensive mine highwalls suggest that faults are widely spaced in the west-central part of the basin. For example, in part of the Navajo mine, only four such faults were visible in approximately 650 ft (200 m) of highwall. Faulting is more intense in the La Plata mine.

West-northwest and northeast-striking fracture zones, where fracture intensity dramatically increases, occur in Pictured Cliffs Sandstone and adjacent Fruitland coal on the western margin of the basin (Laubach and others, 1990, and this vol.). Zones are locally associated with and parallel to small normal faults. In such areas, coal and sandstone have greater fracture frequency and density, have significantly higher fracture connectivity

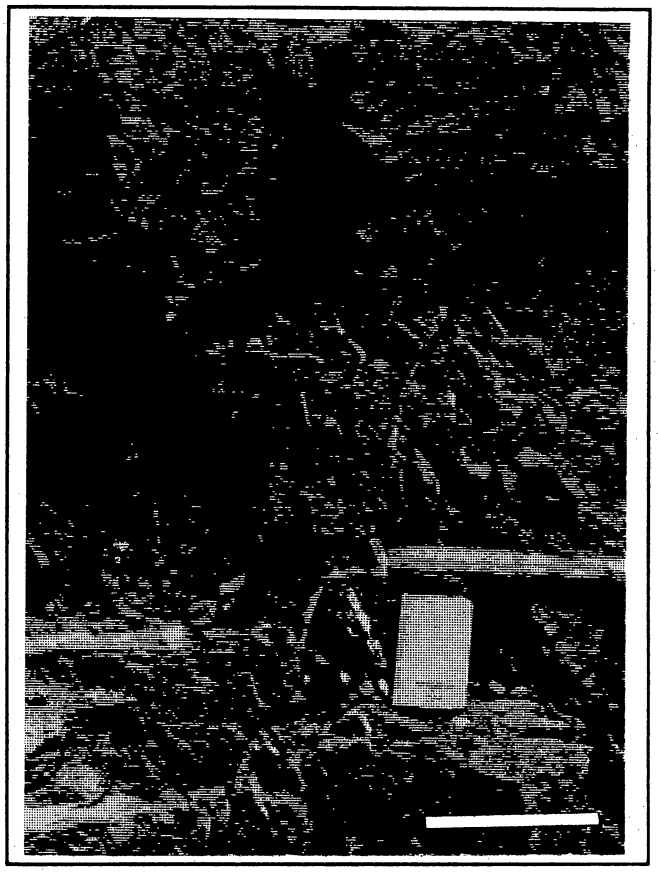

Figure 13. Small normal fault with associated fractures, Navajo mine. Width of fracture zone is indicated by a bar. Note offset tonstein. View is to west. Scale (indicated by arrow) is 11 inches (28 cm).

(Laubach and others, this vol.), and might have greater permeability. Pictured Cliffs fractures that continue into coal seams such as those seen at the Fort Lewis mine and near Durango may be viable exploration targets. Studies are needed to further characterize these fractures to guide exploration and development efforts.

Timing and Cause of Cleat Formation

Cleat sets are a manifestation of some combination of tectonic strain and volume loss/compaction resulting from coal maturation during coalification (McCulloch and others, 1974). Coalification converts initially ductile, fluid-rich sediment into brittle rock at shallow depths. Occurrence of cleat in shallowly buried Tertiary lignites in several basins confirms that fractures can form early in the burial history of coal (Kendall and Briggs, 1933).

Timing of cleat development is constrained by age of cleat relative to dated folds and burial history of the

Fruitland Formation. Where beds are reoriented by folds along the northern and western San Juan Basin margin, systematic regional face and butt cleats remain orthogonal to bedding, indicating that cleat formation predates fold development. Folds on the northern and western basin margin formed during the early Tertiary (Paleocene to Eocene) (Fassett, 1985). Crosscutting relations between cleat and bedding-parallel coal compaction fabrics indicate that brittle failure of coal occurred after a significant amount of compactional flattening. Lack of distorted or folded cleats shows that little vertical shortening of coal occurred after cleat development. Compaction of sufficient magnitude to account for current dimensions of coal beds could have been accomplished at minimum burial depths of approximately 2,000 to 3,000 ft (600 to 900 m) that were achieved prior to Late Cretaceous to early Tertiary tilting and uplift. Early formation of butt cleat is suggested by tilted mineral-filled butt cleat along basin-margin folds and in core from depths of as much as 3,000 ft (900 m). Cleat sets in the San Juan Basin therefore probably formed in the Late Cretaceous (post–Early Maastrichtian?), prior to folds that define the basin margin. Cleat formation was broadly contemporaneous with orogenic shortening of the Cordilleran belt that was already in progress during Campanian deposition of the Fruitland Formation and that continued, marked in the Cordilleran foreland by intermittent uplift, subsidence, or tilting, into the early Tertiary. Other structures in Fruitland coals, such as faults, local fractures discordant to cleat, and some fracture zones, may have developed during Laramide folding and faulting or during one or several of the numerous epeirogenic events that have affected the northeastern Colorado Plateau during the Cenozoic.

Face cleats are opening-mode fractures that form parallel to greatest horizontal compressive stress. Uniformity of face-cleat strikes within large domains in the San Juan Basin indicates that these fractures developed in response to a regionally coherent stress pattern such as could result from orogenic processes of shortening or uplift. This fracture pattern implies lateral elongation of the foreland, a common response to shortening in neighboring mountain belts (Hancock and Bevan, 1987). Similar regional cleat patterns elsewhere in the Rocky Mountains and Appalachian Plateau have been interpreted to result from orogenic compression, and some cleat patterns can be linked to specific structural events (Ver Steeg, 1942; McCulloch and others, 1974; Henckle and others, 1977; Hucka, 1989; Kulander and Dean, 1980). Where orogenic belts are curved or the foreland responds in a nonuniform way to tectonism, stress trajectories and fracture strikes may vary accordingly (Hancock and Bevan, 1987). Paleostress domains with divergent stress trajectories have been inferred in the Appalachian Plateau from face-cleat strike domains (Kulander and Dean, 1980).

Viewed on a regional scale, the San Juan Basin throughout the Late Cretaceous was located in a foreland adjacent to a major bend in the Cordilleran belt (fig. 14). This part of the foreland was probably subjected to both northeast- and southeast-directed tectonic compression events from mid-Cretaceous time through the early Tertiary. Such events could have controlled stress patterns in the basin. Tectonic events are marked by thrusting and volcanism in the orogenic belt, changes in relative sea level as well as unconformities in areas close to the orogenic belt northwest and southwest of the San Juan Basin in Utah and Arizona, and mild tilting and gentle folding within the basin.

In the San Juan Basin, northwest- and northeast-striking cleats in domains 1 and 2 could mark maximum horizontal paleostress trajectories established during episodes of Late Cretaceous southeast and northeast compression. It is not yet possible to link Fruitland cleat

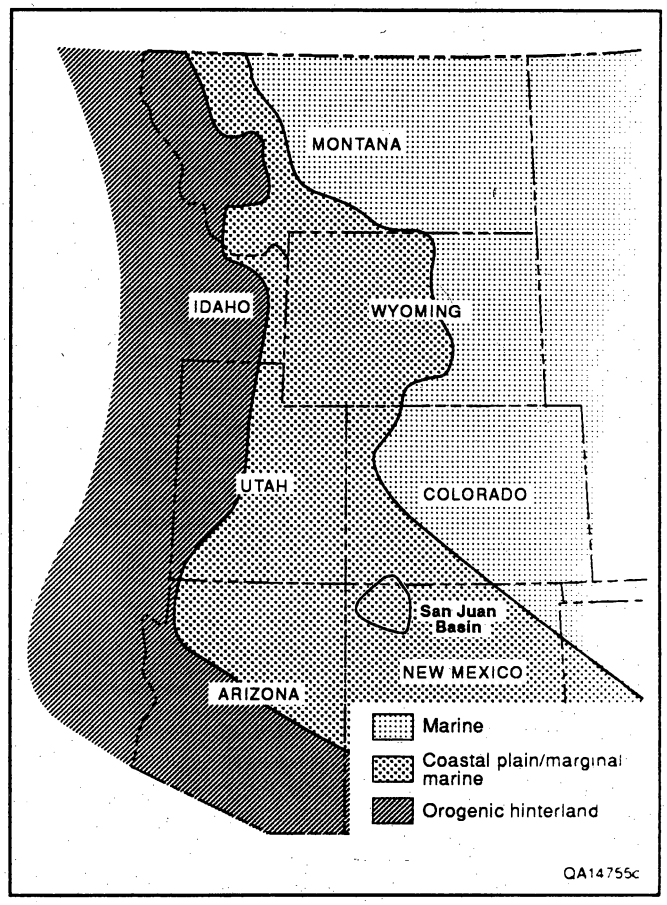

Figure 14. Tectonic/paleogeographic setting of San Juan Basin area in latest Campanian (after Cumella, 1983). Tectonic movements in orogenic hinterland may have affected cleat trends in San Juan Basin.

development to specific tectonic events because the precise time of cleat development is unknown; the Late Cretaceous tectonic setting and history of the basin indicate that several Late Cretaceous tectonic events occurred while coalification was underway in the Fruitland Formation. Coal-occurrence and coal-rank maps indicate that the basin hingeline, and folds such as the Bondad and Ignacio anticline, may have been initiated by late Campanian time (Ayers and others, this vol.; Scott and others, this vol.). During this time, extensive volcanism and possibly fault movement occurred in southeastern Arizona (Cumella, 1983). Orogenic uplift to the southwest may have caused persistent northwest depositional strike and northeast sediment transport direction in the Fruitland Formation, and stresses related to this event may have affected the Fruitland during coalification. In late Maastrichtian (or possibly Paleocene) time, depositional patterns of the McDermott Member of the Animas Formation indicate a short-lived volcanic and tectonic event northwest of the San Juan Basin, and the sub–Ojo Alamo Formation unconformity indicates uplift and erosion of the basin prior to late early Paleocene time (Fassett, 1985). Small basinwide strains could have accompanied early stages of any of these events, accounting for cleat development prior to folding and parallelism of shortening directions indicated by face cleats and northeast- and northwest-trending folds.

Cleat domains may represent separate deformation events or contemporaneous paleostress provinces. Abutting relations in the domain boundary region are inconclusive, but northeast-striking face cleats abut very widely spaced (3 to 6 ft [1 to 2 m]) northwest-striking fractures in the northern Navajo mine, suggesting that domain 1 face cleats in the north formed before domain 2 cleats in the south. If this is the case, it implies early southeast-trending maximum horizontal stress during domain 1 cleat development replaced by northeast-trending maximum horizontal stress during domain 2 cleat development. In the north, coalification may have advanced earlier to the stage where cleat development could occur, as suggested by current pattern of coal rank and deeper burial of the northern section of the basin in the Late Cretaceous. Northwest-striking domain 1 cleats are in highest rank, high-volatile A and B coals, whereas domain 2 cleats are primarily in high-volatile C coal. Multiple cleat-forming events have been inferred in other basins (Spears and Caswell, 1986). Alternatively, crisscrossing or mutually abutting relations and alternations in face-cleat polarity in adjacent beds in the domain 1-2 boundary region may be due to position of this region between two distinct, contemporaneous paleostress provinces, as Kulander and Dean (1980) suggested for some cleat domains in the Allegheny Plateau of West Virginia. The boundary region may have had complex stress patterns during coalification, since the coal-rank map suggests that folds such as the Ignacio Anticline were developing then. Thus the overall tectonic setting and structural history of the San Juan Basin may govern cleat intensity and orientation patterns.

Implications for Coalbed Methane Exploration and Development

Coalbed permeability may be 3 to 10 times greater in the face-cleat direction than in other directions (McCulloch and others, 1974; Ammosov and Eremin, 1960). This permeability anisotropy reflects the strong preferred orientation and greater length of interconnected fractures in the face-cleat direction. Potential permeability anisotropy arising from face cleat, and differences in face-cleat strike in various cleat domains in the San Juan Basin, can be taken into account in the design of development-well-drilling programs and stimulation procedures such as hydraulic fracture treatment. Fruitland face-cleat strike, and thus greatest potential permeability anisotropy, shifts by 90 degrees between domains 1 and 2, from northwest to northeast. However, only in the southern domain and the domain boundary region are face cleats aligned normal to regional least horizontal compressive stress, the most favorable orientation for them to be open in the subsurface.

A closely cleated coal may yield more gas than a coal with wide cleat spacing. For example, cores from some friable coal beds in the Appalachian basin yield approximately 94 percent of total gas content, whereas the same amount of otherwise similar blocky coal from the same area yields only 60 to 65 percent of total gas content (McCulloch and others, 1975). Coal reservoir simulations emphasize the importance of cleat spacing (Paul, 1990), and intense fracture development may enhance the rate of gas production. Cleats are closely spaced in the boundary between domains 1 and 2 because two face-cleat sets overlap and interfere, and coals have relatively high rank. Moreover, folds and faults that locally enhance fracture development occur in this area. High gas yields are suggested by gas seeps along fractures at Soda Springs mine (table 1), and gas evolved from coal core from depths of as little as 200 ft (61 m) (Roberts, 1989). Highly productive Cedar Hill field and Meridian 400 area occur in or near this boundary domain (fig. 1).

Observations of cleat patterns between domains 1 and 2 suggest that two interfering face-cleat sets result in highly cleated coal that may be more isotropic and may have higher overall fracture connectivity and permeability. Furthermore, prevalence of two directions of strongly developed fractures in the domain boundary

region and the resulting increased coal friability may enhance success of well completion by open-hole cavity methods in this area. In cavity completions, the borehole in coal is allowed to collapse, causing adjacent parts of the coal seam to expand toward the cavity. This process tends to open fractures near the borehole and to produce additional fractures (Logan, 1989). Conversely, potential production of coal fines and attendant production problems may be greater here.

Great lateral continuity of volcanic ash layers (tonsteins) on interwell scales, combined with a tendency for cleat to terminate at interbedded noncoal layers, should isolate cleat systems in adjacent beds. This isolation would produce a significant element of layering (heterogeneity) in permeability within Fruitland coal seams and decrease the attractiveness of these seams as targets for horizontal drilling. Because tonsteins are generally thin, however, small faults with net slip of as little as 0.4 inch (1 cm) can interconnect cleat systems in adjacent beds, even without subsidiary fractures along fault zones. On the other hand, some small faults such those at Squaw Creek (table 1) are closed and unlikely to enhance permeability (Raistrick and Marshall, 1939; Ammosov and Eremin, 1960). Local fracture intensification and greater fracture continuity in coal and adjacent sandstone are associated with some faults as well as with folds and fracture zones. Throughgoing fractures may provide significant conduits of gas flow in areas of high gas production. This underscores the importance of determining distribution of faults that are below seismic resolution; they could play a role in connecting otherwise isolated cleat systems.

Acknowledgments

We thank the owners and operators of the Carbon Junction, Chimney Rock, La Plata, and Navajo mines for access to their property.

Fracture Swarms in Upper Cretaceous Sandstone and Coal, Northern San Juan Basin, Colorado: Potential Targets for Methane Exploration

S. E. Laubach, C. M. Tremain, and R. W. Baumgardner, Jr.

Abstract

Northwest-striking fractures in discrete swarms (or zones), separated laterally by unfractured domains typically hundreds of yards (meters) or more wide, characterize Upper Cretaceous Pictured Cliffs Sandstone along the San Juan Basin margin in Colorado. Some fracture swarms in sandstone terminate at overlying Upper Cretaceous Fruitland Formation coal or shale beds, but others extend into them. Fracture connectivity within at least one such swarm in coal is significantly greater than that of adjacent areas. In coal beds, fracture swarms are marked by vertically extensive joints, anomalous cleat strikes, closely spaced fractures, and/or small normal faults. Preliminary results suggest that fracture swarms in sandstone are fractal with fractal dimension D approximately 1.2. Swarms may have enhanced permeability and are potential targets for gas exploration.

Introduction

Fractures enhance fluid flow in low-permeability sandstones and coal beds. With the increasing importance of these rock types as unconventional reservoirs of natural gas, information on their fracture patterns is becoming critical for design of exploration, development, and completion strategy, including application of horizontal drilling (Finley and others, 1990). Accurate determination of subsurface fracture pattern is difficult in mildly deformed sedimentary rocks because fracture detection methods, such as geophysical well logs and core (particularly from vertical wells), may fail to detect fractures and at best sample only a small part of the fracture network. Although many outcrops contain fractures that probably formed at or near surface during erosional unloading or weathering, insight into fracture patterns that exist at depth can be gained from surface studies, especially if fractures in outcrop can be compared with fractures in core from the same formation. Maps of fractures in large exposures provide the most accurate representation of fracture spatial distribution, trace length, connectivity, and size and shape of fracture-bounded blocks. Such information can be used to help understand hydrocarbon production patterns.

Our study focuses on regional fractures in Pictured Cliffs Sandstone and overlying Fruitland Formation coal. We present maps and descriptions of fractures in sandstone and coal in large (up to $\pm 10^6$ ft^2 [$\pm$100,000 m^2]) bedding-plane exposures on the margin of the Late Cretaceous–early Tertiary San Juan Basin of Colorado and New Mexico (fig. 1). Unlike conventional regional fractures, which are envisioned to be regularly spaced and in orthogonal sets (for example, Stearns and Friedman, 1972), Pictured Cliffs fractures are in discrete zones, or swarms, that are separated laterally by domains typically hundreds of yards (meters) wide that lack fractures. Our observations in the San Juan Basin (this vol.) and in the Green River Basin of Wyoming (Laubach, 1991) suggest that *irregularly spaced* swarms with unidirectional strike, such as those in the Pictured Cliffs Sandstone, are typical of many regional fracture sets (figs. 2 to 4).

Previous studies of fractures on the northwestern margin of the San Juan Basin documented joint and coal-fracture (cleat) orientations and distinguished several fracture sets on the basis of abutting relations and orientation (Newman and McCord, 1980; Condon, 1988; Tremain and others, this vol.). Our study builds on this previous work with detailed maps of fracture patterns at selected outcrops, supplemented with examination of core from the basin interior and petrographic study of fracture microstructure. Aims of this paper are to (1) illustrate an example of fracture swarms in sandstone and fracture patterns in adjacent coal beds, (2) discuss observations in context of current models of fracture formation, and (3) present preliminary observations of scale-invariant fracture-swarm characteristics that can be used to help improve engineering models of reservoirs that contain fractures. Results of this study are applicable to the general problems of characterization and interpretation of fractures formed during mild deformation of sedimentary rocks and coalbed-methane exploration.

In Ayers, W. B., Jr., and others, 1991, Geologic and hydrologic controls on the occurrence and producibility of coalbed methane, Fruitland Formation, San Juan Basin: The University of Texas at Austin, Bureau of Economic Geology, topical report prepared for the Gas Research Institute under contract no. 5087-214-1544 (GRI–91/0072), p. 119-140.

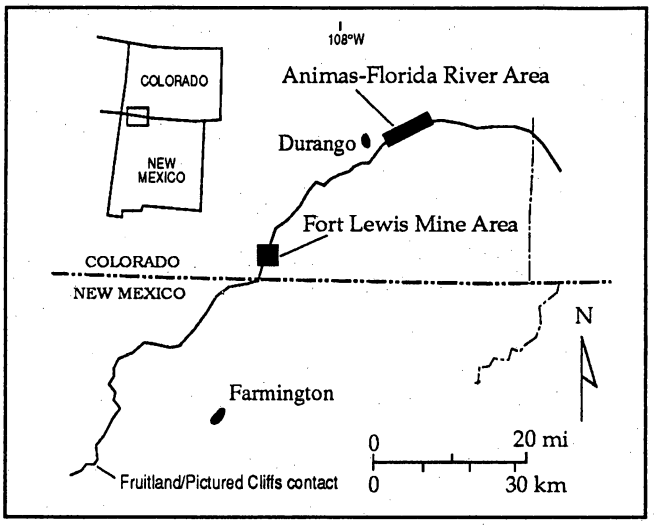

Figure 1. Location map of pavement study areas, northern San Juan Basin, Colorado and New Mexico.

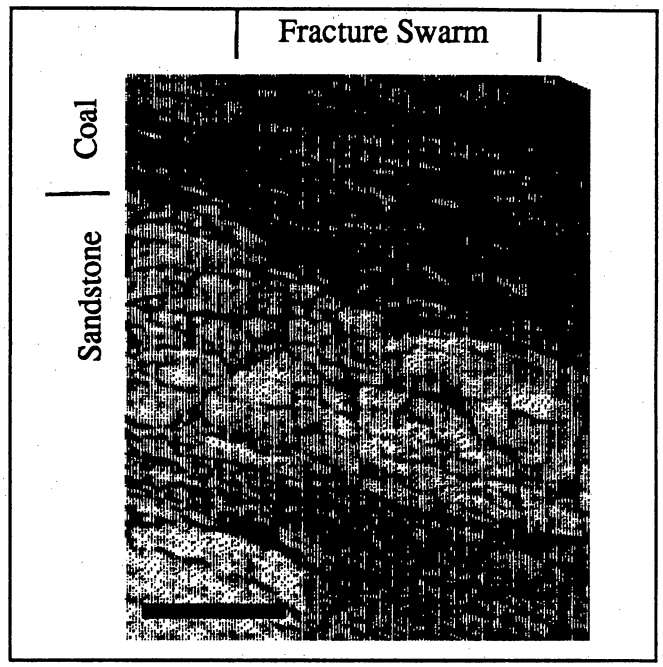

Figure 2. Fracture swarm in upper Pictured Cliffs Sandstone and overlying Fruitland Formation coal. Carbon Junction exposure. Bar scale is 2 inches (5 cm).

Regional Joints and their Stratigraphic Context

The San Juan Basin of the east-central Colorado Plateau, New Mexico and Colorado, is an asymmetrical structural basin of Late Cretaceous to early Tertiary age that contains more than 14,000 ft (4,270 m) of Paleozoic, Mesozoic, and Cenozoic marine and continental rocks. As defined by the Upper Cretaceous Pictured Cliffs Sandstone outcrop, the basin is roughly circular, with an area of approximately 6,700 mi^2 (17,350 km^2). Upper Cretaceous rocks were deposited in or near the Cretaceous intracontinental seaway that was flanked to the west and southwest by the active Cordilleran thrust belt. During late Late Cretaceous to early Tertiary time, folds and reverse faults began to form along the present structural basin margin (Cumella, 1983; Fassett, 1985; Ridgley and Huffman, 1990).

Pictured Cliffs Sandstone and overlying coal-bearing Fruitland Formation were deposited on the western margin of the seaway. The Pictured Cliffs is a coastal facies that overlies marine Lewis Shale. In the northern San Juan Basin it is divisible into a lower unit composed of a series of upward-coarsening mudstone and sandstone interbeds that represent shelf and shoreface deposition, and an upper unit composed of amalgamated sandstone bodies having a composite thickness of 33 to 115 ft (10 to 35 m) representing deposition in barrier-strandplain environments (Ayers and others, this vol.). In the northern basin, the Pictured Cliffs is tightly cemented, primarily with calcite and quartz, and typically has permeability of 0.5 to 1 md (W. B. Ayers, personal communication, 1990).

Fruitland Formation is a continental facies composed of sandstone, mudstone, and coal interbeds deposited landward of barrier-strandplain facies of the Pictured Cliffs Sandstone. It is the primary coal-bearing unit in the San Juan Basin. Coal rests directly on upper Pictured Cliffs sandstone in many exposures in the northern San Juan Basin.

Joints in sandstone on the northwestern margin of the basin are opening-mode fractures that are commonly subvertical and orthogonal to bedding. They generally have northwest and northeast strikes (Newman and McCord, 1980; Condon, 1988; Tremain and Whitehead, 1990). Abutting relations suggest that several generations of joints are present, some of which result from near-surface or surficial processes such as spalling near cliff edges (Tremain and Whitehead, 1990). Previous workers concluded that in Cretaceous rocks many joints predate development of early Tertiary folds because joints remain perpendicular to bedding where beds are tilted (Condon, 1988; Tremain and Whitehead, 1990; Tremain and others, this vol.). Some prominent joints in the Fruitland Formation and the Pictured Cliffs Sandstone parallel northwest-striking face cleat in overlying Fruitland Formation coal beds. Northwest-striking normal faults occur along the western margin of the San Juan Basin (Tremain and Whitehead, 1990, and references therein), and it is possible that some joints and some northwest-striking faults accommodated northeast-southwest extension during Late Cretaceous and/or early Tertiary, possibly at about the same time that regional face cleat was developing (Tremain and others, this vol.). Regional face-cleat patterns are uniform over large areas of the Colorado part of the basin, but significant

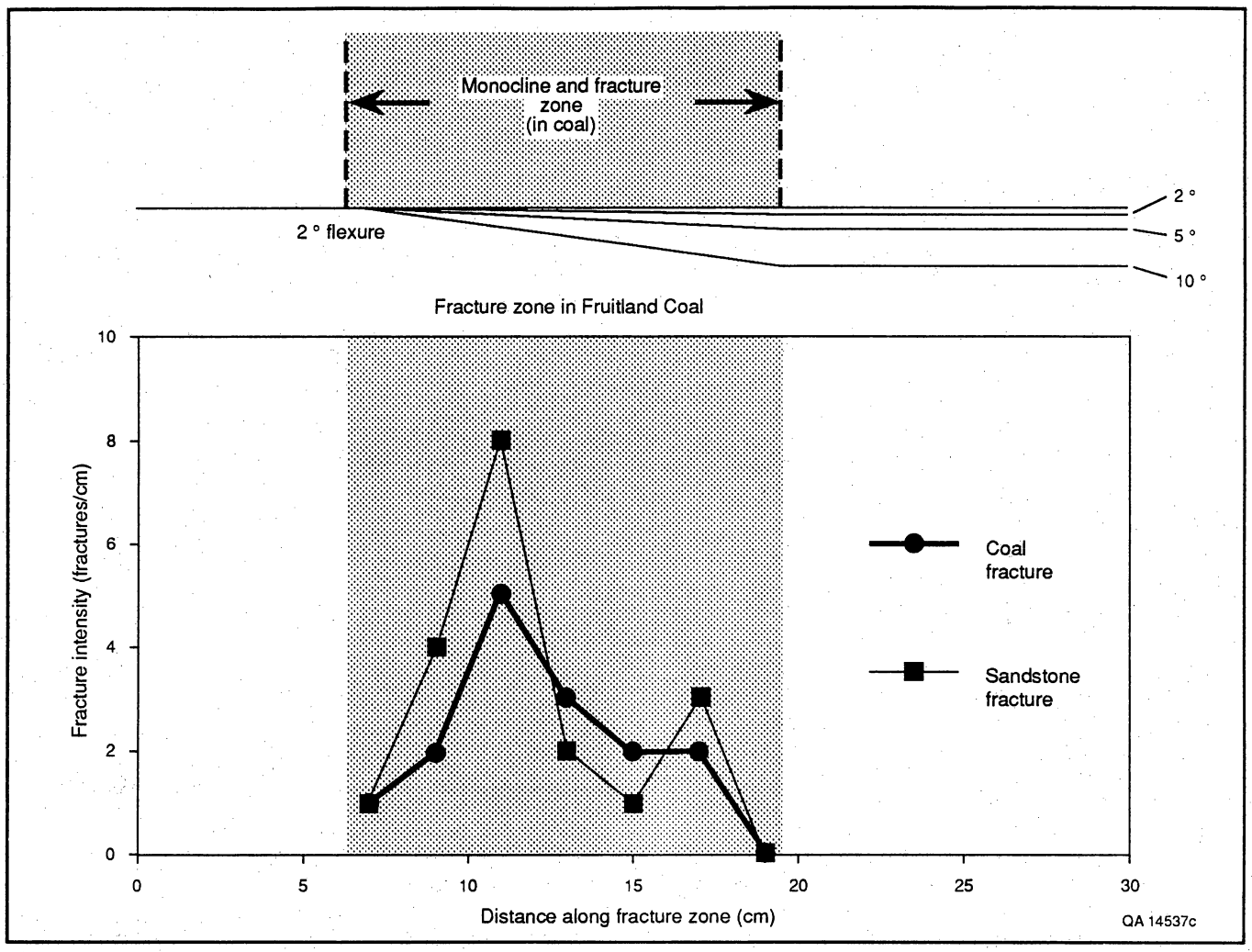

Figure 3. Fracture intensity (fractures/distance) in narrow fracture swarm that crosses both sandstone and coal. Outside the fracture swarm, fracture intensity is less than 0.02. Sandstone/coal contact is deflected by 2° or less across swarm. Carbon Junction exposure.

local variations in cleat strike exist (Tremain and others, this vol.). Exposures near the Animas River south of Durango and at the Fort Lewis mine indicate that variation in cleat strike in some places is associated with fracture swarms that cut both coal bed and sandstone.

Fracture-Trace Maps

Pavement maps that show fracture traces in large bed-parallel outcrops portray fracture network characteristics such as fracture spatial distribution, connectivity, trace length, and fracture-bounded-block size and shape in a way that measurements at isolated stations cannot (LaPointe and Hudson, 1985; Barton and others, 1987; LaPointe, 1988). Barton and others (1987) demonstrated the usefulness of this method in a study that used maps with scales of 1:50, covering areas of approximately 2,150 ft² (200 m²). Because large pavement exposures are rare, pavement maps have been made on quarry floors (LaPointe, 1988) or outcrops that have been artificially cleared (Barton and others, 1987). In our fracture study, we used pavement maps of large natural outcrops and mine floors.

Upper Cretaceous sandstones form natural dip-slope pavements along the margins of many early Tertiary basins in the western United States. On the northwestern and northern margins of the San Juan Basin, numerous bedding-plane Pictured Cliffs Sandstone pavements have areas ranging from hundreds to thousands of square yards (meters). These Pictured Cliffs exposures are nearly devoid of vegetation, debris, and fractures related to surficial processes. Pavements include moderately dipping (~10° to 15°) and steeply dipping (30° to 50°) beds with a range of strikes. Fracture patterns are well exposed in plan view on these bedding-plane pavements, and cross sections of fractures are visible along the upturned edges of the hogbacks. Such exposures are ideal for fracture-trace map studies.

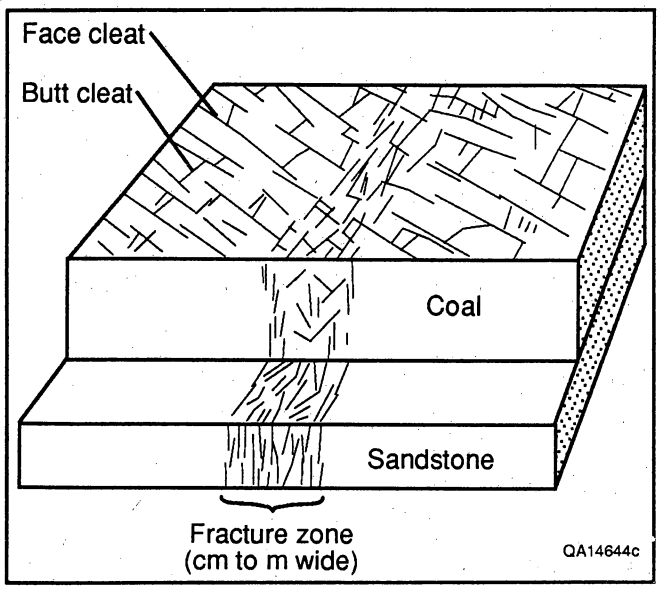

Figure 4. Block diagram illustrating fracture swarm crossing sandstone and coal. Based on relations observed at Carbon Junction exposure (Animas–Florida River area) and Fort Lewis mine.

Map Areas: Fort Lewis Mine and Animas–Florida River Transect

Two large exposures of Pictured Cliffs Sandstone were mapped in detail. The pavements are at the abandoned Fort Lewis coal mine near the Colorado–New Mexico border (sec. 1, R32N, R12W), and along a 2.8-mi-long (4.5-km) ridge southeast of Durango between the Animas and Florida Rivers (fig. 1). These exposures were chosen because they are exceptionally free of debris, vegetation, and surface-related fractures, and because differences in strike between the two areas permit comparison of fracture patterns along different parts of the basin margin. We made observations of fracture patterns at four other pavements in the western and northern parts of the basin to test regional consistency of fracture patterns.

The Fort Lewis mine pavement is a north-northeast-striking (020°) bedding plane of Pictured Cliffs Sandstone that dips southeast between 9° and 13°, forming the dip slope of a subdued northeast-trending hogback (fig. 5). The part of the pavement we mapped is approximately rectangular, with an area of more than 1,000,000 ft^2

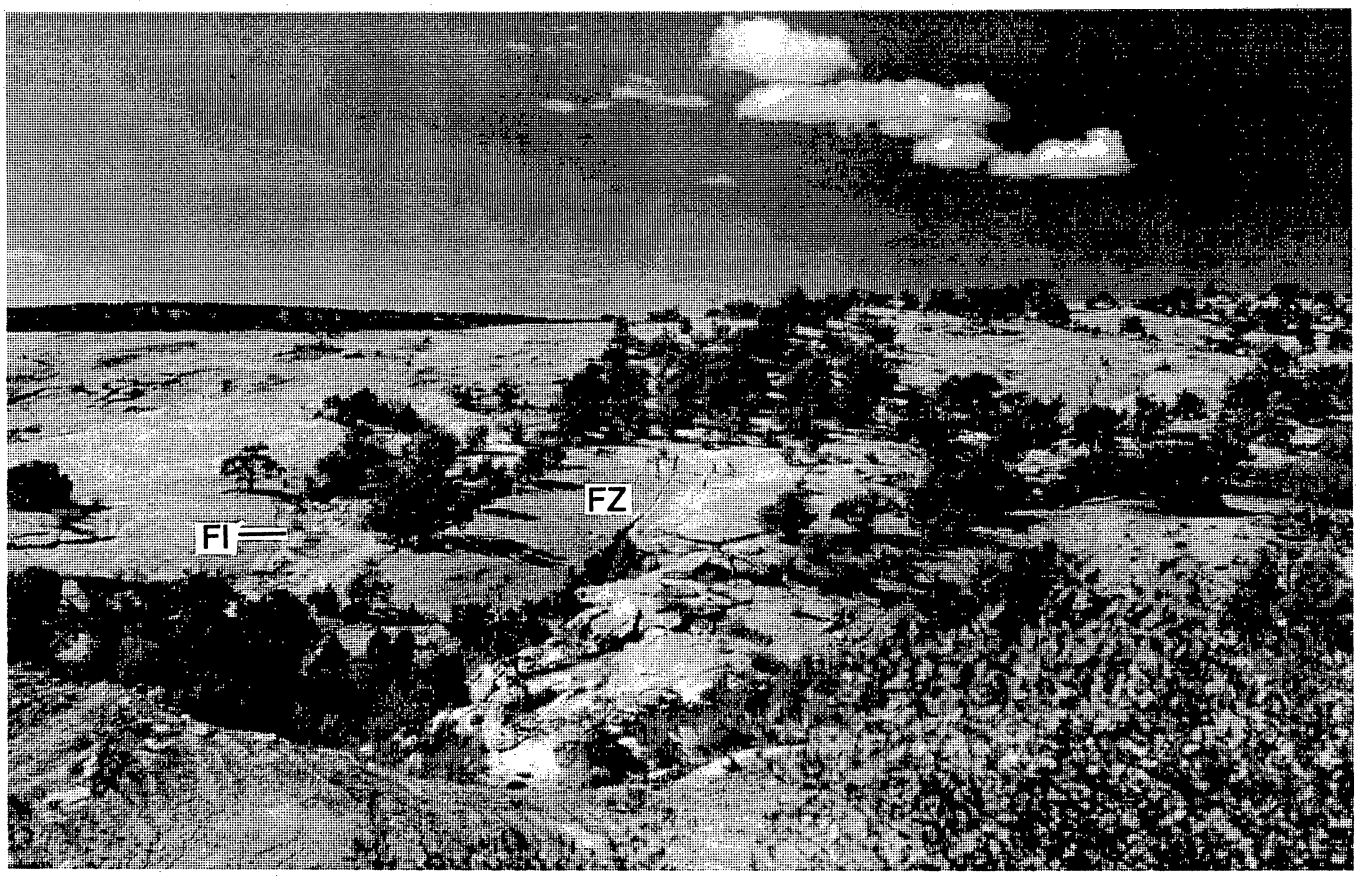

Figure 5. Bedding-plane pavement outcrop, Upper Cretaceous Pictured Cliffs Sandstone, Fort Lewis mine. FZ = fracture swarm; FI = isolated fracture. Note wide extent of unfractured rock between fractures. Scale is indicated by figures in center of outcrop.

(100,000 m²), and a length of more than 1,970 ft (600 m) parallel to strike. Fractures in the pavement are visible in cross section in low cliff exposures on the northwestern side of the hogback. Coal directly overlies sandstone but the sandstone-coal contact is not exposed.

The Animas–Florida River exposure near Durango includes a series of pavements on upper Pictured Cliffs sandstone. Strike is more easterly here than at the Fort Lewis mine, and dips are generally steeper, ranging from 20° to 55°. A sharp contact between sandstone and coal is well exposed in a number of locations along this outcrop. One part of the Animas–Florida River exposure near Durango, on U.S. Rte. 550, has a well-exposed small-scale fracture swarm that illustrates several characteristics of these structures.

Fractures were mapped on large-scale base maps. The Fort Lewis mine pavement was mapped at a scale of 1:1,000 using an air photograph base map, plane table, and SONIN 250 and 150 acoustic distance-measuring devices. Within the Fort Lewis pavement, smaller areas were mapped at approximately 1:50 on unregistered photograph mosaics taken from an elevation of 8 ft (2.5 m). The exposure of Pictured Cliffs Sandstone along the Animas–Florida River transect was mapped at smaller scale (1:24,000 and 1:12,000) on a topographic base map, supplemented with local larger-scale maps and oblique photographs of bed surfaces. The Fort Lewis mine and Animas–Florida River maps therefore provide views of fracture patterns at different scales over distances that are comparable to interwell spacing in some gas reservoirs.

Coal in the Fruitland Formation does not form large pavements in the San Juan Basin, and bedding plane exposures of coal in active open-pit coal mines are difficult to map and interpret because of debris and fractures generated by mining operations. A pavement map of relatively undisturbed coal in the Navajo mine is presented elsewhere (Tremain and others, this vol., their fig. 9). For mapping coal exposures in small natural coal pavements and selected areas of open-pit mine floors, we used color photographs as base maps. Adjacent to sandstone pavements, coal fractures were described in closely spaced outcrops and excavations.

Fracture Swarms

Small-Scale Fracture Swarm: Carbon Junction Outcrop

A narrow zone comprising a swarm of closely spaced fractures that crosses sandstone and overlying coal is exposed in the Pictured Cliffs Sandstone at the top of the U.S. Rte. 550 roadcut near Carbon Junction mine, south of Durango (fig. 1). It is a small example of a type of fracture swarm that occurs on a larger scale elsewhere on the western and northern margins of the basin. This exposure demonstrates that fracture swarms do extend locally from sandstone into overlying coal, with significant effects on fracture patterns in coal. Away from the fracture swarm, sandstone and coal in this outcrop have fracture characteristics that are typical of the northern San Juan Basin. The Pictured Cliffs Sandstone has few fractures, and of these, many are evidently surficial features. Coal has well-developed face cleat with northwest (345°) strike and primary spacing of 1 to 2 inches (3 to 5 cm).

In sandstone, the fracture swarm is composed of numerous curved, anastomosing fractures that are subperpendicular to bedding (figs. 2 through 4). The swarm and most fractures within it strike west-northwest. Some fractures are only slightly curved and have sharp, well-defined boundaries and continuous traces through approximately 5 ft (1.5 m) of exposure. Other fractures are strongly curved, have diffuse margins, and are relatively short (0.4 to 4 inches [1 to 10 cm]). The widest fractures have widths less than 0.02 inch (0.05 cm). Most are marked by a slight orange-brown stain, but no fracture-filling minerals are visible; elsewhere in the basin similar fractures locally have calcite fill. There is no evidence for slip on fractures, and the contact between sandstone and overlying coal is not offset, although it may be slightly tilted, with a change in dip across the swarm of less than 2°.

The tabular fracture swarm is between 5 and 6 inches (12 and 15 cm) wide. Fracture intensity within the swarm is high but variable, ranging from 1 to 8 fractures/cm (fig. 3). Decrease in fracture intensity at the swarm boundary is abrupt. Outside the fracture swarm, fractures with orientation and appearance similar to those within the swarm are absent over an area of at least 30 ft (9 m) wide. Thus, the fracture swarm is isolated by unfractured rock.

In coal, the fracture swarm consists of short (less than 2-inch [5-cm] long) fractures subparallel to the fracture swarm boundary (fig. 4). Only about 25 percent of fractures in sandstone extend into coal. In this area fracture-swarm strike is oblique to face-cleat strike. Consequently, the fracture intensity of 2 to 3 fractures/cm in the fracture swarm (measured perpendicular to the swarm boundary) is considerably higher than that of surrounding coal. Fracture density (fracture length per unit area) is 2 to 10 times greater within the swarm than in adjacent coal. Locally, face cleats terminate against fractures that parallel the fracture swarm, but most abutting relations are consistent with swarm-parallel fractures forming after face cleat. Parallel to the swarm, continuous fracture pathways in coal are tortuous because fractures are arranged in short, curved segments that commonly abut face cleats rather than cross them.

Connectivity, or the proportion of fractures that intersect other fractures, is markedly greater in the swarm than in adjacent coal.

The fracture pattern in the coal has many similarities to "anomalous" coal outcrops that have been described in other parts of the northwestern San Juan Basin (Tremain and others, this vol.). In these outcrops, the usual face and butt cleats are accompanied by additional coal fractures ("third cleat set") having a wide range of strikes. Consequently, cleats have greater dispersion in strike than typical outcrops (Tremain and others, this vol., their table 1). Such fractures locally have inconsistent crosscutting and abutting relations. Coal outcrops with these fractures tend to have greater fracture densities than similar rank and composition coal with only regional cleat.

Structures in the Carbon Junction outcrop indicate north-northeast extension. A small, poorly exposed normal fault that cuts sandstone and coal is about 100 ft (30 m) from the fracture swarm. Strikes of the fault and of the fracture swarm diverge by less than 15°, and fractures in sandstone adjacent to the fault resemble those in the nearby fracture swarm. Elsewhere in the outcrop, isolated opening-mode veins, which locally have widths of as much as 0.2 inch (0.5 cm), cross from sandstone into carbonaceous shale.

Reservoir-Scale Fracture Swarms: Fort Lewis Mine

Zones consisting of swarms of closely spaced west-northwest-striking fractures are exposed at the Fort Lewis mine in a large pavement exposure of upper Pictured Cliffs Sandstone (figs. 5 and 6). General characteristics of the swarms are similar to those at the Durango/U.S. Rte. 550 outcrop, but fracture arrays at the Fort Lewis mine are much larger and have more complex internal patterns. Typically swarms are tens of yards (meters) wide and hundreds of yards (meters) long. Fracture maps from this outcrop provide detailed information on fracture patterns within swarms, evidence for swarm distribution, and evidence for relationships among swarms. Although pavement views of coal fractures are not well exposed at the Fort Lewis mine, it is possible to determine cleat and fault patterns in coals that overlie fracture swarms.

Distinguishing Fracture Sets at Fort Lewis Mine

Fractures striking west-northwest and north are evident in the Fort Lewis pavement. Abutting relations, orientation, and differences in style between these fractures are the basis for distinguishing two fracture sets (I and II). Fracture set I is the most prominent and is composed of steeply dipping, northwest-striking curviplanar frac-

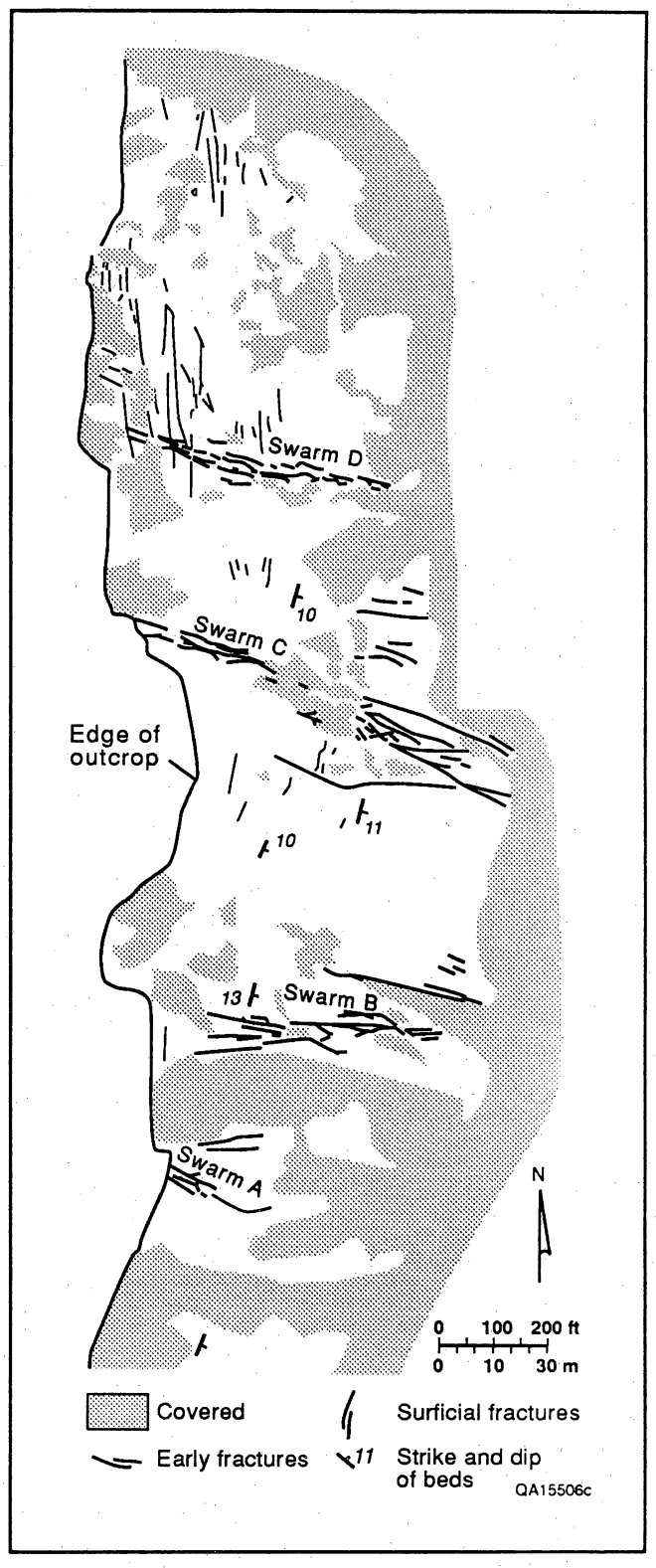

Figure 6. Simplified map of bedding-plane pavement and fracture network in Upper Cretaceous Pictured Cliffs Sandstone, Fort Lewis mine. See figure 1 for location.

tures that occur singly or in swarms. Set II fractures strike north and either cross or abut set I fractures, indicating that set I fractures are older than those of set II. Fractures of both sets are orthogonal to bedding, but the two sets differ in their characteristic shapes, microstructure, and associated alteration. Evidence described below is consistent with set II fractures having formed at shallow depths; they may be surface-related fractures that are not present in buried rocks deeper in the basin. We therefore provide only a brief description of their characteristics.

At the Fort Lewis mine, set II fractures are composed of long, planar segments arranged in en echelon or relay patterns (fig. 6). Overlapping segments of set II fractures are straight rather than curved, and small fractures connecting overlapping segments are rare. Fractures opened by movement normal to fracture walls. No infilling minerals are evident, and fracture widths are 0.008 to 0.02 inch (0.02 to 0.05 cm). Fracture walls are smooth except for arrest lines and plume structures. These characteristics are consistent with opening-mode propagation of set II fractures (Pollard and Aydin, 1988). A reddish-brown to reddish-yellow halo of stained rock that can be as much as 12 inches (30 cm) wide typically surrounds fractures, and fracture surfaces can have a similar but darker stain. Set II fractures are mostly within 150 ft (45 m) of the escarpment of the Pictured Cliffs hogback, which they generally parallel, but some fractures near the cliff edge or local topographic benches curve gradually to approach the free surface at right angles. Fractures are longer, wider, and more abundant near the escarpment.

Set II fractures are similar in appearance to other fractures along the northwestern margin of the basin. In the Pictured Cliffs Sandstone, these fractures tend to be subparallel to topographic escarpments and to be best developed within 75 to 100 ft (20 to 30 m), or less, of cliff edges. Along the Animas–Florida River outcrop belt, similar-appearing fractures parallel the ridge crest and are developed only within 15 ft (4.5 m) of the cliff edge. A younger set of orthogonal, abutting fractures commonly develops where this fracture set is prominent. Similar patterns are common in the southern San Juan Basin (Tremain and Whitehead, 1990). Apparently because their orientation varies with topography, fractures with set II characteristics have a wide range of strikes regionally. If set II fractures are surficial features, caution is warranted in using remote-sensing imagery for characterization of regional fractures present at reservoir depths, because in many outcrops set II fractures are prominent (Tremain and Whitehead, 1990; see also Baumgardner, this vol.).

Several other Pictured Cliffs outcrops and a small part of the Fort Lewis pavement contain additional surficial fracture sets that abutting relations indicate are younger than set II fractures. These include polygonal fractures and exfoliation joints that are locally associated with pop-ups. Polygonal fracture patterns are generally hexagonal and are typically composed of straight and curved fractures. Polygon diameters range from several tens of inches (centimeters) to five yards (meters) or more; locally several scales of polygon are developed in the same exposure. Exfoliation joints are fractures that parallel the outcrop surface; in massive Pictured Cliffs Sandstone they commonly separate a slab of rock 1 to 2 inches (2 to 5 cm) or less thick. On steeply dipping outcrops, downslope movement of thin slabs can result in tentlike pop-up structures consisting of slabs that have fractured and pivoted about an axis generally parallel to the strike of the slope. Lack of vegetation along polygonal and exfoliation-jointed surfaces shows that even where these features are well developed at the surface, the fractures may not extend deeply into bedrock. Extensive development of polygonal fractures, exfoliation joints, and pop-ups can result in a highly disrupted bedding-plane surface where older fracture sets are difficult to recognize. We therefore avoided such surfaces in our mapping.

Morphology and Microstructure of Swarm (Set I) Fractures

The morphology and microstructure of set I fractures distinguishes them from set II fractures. In outcrop, set I fractures are closed. They typically have widths of 0.02 to 0.04 inch (0.5 to 1 mm), although locally fractures have widths of as much as 0.2 inch (0.5 cm). Narrow fractures are marked by a dark-brown seam of infilling of clay and carbonate minerals. Calcite or gypsum is present in some veins at the Fort Lewis mine and in exposures between the Animas and Florida Rivers (fig. 7). Set I fractures commonly are surrounded symmetrically by a halo of lighter colored ("bleached") rock 0.4 to 1.2 inches (1 to 3 cm) wide (fig. 8a).

Many fractures represented by a single trace on the pavement map are actually narrow fracture swarms (figs. 8a through 8c). Set I fractures are composed of short (less than 30 ft [10 m]) segments that either curve gradually throughout their length or curve on the ends. Fractures intersect at a low angle; high-angle abutting relations and crossing fractures are rare (fig. 9). Segments are in turn composed of numerous anastomosing fracture and microfracture strands that give individual fractures a "braided" appearance (figs. 8b and 8c and 10a). These multistrand fractures can be as much as 2 inches (5 cm) wide. Some wide fractures have inclusions of wall rock that combine with anastomosing fracture strands to create irregular or rough fracture cross sections. Such features suggest multiple fracture-opening events.

In map view, set I fractures have distinctive termination styles (fig. 9). Fractures that have isolated

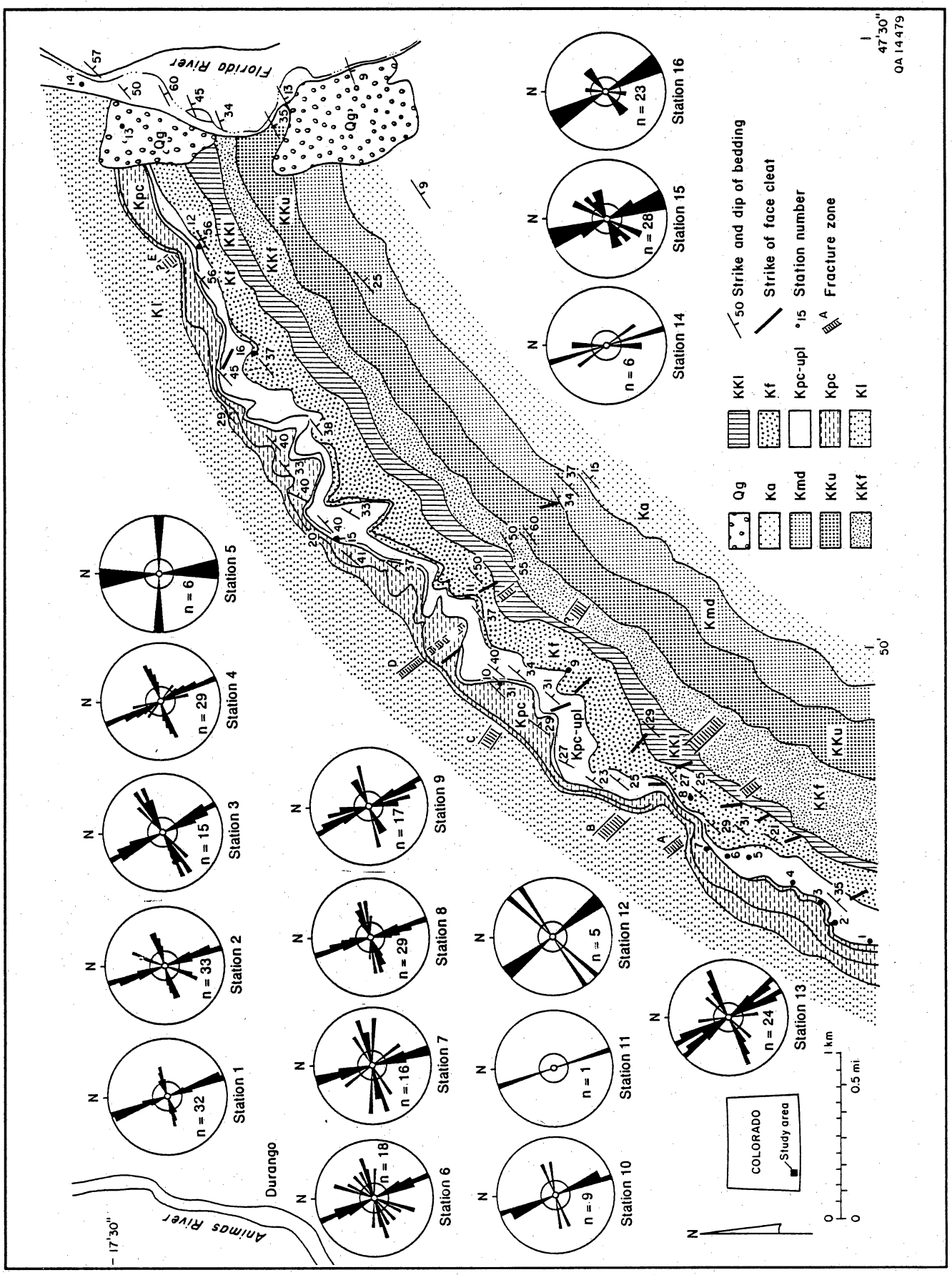

Figure 7. Fracture zones in Pictured Cliffs Sandstone and cleat strike in adjacent Fruitland Formation coal between Animas and Florida Rivers. See figure 1 for location.

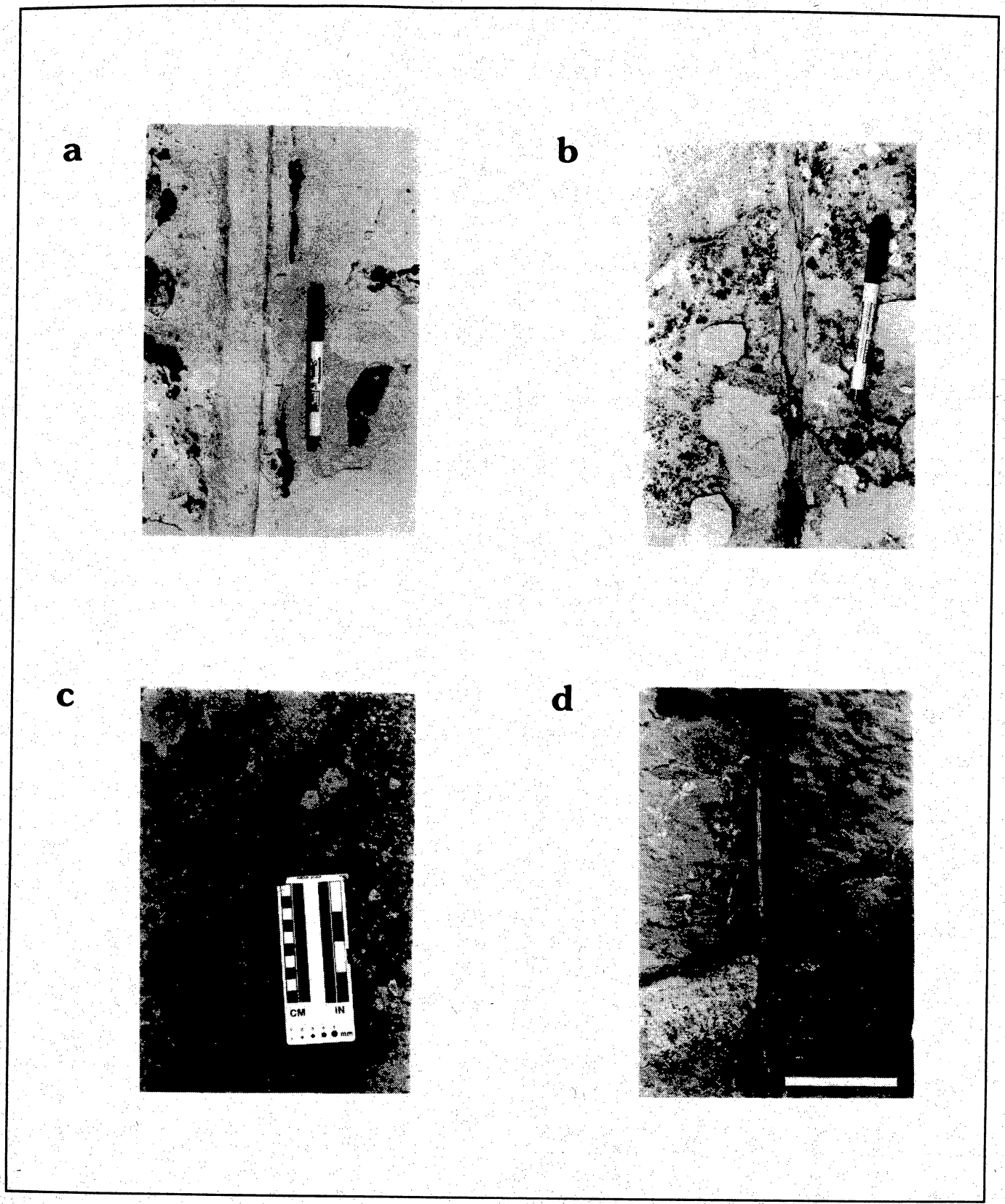

Figure 8. Morphology of individual set 1 fractures, Fort Lewis mine. (a) Single narrow fracture with "braided" appearance and halo of bleached rock (plan view). The morphology superficially resembles that of "deformation bands." (b) Multistrand, macroscopically segmented fracture or narrow fracture swarm with diffuse halo of bleached rock (plan view). (c) Anastomosing fractures in narrow fracture swarm (plan view). (d) Calcite-filled vein (cross-sectional view). Scale bar is 0.5 ft (15.2 cm).

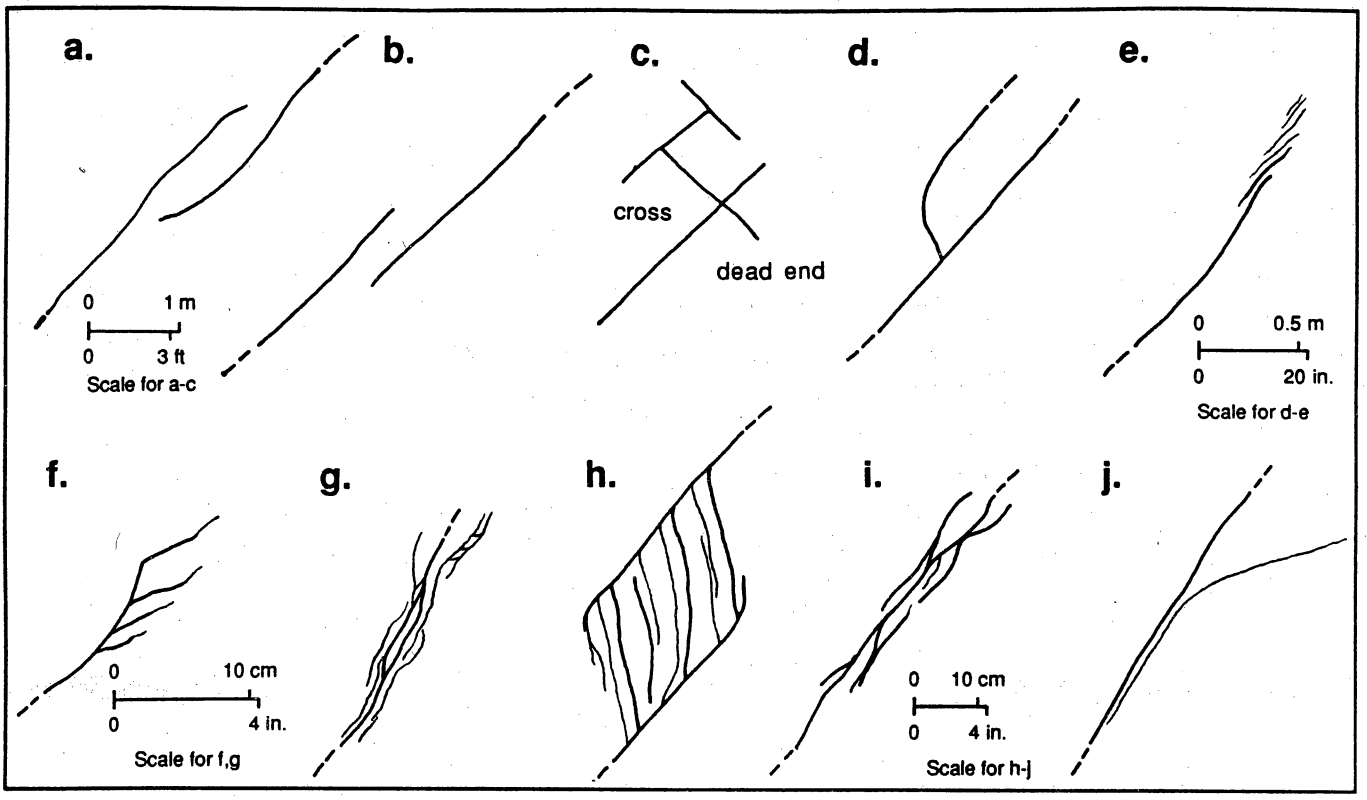

Figure 9. Fracture termination styles. (a) Approaching, nonintersecting. (b) En echelon, no curvature. (c) Abutting, crossing, and dead-end. (d) Hook intersection. (e) Segmented, en echelon step. (f) Asymmetric splay. (g) Horsetail splay. (h) Ladder structure. These patterns resemble fracture patterns developed between strike-slip fault segments. (i) Complex crossing. Examples are from field sketches.

terminations within the rock matrix commonly have small-scale splays, or numerous small segments that may be arranged en echelon or in a diffuse array of parallel microfractures and fracture strands (*horsetail splays*) (fig. 10b). Where fracture segments overlap, fractures curve abruptly (hook) toward adjacent fractures. Within the areas of overlap, various types of interconnected, partly connected, and blind splay fractures and curving fracture strands are developed (figs. 9 and 10b and c). One distinctive overlap pattern is *ladder structure* (figs. 9h and 10b), a pattern in which subparallel, nearly equally spaced straight fractures link two overlapping, parallel strands. Fractures defining ladder structure are at an acute angle (15°–60°) to the main fracture strands, rather than at right angles such as would be expected in a well-designed ladder. Ladder-structure fractures may curve into parallelism with main-strand fractures or may curve abruptly to intersect them. Fracture arrangements associated with terminations and main strands are in larger scale combinations within swarms, defining an overall network pattern discussed below.

Outcrop and petrographic observations are consistent with opening-mode propagation of set I fractures. For most fractures in the outcrop there is no evidence of fracture-parallel slip. Fractographic features such as plume structures and arrest lines are not evident on these fractures, but their microfractured, multistranded aspect and the general lack of exposed fracture surfaces effectively preclude recognition of such features.

Fracture Zone Dimensions and Orientation

Four fracture swarms cross the Fort Lewis outcrop (fig. 6). Swarms are composed of anastomosing and variably interconnected straight and curved fractures with highly variable fracture spacing that ranges from approximately 0.4 to approximately 40 inches (~0.1 to ~1 m). Individual fractures within swarms are perpendicular to bedding and generally terminate vertically within homogeneous sandstone or at shale partings, so that they typically are confined to individual beds. Fracture height is therefore locally only 1.6 to 16 ft (0.5 to 5 m), even where map traces are tens or hundreds of yards (meters) long. Many fractures within swarms are subparallel to the length of the swarm (figs. 11 and 12). Swarm widths are defined by fracture occurrence, as illustrated in figure 13.

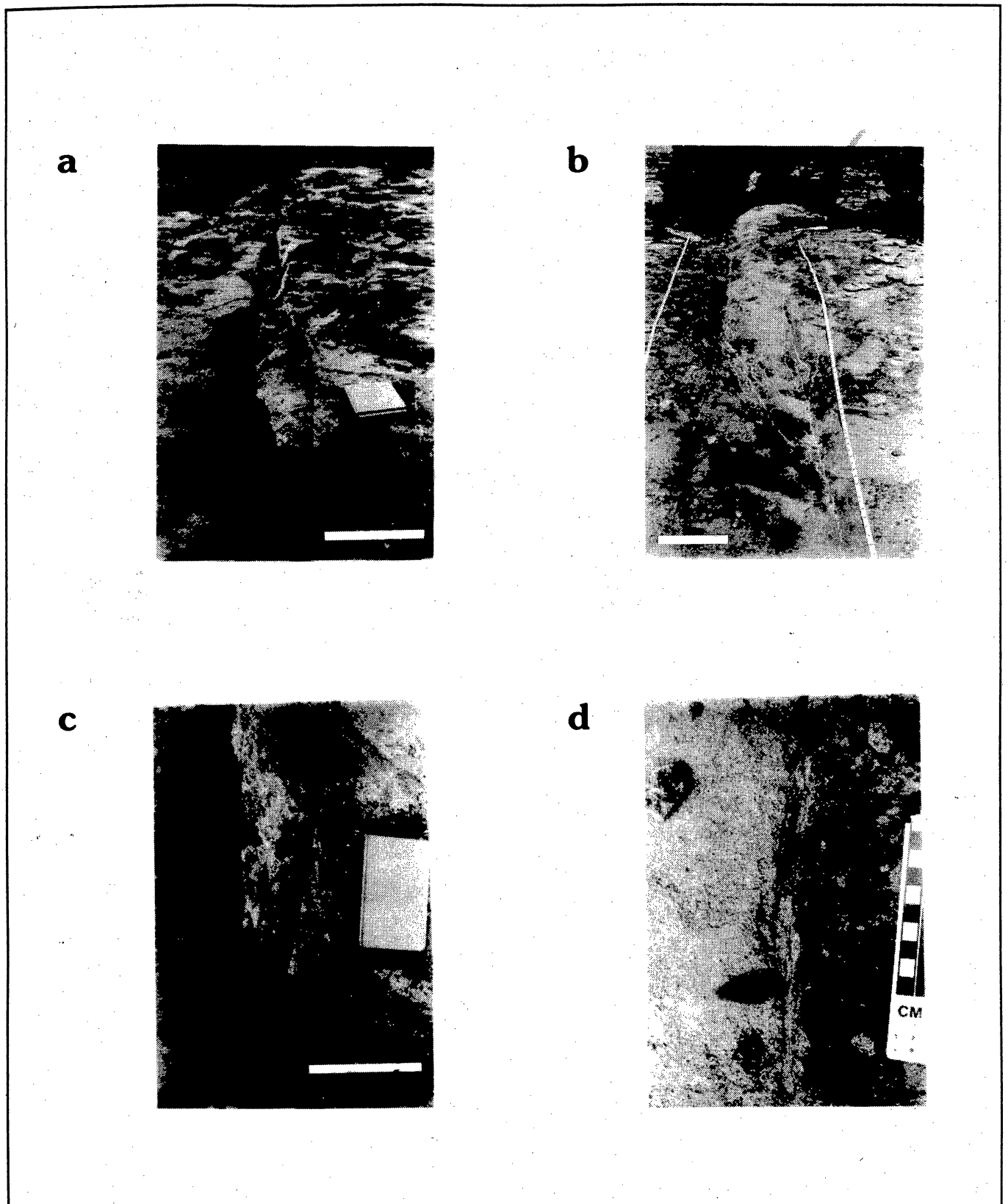

Figure 10. Fracture connectedness and termination style, Fort Lewis mine. (a) Braided fracture strands. Scale bar is 9 inches (23 cm). (b) Overlapping fracture strands connected by an array of thin subsidiary fractures, "ladder" structure. Scale bar is 1 ft (30.4 cm). (c) Curved and branching fracture termination against a larger fracture. Scale bar is 7.5 inches (19 cm). (d) Dead-end fracture termination and associated diffuse microfracture array.

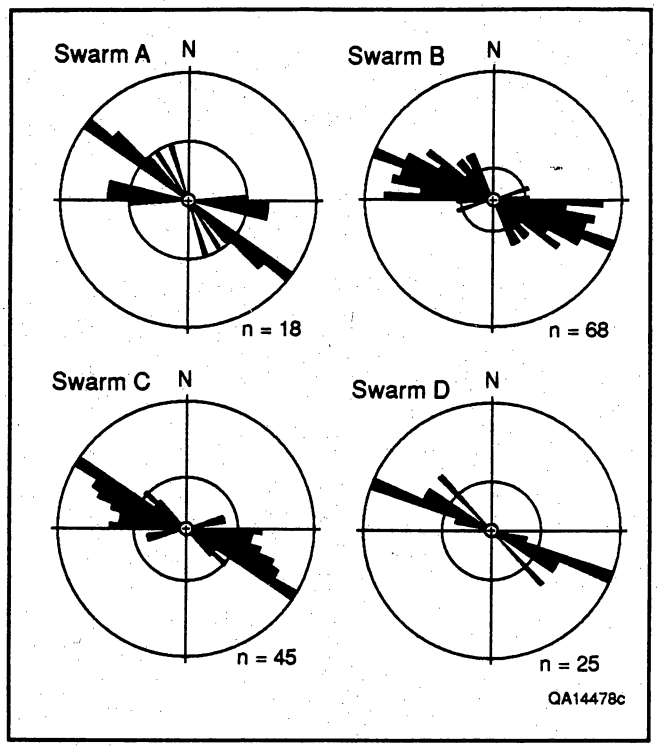

Figure 11. Fracture strikes in four main fracture zones, Fort Lewis mine. Equal-area rose diagrams; data are plotted as percentages of total number of measurements (n) in 5-degree intervals. See figure 6 for locations.

Swarms strike west-northwest, with a range from 290° to 310° (fig. 12). They are tabular and oriented normal to sandstone beds. In plan view, swarm lengths range from 82 ft (25 m) to 755 ft (230 m), and widths range from 23 ft (7 m) to more than 165 ft (50 m). Three of four swarms terminate outside the outcrop, so their lengths cannot be defined precisely, but swarm widths diminish substantially along fracture-swarm strike for several swarms (fig. 13), suggesting that they gradually die out over distances of approximately 1,000 ft (~300 m). The most completely exposed swarm has length/width ratio of greater than 6 (figs. 6 and 14, swarm D). Swarms are separated by domains that lack fractures. These unfractured domains have widths that range from approximately 165 ft (~50 m) to more than 980 ft (300 m), with average width of more than 490 ft (150 m).

The pattern of swarm distribution and the way in which swarms intersect or link are difficult to determine, despite the large size of the Fort Lewis outcrop, because swarms are subparallel and widely spaced. The distribution of fractures in swarm A defines two domains that are separated and offset from each other and that have differing fracture strikes (figs. 6 and 11). These domains might represent an en echelon step between two swarm segments, or the intersection of two nonparallel swarms. The best example of large-scale struc-

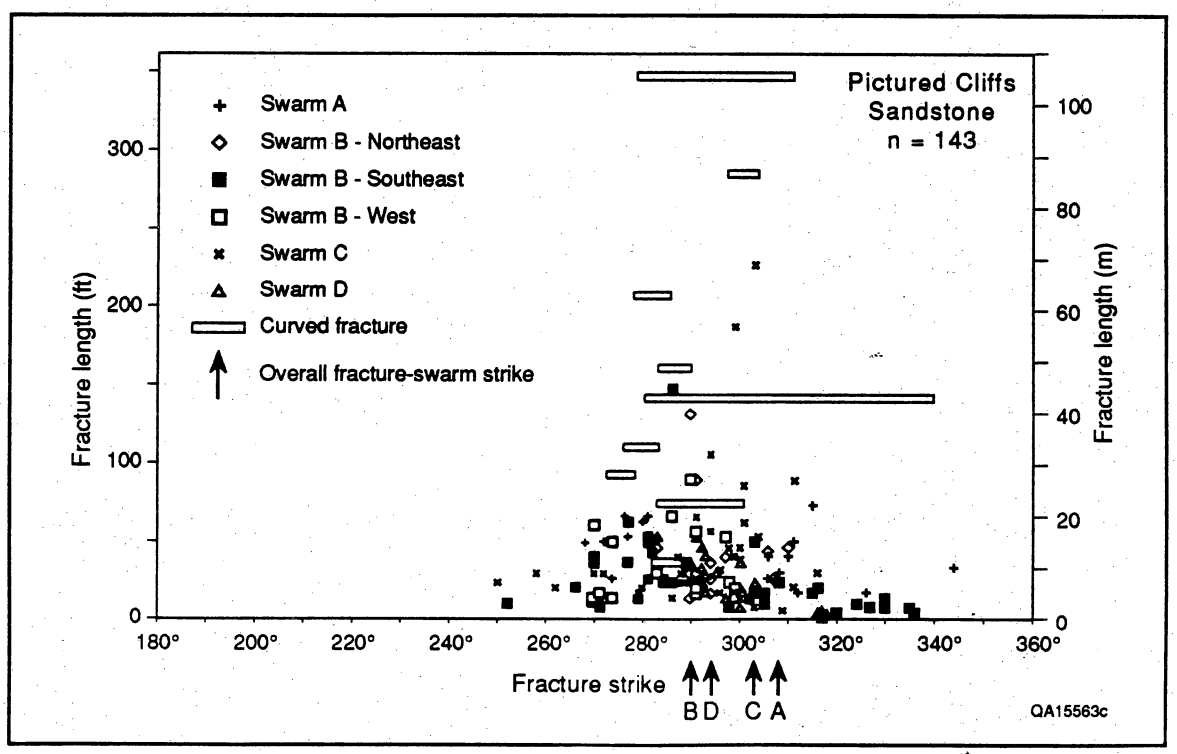

Figure 12. Fracture length versus fracture strike, Fort Lewis mine. Arrows indicate overall strike of four main fracture swarms. Bars indicate strike range of long, curved fractures. Fracture swarms are shown in figure 6.

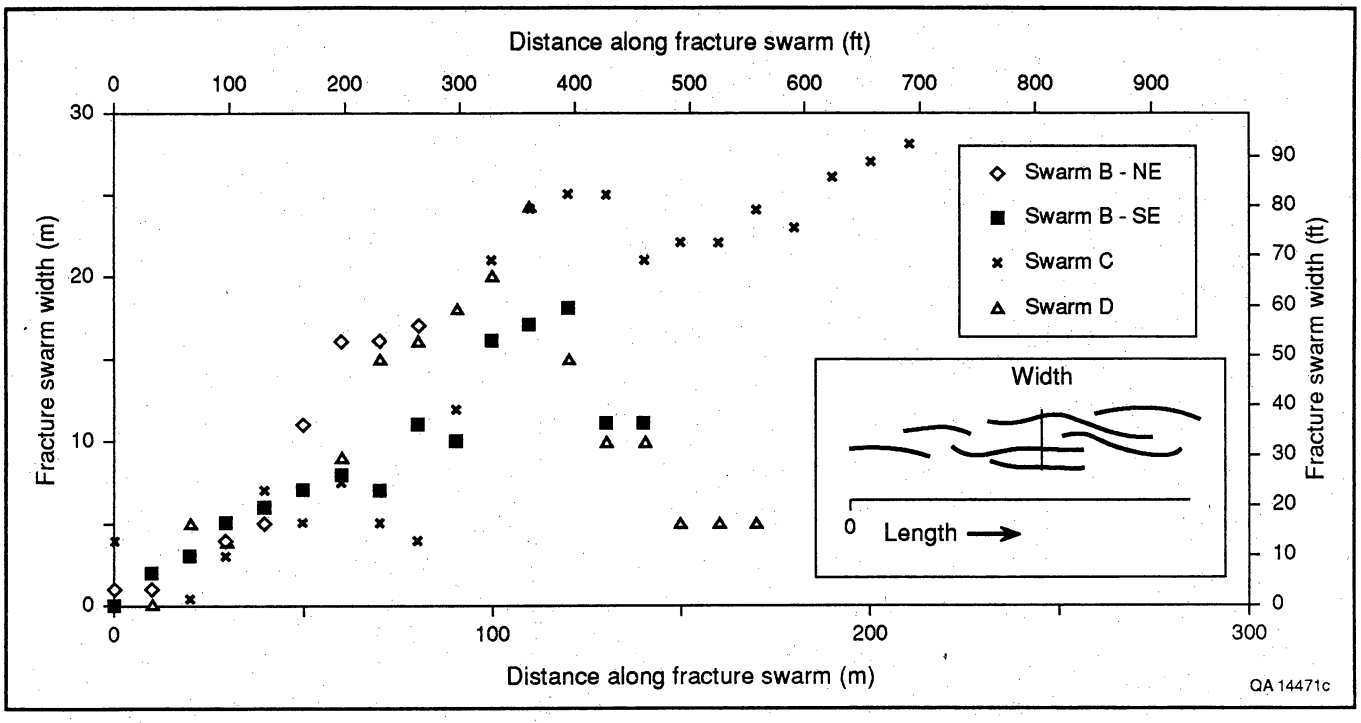

Figure 13. Fracture swarm width versus distance along fracture swarm for swarms B, C, and D. Inset defines fracture swarm width and length.

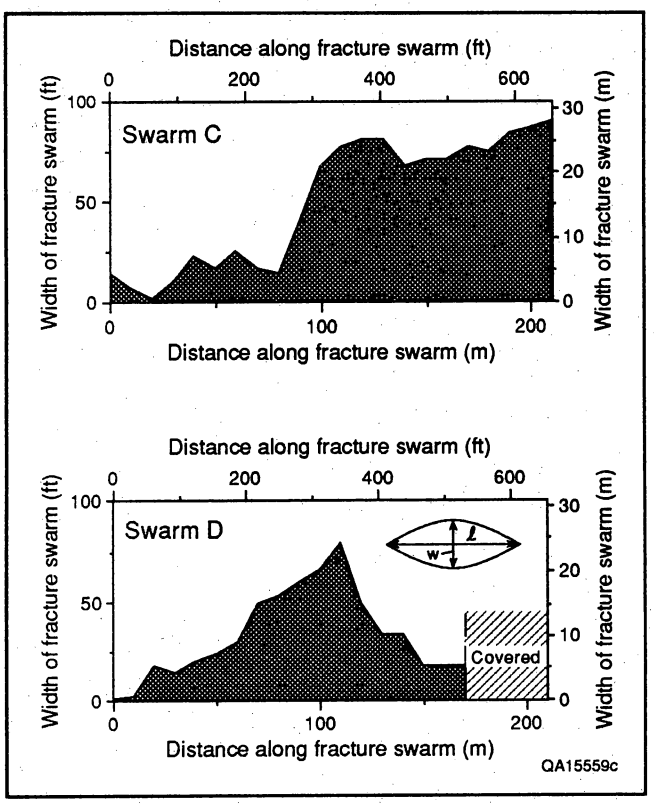

Figure 14. Profiles of fracture swarm width and length for swarms C and D. Swarm C has two sections of approximately constant width, connected by a segment near the middle of the exposure where it abruptly widens, whereas swarm D gradually tapers away from a wide central part.

ture is in swarm B, where two overlapping, curved swarm segments can be distinguished (figs. 6 and 15). The two subparallel main swarm segments are connected by a nonparallel swarm having numerous small fractures arranged in a network of overlapping segments, splays, and ladder structures. Along both main strands, swarm width diminishes as the area of overlap is approached (fig. 15). This macrostructure resembles overlap regions of individual fractures (fig. 10b).

Fracture Patterns within Swarms

Fracture patterns within swarms are defined by fracture spacing, length, shape, orientation, and arrangement. Spacing is highly variable and ranges from 0.5 inch to approximately 3 ft (1 cm to ~1 m) or more. Average between-fracture distance is approximately 3 ft (~1 m), so fracture spacing is close only in comparison to domains adjacent to swarms that lack fractures. Areas within swarms may have regular spacing over large areas. For example, within swarm C, an area of approximately 2,420 ft² (~225 m²) has parallel fractures with approximately 6 ft (~2 m) spacing. These fractures are part of a large ladder structure, and their strike is oblique to that of the swarm as a whole. Fracture density can vary widely within swarms but is generally highest where fracture segments overlap. A general measure of fracture density is the number of fractures within a given swarm. A representative example is swarm C, which consists of 36 individual fractures less than 3 ft (<1 m) long in an area of 36,315 ft² (3,375 m²).

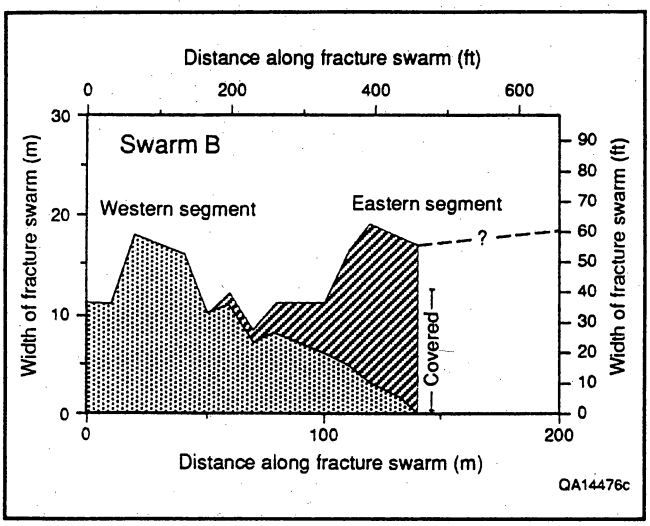

Figure 15. Width versus length measurements of overlapping western and eastern segments of swarm B. Gradual sympathetic narrowing of swarm segments in their region of overlap suggests a pattern of swarm interaction and dilation similar to that observed between segments of individual overlapping fracture segments. Dotted line shows inferred continuation of eastern swarm B segment in covered area.

Individual fractures within swarms have a wide range of trace lengths, ranging from microfractures with millimeter-long traces to fractures with traces longer than 320 ft (100 m). The mean length of individual, continuous fractures in the four swarms is 35 ft (10.5 m) (fig. 16), but this number does not include the many short (< 3 ft [<1 m]) fracture strands and segments that occur within fracture swarms.

Fractures have a wide range of strikes (250° to 340°), but mean fracture strike is west-northwest, similar to overall strike of the swarms (figs. 11 and 12). Mean fracture strikes typically differ from swarm strikes by 10° or less, but individual fractures can differ from swarm strike by 60° to 70°. Fractures with lengths less than approximately 3 ft (~1 m) have the greatest dispersion in strike, reflecting the large number of fractures in this length range that occur in splays, overlap zones, and ladder structures. Many fractures with lengths of 3 to 30 ft (1 to 10 m) have strikes at a high angle (60°) to the strike of the swarm in which they occur, in part reflecting their occurrence in large splays and ladder structures. Most fractures in swarms are straight or slightly curved, but some strongly curved fractures are present. Many fractures with lengths greater than 60 ft (20 m) are significantly curved, and one 130-ft-long (40-m) fracture ranges in strike from approximately 275° to 345°.

Fractures visible on 1:1,000-scale maps are arranged in characteristic patterns that resemble the arrangements associated with terminations of individual fractures

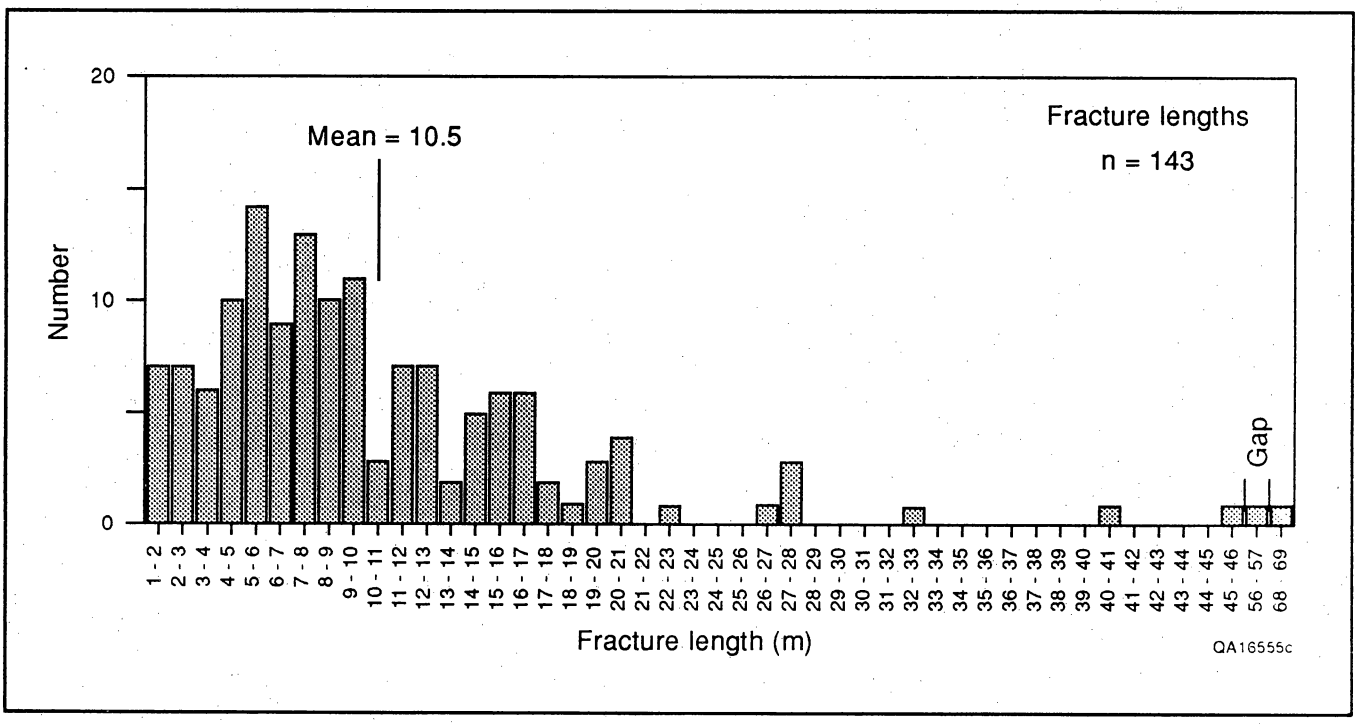

Figure 16. Histogram of fracture segment lengths greater than 3 ft (1 m) long, Fort Lewis mine pavement.

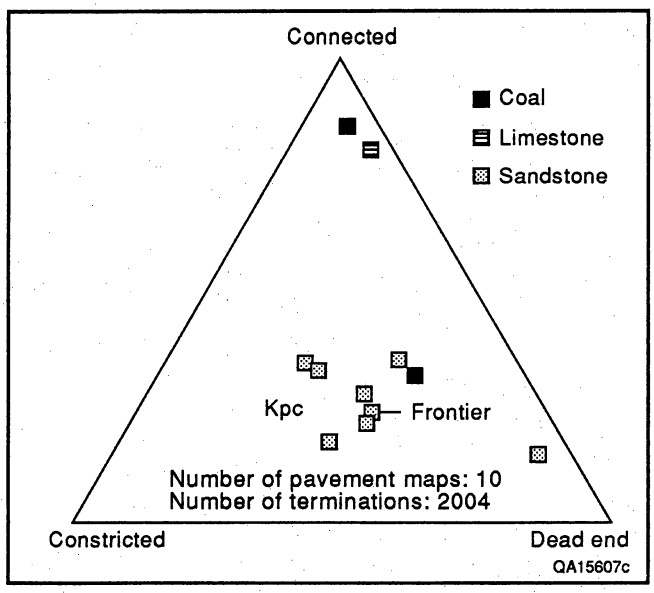

Figure 17. Termination-type diagram showing proportion of connected, constricted, and dead-end fracture terminations. Connected fractures are those that abut or cross. Constricted fractures are those connected only by narrow subsidiary fractures or microfractures; typically these are where segmented fracture strands overlap (see figure 10). Dead-end (or blind) fractures have isolated terminations. Sandstone measurements are from seven detailed maps of the Fort Lewis mine near the Colorado–New Mexico border and of a pavement in the Cretaceous Frontier Formation in Wyoming (Laubach, 1991). Coal measurements are from a map of lower Fruitland Formation coal at the Navajo mine in New Mexico (Tremain and others, this vol.); a seemingly anomalous pattern of poor interconnectedness in coal is evident. For comparison, Cretaceous Edwards Limestone, Balcones Fault Zone, Central Texas, shows a well-interconnected fracture pattern (Collins and others, 1990).

(fig. 9). The most distinctive macro-scale arrangements include abruptly curving fracture segments and ladder structures. Along their strike or near their terminations, many large fractures split into smaller en echelon or arborescent arrangements of segments.

Fracture Connectedness

The degree to which fractures are interconnected will affect the flow properties of a fracture system (Long and Billaux, 1987; Barton and Hsieh, 1989). Fractures that are not interconnected cannot contribute to fracture flow. Connectedness can be assessed by noting the proportion of fractures that intersect or that *connect* with other fractures by abutting, crossing, or splaying relations relative to those that terminate within the rock matrix with *dead-end* terminations or that are partly (or poorly) interconnected with other fractures, such as where fractures are linked by *constricted* thin, tapering tips or microfractures. Connectedness is represented on a triangular graph (CCD plot) that shows the ratios of connected, constricted, and dead-end termination types (fig. 17). Detailed outcrop maps, such as the field maps that form the basis of figure 6, are needed to assess interconnectedness and to count fracture termination types. Another measure of fracture linkage is the connectedness index, which is the number of connected fracture terminations divided by the number of blind and constricted fracture terminations. It gives a measure of the proportion of well-connected fractures in a network. High values of connectedness index indicate more connected fractures. The number of terminations increases with map area, but the degree of connectedness does not vary systematically with size of the area mapped (fig. 18a, b).

In Pictured Cliffs outcrops, fracture connectedness is surprisingly low in comparison with what might be expected for orthogonal arrays of regional fractures (Stearns and Friedman, 1972) or simple cubic networks of current fractured-reservoir models (for example, Aguilera, 1980). Such networks would be well connected by numerous abutting intersections and would plot near or on the "connected" apex of the CCD plot. At the Fort Lewis mine, fracture connections across the width of fracture swarms (normal to overall fracture strike) are infrequent. Few abutting or crosscutting fractures occur within swarms, except between set I and set II fractures–and these would be irrelevant for subsurface fluid flow if set II fractures are surficial phenomena. Most connections at the mapped level of exposure are through low-angle intersections and microfracture arrays where fracture strands overlap. Such intersections tend to connect fractures parallel to the length of the fracture swarm, but not across the width, so some sections of fracture swarms may be partly or completely isolated from others. Some fractures appear to be completely isolated both along and across strike, and many fractures or linked arrays of fractures have one blind termination.

In coal, high fracture connectivity is expected because numerous abutting relations are evident in most outcrops in the San Juan Basin. Surprisingly, a detailed map of a large exposure of Fruitland coal in the Navajo mine shows connectivity ratios similar to Pictured Cliffs fracture swarms (fig. 17; Tremain and others, this vol., fig. 9). This area may be anomalous, or the degree of connection among cleats may be overestimated in other exposures where weathering or other disturbances enhance fracture development. This outcrop is not near any known fracture swarm in sandstone or any other structure, but in the clustering of long fractures there is an indication that the fracture pattern has domains of contrasting fracture density. This observation suggests

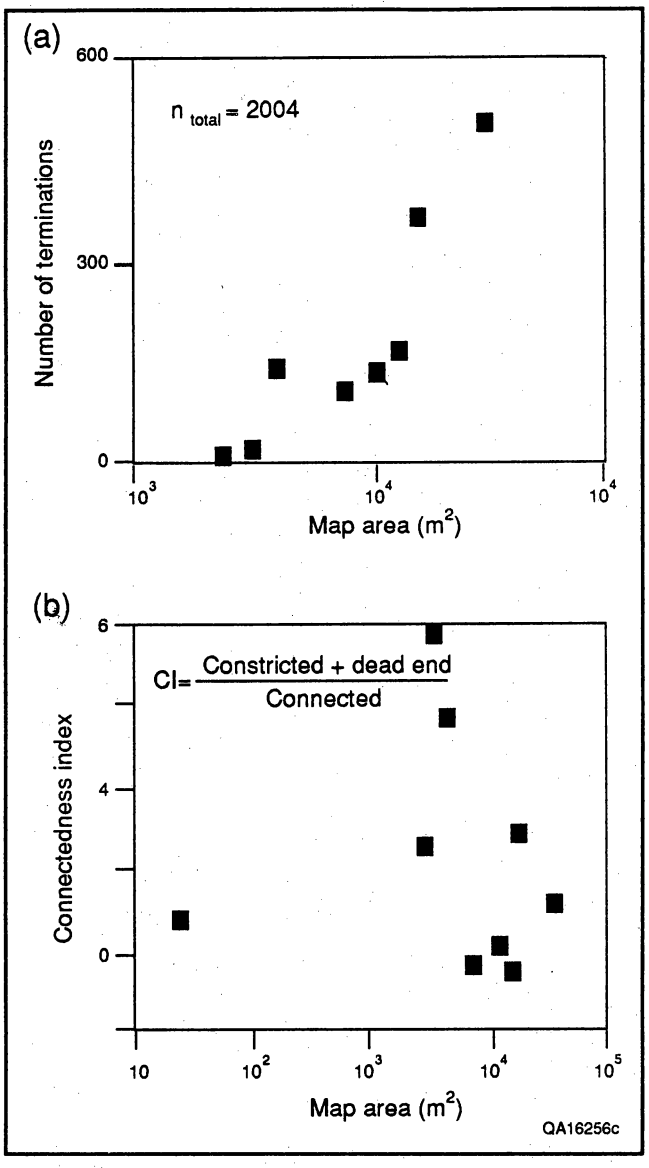

Figure 18. Fracture connectedness. (a) Number of fracture terminations versus size of map area and (b) connectedness index versus map area. As expected, larger maps have more terminations, but the proportions of termination types relative to the degree of connectedness does not change systematically with map size.

that domains with varying degrees of cleat development may exist within regional coal fracture patterns in Fruitland Formation coal beds.

Relation of Swarms in Sandstone to Coal Fracture Patterns

At the Fort Lewis mine, coal directly overlies sandstone, but the mine has been reclaimed and the contact between coal and sandstone is not exposed in remaining outcrops. Coal is exposed within 10 ft (3 m) of the coal-sandstone contact, and cleat patterns were studied in 20 small natural outcrops and shallow excavations adjacent to the pavement. Cleat strikes and spacing are typical for the northern San Juan Basin throughout much of the outcrop. Face cleats strike northwest and have little dispersion in strike. In contrast, where fracture swarm D projects into the coal outcrop, numerous small normal faults and highly variable cleat patterns are evident. We interpret this to be the continuation of fracture swarm D in the Fruitland coal seam.

The disturbed zone in coal is approximately 90 ft (30 m) wide. Within it, six map-scale normal faults have west-northwest strikes and throws of 3 ft (1 m) or less. Fractures in coal include small faults, "third" cleats with a range of strikes, curved cleat, and vertically extensive joints. Fracture density is greatest near faults. Changes in cleat strikes are evident at distances of as much as 50 ft (15 m) from mapped faults. These characteristics resemble the fracture pattern in coal associated with the fracture swarm at Durango/U.S. Rte. 550 described above.

Regional-Scale Fracture Swarms: Animas–Florida River Exposure

Discrete west-northwest, northwest-, and north-striking fracture swarms are present in Pictured Cliffs pavements between the Animas and Florida Rivers, southeast of Durango (fig. 7). Preferential erosion along north-striking fracture swarms may account for some of the linear topographic features along this outcrop. West-northwest fracture swarms tend to be less well exposed. The northwest-striking fracture swarms are subparallel to face-cleat strikes in overlying Fruitland Formation coal. Exposed swarm lengths are as much as 1,000 ft (305 m), and widths range from 50 to greater than 100 ft (15 to >30 m). Smaller swarms, such as the one that occurs at Carbon Junction (fig. 2), at the western end of the Animas–Florida River exposure, are present locally elsewhere along the ridge. Spacing between large fracture swarms is irregular and ranges from over 4,000 ft (1,220 m) to approximately 200 ft (60 m).

Because of limited coal exposures adjacent to this outcrop, our mapping did not link large fracture swarms in sandstone to specific coal-fracture anomalies or faults. Local changes in mean face-cleat strike and development of "third cleat" trends in some exposures in this area suggest that fracture swarms may exist in coal. Several of the fracture swarms in the Pictured Cliffs Sandstone do not extend into the overlying upper Pictured Cliffs tongue or Fruitland sandstones. Just as at the Fort Lewis mine, many fracture swarms are isolated vertically as well as laterally by rock that lacks fractures.

Swarms in the Animas–Florida River exposure show that the Fort Lewis mine fracture network is not an

isolated occurrence. Discrete, irregularly spaced swarms of concentrated fractures is the structural style on a regional scale in Pictured Cliffs Sandstone. Fracture swarms can be larger than those exposed at the Fort Lewis mine, and they may be more widely and irregularly spaced. Fracture swarms have strikes similar to those in the Fort Lewis exposure, although most mapped swarms have a somewhat more northerly strike near Durango. This change in strike corresponds broadly to regional variation in face-cleat orientation in Fruitland coal across the northern San Juan Basin.

Preliminary Core Observations

Fractures are evident in several Fruitland Formation and Pictured Cliffs Sandstone cores from vertical wells (table 1). Preliminary observations of these fractures indicate that some resemble set I fractures at the Fort Lewis mine. Fractures in sandstone are subvertical and are composed of multiple strands; several have calcite vein-fill. Striated and inclined fractures not evident at the Fort Lewis mine are present in these cores, but they are generally found only in shales.

Limited core orientation data indicate north, northeast, and east strikes for some of the steeply dipping sandstone fractures, but further oriented core and borehole-imaging log studies are needed to establish subsurface fracture trends across the basin. If face-cleat strikes are a guide to sandstone fracture patterns, fracture strikes may vary considerably in the northern part of the basin. If fractures are associated with faults, then northwest and northeast strikes should be expected.

Scale-Invariant Characteristics of Fracture Patterns

In Pictured Cliffs Sandstone at the Fort Lewis mine, several characteristic fracture patterns are repeated on scales ranging from inches (centimeters) or less to hundreds of yards (meters) or more. These patterns include anastomosing, segmented, parallel, en echelon, and relay fracture strands and structures developed near fracture terminations such as horsetail and asymmetric splays, curved overlapping, and smoothly and abruptly hooking fracture segments and ladder structures. The ratios of overlap length to width for segments of small, intermediate, and large fractures are similar, and fracture patterns within swarms resemble the overlap patterns of whole fracture swarms, such as the western and eastern segment of swarm B (fig. 15). Furthermore, fracture connectivity index and ratios of fracture termination types are the same when measured for small (yards to tens of yards [meters to tens of meters]) parts of the map or for the entire pavement (fig. 17).

Fractal geometry is one way to quantify heterogeneity of two-dimensional fracture-trace networks (Barton and Larsen, 1985; Barton and others, 1987; LaPointe, 1988; Velde and others, 1990). Fractal geometry is particularly useful for quantifying scaling properties of complex patterns, and such information is being incorporated increasingly in fractured-reservoir models (Matthews and others, 1989). The impetus for this is the realization that transport processes in fractal systems are likely to be substantially different from those in nonfractal (Euclidian) networks. Reservoir simulations using a fractal network of fractures may provide useful predictions of hydrocarbon reservoir production characteristics (Matthews and others, 1989). Moreover, the fractal dimension (D) provides an objective standard of comparison between various fracture patterns. If D is constant over a range of sampling scales, the pattern is statistically self-similar over that range of scales. "Self-similarity" is repetition of the fracture pattern over a wide range of scales. Information on characteristic scaling properties of fracture systems may be useful for extrapolating outcrop and core observations of fractures in sandstone and coal to subsurface exploration and development.

We used the "box method" to estimate fractal dimension of the Fort Lewis fracture network (Barton and Larsen, 1985; see also LaPointe, 1988). Grids of various sized square elements (r) are successively placed over the map, and the number of grid elements containing a fracture trace (N) is counted. $Nf^D = 1$, or equivalently, $D = \log N/\log (1/r)$, are relationships that define the fractal distribution of lines on a map, with D (the fractal dimension) being the slope of the best-fit line on a log-log plot. We used grid elements with sizes (r) ranging from less than 2 ft (0.5 m) to more than 160 ft (50 m) in our preliminary study (fig. 19). The fractal dimension D for the entire pavement is 1.2 ($R^2 = 0.98$). Applying the same technique to individual swarms and inch-scale (centimeter-scale) segments of individual braided fractures gives the same fractal dimension. Similar results are obtained if maps are used that have been filtered such that only fractures that have lengths less than 0.5(r) are counted. The smooth line on the fractal plot indicates that the fracture pattern is self-similar over the range 2 to 160 ft (0.5 to 50 m), consistent with observations of a range of sizes for a variety of fracture configurations. Swarm patterns at the Fort Lewis mine, and the distribution of swarms along the Animas–Florida River transect suggest that swarm distribution at a scale of approximately 3,000 ft (~1,000 m) could resemble the distribution of fractures within swarms.

It is well known that natural fracture systems have fracture distributions at many length scales. Such features are consequences of fracturing processes and the stress field during fracture propagation (Pollard and Aydin, 1988). For example, the curvature of overlapping fracture segments results from interaction of regional

Table 1. Fractures in cores (excluding coal).

Well name, location	Fm	Core depth (ft)	Lithology	Fracture description and mineralization	References
USGS Core[2] Hole A-15 Sec. 1, T23N, R13W	Kf	248-257	ss	Gypsum veins.	Wilson & Jentgen, 1980
El Paso Natural[2] Gas Gasbuggy No. 1 Sec. 36, T29N, R4W	Tn, Tka, Kkf, Kf, Kpc, Kl	3436-4316	ss, siltstone, shale	Shale in all fms. striated; vert. fracs. in sh. in Kkf & Kf, & Kl—often filled with calcite in Kkf & Kf plus some clay. Sandstones in Tn & Tka have 75° to vert. fracs.; ss & siltstones in Kkf, Kf & Kpc have many 70° to vert. fracs. often lined with calcite plus low-angle (<30°) fracs. Kpc ss has one 10-ft wet vert. frac. with gas odor.	Fassett, 1967
Blackwood & Nichols[1,2] NEBU No. 403 Sec. 9, T30N, R7W	Kf	3025-3192	ss, siltstone, & shale	Fractures are open to filled; open trend N & E, partially open N & NE, filled N & NE. Fractures arranged in strands.	Mavor and Close, 1989a, GRI-90/0041
Western Coal[2] P-70 Sec. 22, T30N, R15W	Kf	370-414	carb. shale	Horizontal fracs. with calcite veins & pyrite on glossy surfaces.	TRW Preliminary Well Test Report, 1978
Tiffany[1,2] Glover No. 1 Sec. 2, T32N, R6W	Kf	3062-3111	siltstone	Horizontal to vertical microfractures (0.5 mm wide) filled with white mineral (calcite?).	COGCC files
Mobil Colorado[1,2] 32-7, No. 9 Sec. 4, T32N, R7W	Kf	2759-3064 2899-2927	ss, shale	"Some gouge and calcite filled fracs. in ss below coals, strike same as cleats." Low-angle striated in shale; Mod.-high angle filled fracs. in ss avg. 7 cm long & 0.1 mm wide + high-angle calc.-filled fracs. 0.2 mm wide & 10 cm long (one 24 cm)—not visibly porous, 28 filled fracs.	GRI-90/0043 Mavor and Close, 1989c
Ladd 2-3 North Cox Canyon Sec. 3, T32N, R10W	Kf	3084-3114	carb. shale	4 striated horizontal to 40°, one with calcite.	CGS files
Mesa Hamilton No. 3[1] Sec. 30, T32N, R10W	Kf	2652-2887	ss & shale enclosing coals	Prominent set of open fractures N70-80E.	Mavor and Close, 1989d, GRI-90/0040
USGS No. 1 Sec. 23, T32N, R12W	Kf	181-226	siltstone	45° fractures.	Roberts, 1989
USGS No. 2[2] Sec. 23, T32N, R12W	Kf	61-119	shale & siltstone	Two 45° fractures.	Roberts, 1989
El Paso Natural Gas 14-20, 33-7 Sec. 20, T33N, R7W	Sano-stee Kd	7253-7418 7646-7694	ss ss & shale	Calcite veins. Vert. & horizontal fractures.	COGCC; Petroleum Information completion card
Amerada No. 1 Harmon Sec. 17, T33N, R8W	Kd	7796-7810	ss	Fractures	COGCC files

Table 1 (cont.)

Well name, location	Fm	Core depth (ft)	Lithology	Fracture description and mineralization	References
U.S. Smelting-Mining 1-x Brown Sec. 15, T33N, R9W	Kf Kd	2669-3086 7725-7965	ss, shale ss	Fracs., with gas odor in ss fractures, vert.	COGCC; Petroleum Information completion card
USGS No. 17 Sec. 17, T33N, R11W	Kf	226-271	.8 ft siltstone 1 ft claystone	High-angle frac. Two 45° fracs.	Roberts, 1989
USGS No. 14 Sec. 30, T33N, R11W	Kf	46-58 161-265	siltstone	45° frac.	Roberts, 1989
USGS No. 11 Sec. 31, T33N, R11W	Kf	71-137	siltstone ss	45° frac. Calcite-filled fracs.	Roberts, 1989
Benson-Montin Greer Ute A-1 Sec. 35, T33N, R12W	Kd	3634-3686	ss	Good fracture system at 3662-3686.5 ft.	COGCC files
USGS No. 8[2] Sec. 36, T33N, R12W	Kf	75-129	siltstone	Pyrite on fracs.	Roberts, 1989
SUTEC[2] Oxford No. 1 Sec. 25, T34N, R8W	Kf	2769-2787 2804-2822	shale	Striations with calcite, pyrite, & gypsum.	CGS files
SUTEC[2] Oxford No. 2 Sec. 25, T34N, R8W	Kf	2832-2850	carb. shale & siltstone	Striations with calcite on faces, trace pyrite.	CGS files
Bowen & Edwards SE Durango Federal 3-1 Sec. 3, T34N, R9W	Kf	1890-1918 2010-2040 2132-2160	shale	Fracs. at 2040 ft.	COGCC files
Tenneco[2] Fassett 2-13 Sec. 13, T34N, R9W	Kf	2468-2482	carb. shale	Striations dipping 30-50°, two vert. fracs.	CGS files
Tenneco Larson 1-12 Sec. 13, T34N, R9W	Kf	2291-2297 2303-2361	carb. sh. ss	2 striations at 50-60°. 60° vert. fracs.	CGS files
Bowen & Edwards[1] McCulloch Well No. 28-1 Sec. 28, T34N, R10W	Kf	3140-3168	shale	Striations.	COGCC files
Bayless Jicarilla 459 No. 5	Kf	3803-3883	carb. sh. ss	Fracs. with striations. Vert. fracs.	BEG files

[1]Oriented cores.

[2]Also have mineralized coal cleats (see table 2, Tremain and others, this vol.).

Tn = Nacimiento Formation; Tka = Animas Formation; Tkkf = Kirtland Shale; Kf = Fruitland Formation; Kpc = Pictured Cliffs Sandstone; Kl = Lewis Shale; Kd = Dakota Sandstone.

CGS = Colorado Geological Survey; COGCC = Colorado Oil and Gas Conservation Commission (geological well report); BEG = Bureau of Economic Geology, The University of Texas at Austin.

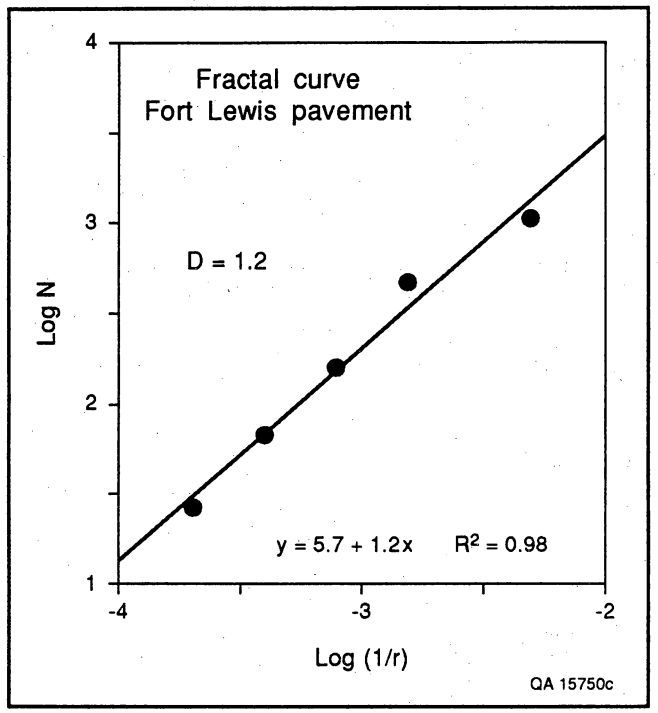

Figure 19. Fractal curve for Fort Lewis pavement, showing number of elements containing fracture traces (N) and length of counting element sides (r). Counting element sizes shown here range from 6.5 to 167 ft (2 m to 51 m).

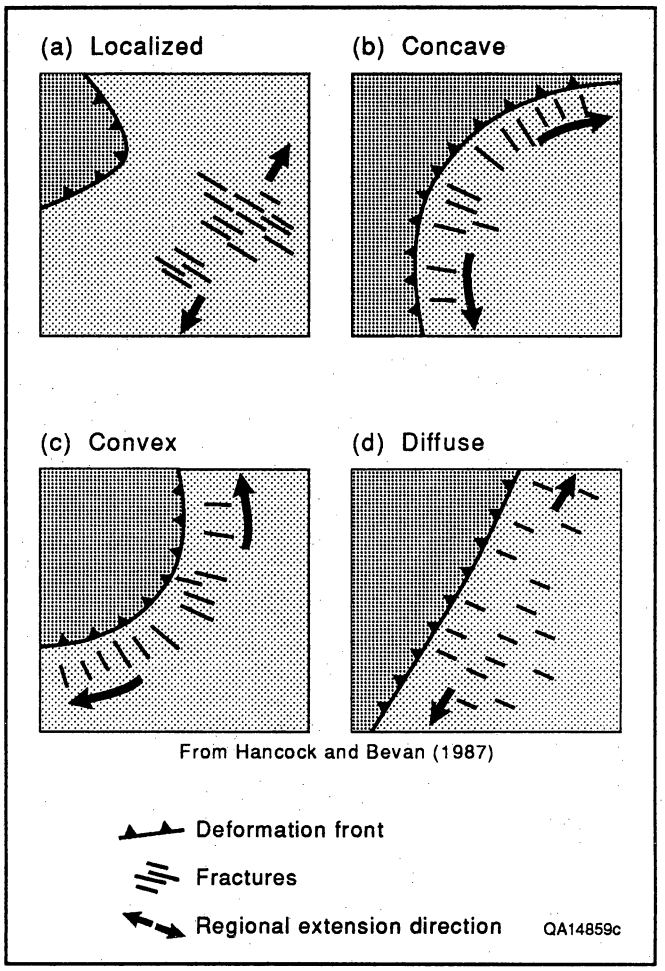

Figure 20. Map view of deformation fronts of various shapes and fracture strikes in foreland areas that may result from lateral foreland extension (modified from Hancock and Bevan, 1987). (a) Uniform extension direction and localized extension in advance of convex front. (b) Concave arc of extension directions with concave front. (c) Convex arc with convex front. (d) Slightly convex arc of extension directions with nearly rectilinear front. Fracture strikes are not precisely parallel to shortening directions, but rotate in sympathy with them. Obstacles and indentors within the foreland and the deformation front may cause fracture strikes to vary on subregional scale.

and local stresses near fracture tips. Where regional (or far-field) stress contrasts are low, stresses induced by growing fractures may interfere, causing overlapping fracture tips to curve. On the other hand, where regional horizontal stress contrast is high, overlapping segments will tend to follow regional stress trajectories, and hooking will not be favored (Olson and Pollard, 1989). Fracture length and spacing may be interrelated, since fracture development relieves stress in a volume of rock proportional to fracture length. Such a process can control where subsequent fractures form relative to early formed fractures, and can lead to a network with a hierarchy of fracture lengths and fracture spacing (Nur, 1982), with oldest fractures being longest and farthest apart. Such processes could be responsible for aspects of the Pictured Cliffs fracture patterns. The cause of localized fracture development and the formation of swarms may reflect interference between swarms and regional deformation patterns.

Causes of Fracture Development

Most rocks near the Earth's surface behave as brittle-elastic materials in response to natural stresses. Consequently, under the influence of compression, extension, flexure, uplift, cooling, and fluid migration, many rocks acquire networks of fractures of various types and sizes. Determining which process(es) caused a given fracture set is important because this information can provide insight into the probable distribution and orientation of fractures on local and regional scales. This determination is commonly difficult, however, because many loading paths can result in fractures that appear similar (Engelder, 1985).

We interpret fractures in Pictured Cliffs Sandstone to have formed in response to west-northwest tectonic shortening that caused lateral elongation subparallel to the Cordilleran overthrust belt (fig. 20). This model is basically the same as that proposed to explain regional face-cleat patterns in the San Juan Basin (Tremain and others, this vol.).

Fractures in the Pictured Cliffs share several characteristics with fracture sets in other foreland areas (Hancock and Bevan, 1987). Fractures have average strikes that are normal to the folded and reverse-faulted northwestern margin of the basin. This pattern relative to the orogenic belt is similar to that of unidirectional regional fracture sets in the foreland of the Appalachian thrust belt (Engelder, 1985) and several other thrust belts (Hancock and Bevan, 1987; Dunne and North, 1990). Since opening-mode fractures are initiated at right angles to the minimum principal stress, vertical fractures in Pictured Cliffs swarms indicate a horizontal minimum stress during fracture development. Evidence that fractures grew before folding is consistent with orientation of fractures normal to bedding, and with similar fracture strikes at the Fort Lewis mine and Animas–Florida River exposure, despite regional change in fold trend. Timing is broadly consistent with fracture growth driven by movements in the adjacent orogenic belt. Strongly curved intersections between overlapping fracture segments and fracture terminations at thin shale partings suggest fractures propagated when low differential regional stresses prevailed (Olson and Pollard, 1989). Elevated pore-fluid pressure is likely to have accompanied fracturing (Lorenz and others, in press).

Faults in coal are associated with fracture swarms in sandstone at the Fort Lewis mine, and some swarms are associated with small normal faults in sandstone, suggesting that fractures locally represent deformation in advance of lateral tips of growing normal faults (Laubach and Marshak, 1987). This interpretation is compatible with the foreland extension model; such faults are common features of foreland extension (Hancock and Bevan, 1987). Prominent examples in the foreland of the Cordilleran belt are the east-northeast-striking Laramide normal faults of the Rocks Springs Uplift in Wyoming that are aligned normal to the adjacent Idaho-Wyoming thrust belt.

Tremain and others (this vol.) describe northeast- and northwest-striking normal faults in Cretaceous and Tertiary rocks in the San Juan Basin. Evidence from reflection seismic data cited by Taylor and Huffman (1988) indicates that these fault trends have a long movement history. They have inferred that during the Laramide, east-west shortening resulted in left-lateral movement on northwest-striking faults, and right-lateral movement on northeast-striking faults, but evidence for transcurrent slip is not apparent on the faults and fractures we studied. Ladder structures resemble fracture patterns associated with small strike-slip faults, but strike-slip motion does not appear to have occurred on the Fort Lewis fracture zones.

Fracture Swarms: Targets for Natural Gas Exploration?

Although the existence of fracture swarms in the subsurface of the San Juan Basin has yet to be demonstrated, fractures in some Pictured Cliffs and Fruitland core from coalbed methane wells resemble fractures in outcrop swarms, and our genetic model predicts that swarms should exist within the basin. Predicting the location and pattern of fractures in the subsurface is important for exploration, engineering evaluation, and development of many hydrocarbon reservoirs because fractures may control the size and shape of the rock volume contacted by a given borehole (Long and Witherspoon, 1985; Long and Billaux, 1987; La Pointe, 1988). Insight from outcrop examples can help guide completion and stimulation strategies. In the San Juan Basin, Pictured Cliffs sandstones and Fruitland coal beds form gas reservoirs (Ayers and others, this vol.), and local high gas and/or water production and abrupt differences in well performance that cannot be explained by other aspects of reservoir geology or completion practices indicate that fracture-enhanced permeability is present (fig. 21) (Gorham and others, 1979; DuChene, 1989; Kaiser and others, this vol.).

Predicting reservoir behavior where fractures play an important role is currently hindered because even simple fracture-network patterns are difficult to document with conventional methods in vertical boreholes. Fracture-detection methods used in our study did not document fracture swarms in the subsurface, but the abrupt contrast in fracture intensity (or density) between swarms and adjacent rocks suggests that these features may be visible with advanced seismic techniques (such as cross-polarized S-waves) and possibly as velocity anomalies on conventional seismic lines. Our observations indicate that it may be difficult to fully assess the role of fractures in Rocky Mountain low-permeability gas reservoirs with current fracture-detection methods or fractured-reservoir models. These conclusions are likely to apply elsewhere in the western United States because the Pictured Cliffs and Fruitland share a similar tectonic setting and other characteristics with many Cretaceous gas reservoir rocks of this region.

The essentially discontinuous nature of Pictured Cliffs fracture networks should be incorporated in exploration concepts and reservoir simulators, perhaps through application of fractal geometry. In contrast to conventional views of regional fracture patterns, in which fractures are regularly spaced in orthogonal arrays, fractures in the Pictured Cliffs Sandstone occur in discrete swarms with a range of sizes, separated laterally by domains

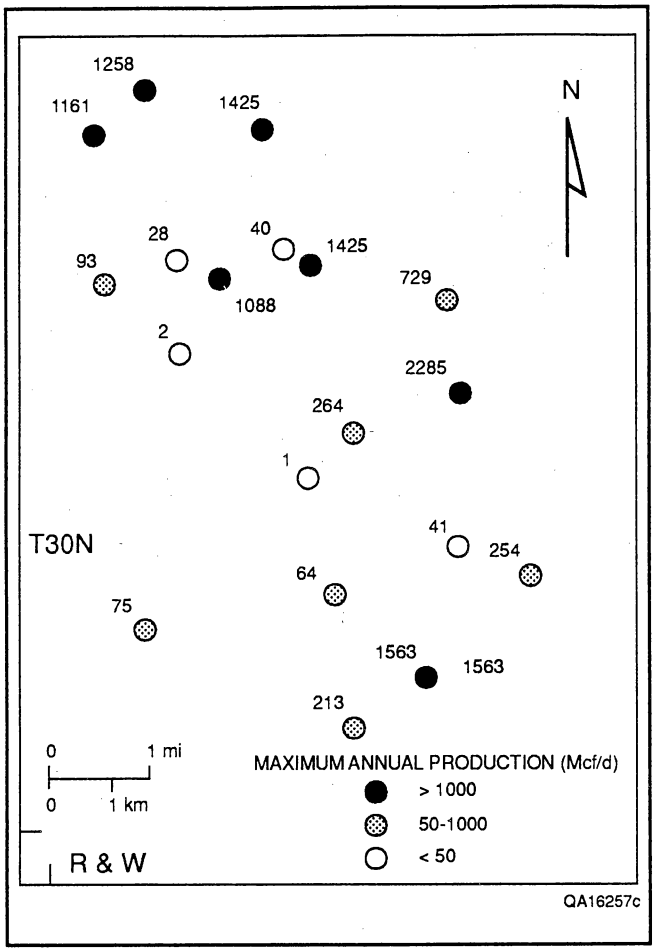

Figure 21. Maximum annual production maps of coalbed methane wells from an area in the northern San Juan Basin (Joseph Yeh and W. R. Kaiser, personal communication, 1990). Abrupt and substantial differences in maximum annual production may indicate local differences in reservoir quality that could in part be accounted for by discrete fracture zones such as those at Fort Lewis mine. Map is not contoured; this emphasizes that "sweet spots" may be controlled by fracture swarms of unknown size and position. If patterns such as those at Fort Lewis mine extend to field-scale fracture zones, outcrop examples could provide a guide for understanding distribution of exceptionally productive wells.

typically hundreds of yards (meters) wide that lack fractures. Fractures are poorly connected across strike, and even within swarms fractures are moderately to poorly interconnected, having a high proportion of constricted, narrow links between fractures. We postulate that distribution of swarms on a scale of 1,500 to 3,000 ft (500 to 1,000 m) resembles the pattern of fractures within swarms, but degree of inter-swarm connectedness is likely to be poor, resulting in elliptical, northwest-trending islands of fracture permeability surrounded by intact rock.

Fracture spacing and connectedness are key parameters in fractured reservoirs, but currently even highly sophisticated reservoir simulators use fracture networks that are greatly simplified. Evenly spaced fracture sets arranged in parallel or orthogonal Euclidian patterns are commonly incorporated in these models, not variably spaced fracture swarms with fractal characteristics such as those in the northwestern San Juan Basin. Future work should take these differences into consideration.

Summary

1. On the northwestern margin of the San Juan Basin, a prominent set of fractures in the Pictured Cliffs Sandstone occurs in west-northwest-striking swarms. Small-scale (~inches [centimeters]) fracture patterns within swarms resemble patterns developed on much larger scales (fractal dimension D ~ 1.2).

2. Locally, fracture swarms extend into overlying Fruitland coal seams, where they are marked by more, and better interconnected, fractures and small normal faults.

3. Swarms may be areas of enhanced permeability and are potential targets of coalbed methane exploration. Studies are needed to further characterize these fractures to guide exploration and development efforts.

Acknowledgments

We thank W. A. Ambrose, W. B. Ayers, Jr., and N. H. Whitehead III for assistance and discussions, and W. B. Ayers, Jr., and Roger Tyler for reviews.

Effects of Compaction on Cleat Characteristics: Preliminary Observations

Roger Tyler, S. E. Laubach, and W. A. Ambrose

Abstract

A preliminary survey of outcrops and mine highwalls of interbedded lenticular, channel-fill sandstones and coal beds in several basins of the western United States indicates that cleat variations can develop as a result of differential compaction between coal and sandstone. Variations include increases in cleat frequency and development of throughgoing fractures and faults. If such fracture systems are sufficiently developed they could either enhance, or detract from, coalbed permeability. If these fracture systems prove to be widespread, then coalbed methane exploration targets could be identified using structural and lithofacies maps.

Introduction

Fractures are the primary factor controlling permeability in coal beds. The most pervasive fractures in coal, termed "cleat," are those formed during coalification. Cleats are opening-mode (mode I) fractures that are perpendicular to bedding; they are composed of two fracture sets—the face and butt cleat—that are commonly orthogonal to each other. Face cleats are the dominant fracture set, against which other fractures may terminate. They are thought to strike parallel to the principal compressive stress that existed during coalification and perpendicular to axial trends of folds (Diamond and others, 1976). Butt cleats are short, poorly developed fractures that commonly extend no further than the width between two face cleats. Butt cleats are thought to form perpendicular to the principal compressive stress that existed during coalification (Diamond and others, 1976). Cleats in coal beds enhance methane migration through coal (fig. 1). In some cases, boreholes drilled perpendicular to face cleats have yielded 2.5 to 10 times as much gas as holes drilled perpendicular to butt cleats (McCulloch and others, 1974).

Variations in fracture patterns can occur as a result of tectonism or differential compaction (fig. 1). Because mudstone and coal beds compact more than sandstone during burial, interbedded mudstone and coal compact around and/or under lenticular channel-fill sandstone bodies, resulting in divergent coalbed contacts. Most differential compaction probably occurs before coalification has advanced far enough for the peat bed to fracture. However, if even small amounts (possibly 10 percent or less) of differential compaction occur after coal has become brittle (postcoalification), irregular or lenticular sandstone bodies could potentially cause enhanced-fracture development. Thus, fracture style near lenticular channel-fill sandstones may differ from that of regional cleat systems. Stress concentrations occurring at the irregular, divergent coalbed contacts may potentially cause enhanced fracture development, manifested as long, more interconnected, or more frequent fractures, even where differential compaction *per se* is minimal. If these fracture systems are sufficiently developed, they may enhance coalbed permeability. Therefore, predictions of cleat variations near lenticular channel-fill sandstone bodies could aid coalbed methane exploration and development. On the other hand, if syncoalification faults rather than opening-mode cleats develop in this setting, fractures might be less conductive for fluids, detracting from coalbed permeability.

Scope of the Study

This study, part of an investigation of controls of coalbed methane producibility in the San Juan Basin, also involves examination of coal beds from other western coal basins. Lenticular, fluvial-deltaic sandstones and associated coal beds of the Fruitland Formation in the San Juan Basin are possible areas for compaction-related fracture enhancement, but these sandstones and coal beds are poorly exposed. We therefore studied exposures of coal beds from other basins that are similar to Fruitland Formation coal beds but have well-exposed divergent coalbed contacts. The examples in this report represent a range from parallel to strongly divergent coalbed contacts.

We studied examples of lenticular sandstone bodies interbedded with coal beds to determine if there is any variation in cleat fracture systems associated with channel-fill sandstones, and to establish the relation of any variations to the shape of coalbed-sandstone

In Ayers, W. B., Jr., and others, 1991, Geologic and hydrologic controls on the occurrence and producibility of coalbed methane, Fruitland Formation, San Juan Basin: The University of Texas at Austin, Bureau of Economic Geology, topical report prepared for the Gas Research Institute under contract no. 5087-214-1544 (GRI-91/0072), p. 141-151.

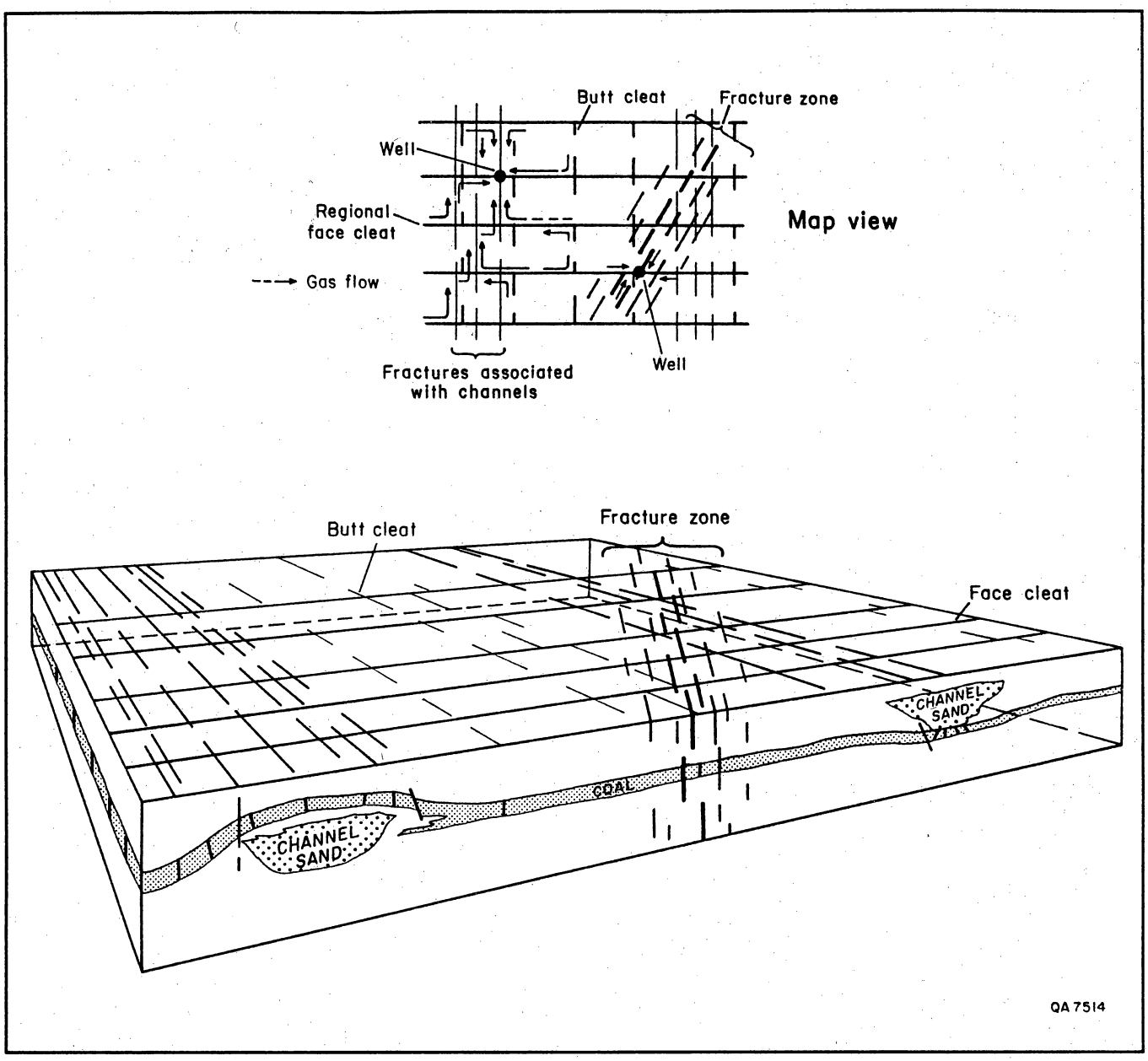

Figure 1. Face-cleat fracture systems may constitute the principal source of permeability in coal beds. Variations in cleat systems, occurring as a result of tectonism and/or differential compaction, may enhance coalbed permeability.

contacts. A description of cleat patterns where coal beds and sandstones have parallel contacts is presented as a basis for comparison. We present preliminary observations of cleat characteristics associated with coalbed contacts at the Navajo mine (San Juan Basin, New Mexico), the Emery coal field (Uinta Basin and Wasatch Plateau, Utah), and the Kemmerer and Rock Springs mines (Greater Green River Basin and Rock Springs Uplift, Wyoming). Examples range from parallel, nonlenticular coalbed contacts to strongly divergent contacts where the local coalbed contacts diverge by 10 to 15 degrees. In the Emery coal field, lenticular channel-fill sandstones split slightly divergent coalbed contacts by 3 to 5 degrees. Lenticular channel-fill sandstones in the Kemmerer mine split slightly to moderately divergent coalbed contacts by 7 to 9 degrees, whereas in Rock Springs, they split moderately to strongly divergent coalbed contacts by 10 to 15 degrees.

Stratigraphic sections were measured to document depositional systems and to evaluate sandstone geometries at each location. An average of 50 measurements of cleat strike, dip, height, spacing, frequency, and

aperture (width) were made at each location, resulting in approximately 900 field measurements of fracture geometry. Rose diagrams, graphs, and/or histograms of cleat strike and spacing versus distance were plotted for evaluation of structural style relative to coalbed contacts.

Cleat Patterns Near Parallel and Divergent Coalbed Contacts

Parallel Coalbed Contacts

Many coal basins have areas where coalbed contacts are virtually parallel on the scale of extensive mines. In such settings, it is unlikely that differential compaction effects could be discerned. These areas provide insight into the degree of cleat variation that exists where no (or only regional-scale) differential compaction has occurred. In the San Juan Basin of New Mexico and Colorado, Fruitland Formation coals overlie and have planar contacts with laterally extensive, barrier-strandplain sandstones of the Pictured Cliffs Sandstone (Ayers and others, this vol.). Tremain and others (this vol.) describe uniform face- and butt-cleat strikes in this setting. Extensive coalbed exposures occur in the Navajo mine, where we documented cleat patterns associated with parallel coalbed contacts.

A 900-ft-long (275-m) section of coal and interbedded shale and sandstone in the Upper Cretaceous Fruitland Formation is exposed in the Pinto pit of the Navajo mine (Tremain and others, this vol., their table 1). In this exposure, parallel-bedded, subbituminous coal is divided into two horizons, a lower 2-ft-thick (0.6-m) seam (number 7) and an upper 25-ft-thick (8-m) seam (number 8), separated by a 10-ft-thick (3-m) sandstone. In the pit, the parallel coalbed contacts of the lower coal seam are laterally continuous and readily accessible. Locally, cleats show minor variation in strike, dip, spacing, frequency and aperture. Face- and butt-cleat strikes are northeast (040 degrees) and northwest (310 degrees), respectively, and cleat dips are orthogonal to bedding. Spacing remains constant at less than 0.5 inch (1.3 cm) for tertiary cleats, 0.5 to 2 inches (1.3 to 5 cm) for secondary cleats, greater than 2 inches (5 cm) for primary cleats, and greater than 12 inches (30 cm) for master cleats (see Tremain and others, this vol., for definition of terms). Most cleat-spacing values fall within one standard deviation of the mean of the entire data set (Tremain, and others, this vol., their fig. 6). Cleat frequency, the inverse of spacing, ranges from less than 1 cleat per inch (2.5 cm) to greater than 5 cleats per inch (2.5 cm). Cleat characteristics therefore show only minor variation where coalbed contacts are parallel.

Slightly Divergent Coalbed Contacts

Exposures along Interstate Highway 70 in central Utah in the Upper Cretaceous Ferron Sandstone Member of the Mancos Formation contain lenticular channel-fill sandstones associated with the "I" coal seam of Emery coal field (fig 2). Coal seams are commonly split, absent, or thin over these channel-fill sandstones; one sandstone body approximately 3.8 mi (6 km) east of the intersection between IH-70 and Utah Highway 10 displays slightly divergent coalbed contacts. In this exposure the channel-fill sandstone extends along strike for 200 ft (61 m) and varies in thickness from 3 to 20 ft (0.9 to 6.1 m). The 2- to 4-ft-thick (0.6- to 1.2-m) coal beds diverge over and under the channel-fill sandstone, forming low-amplitude folds. The angle of divergence between the coalbed contacts is 3 to 5 degrees.

The low-amplitude folds in these exposures have been inferred to be caused by compaction of sand, clay, mud, and peat. Average compaction ratios in a peat-to-coal transformation for bituminous coals are 11:1 (Ryer and Langer, 1980). Sections measured along the slightly divergent coalbed contacts are through semibright, high-volatile bituminous coal beds. Within the lower 2-ft-thick (61-cm), folded coal bed, face cleats are well developed. In general, face cleats strike northeast (038 degrees) and butt cleats strike northwest (320 degrees), and cleat dips are orthogonal to bedding. Primary face cleats have an average height of 1 to 2 ft (30 to 61 cm), spacing of 2 to 4 inches (5 to 10 cm), and frequency of less than 1 cleat per inch (2.5 cm). Primary butt cleats are not as well developed as face cleats, averaging 6 to 12 inches (15 to 30 cm) in height, 1 to 2 inches (2.5 to 5 cm) in spacing, and less than 2 cleats per inch (2.5 cm) in frequency. Secondary and tertiary face and butt cleats have average heights of 0.3 to 12 inches (0.8 to 30 cm), spacing of less than 0.5 to 2 inches (1.2 to 5 cm), and frequencies of greater than 2 cleats per inch (2.5 cm). In general, cleat spacing is 0.8 to 2.2 inches (2.0 to 5.5 cm), frequency is 2.3 to 3.5 cleats per inch (2.5 cm), and aperture width is less than 0.1 inch (0.3 cm). Locally, intermediate (third) cleats which strike north-northeast (340 degrees) are present under the flanks of the channel-fill sandstone.

These cleat characteristics are modified by the compaction-induced folding on the flanks of the channel-fill sandstone. On the flanks, average face-cleat frequencies increase and primary face-cleat spacing shows a corresponding decrease toward the axis of the sand body (fig. 2). Butt cleats have similar increases in average cleat frequencies toward the axis of the sand body (fig. 2) and decreases in primary cleat spacing on the flanks and under the sand body. These preliminary observations show structures to be similar to low-amplitude folds and intense fracture development in

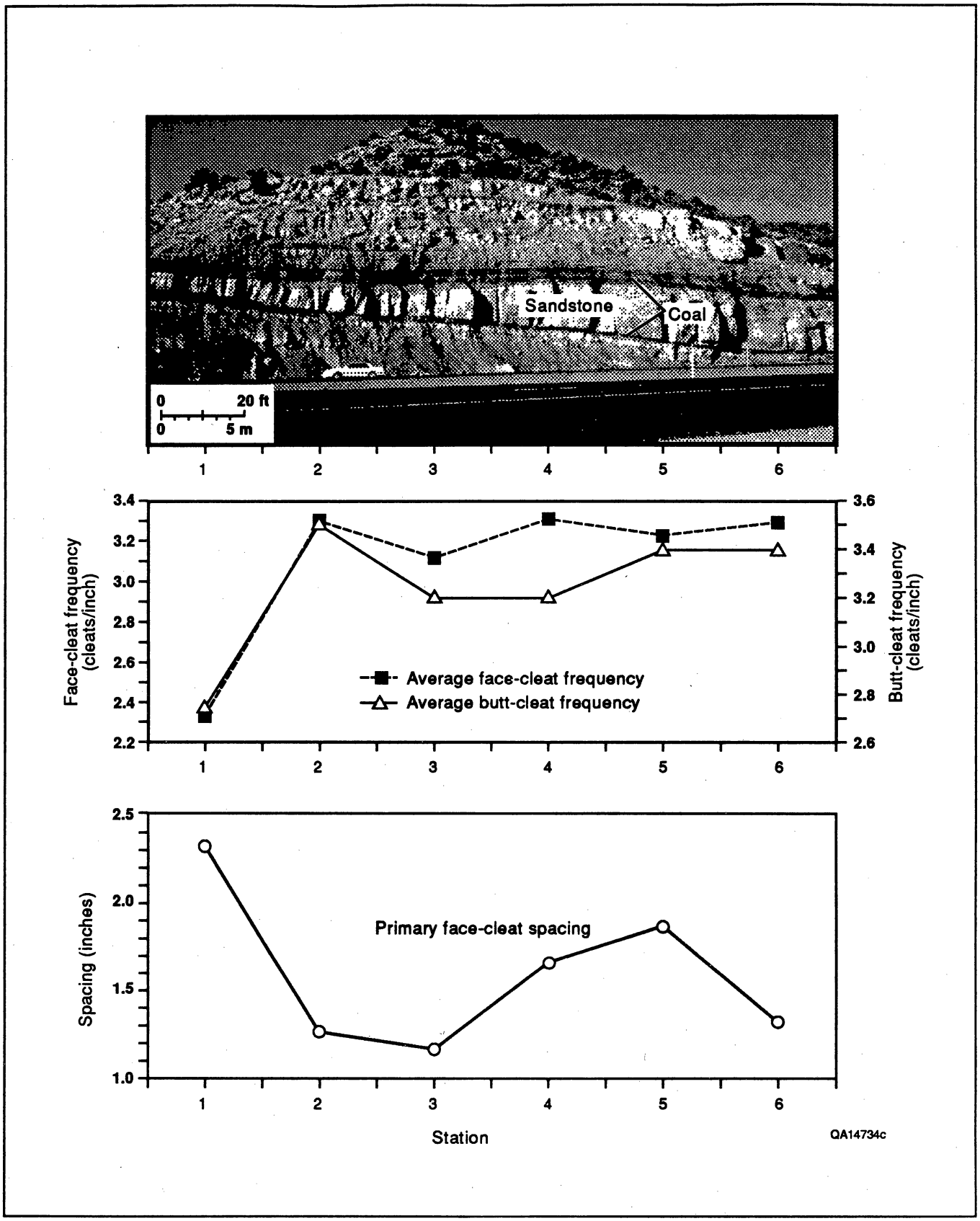

Figure 2. Frequency of cleats in Emery coal field, Interstate Highway 70, Utah. Average frequencies of primary, secondary, and tertiary face and butt cleats in the coal bed below the channel-fill sandstone increase toward the axis of the sand body. Primary-face-cleat spacing, the inverse of frequency, shows a corresponding decrease.

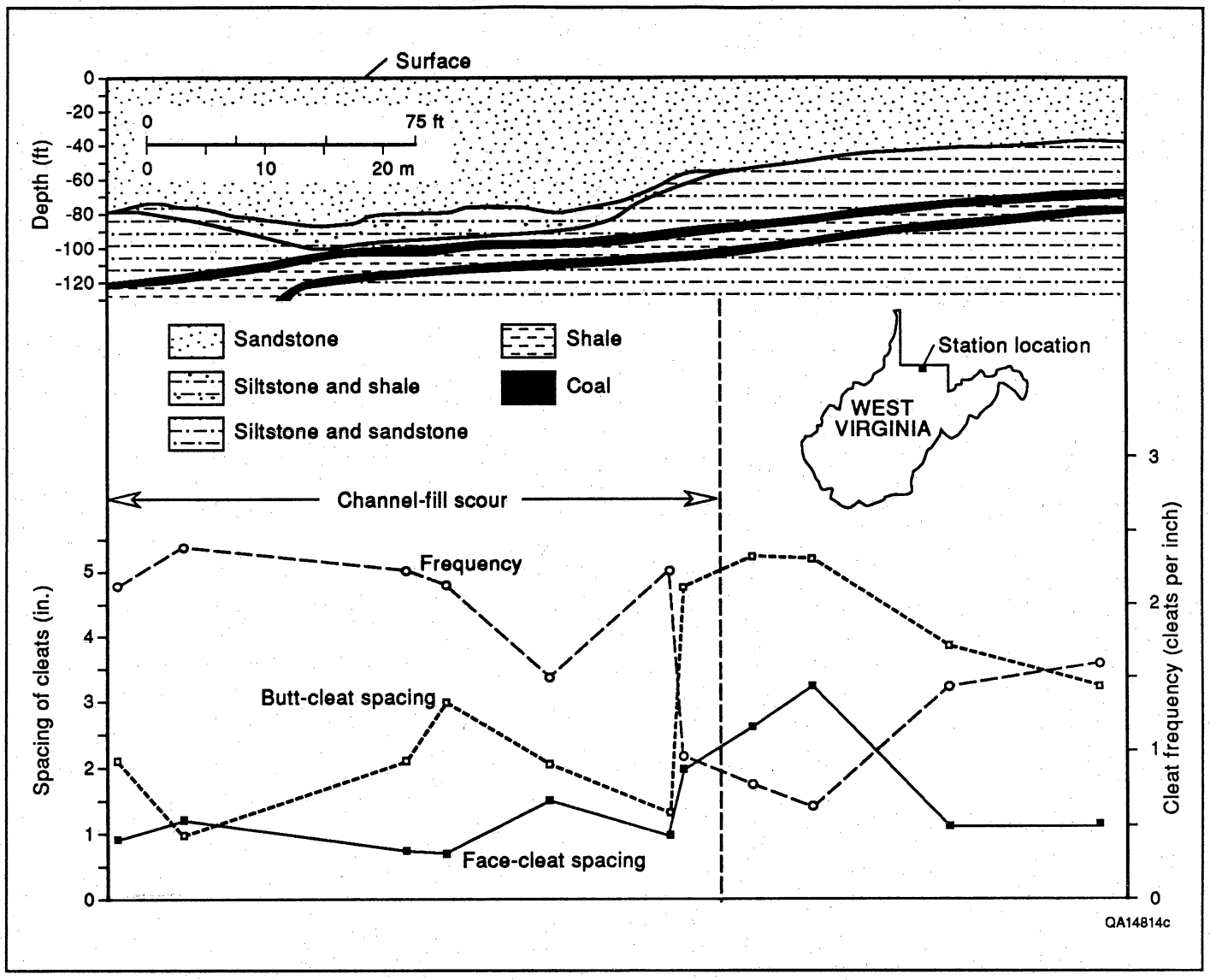

Figure 3. Variations in cleat frequencies in proximity to the axis of channel-fill sandstones, near Morgantown, West Virginia (modified from Dixon and Jake, 1979).

the Upper Freeport coals, near Morgantown, West Virginia (fig. 3), that are interpreted to be compaction induced. Therefore, coal beds are more intensely fractured where folded under (and/or over) channel-fill sandstones than where adjacent to channels, although the differences from regional patterns are slight.

Slightly to Moderately Divergent Coalbed Contacts

The Kemmerer mine is one of the largest open-pit coal mines in the United States. It is located 3 mi (5 km) southwest of Kemmerer, in southwestern Wyoming. At the Kemmerer mine, high-volatile subbituminous B coal of Late Cretaceous age is mined from the Adaville Formation, which consists predominantly of sandstone, mudstone, and carbonaceous shale interbedded with coal beds. Channel-fill sandstone complexes (approximately 900 to 2,000 ft [275 to 610 m] wide and 200 ft [61 m] thick) split coal beds that are 50 to 100 ft (15 to 31 m) thick. Where visible, laterally continuous tonsteins are less than 6 inches (15 cm) thick.

In the 1-UD pit of the Kemmerer mine, strata strike northward, and dip 10 to 28 degrees westward. The lowest coal bed, number 1, is the thickest, averaging 90 ft (27 m) at the bottom of the 1-UD pit. A lenticular

channel-fill sandstone splits the number 1 coal bed into two subparallel beds. The channel-fill sandstone extends updip for approximately 2,000 ft (610 m) and attains a maximum thickness of approximately 200 ft (61 m). Where unsplit, the number 1 coal bed is 100 to 120 ft (31 to 37 m) thick. The coal split that underlies the sandstone is 80 ft (24 m) thick, and the bed above it is 40 ft (12 m) thick. As a result, the coal beds diverge from being parallel to conform to the bedding of the sandstone body. The angle of divergence between the slightly to moderately divergent coalbed contacts is approximately 7 to 9 degrees.

Within the number 1 coal bed, and throughout the mine, the average face- and butt-cleat strikes are 055 and 325 degrees, respectively. Cleat dip is orthogonal to bedding. Cleat spacings of 0.1 to 2 inches (0.3 to 5 cm) for primary and secondary cleats and less than 0.1 inch (0.3 cm) for tertiary cleats result in an intense cleat development. The uniform, close cleat spacing is evident throughout the coal bed and therefore comparisons between primary, secondary, and tertiary cleat spacings are not possible. No variation in cleat strike, frequency, or aperture was found. Cleat frequency is generally greater than 3 cleats per inch (2.5 cm) and aperture less than 0.06 inch (0.2 cm).

The number 4 coal bed, in the 1-UD pit, is also split by a channel-fill sandstone. Coal-sandstone geometries and cleat characteristics in the number 4 coal bed are similar to those in number 1. Under the channel, no variations in cleat strike, spacing, frequency, or aperture were recorded. However, some fractures and faults are localized near the pinch-out of the channel-fill sandstone. In an area approximately 12 ft (4 m) wide, tonsteins are folded and contorted, intermediate (third) cleat strikes (000 to 010 degrees) are present, and slickenside striations, defined by aligned secondary minerals and grooves in cleat surfaces, are evident on some cleat and bedding-plane surfaces. Of possible significance to enhanced permeability, intermediate (third) cleats are throughgoing fractures that are as much as 20 ft (6 m) tall. They are irregularly spaced, nonparallel, and curviplanar, both in plan and cross-sectional view, and they cut through some tonsteins.

Several Tertiary normal faults occur in the mine, and the Absaroka thrust fault is located approximately 1 mi (1.6 km) west of the mine. These faults are part of the Overthrust Belt, which was active during early Tertiary, when upper Cretaceous sediments of the Adaville Formation were rapidly buried and coalified. Additional fracture development near coal-sandstone splits may therefore partly reflect thrust-related deformation in addition to coalification and compaction. Further study would be required to separate effects of these two processes.

Moderately to Strongly Divergent Coalbed Contacts

In the Rock Springs Formation of the Rock Springs Uplift, southwestern Wyoming, both parallel and divergent coalbed contacts are present. Divergent coalbed contacts are associated with interbedded channel-fill sandstone, levee, and crevasse-splay deposits. Within these semibright subbituminous coal beds, where coal and sandstone deposits are parallel, opening-mode face and butt cleats are orthogonal to each other, having strikes of between 060 to 070 degrees and 335 to 340 degrees, respectively. Face cleats are well developed in semibright coal seams. In areas of parallel coalbed contacts, primary face cleats have an average height of 2 ft (61 cm), spacing of 2 to 6 inches (5 to 15 cm), and frequency of 1 to 2 cleats per inch (2.5 cm). Primary butt cleats average 6 to 12 inches (15 to 30 cm) in height, 1 to 2 inches (2.5 to 5 cm) in spacing, and less than 2 cleats per inch (2.5 cm) in frequency. Secondary and tertiary face and butt cleats have average heights of 0.3 to 12 inches (0.8 to 30 cm), spacings of less than 1 inch (2.5 cm), and frequencies of greater than 2 cleats per inch (2.5 cm). Cleat frequencies of 3 to 7 cleats per inch (2.5 cm) and apertures of less than 0.1 inch (0.3 cm) are typical. Because these cleats are closely spaced and uniformly developed throughout, the distinction between primary, secondary, and tertiary cleats is difficult.

On the western flank of the Rock Springs Uplift, in outcrops west of Interstate 80 and within the town of Rock Springs, north- to northeast-striking mine highwalls exhibit moderately to strongly divergent coalbed contacts associated with lenticular point-bar deposits. In one example, the point bar extends along strike for 450 ft (137 m) and is 40 ft (12 m) high at its thickest development. Local paleoflow within the channel was eastward, and lateral accretion surfaces dip 11 degrees southwest. The point bar splits and folds two 3- to 6-ft-thick (1- to 2-m), semibright, subbituminous coal beds. The angle of divergence between the moderately to strongly divergent coalbed contacts is between 10 and 15 degrees. Dip of the coal bed where folded under the channel is 21 degrees southwest. Therefore, the coal bed is tilted with respect to the lateral accretion surfaces, and discordances between dips of the point bar and coal bed are greatest at the flanks of the channel.

Unusual and previously undescribed cleat fracture systems occur in the subbituminous coal beds adjacent to the lenticular sandstones (fig 4). No typical regional face cleats are evident; instead, closely spaced normal faults replace face cleats. These faults have slip surfaces that are mineralized, striated in a downdip orientation, and curviplanar. The curviplanar slip surfaces are

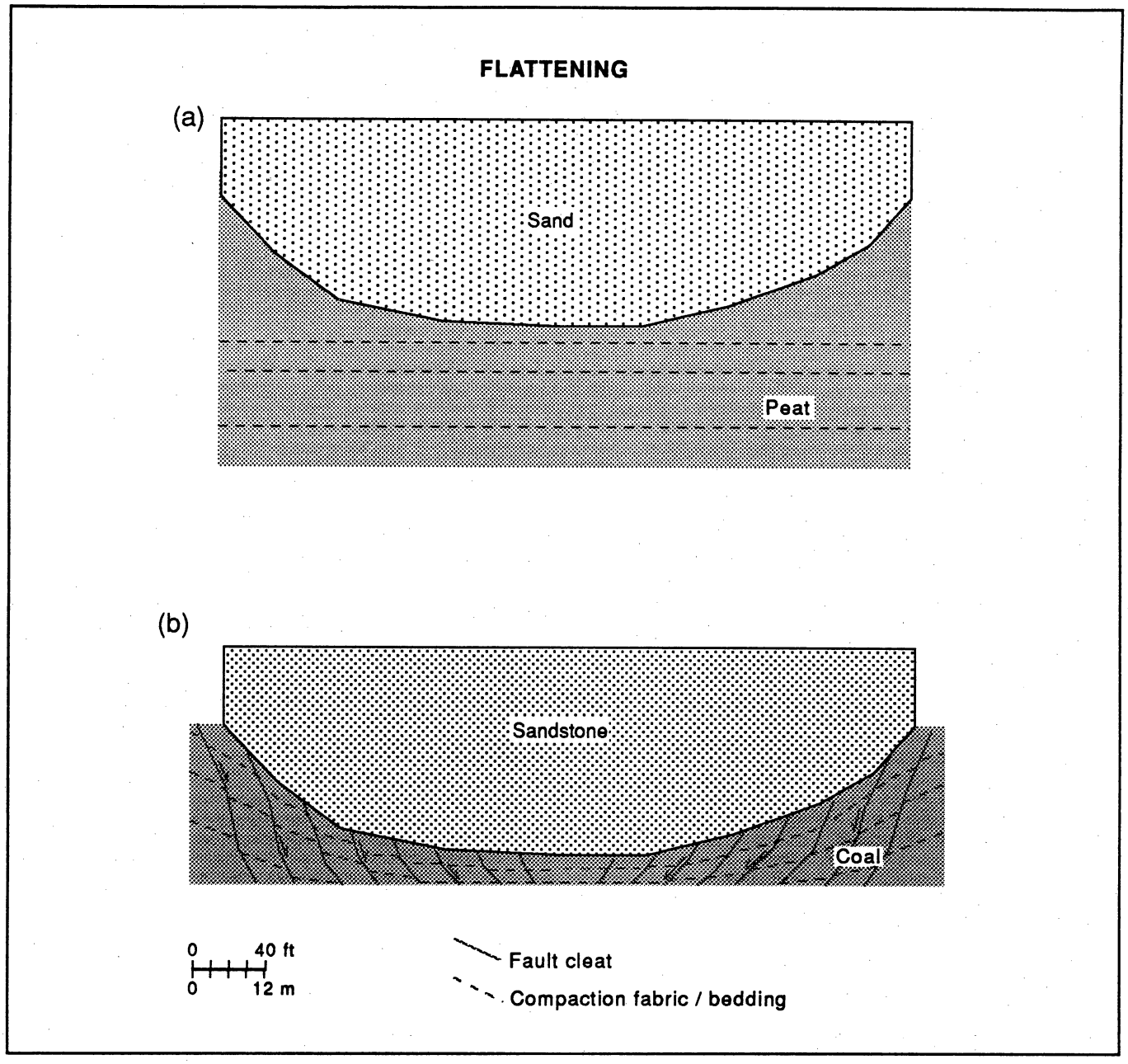

Figure 4. Model for fault-cleat development by compaction and differential flattening of coal. (a) Lenticular channel-fill sand bodies differentially compact and flatten peat. (b) Syncompactional fault cleats develop that offset coal bedding. Note the range of cutoff angles between the coal bedding and fault cleats. The process is thought to occur at a late stage of coalification.

concave and convex to each other, forming sigmoidal patterns. The spacing of the faults, from 1 to 6 inches (2.5 to 15 cm), is similar to regional face-cleat spacing. The faults in the upper 3 ft (1 m) of the folded coal beds strike northeast (065°), in the same direction as regional face cleats, and do not extend more than 5 inches (13 cm) into adjacent sediments. Toward the upper contact of the coal bed, some faults have highly variable dips. Fault dips range from perpendicular to 60 degrees northwest. The cutoff angles between coal bedding and faults range from 45 to 90 degrees but are typically 45 to 60 degrees. Therefore,

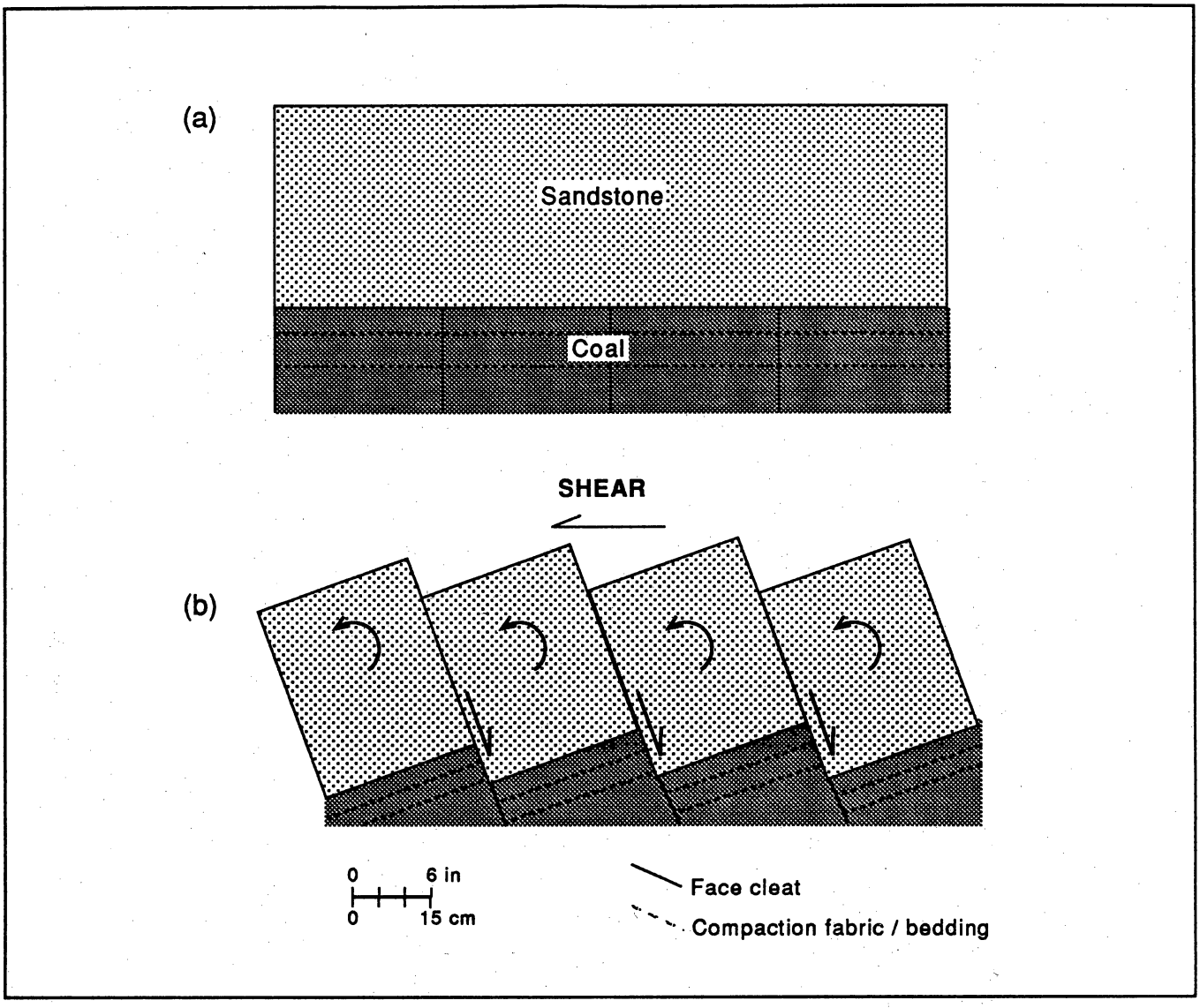

Figure 5. Effect of rotating normal fault blocks on coal bedding. (a) Parallel coalbed contacts with face cleats developed orthogonal to coal bedding. (b) Lateral shear within coalbed contacts, resulting in the rotation of face cleats and the development of normal faults. Near Superior, Wyoming, faults like this result from slip on preexisting face cleat. Note 90-degree cutoff angle between coal bedding and faults.

the faults cannot be reactivated face cleats, but are instead fault cleats that we infer to be syncompactional faults (fig. 4). Tilting of the coal beds between rotating (mode II) fault cleats is probably responsible for the angular discordances between coal bedding and lateral accretion surfaces on the flanks of the channel-fill sandstone.

Fault cleats in the Rock Springs outcrop are kinematically compatible with lateral extrusion of coal from beneath a sandstone indentor (fig. 4). We envision faults to have developed at a late stage of coalification, contemporaneous with development of normal face cleat elsewhere in the Rock Springs Formation. If faults formed instead by slip on preexisting vertical face cleats, then cutoff angles between faults and coal bedding of 90 degrees (rather than the observed 45 to 60 degrees) would be expected (fig. 5). Cutoff angles that are consistently 90 degrees occur in Cretaceous coal beds

in the Green River Basin, but they are generally associated with tilted and rotated normal fault blocks in sandstones.

In cross-sectional and plan view, below and on the flanks of the channel, cleat-strike variations indicate the presence of intermediate or third cleat orientations (020 to 040 degrees) in the coal beds (fig. 6a). Intermediate cleats, which are curviplanar and discontinuous, abut and crosscut butt cleats, but they terminate against fault cleats (fig. 6b). Away from the channel-fill sandstones, the curviplanar cleats are absent.

In summary, the low-amplitude folds of compaction origin associated with moderately to strongly divergent coalbed contacts locally contain a previously undescribed style of coal fracture. These fault cleat systems may be discontinuous, curviplanar, striated, mineralized, and commonly have strikes that parallel regional face-cleat trends.

Structures Associated with Divergent Coalbed Contacts

Coal seams that have parallel coalbed contacts over a scale of 1,500 to 2,000 ft (457 to 609 m), have uniformly developed, opening-mode face and butt cleats that show little variation in strike, dip, spacing, or frequency. Studies of slightly to strongly divergent coalbed contacts at the Emery, Kemmerer, and Rock Springs mine areas suggest that cleat strike, dip, spacing, frequency, and type can vary on the flanks and under fluvial-deltaic channel-fill sandstones. Below these channels, differences in cleat characteristics associated with low-amplitude folds in coal beds are most likely the result of compaction. Throughgoing fractures and intermediate (or third) cleat strikes, such as those at Emery, Kemmerer, and Rock Springs, may reflect brittle failure as a result of stress concentration caused by compactional loading of rigid lenticular sandstone encased in brittle coal. Closely spaced fault cleats (mode II) that develop instead of normal face cleats, such as those at Rock Springs, most likely accommodate flow of material from beneath lenticular, channel-fill sandstones (fig. 4). This fracture system probably forms at an earlier stage of compaction when substantial strain in coal is being accommodated by fractures. These fault cleats may be poor fluid conduits because they are faults rather than opening-mode fractures. However, fault-cleat development could increase vertical connectivity between adjacent coal beds, especially if coal beds are separated by noncoal, tonstein layers, as in the San Juan Basin (Tremain and others, this vol.). Fault cleats occurring together with throughgoing fractures, and localized zones of opening-mode cleat systems, such as those developed under fluvial-deltaic channel-fill sandstones, could enhance coalbed permeability.

Summary

Studies within the Navajo mine determined that the parallel coalbed contacts have uniformly developed opening-mode face and butt cleats that show little variation in strike, dip, spacing, or frequency. Studies of slightly to strongly divergent coalbed contacts at the Kemmerer, Emery, and Rock Springs mine areas suggest that cleat characteristics vary on the flanks and under fluvial-deltaic channel-fill sandstones. Differences in cleat strike, dip, and frequency, associated with low-amplitude folds below these channels, are the result of compaction.

In the Emery coal field, the average face- and butt-cleat frequencies in the coal bed below the channel-fill sandstone increase toward the axis of the sand body. An intermediate or third cleat strike is also present. At the Kemmerer mine, tonsteins are folded and contorted, and a third throughgoing cleat orientation indicates that compaction played a role in the formation of cleats.

In the Rock Springs area, fault cleats formed at various dip angles below the folded portion of the moderately to strongly divergent coalbed contacts. These fault cleats have strikes and spacings similar to those of face cleats in adjacent outcrops. Cutoff angles of 45 to 60 degrees between coal bedding and fault cleats indicate that they are not simply reactivated face cleats; they are closely spaced mode II cleat sets that formed instead of mode I cleats during coalification. We suggest, therefore, that compaction was active below the folded portion of the channel-fill sandstone and that these fault cleats are a variety of face cleat.

Fault cleats occurring together with localized zones of opening-mode cleat systems, such as those developed under fluvial-deltaic channel-fill sandstones, could enhance coalbed permeability. Any ability to predict these cleat characteristics could be useful for methane exploration, as areas for vertical degasification may then be identified using structural and lithofacies maps.

Compaction-Related Cleat Variations: Ongoing Research

Comparisons between parallel and divergent coalbed contacts indicate enhanced development of cleat systems on the flanks of channel-fill sandstones. In some

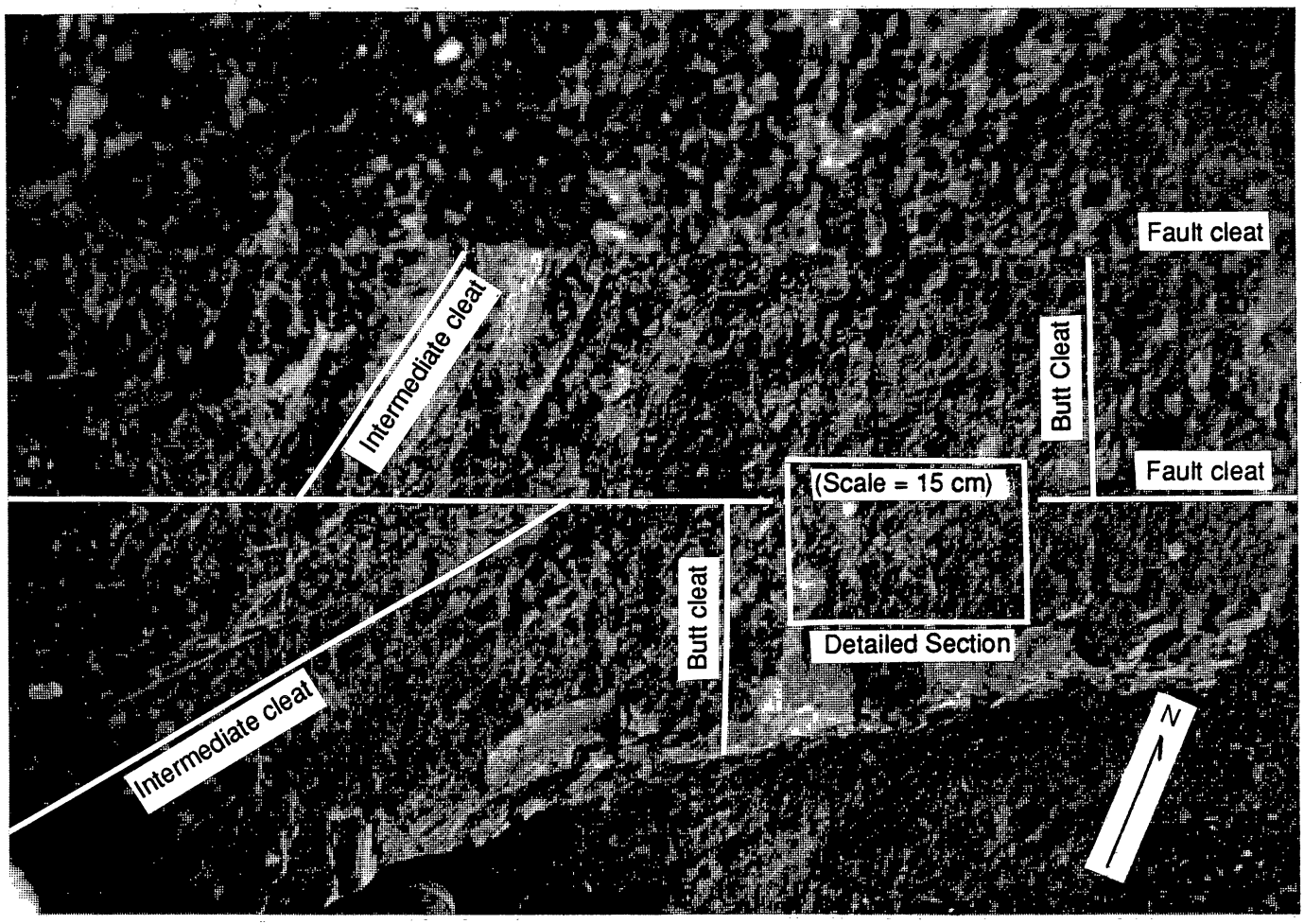

Figure 6a. Plan view of cleat-strike variations on the flanks of channel-fill sandstone. Fault cleats (strike 065°) are orthogonal to butt cleats (strike 335°). Curviplanar and discontinuous intermediate cleats strike between 020 and 040 degrees.

cases, such as in the Emery coal field, the effect of irregular coalbed contacts on regional cleat patterns is subtle. Elsewhere, in Kemmerer for example, through-going fractures could potentially contribute to fracture permeability and be a target for exploration. Locally, as in the Rock Springs example, fault cleats could increase vertical connectivity between coal beds; if such fracture systems were sufficiently developed, they would be potential sites for coalbed methane exploration. Therefore, the abundance of low-amplitude folds associated with fluvial-deltaic channel-fill sequences—and their potential contribution to enhanced methane production—suggests the need for further research.

Acknowledgments

The authors wish to thank the Pittsburgh and Midway Coal Mining Company (Kemmerer mine), the Nerco–Bridger Coal Company, and the BHP–Utah International Inc. (Navajo mine) for allowing access to coal exposures within their mines.

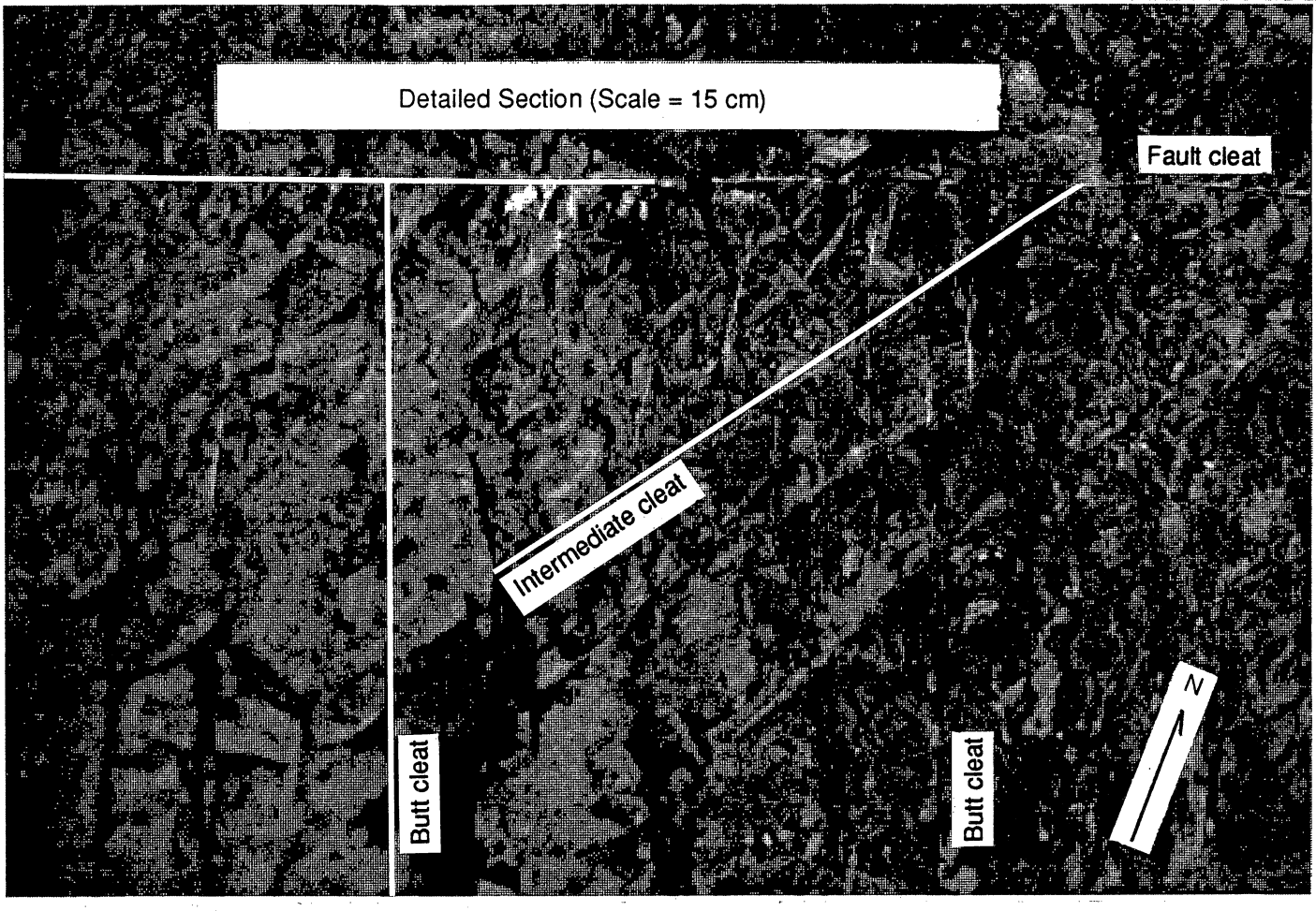

Figure 6b. Detailed plan view of cleat-strike variations (from fig. 6a). Abutting relations suggest that the intermediate cleats abut and cross butt cleats but terminate against fault cleats.

Comparative Lineament Analysis of the San Juan Basin: Relationships between Lineament Attributes and Coalbed Methane Production

Robert W. Baumgardner, Jr.

Abstract

Lineament attributes were correlated with production data from Fruitland Formation wells. The data showed that wells on lineaments do not have consistently higher production values than those not on lineaments. There was no consistently significant correlation between production and lineament attributes. Independent studies did not show consistent lineament attributes. Therefore, lineament attributes cannot be used to predict production values examined in this study.

Introduction

Coal beds are fractured reservoirs for natural gas. Anomalously high production of coalbed methane is commonly attributed to fractures that formed subsequent to coalification and cleat development. This study tested the utility of lineaments for identifying highly productive coalbed methane trends in the Fruitland Formation of the San Juan Basin. Presumably, these trends are associated with fractures, which may be represented at the surface as lineaments.

In this study, lineaments were mapped on 1:250,000-scale Landsat Thematic Mapper (TM) images. Lineament azimuth, length, density (length/area), and proximity were compared with initial water production (IPW) data from 420 Fruitland wells in the northern half of the basin. Linear regression analysis was used to quantify the relationship between lineament attributes and production data.

Landsat lineaments in the northwestern San Juan Basin were compared with lineaments derived from six different scales of imagery that were published in three previous studies. Lineament attributes (azimuth, length, and proximity) from these studies and the current study were compared with initial water production (IPW) and maximum monthly gas production (MMG) from wells in the northwestern San Juan Basin.

Purpose

The purpose of this study was to map lineaments and to assess their relationships with Fruitland coalbed methane production. Depth to the gas-producing intervals in the Fruitland Formation varies from 150 ft (45 m) near the basin margins to 4,000 ft (1,200 m) near the center of the basin (W. R. Kaiser, personal communication, 1990). Permeability in conventional reservoirs is enhanced by fractures in many areas of the San Juan Basin (Gorham and others, 1979). Lineaments may be spatially correlated with fractures in the subsurface. If a correspondence between lineaments and subsurface fractures can be demonstrated, then the location and orientation of these surface features can be used to assist selection of drilling sites for enhanced production of coalbed methane from fractured reservoirs.

The approach taken in this study was to test the relationship between lineament data and production data. Unlike some empirical studies, which regard spatial coincidence between lineaments and highly productive wells as proof that the lineaments or their subsurface counterparts are enhancing production, in this study strict statistical criteria were applied to determine whether lineament attributes have a statistically significant correlation with production data.

First use of the word "lineament" was attributed to Hobbs (1904) by El-Etr (1976) in a review of the terminology applied to linear features on the Earth's surface. The definition formulated by Woodruff and Caran (1984, their p. 8) describes the lineaments mapped in this study: "a pattern of tones, textures, contours and other such features that is straight, linear and more or less continuous, has definable end points and lateral boundaries (high length/width ratio), and hence a discernible azimuth." Features that fit this definition but proved to be man-made were excluded from this analysis.

Review of Previous Lineament Studies in the San Juan Basin

Previous studies used imagery at scales different from that used in the present study (fig. 1; table 1). Kelley and Clinton (1960) produced a fracture map of the entire San Juan Basin (fig. 1) based on aerial photographs and photoindices (table 1). They grouped

In Ayers, W. B., Jr., and others, 1991, Geologic and hydrologic controls on the occurrence and producibility of coalbed methane, Fruitland Formation, San Juan Basin: The University of Texas at Austin, Bureau of Economic Geology, topical report prepared for the Gas Research Institute under contract no. 5087-214-1544 (GRI-91/0072), p. 153–179.

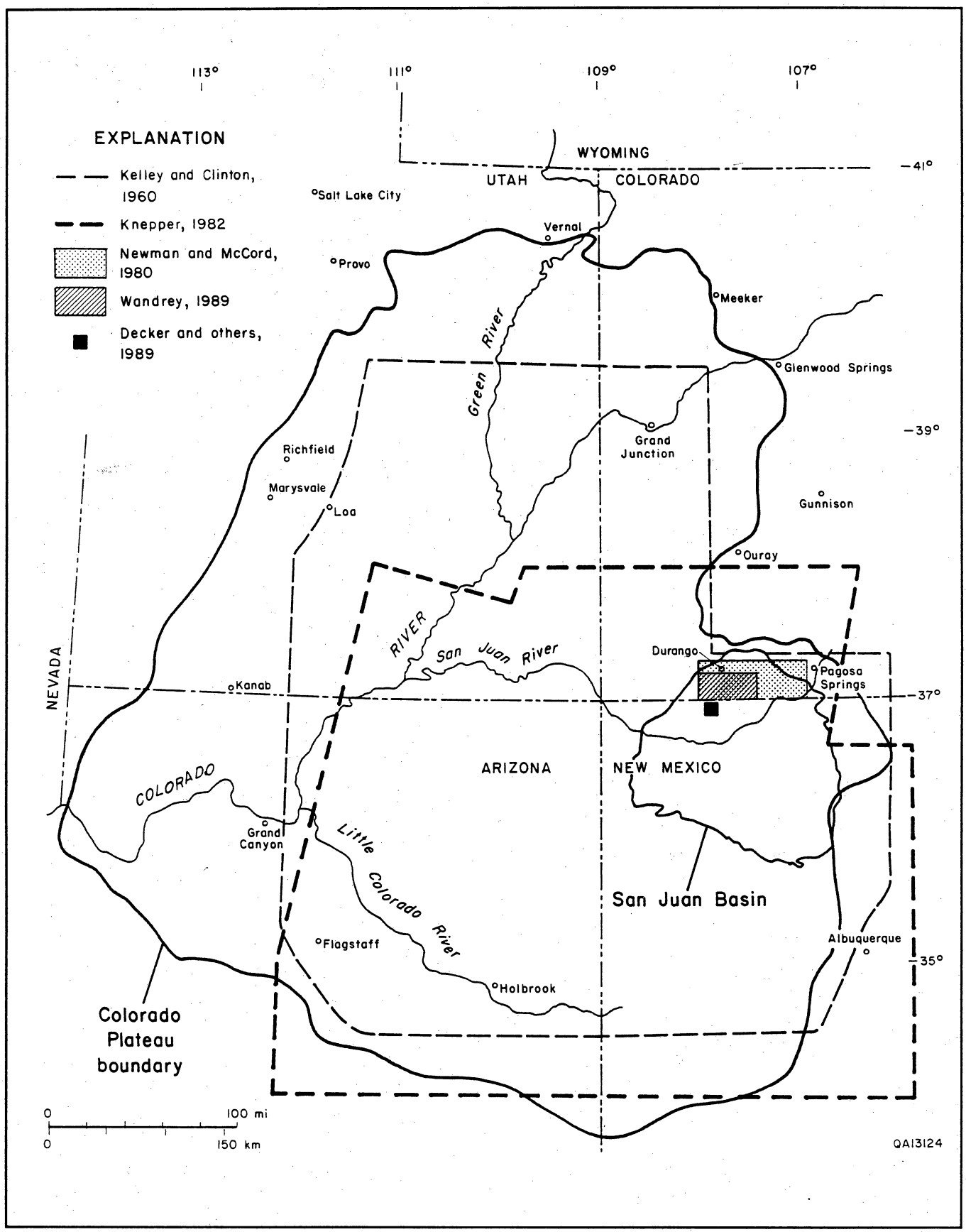

Figure 1. Previous lineament studies in the vicinity of the San Juan Basin. From Tremain and Whitehead (1990).

Table 1. Imagery used for lineament studies in the San Juan Basin.

Authors (date)	Scale	Imagery type
Kelley and Clinton (1960)	?	aerial photos
Kelley and Clinton (1960)	1:62,500	photoindex
Newman and McCord (1980)	1:160,000	Landsat MSS, FCC image
Knepper (1982)	1:800,000	Landsat MSS, black-and-white image
Decker and others (1989)	1:28,000	aerial photographs, black-and-white
Decker and others (1989)	1:58,000	aerial photographs, color infrared
Decker and others (1989)	1:80,000	aerial photographs, black-and-white
Decker and others (1989)	<1:80,000	Landsat image
Wandrey (1989)	1:15,840	aerial photographs, color
Wandrey (1989)	1:20,000	aerial photographs, black-and-white
Baumgardner (this study)	1:250,000	Landsat TM[3] FCC (bands 7, 4, 2)

MSS = multispectral scanner
FCC = false-color composite
TM = thematic mapper

fractures in the basin into six trends and concluded that the fracture pattern was too complex to be the result of uniform stress. The pattern reflected irregular deformation of the basin from place to place. They identified a "dominant" fracture trend between 45° and 60°.

Newman and McCord (1980) mapped 333 lineaments on Landsat images covering the northern San Juan Basin (southern Colorado) (fig. 1; table 1). Thirty percent of their lineaments had orientations from 350° to 20°, and 37 percent had orientations from 10° to 50°. They inferred that the northern trend might reflect Laramide structural deformation, and that the northeastern trend might be related to basement structure. The northeastern lineament trend in the southern part of their study area agreed with Kelley and Clinton's (1960) trends in northern New Mexico. Newman and McCord (1980) reported localized similarity between linear features and mapped fracture patterns, which are oriented predominantly north-northwest in the northern part of their study area.

Knepper (1982) mapped more than 6,000 lineaments in the southern Colorado Plateau (fig. 1) using Landsat images (table 1). Then, he interpreted 19 "derivative" lineaments, which mark clusters of linear features interpreted from maps of trend interval concentration and linear features. Knepper assumed that these "derivative" lineaments reflect major tectonic lines. Three of these derivative lineaments are in the San Juan Basin. They correspond spatially to gravity highs, magnetic anomalies, and dike swarms.

Decker and others (1989) mapped lineaments on aerial photographs and Landsat images of the Cedar Hill field area, northern San Juan Basin, New Mexico (fig. 1; table 1). Their study revealed linear features oriented predominantly 20° to 40°, 300° to 310°, and 80° to 90°. They concluded that although Landsat images were useful for determining regional structural trends, only aerial photos could be the basis for detailed photolinear maps. In their view, satellite imagery cannot provide detailed information on fracture orientation and location that is needed for most exploration programs. Photolineaments (derived from photographs) mapped by Decker and others (1989) were oriented predominantly 10° to 20°, 30° to 60°, 280° to 290°, and 300° to 310°. Landsat lineaments had azimuths of 20° to 30°, 45° to 50°, 300° to 310°, 340° to 350°, and E–W. These data were reanalyzed in this study and a smaller number of statistically significant peaks were defined. Results of this analysis are presented in a subsequent section. Locally, linear features on aerial photos are parallel to cleat directions and subparallel to open fractures in core from the Mesa Hamilton No. 3 well in Cedar Hill field. However, not all photolinears were faults or fractures.

Wandrey (1989) mapped lineaments on aerial photographs of the northwestern San Juan Basin, La Plata County, Colorado (fig. 1; table 1). He found recurring trends at 60° to 80° and 290° to 325°. They were revealed to be joints on larger scale photos.

Summary of Cleat, Joint, and Fracture Studies in the San Juan Basin

Because fractures enhance oil and gas production in the San Juan Basin, several authors have studied fractures at the surface and in the subsurface. Gorham and others (1979) studied fractures in the Verde, West Puerto Chiquito, and East Puerto Chiquito oil fields of the San Juan Basin (fig. 2). They found competent beds are fractured in areas of maximum curvature along the Hogback Monocline. Open joints trend parallel to axes of local folds. In Puerto Chiquito field, oil reservoirs are composed of low-permeability blocks separated by highly permeable fractures. Apparently the fracture zones extend horizontally for miles, but their height is mostly restricted to less than 100 ft (30 m). Gorham (1979) and his coworkers observed that joint trends in older rocks do not necessarily appear in overlying strata.

Condon (1988) studied fractures on the northwestern side of the San Juan Basin (fig. 2). There, he documented four discrete sets of joints, distinguished by their degree of development, abutting relationships, and orientation. Joint sets were designated J1 through J4, in order of decreasing age. Average orientations of the joint sets were 15°, 282°, 53°, and 317°, respectively. The mean orientation of face cleats was 339°; that of butt cleats was 48°.

Emmendorfer (1989) studied dipmeter fracture logs from 15 wells in the Gavilan Mancos oil field in the eastern San Juan Basin, Rio Arriba County, New Mexico (fig. 2). Most fractures are oriented north-northwest.

Orientations of cleats and joints in the San Juan Basin range from northeast to northwest. Face cleats along the southern and western margins of the basin predominantly trend northeastward (fig. 2) (Tremain and others, this vol.). Along the northern and northwestern sides of the basin (southern Colorado), face cleats trend mostly northwestward (Condon, 1988; Tremain and others, this vol.). Joints near the center of the basin trend mostly northwestward (Tremain and Whitehead, 1990, their figure 37), and face cleats trend northeastward and northwestward in cores from the northern half of the basin (fig. 2).

These studies indicate that for the San Juan Basin as a whole there is a bimodal distribution of cleat and joint orientations. In the northwestern part of the basin this probably is also true, on the basis of Condon's (1988) joint and cleat measurements and Tremain and others' (this vol.) cleat studies. However, a northwestern face-cleat trend may predominate locally.

These results suggest that if lineaments are controlled by surface fractures, there may be considerable local variability in lineament azimuth, as a function of local folding. Furthermore, lineaments may be perpendicular to each other, as cleats are, if these fracture trends are continuous into rocks overlying coals. If the trend of lineaments is controlled by fractures, then orientations of lineaments should change as cleat and joint directions change across the basin.

Data Sources and Procedures

Landsat Imagery

Four Landsat Thematic Mapper (TM) images (scale 1:250,000) were used for this study (fig. 3). These false-color composite (FCC) images were generated with data from bands 7 (red), 4 (green), and 2 (blue) (table 2). These bands detect reflective infrared and visible light between wavelengths of 0.52 and 2.35 μm (fig. 4). In bands 4 and 7 the contrast between vegetation and soil is relatively large (fig. 4). Some variations in soil and rock composition, such as might occur along a fault or a formation contact, are more visible in FCC images composed of these three bands. The visibility of lineaments demarcated by vegetation changes, faults, or formation contacts is enhanced by these image characteristics.

These four images provide complete coverage of the San Juan Basin and extend several miles beyond the basin boundary as defined by the outcrop contact between the Pictured Cliffs Sandstone and Fruitland Formation. These Cretaceous-age rocks crop out concentrically around the margins of the basin. The most common rock units at the surface in the basin are the San Jose (Eocene) and Nacimiento (Paleocene) Formations (O'Sullivan and Beikman, 1963; Steven and others, 1974; Manley and others, 1987).

The resolution of the Thematic Mapper in bands 7, 4, and 2 is 100 ft (30 m). Under most conditions, an object on the ground must be 100 ft (30 m) wide to be detected by the satellite sensor. An exception to this general rule occurs when an object less than 100 ft (30 m) wide having very high reflectance, such as a dry, gravel-topped road, is located in low-reflectance surroundings, such as a wet, grass-covered field. Because of the large difference in reflectance, the sensor will detect the narrow road. However, natural land surface features seldom display such contrast.

These four images were selected for two reasons: (1) no other set of four images with the same (highest possible) quality had been acquired during such a short time period (39 days) (table 2), and (2) they had the least amount of snow and cloud cover of all available images.

The sun's azimuth for all scenes is between 133° and 148° (table 2). As a result, linear features perpendicular to the sun's azimuth (43° to 58°) may be preferentially illuminated or shaded, similar to the effect of look direction (of the radar signal) on features detected

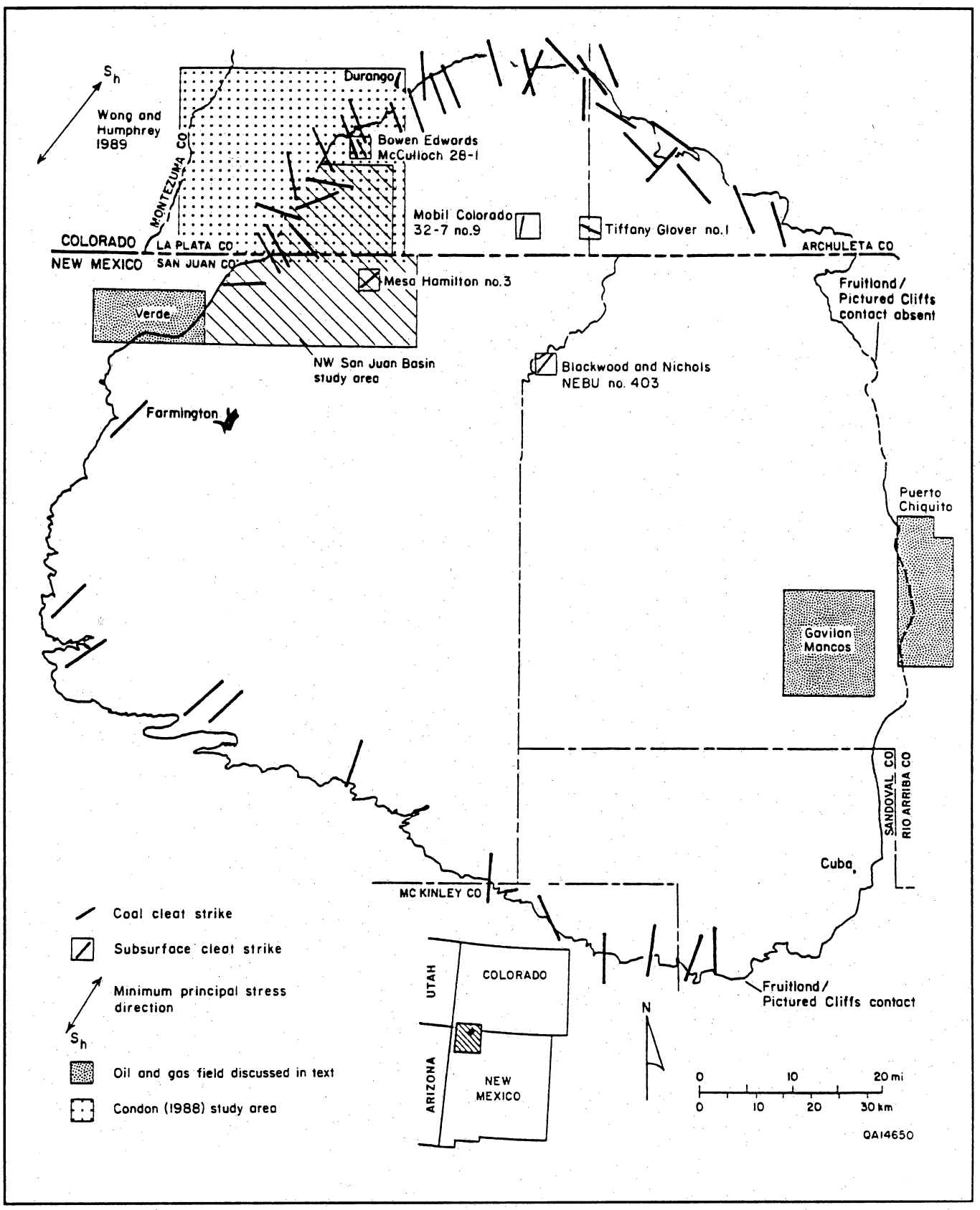

Figure 2. Face-cleat orientations and in situ stress in the San Juan Basin. Cleats in Colorado are from Newman and McCord (1980), Condon (1988), and Tremain and Whitehead (1990). Cleats in New Mexico are from Tremain and Whitehead (1990). After Tremain and others, this volume.

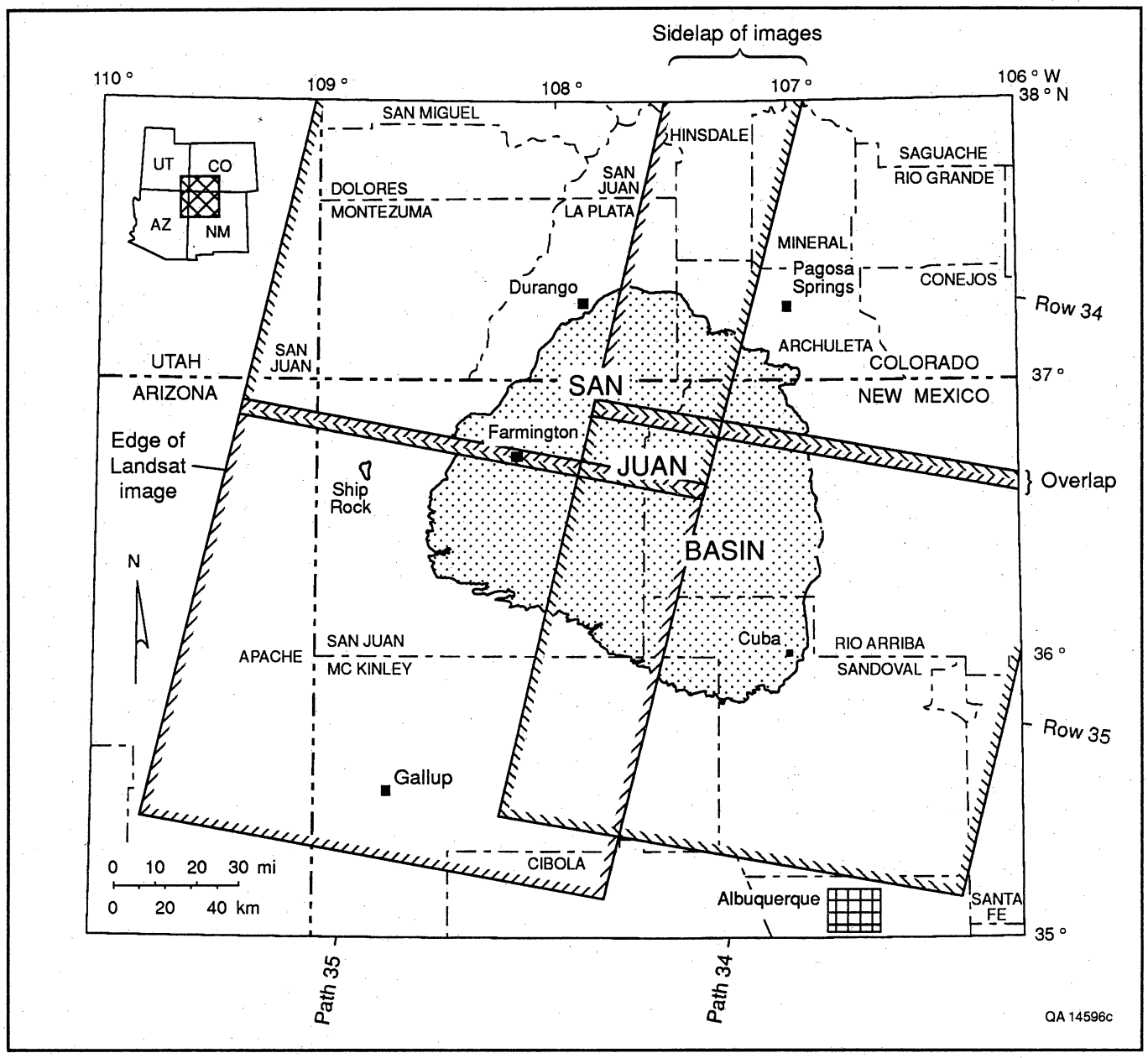

Figure 3. Landsat images used to map lineaments in this study.

Table 2. Landsat Thematic Mapper images used in this study.*

Path/row	Scene identification number	Date	Sun elevation (°)	Sun azimuth (°)	Lineament mapping time (hr)
34/34	51304-17112	9/26/87	44	141	5.5
34/35	51288-17112	9/10/87	49	133	6.1
35/34	51327-17175	10/19/87	37	148	5.8
35/35	51327-17182	10/19/87	38	147	7.0

*All images were generated as false-color composites (FCC's) using bands 7 (red), 4 (green), and 2 (blue). See figure 3 for location of images.

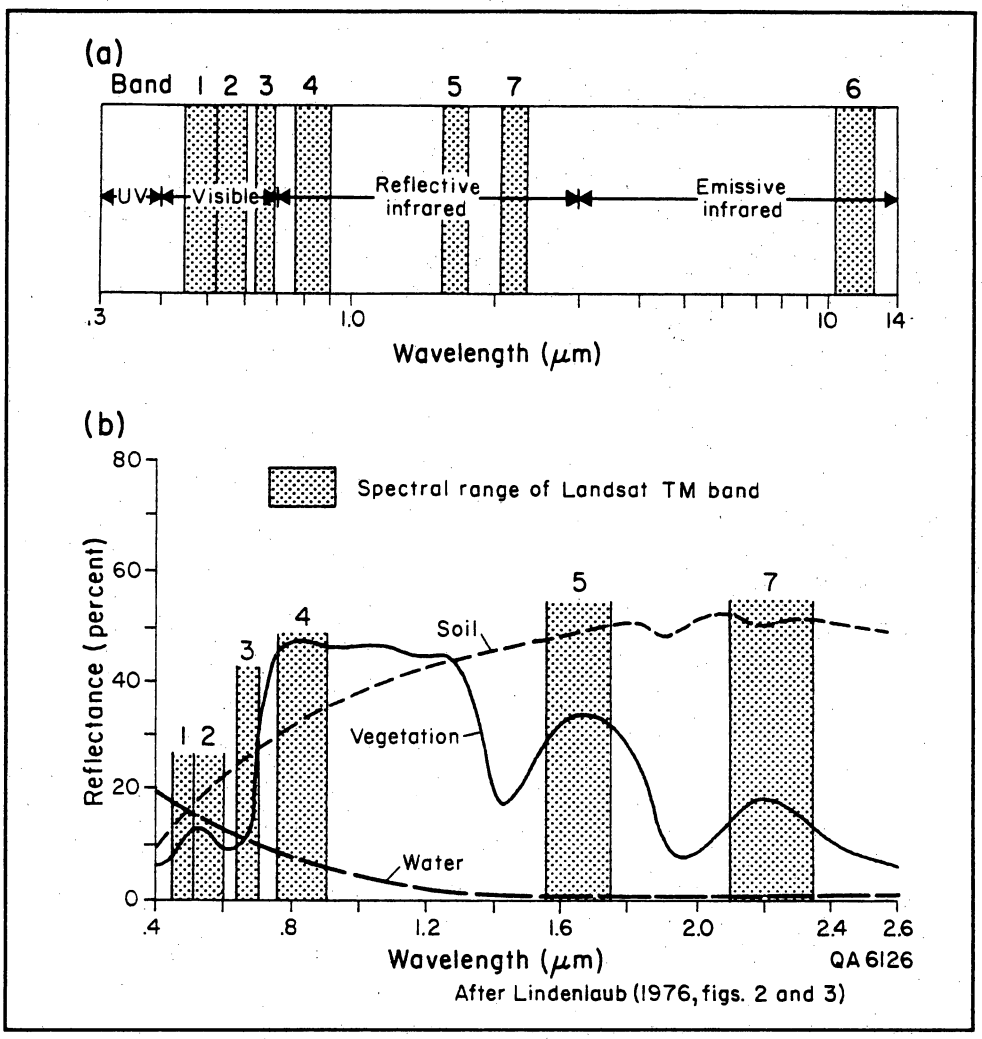

Figure 4. Spectral range of Landsat satellite Thematic Mapper (TM) sensors. Each band represents that part of the electromagnetic spectrum that each of the sensors detects. (a) Distribution of Landsat bands in visible, reflective infrared, and emissive infrared wavelengths. (b) Reflectance of three basic land-cover types in the visible and reflective infrared wavelengths. Percent reflectance is a measure of relative brightness on a Landsat image. For example, in band 7 bare soil is the most reflective cover type, water appears black or near-black, and vegetation displays an intermediate brightness.

by side-looking radar (Yamaguchi, 1985). However, as is discussed in a subsequent section of this report, no significant preferential enhancement was detected.

Lineaments from Other Studies

Lineaments from other studies that covered a selected area in the northwestern San Juan Basin were digitized directly from published maps. They were not checked against original imagery. No judgment was made in this study regarding the "validity" of the lineaments in previous studies. Their azimuths were analyzed just as those from this study were, using the techniques described in the following sections.

Production Data

Values of initial water production (IPW) and maximum monthly gas production (MMG) were obtained from private and public sources: Petroleum Information, Dwight's Oil and Gas Reports (1990a, b), and the Colorado Oil and Gas Conservation Commission. Initial water production is assumed to be a positive function of fracture permeability. Wells with high IPW and MMG values are assumed to be draining more permeable fractures than wells with low values. Values of IPW and MMG were not "normalized" for different well-completion techniques, different completion dates, or possible interference effects from nearby wells. Nor were

wells from overpressured and underpressured areas examined separately. At the time of this study MMG data were available for wells in the northwestern part of the basin, but only for 1988 and 1989. Whereas both of these measures of production data may be related to long-term gas production, the nature of this relationship is not well known for the study area. There is no statistically significant correlation (at p = .05 level) between MMG and IPW values in this study. No normalized, long-term gas production data were available at the time of this study.

Lineament Mapping Procedures

Lineaments were mapped in a series of steps. The Landsat image was placed on a light table and viewed with transmitted light in a darkened room. A transparent sheet of mylar was placed over the image, and the end points of each lineament were marked. To ensure that each image was given equally rigorous inspection, records were kept of time spent per image. Each scene was examined for 5.5 to 7.0 hr (table 2). This time included using a mask to view 1/9 of an image at a time. The mask was placed over the image, and each 1/9 of the image was studied for 10 minutes. During this procedure all parts of the image received equal attention. Differences in time spent on each image were caused by differences in complexity of features on each image, but this probably did not significantly affect mapping of the lineaments.

After thorough visual inspection was completed, a second sheet of transparent mylar was placed over the first, and the end points were connected by a line drawn on the second sheet. In this way the image was not obscured during the initial visual inspection by a growing network of lines. Then, the mapped lineaments were checked against U.S. Geological Survey topographic maps and some were field checked. All lineaments were checked against maps at the same scale (1:250,000), and 116 of these lineaments were also checked against 1:24,000-scale maps. Another 23 lineaments were checked in the field in the vicinity of Durango, Colorado, and Farmington, New Mexico. Forty-nine other lineaments were determined to be linear sand dunes during field-checking. Because they were presumed to not reflect geologic structure, they were removed from the data before being analyzed further. Lineaments corresponding to man-made features such as fences, straightened river channels, levees, power line rights-of-way, and the like, were erased from the overlay. The number of man-made features that were erroneously mapped as lineaments (53) amounted to 5.7 percent of the lineaments checked (925). It is possible that other man-made features were mapped as lineaments but were not detected. Therefore, this error rate should be considered a minimum. Lineaments that were neither man-made nor clearly associated with some natural feature, such as a straight stream valley, were not erased. These were usually mapped on straight tonal boundaries that were visible on the Landsat images but were not apparent on the topographic maps or in the field.

In the next step, those lineaments confirmed as natural features were transferred from the second mylar overlay to U.S. Geological Survey topographic maps at the same scale (1:250,000). In areas where images overlapped (between rows) or sidelapped (between paths) (fig. 3), lineaments from only one image were transferred to the topographic maps. This prevented creation of false high-lineament density along image boundaries. At this point, lineaments were compared with maps of surface geology (scale 1:250,000) to determine whether spatial correspondence existed between lineaments and mapped geologic features, such as faults and formation contacts. Finally, from the maps 969 lineaments (fig. 5) were digitized for computer-assisted analysis.

Results

Definition of Lineaments

Of the 5,855 lineaments mapped edge to edge on the Landsat images (fig. 3) in this study, 969 are within the boundary of the San Juan Basin (fig. 5). Of these, 925 (95 percent) were checked against geologic maps. More than a third (35 percent) are straight streams or valley axes (table 3). Because the visibility of streams is not affected by land cover or land use, it is unlikely that differences in these factors affected the detection of these lineaments. Straight formation contacts account for 11 percent of the lineaments checked. These probably are represented on the ground by slight topographic relief, locally. No mapped faults were recognized on Landsat imagery. More than half of the lineaments checked are straight ridges, tonal anomalies, and other linear features. The relationship between lineaments and geologic structure or fractures is discussed in a subsequent section of this report.

Length-Weighted Frequency of Lineament Azimuths

To an extent, lineament analysis is subjective, depending on vagaries of interpretation (including operator bias) more than most other kinds of geologic analysis. To compound this problem, in many studies lineament trends are referred to in qualitative terms such as "prominent" and "dominant." In this study lineaments were checked against other maps and were field checked; numerically significant lineament trends were defined by standard statistical analysis of orientation data. Length-weighted frequency (F) and Bernshtein

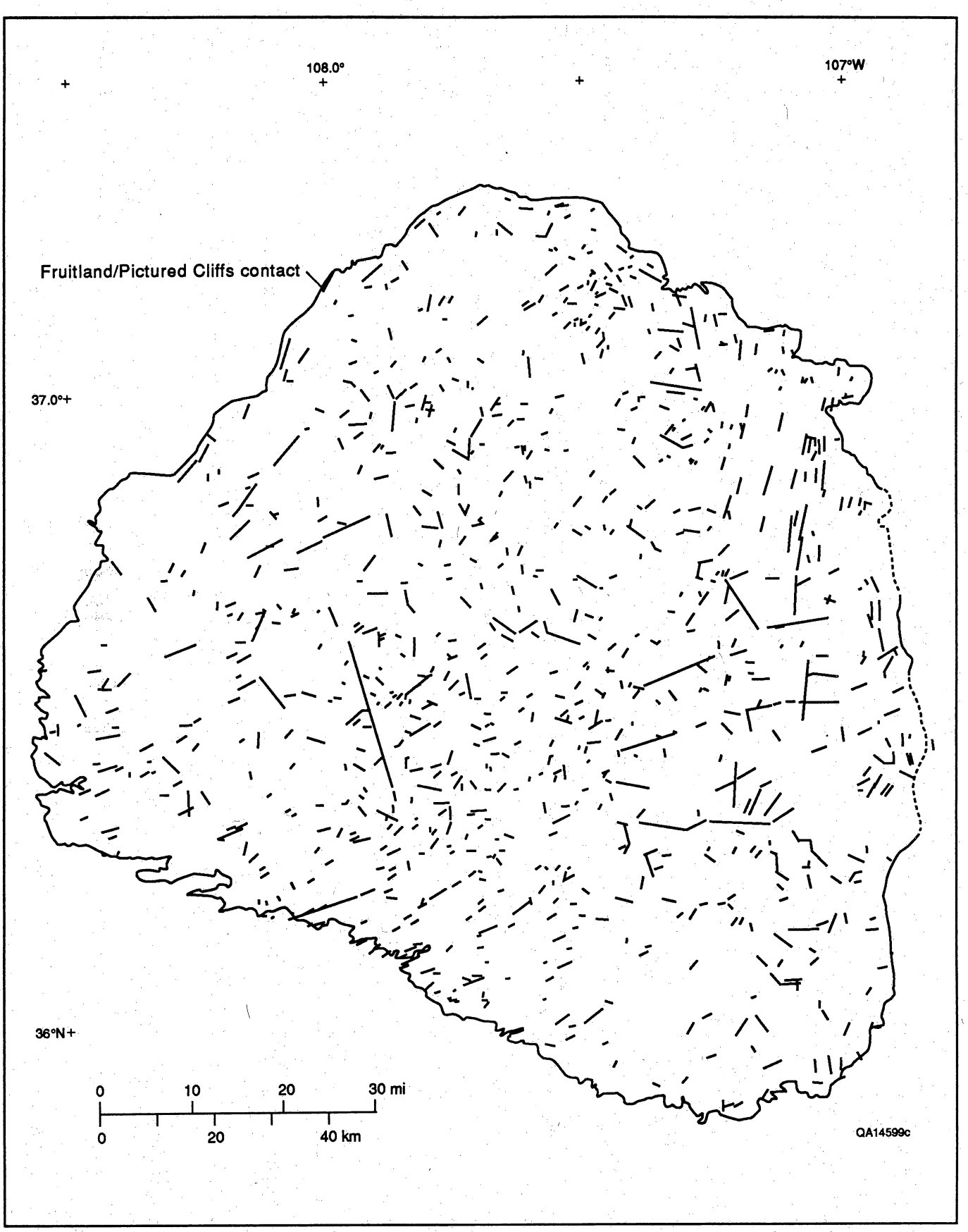

Figure 5. Landsat lineaments in the San Juan Basin mapped in this study. See figure 1 for location of study area.

Table 3. Descriptions of Landsat lineaments mapped in the San Juan Basin that were checked against geologic maps.

Description	Number	Percent
Straight stream or valley	320	35
Straight formation contact	103	11
Straight fault	0	0
Straight igneous dike	22	2
Other (tonal anomaly, etc.)	480	52
TOTAL	925	100

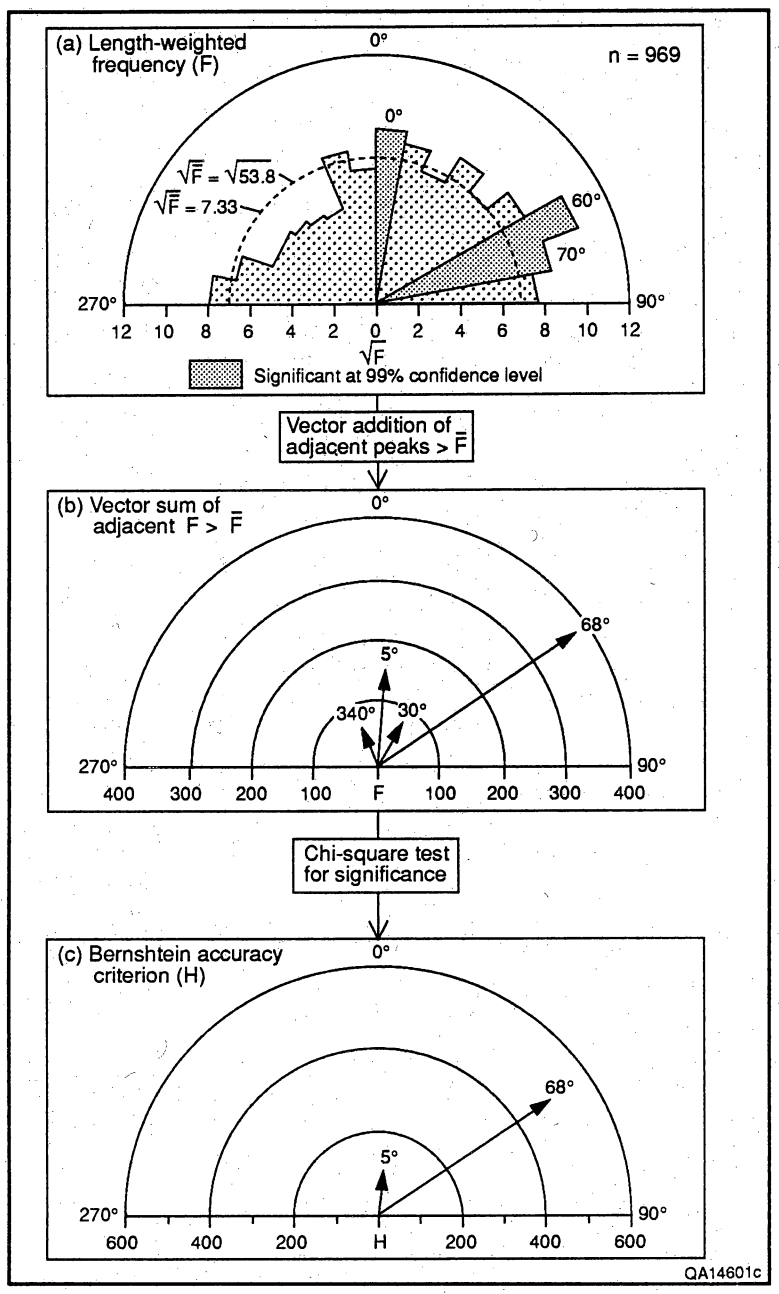

Figure 6. Procedure for statistical evaluation of lineament orientation data; polar graphs of orientation data for all 969 lineaments in the San Juan Basin. (a) Length-weighted frequency (F) of lineaments has three peaks significant at the 99-percent confidence level, as determined by a chi-square test. The square root of F is plotted to prevent areal exaggeration of large peaks. (b) The vector sum of adjacent larger-than-average peaks of F has four peaks, but orientations are different from the F peaks. The data at 270° (=90°) are adjacent to the 80° peak and are added to them in this step. (c) Two peaks of Bernshtein accuracy criterion (H) are significant at the 99-percent confidence level: 5° and 68°. These are referred to as the significant basinwide peaks.

accuracy criterion (H) (Dix and Jackson, 1981) were defined for each set of lineament data. In this way, the interpretation of the data is as objective as possible, although some subjectivity of the original mapping probably remains.

Lineament-azimuth data were initially displayed as rose diagrams of length-weighted frequency (F) (fig. 6a). This parameter expresses the total lineament length in a 10-degree-wide sector of the graph, weighted in proportion to the number of lineaments in the area in question (Dix and Jackson, 1981):

$$F = \frac{L_s \times n}{L_t}$$

where

F = length-weighted frequency,
L_s = total lineament length in 10-degree sector,
L_t = total lineament length in area, and
n = number of lineaments in area.

Length-weighted frequency combines lineament length and number of lineaments in a single parameter. The advantage in using this measure is that values from different areas or studies can be compared while allowing for differences in number of lineaments in each area or study.

Graphical Display of Results

Selection of Polar Graphs

Polar graphs are used in this study to display orientation data because of their familiarity and ease of interpretation (fig. 6). Because lineament data are symmetrical about the axis of a polar diagram, only the northern half, from 270° through 360° to 90°, of these diagrams is used. To avoid areal exaggeration of high F values, all orientation data were plotted as the square root of F (fig. 6a) before being converted to the vector sum of adjacent sectors greater than the mean (fig. 6b).

Statistical Significance of Lineament Azimuths

The statistical analysis of lineament azimuths used in the current study is explained fully in the following sections. However, the reader desiring more background on these techniques is referred to Dix and Jackson (1981).

Definition and validity of peak values

In this study a peak on a polar graph of $\sqrt{F}$ is defined as any 10-degree-wide sector with a magnitude larger than the average for that graph. To determine which greater-than-average peaks were significant, a chi-square test was used to measure the difference between each peak and the mean F value for each data set (Siegel, 1956). Dix and Jackson (1981) concluded that the 99-percent confidence level (p = .01 level) should be used to define geologically meaningful peaks because none of their samples with more than 100 computer-generated "lineaments" had statistically significant peaks at that level. In this study, we applied the same standard (p = .01 level) to define significant lineament azimuths (fig. 6a), even though there are two data sets for the northwestern San Juan Basin that comprise fewer than 100 lineaments.

Vector sums of greater-than-average peaks

Although the significant azimuths of lineament orientation data can be determined using 10-degree-wide sectors, significant trends that are split between two adjacent sectors may be obscured. To avoid this potential loss of important data, vector sums of adjacent greater-than-average peaks were calculated. A greater-than-average peak is any sector with a value of F greater than the mean (fig. 6a). The greater-than-average peaks (and their vector sums) for all 969 Landsat lineaments in this study are 0° and 10° (5°), 30° (30°), 50° through 80° and 270° (68°), and 340° (340°) (fig. 6b).

Vector sums of greater-than-average peaks are not always statistically significant, however. To determine which peaks are significant, a chi-square test was applied to each one (fig. 6c). In this study, the 5° and 68° peaks are significant (fig. 6c). As a further refinement, the chi-square value for each significant peak was divided by the degrees of freedom (v = k–1, where k equals the number of 10-degree sectors forming the peak) to yield the Bernshtein accuracy criterion (H) (Vistelius, 1966; Dix and Jackson, 1981). The values for the significant peaks were plotted using magnitude of the Bernshtein criterion and azimuth of the vector sum peak (fig. 6c).

The distribution of Bernshtein values for the lineament data in this study is bimodal. Significant azimuth peaks are present at 5° and 68° (fig. 6c). Neither of these peaks falls in the interval between 43° and 58°, so it appears that preferential enhancement of linear features perpendicular to the sun's azimuth (table 2) has not affected these lineament peaks.

Lineament Density

Lineament density was measured to determine whether it corresponds to known geologic structures. Lineament density was calculated by measuring lineament length in 100-km² grid cells. The results, expressed as lineament length/100 km², are contoured as shown in figure 7. High values (≥20 km/100 km²) neither delineate the boundaries of the San Juan Basin at the surface nor coincide with any geologic structures in the basin on the base of the Ojo Alamo Formation or on the top of the Pictured Cliffs Formation. This lack of correspondence probably reflects the structural and topographic diversity of the study area. A similar analysis of the East Texas Basin (Baumgardner, 1987) showed

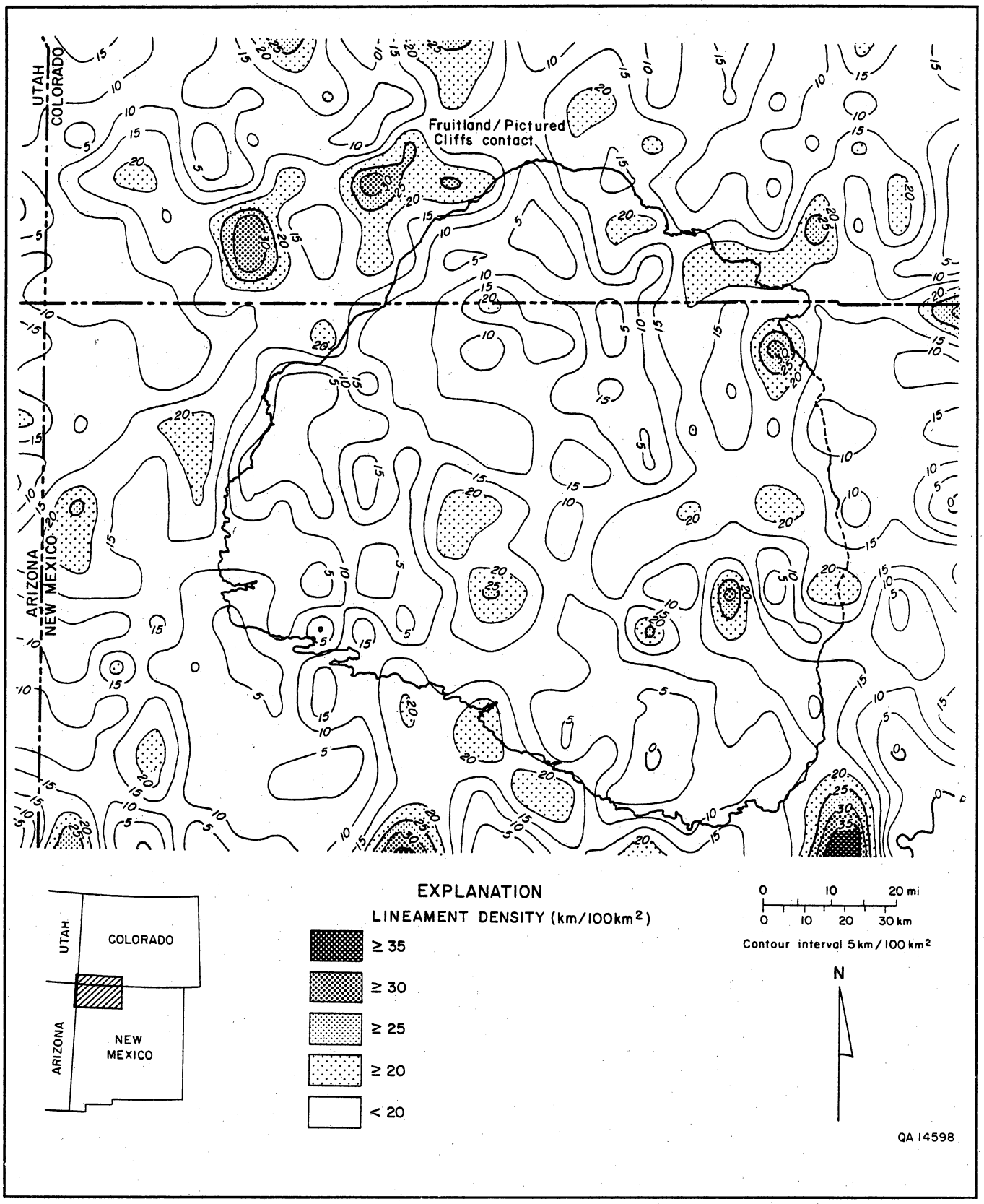

Figure 7. Lineament density in study area. Note that high values (≥20 km/100 km²) do not show any spatial correspondence with boundary of the San Juan Basin.

high values of lineament density outlining its boundaries. However, the topographic relief in and around the San Juan Basin is much more variable than in the relatively uniform, low-relief area in East Texas.

Production Data Versus Lineament Attributes

To assess the possible effect of lineaments on coalbed methane production in the San Juan Basin, production data from wells were compared with various attributes of the nearest lineament. At the time of this study, initial water production (IPW) data were available from 420 wells in the northern San Juan Basin (fig. 8). Maximum monthly gas production (MMG) data were available only for wells in a small area in the northwestern part of the basin. Linear regressions were carried out between lineament attributes (independent variables) and production data (dependent variables). As in most statistical analyses, only correlation coefficients significant at a confidence level of $p = .05$ or better were accepted as significant. More than 70 linear regressions were done (fig. 9), but only 8 were statistically significant.

San Juan Basin

Lineament attributes (distance to nearest lineament from well, length of nearest lineament, and azimuth of nearest lineament) were correlated with initial water production (IPW) from gas wells in the northern San Juan Basin (fig. 8). Initially, lineament attributes were compared with all IPW values and all nonzero IPW values. Then, IPW values were subdivided into groups defined by natural groupings in the data (W. R. Kaiser, personal communication, 1990): 1 to 99 bwpd, 100 to 249 bwpd, 250 to 400 bwpd, and more than 400 bwpd. No lineament attributes were significantly correlated (at $p = .05$ level) with IPW data or any subset of those data.

Next, the lineament data were separated into northeast- (1° to 89°) and northwest-trending (273° to 358°) groups, and the regressions were repeated. The assumption behind this analysis was that lineaments in one azimuthal range (northeast or northwest) might represent similarly oriented subsurface fractures that are more permeable than those in the other azimuthal range because of in situ stress differences. If one azimuthal set is more permeable than the other, this should be manifested in the IPW values of nearby wells. However, out of 24 linear regressions, only two significant (at $p = .05$ level) correlations were found in these azimuthal subsets of the data (figs. 9 and 10). Both correlations suggest that nearby lineaments have a "negative" effect on initial water production (IPW), the reverse of the expected results. But both correlation coefficients are quite small ($|r| < .28$), and they explain less than 10 percent of the variability in the IPW values ($r^2 < .10$). Thus, these lineament attributes cannot be used to reliably predict IPW.

In the first correlation, IPW values between 100 and 249 bwpd decrease as length of the nearest northeast-trending lineament increases (fig. 10a). This suggests that lineaments near wells with IPW values in the upper part of this range (100 to 249 bwpd) are shorter than those in the lower part of this range. This result is the opposite of what would be expected if lineaments were the surficial equivalents of permeable subsurface fractures. A longer fracture drains more of the reservoir than a shorter fracture (other things being equal), and a well draining a longer fracture should have higher IPW. In addition, longer lineaments are generally thought to be functions of deeper seated, perhaps tectonic, processes (Williams, 1983), whereas shorter lineaments may result just from surficial processes (Tremain and Whitehead, 1990). But, even this weak correlation ($r = -.27$) does not hold for any other range of IPW values. Thus, it has not been shown that lineament length is a consistent indicator of IPW values.

In the second correlation, IPW increases as distance to the nearest northeast-trending lineament increases (fig. 10b). This result suggests that the farther a well is from a northeast-trending lineament, the higher its IPW (only for values between 1 and 99 bwpd). This result, like the previous one, is the reverse of what would be expected if lineaments were expressions of permeable fractures in the subsurface. As before, this correlation applies to only part of the range of all IPW values, and it cannot be extended beyond that range.

More important than either of these two weak correlations is the absence of any significant correlation (at $p = .05$ level or better) between lineament attributes and the highest values of IPW (≥250 bwpd) (fig. 9). Presumably, high IPW values are the ones enhanced most by fracture permeability, yet they show no correlation with lineament length or proximity.

Lineament azimuth cannot be used to differentiate between high and low values of IPW, either. The vector mean azimuth (27°) of lineaments nearest wells with IPW greater than 400 bwpd is the same as the vector mean azimuth (27°) for those nearest wells with IPW between 1 and 99 bwpd. These results bolster our conclusion that the Landsat lineaments mapped in this study are not consistent indicators of subsurface fracture permeability.

Lineament density (length/area) was compared with values of IPW (figs. 7 and 8). No spatial correspondence between lineament density and IPW values was seen. This is not surprising. The "coarseness" of the lineament density data, which were contoured on 10-km centers, is much greater than the minimum spacing between

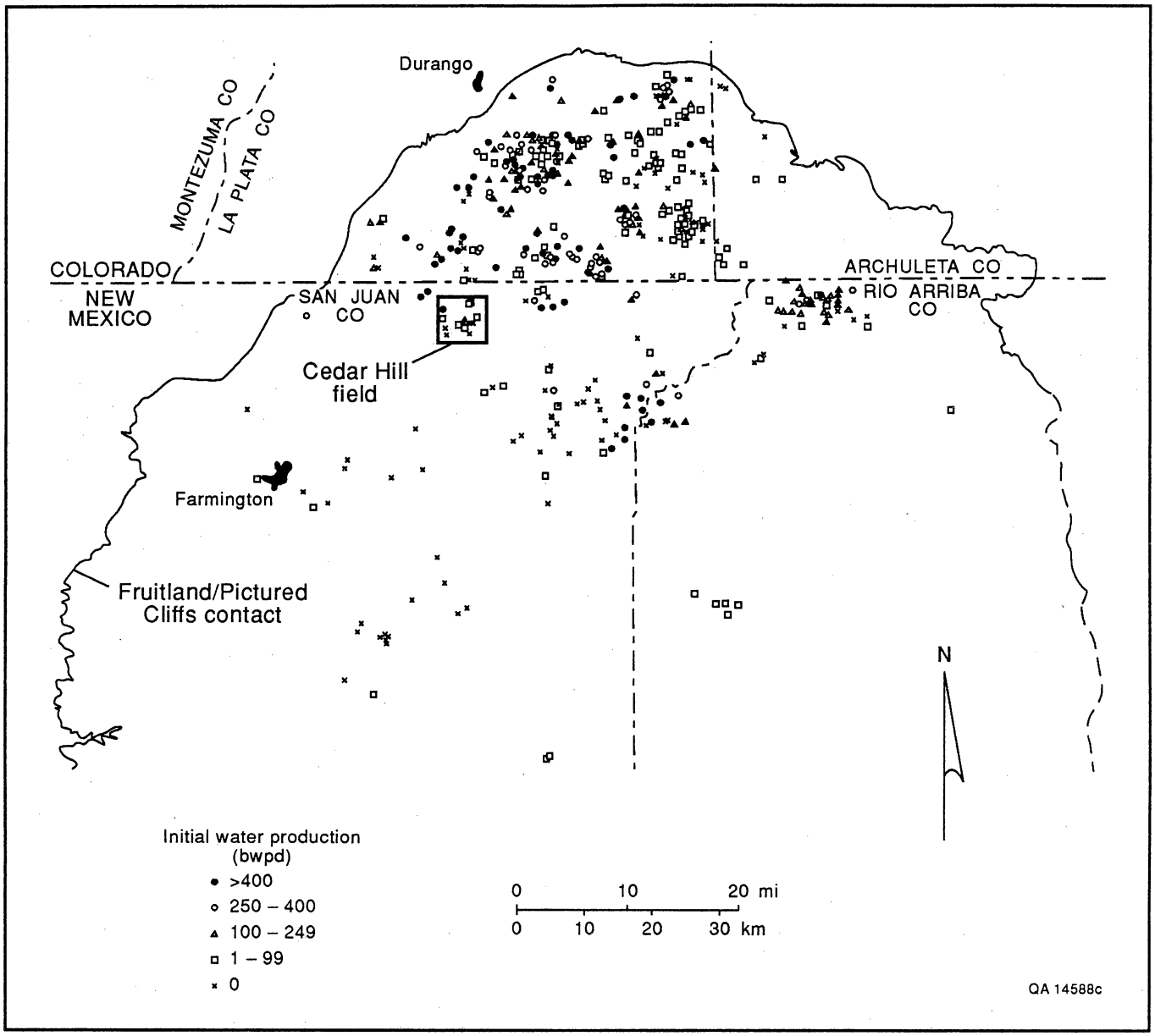

Figure 8. Map of northern San Juan Basin showing locations of 420 coalbed methane wells with initial water production (IPW) data.

many wells (<1 km). Some adjacent wells have vastly different values of IPW (fig. 8); hence, the lack of spatial correspondence between lineament density and IPW. Lineament density in Cedar Hill field, an area of high gas production, is less than 20 km/100 km² (figs. 7 and 8).

Detailed Study Area (Northwestern San Juan Basin)

Lineament attributes and production data were analyzed in more detail in an area in the northwestern San Juan Basin (fig. 11). Besides initial water production (IPW), lineament attributes were compared with maximum monthly gas (MMG) production for 1988 and 1989 (Dwight's Oil and Gas Reports, 1990a, b). Lineaments from three previous studies that covered the northwestern San Juan Basin (figs. 12 through 14; table 4) were compared with one another and with lineaments mapped in this study (fig. 11); the lineaments also were correlated with production values from wells in the basin. Because the previous studies were based on imagery at scales different from that in the present study, this allowed comparison of the coincidence of lineaments mapped on different images by different observers. Of 1,284 lineaments from all studies, only

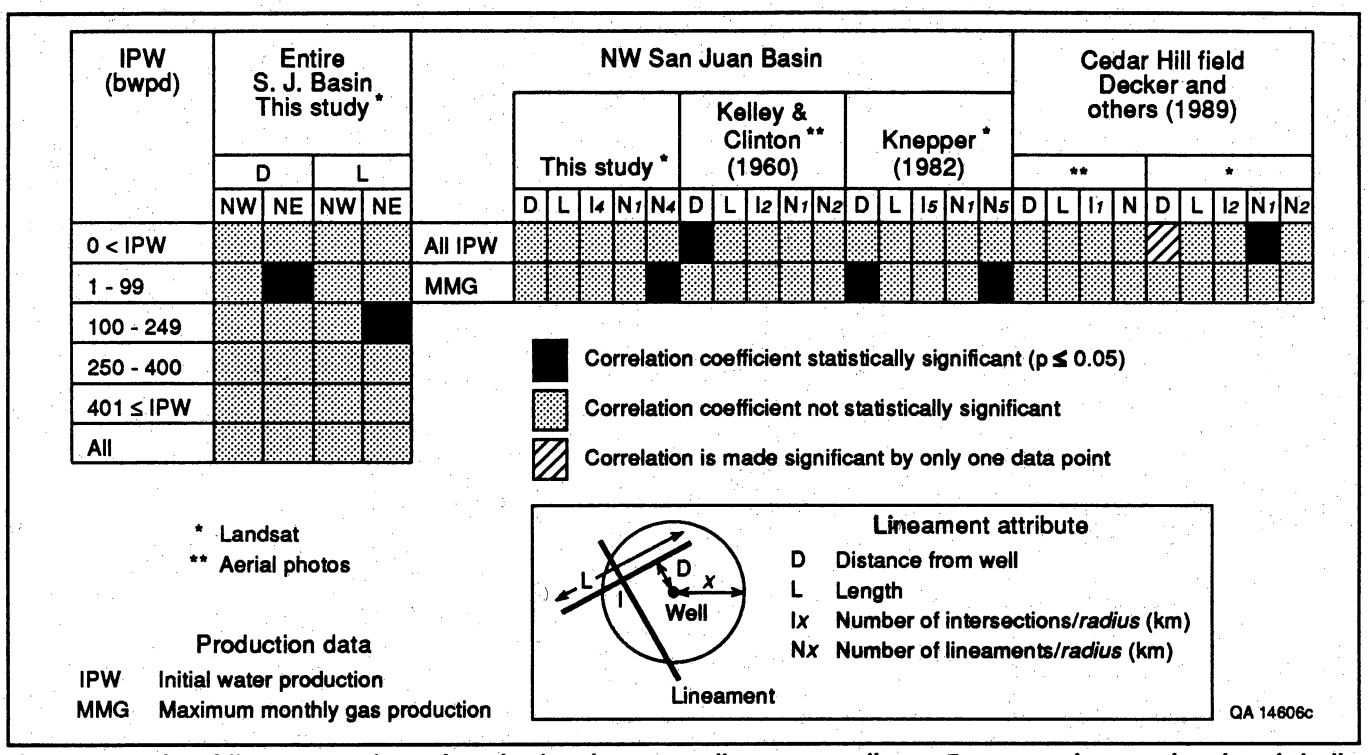

Figure 9. Results of linear regressions of production data versus lineament attributes. Few regressions produced statistically significant (p = .05) correlation coefficients.

52 coincided between 2 different studies. Of these 52 lineaments, only 2 coincided with lineaments from more than 1 other study. Lineaments were considered to coincide if they (1) had the same azimuth within ±5°, (2) overlapped for part of their length, and (3) were less than 1 mm apart, as measured on the original imagery. For a Landsat image at 1:250,000 scale, this 1 mm represented 250 m on the ground.

These and the following results indicate that lineament mapping is strongly dependent upon the interpreter, the type of data base, and the scale of the data base used. For the same area of the northwestern San Juan Basin, the number of lineaments ranged from 51 to 914, largely as a result of differences in scale (table 4). For a smaller area near Cedar Hill field (fig. 14), Decker and others (1989) mapped 11 lineaments on Landsat images and 249 lineaments on aerial photos (table 4).

Lineament azimuth

Lineament azimuths were analyzed to determine (1) if a consistent lineament trend existed for all studies, and (2) if that trend was associated with production values. For two of the three studies that cover the northwestern San Juan Basin (fig. 15, inset), statistically significant lineament azimuths are similar. The maximum lineament azimuth for Landsat lineaments in the present study (35°, fig. 15b) is practically the same as the significant lineament azimuth (38°, fig. 15c) on the basis of aerial photographs interpreted by Kelley and Clinton (1960). However, the maximum lineament azimuth (302°, fig. 15d) mapped on Landsat images by Knepper (1982) is nearly perpendicular to these azimuths. These results indicate that the maximum lineament azimuth can vary widely depending on the interpreter and on the scale and type of imagery used to map the lineaments.

The effect of this variability in lineament azimuth is shown in figure 16. Maximum monthly gas production (MMG) is plotted against the azimuth of the nearest lineament. The highest values of MMG are closest to northeast-trending lineaments in this study (fig. 16a). However, the same high values of MMG, which are from the same wells, are closest to northwest-trending lineaments from Knepper's (1982) study (fig. 16b). Clearly, a lineament azimuth from one study cannot be used in other lineament studies to predict MMG values.

This comparison also shows that fracture trends inferred from well data in one location cannot be used to define "geologically significant" lineaments elsewhere. One cannot assume that lineaments of a given azimuth near wells with high production values are evidence of higher permeability because there is no lineament azimuth consistently associated with high MMG values in all studies.

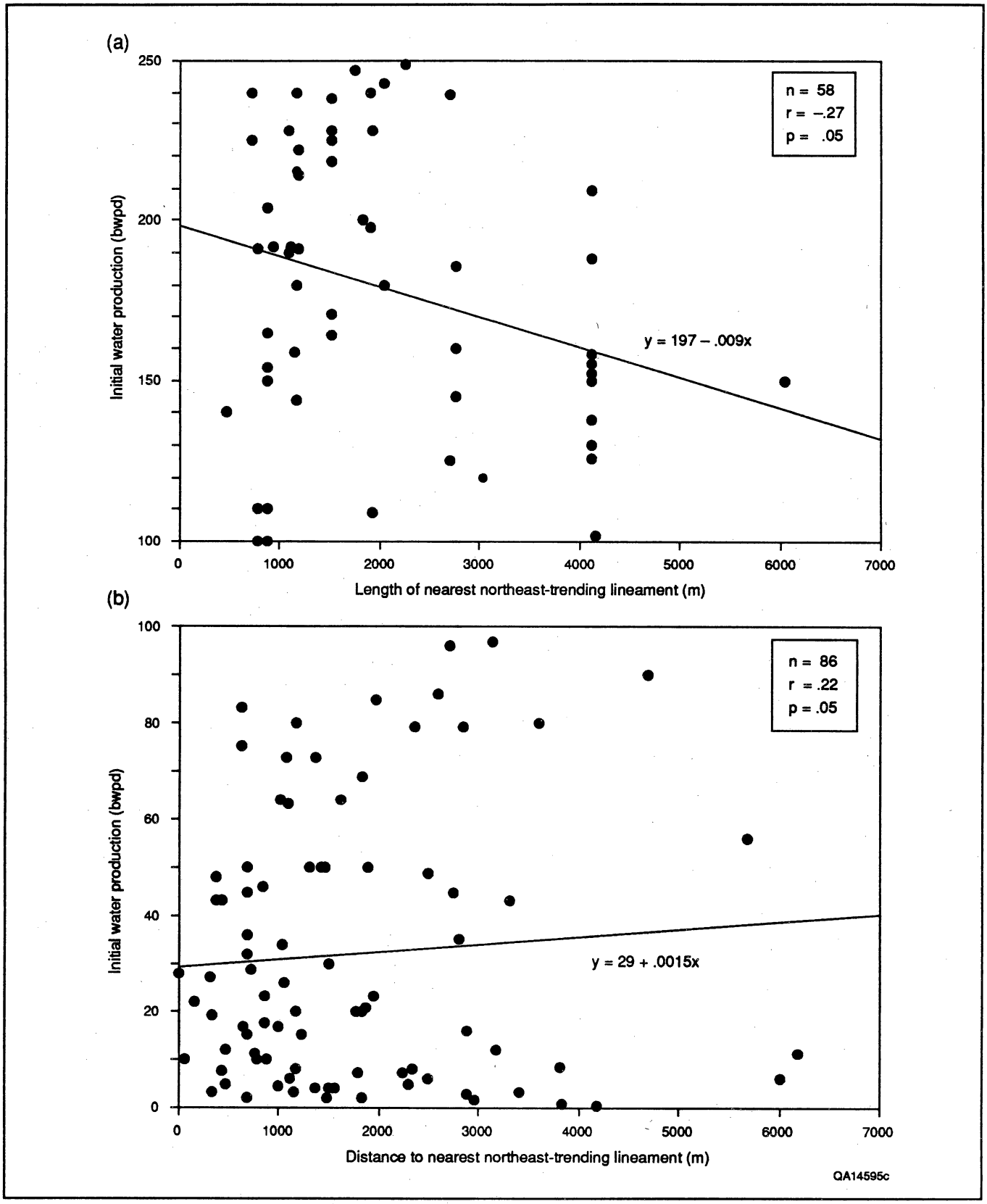

Figure 10. Graphs of initial water production (IPW) versus attributes of lineaments mapped in this study. (a) IPW (100 to 249 bwpd) versus length of nearest northeast-trending lineament. IPW decreases as lineament length increases—the reverse of the expected result. (b) IPW (1 to 99 bwpd) versus distance to nearest northeast-trending lineament. IPW increases as distance to nearest lineament increases—the reverse of the expected result.

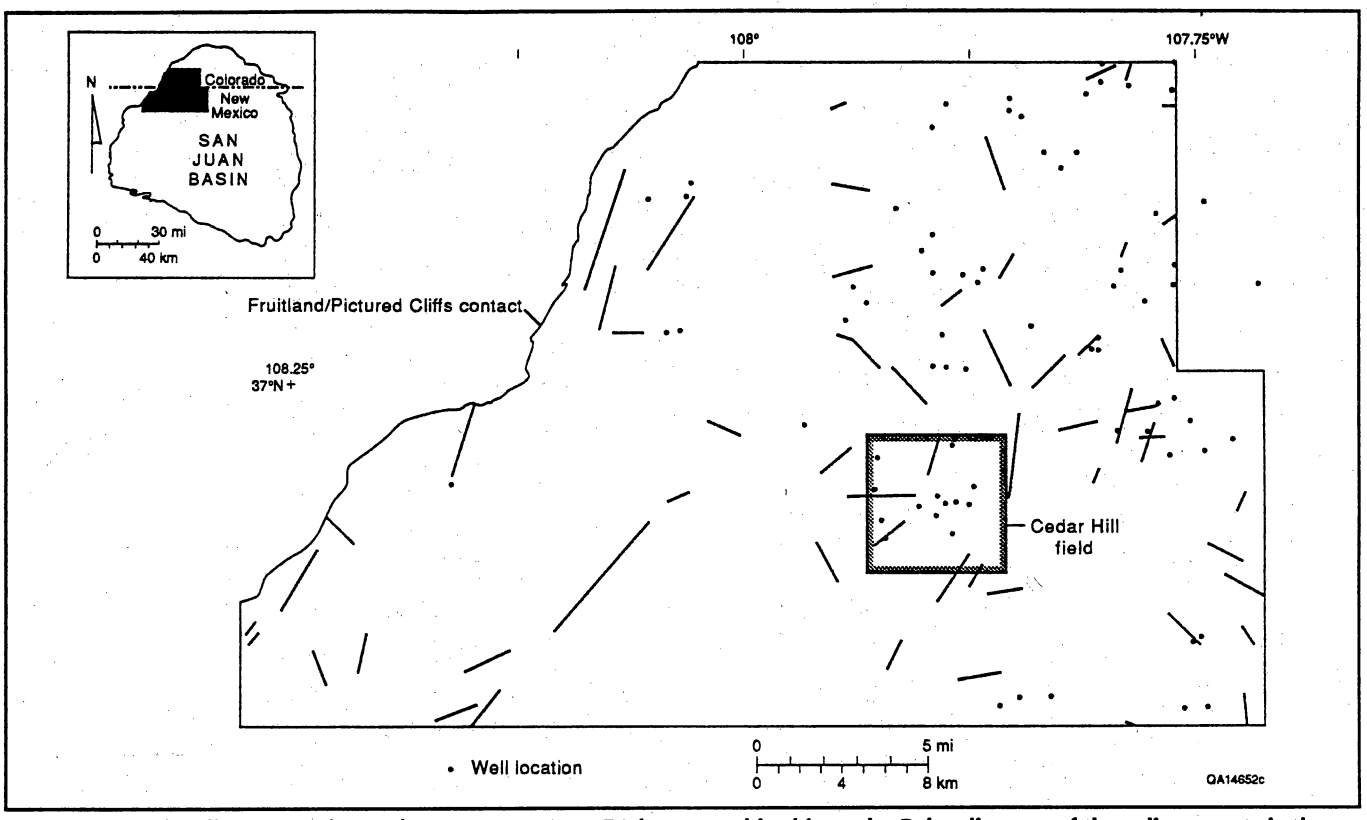

Figure 11. Landsat lineaments in northwestern San Juan Basin mapped in this study. Polar diagram of these lineaments is shown in figure 15b.

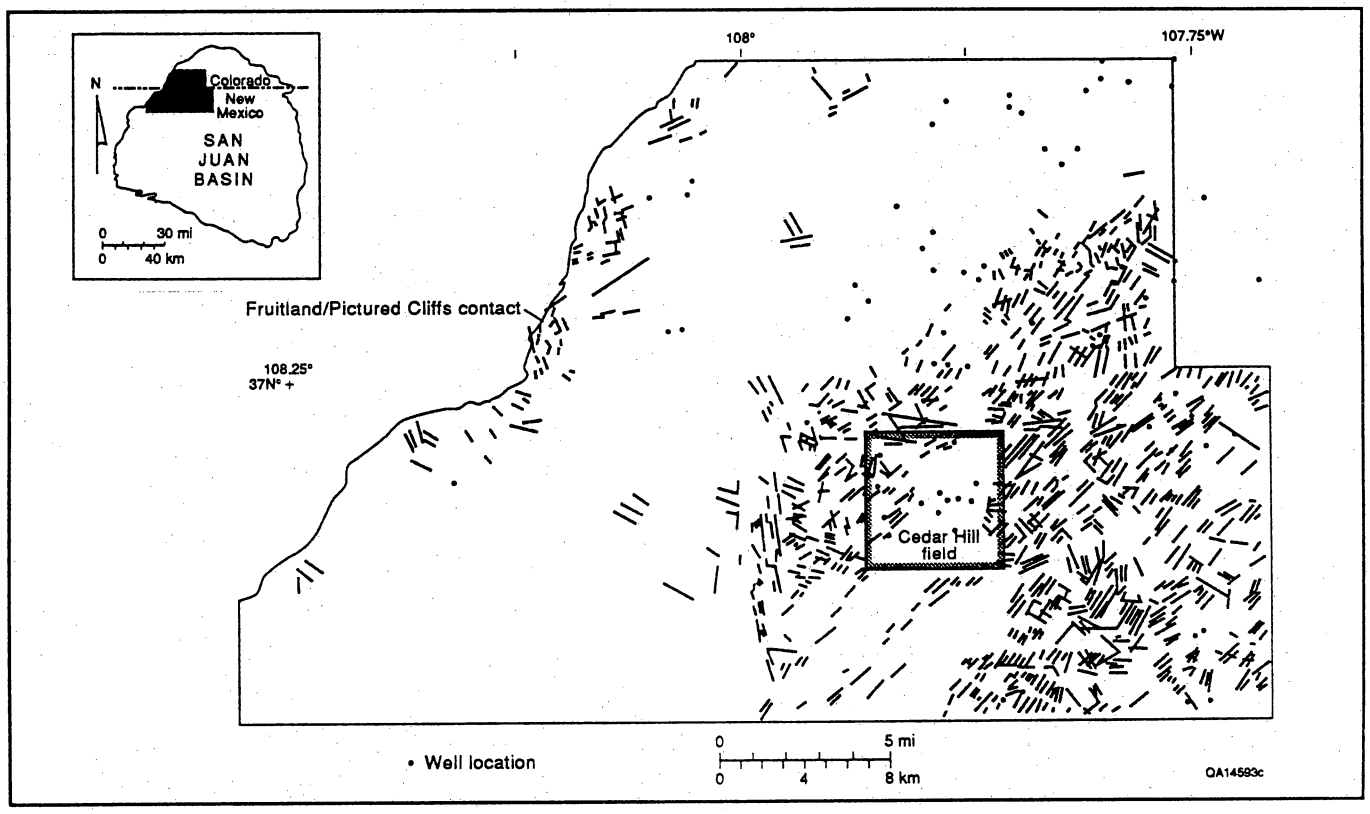

Figure 12. Aerial photolineaments in northwestern San Juan Basin mapped by Kelley and Clinton (1960). Polar diagram of these lineaments is shown in figure 15c.

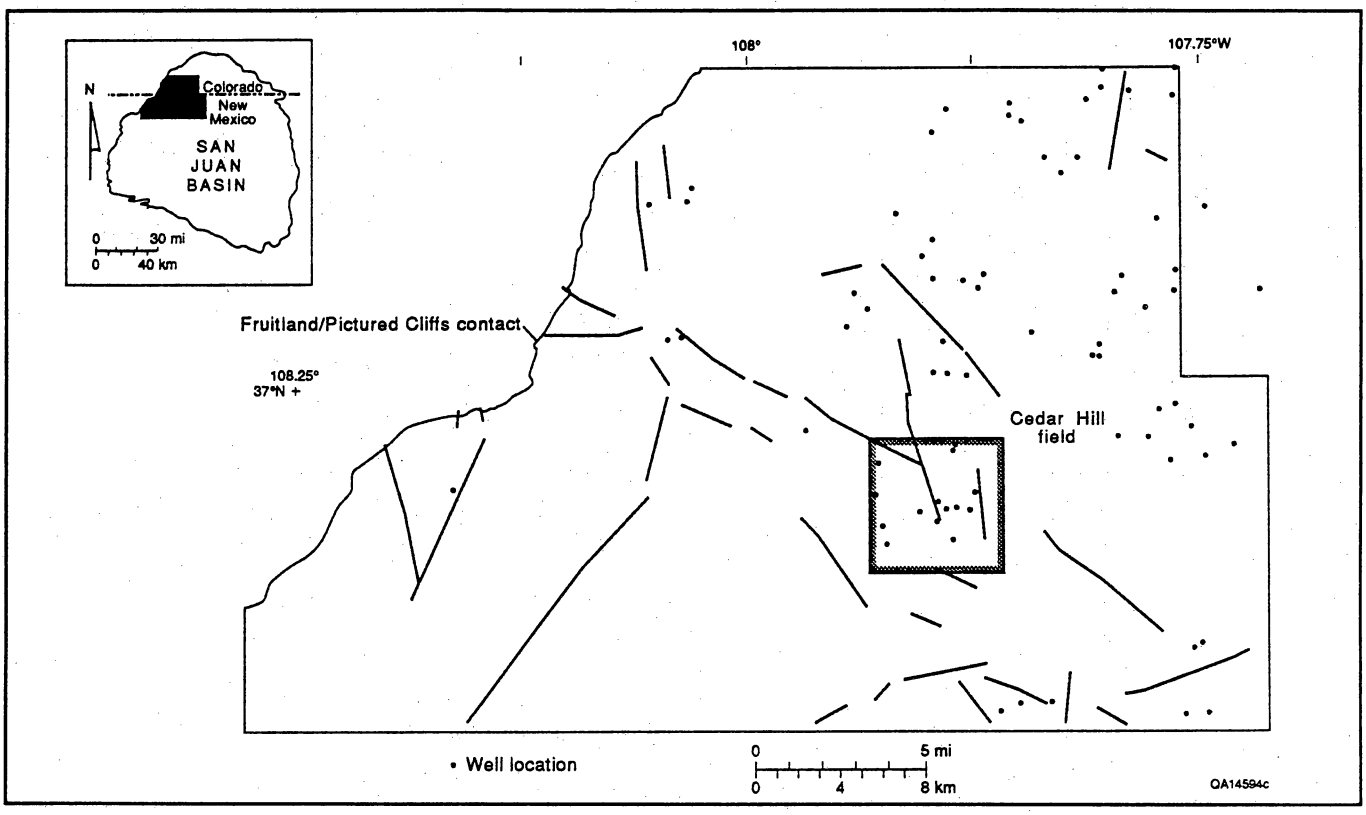

Figure 13. Landsat lineaments in northwestern San Juan Basin mapped by Knepper (1982). Polar diagram of these lineaments is shown in figure 15d.

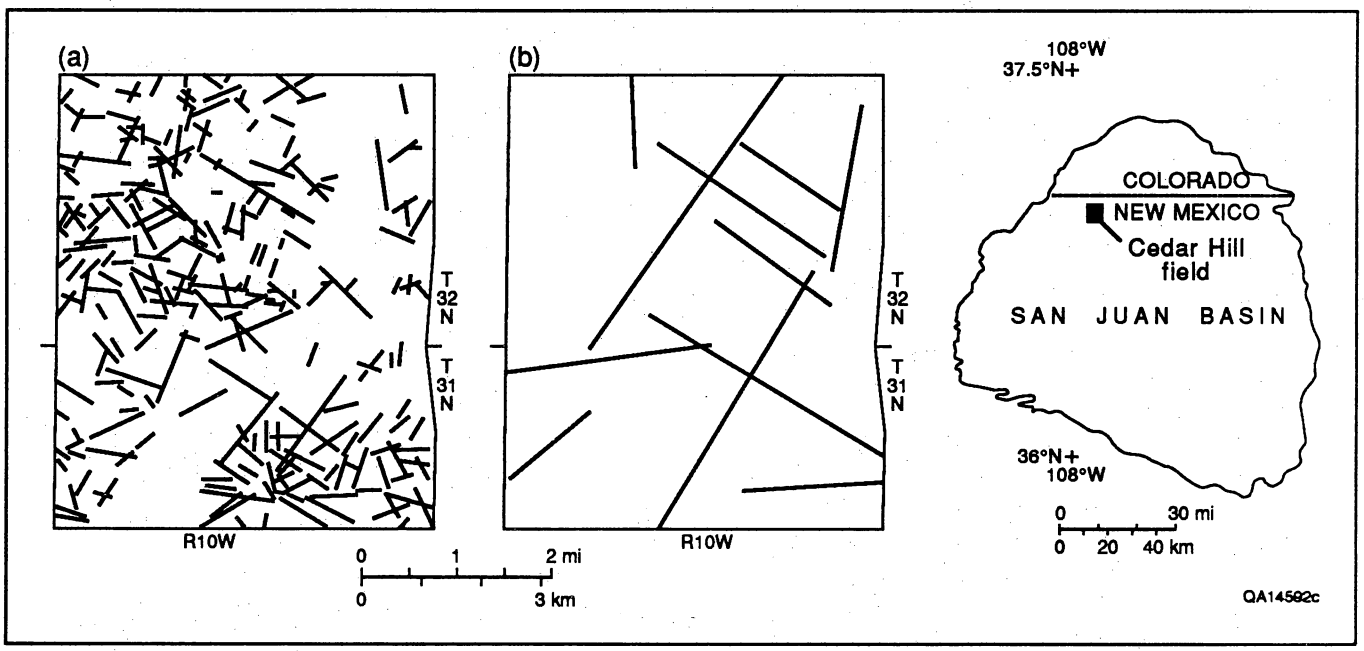

Figure 14. Lineaments in Cedar Hill field area mapped by Decker and others (1989). (a) Aerial photolineaments. (b) Landsat lineaments. Polar diagram of aerial photolineaments is shown in figure 15e.

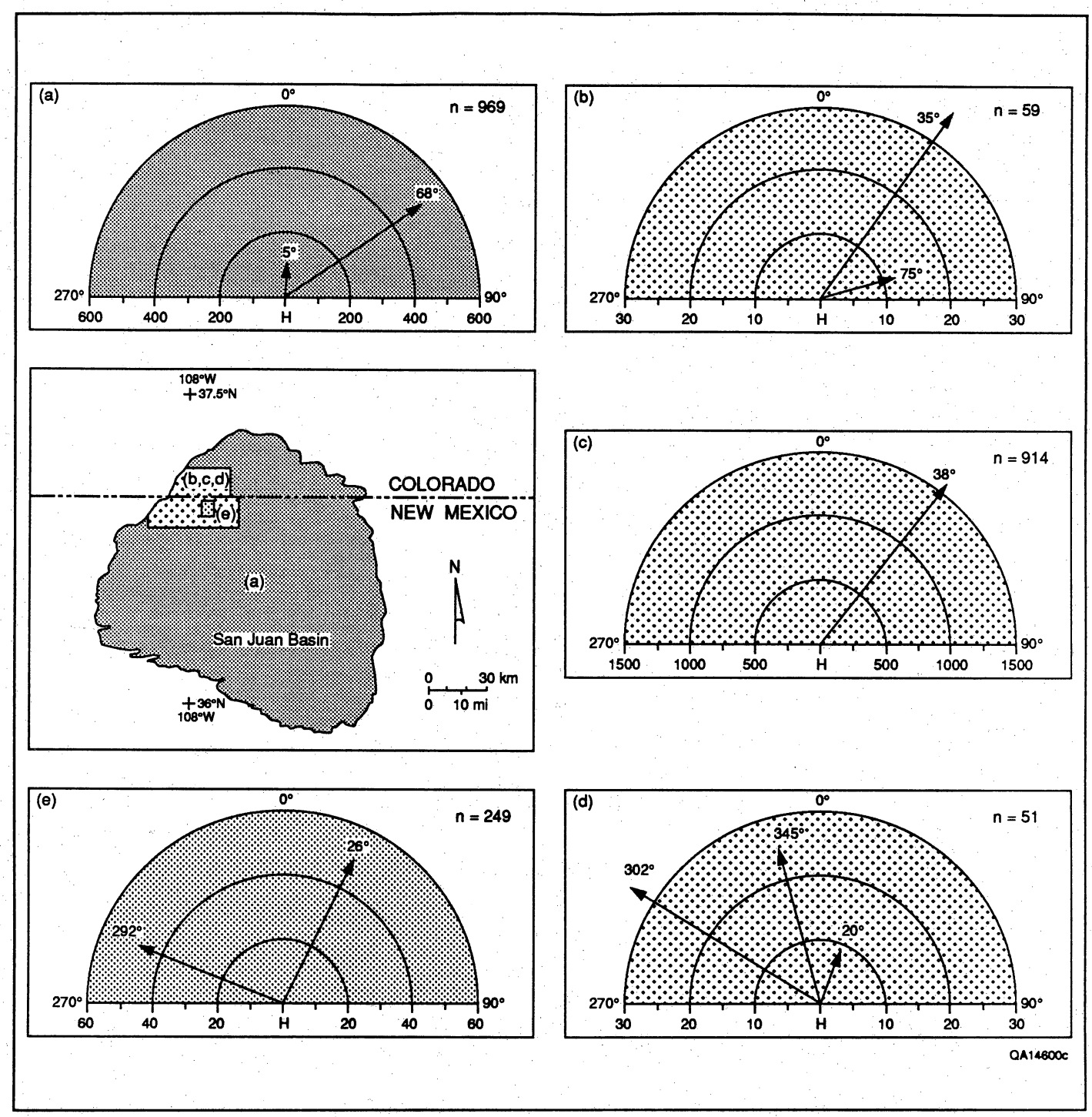

Figure 15. Polar graphs of Bernshtein accuracy criterion (H) for lineaments in this and three previous studies. Only vector sums of lineament azimuths that are significant at the p = .01 level are shown. See inset for area covered by each study. Stipple patterns represent areas that correspond to like data on graphs. (a) This study, entire San Juan Basin. Note that b, c, and d lineaments are from different studies in the northwestern San Juan Basin. (b) Landsat lineaments, this study. (c) Aerial photolineaments, Kelley and Clinton (1960). (d) Landsat lineaments, Knepper (1982). (e) Aerial photolineaments in Cedar Hill field area, Decker and others (1989). Landsat lineaments mapped by Decker and others (1989) are insufficient (n = 11) to produce a meaningful value for H (fig. 6).

Table 4. Lineaments in the northwestern San Juan Basin mapped in different studies.*

Authors (date)	Number of lineaments	Scale of imagery	Well-lin. dist. (ft) min.	Well-lin. dist. (ft) max.	Radius (mi)
Decker and others (1989)	249	≥1:80,000	20	1,200	0.6
Decker and others (1989)	11	<1:80,000	90	7,100	1.2
Kelley and Clinton (1960)	914	1:62,500	70	13,500	1.2
This study	59	1:250,000	100	7,700	2.5
Knepper (1982)	51	1:800,000	430	25,900	3.1
TOTAL	1,284				

*Area covered by Decker and others (1989) (fig. 14) is only a small part of the area covered by the other studies (figs. 11–13). Wells were paired with the nearest lineament. Distance to nearest lineament varies with scale of the imagery. The number of lineaments and lineament intersections were counted within the radius around a well and compared with production data. Radius increases as scale of imagery decreases to compensate for loss of resolution.

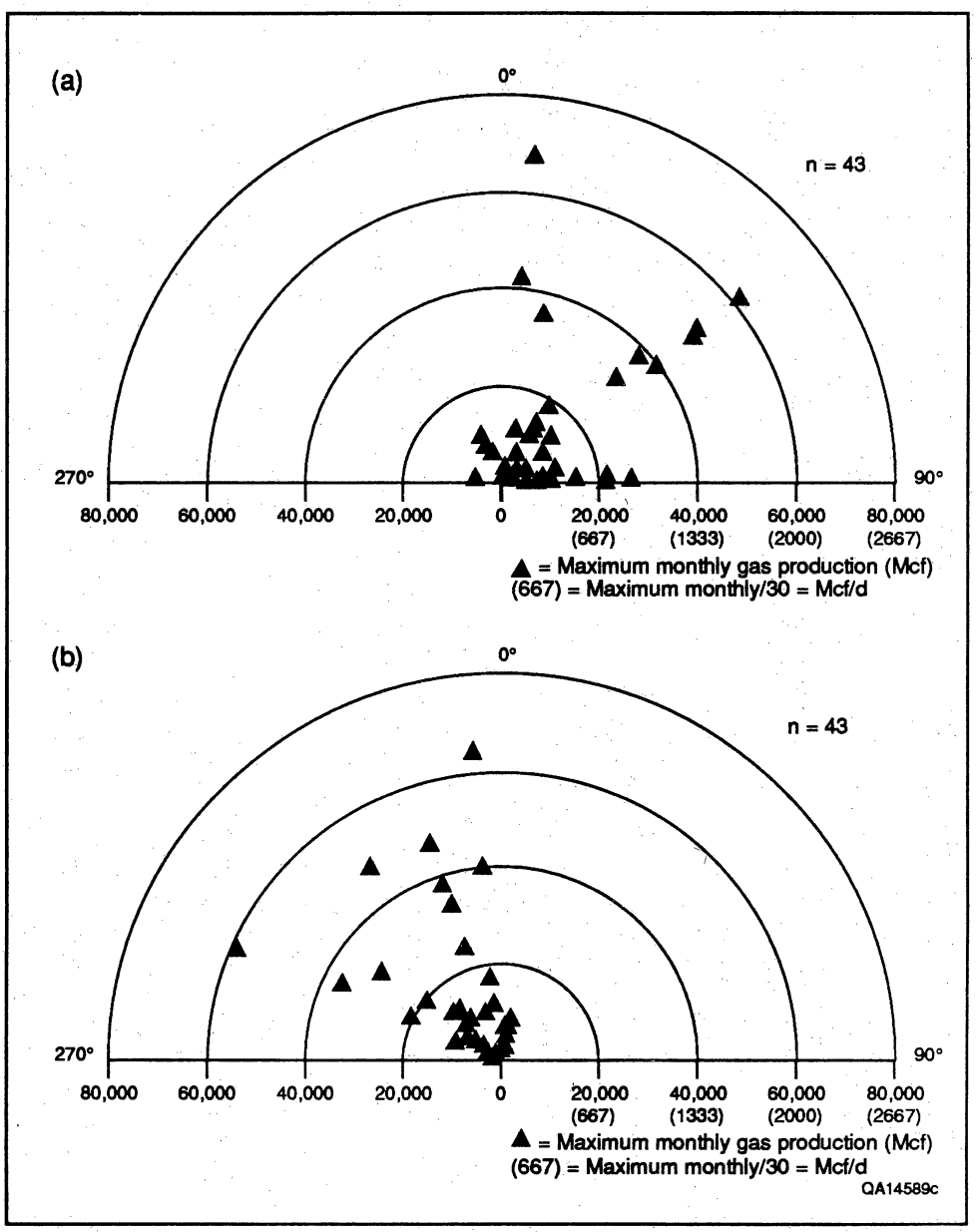

Figure 16. Polar graphs of maximum monthly gas production (MMG) versus azimuth of nearest lineament. MMG data are from wells in northwestern San Juan Basin (fig. 12) for 1988 and 1989. (a) This study: all values of MMG greater than 11,000 Mcf are in the northeastern quadrant. (b) Knepper (1982): all values of MMG greater than 11,000 Mcf are in the northwestern quadrant. MMG values are from the same wells in both studies. This relationship shows that lineament azimuth for the same area may be quite different, depending on the study.

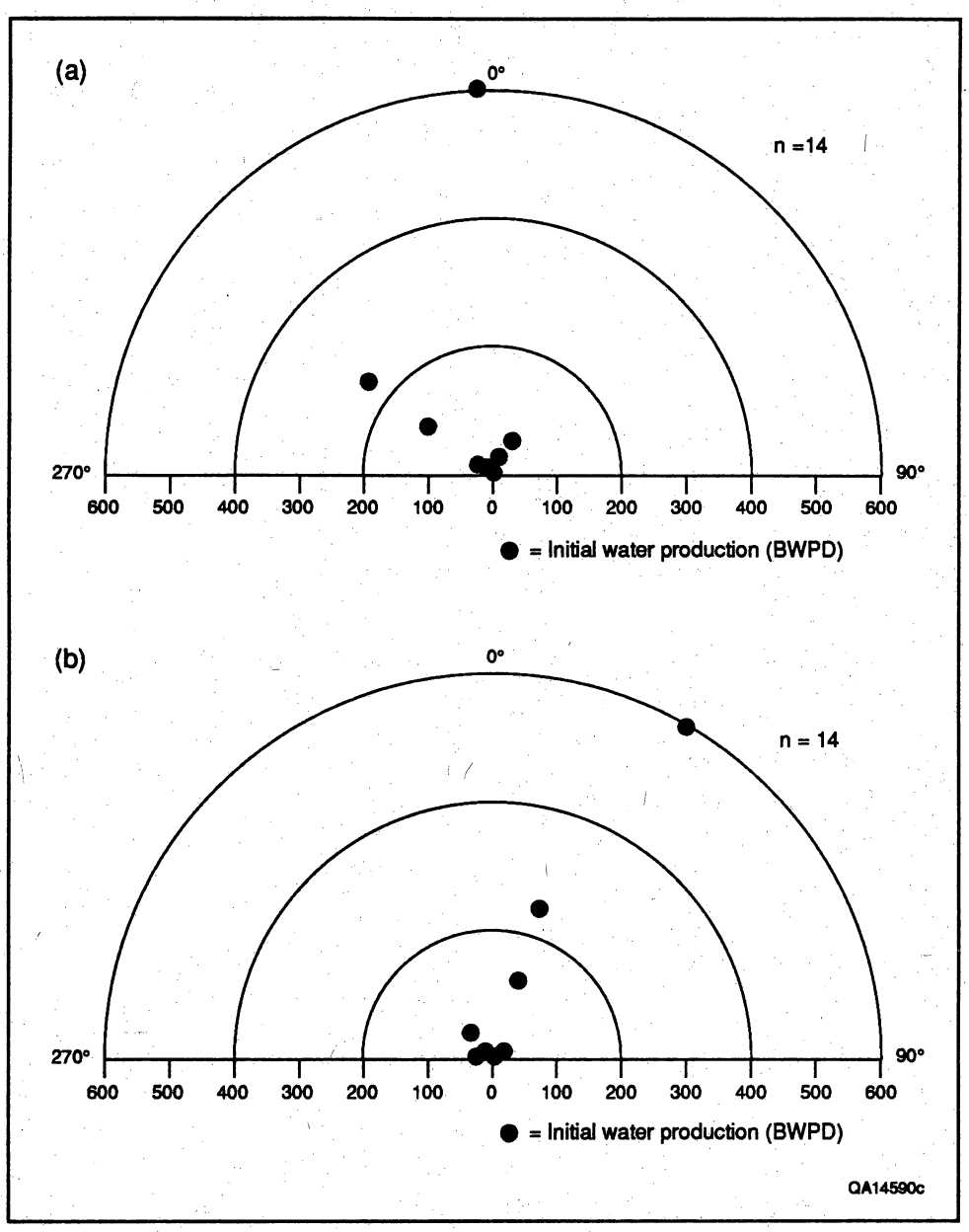

Figure 17. Polar graphs of initial water production (IPW) versus azimuth of the nearest lineament. All IPW data are from the same wells. Lineament azimuth data are from different data bases in the same study by Decker and others (1989). (a) Landsat lineaments: all IPW values greater than 100 bwpd are in the northwestern quadrant. (b) Aerial photolineaments: all IPW values greater than 100 bwpd are in the northeastern quadrant. This relationship shows that lineament azimuth in the same study is dependent on data base.

Even different types of imagery in the same study can produce divergent azimuths. Decker and others (1989) reported lineaments mapped from aerial photographs and Landsat images. Highest values of initial water production (IPW) (>100 bwpd) are closest to northwest-trending Landsat lineaments (fig. 17a), but the same wells are closest to northeast-trending aerial photolineaments (fig. 17b). It is clear from these comparisons that the azimuths of nearest-well lineaments from different studies or even from different imagery in the same study can be quite different, even perpendicular, and that no lineament azimuth can be described as more useful than any other for predicting these production values. Furthermore, most other comparisons between lineament azimuth and production data (for example, IPW versus azimuth for Kelley and Clinton [1960], Knepper [1982], and this study) showed no preferential distribution of high values relative to lineament azimuth.

Wells on lineaments

Two comparisons were made to determine whether wells on lineaments had higher production values than wells not on lineaments. First, mean production values from wells less than 660 ft (200 m) from a lineament were compared with mean production values from wells more than 660 ft (200 m) from a lineament (table 5a). Wells less than 660 ft (200 m) from a

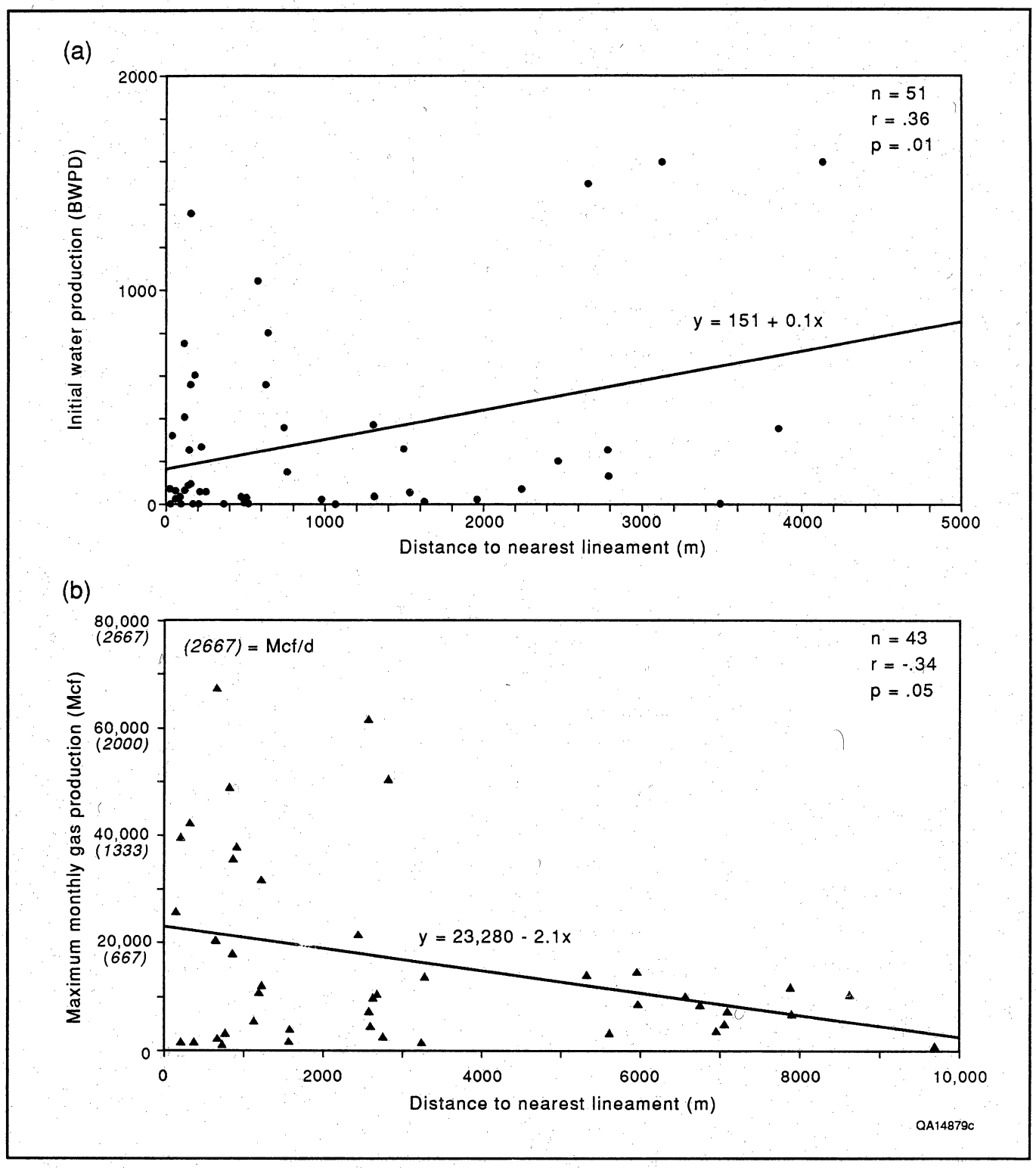

Figure 18. Graphs of production data versus distance from well to nearest lineament. (a) IPW versus distance to nearest lineament (Kelley and Clinton, 1960). Positive correlation coefficient indicates that IPW increases as distance to lineament increases, contrary to the expected result. (b) MMG versus distance to nearest lineament (Knepper, 1982). Negative correlation coefficient shows that MMG decreases as distance to lineament increases, as expected.

Table 5. Comparison between distance to nearest lineament and production data for wells in this study. (Wells less than 660 ft [200 m] from a lineament are considered to be on a lineament.)

a. Mean production data from wells on lineaments (well-lineament distance <660 ft [200 m]) and wells not on lineaments (well-lineament distance >660 ft [200 m]).

	Mean MMG production (Mcf) at well-lineament distance:		Mean IPW (bwpd) at well-lineament distance:	
Study	**<660 ft**	**>660 ft**	**<660 ft**	**>660 ft**
Decker and others (1989)[1]	39,877	30,071	100	4
n	9	3	11	3
Decker and others (1989)[2]	46,997	34,235	0	*101
n	3	9	3	11
Kelley and Clinton (1960)[1]	15,220	17,278	210	278
n	11	32	22	54
Knepper (1982)[2]	14,270	16,873	50	*267
n	2	41	3	73
This study[2]	13,712	16,980	137	265
n	3	40	4	72

Note: If lineaments are enhancing production, MMG and IPW values should be higher at well-lineament distance <660 ft (200 m). This occurs only for the lineaments from the study by Decker and others (1989), but these mean values are not significantly higher than those from wells more than 660 ft (200 m) from a lineament. In fact, the only mean production values that are significantly higher are IPW values from wells more than 660 ft (200 m) from the nearest lineament, the opposite of the expected result.

b. Mean distance from well to lineament for wells with production values greater than and less than the mean.

	Mean distance from well to nearest lineament (ft) for MMG (Mcf):		for IPW (bwpd):	
Study	**> mean**	**< mean**	**> mean**	**< mean**
Decker and others (1989)[1]	512	384	295	449
n	7	5	3	11
Decker and others (1989)[2]	1,854	2,507	3,317	1,595
n	7	5	3	11
Kelley and Clinton (1960)[1]	*3,015	6,004	7,336	4,675
n	13	30	23	53
Knepper (1982)[2]	*4,807	13,114	12,947	8,793
n	13	30	23	53
This study[2]	*3,767	5,692	5,853	4,734
n	13	30	23	53

Note: If greater-than-average production is a result of lineament proximity, then mean distance should be less for MMG and IPW values greater than the mean. This holds true for MMG data in most studies, but the MMG values from the study by Decker and others (1989) are not significantly different.

[1]Based on aerial photographs.
[2]Based on Landsat images.
*Mean values are significantly different at p = .05 level.

lineament were considered to be on the lineament. A distance of 660 ft (200 m) was chosen on the basis of the width of a pencil line at the original scale of the imagery and possible positioning error when digitizing the lineaments. Second, mean distance to the nearest lineament from wells with greater-than-average production values was compared with mean distance from wells with less-than-average production values (table 5b). This comparison tested whether wells with greater-than-average production were significantly closer to lineaments than wells with production less than the average. No distinction was made for the relative position of the well-lineament pairs. Wells along the trend of a lineament were treated the same as wells off the trend of, but near, a lineament.

Briscoe and others (1988) conducted a similar study and reported higher production from wells near lineaments. They mapped joints and lineaments in the Oak Grove field of the Warrior Basin, Alabama on aerial photographs. Wells "connected to fracture systems" (Briscoe and others, 1988, their p. 242), in the form of major linear features and/or closely-spaced joints, had higher production. Wells within 200 ft (60 m) of fracture zones obtained 25 percent greater methane production and 50 percent greater water production than wells in unfractured areas. Field mapping revealed that fractures at the surface extend to subsurface coal seams, as shown by continuous streams of methane bubbles in creeks.

However, the current analysis revealed that there is no consistent relationship between production data and a well's position on or off a lineament. Few mean values of MMG and IPW are significantly different for wells on or off lineaments (table 5a). For data from Knepper (1982) and Decker and others (1989), IPW values are significantly higher from wells that are off lineaments, the opposite of the expected result. Wells with above-average MMG values are closer to lineaments than those with below-average MMG values in three studies (table 5b). This result is consistent with the hypothesis that lineaments enhance gas production, but it was not obtained for the Cedar Hill field area (Decker and others, 1989), where some of the highest gas production values in the San Juan Basin have been observed (MMG as high as 67,837 Mcf, equivalent to 2,261 Mcf/d).

Distance from well to nearest lineament

The comparison of wells on and off lineaments was followed by linear regression of production data versus distance to the nearest lineament (fig. 9). Distance varied according to scale of the imagery (table 4). For the study by Decker and others (1989), based on aerial photographs (scale 1:28,000 to 1:80,000), this distance ranged from 20 to 1,200 ft (6 to 370 m). For the Knepper (1982) study, based on 1:800,000-scale Landsat imagery, the distance ranged from 430 to 25,900 ft (130 to 7,900 m). Only 3 out of 10 linear regressions (2 kinds of production data versus 5 sets of lineaments) produced significant correlation coefficients (fig. 9). One of those is made significant by a single data point. The correlation coefficient for Kelley and Clinton (1960) data is positive (fig. 18a), indicating that the farther away the well is from a lineament, the higher the IPW is, the opposite of the expected effect of lineaments on production data. The Knepper (1982) data show a negative correlation between MMG and distance to lineament (fig. 18b), but this correlation (–.34) explains only 12 percent (r^2 = .12) of the variability in MMG values.

Length of nearest lineament

The length of the nearest lineament had no significant effect on the production data tested (fig. 9).

Lineament intersections within a given radius

The number of nearby lineament intersections was compared with production data; if lineaments represent fractures or other zones of enhanced permeability in the subsurface, then intersections of these zones should represent areas of increased permeability in the subsurface, which should be reflected in production data. The number of lineament intersections was counted within a given radius of each well. The size of the radius varied with the scale of the original imagery to allow for differences in the density of lineaments, which is a function of the scale and resolution of the original imagery (table 4). Then, the number of lineament intersections was correlated with the production data for each well. There was no significant correlation between intersections and production (fig. 9). It is especially noteworthy that the lineament data for the Cedar Hill field are not significantly correlated with production data, because this field includes some of the most productive wells in the northern San Juan Basin, presumably because permeable fractures are present in the Fruitland Formation there.

Number of lineaments within a given radius

Finally, the number of lineaments within a given radius of each well was correlated with production values. To this point in the study, results showed that no lineament attributes could be used consistently to predict production values. The following comparison tests whether the number of lineaments, regardless of length, azimuth, or relative distance from a well, is correlated with IPW or MMG.

Radii of 0.6 mi (1 km) and the "scale-determined" radius discussed above were used. Of 18 regressions (2 kinds of production data versus 2 radii, except for the aerial photolineaments in Decker and others [1989]), only 3 produced significant correlation coefficients (figs. 9 and 19). The correlation coefficients ($|r| \leq .59$ explain only about one-third of the variability in the

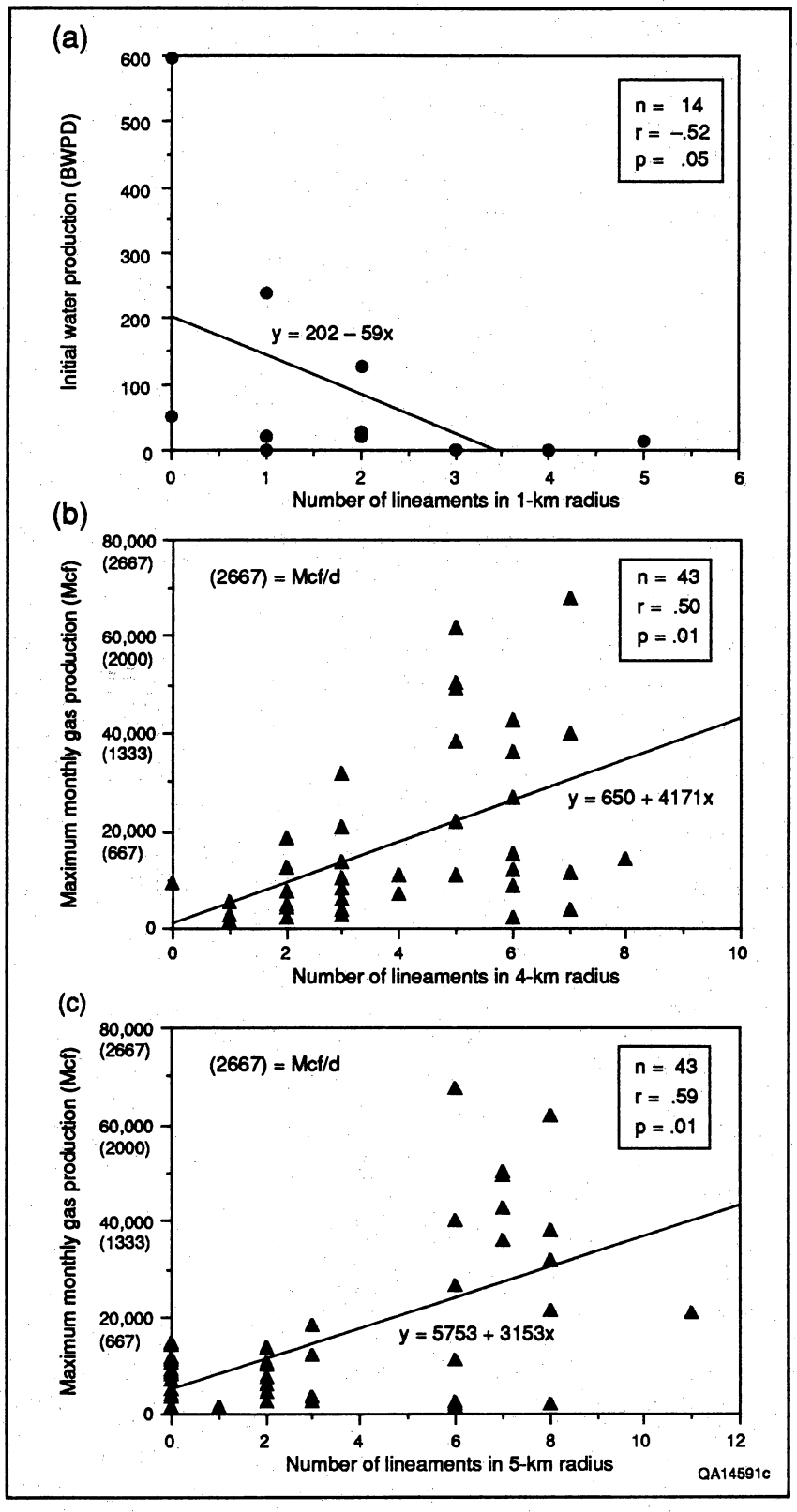

Figure 19. Graphs of production data versus number of Landsat lineaments within a given radius of a well. (a) IPW versus lineaments in a 0.6-mi (1-km) radius (Decker and others, 1989). Negative correlation coefficient indicates that as number of lineaments near a well increases, IPW decreases—the reverse of the expected result. (b) MMG versus Landsat lineaments in a 2.5-mi (4-km) radius (this study). (c) MMG versus Landsat lineaments in a 3.1-mi (5-km) radius (Knepper, 1982). Applicability of these correlations to exploration is questionable, given the size of the radii around the wells.

production data ($r^2 \leq .35$). These correlations are surprising for two reasons. First, all significant correlations are for Landsat lineaments, not aerial photolineaments. A previous study of lineaments in the Cedar Hill field area concluded that aerial photolineaments are more useful for exploration programs (Decker and others, 1989). Second, these results show that the *only* lineament attribute that is significantly correlated with production values from Cedar Hill field is the number of Landsat lineaments within a given radius of the well. However, the number of lineaments is negatively correlated with IPW (fig. 19a), indicating that the fewer lineaments there are within a 0.6-mi (1-km) radius of a well, the higher its IPW. This is the reverse of the relationship usually expected in lineament studies. Even where a positive correlation with production values was seen, for the data from Knepper (1982) and from this study (fig. 19b and 19c), the utility of this relationship for exploration purposes is questionable because the radii used are as large as 3.1 mi (5 km).

Discussion

Lineaments and Stress

Most linear topographic features probably form as a result of weathering and erosion along linear fractures. Surface fractures form in response to stresses in near-surface rocks, which may be different from those in the deep subsurface. Differences in age, thickness, and tectonic history of rocks at the surface and those at depth are likely to produce differences in orientation, length, and location of fractures at the surface and those at depth. Local topography, weathering, and erosion may cause shallow, horizontal stresses (less than 330 ft [100 m] deep) to differ from deeper stresses at the same site (Haimson, 1978, 1979; Zoback and others, 1980; Zoback and Zoback, 1980). As a result, lineaments that form along surface fractures may not be representative of fractures or stress directions at depth in reservoir rocks.

However, measurement of lineaments over a large area may cancel the random effects of local topography and reveal patterns that are related to more deeply seated stresses. Longer lineaments may result from deeper fractures (Nur, 1982). If these linear patterns are the result of present-day stresses or deep fractures in the rock, they could provide information about the orientation of permeable fractures in the subsurface. The minimum horizontal compressive stress direction determines the orientation of open vertical fractures in the subsurface.

Even so, the relationship between lineaments and fractures commonly is not straightforward in sedimentary basins. Natural fractures in the subsurface may parallel joints mapped at the surface (Hickman and others, 1985). One study in an area of flat and gently dipping rocks reported vertical fractures in the subsurface subparallel to lineaments, but nearly perpendicular to surface fractures (Komar and others, 1971). Apparently, the relationship between orientations of linear features at the Earth's surface and in the subsurface is not the same everywhere. Indeed, in an area of complex fracture patterns, surface and subsurface fractures may range from parallel to perpendicular in the same sedimentary basin because of differences in lithology and burial and thermal histories of the rocks involved (Grout and Verbeek, 1985).

Stress in the Study Area

The present stress regime in the San Juan Basin is extensional, with minimum horizontal stress oriented northeast (fig. 2) (Wong and Humphrey, 1989). Regional opening-mode fractures in this stress field would be oriented west-northwest. Near the boundary between the Colorado Plateau and Rio Grande Rift provinces, which is adjacent to the eastern side of the San Juan Basin, maximum compressive horizontal stress is predominantly north-northeast (Zoback and Zoback, 1989, their fig. 1). Opening-mode fractures formed in this stress regime would be oriented north-northeast if aligned with maximum horizontal stress, approximately perpendicular to fractures farther to the northwest.

Independent studies have shown that northeast- and northwest-trending faults, fractures, and foliations are present in the San Juan Basin. Precambrian foliation trends and age-province boundaries trend predominantly northeastward beneath the San Juan Basin (Kelley, 1955). Northeast-trending fault zones with major displacements of Precambrian age have influenced later Phanerozoic fracture trends (Shoemaker and others, 1974). Northeast-northwest conjugate joint sets and northeast-trending extensional fractures were recognized by Woodward and Callender (1977). Statistically significant ($p = .01$ level) cleat directions from the Mesa Hamilton No. 3 well in Cedar Hill field are 032° and 303°. These orientations are very similar to the significant lineament azimuths (026° and 292°) for the data from Decker and others (1989) (fig. 15e).

Lineaments and Production from Coal Beds

The results of this analysis suggest that lineament studies, on any imagery, are not very useful for locating highly productive coalbed methane wells in the San Juan Basin. No consistent significant difference was found between production data from wells on lineaments and those not on lineaments (table 5). No consistent relationship was found between any lineament attribute and the entire range of values of IPW or MMG

(fig. 9). These results do not replicate those reported in a study of coalbed methane in the Warrior Basin, Alabama (Briscoe and others, 1988). The wells within 200 ft (60 m) of fracture zones in that basin had higher methane and water production. Since this work was completed, lineament attributes have been correlated with the daily average of the maximum annual water (MAW) and gas (MAG) production. Few correlations were significant, confirming that the lineament attributes tested cannot be used to predict these production data in the San Juan Basin.

Conclusions

This study has shown that lineaments in the San Juan Basin are not reliable indicators of geologic structure or predictors of production results from wells in the Fruitland Formation. Density of lineaments mapped in this study does not demarcate geologic structures in the subsurface. There is little agreement between lineaments mapped in independent studies of the San Juan Basin. More than 95 percent of lineaments mapped in four separate studies do not coincide. The statistically significant ($p = .01$) vector sums of lineament azimuths in each study vary from subparallel to perpendicular to those in the other studies. Azimuths of lineaments nearest wells with high values of IPW and MMG vary between studies and even within one study, for lineaments derived from different imagery. Wells on lineaments do not have consistently higher production values than those not on lineaments. There is no significant correlation between production data and the length of, or distance to, the lineament nearest each well. However, there is a relatively weak correlation ($|r| \leq .59$, $p = .01$) between the number of lineaments within a given radius and IPW or MMG. The bimodal distribution of lineaments (northeast and northwest) in some studies may reflect joint patterns in the San Juan Basin, but this connection remains unproven.

Lineament attributes examined in this study are not useful for predicting either IPW or MMG values from coalbed methane wells. It is possible that lineament attributes may effectively predict other production parameters, such as average daily gas production or mean annual gas production. Further study should examine the relationship between production values such as these and lineament attributes. Dividing the basin into underpressured and overpressured areas and reexamining the data may reveal more significant relationships. In addition, a multivariate analysis of lineament attributes and production values could be done. It is possible that better correlations between lineament attributes and production values may result from this type of study.

Acknowledgments

The author wishes to acknowledge the following persons who assisted in completion and improvement of this report. Consultation with Walter B. Ayers, Jr., and William R. Kaiser improved the analysis and presentation of results. Neil H. Whitehead III assisted with field-checking of lineaments. Rick Edson, Joseph Yeh, and Arten J. Avakian provided invaluable assistance in the use of computer-based mapping and contouring programs. Ting-Ya Hsieh assisted with integration of lineament and well-data files. Insightful reviews by Walter B. Ayers, Jr., Tucker F. Hentz, William R. Kaiser, and Stephen E. Laubach improved the report and the conclusions presented herein. Figures were drafted by Wade W. Kolb, Joel L. Lardon, Kerza A. Prewitt, and Tari Weaver under the direction of Richard L. Dillon, Chief Cartographer.

Predicting Fracture Permeability from Bed Curvature

Joseph Yeh, D. D. Schultz-Ela, and S. E. Laubach

Abstract

Predictions of fracture occurrence using quantitative analysis of bed curvature may be useful in the design of coalbed methane exploration and development strategy. Valid application of computer-based methods of curvature analysis requires an appreciation of the theoretical and practical limitations and assumptions involved.

Introduction

Improved methods for accurately predicting occurrence and effect on permeability of fractures in coal seams could enhance coalbed methane resource development. One method that has been used for predicting fracture occurrence and fracture-related permeability in fractured reservoirs is the "curvature method," or "second derivative method," of Murray (1968). We review and reassess the theoretical underpinnings of this method and apply the technique to a part of the Cedar Hill field of the northwestern San Juan Basin, where predictions of the method can be compared with production data. Our results suggest the types of theoretical and practical improvements to the method that are required before results can be applied with confidence to coalbed methane exploration and development.

Background and Basic Principles

Reasons for Analyzing Curvature

In general, sediments are deposited in near-horizontal layers. Any significant curvature now present in the rock layer is the result of folding (or perhaps differential compaction effects). Stress is required to bend the rocks into folds, which will increase the strain energy in the rocks. In brittle rocks, fracturing and faulting relieves this energy when it exceeds failure levels specific to the rock type. Thus, there should be some relationship between the amount of bending in the rock and the amount of fracturing. If these fractures are the primary contributor to the permeability of a rock containing an economically important fluid, identifying areas of increased folding may indicate areas of high production.

The theoretical relationship between bed curvature and fractures rests on several key assumptions. A bed is assumed to be brittle and to fracture in tension when it is folded. A simplified geometrical analysis of the fractures then relates increased bending of the bed to increased permeability (Murray, 1968; Pirson, 1977). Therefore, the permeability of appropriate beds should be indicated by the curvature of the beds, a property which is relatively easy to calculate from structure maps. The theory and its practical application will be reviewed, followed by a discussion of the assumptions used and sources of difficulty in establishing a quantitative relationship between structures and fracture permeability.

Theoretical Relationship between Fracture Permeability and Curvature

Murray (1968), and in a more abridged version Pirson (1977), developed a simple theory for the intuitive relationship between structural curvature and fracture permeability. The theory strictly applies to only two-dimensional structures, that is, cylindrical folds that formed in plane strain. Individual competent beds fold by flexure, with their neutral surfaces (surface of no length change) at the bed surface on the inner arc of the fold. Bending stresses the beds in tension as the bed stretches around the fold, and extensional fractures form when the tensional stresses exceed the tensional strength of the bed.

Given that behavior of the beds, Murray (1968) analyzed the geometry of the fractures formed. His theory will be summarized here, emphasizing the simplifying assumptions used to make the problem tractable. The first of the series of assumptions is that the fractures open as wedges separated by rectangular blocks of the unfractured bed (fig. 1). The fractures are further assumed to be sufficiently closely spaced that the top and bottom surfaces of a bed may be approximated as sectors of a

In Ayers, W. B., Jr., and others, 1991, Geologic and hydrologic controls on the occurrence and producibility of coalbed methane, Fruitland Formation, San Juan Basin: The University of Texas at Austin, Bureau of Economic Geology, topical report prepared for the Gas Research Institute under contract no. 5087-214-1544 (GRI-91/0072), p. 181-192.

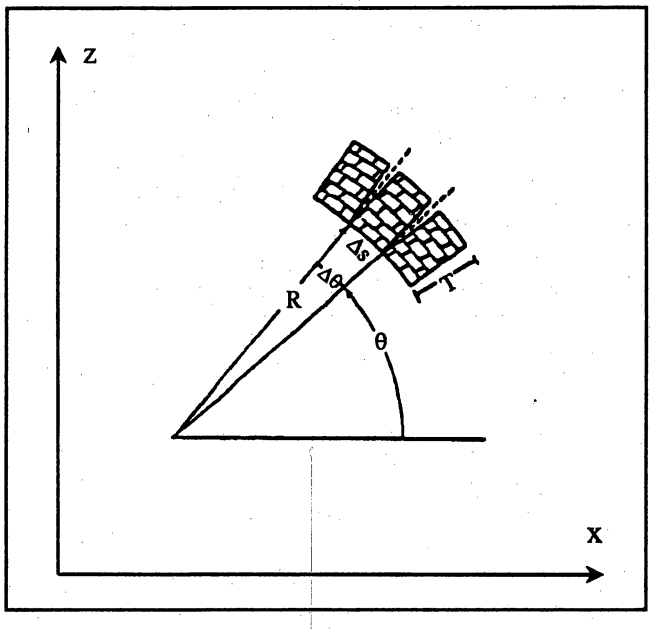

Figure 1. Geometry of fracture system used in deriving expressions for fracture porosity and permeability (from Murray, 1968).

circle. Then the fractional porosity for a new fracture, φ, is simply

$$\varphi = \frac{\text{(area of fold sector)} - \text{(area of intact rock)}}{\text{(area of fold sector)}}, \quad (1)$$

that is, the area of the newly opened fracture divided by the area of the fold between the centers of two fractures (fig. 1). Areas are used because the analysis is in two dimensions; they can be converted to volumes by multiplying by a unit distance of rock in the third dimension.

If the fractures are closely spaced and the bending is small, the angular separation, $\Delta\theta$, of fractures around the fold arc is small. The width of a section of intact rock, $R\sin(\Delta\theta)$, is then approximately equal to $R\Delta\theta$, where R is the radius of the inner arc of the fold. The area of intact rock between fractures is the bed thickness, T, multiplied by $R\Delta\theta$. If the standard formula for circle areas is used to find the area of the fold sector, then substituting into the above equation yields

$$\varphi = \frac{T}{2R+T}. \quad (2)$$

The assumption of gentle bending implies a large R, and if T is relatively small then φ can be approximated by T/2R.

The next step is to relate the radius of the curve, R, to a more easily measured quantity. If z is the depth coordinate and x the horizontal coordinate, the dip of a bed at any point is the infinitesimal change of horizontal distance divided by the infinitesimal change of depth of the bed, or the familiar derivative dz/dx. It is then relatively simple to calculate the change in dip with horizontal distance, or d^2z/dx^2. Calculus is used to express the curvature of a circle as a function of these first and second derivatives of depth. Because the first derivative is a squared term in the curvature equation, it can be neglected for small dips. The curvature is the reciprocal of the radius of the curve, so for small dips we have

$$\varphi = \frac{1}{2} T \frac{d^2z}{dx^2}. \quad (3)$$

This equation represents a practical way to measure fracture porosity from measurements of bed thickness and change of bed dip.

If the goal of predicting fracture intensity is to predict the production from a fractured reservoir, the fracture permeability, K, is of greater interest than the fracture porosity. Murray (1968) expands the geometric analysis above to analyze fracture permeability using a simple fluid mechanics approach. The volume of fluid flow through a straight-sided channel can be expressed in terms of the distance between the channel walls, the fluid viscosity (μ), and the pressure gradient in the direction of flow dp/dy. If it is accepted that the same equation describes flow through a wedge-shaped fracture with a very small opening angle, the volume of flow through a fracture is found by integrating the fluid flow equation along the diverging fracture sides. This flow volume can be converted to an average flow per unit area by dividing by the average bed area between fractures, assuming that the fractures have negligible area relative to the intact rock (that is, very small φ). After some algebraic manipulation, the average flow becomes

$$q = -\frac{A^2}{48T^2\mu}\left(T\frac{d^2z}{dx^2}\right)^3 \frac{dp}{dy}. \quad (4)$$

This flow needs to be converted to a permeability, which requires a model of fluid flow through the whole rock instead of through a single fracture. The most common model is Darcy's law for flow through a porous medium, where

$$q = -\frac{K}{\mu}\left(\frac{dp}{dy}\right). \quad (5)$$

Darcy's law assumes that the flow is through some matrix of interconnected passages, here represented by fractures. The most important assumption is that the dimensions and spacing of fractures is small compared with the scale of the overall flow, which corresponds to the thickness of the bed. The flow must also be laminar. Factors favoring laminar flow are narrow fractures, low fluid density, and high fluid viscosity.

Equating the last two equations and solving for the permeability, K, yields the desired relation between curvature and fracture permeability:

$$K = -\frac{1}{48}\left(\frac{A}{2}\right)^2\left(T\frac{d^2z}{dx^2}\right)^3, \quad (6)$$

where A/T is the fracture spacing and d^2z/dx^2 has units of $(\text{length})^{-1}$ because it is essentially a change in angle per distance. Note that because of the cubed term, permeability increases greatly with increases in bed thickness and curvature.

The analysis can be carried one step further by applying it to an actual rock type (Murray, 1968). Simple bending theory relates the stress, F, in the outer arc of a bed to its thickness, curvature, and Young's modulus, E, for a particular rock:

$$F = ET\frac{d^2z}{dx^2}. \quad (7)$$

If the thickness and curvature are sufficiently large that F exceeds the tensile strength of the bed, the rock will fracture. For curvatures below this threshold, there will be no fracture permeability induced by the bending. Values of Young's modulus and tensile strengths are tabulated in various references (for example, Brace, 1964; Jaeger and Cook, 1979; Turcotte and Schubert, 1982).

Application of the Curvature Method

Quantitative estimates of the fracture permeability require information on fracture spacing, bed thickness, and bed curvature. However, because of the many simplifying assumptions embodied in the theory, it may be more fruitful to (at least initially) concentrate on identifying *relative* changes in permeability within a target region. A sedimentary bed commonly has reasonably uniform thickness, so mapping changes in the curvature of the bed becomes the most important objective. Zones of relatively high curvature will have high fracture permeabilities.

Mapping bed curvature requires a basic structure map of the bed of interest, or of another bed which parallels it. Such a map describes the depth, z, associated with each (x, y) location on the bed's surface. At each point on the bed, a dip may be calculated. Therefore, curvature describes the change of dip with movement across the surface. The larger the curvature of an arc, the smaller the radius of the arc, and therefore the "tighter" the curve (that is, the greater the change in dip for a given horizontal change). As shown above, curvature is approximately equal to the second derivative of the bed depth with respect to a horizontal coordinate. Thus, mapping curvature reduces to mapping this second derivative.

Several methods are available for calculating the second derivative from a structure map. We will describe three approaches to calculating second derivative values: the ring method, the trend surface method, and the direct method based on finite difference equations.

Ring Method

The ring method is an approach suggested by Muñoz-Espinoza (1968) and Pirson (1977) for calculating the second vertical derivative of potential fields from their values at equally spaced points on a horizontal grid. The derivative value is found by averaging the grid point values on successively larger rings about the point of interest, then multiplying those averages by weighting factors and summing. The size and number of rings and the weighting factors are empirically derived with a Lagrange interpolation polynomial to best approximate known potential functions (Henderson, 1960). Dobrin (1976) describes the justification for this method in a particularly understandable way. Given measured values of the field, H, on one horizontal plane, say (x, y, z_o) where z_o is constant, the ring calculation was developed to find the values of gravity and magnetic fields (both examples of potential fields) on planes with different constant z values (called upward and downward continuation). The property of potential fields that makes this possible is that they satisfy Laplace's equation, where

$$\frac{d^2H}{dz^2} = -\left(\frac{d^2H}{dx^2} + \frac{d^2H}{dy^2}\right). \quad (8)$$

In other words, the horizontal (x and y) changes in H completely determine the vertical (z) change in H. To apply this method to curvature analysis, Muñoz-Espinoza (1968) and Pirson (1977) take H to be the structural height of the bed, then calculate its vertical second derivative, d^2H/dz^2, using the ring method. A computer source code implementing the ring method with Henderson's (1960) constants appears in Muñoz-Espinoza (1968) and is also published in Pirson (1977).

In detail, Muñoz-Espinoza presented the structural surface as a function in space, H(x, y, 0). A right-handed system of coordinates is adopted in which the origin is taken at each node of a grid and the z axis is taken with positive vertically upward. An evenly spaced grid system with mesh interval "a," where "a" is a specified distance appropriate to the area of interest, is laid on the structure map. Figure 2 shows the representation of structural contours on the plane of observation and the grid system. The function H has dependent variables of x and y, where H is structural height at each (x, y) location on a horizontal plane (z = 0), represented on a map by contour lines. Henderson (1960) and Muñoz-Espinoza (1968) described a comprehensive formula from which the second derivative of potential field or structural surface can be obtained; an outline of it follows.

The structural surface function H(x, y, z) is purported to satisfy Laplace's equation, and accordingly is treated

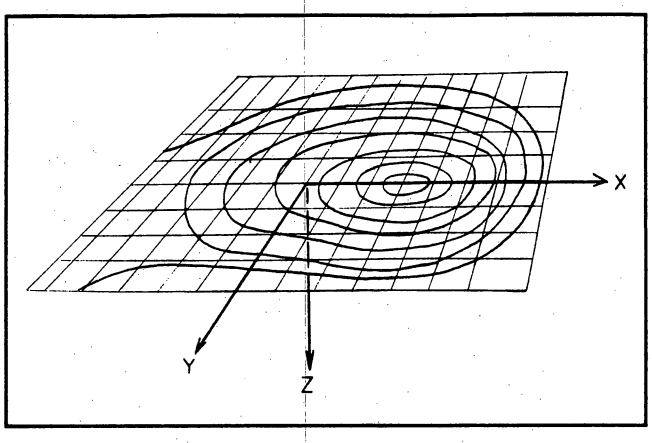

Figure 2. Representation of the structural surface as a contour and its grid system.

with the same methods as applied to potential fields. The usual continuation problem is to derive H(x, y, z), $\partial H/\partial z$, and $\partial^2 H/\partial z^2$ beyond the plane of observation (z = 0) with the interpolated boundary condition of structural height, H(x, y, 0). In mathematics, this problem is known as the first boundary problem (or Dirichlet problem).

The integral solution of the Dirichlet problem for a surface is used to compute H(z) at n points of interval "a" along the vertical line x = y = 0 above the plane. The integral in polar coordinates is

$$H(-ma) = \int_0^{\infty} \frac{ma\bar{H}(r)rdr}{(r^2+m^2a^2)^{3/2}} \quad m = 1, 2, \ldots . n , \qquad (9)$$

where

$$\bar{H}(r) = \frac{1}{2\pi}\int_0^{2\pi} H(r,\theta)\, d\theta$$

is the average value of H along a circle having a radius of r about the point. An equation accurately represents a structural surface at a certain point if there are a number of progressively larger concentric rings about the center point, with continuous data around each ring. Ten rings with radii r = 0, a, a√2, a√5, a√8, a√13, a√25, a√50, a√136, a√274, and a√625 are used to sample the field (Henderson, 1960). The number of mesh points falling on the circles having these radii is respectively 1, 4, 4, 8, 4, 8, 12, 12, 8, 8, and 12. Figure 3 shows the mesh points falling on the first seven rings, which are adequate to sample the field (Muñoz-Espinoza, 1968).

An approximation formula is obtained by employing the Lagrange interpolation,

$$H(z) \approx \sum_{m=0}^{n} \frac{(-1)^m z(z+a)(z+2a)\cdots(z+na)}{a^n(z+ma)(n-m)!m!} H(-ma) . \qquad (10)$$

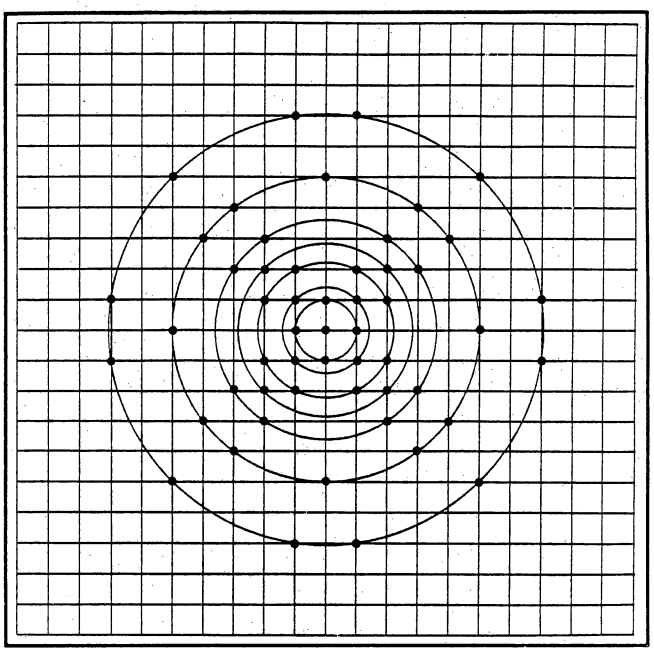

Figure 3. Mesh points of the grid falling on rings of radii 0, a, a√2, a√5, a√8, a√13, a√25, a√50, a√136, a√274, and a√625 (from Muñoz-Espinoza, 1968); "a" is the grid interval.

The values of the parameters "n" and "a" are unspecified. By applying the formula to a variety of theoretical and experimental data for which H(–ma) and H(z) were known, Henderson (1960) determined that satisfactory results were achieved with n = 5. The determination of mesh grid interval "a" depends upon the spacing of wells, lateral extent of the structure, and sharpness of structural feature. If "a" is too small, bull's-eyes are likely to develop; if "a" is too large, the coverage will be inadequate to delineate small features. The rule of thumb for selecting the grid interval is the "smallest feature" rule. That is, the smallest "nib" or feature must straddle at least two grid cells.

Derivative formulas can be obtained from the general expression by differentiation (Henderson, 1960). Differentiating H(z) with respect to z yields the second vertical derivative formula,

$$\left[\frac{\partial^2 H}{\partial z^2}\right]_{z=k} = \sum_{i=0}^{10} \bar{H}(r_i) \bullet D''(r_{i,k}) , \qquad (11)$$

where $\bar{H}(r_i)$ is the average value for H(r) on the circle with a radius of "r" at the point where the derivative is desired, and $D''(r_{i,k})$ is a set of coefficients which weight the center value and seven-ring average values, $\bar{H}(r_i)$ (table 1).

The second derivative calculation is carried out in two steps. First, the average structural height for individual rings is found from a gridded contour map. Next, the center node value and its associated ring-average values are multiplied by the appropriate

Table 1. Coefficients for calculating second derivative of a surface (from Henderson, 1960).

i	$H(r_i)$	$D''(r_{i,0})$
0	$H(0)$	2.82994
1	$H(a\sqrt{1})$	–2.49489
2	$H(a\sqrt{2})$	0.05173
3	$H(a\sqrt{5})$	–0.39446
4	$H(a\sqrt{8})$	0.00932
5	$H(a\sqrt{13})$	–0.00732
6	$H(a\sqrt{25})$	0.00304
7	$H(a\sqrt{50})$	0.00219
8	$H(a\sqrt{136})$	0.00040
9	$H(a\sqrt{274})$	0.00004
10	$H(a\sqrt{625})$	0.00000

coefficient $D''(r_{i,k})$, and the products are summed. A computer program "Deriv7" from Muñoz-Espinoza (1968) was modified to calculate the second derivatives. Because of the negative sign in Laplace's equation, concave-downward curvature is positive and concave-upward curvature is negative. Note that this sign convention is the *opposite* of the normal convention for second derivative curvatures.

Using the ring method to calculate curvature has several troubling flaws. First, the structural height of the bed is not a potential function. Indeed, if H is the vertical coordinate of the bed, it is a *dependent* variable of x and y, that is, H is uniquely determined at each (x, y) location. A potential field in space is a function of three *independent* variables. If (x, y, z) are locations on the bed's surface, then H = z. In this case, Laplace's equation is not satisfied because it would imply that

$$-\frac{d^2z}{dx^2}=\frac{d^2z}{dy^2}. \qquad (12)$$

Because the bed surface can be any arbitrary shape, there is no necessary relation between depth changes in the x and y directions. The second problem with using the ring method is that we are interested in calculating changes in bed depth with *lateral* changes, not a nonsensical change in depth with depth. The third problem relates to the practical use of the ring method: the spacings of the rings and their weighting factors are empirically calculated from functions which satisfy Laplace's equation, that is, potential functions. The applicability of these constants to other functions is debatable.

In spite of the problems with strictly applying the ring method to curvature calculation, that method may still have approximate validity. As Pirson (1977) correctly points out, we are interested in calculating the total porosity, which is related to the curvature in three dimensions by

$$\varphi=\frac{1}{2}T\left(\frac{d^2z}{dx^2}+\frac{d^2z}{dy^2}\right). \qquad (13)$$

The problem with Pirson's analysis is that he next uses Laplace's equation to equate j to the vertical derivative so that the ring method may be applied. However, as Dobrin (1976) demonstrates, the ring method actually is based on the second derivative of potential with x and y, which is then converted to the vertical second derivative using Laplace's equation. The restriction that the function describes a potential field is *only* made to relate those horizontal changes of a function to vertical changes through Laplace's equation, so the ring method fundamentally *does* describe the horizontal second derivatives of an *arbitrary* function. Therefore, the principles of the ring method are valid for bed curvature analysis. The only remaining problem is that the weighting factors have been calculated specifically for potential functions. As such, they are not strictly applicable to an arbitrary function describing the bed surface. The errors incurred by using the published weighting constants and ring spacing for curvature analysis have not been assessed. However, the method has been applied with some success (this report and Muñoz-Espinoza, 1968) so it appears to be at least approximately applicable.

The ring method requires data at evenly spaced gridpoints. Other methods of calculating the second derivative can be devised using these data. Field data are commonly subject to minor errors and some

amount of variability, or "noise," which only obscure the trends of interest. The ring method solves this problem by averaging on a number of rings covering a substantial area around the calculation point. Other common approaches to smoothing the data involve trend surfaces, finite difference equations, and Fourier transforms. Each method holds promise for extracting curvature information.

Trend Surface Method

If an actual polynomial equation (which graphs as a surface) can be found that represents the data, the curvature can be calculated by solving the second derivative equation at points of interest. Taking the derivative at a point on a three-dimensional surface is not as simple as on a two-dimensional curve. If the structural height of the bed, z, is considered a scalar function of x and y, that is z = z (x, y), then the first derivative of z is a *vector* given by

$$\text{grad } z = \nabla z = \frac{\partial z}{\partial x}\mathbf{i} + \frac{\partial z}{\partial y}\mathbf{j}, \qquad (14)$$

where **i** and **j** are unit vectors in the x and y directions. This vector has a direction and magnitude, so it is not straightforward to represent on a map. However, the "derivative" of a vector field is a scalar again, found by taking the divergence, or

$$\text{div (grad } z) = \nabla^2 z = \frac{\partial^2 z}{\partial x^2} + \frac{\partial^2 z}{\partial y^2}. \qquad (15)$$

This quantity corresponds to the derivative term in the porosity equation (Murray, 1968; Pirson, 1977), and can be easily calculated from the equation for a polynomial surface. Note also that $-\nabla^2 z = d^2H/dz^2$ from the ring method, underscoring the similar fundamental formulas for curvature in both methods and accounting for the sign difference between them. Differences in computed values arise from how those values are actually calculated.

Statistically fitting a polynomial surface, or trend surface, to the data is a common means of smoothing data, identifying trends, or removing regional effects that are not of interest (for example, Davis, 1986). Changing the order of the polynomial results in different degrees of smoothing. Once a balance is obtained between filtering out noise and revealing significant detail, the second derivative of the polynomial function may be taken at any point. In this study we fitted high-order (from 3 to 28) polynomial equations to the structural surface with the aid of computer mapping software (PCMS by Zycor; CPS-1 and CPS-PC by Radian*). This method successfully separates regional structures from local, "residual" structures. If regional production trends are of interest, the trend surfaces are useful for identifying regional curvature variations. Although a polynomial equation represents the trend surface, the coefficients of the equation were not directly available in the software we used (other versions offer this option). Therefore, we could not analytically calculate the second derivative of the equation (the approximate curvature) at points on a structure. The surface must be gridded, then analyzed by either the ring or the direct method, which introduces a dependency on the gridding method.

Direct Method

As in the ring method, a right-handed system of coordinates was adopted in which the origin is taken at each grid node and the z axis is taken with positive vertically upward. An even-spaced grid system with a mesh interval of "a," where "a" is a specified distance appropriate to the area of interest, was laid on the structure map. Figure 2 shows the representation of the structural contour on the plane of observation and the grid system.

The direct method calculates the second derivative of a point on a structural surface by means of its partial derivatives with respect to x and y. An equation for the actual surface is not explicitly found. The finite difference equation was used to approximate the partial derivatives,

$$\frac{\partial^2 z(x_i, y_j)}{\partial x^2} = \frac{(z_{i,j+1} + z_{i,j-1} - 2z_{i,j})}{\Delta x^2}$$

and

$$\frac{\partial^2 z(x_i, y_j)}{\partial y^2} = \frac{(z_{i-1,j} + z_{i+1,j} - 2z_{i,j})}{\Delta y^2}, \qquad (16)$$

where $z(x_i, y_j)$ is the structural height at point (x_i, y_j).

$$\frac{\partial^2 z(x_i, y_j)}{\partial x^2} \text{ and } \frac{\partial^2 z(x_i, y_j)}{\partial y^2}$$

are second partial derivatives with respect to x and y, and Δx and Δy are the grid intervals for the grid system. Mathematically, the second derivative, $\nabla^2 z$, of $z(x_i, y_j)$ is defined as above, where

$$\nabla^2 z(x_i, y_j) = \left[\frac{\partial^2 z(x_i, y_j)}{\partial y^2} + \frac{\partial^2 z(x_i, y_j)}{\partial x^2}\right]. \qquad (17)$$

The scalar nature of this quantity gives a single number for the curvature at each location on the data surface. Positive values indicate concave-upward curvature; conversely, negative values indicate concave-downward curvature. The magnitude of the value indicates the "tightness" of the curvature. A zero value indicates a flat data surface *or* a saddle point in the surface where the opposite directions of curvature cancel out. In the latter case, the second derivative may not identify areas

*The use of firm and brand names in this report is for identification purposes only and does not constitute endorsement by the Gas Research Institute or the Bureau of Economic Geology.

of rock that are likely fractured because of opposite vertical curvature in different horizontal directions, for example, concave up in an eastern direction and concave down in a northern direction.

Some computer packages (for example, CPS-1) use finite differences in other ways to calculate the second derivative. In this case, the second derivative is a gradient **vector**, $\nabla^2 z(x_i, y_j)$, where

$$\nabla^2 z(x_i, y_j) = \left[\frac{\partial^2 z(x_i, y_j)}{\partial y^2}, \frac{\partial^2 z(x_i, y_j)}{\partial x^2}\right] \qquad (18)$$

(note the second partial derivatives are x and y components of the vector rather than added to form a scalar). This vector consists of the direction on the xy plane and the magnitude of the vector:

$$\text{direction of } \nabla^2 z(x_i, y_j) = \tan^{-1}\left[\frac{\partial^2 z(x_i, y_j)}{\partial y^2} \Big/ \frac{\partial^2 z(x_i, y_j)}{\partial x^2}\right]$$

and

$$\text{magnitude of } \nabla^2 z(x_i, y_j) = \sqrt{\left(\frac{\partial^2 z(x_i, y_j)}{\partial x^2}\right)^2 + \left(\frac{\partial^2 z(x_i, y_j)}{\partial y^2}\right)^2}, \qquad (19)$$

where magnitude of $\nabla^2 z(x_i, y_j)$ is the "curvature" of the surface at point (x_i, y_j) in the specified direction. A curvature contour map generated by CPS-1 with this method shows high mean curvature magnitude and large mean curvature change, but it has two drawbacks. First, the arithmetic sign (positive or negative) of the partial derivative is lost during calculation of the magnitude; the map shows the magnitude only as a combination of absolute values of the second derivative components across the structure. The second problem with this method is that the second partial derivatives are based solely on three-point differential approximation with data along x and y axes, ignoring other data around that point on the surface. The end result is that artificial trends appeared along the x and y axial directions, causing localized bull's-eyes on the curvature map.

Fourier Transform

An alternative approach to the second derivative method also identifies areas where the dip of the bed changes rapidly. Bed structure data defined on a grid can be transformed with a discrete Fourier transform (for example, Dobrin and Savit, 1988). This transform approximates the bed surface with a set of sine and cosine terms, roughly corresponding to waves of different wavelengths. Each wave is weighted differently so that the set approximates the surface form. The advantage of transforming the data is the ease with which certain wavelengths, or ranges of wavelengths, can be deleted before transforming the data back to the standard domain. By removing long wavelength terms, regional trends and low curvature are filtered from the data, leaving only short wavelength terms. The transformed short wavelength terms will result in a map depicting areas of high curvature, somewhat analogous to removing a low order trend surface from the observed data. High frequency "noise" can also be filtered out if it is not judged to indicate significant structure. If curvature in a certain direction is not significant, for example, compaction-created folds over topographic variations with a directional "grain," then a directional filter may be applied to the transformed data to suppress curvature in that direction.

Assumptions Used and Limitations of the Method

As quickly becomes obvious in the derivation of the relation of fracturing to bed curvature, many assumptions are required to simplify the results into a useful form. The methods summarized above should be applied only when the conditions roughly satisfy the various assumptions.

The major assumption of the theory is that bending of a bed induces brittle failure expressed as one family of evenly spaced fractures in a single orientation (two orientations in three dimensions). An increase of curvature causes an increase in stress and strain, and fractures only appear when the bending-induced stress exceeds the tensile strength of the rock. Further bending opens the fractures more but does not produce any new fractures. The neutral surface of the bed coincides with the inner arc of the fold, implying that folding only results in effective tensile stresses throughout the bed. The validity of these assumptions is questionable in many cases. It is debatable whether fractures form in only one orientation. Coincidence of the neutral surface with the inner surface of the fold requires a particular type of loading. This situation, leading to tension throughout the bed, should be relatively rare, particularly when lateral compression causes buckle folding. Lacking a general, comprehensive theory of how fractures form and propagate in a brittle bed subjected to bending, the departure from realism by the assumptions used here cannot be evaluated, particularly when the cause of the bending cannot be specified. However, there *is* good qualitative evidence that some fractures form on the outer arcs of folded brittle beds in the orientations expected, so that there is little doubt that an increase in bed curvature causes some increase in fracture intensity or opening. How this fracturing quantitatively relates to permeability is only suggested by the above analysis.

Given the assumptions about the formation of the fractures, the assumptions used in deriving the fracture porosity are not difficult to meet. The major assumptions are that the bed's curvature is small relative to its thickness and, similarly, that the dips of the bed are small. Fractures formed are assumed to be close together relative to the curvature, so that the angular divergence between fracture faces is small and the intact rock between them approximates an arc. Small dips in absolute terms are required to equate the second derivative with the curvature. This implies that if there is a large regional dip induced by tilting, it should be removed (mathematically of course) before analyzing curvature variations superimposed on it.

Relating the fracture porosity to permeability requires a model of fluid flow that may not strictly apply. Flow through a porous media described by Darcy's law requires that the flow passages, or fractures, be closely spaced relative to the scale of the media. With sedimentary rocks, the fracture spacing must be small relative to the layer thickness. This requirement may explain why Murray (1968, p. 61) found that "wider spacing [greater than 6 inches] leads to unreasonably large values of calculated permeability" in a bed with a thickness of 5 to 10 ft (2 to 3 m). Choice of a single value for the fracture spacing may be a difficult task, particularly if the fractures have a fractal distribution. If there is doubt about the fracture spacing value or if the spacing varies with curvature, the curvature analysis can still be used to indicate areas of *relatively* high permeability, which is useful if the absolute permeability can be measured in a few places in the study area. Similarly, the fracture spacing can be measured in areas of known permeability and curvature to construct an empirical relation similar to the permeability equation, which could be used elsewhere to predict permeability from curvature and thickness information.

Test of the Curvature Method

To evaluate the utility of curvature analysis for predicating fracture density, we analyzed three methods of determining the second derivative of a surface to discover their strengths and limitations. Two of the three methods were applied to idealized structural models and to structure of a Fruitland Formation coal bed at Cedar Hill field. The maps resulting from curvature analysis were compared with coalbed methane production.

Three idealized structure maps, prepared for testing the second derivative ring and direct methods, portray structures that resemble features in the San Juan Basin. Curvature of a coal seam in the Cedar Hill field was analyzed using an actual structure map of the base of the basal Fruitland coal seam.

There are several requirements for use of the curvature methods. First, a good structure map is needed. Second, the interpolation of structural height at each grid point must be performed flawlessly, so that the grid can truly represent the structure. And finally, the grid system must extend beyond the area of interest so that the derivatives near the boundary will be valid when calculations reach out seven rings from the grid point.

Idealized Structures

The ring method was applied first to a simple plunging noncylindrical anticline (nose) structure with variable fold magnitude (fig. 4a). Such structures are common in the San Juan Basin. The curvature map (fig. 4b) exhibits high contour values along the structural axis that conforms to the shape of the nose. Areas of high curvature are not distributed uniformly along the axis of the nose; instead, they are in discrete patches along the trace of the contour lines. This distribution is an artifact of the method of gridding the structure-contour map. The grid spacing is smaller than the horizontal contour separation; therefore, several grid points lie between each contour. Although the software does some smoothing, the slope of the gridded surface is approximately constant between contours, with relatively sharp slope changes at the contour locations. The ring method correctly identifies the local high curvature along the contours. The curvature map generated therefore depends strongly on the gridding algorithm used and the grid spacing relative to the contour spacing.

The plunging anticline pattern differs from those associated with simple open folds of nonuniform plunge (fig. 5a) or cylindrical plunging syncline/anticline pairs (fig. 6a). The curvature map made by the ring method shows positive and negative curvatures associated with anticlines and synclines, and positive and negative plunge culminations (figs. 5b and 6b). The patchiness and zigzags of the curvature contour lines on these maps belies the grid system derived from the original smooth surface. The direct method of calculating the second derivative was also applied to the plunging syncline/anticline map. The results are virtually identical to those of the ring method (fig 6c). Here positive and negative curvatures are associated with synclines and anticlines, respectively. Because the direct method relies on finite differences between grid point values, it shows a similar dependency on the gridding method.

Structures in Cedar Hill Field

The structure map of lower Fruitland coal seam was hand drawn using data from 96 wells in the Cedar Hill field and surrounding area. The contour map was digitized and the structure grid was interpolated with computer mapping software (PCMS). Valid application

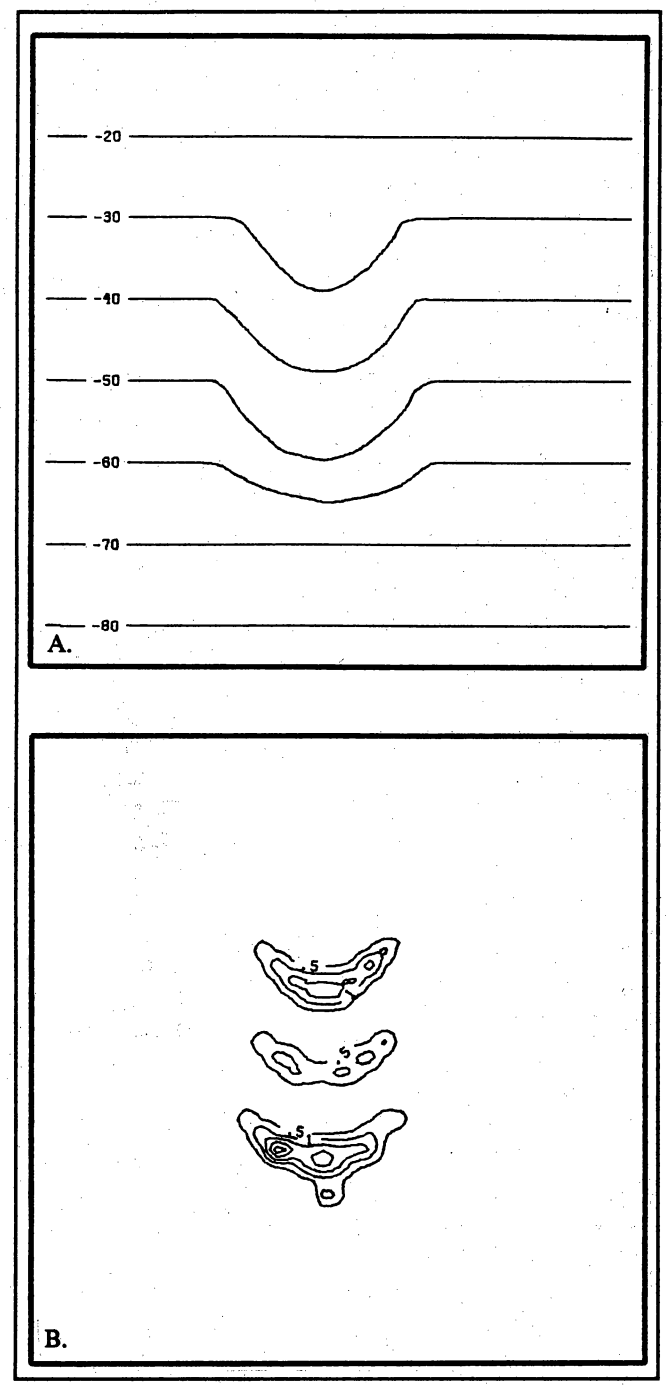

Figure 4. Structure (a) and curvature (b) contour maps for a simplified plunging anticline structure.

of the method requires a grid system that is representative of the structure. Satisfactory results were achieved after several attempts by adjusting the size of the grid interval "a," the smoothing coefficients, and editing the grid (fig. 7) . The ring method curvature of the structure was then calculated from the grid with a FORTRAN

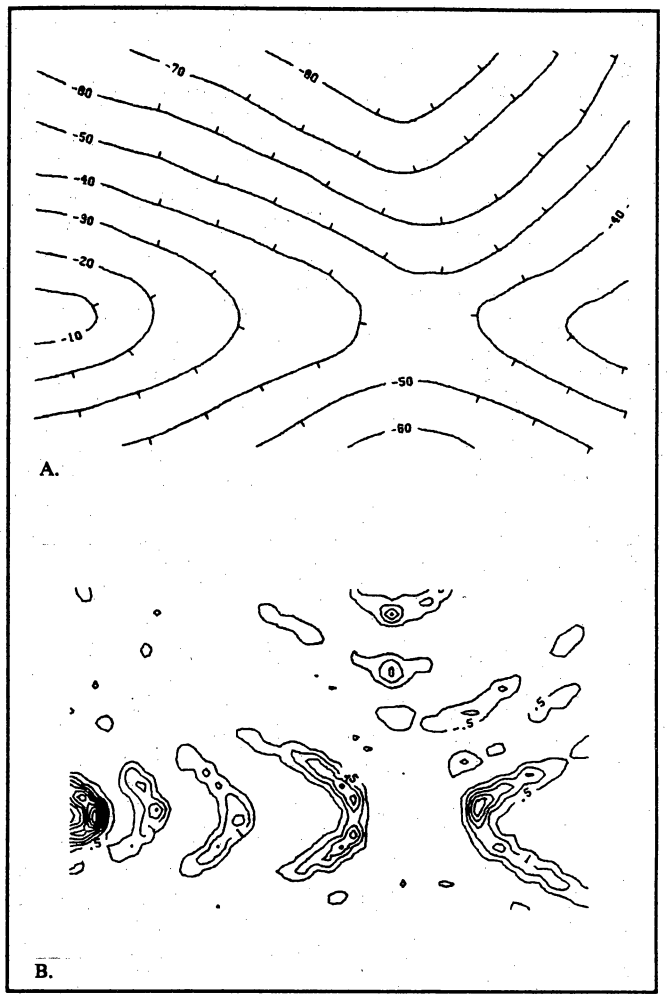

Figure 5. Structure (a) and curvature (b) maps for a fold with nonuniform plunge.

program (Deriv7). The curvature maps highlight the positive and negative curvatures of the lower Fruitland coal bed (figs. 8 and 9). Results using the direct method are similar, but with the signs reversed.

Publicly available gas production data (maximum annual gas production, where maximum annual production is greatest annual production normalized to Mcf/d) show an eastward-trending zone of high production subparallel to the structural axis of the Cedar Hill field (fig. 10). Part of the area with highly productive wells corresponds to areas that have moderate to high curvature, but many areas that are indicated to have high curvature are in less productive areas. Conversely, anomalously high production values in the east central part of the map do not fall in areas of high curvature. Most of the high curvatures correspond to local structures and generally are not indicative of high production. These results show that, for these maps,

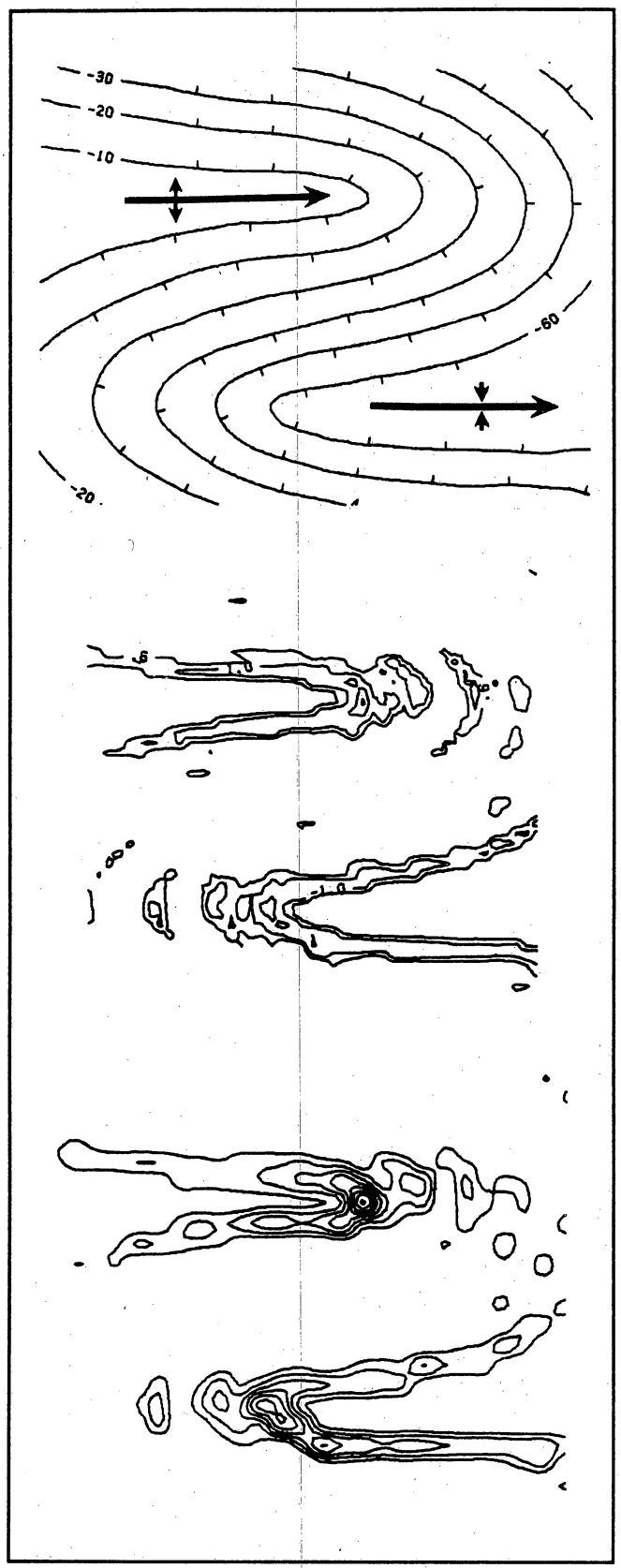

Figure 6. Structure map (a) and curvature maps calculated with the ring method (b) and direct method (c) for a plunging anticline and syncline pair.

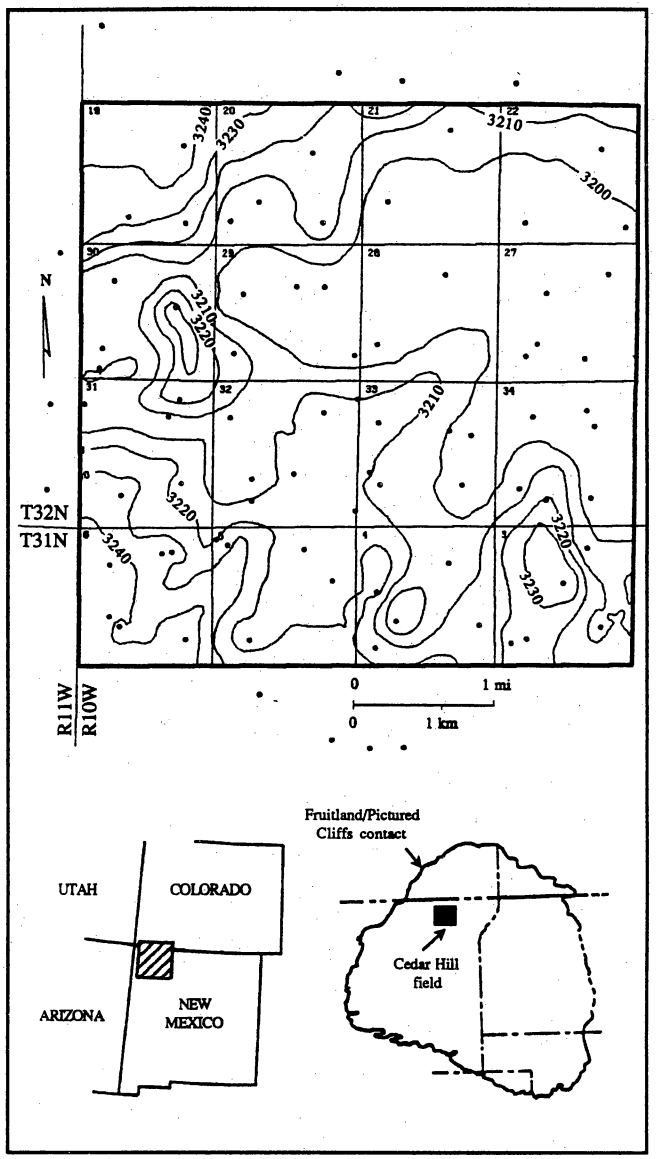

Figure 7. Structure map of the base of the basal Fruitland coal seam at Cedar Hill field, showing well control. Contour interval is 10 ft (~3 m).

the areas of highest curvature are not good guides to highly productive areas, but areas of more widespread moderate curvature may be predictors of production. Such maps may be useful, in conjunction with information on other geologic factors as well as completion techniques and production history, for assessment of coalbed methane production patterns.

A trend surface fitted to the structure map shows a more consistent correlation with the production pattern. Figure 11a shows a 28th-order polynomial surface calculated for the Fruitland coalbed structure map. The regional structure highlighted by this technique is an

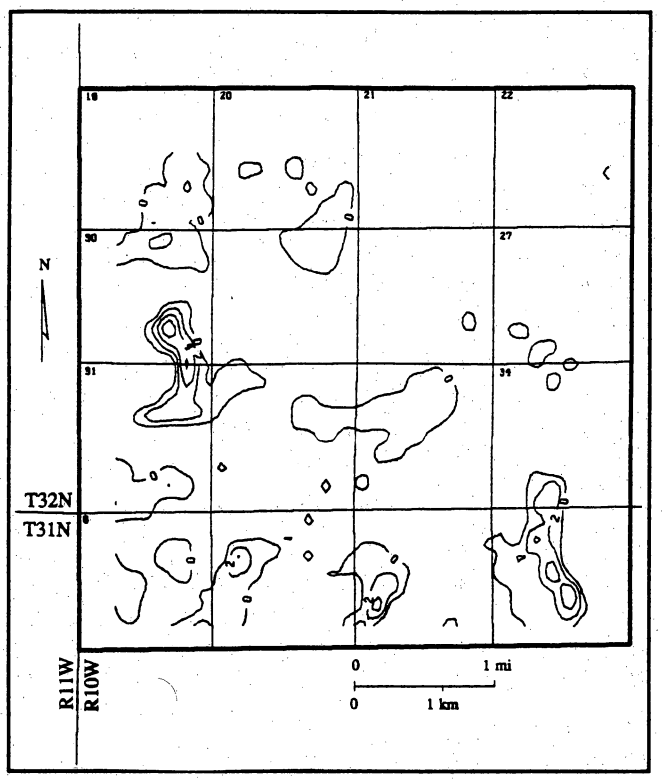

Figure 8. Positive curvature contour map of the base of the basal Fruitland coal seam at Cedar Hill field (fig. 7). Contour interval is 0.5×10^{-5}/ft curvature unit.

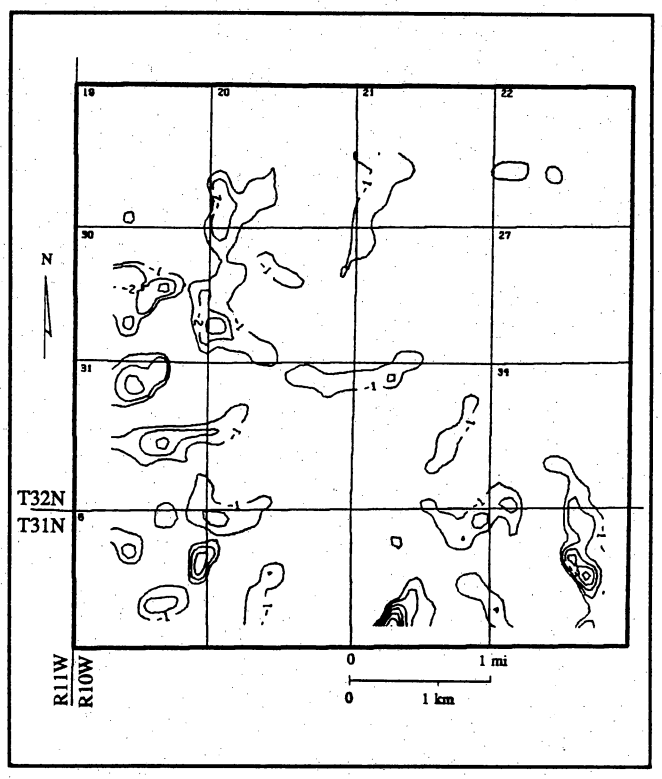

Figure 9. Negative curvature contour map of the base of the basal Fruitland coal seam at Cedar Hill field (fig. 7). Contour interval is 0.5×10^{-5}/ft curvature unit.

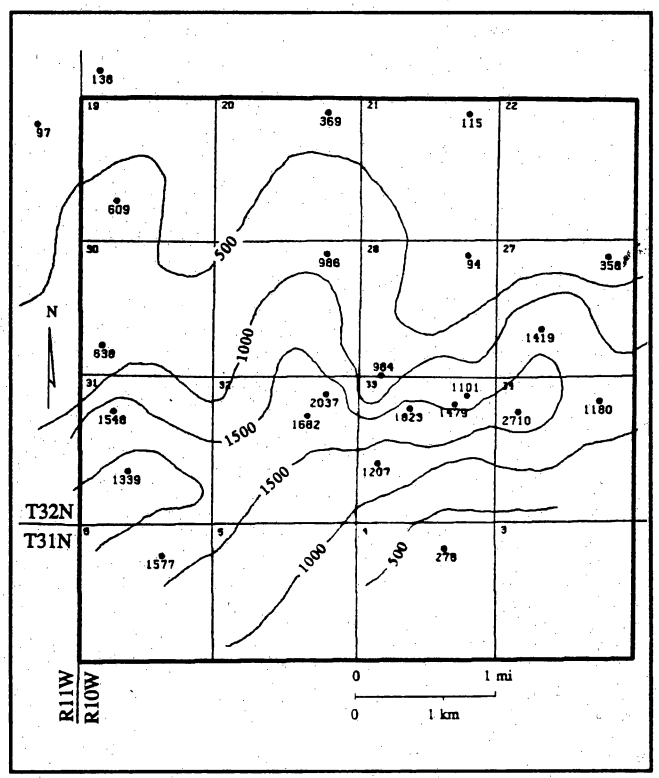

Figure 10. Maximum annual gas production in Cedar Hill field. Gas production has been normalized to per day basis (Mcf/d).

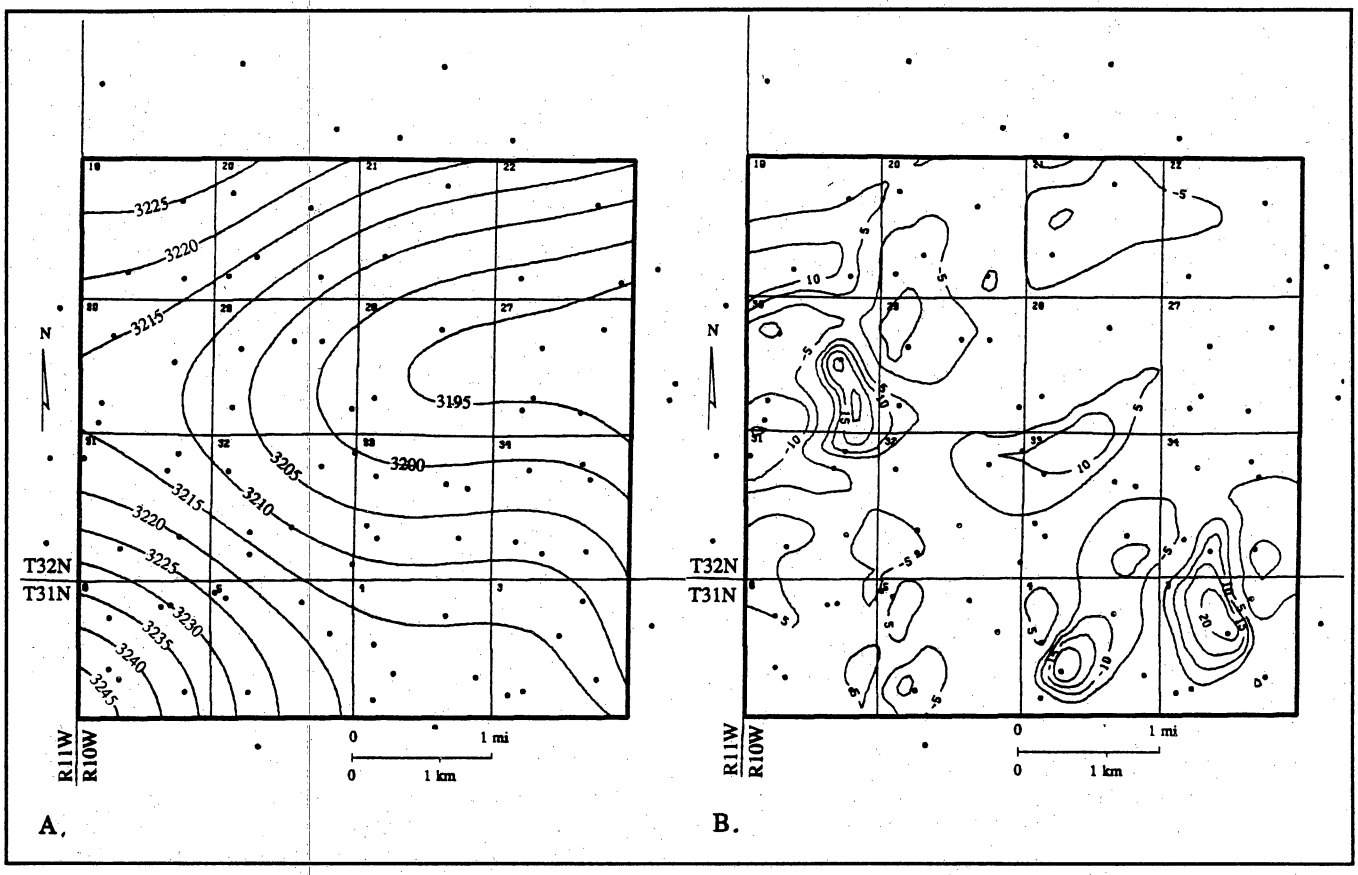

Figure 11. Contoured 28th-order trend surface (a) and residual surface (b) calculated for the structure map of the basal Fruitland coal seam (fig. 7).

eastward-plunging syncline across the middle of the area. The axis of this fold closely follows the zone of high gas production (fig. 10). The residual structures, or deviations of the actual data from the trend surface, are plotted in figure 11b. Many of these local structures correspond to highs on the curvature maps (figs. 8 and 9), emphasizing the sensitivity of the curvature method to local structural variations. Curvature calculated from the trend surface data showed a haphazard distribution of very low curvature contours. Experimenting with the grid method and grid spacing may improve the identification of high curvature areas of the trend surface, which appear to correlate well with high gas production zones of the Cedar Hill field. Alternatively, implementation of a method that allows direct calculation of the second derivative from the polynomial coefficients of the trend surface should avoid the artifacts introduced by the gridding and ring or finite difference steps.

Conclusions

Bed curvature methods for predicting fracture permeability have certain theoretical and practical limitations that need to be appreciated for valid use of the technique. The application of computerized mapping, trend surface, and curvature-calculation techniques to the Cedar Hill field identifies areas of high bed curvature and predicted high permeability. These areas appear to correlate well with high gas production zones.

Hydrology, Thermal Maturity, and Gas Composition

Hydrology of the Fruitland Formation, San Juan Basin

W. R. Kaiser, T. E. Swartz, and G. J. Hawkins

Abstract

Hydrology of the Upper Cretaceous Fruitland Formation was evaluated from its potentiometric surface, pressure regime, and hydrochemistry and through numerical ground-water modeling. The Fruitland Formation receives recharge mainly from the elevated, wet, northern and northwestern margins of the basin, where aquifer coal seams crop out. Regionally, the Fruitland Formation is a single hydrologic unit. Compartmentalization is indicated locally by large vertical and lateral pressure gradients. Abnormal pressuring requires permeability contrasts in the Fruitland and is explained hydrodynamically; overpressuring is artesian in origin. Underpressuring endures because discharge exceeds recharge and the two areas are hydraulically separated. Fruitland formation waters reflect their hydrologic setting. Na-HCO_3 waters coincide with overpressure and Na-Cl waters with underpressure. These waters are meteoric in origin and HCO_3^- is mainly of bacterial origin. Fruitland hydrodynamics were simulated in a regional, cross-sectional, ground-water model by reflecting regional permeability contrasts. Enhanced permeability is inferred from gentle hydraulic gradients, overpressuring, and low-chloride formation waters.

Introduction

Little is known about the hydrology of coal basins and its relation to the producibility of coalbed methane. Locally its significance is evident in the need to dewater (depressure) some coal seams to stimulate gas desorption for commercial production. However, beyond this correlation, few associations have been established between the regional hydrologic setting and methane producibility. Lacking knowledge of ground-water circulation and hydrochemistry, we can say little about favorability of production in recharge or discharge areas or its association with potentiometric anomalies. Moreover, the relative importance of unconventional and conventional structural/stratigraphic trapping remains clouded without a hydrologic framework and understanding of the pressure regime. Thus, the objective of this study was to establish the Fruitland Formation's hydrologic setting for subsequent evaluation of its role in the producibility of coalbed methane.

Fluid dynamics and trapping mechanisms in coal seams are poorly understood. Decker and Horner (1987) suggested that overpressured coal beds have better deliverabilities and are preferred exploration targets, overlooking sustained production from underpressured coal beds. They contended that overpressure is relict, a product of earlier compaction, dewatering, and reservoir isolation. However, we conclude that overpressuring and trapping mechanisms in the Fruitland Formation can alternatively be explained, as proposed here, in the context of the regional hydrology and hydrodynamics. Furthermore, Decker and others (1987) concluded that bicarbonate-rich water in coal seams indicate reservoir isolation and the presence of fresh connate water. In contrast, our study indicates that low-chloride water reflects active ground-water circulation and the presence of meteoric water and is an indicator of enhanced permeability.

Whether hydrologic parameters such as fluid flow, pressure regime, and chemical composition of formation waters are important controls of methane producibility or simply indicators of permeability has not been previously established. To evaluate these parameters in the San Juan Basin, we made (1) regional Fruitland potentiometric-surface, pressure-gradient, and bottom-hole pressure (BHP) maps using shut-in pressures (SIP) recorded in drill-stem tests (DST) and bottom-hole pressures (BHP) calculated from wellhead SIP's (WHSIP), (2) pressure-elevation and pressure-depth plots, (3) Piper (trilinear) and Stiff ionic-ratio diagrams and histograms of Fruitland formation waters, and (4) a Fruitland chlorinity map. The ground-water flow system was further conceptualized in numerical modeling.

A discussion of the elements of Fruitland hydrodynamics (hydraulic head, pressure regime, and hydrochemistry) is followed by examination of hydrostratigraphy and regional ground-water flow. Hydrodynamic elements are used to define components of the Fruitland–Pictured Cliffs aquifer system and the degree of hydraulic communication between coal beds and sandstones. Abnormal formation pressure and the origin of overpressuring in the Fruitland are explained hydrodynamically. Lastly, our assumptions about ground-water flow in the San Juan Basin were tested in a regional cross-sectional model.

In Ayers, W. B., Jr., and others, 1991, Geologic and hydrologic controls on the occurrence and producibility of coalbed methane, Fruitland Formation, San Juan Basin: The University of Texas at Austin, Bureau of Economic Geology, topical report prepared for the Gas Research Institute under contract no. 5087-214-1544 (GRI-91/0072), p. 195–241.

Hydrodynamics

The hydrodynamics of the Fruitland Formation were established from its potentiometric surface, formation fluid pressure, and hydrochemistry. A potentiometric-surface map shows hydraulic head in a confined aquifer. Hydraulic head is the height above mean sea level (msl) to which the fluid column freely stands, or rises, and is the sum of the elevation head and pressure heads (Freeze and Cherry, 1979). Elevation head is the distance from msl to the point where the pressure head is determined from the fluid pressure. Data used to prepare the potentiometric-surface map were approximately 250 wellhead shut-in pressures (WHSIP), 50 SIP's recorded in drill-stem tests (DST), and 10 BHP's measured or extrapolated in well tests. Static water levels (approximately 30) along the northern and southern margins of the basin and outcrop elevations of perennial streams at the northern margin were used to map the Fruitland water table.

Static BHP equals the sum of the surface pressure, gas-column pressure, and liquid-column pressure; its estimation from WHSIP's involves calculating the additive pressure exerted by the weight of the static fluid column. In this study, BHP's were calculated using the Cullender and Smith (1956) method, the most accurate method for calculating BHP's in dry-gas wells. To accommodate water production, we modified Cullender and Smith's method by treating the gas-liquid system as a pseudohomogeneous mixture (Peffer, 1985; Peffer and others, 1986). Gas-compressibility factors (Z-factors) were calculated using Hall and Yarborough's equation of state, which accurately represents the Standing-Katz Z-factor chart for calculation of Z-factors as a function of pressure and temperature (Hall and Yarborough, 1973; Yarborough and Hall, 1974).

We tested our modified Cullender and Smith method on three wells in Cedar Hill field (Cahn 1, Schneider B 1S, and State BW 1) for which measured BHP's, WHSIP's, and associated production data were available. When average daily water and gas production were matched with the month of the well test, good agreement between measured and calculated BHP's was achieved (table 1). Absolute deviation (DP) from the measured BHP ranged from 9 to 92 psi; most calculated BHP's were within 9 to 60 psi of the measured value. The most difficult problem was matching appropriate WHSIP's with the corresponding production data. However, in most cases only surface pressures were available, and the calculated BHP's in effect represent those of dry-gas wells. Extremely high water productivities may cause calculated BHP's to be too high.

In a comparison of calculated BHP's and DST SIP's in the same well, absolute differences in pressure were as large as 151 psi (table 2). Typically, the DST SIP is higher than the calculated value. There is no single

Table 1. Comparison of calculated and measured BHP[a], Cedar Hill field.

Well	Water[b] bwpd	Gas[b] Mcf/d	WHSIP[c]	BHP calculated	BHP[d] measured	$\lvert\Delta P\rvert$[e]
Amoco	0	694	1,293	1,396	1,362	34
Schneider B 1S[f]	0	356	1,313	1,418	1,362	56
	83	661	1,208	1,371	1,362	11
Amoco	0	547	1,293	1,391	1,421	30
State BW 1	0	272	1,313	1,412	1,421	09
	44	784	1,208	1,329	1,421	92
Amoco	239	350	1,098	1,405	1,465	60
Cahn 1	207	738	1,258	1,494	1,465	29
	126	901	1,323	1,507	1,465	42
	120	976	1,323	1,498	1,465	33

[a] All pressures in psi.

[b] Average daily water and gas production for month of well test. Zero indicates no water reported, not necessarily that none was produced.

[c] Surface pressure on date of well test as reported by Amoco.

[d] BHP reported to NMOCD by Amoco June 8, 1983.

[e] Absolute pressure difference.

[f] BHP in well B 1S approximately 1,525 psi in 1979 prior to production (Amoco to NMOCD July 6, 1988).

Table 2. Comparison of calculated BHP and DST SIP[a].

Well	Location	BHP calculated	DST SIP	|ΔP| [b]
Bondad 3-8	8 33N 9W	1,367	1,365	02
Gallegos 1	12 33N 8W	1,439	1,525	86
Ute 1	36 33N 7W	1,249	1,370	121
Mesa 3-18	18 32N 7W	1,534	1,610	76
San Juan 32-5, 2	35 32N 5W	1,597	1,550	47
Northeast Blanco Unit 212	1 31N 7W	1,640	1,675	35
San Juan 29-4, 2	35 29N 4W	1,214	1,375	151

[a] All pressures in psi
[b] Absolute pressure difference

explanation for this, but it probably reflects such factors as pressure depletion caused by production, shut-in time, and unreported water production. Certainly the former is evident in the Schneider B 1S (table 1), where original reservoir pressure of approximately 1,525 psi declined to less than 1,400 psi upon production. In low-permeability strata such as the Fruitland, pressure equilibrium is attained slowly, if at all, and shut-in times probably were never long enough to achieve equilibrium. Thus, we classified DST's on shut-in time, using the highest pressure recorded, whether initial or final SIP. Approximately two-thirds of the DST shut-in times were between 30 and 60 min. WHSIP's were not classified because shut-in times were seldom recorded; rarely did they exceed 7 days. In general, most of the BHP's used here represent something less than original reservoir pressure.

Hydraulic Head

Equivalent Fresh-Water Head

BHP's were converted to pressure heads using a fresh-water hydrostatic gradient of 0.433 psi/ft and were combined with elevation heads to calculate equivalent fresh-water heads. Although equivalent fresh-water heads may be inexact because of variable density, they are commonly used for representing heads in aquifers containing fluid of varying density where the prime concern is lateral flow (Bair and others, 1985). Dealing with variable density is not a trivial matter and usually only done in modeling studies. One must consider the density of water in the formation at the sample point and the integrated density of all water in the formation at higher points on the potentiometric surface. Furthermore, as additional chemical analyses become available one may have to completely revise the map. The effect of increased salinity is to steepen the potentiometric surface basinward because saline water is denser and will not freely rise as high as fresh water. In the north-central part of the basin, formation waters are fresh to brackish and rarely exceed total dissolved solids (TDS) contents of 30,000 mg/L. In the south, waters are more saline, exceeding 35,000 mg/L in some cases, and the potentiometric surface actually may be somewhat steeper than shown in figure 1. For example, if BHP were 433 psi, equivalent fresh-water and seawater pressure heads would be 1,000 (305 m) and 975 ft (297 m), respectively.

The calculation of heads is also affected by the presence of a gas phase. The effect is negligible in coal seams prior to gas production, where water and gas reservoir pressure are approximately equal (McKee and others, 1987). Thus, BHP's measured early in the well history are representative of formation water pressure. Furthermore, available gas-water capillary pressure measurements in coal seams (Dabbous and others, 1976; Way and others, 1985) show low capillary pressures (<10 psi) at high water saturations, which usually exist initially in most coal seams. Free gas may also be present to contribute a buoyant force (the difference between hydrostatic and gas gradient). However, BHP's were not computed back to the gas/water contact either because there are no contacts or because data on such contacts were unavailable. Moreover, Fruitland sandstone gas reservoirs, where a buoyant force is most likely, are at most a few tens of feet thick and the corresponding gas caps would be thin. Hence, if the buoyant force is unaccounted for, only a small error (flattening of the potentiometric surface) would be introduced relative to the 200-ft (61-m) contour interval of figure 1. For example, the presence of a 50-ft (15-m) gas column would cause the head to be approximately 43 ft (13 m) too high. A 232-ft (71-m) gas column

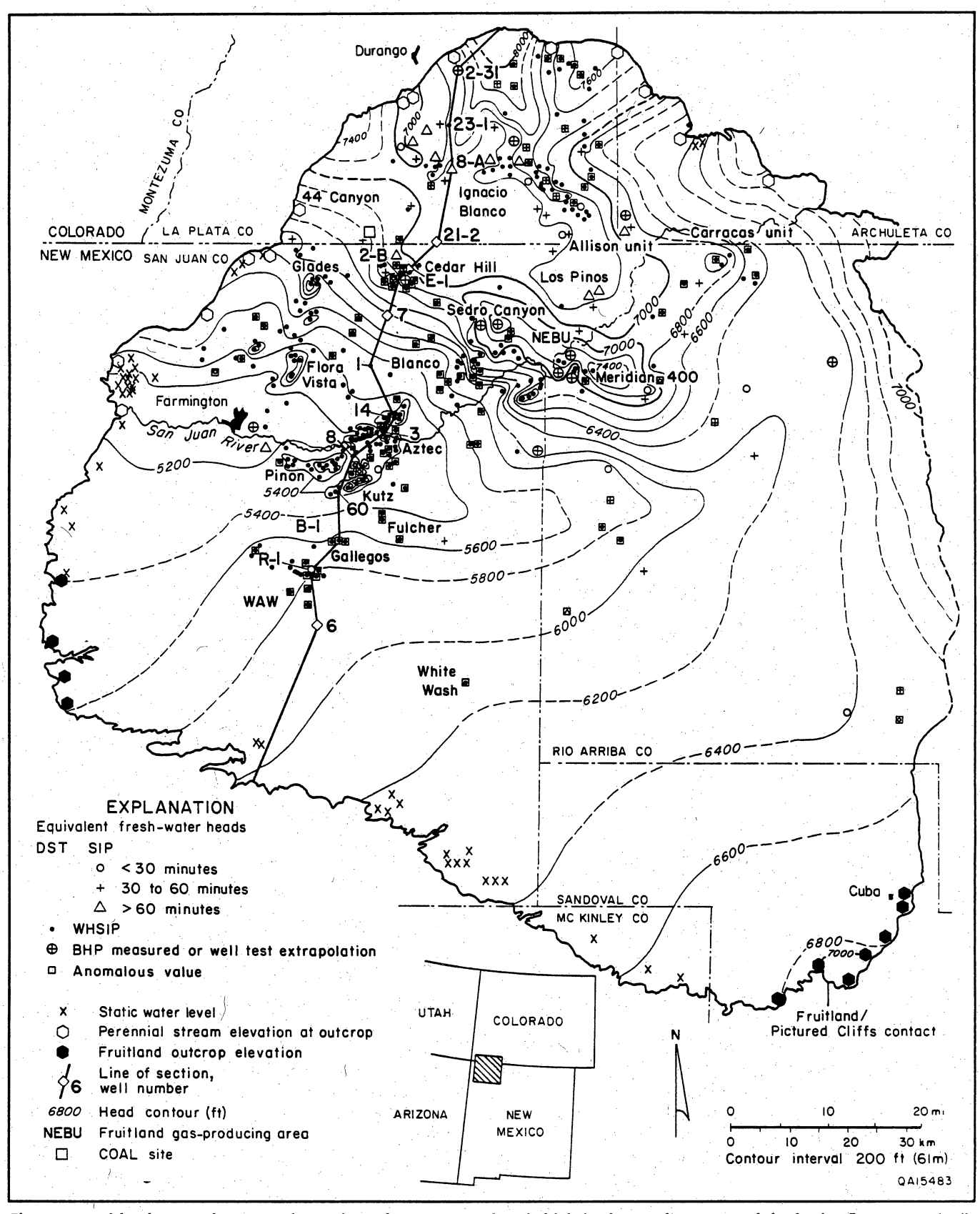

Figure 1. Fruitland Formation potentiometric-surface map. Surface is high in the northern part of the basin, flattens markedly basinward, and shows recharge is from the northern margin of the basin. Marked steepening of surface coincides with southwestward pinch-out of aquifer coal seams (see fig. 25).

would be required to introduce an error equal to the contour interval. Finally, if water is in transit through the sandstones, as implied by the potentiometric-surface map, then capillary pressures will be low (Berry, 1959) and BHP's will reflect formation water pressure.

Potentiometric Surface

A Fruitland potentiometric-surface map was made from equivalent fresh-water heads (fig. 1). The surface is high in the north-central part of the basin, flattens conspicuously basinward, and shows that recharge is at the elevated northern and northwestern margins of the basin (fig. 2) in the foothills of the San Juan Mountains, where numerous thick coal seams crop out in the wettest part of the basin (precipitation 20 to 30 inches/yr [51 to 76 cm/yr]). Recharge from the eastern margin is limited because (1) the Fruitland is absent along much of the margin (Ayers and others, this vol., their figs. 3 and 14) and where present is dominated by low-permeability, fine-grained rocks, (2) there is less annual precipitation (12 to 20 inches [30 to 51 cm/yr]), and (3) the continental divide lies within the basin, diverting potential recharge eastward out of the basin that would otherwise be available through leakage. Moreover, much of the recharge is captured by the overlying, high-permeability Ojo Alamo Formation (Ayers and others, this vol., their figs. 2, 3, and 4). Recharge from the southern and western margins of the basin also is limited, with annual precipitation being lower than it is on the east (4 to 12 inches/yr [10 to 30 cm/yr] versus 12 to 20 inches/yr [30 to 51 cm/yr]). Furthermore, the Fruitland–Pictured Cliffs outcrop along the southwestern margin of the basin is topographically lower than the basin interior (fig. 2) and lies just east and northeast of the Chaco River. Consequently, potential recharge to the unconfined Fruitland–Pictured Cliffs aquifer is diverted westward out of the basin as discharge to the Chaco River and its tributaries and is thus unavailable as recharge basinward to the confined aquifer system. This is demonstrated on the southern margin, where saline springs issue from Fruitland coal seams in topographically low areas associated with tributaries of the Chaco River. Widely spaced head contours in the southeastern part of the basin reflect limited recharge from the southern margin of the basin and reduced fluxes in low-permeability strata, whereas widely spaced contours in the San Juan River valley reflect discharge (upward flow) to the river.

Potentiometric Mounds

Topography, elevation of completion intervals, presence of free gas, and cross-formational flow were examined to explain potentiometric mounds at Sedro Canyon, Meridian 400, Aztec, Kutz, Pinon, Flora Vista, and Glades areas (figs. 1 and 2). Potential for upward flow was determined from the vertical pressure gradient, or slope of the line established by plotting BHP versus elevation above mean sea level (msl). The largest mounds are in the Sedro Canyon–Meridian 400 area (SC-M) and the Aztec-Kutz-Pinon area (A-K-P) (figs. 1 and 2). The mound in the SC-M area trends northwest-southeast as a continuous potentiometric ridge 25 mi (40 km) long, as defined by the 7,000-ft (2,134-m) head contour, and mounds in the A-K-P area trend northeast-southwest and east-west for 4 to 8 mi (6.4 to 13 km). These mounds probably do not represent recharge mounds (downward flow) because there is no apparent source for the recharge. The SC-M area is well basinward and unassociated with any topographic highs. In fact, topography is higher northwest of SC-M and elevations of test intervals at SC-M are lower than those to the southwest, proving that elevation head cannot explain the high heads at SC-M. On the other hand, A-K-P is located in the San Juan River valley, the regional discharge area where upward flow is expected. Some A-K-P wells are slightly overpressured and located mainly along the San Juan River. Overpressuring in these wells is explained hydrodynamically as evidence for upward flow.

The presence of free gas causes heads to be higher, which may contribute to the potentiometric anomalies, particularly at A-K-P, where gas is conventionally trapped in sandstone reservoirs. However, free gas is not the main contributory factor. Gas columns that are many times the thickness of sandstone reservoirs at A-K-P would be required to account for these anomalies. At SC-M, the presence of gas has a negligible effect on heads as water and gas reservoir pressures are approximately equal.

The alternative explanation for potentiometric mounds at SC-M and A-K-P, having eliminated recharge, topography, and buoyant force as primary causes, is that they indicate areas of upward flow. Pressure-elevation (msl) plots for SC-M and A-K-P show vertical pressure gradients of approximately 0.80 psi/ft, indicating a very strong potential for upward flow (figs. 3 and 4). The large vertical pressure gradients imply that the Fruitland strata are not well interconnected vertically and that a large driving force is needed to move fluid vertically. Shale interbeds and abundant tonsteins limit vertical connectivity between and within coal seams, contributing to reservoir compartmentalization.

The SC-M area is thought to represent a pressure ridge coinciding with upward ground-water flow caused by pinch-out of thick, laterally continuous coal seams (aquifers) in the area and possible offset by faulting along the basin's structural hingeline (Ayers and Zellers, this vol.). Wells in the SC-M area are overpressured and have the highest reported Fruitland bottom-hole temperatures (up to 140°F [60°C]). Aquifer coal seams transmit ground water from the northern and northwestern margins of the basin under high pressure; upon

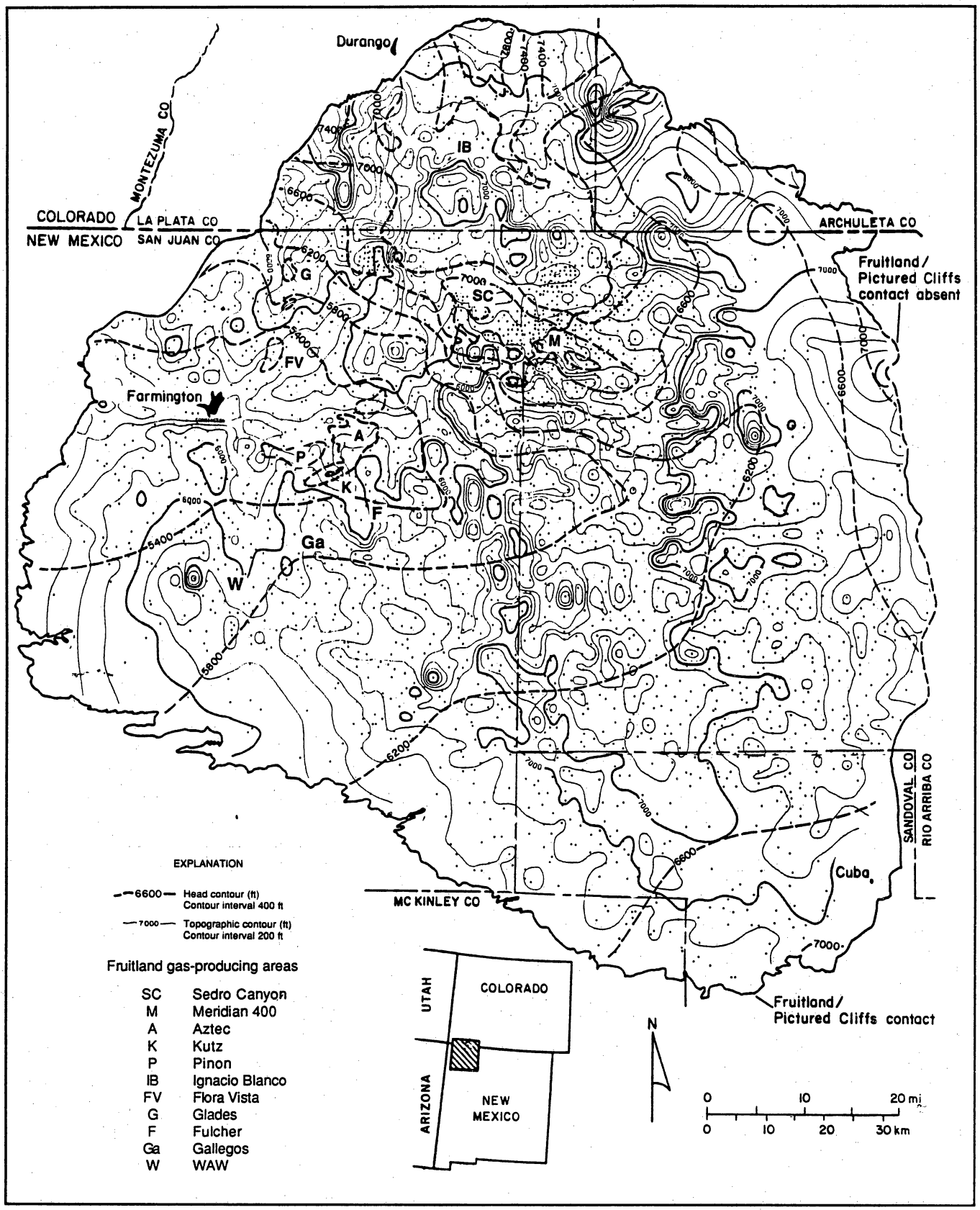

Figure 2. Fruitland Formation potentiometric-surface map and topographic map of land surface, San Juan Basin (from Kaiser and Swartz, 1990).

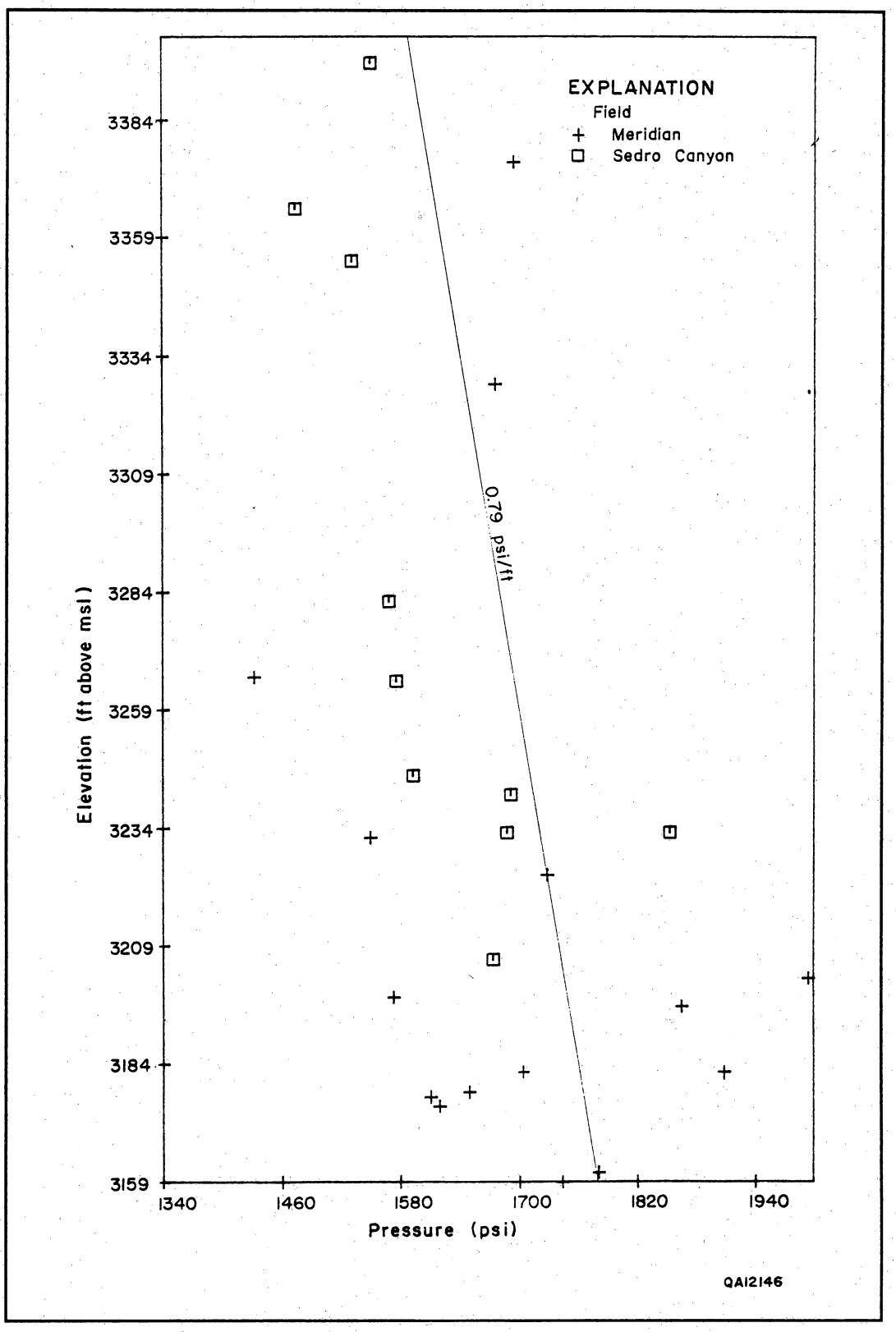

Figure 3. Fruitland Formation pressure-elevation plot, Sedro Canyon–Meridian 400 area (from Kaiser and Swartz, 1990). See figure 1 for area location. Vertical pressure gradient (~0.79 psi/ft) is the slope of the trend line and is much larger than the hydrostatic pressure gradient (0.433 psi/ft), which indicates strong potential for upward flow. Large vertical pressure gradient indicates reservoir heterogeneity and low vertical permeability. Large lateral pressure gradient (note wide pressure range at 3,184 ft [970 m]) also indicates reservoir heterogeneity.

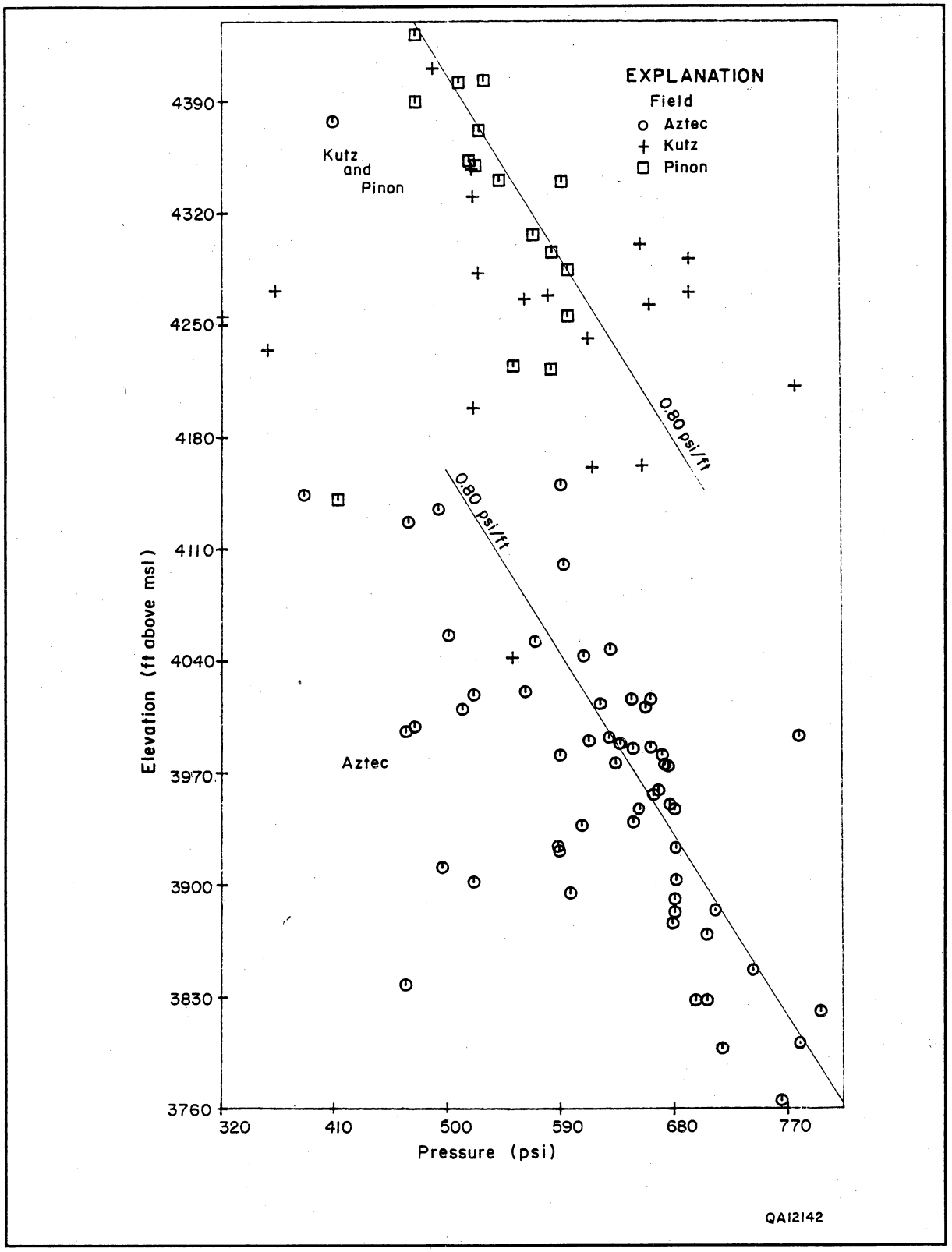

Figure 4. Fruitland Formation pressure-elevation plot, Aztec-Kutz-Pinon area (from Kaiser and Swartz, 1990). See figure 1 for area location. Vertical pressure gradient (~0.80 psi/ft) is the slope of the trend line and shows strong potential for upward flow.

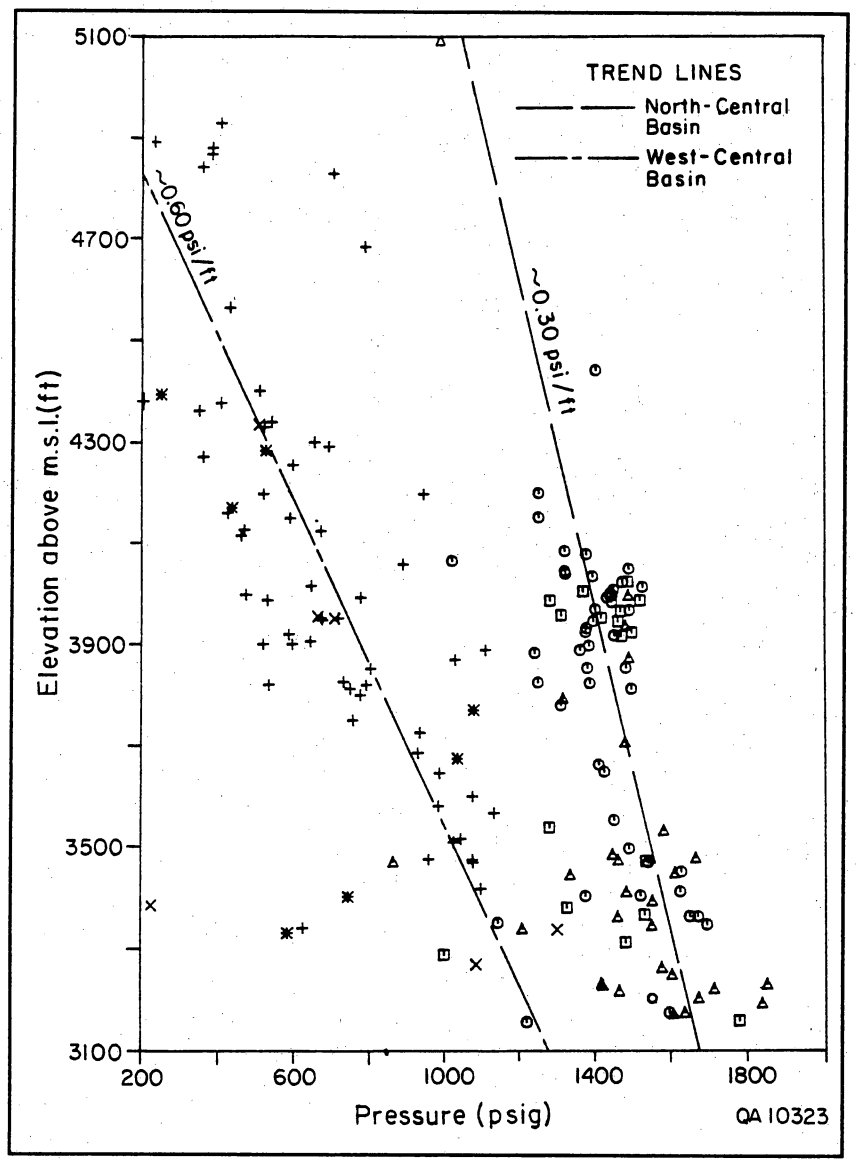

Figure 5. Fruitland Formation pressure-elevation plot, San Juan Basin (modified from Kaiser and Swartz, 1988) Vertical pressure gradient (~0.30 and ~0.60 psi/ft) is the slope of the respective trend line. Groundwater flow is potentially downward in the north-central part of the basin (vertical gradient <hydrostatic gradient, 0.433 psi/ft) and upward in the west-central part of the basin (vertical gradient >hydrostatic). Coal and sandstone values lie along the same trend lines, indicating regional pressure communication between interbedded coal seams and sandstones.

pinch-out this water must turn upward. Note that the potentiometric mound is associated with thick coal seams (Ayers and others, this vol., their figs. 23 and 25) and marked steepening of the potentiometric surface (fig.1), indicative of lower permeability across a facies change. This resistance to horizontal flow causes a buildup of fluid pressure and, in turn, a reversal of the vertical pressure gradient from downward, which is shown regionally for the north-central part of the basin (fig. 5), to upward (fig. 3). Vertical pressure gradient at A-K-P (fig. 4) exceeds the regional gradient (~0.60 psi/ft) and is consistent with upward vertical flow.

Pressure Regime

Two Fruitland pressure gradients were calculated, simple pressure gradient and vertical pressure gradient. Each has a different meaning and use. Simple pressure gradient is the quotient of BHP divided by the depth from land surface of the test interval's midpoint and is used to define the pressure regime in the Fruitland. Vertical pressure gradient, or slope of the pressure-elevation plot, is used to indicate vertical flow direction. The simple pressure gradient is usually calculated over a much larger interval than is the vertical pressure gradient, which is usually determined for a specific formation or aquifer.

The Fruitland Formation is abnormally pressured relative to the fresh-water hydrostatic gradient (0.433 psi/ft) and is divided into overpressured and underpressured areas. The north-central part of the basin is overpressured and is surrounded by a much larger underpressured area (fig. 6). The overpressured area (simple pressure gradient >0.44 psi/ft) is a large, roughly rectangular area (~1,000 mi² [~2,590 km²]), trending northwest-southeast from the outcrop in T34N, R10W basinward to T31N, R5W and extending north and northeast to the outcrop. Note that the overpressured

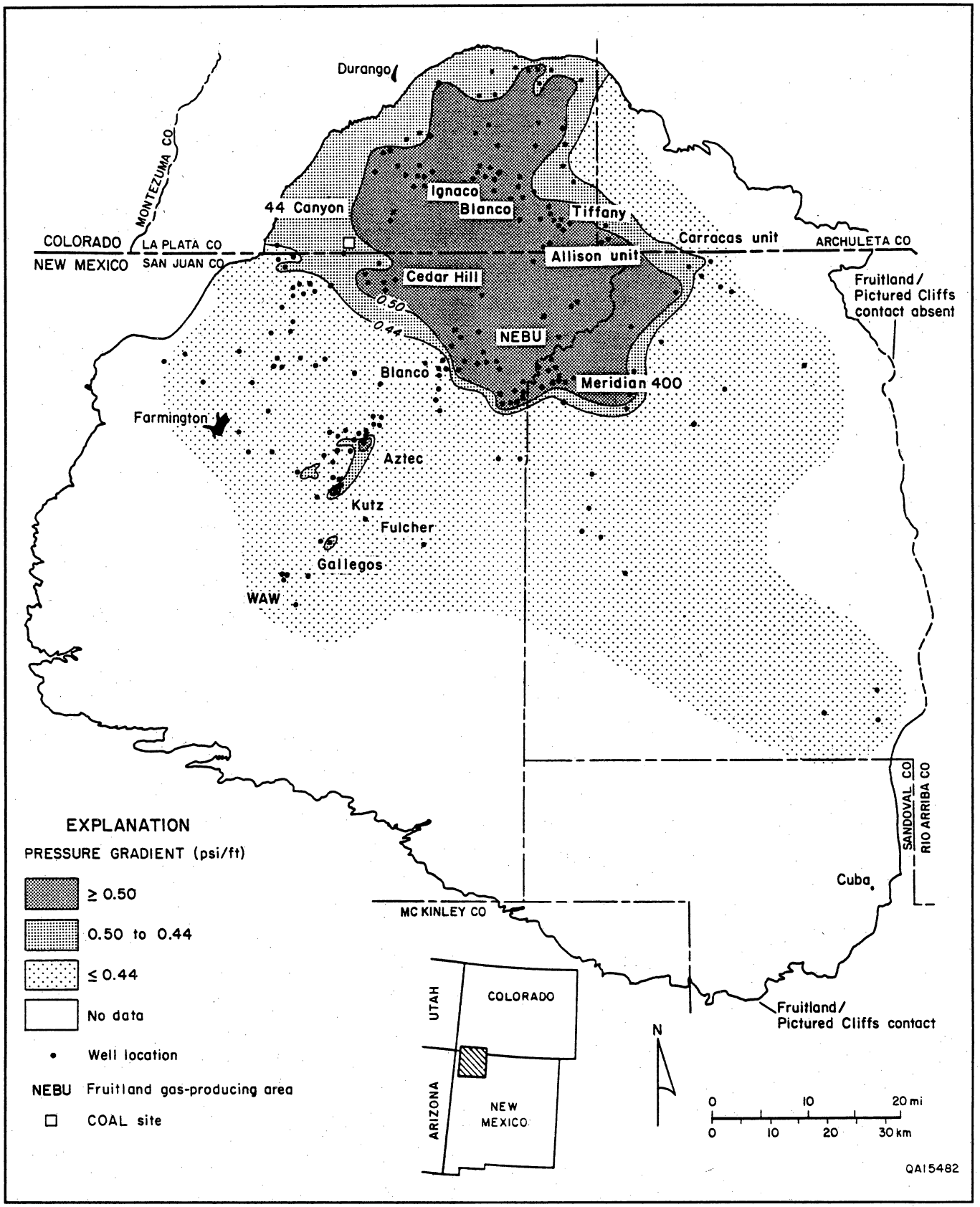

Figure 6. Fruitland Formation pressure-gradient map, San Juan Basin. Gradients are pressure-depth quotients. Overpressure is adapted to the basin's present geomorphology, extending to the northern outcrop (recharge area), and is nearly coincident with thick aquifer coal beds and freshest formation waters.

area is regional in extent and is not confined to isolated areas delineated by drilling mud weight (Kelso and others, 1988). Except to the northwest, the overpressured area is surrounded in all directions by an area of underpressure (pressure gradient <0.44 psi/ft). The transition between the pressure regimes is marked by pronounced steepening of the potentiometric surface (figs. 1 and 6) and coincides with pinch-out of thick aquifer coal seams and possible faulting along the basin's structural hingeline (Ayers and others, this vol.).

In the north-central part of the basin, BHP's typically range from 1,400 to 1,900 psi, translating into simple pressure gradients of 0.50 to 0.63 psi/ft, whereas BHP's in the southern part of the basin commonly range from 400 to 1,000 psi (0.30 to 0.40 psi/ft). The 1,200-psi contour (fig. 7) encloses the approximate area of overpressure. The area of highest pressure (BHP's greater than 1,600 psi) is northwest-trending, parallel to depositional strike (fig. 7), and is south of the basin's structural axis (Ayers and others, this vol., their fig. 5). Meridian 400, Northeast Blanco (NEBU), Sedro Canyon, and Los Piños are in this region. To the southwest, between Sedro Canyon and Blanco, the pressure drops abruptly from approximately 1,500 psi to 800 psi over a distance of approximately 10 mi. Low permeability and reservoir compartmentalization are inferred from this steep, lateral pressure gradient, which coincides with the pinch-out of thick coal seams (Ayers and others, this vol., their fig. 2) and conspicuous steepening of the potentiometric surface (fig. 1). From Blanco, pressure uniformly decreases southwest to approximately 700 psi at Aztec and to less than 400 psi at Gallegos South. The lowest reported BHP's (less than 200 psi) occur in the San Juan River valley near the western margin of the basin.

Pressure-depth and pressure-elevation plots (figs. 5 and 8), prepared by geographic area and lithology, show two distinct populations, reflecting the overpressured north-central part of the basin and the underpressured west-central part of the basin. North-central BHP's are greater than fresh-water hydrostatic pressure (fig. 8) and lie along a trend having an approximate vertical pressure gradient of 0.30 psi/ft (fig. 5), whereas west-central BHP's are less than hydrostatic and lie along a trend having an approximate vertical pressure gradient of 0.60 psi/ft (fig. 5), indicating, respectively, potential for downward and upward vertical flow. In both areas, coalbeds and sandstones cluster together, falling along the same trend lines, showing no significant difference in pressure, indicating regional pressure communication between interbedded coal seams and sandstones.

Anomalous islands of overpressure in the regionally underpressured west-central part of the basin occur at Kutz, Aztec, Flora Vista, and Glades and are explained hydrodynamically by local upward flow of ground water. Flora Vista and Glades lie in a dip-elongate belt of thick coal seams (Ayers and others, this vol., their fig. 25) and thus may receive recharge from the outcrop to the north, contributing to overpressure. Anomalous underpressuring in the overpressured north-central part of the basin is attributed to pressure decline because of production in the Ignacio Blanco field. Seventeen wells clustered in the vicinity of the Ignacio Anticline (T34N, R7W and T33N, R6W), completed in the early 1980's, are thought to have undergone pressure decline caused by long-term production from nearby wells dating from the 1950's.

Hydrochemistry

Hydrochemistry indicates ground-water circulation through distribution of mass or dissolved solids in ground water, whereas hydraulic head indicates circulation through distribution of potential energy. In other words, chemical composition records actual ground-water movement (mass transfer), whereas head shows the direction of force that drives ground-water flow. The two kinds of data are complementary: hydrochemistry is particularly useful for delineating flow patterns if head data are sparse or ambiguous. Hydrochemistry reflects rock-water interaction and prevailing ground-water flow rates and directions. Because ground water evolves chemically along its flow path, hydrochemistry can be used to define recharge and discharge areas. Generally, ground water is freshest at the outcrop in recharge areas and penetration of this fresh water into a basin marks the most permeable flow paths and implies an active, dynamic flow system.

To evaluate Fruitland hydrochemistry, Piper (trilinear) and Stiff ionic-ratio diagrams, histograms, and a chlorinity map were prepared from approximately 250 chemical analyses that were separated by geographic region and producing lithology. Most of the analyses are from the north-central part of the basin. Few analyses were available from other parts of the basin. Ten GRI/BEG samples were collected, preserved, and analyzed for major ions, organic acids, stable isotopes, and selected trace metals to investigate sources of alkalinity and CO_2 in Fruitland waters and the extent of meteoric circulation in the basin. Chemical analyses were performed by the Bureau of Economic Geology's Mineral Studies Laboratory. Stable isotope analyses were done by Coastal Science Laboratories, Inc., Austin, Texas.

Piper diagrams were used to identify chemical facies or water type. However, Piper diagrams cannot be used to differentiate among waters of the same type, whereas ionic ratios can be used to fingerprint waters of the same facies (Novak and Eckstein, 1988). Thus, we modified the Stiff diagram and plotted eight ionic ratios: (Ca+Mg)/(Na+K), Mg/Ca, Ca/(Na+K), SO_4/(Na+K), (Na+K)/(HCO_3+CO_3), (Ca+Mg)/(HCO_3+CO_3), Cl/(Na+K), and SO_4/Cl.

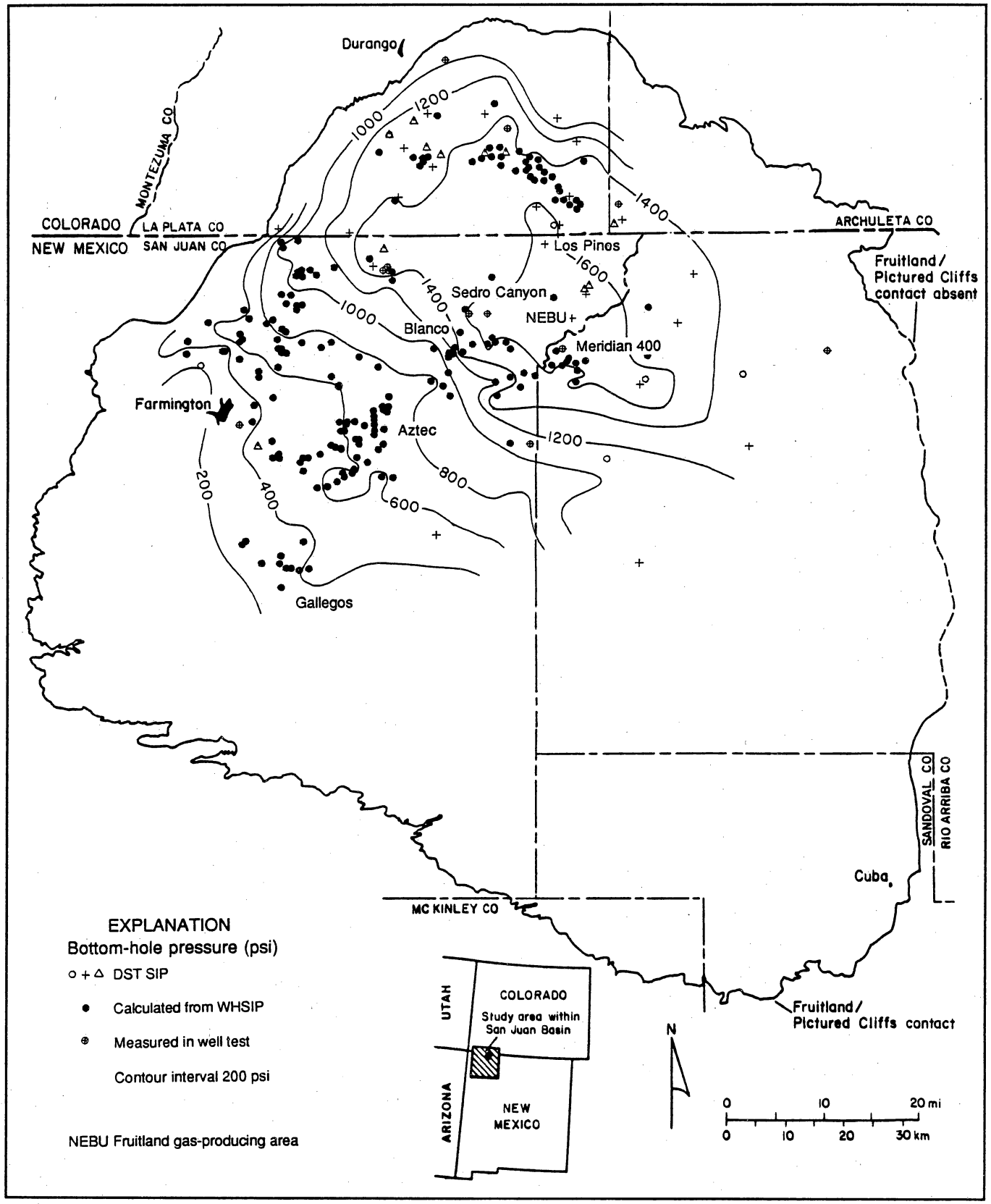

Figure 7. Fruitland Formation bottom-hole pressure map, San Juan Basin (from Kaiser and Swartz, 1990). Typical BHP's are 1,500 psi in the north-central part of basin, and 600 psi in the west-central part of basin. Highest pressures (>1,600 psi) occur south of the structural axis of the basin. Note steep pressure gradient in northeast San Juan County at transition between overpressuring and underpressuring (fig. 6).

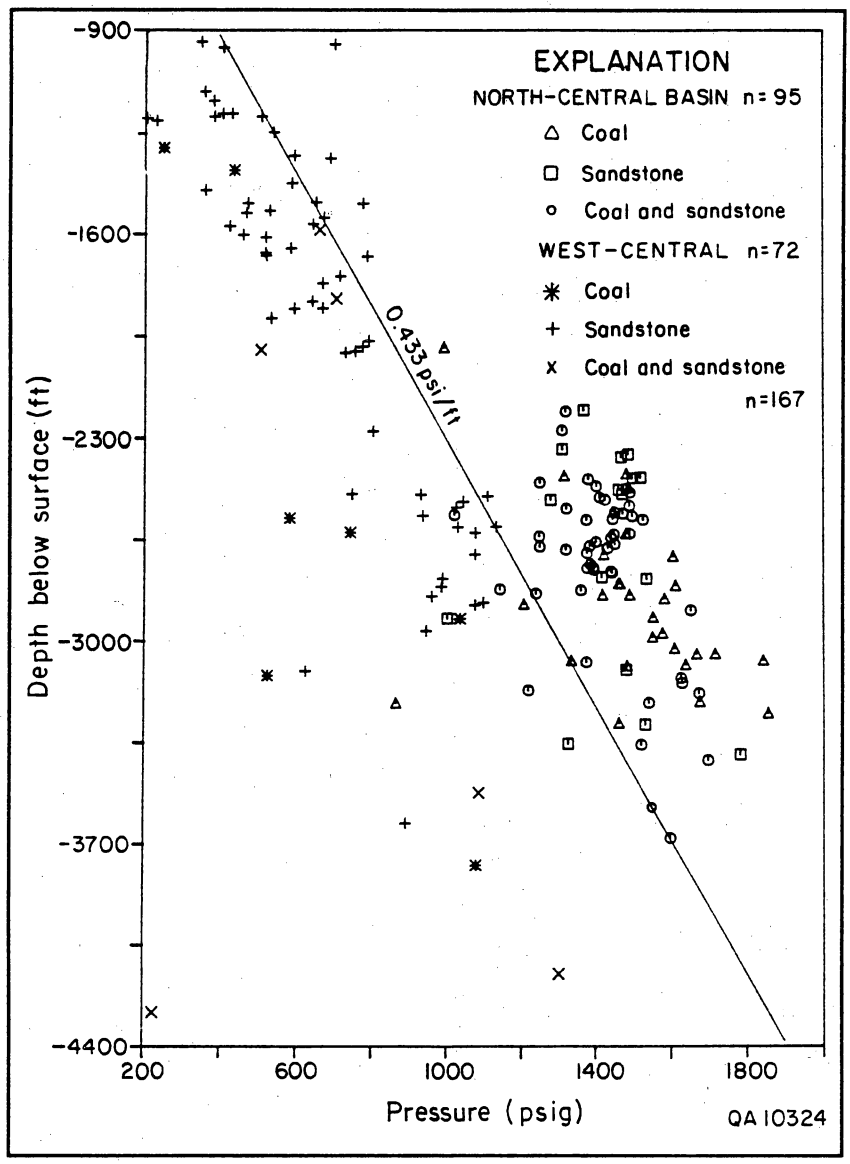

Figure 8. Fruitland Formation pressure-depth plot, San Juan Basin (from Kaiser and Swartz, 1988). Depth relative to land surface.

North-Central Basin

Chemical analyses of Fruitland waters produced from coal seams were selected from across the north-central part of the basin for wide geographic coverage. They are Na-HCO_3-type waters, complemented by a smaller number of Na-Cl waters (fig. 9a). At least five Na-Cl waters came from wells that were stimulated with HCl or KCl, or both, and may not represent formation water. One Na-Cl water sample came from coal in the shallow subsurface on the western basin margin. These waters are mainly brackish and saline but not brines (fig. 10a and b). Fruitland waters produced from sandstone in the north-central part of the basin are also mainly Na-HCO_3 type, with only a few Na-Cl-type waters (fig. 9b), contrary to previous reports on chemical facies of sandstone waters (Decker and others, 1987). Only waters produced from intervals thought to be mainly sandstone (based on log analysis) were plotted in figure 9b. Several of the Na-HCO_3 waters came from open-hole completions in upper Fruitland sandstone in the Ignacio Blanco field made in the 1950's by Stanolind Oil & Gas; one sample came from a perforated interval in a well in Cedar Hill field. Apparently, sandstone waters are somewhat less saline (fresher) than coal waters, being lower in TDS and Cl (fig. 10c and d).

To further evaluate chemical characteristics of Fruitland waters produced from coalbeds and sandstones in the north-central basin, we plotted Stiff ionic-ratio diagrams of samples from wells in T33N, R7W. Waters from coal and sandstone are Na-HCO_3 type and have ionic-ratio diagrams of similar shape and ionic ratios (figs. 11 and 12); that is, the variations are common to waters from both lithologies, showing that chemical

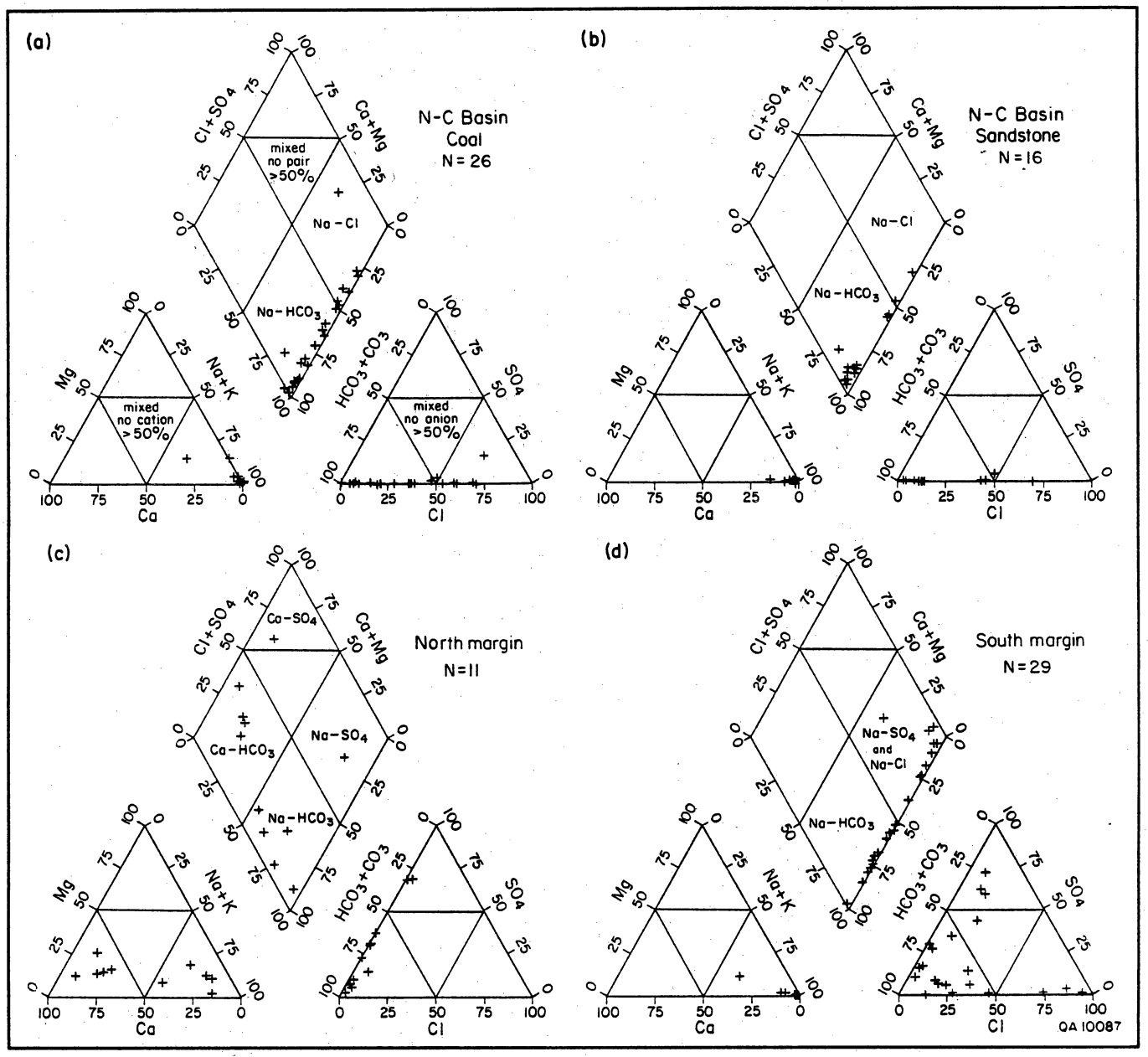

Figure 9. Piper diagrams of Fruitland waters, San Juan Basin (from Kaiser and Swartz, 1988). North-central part of basin by lithology (a and b), and northern (c) and southern (d) margins of basin undifferentiated by lithology. Similar chemical facies in coalbed and sandstone waters indicates hydraulic communication between strata. Note diversity of facies types in Fruitland waters. Diagrams plotted in meq/L.

composition cannot be used to identify completion lithology. Moreover, similar chemical facies and diagram shapes for waters from both lithologies indicate hydraulic communication between coal seams and sandstones. For example, coal and sandstone waters are similar at Cedar Hill field (fig. 13). Commonly, coal waters have large Mg^{2+}/Ca^{2+} ratios, giving the diagram a distinctive triangular segment, or magnesium triangle. Coal waters from the Meridian 400 area have Mg^{2+}/Ca^{2+} ratios as large as 12 (fig. 14), whereas those from Cedar Hill (fig. 13) are not unusually large but are similar to those in T33N, R7W, and the NEBU area (fig. 15). Apparently, the Mg^{2+}/Ca^{2+} ratio increases basinward down hydraulic gradient along the flow path (figs. 15 and 16). Magnesium enrichment and/or Ca^{2+} depletion basinward is evident in a number of analyses in the Meridian 400 and NEBU areas. Ca^{2+} concentration may be reduced by precipitation of calcite and gypsum and in ion exchange. Fibrous calcite and gypsum occur as discontinuous mineral fill along the primary coal cleat

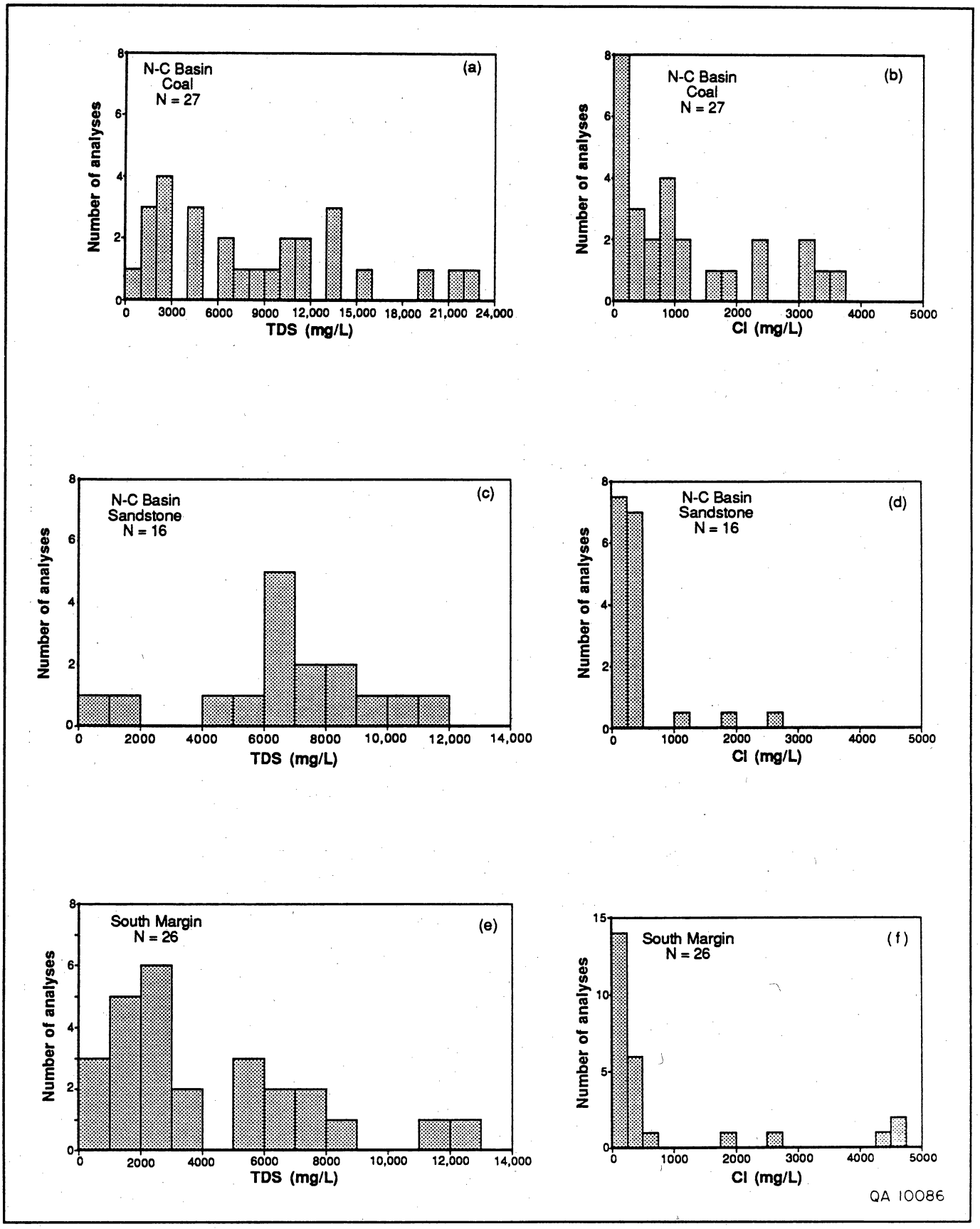

Figure 10. Histograms of Fruitland water composition, San Juan Basin (from Kaiser and Swartz, 1988). North-central part of basin by lithology, southern margin undifferentiated.

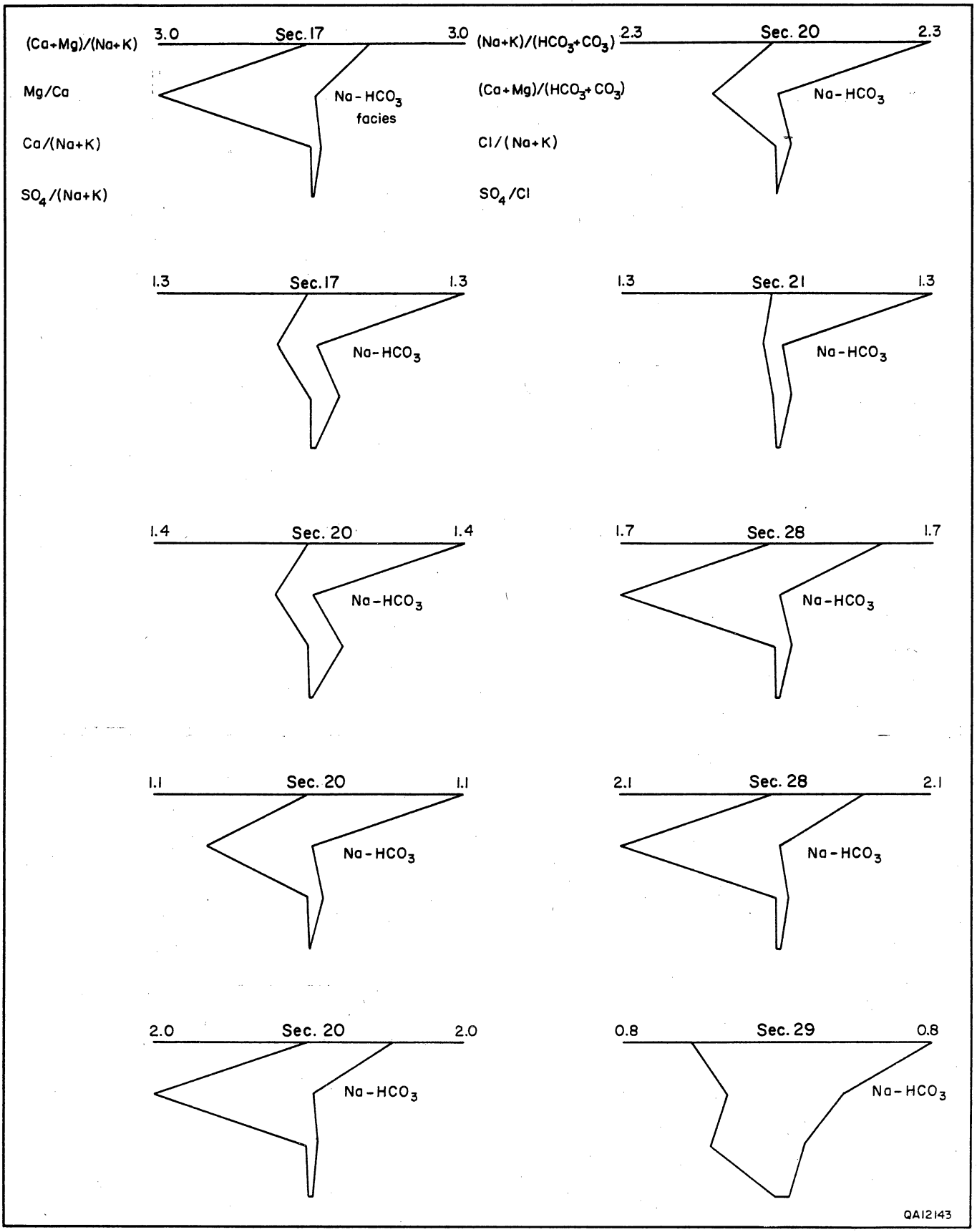

Figure 11. Stiff ionic-ratio diagrams, Fruitland coalbed waters, T33N, R7W, San Juan Basin (from Kaiser and Swartz, 1990). Diagrams plotted in meq/L. See figure 16 for area location.

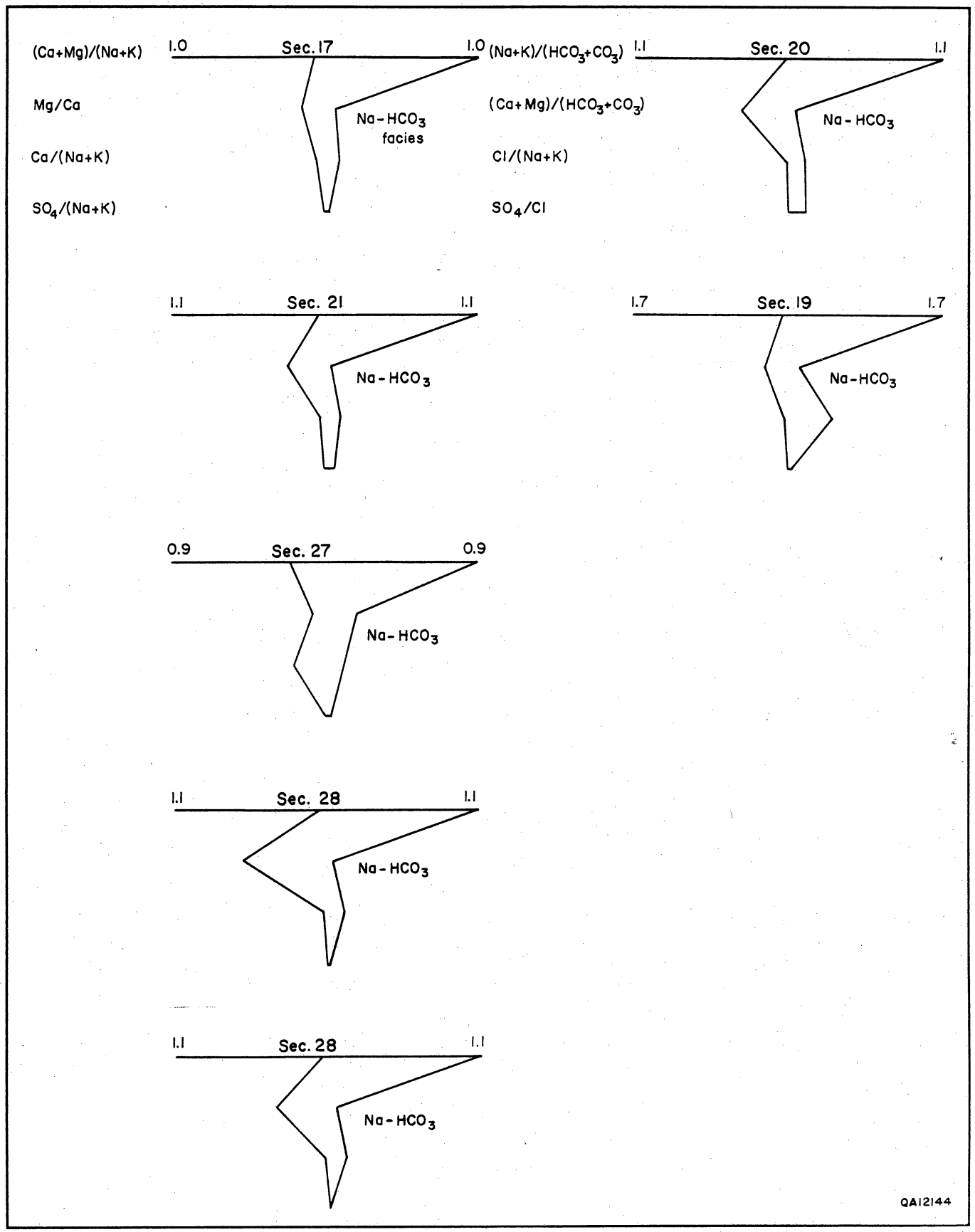

Figure 12. Stiff ionic-ratio diagrams, Fruitland sandstone waters, T33N, R7W, San Juan Basin (from Kaiser and Swartz, 1990).

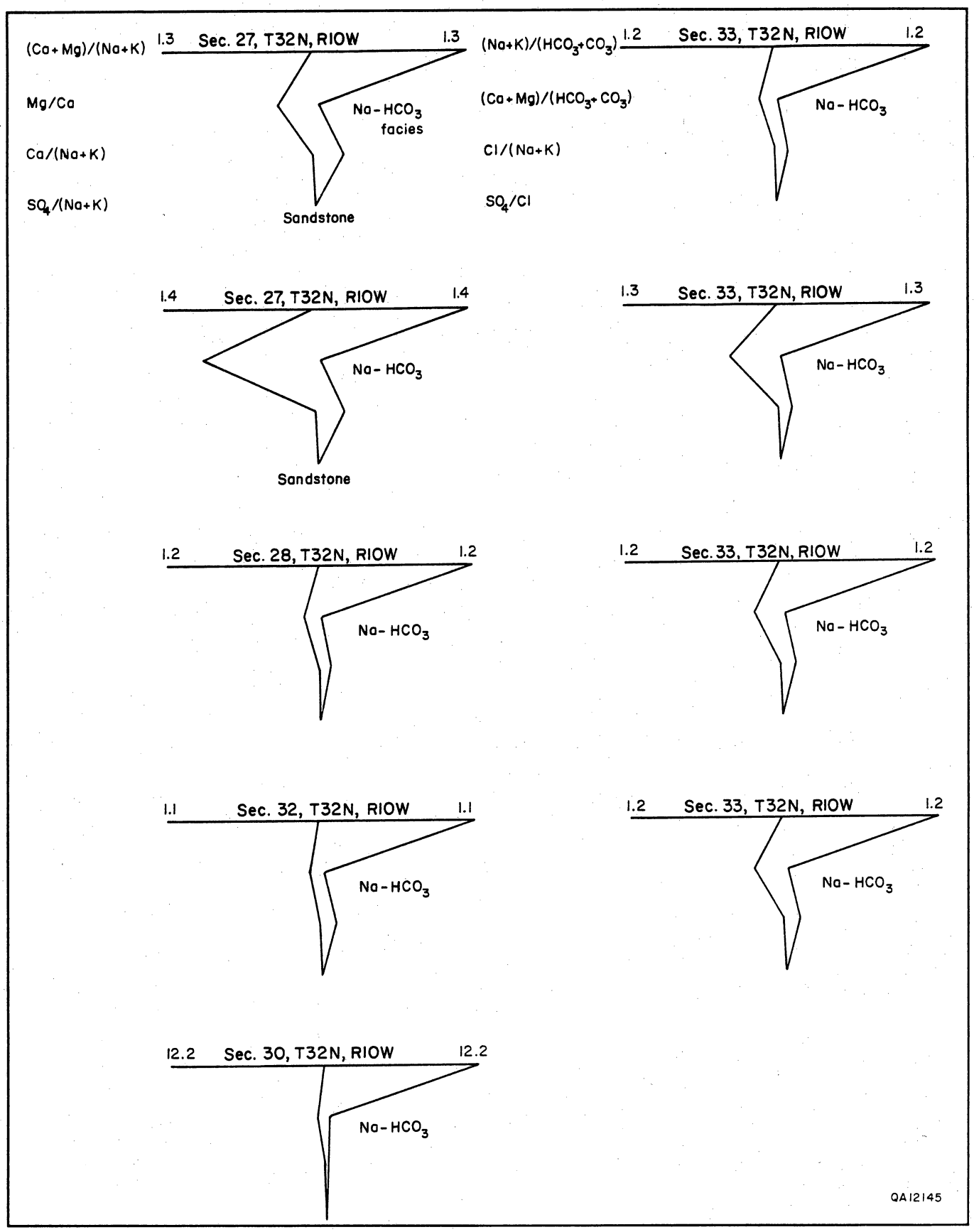

Figure 13. Stiff ionic-ratio diagrams, Fruitland coalbed and sandstone waters, Cedar Hill field, San Juan Basin (from Kaiser and Swartz, 1990).

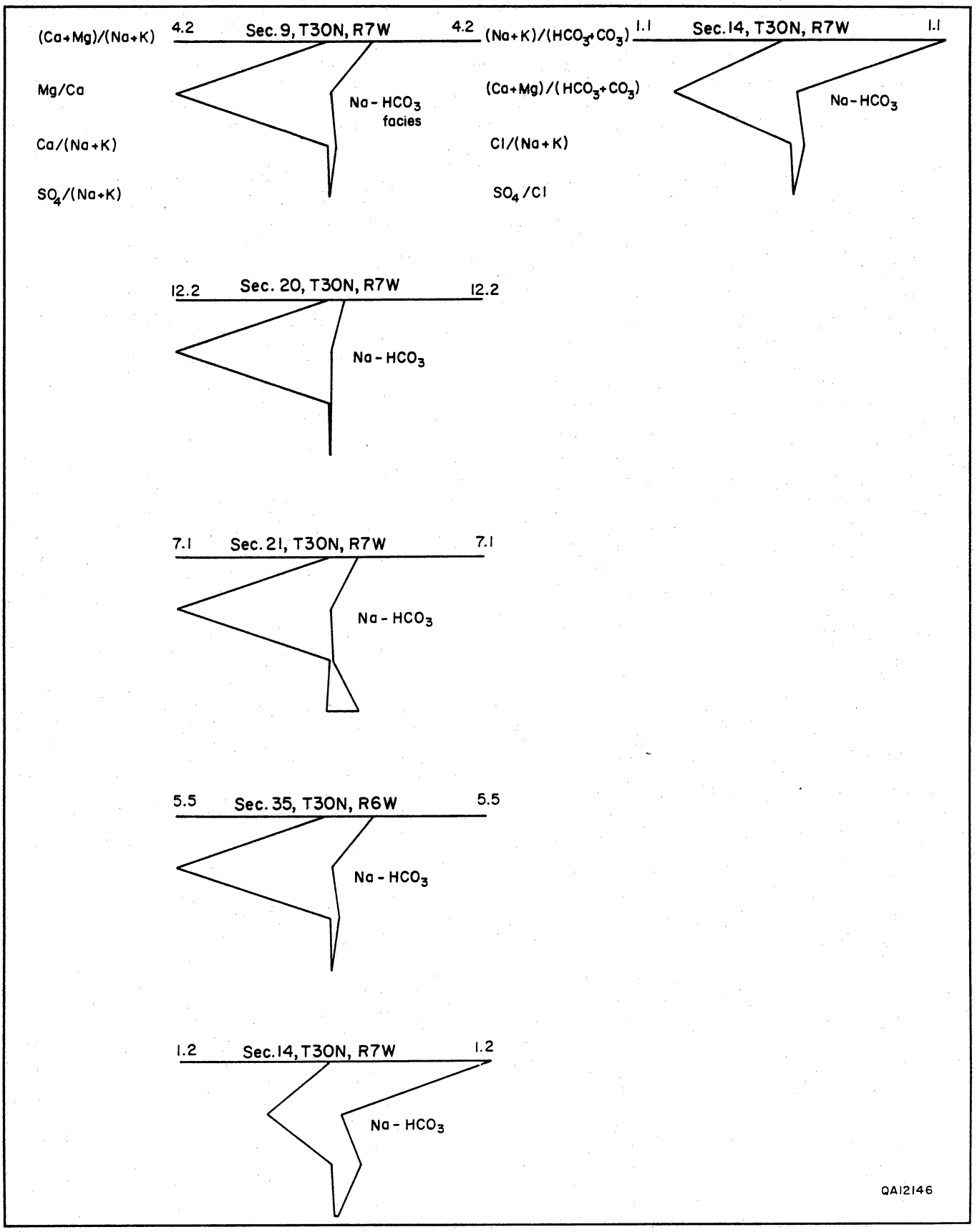

Figure 14. Stiff ionic-ratio diagrams, Fruitland coalbed waters, Meridian 400 area, San Juan Basin (from Kaiser and Swartz, 1990).

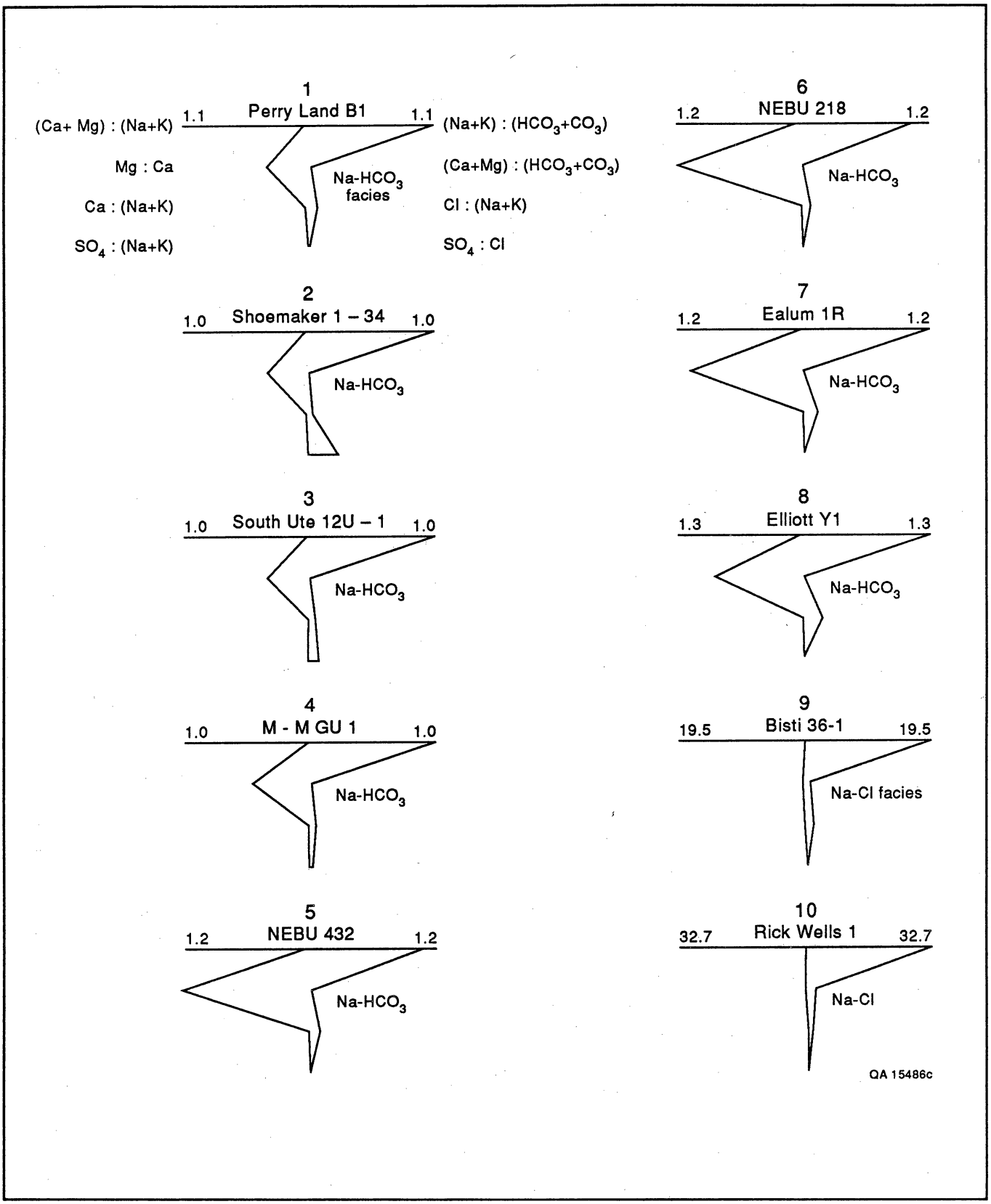

Figure 15. Stiff ionic-ratio diagrams, GRI/BEG Fruitland coalbed water samples (see fig. 16 for location and table 3 for analyses). Northern waters are Na-HCO_3 type and southern waters Na-Cl type. Note increase in Mg^{2+}/Ca^{2+} ratio down flow path (samples 2, 3, 4, and 7). Samples 9 and 10 resemble seawater (see fig. 23); meteoric dilution is indicated by $\delta^{18}O$ and δD values (see fig. 18) and small $(Na+K)/(HCO_3+CO_3)$ ratios.

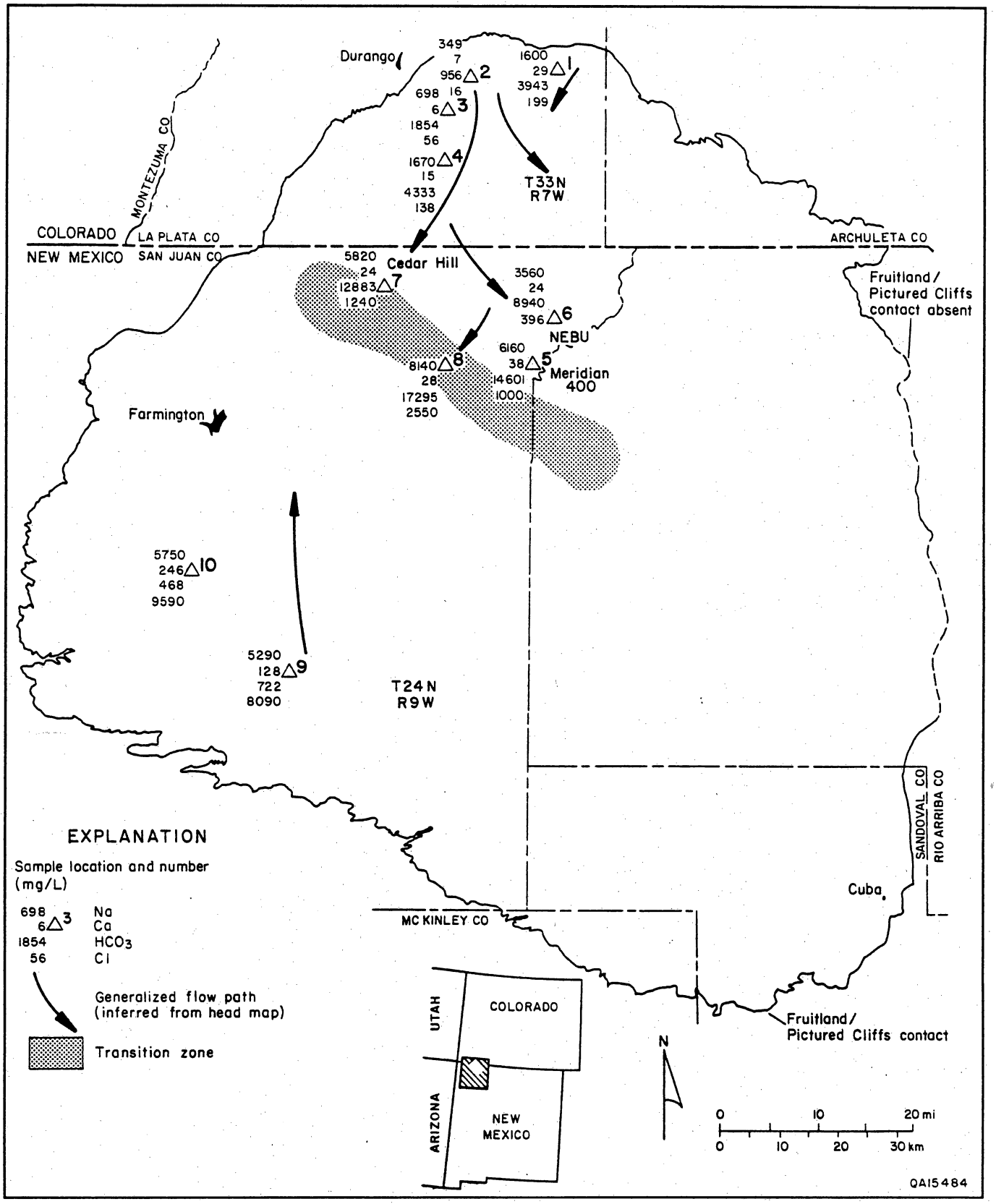

Figure 16. Location of GRI/BEG Fruitland coalbed water samples. In the north-central part of the basin, Na^+ and HCO_3^- increase down flow path, reaching their highest concentration in the transition zone. Southern waters are enriched in Cl^- and Ca^{2+}. The transition zone is a regional facies, potentiometric, pressure, and hydrochemical boundary. Complete chemical analyses in table 3.

(Tremain and others, this vol., their table 2). Moreover, solubility of calcite is less than that for Mg-carbonates, and in ion exchange, Ca^{2+} is more strongly adsorbed than Mg^{2+}.

Waters in the north-central part of the basin are unique in their very high HCO_3^- contents (several thousand mg/L up to 20,000 mg/L), high Na^+ contents (thousands of mg/L), low Ca^{2+} and Mg^{2+} contents, low Cl^- contents (tens to hundreds of mg/L), negligible SO_4^{2-} content, and Ba^{2+} enrichment (table 3). Earlier, on the basis of the existing suite of water analyses, organic-acid anions were thought to be important contributors to total alkalinity (Kaiser and Swartz, 1990). Very high reported HCO_3^- contents and neutral to slightly alkaline pH's (7 to 8) of produced waters suggested that organic acids were abundant and that inorganic alkalinities (HCO_3^-contents) were lower than those reported in available analyses. Commonly, HCO_3^- values (total alkalinity) in excess of several hundred mg/L in oil and gas field waters are attributed to organic acids such as acetic and propionic, where 100 percent of field-determined alkalinities may be contributed by organic species (Carothers and Kharaka, 1978; Kharaka and others, 1985, 1986; Lundegard and Land, 1986; Morton and Land, 1987).

Although organic acids are present (200 to 300 mg/L as acetic acid), they are secondary contributors to the very high total alkalinities that are due mainly to HCO_3^- (table 3). Samples effervesced upon acidification in the laboratory. Inorganic C analyses and field alkalinities expressed as HCO_3^- are almost identical. Shapes of titration curves are typical of waters dominated by inorganic alkalinity (fig. 17). Bicarbonate content shows no correlation with pH, suggesting an open chemical system and addition of CO_2. Results of analyses for ^{13}C of total dissolved carbonate species (HCO_3^-, H_2CO_3, CO_2, and CO_3^{2-}) show extreme enrichment in ^{13}C: values of $\delta^{13}C$ range from +16.7 to +26.0‰ (table 3). Formation of CH_4 by degradation of organic acids and reduction of CO_2 by methanogenic bacteria yield isotopically heavy HCO_3^- (Carothers and Kharaka, 1980; Grossman and others, 1989). Lower $\delta^{13}C$ values (+16.7 and +17.5‰) near the northern outcrop (recharge area) may reflect dilution by isotopically light CO_2 formed diagenetically in the soil zone (Phillips and others, 1989) or greater abundance of isotopically light thermogenic CO_2. Heavier values basinward (+24.0 to +26.0‰) may indicate less dilution or that little CO_2 is being generated, while CH_4 continues to form by reduction, enriching the remaining CO_2 in ^{13}C (Carothers and Kharaka, 1980).

Abundant organic acids are thought to have been generated by the late Oligocene thermal event (Bond, 1984). Organic acids probably are not forming today because subsurface temperatures are too cool (~125°F [~50°C]). At 158°F (70°C), organic acids are generated faster than they are destroyed by bacteria (Y. K. Kharaka, 1989, personal communication). In waters low in Ca^{2+} and Mg^{2+} such as these, HCO_3^- contents of more than 1,000 mg/L can be generated when CO_2-releasing processes (methanogenesis and sulfate reduction) occur. Methanogenesis is dominant here because sulfate reduction produces isotopically light HCO_3^- and is pervasive at low SO_4^{2-} concentrations (Claypool and Kaplan, 1974; Whiticar and others, 1986). Sulfate reduction and methanogenesis in peat swamps were postulated by Decker and others (1987) to account for high HCO_3^- contents in coalbed waters. However, these waters are meteoric and not fresh connate waters. They plot above and close to the meteoric water line, showing enrichment of D but not of ^{18}O (figs. 18 and 19). A possible explanation of D enrichment is isotopic exchange with hydrogen gases (CH_4, C_2H_6, H_2, and H_2S) (Welhan, 1987) or between H_2O and HCO_3^- in methanogenesis. During methanogenesis, coexisting formation waters are enriched in D (values of δD range from 0.0 to –80‰) (Whiticar and others, 1986). This enrichment in Fruitland waters is shown by a close correlation between δD of water and $\delta^{13}C$ of total dissolved carbonate species (fig. 19). Exchange with H_2S is not likely because it is not present in these waters. Basinward enrichment of ^{18}O (samples 5 through 8) may, in view of isotopically light oxygen upflow, represent mixing of lighter water with older, isotopically much heavier water downflow or it may represent older recharge events, when past recharge was enriched in ^{18}O.

Basin Margins

Waters from the northern and southern margins of the basin are included for comparison with basinal waters to show the diversity of chemical facies in the Fruitland Formation. Waters from the basin margins are discussed collectively because host lithology is usually not reported. Waters from the northern margin are dominantly Ca-Mg-HCO_3 and Na-HCO_3 types (fig. 9c), whereas those from the southern margin are sodium dominated, showing Na-HCO_3, Na-SO_4, and Na-Cl types (fig. 9d). Waters from the northern margin are fresh to brackish (TDS content of 180 to 3,015 mg/L and chlorinities of 2 to 45 mg/L), whereas waters from the southern margin (fig. 10e and f) have salinities similar to those in the north-central part of the basin.

Waters from the northern margin of the basin graphically differ from those of the north-central part of the basin. Those of the northern margin are Ca-Mg and Na-HCO_3-type waters that have large SO_4^{2-}/Cl^- ratios (up to 116), giving the Stiff ionic-ratio diagram a distinctive triangular foot, or sulfate triangle (fig. 20). This allows

Table 3. Chemical analyses of produced Fruitland coalbed waters.

Sample Number	1	2	3	4	5	6	7	8	9	10
Well	Perry Land GU B 1	Shoemaker 1-34	Southern Ute 12U-1	Mayfield-Melton GU 1	NEBU 432	NEBU 218	Ealum Gas Com C 1R	Elliott Gas Com Y 1	Bisti Coal 36-1	Rick Wells 1
Location	30 35N 6W	34 35N 8W	12 34N 9W	1 33N 9W	7 30N 7W	16 31N 7W	33 32N 10W	9 30N 9W	36 25N 12W	8 26N 13W
Production interval	1,304-1,480	1,896-2,026	2,400-2,478	2,530-2,747	3,004-3,216 (OH)	3,200-3,346 (OH)	2,777-2,813	2,790-2,944	1,074-1,092	1,383-1,427
Source	wellhead	wellhead	wellhead	separator[a]	separator[a]	wellhead	wellhead	wellhead	wellhead	wellhead
TDS	5,820	1,360	2,650	6,220	21,970	13,030	20,110	28,210	14,330	16,190
Na	1,600	349	698	1,670	6,160	3,560	5,820	8,140	5,290	5,750
K	9.9	4.3	5.8	5.4	19.5	13.2	33.3	53.1	22.5	27.5
Ca	28.8	6.5	5.8	15.1	37.7	24.4	23.6	28.1	128	246
Mg	6.2	1.2	1.2	4.2	27.4	17.3	15.5	15.1	36.4	57.7
Sr	4.3	0.6	0.7	5.0	17.7	13.2	12.3	19.4	6.9	12.3
Ba	6.5	0.7	1.1	6.1	62.9	21.1	36.2	51.5	8.4	7.6
Fe	0.12	0.80	0.04	0.05	0.64	0.72	1.24	0.59	0.57	2.37
Mn	0.06	0.03	0.03	0.01[b]	0.01	0.01	0.03	0.01	0.49	0.15
Li	0.88	0.34	0.94	1.54	1.39	1.11	0.58	1.13	0.50	0.53
B	1.08	0.21	0.63	1.55	2.15	0.98	8.54	9.17	1.18	1.09
SiO_2	21.0	22.8	26.1	31.5	26.6	27.1	24.7	26.1	12.5	15.0
Field alkalinity (as HCO_3^-)	3,943	956	1,854	4,333	14,601	8,940	12,883	17,295	722	468
Organic acids (as CH_3COOH)	270	220	210	330	330	210	210	220	120	160
NH_3	2.53	1.50	1.11	4.47	11.3	8.57	9.13	16.2	4.99	6.20
organic-N	0.39	0.78	0.85	1.04	1.45	1.59	0.85	1.50	0.60	0.48
Cl	199	16	56	138	1,000	396	1,240	2,550	8,090	9,590
SO_4	<5[c]	<5	<5	<5	<5	<5	<5	<5	<5	10.4
Br	0.85	0.14	0.50	0.76	4.65	3.49	3.99	6.19	7.64	8.68
I	0.38	0.10	0.33	1.13	0.41	0.11	0.52	0.87	0.60	0.56
Field pH	7.65	8.21	8.23	7.73	7.62	7.89	8.06	8.02	7.39	7.33
$\delta^{18}O$[d]	-14.0	-14.6	-14.6	-14.1	-7.4	-7.9	-7.7	-7.6	-10.8	-10.5
δD	-85	-98	-102	-85	-32	-43	-28	-36	-81	-80
$\delta^{13}C$[e]	+23.5	+17.5	+16.7	+24.0	+25.6	+24.7	+26.0	+24.9	+19.7	+19.5
Σ cations (meq/L)	71.94	15.73	30.92	74.03	273.71	158.30	257.14	359.07	240.27	268.10
Σ anions (meq/L)	70.28	16.13	31.98	74.95	267.66	157.78	246.25	355.55	239.98	278.33

[a] Flowing well; [b] near detection limit of 0.01 mg/L; [c] detection limit 5 mg/L; [d] $\delta^{18}O$ and δD in per mil relative to SMOW; [e] $\delta^{13}C$ of total dissolved carbonate species in per mil relative to PDB.

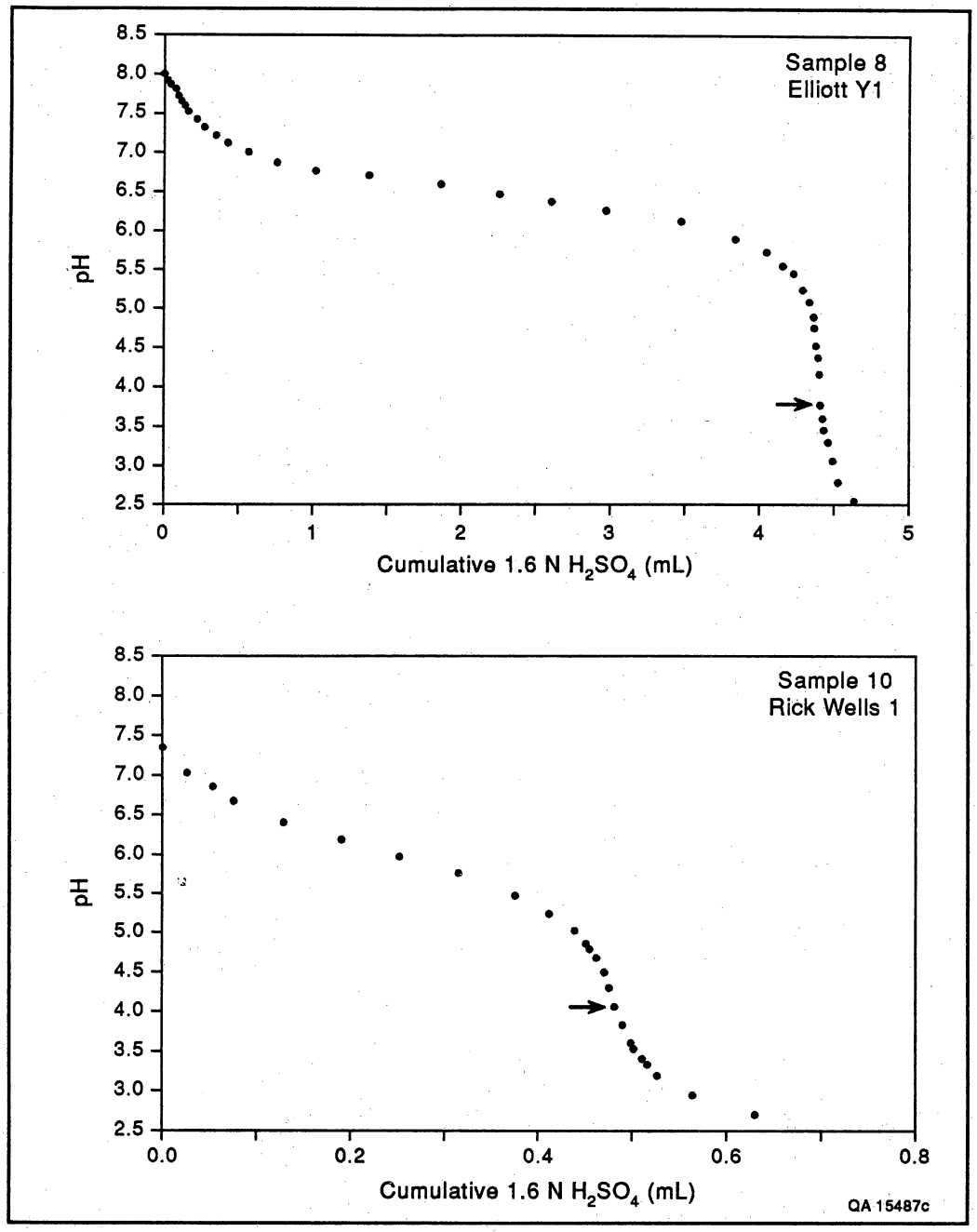

Figure 17. Representative titration curves for field alkalinity, GRI/BEG water samples. Curve shape is characteristic of waters dominated by inorganic alkalinity. Inflection points (arrows) are shifted to lower pH by organic acids. Curve flattens and inflection point becomes less well defined as relative percent of organic acids increases (sample 10, table 3).

easy differentiation among Na-HCO_3-type waters from the northern margin and north-central part of the basin and shows that Stiff ionic-ratio diagrams can be used to characterize waters of the same chemical facies. The pattern for world-average river water is shown for comparison. Note the absence of sulfate and magnesium triangles in the river water. Apparently, meteoric waters in the northern part of the basin evolved from average river water by addition of SO_4^{2-} and Mg^{2+}, followed downflow by loss of SO_4^{2-}, addition of Cl^-, Na^+ (ion exchange), and HCO_3^- (methanogenesis), and possible addition of Mg^{2+} as well as loss of or no addition of Ca^{2+} (mineral precipitation and ion exchange) to become Na-HCO_3 waters. Sulfate reduction occurs rapidly along the flow path because waters within 2 mi of the outcrop have negligible SO_4^{2-} contents (fig. 16 and table 3).

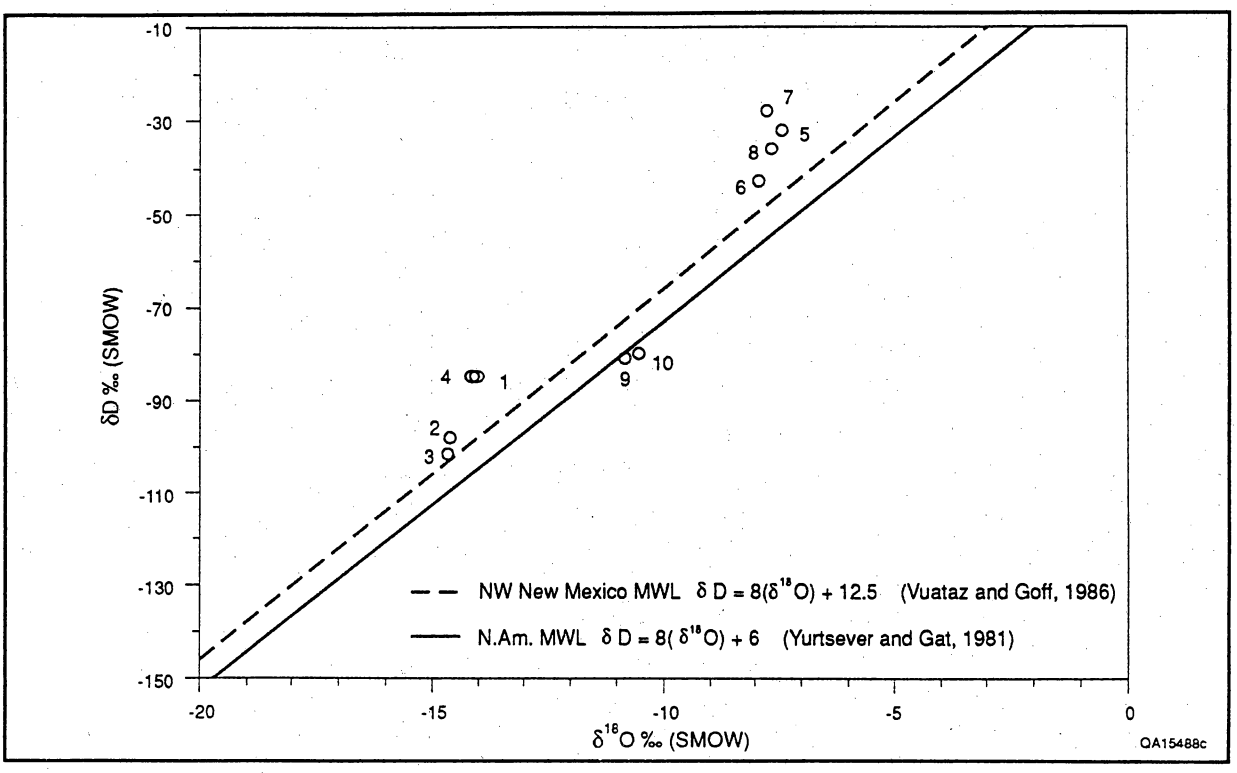

Figure 18. Plot of δD and $\delta^{18}O$, GRI/BEG water samples. Northern waters plot above the meteoric water line (MWL) and are enriched in D but not ^{18}O, which indicates isotopic exchange with hydrogen gases or bicarbonate in methanogenesis. Southern waters (samples 9 and 10) plot to right of New Mexico MWL, indicating evaporation during recharge in the semiarid climate.

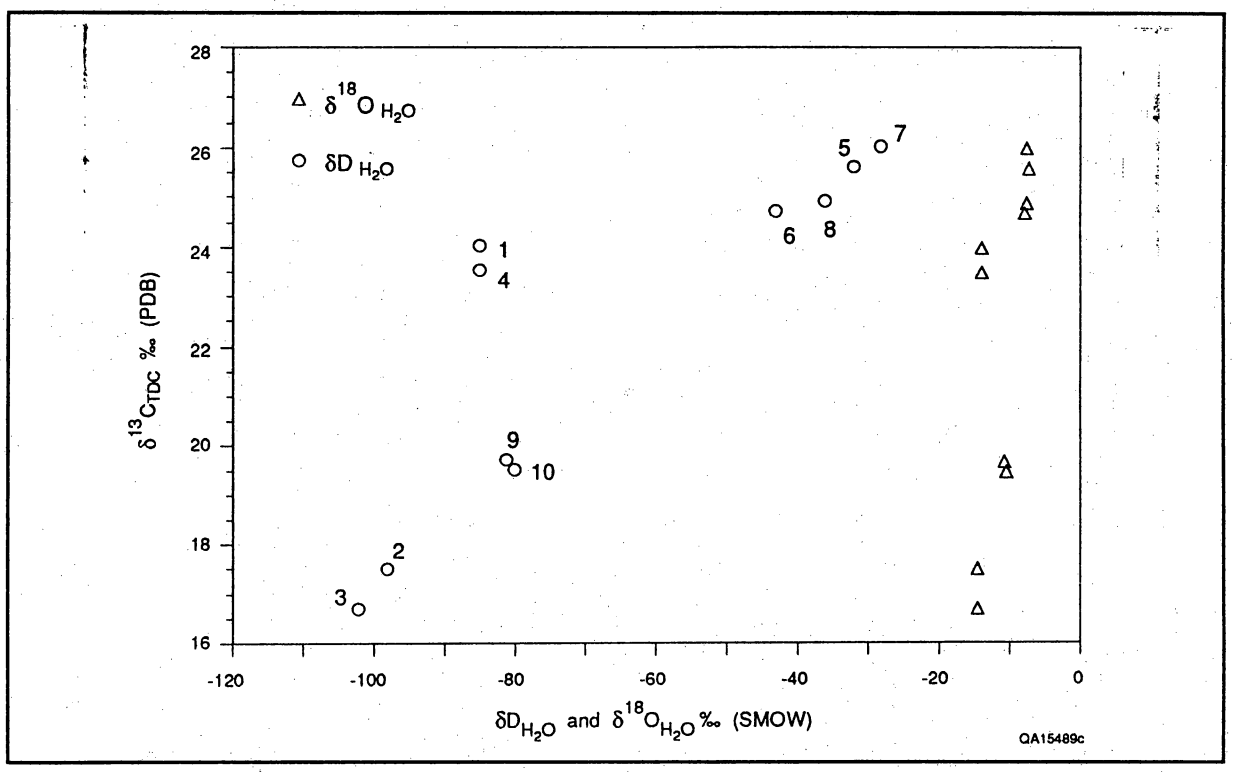

Figure 19. Plot of δD and $\delta^{18}O$ in water versus $\delta^{13}C$ of total dissolved carbonate species (TDC). D enrichment during methanogenesis is indicated by correlation of δD with $\delta^{13}C$.

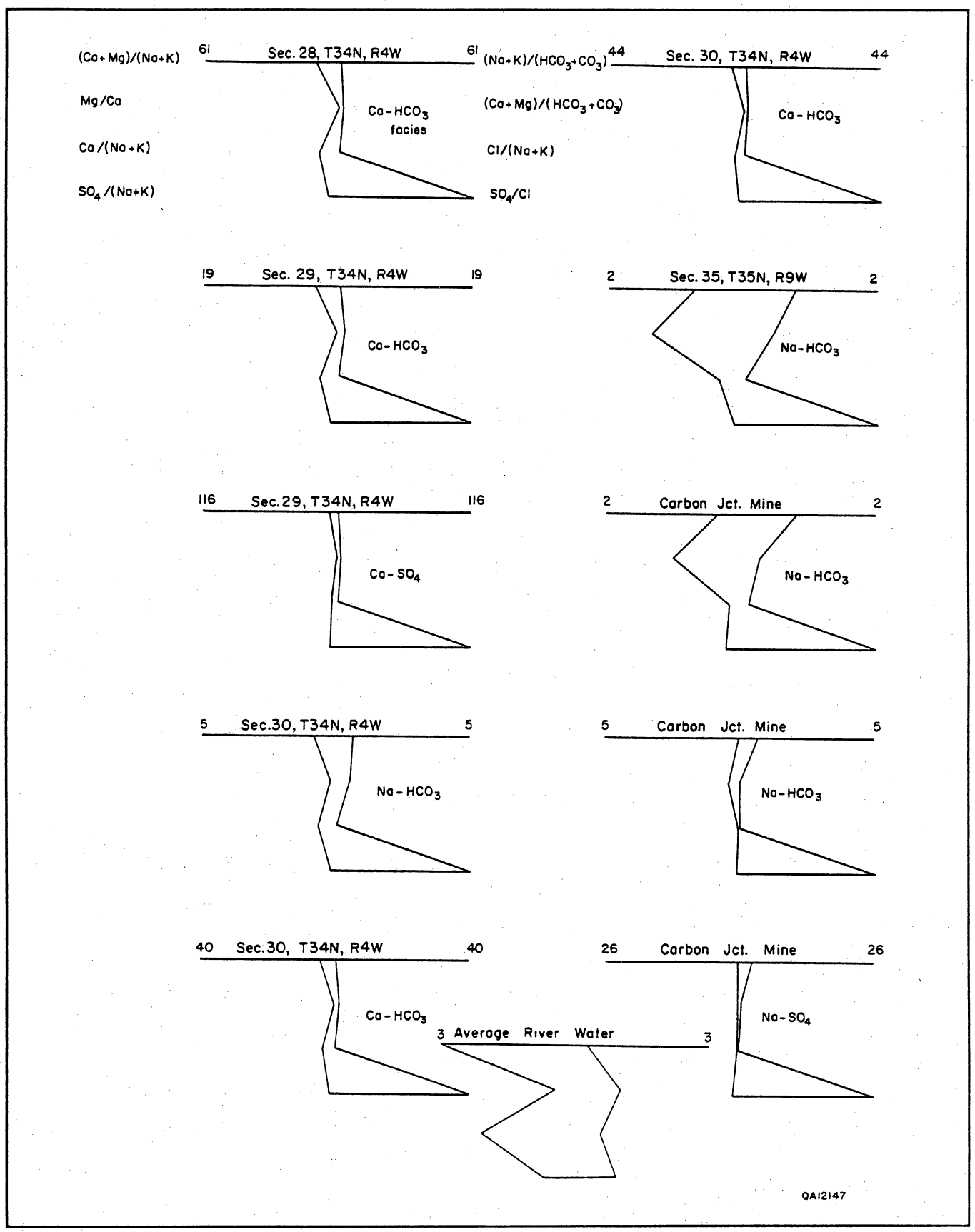

Figure 20. Stiff ionic-ratio diagrams, Fruitland waters, northern margin of the San Juan Basin (from Kaiser and Swartz, 1990). Diagrams plotted in meq/L.

Waters from the southern margin of the basin are sodium dominated, with Na-HCO_3, Na-SO_4, and Na-Cl types present. Consequently, waters display a variety of diagram shapes (figs. 21 and 22), illustrating the diversity of chemical facies in the Fruitland Formation. Na-SO_4 waters are thought to be the chemically evolved shallow ground water because thenardite (Na_2SO_4) is deposited by spring waters (Stone and others, 1983). Diagrams of Na-Cl-type waters resemble those basinward (figs. 15 and 23) but have smaller (Na+K)/(HCO_3+CO_3) ratios. Among 29 analyses plotted from the southern margin of the basin, 19 have a sulfate triangle, 7 a magnesium triangle, and 3 a north-central basin signature (similar facies and diagram shape). All diagrams from the southern margin are dissimilar to those of world-average river water and seawater (figs. 20 and 23). Coal waters sampled basinward of the southern margin have diagrams very similar to that for seawater (figs. 15 and 23), especially those in T24N, R9W. These waters have TDS contents of 14,000 to 42,000 mg/L, chlorinities of 8,000 to 26,000 mg/L, and are the only brines identified in the Fruitland Formation. Their (Na+K)/(HCO_3+CO_3) ratios are less than that of seawater, suggesting meteoric dilution, which is confirmed by stable isotope analysis for samples 9 and 10 (fig. 18 and table 3). Their $\delta^{18}O$ and δD values are similar to those of Holocene Ojo Alamo and Nacimiento ground waters (Phillips and others, 1986). They plot near the meteoric water line for northwest New Mexico but are shifted somewhat to the right, which strongly suggests evaporation during recharge, a common process in semiarid environments (Phillips and others, 1986). Thus, these Fruitland waters probably represent modified marine waters. Apparently, coal beds have been flushed of their fresh connate water by saline waters moving upward and laterally toward the San Juan River valley. Their presence further indicates limited recharge from the southern margin of the basin and implies low permeability. These waters can be preserved only where strata are tight and poorly flushed by meteoric recharge.

Chlorinity

Ground-water flow patterns were also defined by a chloride map. Chloride was mapped because it is a conservative chemical species unaffected by rock-water interaction. In the north-central part of the basin, the chlorinity map (fig. 24) and isotopic data (fig. 18) show a fresh-water plume of meteoric origin extending basinward from the northern and northwestern margins, as predicted from the potentiometric-surface, or head, map (fig. 1). The distribution of dissolved solids, or mass, shows that low-chloride water coincides with flow patterns inferred from the head map and that flow is in the directions inferred from the map. For example, the Southern Ute-Mobil 36-1 well receives recharge directly from the northwestern margin of the basin; its produced waters have a TDS content of approximately 1,500 mg/L and contain 2 mg/L chloride. In contrast, the Southern Ute 1-24 well, although closer to the outcrop, should, as predicted from the chloride (fig. 24) and head (fig. 1) maps, receive little direct recharge from the outcrop. Indeed, its produced waters have a TDS content of approximately 10,000 mg/L and contain about 600 mg/L chloride. The correlation between chlorinity and the present-day flow system and the presence of meteoric water show conclusively that these low-chloride waters are not fresh connate waters but evolved meteoric waters.

Tongues of low-chloride water project basinward along generalized flow paths inferred from the head map, defining the configuration of fresh-water recharge (fig. 24). Major tongues are oriented northwest-southeast, parallel to depositional strike and to the orientation of aquifer coal seams. The northerly tongue in eastern La Plata County coincides with thick coal seams that extend to the outcrop (Ayers and others, this vol., their fig. 25), possibly serving as avenues for recharge. A basinward protrusion of low-chloride water from the northwestern margin also coincides with thick coal seams. Secondary tongues are oriented northeast-southwest and may reflect the dominant fracture trend (Tremain and others, this vol., their fig. 12), dip-elongate coal seams (Ayers and others, this vol., their fig. 25), Fruitland channel sandstone belts (Ambrose and Ayers, this vol., their fig. 6), or a combination of all three.

Some extremely low-chloride waters, located in T33N, R6W at the end of a 20-mi flow path, have chloride contents of less than 5 mg/L. Their meaning is ambiguous. Analytical error has been eliminated because the technique used (argentometric titration) tends to produce results that err on the high side. Possibly, the low chlorinities reflect recharge of fresh Pleistocene waters, which commonly are very low in chloride and depleted in ^{18}O and D (Phillips and others, 1986), and therefore indicate relatively fast ground-water flow rates and short residence times. The age of ground water from the Ojo Alamo Sandstone in the southwestern part of the basin, based on ^{14}C dating, ranges from very young to 26,000 yr B.P. (Phillips and others, 1989). Calculations based on heat-flow data (McCord, 1988) and highest permeability values from well tests (50 md) yield, respectively, ground-water velocities of 6.1 and 6.4 ft/yr (1.9 or 2.0 m/yr), which translates to travel (residence) times of approximately 17,000 yr (20 mi [32 km] at 6.1 or 6.4 ft/yr [1.9 or 2.0 m/yr]). This age corresponds almost exactly to that of a major recharge event in the San Juan Basin and is close to another event dated at approximately 22,000 yr B.P. (Phillips and others, 1986). Use of Fruitland aquifer permeabilities (10 md or less)

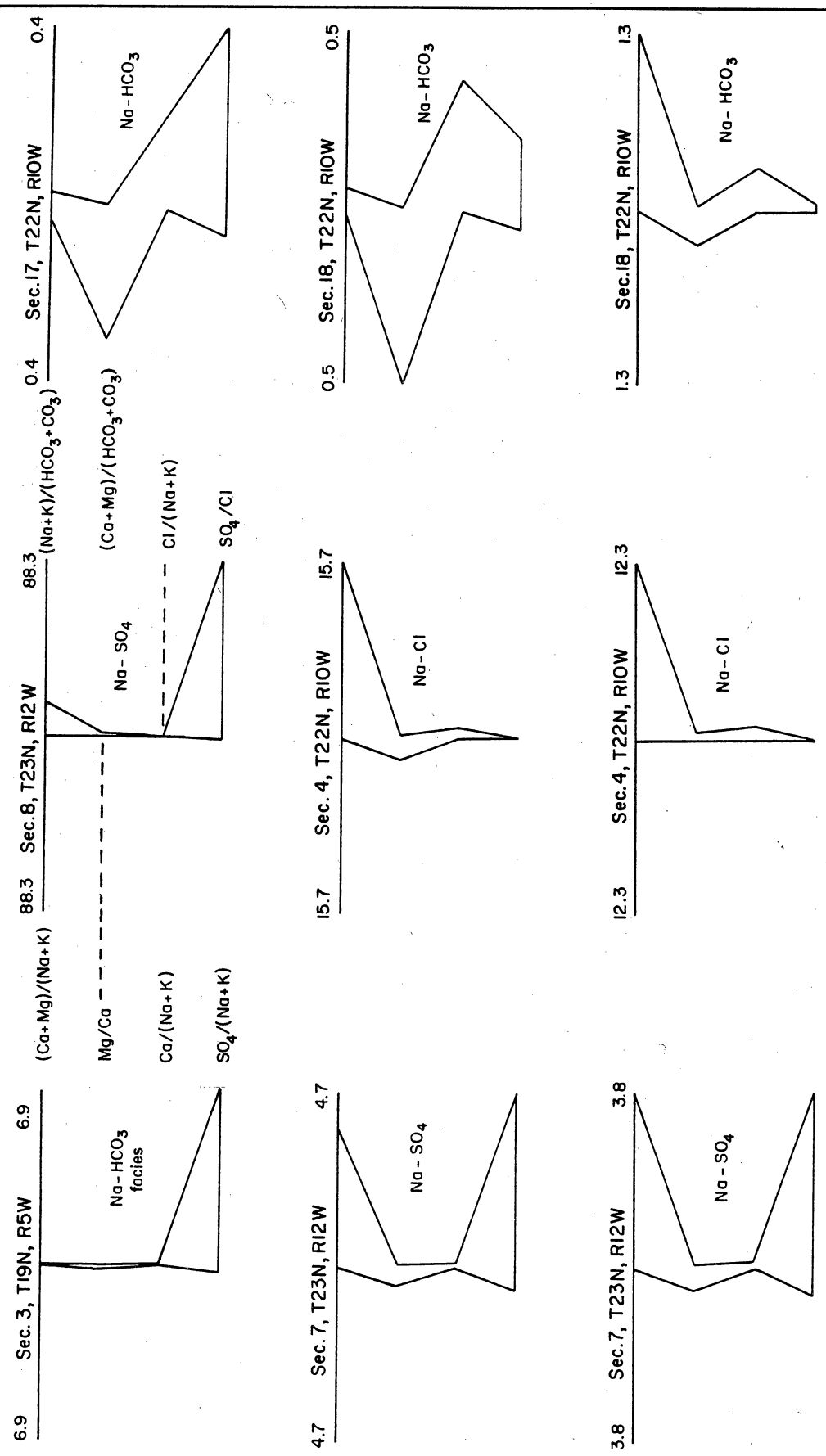
6.9
Sec. 3, T19N, R5W
6.9
Na-HCO3 facies
4.7
Sec. 7, T23N, R12W
4.7
Na-SO4
3.8
Sec. 7, T23N, R12W
3.8
Na-SO4
15.7
Sec. 4, T22N, R10W
15.7
Na-Cl
12.3
Sec. 4, T22N, R10W
12.3
Na-Cl
0.5
Sec. 18, T22N, R10W
0.5
Na-HCO3
1.3
Sec. 18, T22N, R10W
1.3
Na-HCO3
0.4
Sec. 17, T22N, R10W
0.4
Na-HCO3
88.3
Sec. 8, T23N, R12W
88.3
Na-SO4
(Ca+Mg)/(Na+K)
Mg/Ca
Ca/(Na+K)
SO4/(Na+K)
(Na+K)/(HCO3+CO3)
(Ca+Mg)/(HCO3+CO3)
Cl/(Na+K)
SO4/Cl

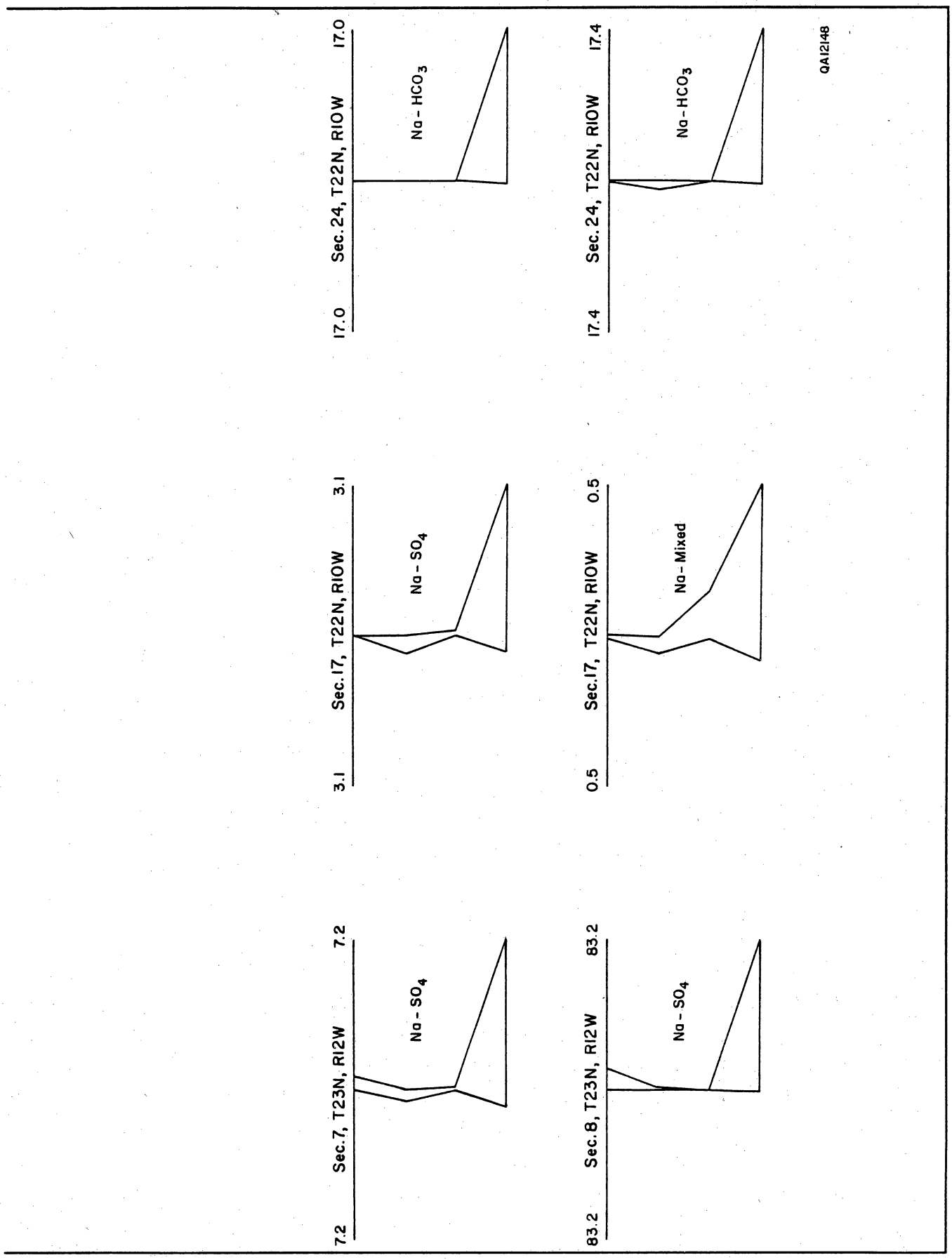

Figure 21. Stiff ionic-ratio diagrams, Fruitland waters, southern margin of the San Juan Basin (from Kaiser and Swartz, 1990).

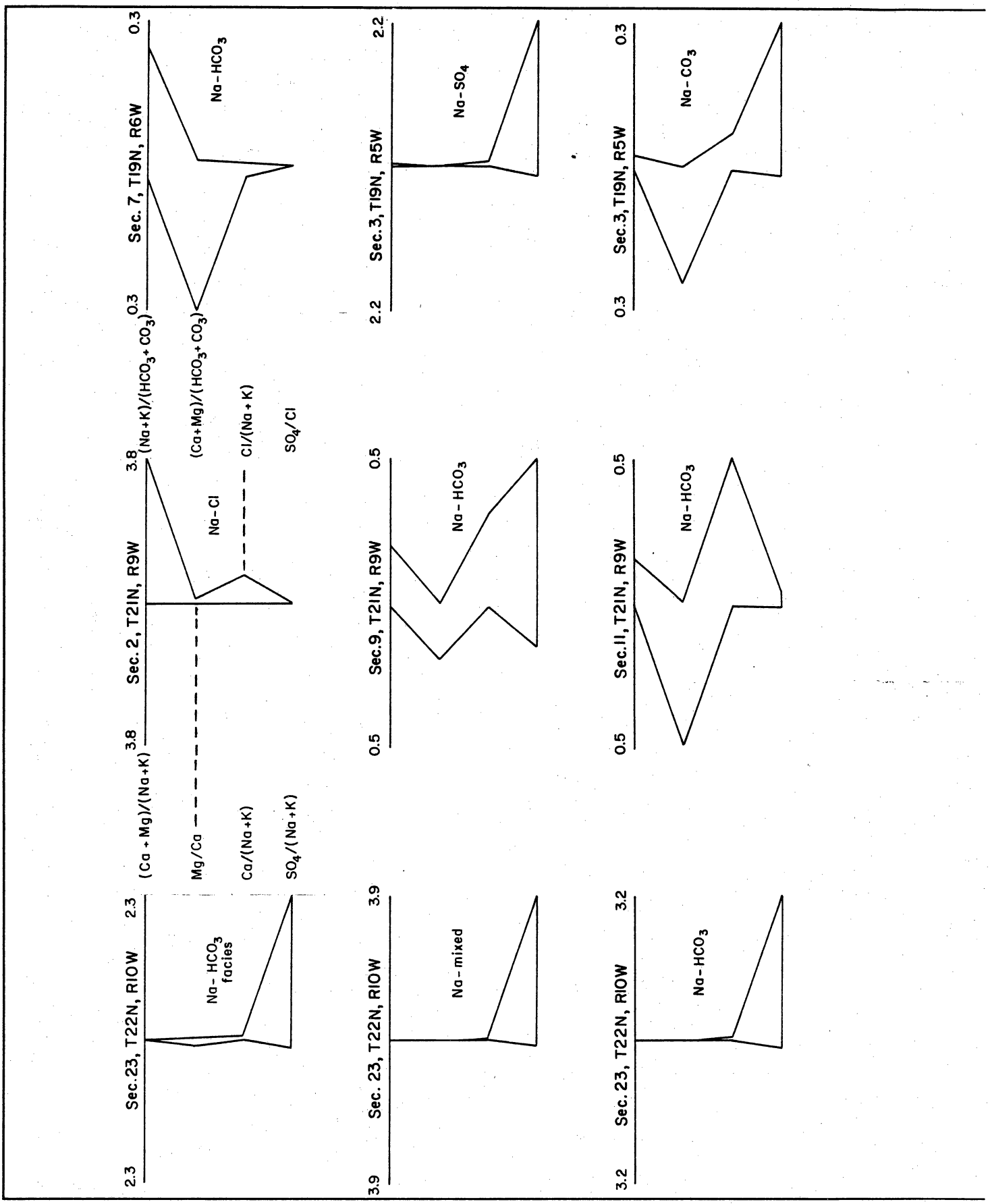
(Ca + Mg)/(Na+K)
Mg/Ca
Ca/(Na+K)
SO4/(Na+K)
(Na+K)/(HCO3+CO3)
(Ca+Mg)/(HCO3+CO3)
Cl/(Na+K)
SO4/Cl
Sec.23, T22N, R10W
Na-HCO3 facies
Sec. 2, T21N, R9W
Na-Cl
Sec.9, T21N, R9W
Na-HCO3
Sec.11, T21N, R9W
Na-HCO3
Sec. 7, T19N, R6W
Na-HCO3
Sec.3, T19N, R5W
Na-SO4
Sec.3, T19N, R5W
Na-CO3
Sec. 23, T22N, R10W
Na-mixed
Sec. 23, T22N, R10W
Na-HCO3

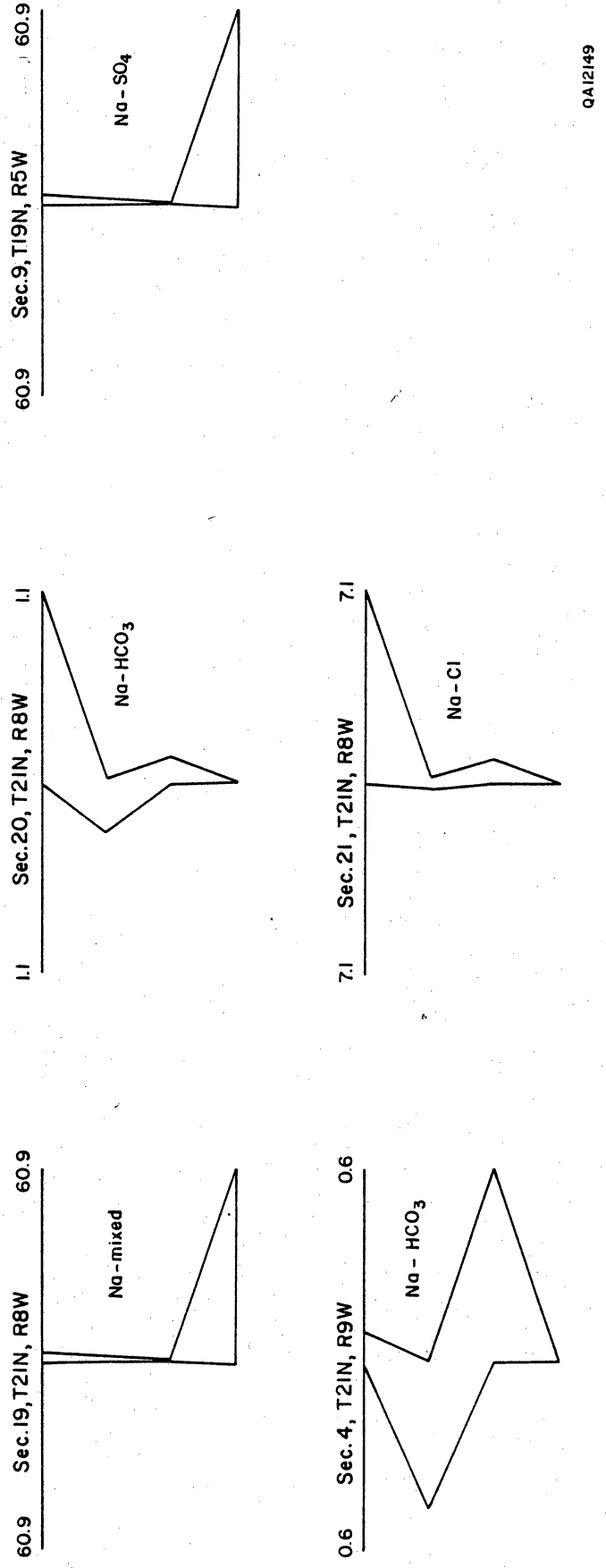

Figure 22. Stiff ionic-ratio diagrams, Fruitland waters, southern margin of the San Juan Basin (from Kaiser and Swartz, 1990).

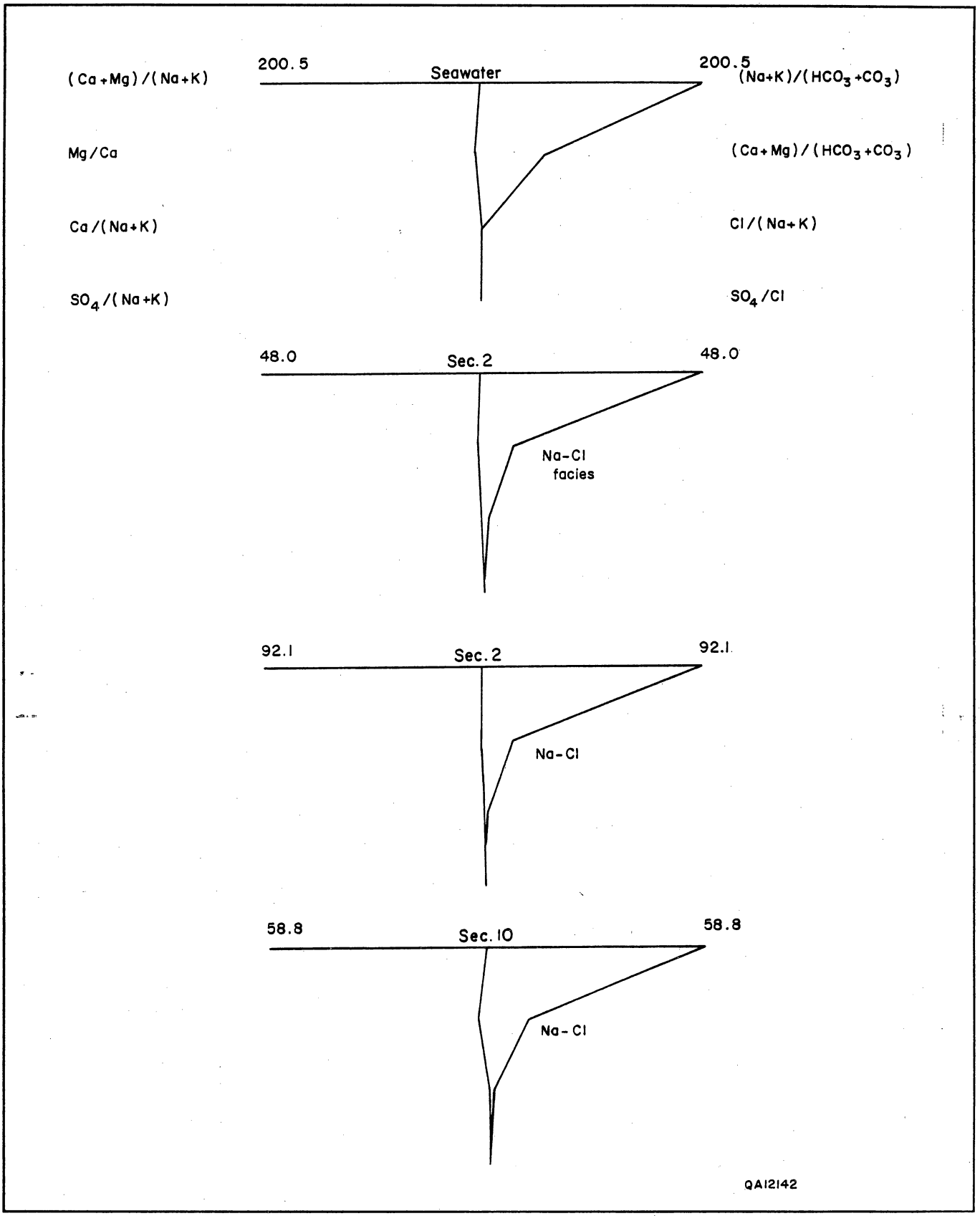

Figure 23. Stiff ionic-ratio diagrams, Fruitland coalbed waters, T24N, R9W, San Juan Basin (from Kaiser and Swartz, 1990). Their similarity to seawater suggests the presence of marine waters. See figure 16 for area location.

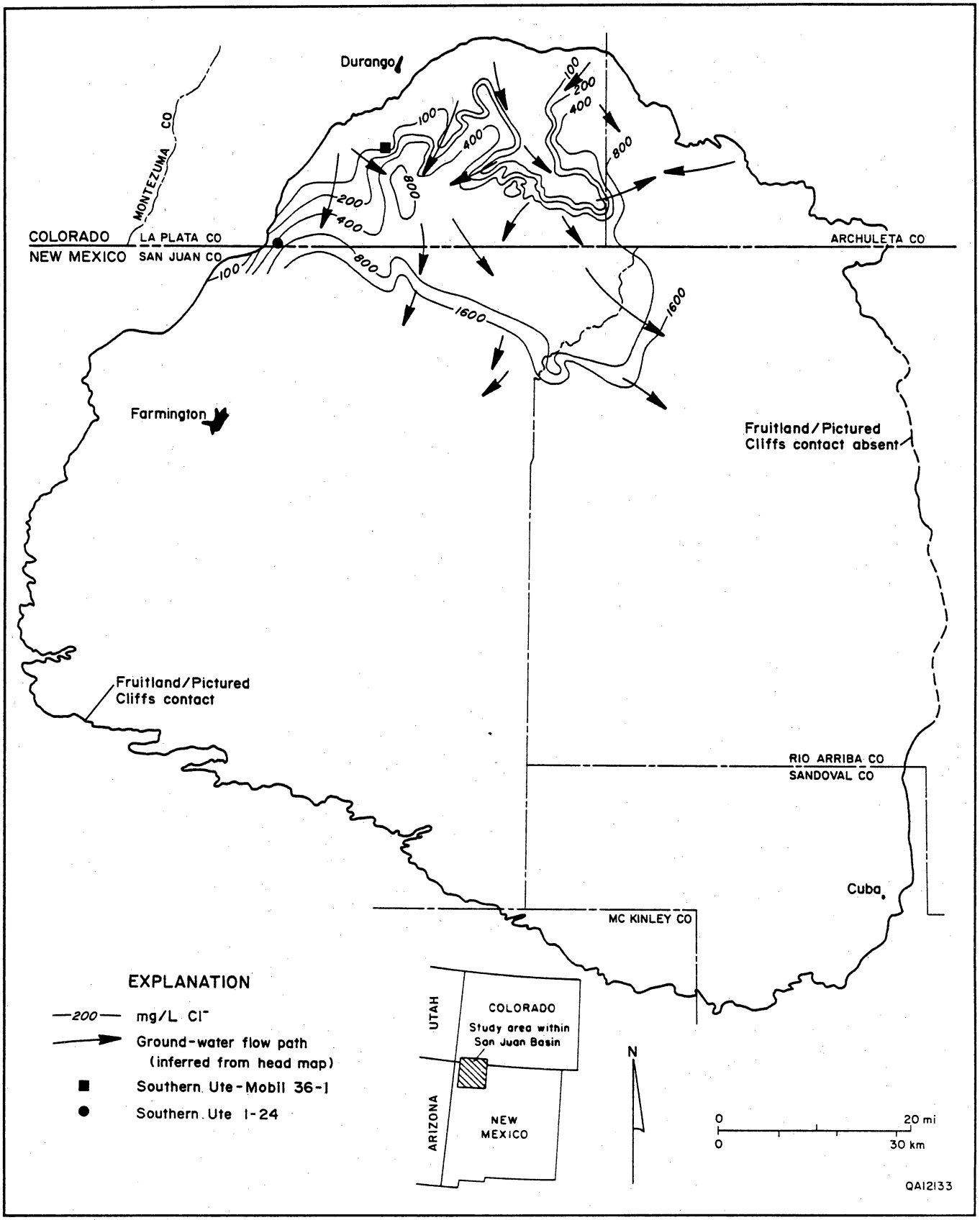

Figure 24. Chlorinity map of Fruitland waters, north-central part of the San Juan Basin (from Kaiser and Swartz, 1990). Distribution of chloride shows that flow is in directions inferred from the head map (fig. 1). Low chlorinities coincide with overpressure (fig. 6).

that are typically reported from well tests yield relatively long travel times of greater than 80,000 yr. Because permeability in a fractured reservoir is scale dependent, or increases with sample size (Garven, 1986), high permeabilities (fast ground-water flow times) are predictable from regional heat-flow data. Higher regional than local permeability is inferred from scale dependency. Consequently, the Fruitland Formation regionally is a homogeneous, hydraulically interconnected aquifer, or single hydrologic unit, but locally is a heterogeneous, disconnected aquifer. Local heterogeneity is indicated by large vertical and lateral pressure gradients (fig. 3).

Hydrostratigraphy and Regional Flow

The Fruitland–Pictured Cliffs aquifer system is defined to include the Fruitland Formation, upper Pictured Cliffs sandstone tongues that intertongue with the Fruitland, and the Pictured Cliffs Sandstone, which underlies the coal-bearing Fruitland (Ayers and others, this vol., their figs. 1 and 19; Ayers and Zellers, this vol., their fig. 1). The aquifer system is confined by shale and is overlain and underlain, respectively, by the Kirtland Shale and Lewis Shale. Components of the Fruitland–Pictured Cliffs aquifer system were illustrated earlier (Kaiser and Swartz, 1988) in a regional hydrostratigraphic cross section and are defined by hydraulic head, pressure gradients, hydrochemistry, relative permeability, topography, and geography.

The potentiometric surface slopes from the basin margin toward the San Juan River valley, and ground water flows laterally, mainly from the northern and northwestern basin margins toward the river valley (fig. 1). Vertical flow is down the steep northern flank (fig. 25), as indicated by a regional vertical pressure gradient (~0.30 psi/ft) that is less than the hydrostatic gradient (fig. 5). At the north, the potentiometric surface is above land surface (overpressured conditions) to a point just beyond the Crandell 7 well; southward it is below land surface (underpressured) (fig. 25). Note that the pronounced steepening of the potentiometric surface between the Southern Ute 21-2 and Crandell 7 wells coincides with basinward pinch-out of thick, continuous coal seams and upper Pictured Cliffs sandstone tongues in the vicinity of the Cedar Hill field (Keys E-1 and Schneider B 1S) (fig. 25).

The Fruitland Formation is a single hydrologic unit, as shown by similar heads and water chemistry in interbedded coalbeds and sandstones. In the north, hydraulic communication between the Fruitland Formation and upper Pictured Cliffs sandstone tongues is inferred from similar heads and their intertonguing relation (Ayers and Zellers, this vol., their fig. 1; Ayers and others, this vol., their fig. 2). Therefore, the two are considered a single hydrostratigraphic unit that transmits ground water mainly south and southwest. Almost nothing is known about their relative permeabilities. The hydraulic relation of the Fruitland–upper Pictured Cliffs hydrostratigraphic unit to the underlying main Pictured Cliffs Sandstone, or to that exclusive of the sandstone tongues, is uncertain. Available pressure data indicate that Fruitland heads are considerably higher than those of the low-permeability main Pictured Cliffs Sandstone and that the two are not in hydraulic communication in the northern part of the basin. Pictured Cliffs heads are highest (6,200 to 7,000 ft [1,890 to 2,134 m]) in the northwestern part of the basin, adjacent to the outcrop, and decrease southeast to approximately 6,000 ft (1,829 m), parallel to the Pictured Cliffs depositional strike. Except for the northwestern part of the basin, Pictured Cliffs heads in the northern basin are 800 to 1,000 ft (244 to 305 m) lower than those in the Fruitland Formation (Kaiser, Bureau of Economic Geology unpublished map). This large head difference partly reflects failure to attain pressure equilibrium during short-term well testing, which implies low permeability in the Pictured Cliffs Sandstone. Even though strong potential for downward flow (leakage) is indicated from the Fruitland Formation to the main Pictured Cliffs Sandstone, this potential, particularly in low-permeability strata, does not mean that significant flow actually occurs. The very large head difference between the Fruitland Formation and main Pictured Cliffs Sandstone indicates hydraulic separation and low permeability in the main Pictured Cliffs Sandstone, which is too tight to receive and transmit appreciable recharge basinward (Cumella, 1981; Kaiser and Swartz, 1988, 1989). If this were not the case, head differentials and vertical pressure gradients would be much less. Separation is further indicated in the hydrochemistry; Pictured Cliffs waters are Na-Cl type, whereas Fruitland waters are a unique, low-chloride, Na-HCO_3 type (table 3). Thus, ground-water flow is mainly in the Fruitland Formation, especially in more permeable coal seams, and in the upper Pictured Cliffs sandstone tongues, which are confined by the low-permeability main Pictured Cliffs Sandstone below and the Kirtland Shale above. Consequently, in the northern part of the basin, the Fruitland–Pictured Cliffs aquifer system consists of the Fruitland Formation and upper Pictured Cliffs sandstone tongues (fig. 25; Ayers and others, this vol., their fig. 2).

In the southern part of the basin, major upper Pictured Cliffs sandstone tongues are absent and the Fruitland Formation rests conformably on the Pictured Cliffs Sandstone. Heads and hydrochemistries in the basal coal beds and Pictured Cliffs Sandstone are similar; the waters of both are dominantly Na-Cl type with similar salinities. In the San Juan River valley, Pictured Cliffs

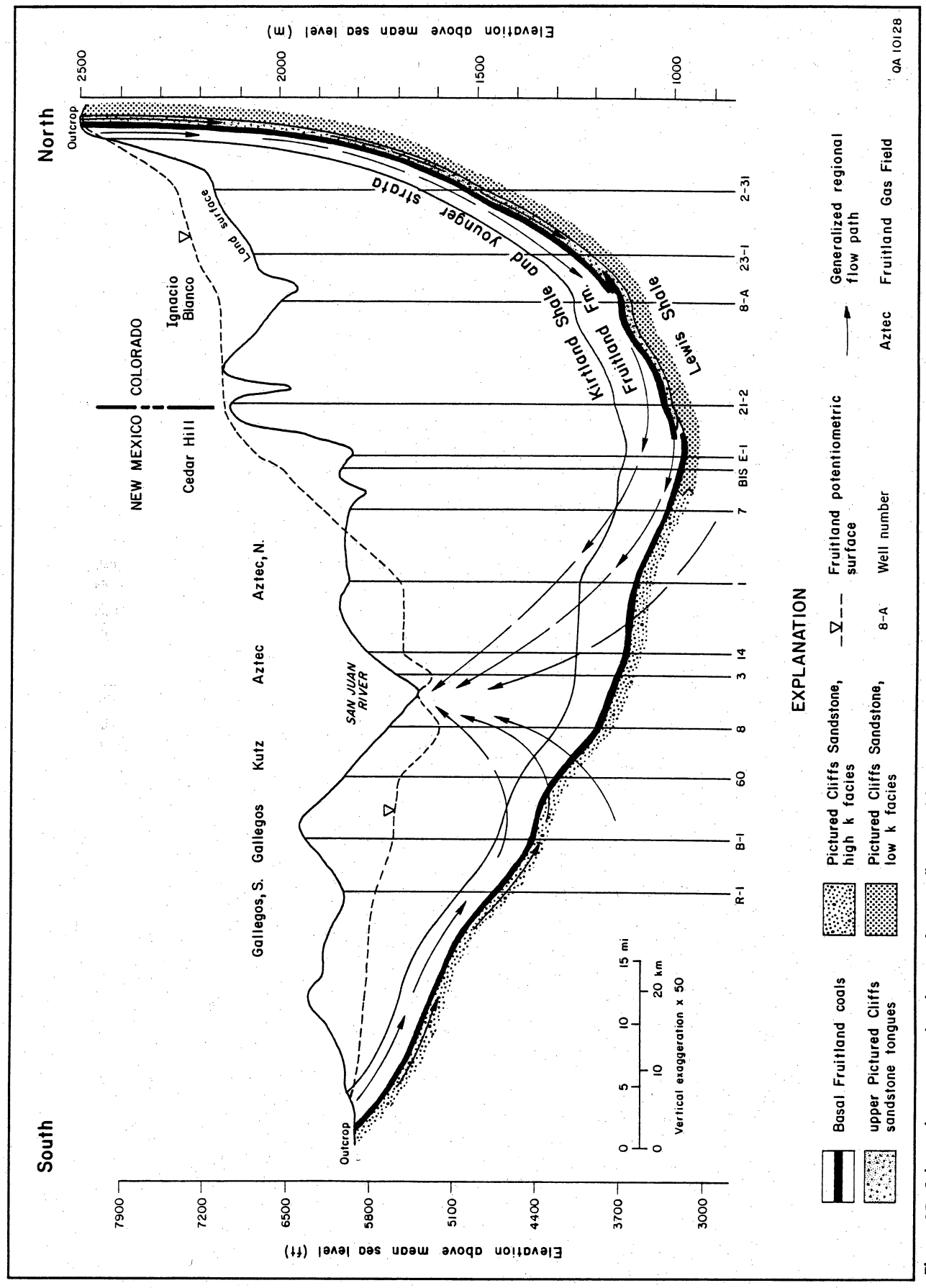

Figure 25. Schematic cross-sectional ground-water flow, Fruitland–Pictured Cliffs aquifer system (modified from Kaiser and Swartz, 1988). See figure 1 for line of section. Basal Fruitland coal seams pinch out in vicinity of Cedar Hill field between wells 21-2 and E-1 and upward flow is initiated at this point. In the north, the potentiometric surface is above and independent of land surface, indicating artesian overpressured conditions.

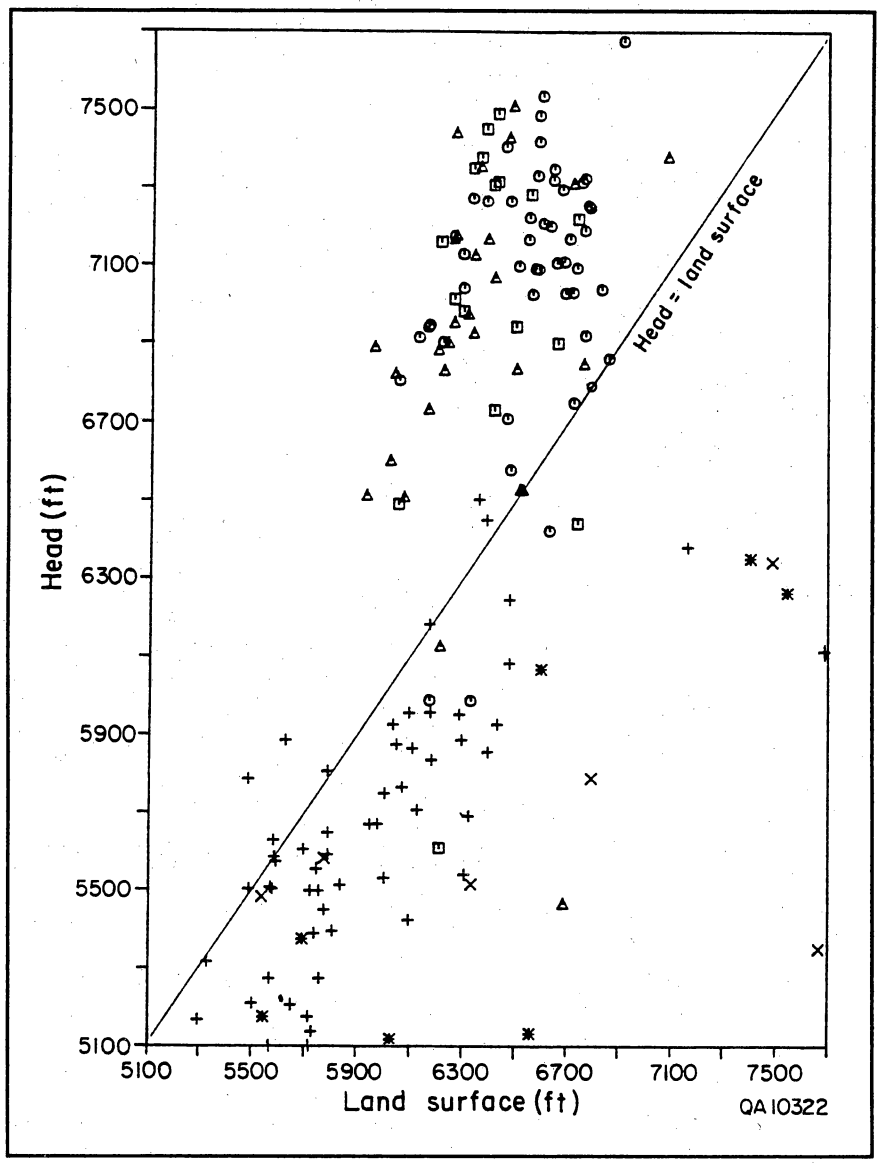

Figure 26. Fruitland fresh-water equivalent head versus land surface (from Kaiser and Swartz, 1988). Geometric symbols for north-central part of basin, stick symbols for west-central part of basin. In the north, independence of head and land surface indicates artesian conditions, whereas in the southwest, dependence indicates cross-formational flow.

heads are similar to or slightly greater than those of the Fruitland. Elsewhere, in the west-central part of the basin, Pictured Cliffs heads are somewhat less or about equal to Fruitland heads, indicating a single aquifer system. Thus, hydraulic communication between the basal Fruitland Formation and Pictured Cliffs Sandstone is inferred from their similar heads and water chemistries. This communication accounts for occasional water production in wells completed in the basal coal. However, in the southeastern part of the basin where Pictured Cliffs heads are as much as 700 ft (213 m) lower than Fruitland heads, the two units are hydraulically separate. Consequently, in the west-central part of the basin, the Fruitland–Pictured Cliffs aquifer system consists of the basal Fruitland Formation and the Pictured Cliffs Sandstone (fig. 25); it transmits ground water from the northeast and southeast for eventual discharge to the San Juan River.

In the northern part of the basin, the aquifer transmits ground water under high head from the northern and northwestern margins of the basin. Basinward, flow must eventually turn upward as cross-formational flow along the pinch-out of thick aquifer coal seams and upper Pictured Cliffs sandstone tongues (fig. 25). Hydraulic head is independent of land surface, indicating a confined aquifer and little gravity-driven cross-formational flow; that is, artesian conditions (fig. 26). In the west-central part of the basin, upward cross-formational flow is centered on the San Juan River valley, where the potential for upward flow is indicated by a regional vertical pressure gradient (~0.60 psi/ft) that is greater than the hydrostatic gradient (fig. 5). The plot of head versus land surface (fig. 26) shows correlation of head and land surface, indicating a partially confined aquifer experiencing gravity-driven cross-formational flow (Tóth, 1978).

Abnormal Formation Pressure

The Fruitland Formation is both overpressured and underpressured, having an overpressured area surrounded by a much larger underpressured area (fig. 6). Factors contributing to underpressuring are reduced temperature, uplift, and erosion (Bradley, 1975), poor vertical hydraulic connection with shallow water-table aquifers, heterogeneous permeability or variable hydraulic conductivity, recharge and discharge areas hydraulically disconnected, and basinal discharge in excess of recharge (Belitz and Bredehoeft, 1988). Overpressuring is indicative of increased temperature, basinal subsidence, compaction, and hydrocarbon generation or artesian conditions.

Temperature reduction is thought to be an important cause of abnormal pressure, especially underpressuring (Bradley, 1975), which in the San Juan Basin can be explained in the context of basin evolution. During the Oligocene Epoch the Fruitland Formation was buried under approximately 9,000 ft (2,743 m) of sediment and subjected to igneous intrusion (Bond, 1984). Overpressuring developed in response to burial and intense hydrocarbon generation. Subsequent to the Oligocene thermal event there was basinwide deterioration to an underpressured state following uplift and erosion.

An example serves to illustrate evolution of the basinal pressure regime. First, assume that the Oligocene overpressured gradient was a realistic 0.80 psi/ft; formation pressure at 9,000 ft (2,743 m) would have been 7,200 psi. Next, assume the formation was sealed and that 6,000 ft (1,829 m) of sediment was eroded in post-Oligocene time, yielding a burial depth similar to that of today (3,000 ft [914 m]). Finally, using today's temperature gradient (1.9°F/100 ft [1.1°C/30 m]), a pressure change of 75 psi/°F, and a hydrostatic gradient of 0.433 psi/ft, one can calculate the pressure gradient per foot of depth change according to Bradley (1975):

$$\Delta PG_f - \Delta PG_h = PG_{\Delta d}$$
$$(0.019°F/ft \times 75\ psi/°F) - 0.433\ psi/ft = 0.992\ psi/ft \quad (1)$$

This corresponds to a pressure reduction of 5,952 psi (6,000 ft × 0.992 psi/ft) due to temperature reduction, uplift, and erosion. Predicted formation pressure is 1,248 psi (7,200 psi – 5,952 psi), 51 psi less than hydrostatic pressure at 3,000 ft (1,299 psi) and underpressured as observed throughout most of the basin.

Fruitland overpressuring is not an artifact of Oligocene hydrocarbon generation and overpressuring, or a fossil geopressure; it is thought to represent a repressuring event of probable Pliocene age that occurred after basinwide deterioration to an underpressured state. Overpressuring originated in response to establishment of the basin's present topography and hydrodynamics in middle Pliocene time (Kelley, 1955; Berry, 1959); it is attributed to artesian conditions; that is, to an elevated recharge area on the basin's northern margin and to aquifer confinement and basinward pinch-out (fig. 25). In other words, hydraulic head is elevated, raising pressures down hydraulic gradient well above hydrostatic so that head rises above land surface (overpressured). This interpretation is supported by the fact that overpressuring is adapted to the present geomorphology and not to the basin's tectonic axis (Ayers and others, this vol., their fig. 5) or most thermally mature area (Scott and others, this vol., their fig. 3). The overpressured area is located north and west of the basin axis and extends northward to the recharge area at the basin rim. Most of the overpressured area lies south of the area of highest vitrinite reflectance and only partially overlaps the highest rank coals. The pressure transition parallels the 0.78 isoreflectance line (boundary between high-volatile A and B bituminous) on the southwest but is discordant to isoreflectance in the remainder of the basin (Scott and others, this vol., their fig. 3). Disparity between overpressuring and the inferred region of maximum Oligocene gas generation is not surprising, since today's formation temperatures are too low to generate gas (Spencer, 1987). Moreover, overpressure coincides with modern hydrologic elements such as the freshest (low-chloride) formation waters (meteoric water) (figs. 6, 18, and 24) and distribution of aquifer coal seams and upper Pictured Cliffs sandstone tongues (Ayers and others, this vol., their fig. 21).

Cross-Sectional Modeling

Regional ground-water flow was modeled in a cross section across the San Juan Basin to further conceptualize ground-water flow and to elucidate cross-formational flow. Numerical modeling is a logical extension of head, pressure, and hydrochemical mapping and was done to test assumptions about ground-water circulation patterns, causes of abnormal pressuring, and regional permeability contrasts made from potentiometric-surface and pressure-gradient maps (figs. 1 and 6) and from stratigraphic cross sections (Ambrose and Ayers, this vol., their fig. 3; Ayers and others, this vol., their fig. 2). Modeled strata include the Pictured Cliffs Sandstone and all younger strata. FREESURF (Neuman and Witherspoon, 1970), a two-dimensional, steady-state flow model, was used to solve the equation describing ground-water flow in porous media. Specifically, our objective was to better understand Fruitland hydrodynamics by simulating potentiometric anomalies and abnormal pressuring.

Hydrostratigraphy

The ground-water flow model was constructed from geophysical logs along a 90-mi (145-km), north-south cross section in the western San Juan Basin oriented nearly perpendicular to the head contours, or parallel to the inferred flow path (fig. 1). Hydrostratigraphic boundaries follow the stratigraphy of Ayers and others (this vol.) and were chosen on the basis of hydrologic characteristics and log response. Three major units were defined in the Cretaceous (Pictured Cliffs Sandstone, Fruitland Formation, and Kirtland Shale) and two in the Tertiary (Ojo Alamo Sandstone and undivided Tertiary).

The base of the Pictured Cliffs Sandstone is defined on geophysical logs as the base of upward-coarsening log patterns above the Lewis Shale. Its top is directly below the lowest Fruitland coal seams. On the northern limb of the basin, upper Pictured Cliffs sandstone tongues are included in the Pictured Cliffs Sandstone, but basinward, where the basal Fruitland coal is thick, a separate basal coal/upper Pictured Cliffs Sandstone unit is defined. The Fruitland Formation was divided for modeling into three units. In the lower Fruitland Formation, northern and southern coal units containing coal, sandstone, and shale are defined. The northern coal unit contains numerous, thick, continuous coal seams, whereas the southern coal unit contains fewer, thinner, and less continuous coal seams. The upper Fruitland Formation is defined as a sandstone unit, composed mainly of sandstone and shale. The Kirtland Shale was divided into three units: lower Kirtland Shale, Farmington shale and sandstone unit, and upper Kirtland Shale. The Farmington unit is a sequence of interbedded shale and thin sandstones (Ayers and others, this vol., their fig. 1).

The Ojo Alamo Sandstone unconformably overlies the Kirtland Shale and is defined by its blocky log pattern. The Ojo Alamo Formation is continuous throughout the southern part of the basin but is indistinguishable from other Tertiary units in the northern part. The undivided Tertiary includes the Nacimiento–Animas Formations and San Jose Formation, which consist of alluvial sandstones and mudstones. The Nacimiento and Animas Formations are stratigraphic equivalents and are considered a single hydrostratigraphic unit (Stone and others, 1983; Phillips and others, 1989); this unit is overlain by the San Jose Formation.

Computer Program

The ground-water flow model was implemented with FREESURF, a computer program developed by Neuman and Witherspoon (1970). FREESURF solves the partial differential equation describing two-dimensional steady-state flow through porous media:

$$\frac{\partial}{\partial x}\left(K_x \frac{\partial h}{\partial x}\right) + \frac{\partial}{\partial z}\left(K_z \frac{\partial h}{\partial z}\right) = 0 \qquad (2)$$

using a finite-element method and noniterative Gaussian elimination scheme (variational method of Rayleigh-Ritz). FREESURF computes hydraulic head at each node and calculates fluxes (recharge and discharge) along a prescribed head boundary; it was modified to compute stream functions (streamlines) and Darcy velocities (Fogg and Senger, 1985; Senger and others, 1987; Senger, 1989) to show ground-water flow patterns and fluxes. These are difficult, if not impossible, to establish from contour maps of computed hydraulic heads, because of permeability anisotropy and extreme vertical exaggeration on cross-sectional models.

FREESURF output was evaluated using three plotting routines developed by R. K. Senger of the Bureau of Economic Geology (personal communication, 1990). One routine contours hydraulic head and delineates the pressure regime. Another plots velocity vectors to show direction and rate of flow. The third routine uses velocity and a unit thickness of 1 ft (0.3 m) to plot stream tubes that show magnitude of flow for consequent delineation of the most transmissive units.

Modeling

The finite-element mesh was designed to represent the cross-sectional model's hydrostratigraphy and basin geometry (fig. 27). The steep northern limb was designed by manually projecting modeled units updip from the northernmost geophysical log to the outcrop along a section parallel to the lateral flow direction inferred from the head map (fig. 1). The southern limb was similarly designed, but along a section oblique to flow direction, into an area having values of Fruitland static-water levels.

The model's lower boundary is the contact between Pictured Cliffs Sandstone and Lewis Shale, a thick 600-ft (183-m) marine shale and regional confining unit. This contact is a no-flow boundary (fig. 27). The model's upper boundary is the water table in the undivided Tertiary. To establish the water table, a topographic profile was made along the model's line of section, and static-water levels in the vicinity of the section were documented from the literature. The water table was approximated by assuming that it mirrors topography at depths below land surface estimated from actual water levels. Where the section crosses perennial rivers, the water table was set to their surface elevation. The water table is a constant head boundary for the model simulations and a prescribed flux boundary for investigation of recharge and discharge.

The finite-element mesh was constructed (discretized) by passing vertical (transverse) lines through the cross

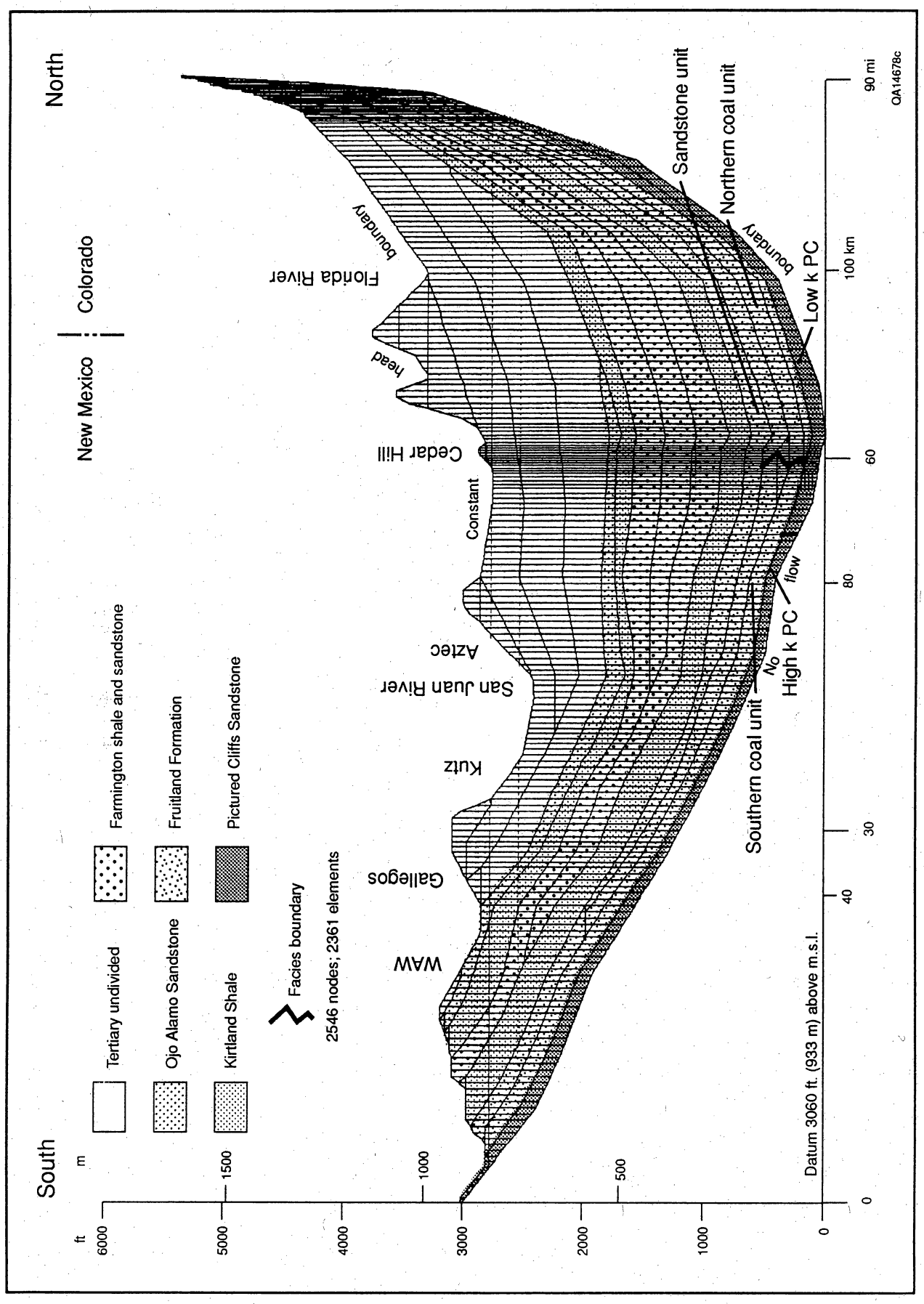

Figure 27. Finite-element mesh of major hydrogeologic units above the Lewis Shale, San Juan Basin. Units are assigned permeabilities that vary among simulations. The upper surface is a constant head boundary corresponding to the water table. The lower surface is a no-flow boundary corresponding to the contact between the Pictured Cliffs Sandstone and Lewis Shale. Vertical exaggeration 50×.

section and lateral lines parallel to hydrostratigraphic boundaries. Transverses are approximately 0.5 mi (0.8 km) apart, except at the regional facies change and on the basin's steep northern limb. Additional transverses were added in those areas to ensure more accurate modeling of flow. Additional lateral lines were placed parallel to hydrostratigraphic boundaries to more uniformly subdivide the units and decrease their thickness for more accurate modeling. Intersection of transverse lines with the lateral lines define 2,546 nodes, which in turn enclose the model's 2,361 elements (fig. 27).

Model Limitations

The largest potential source of error is in the permeability distribution and assumed anisotropies of hydrostratigraphic units, that is, in the ratio between horizontal and vertical permeability (k_h/k_v). Only meager permeability data are available, which indicate low permeabilities (0.1 to 10 md) in the Fruitland Formation and Pictured Cliffs Sandstone. Permeability of Fruitland coal seams is orders of magnitude higher than sandstones. Moreover, discretization required simplification of the hydrostratigraphy. Complexity at the local scale (Ambrose and Ayers, this vol., their fig. 3; Ayers and Zellers, this vol., their fig. 17) is far greater than can be depicted in a regional model. The model simulates ground-water flow north-south across the San Juan Basin, which is oblique to the direction of regional flow south of Gallegos (fig. 1). Thus, results of the model may not be directly comparable to observed conditions.

The model assumes steady-state conditions; that is, ground-water flow pattern and velocity do not change with time and are governed by basin geometry, topography, and permeability distribution. The present flow system was established in the Pliocene upon establishment of the basin's present topography. Uplift, erosion, and retreat of the basin margins since then have been limited and have had minor effect on the flow system. One possible cause of transient conditions is extensive hydrocarbon production from the Pictured Cliffs Sandstone and subsequent decline of reservoir pressure below virgin conditions.

Although Darcy's law assumes flow through porous media, the strata in this model have low matrix permeability and are fractured. Fracture flow dominates in coal beds. Nevertheless, because the Fruitland coal beds are pervasively fractured (cleated), they should behave regionally as a porous medium. Sandstone, however, is discretely fractured (Tremain and others, this vol.), and local fracture flow is possible if fracture permeability exceeds matrix permeability.

Another limitation of the model is the assumption of a homogeneous fluid (fresh water) throughout the basin, which neglects effects of variable density and temperature. A denser, more viscous fluid basinward would result in a decrease of hydraulic conductivity, which influences flow rates linearly. TDS content of formation waters increases basinward along the cross section, but does not exceed 35,000 mg/L. Because hydraulic gradients are steep, topographically driven flow undoubtedly dominates buoyancy-driven flow associated with these slightly denser formation waters (Senger, 1990). Thus density and viscosity effects are probably minimal and may even be balanced by a basinward increase in temperature. Other factors that may affect the model are the assumption of no flow into or out of the Lewis Shale and no consideration of flow perpendicular to the cross section.

Model Simulations

The simulations were done to investigate the relative importance of such factors as permeability anisotropy and confinement on ground-water flow in the San Juan Basin. Three simulations are presented here to illustrate the interactions of geology and hydrology that explain the hydrodynamics of the Fruitland–Pictured Cliffs aquifer system. Because of uncertainty about permeability and inherent limitations of the model, simulation design was kept simple to reduce the chance for error and to facilitate interpretation of results. The simplest simulation is Model Simulation 1, in which all hydrostratigraphic units were assigned the same permeability. In Model Simulation 2, the Kirtland Shale is a confining unit. The most complex simulation is Model Simulation 3, where regional permeability contrasts were imposed to approximate observed data. Recharge and discharge were also investigated to further test Simulation 3. Permeabilities assigned for each simulation are given in table 4. Flow paths reflect direction and magnitude shown on plots of flow velocity and stream tubes for each simulation.

Model Simulations 1 and 2

In Simulation 1, no permeability constraints were imposed. Consequently, gravity-driven, cross-formational flow dominates the entire section (fig. 28). Flow is downward under topographic highs and upward under topographic lows. Note slight underpressuring (deep heads lower than surface heads) at the base of the cross section on either side of the state line. This reflects topographic highs in the area and the absence of confinement.

In Simulation 2, a low-permeability confining layer (Kirtland Shale) was added to the section, whereas permeability values in the upper and lower sections were unchanged (fig. 29). The Kirtland Shale in the center of the section isolates two flow systems: (1) one above that consists of a series of intermediate flow systems and (2) the other below that is regional. Flow

Table 4. Model permeabilities and k_h/k_v ratios.

Modeled hydrostratigraphic units	Simulation 1 md, k_h/k_v	Simulation 2 md, k_h/k_v	Simulation 3 md, k_h/k_v
Undivided Tertiary	1.0, 100	1.0, 100	10.0, 100
Ojo Alamo Sandstone	1.0, 100	1.0, 100	10.0, 100
Kirtland Shale			
Upper shale unit	1.0, 100	0.01, 1,000	0.01, 100
Farmington shale and sandstone unit	1.0, 100	0.01, 1,000	0.1, 100
Lower shale unit	1.0, 100	0.01, 1,000	0.01, 100
Fruitland Formation			
Sandstone unit	1.0, 100	1.0, 100	0.1, 100
Southern coal unit	1.0, 100	1.0, 100	0.1, 100
Northern coal unit	1.0, 100	1.0, 100	10.0, 100
Basal coal/upper Pictured Cliffs sandstone unit	1.0, 100	1.0, 100	10.0, 100
Pictured Cliffs Sandstone			
Southern unit	1.0, 100	1.0, 100	1.0, 100
Northern unit	1.0, 100	1.0, 100	0.1, 10,000

in the upper section is similar to that of Simulation 1, but is now cross-formational only to the top of the confining layer. Recharge over topographic highs and discharge to topographic lows divides flow into a series of intermediate cells.

In the lower section, ground water enters the basin at the northern margin, flows basinward, passes beneath the San Juan River, and exits at the southern margin. Overpressured conditions are simulated and extend nearly across the entire basin. Agreement between simulated and observed heads in the Fruitland Formation is good in the northern part of the basin and poor in the southern part. Note that the hydraulic gradient shows no change as flow turns updip (fig. 29), indicating that this is not the cause of the steep gradient mapped south of Cedar Hill field (fig. 1).

If k_h/k_v of the Kirtland Shale is reduced to 100, flow is still confined but would turn upward at the San Juan River, converging from the north and south. If k_h/k_v is reduced to 10, the Kirtland Shale is no longer a confining unit and gravity-induced cross-formational flow extends across the entire cross section to hydraulically connect all units. A k_h/k_v of 10 was too low (vertical permeability too high) and allowed heads to equilibrate readily in the vertical direction. Flow increases because the cross-sectional area through which vertical flow can take place is large compared with that for horizontal flow.

Model Simulation 3

In Simulation 3, we described the system to yield good agreement between computed and observed data. To approximate observed Fruitland heads, we imposed permeability contrasts that were inferred from the head map (fig. 1) and stratigraphic studies (Ambrose and Ayers, this vol.; Ayers and others, this vol.). Permeabilities assigned to the hydrostratigraphic units are consistent with available permeability data.

Flow patterns in Tertiary strata, despite an increase in lateral permeability from 1.0 to 10 md (table 4), differ little from those in Simulation 2 (figs. 29 and 30). Flow in these strata is separated from that in the lower section by the Kirtland Shale. Plots of velocity vectors and streamlines show that ground-water flow is concentrated in the permeable Tertiary section. The Fruitland–Pictured Cliffs aquifer system is isolated in the north and is in poor communication with Tertiary strata on the south, experiencing minor cross-formational flow. Only on the southern end of the section, where strata approach the outcrop, does appreciable flow move downward across the Kirtland Shale into the Fruitland–Pictured Cliffs aquifer. Correlation of Fruitland heads and land surface in the southern part of the basin indicates a poorly confined aquifer experiencing cross-formational flow (fig. 26). The southern outcrop is a discharge area. Consequently, on the southern margin

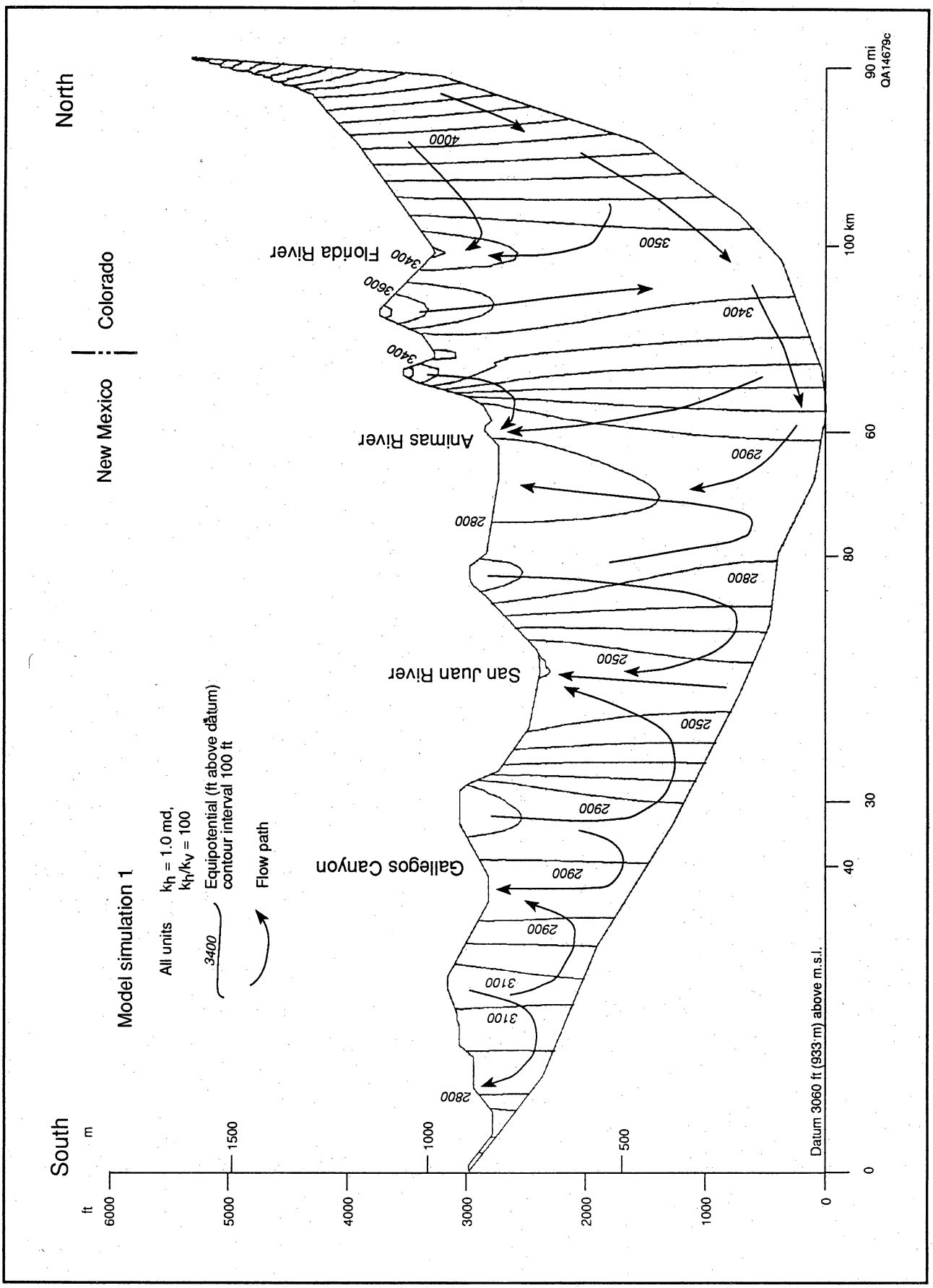

Figure 28. Equipotentials and generalized flow paths from Model Simulation 1, San Juan Basin. All units have the same permeability. Gravity-driven cross-formational flow dominates the entire section. Flow is downward under topographic highs and upward under topographic lows.

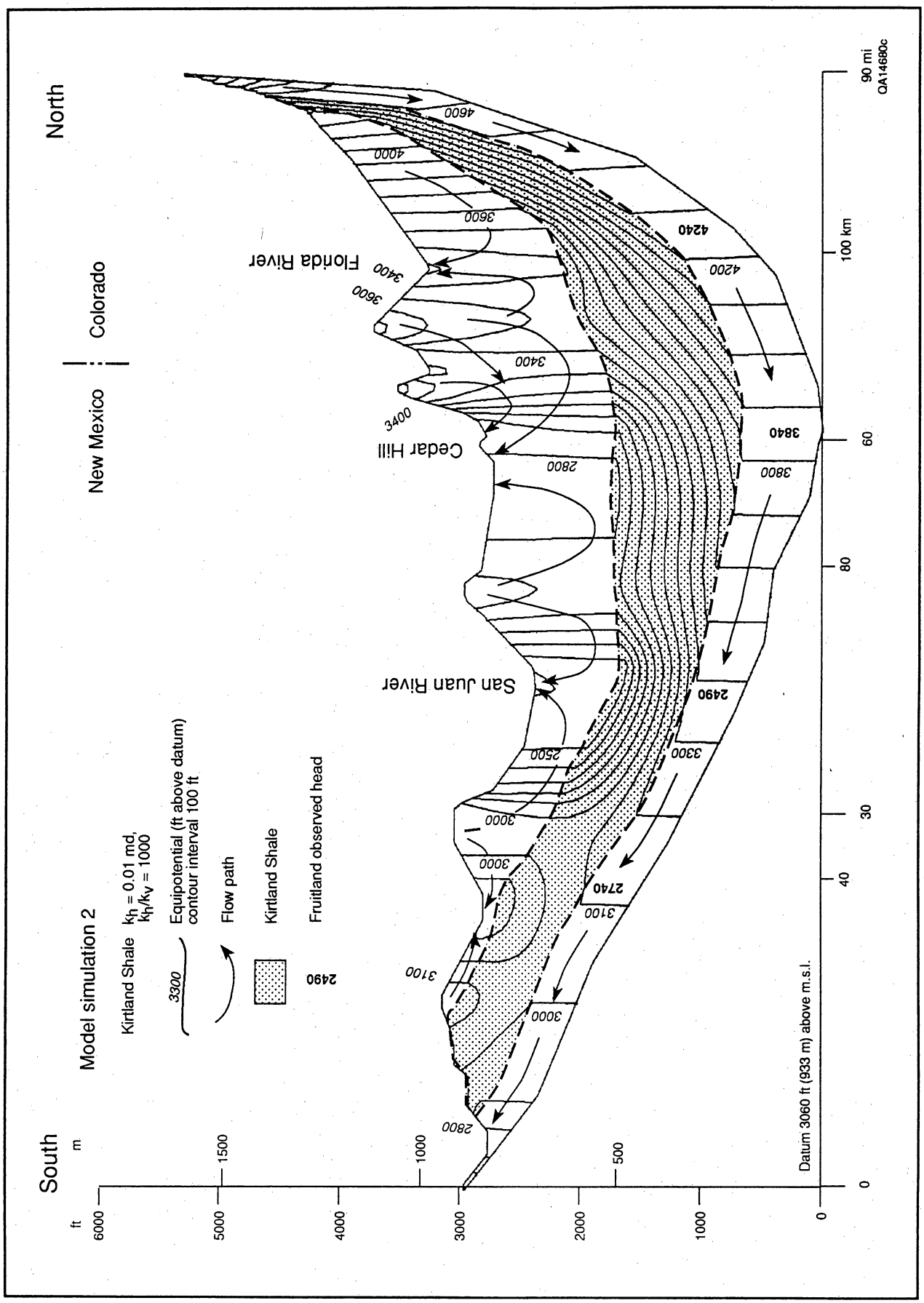

Figure 29. Equipotentials and generalized flow paths from Model Simulation 2, San Juan Basin. Kirtland Shale is an aquitard. Flow in Tertiary strata is cross formational, whereas that in the Fruitland Formation is lateral (confined). Ground water enters the basin at the northern margin, flows across the basin, and exits at the southern margin. Overpressure extends almost across the entire basin. Note the close agreement of simulated and observed heads in the northern part of the basin.

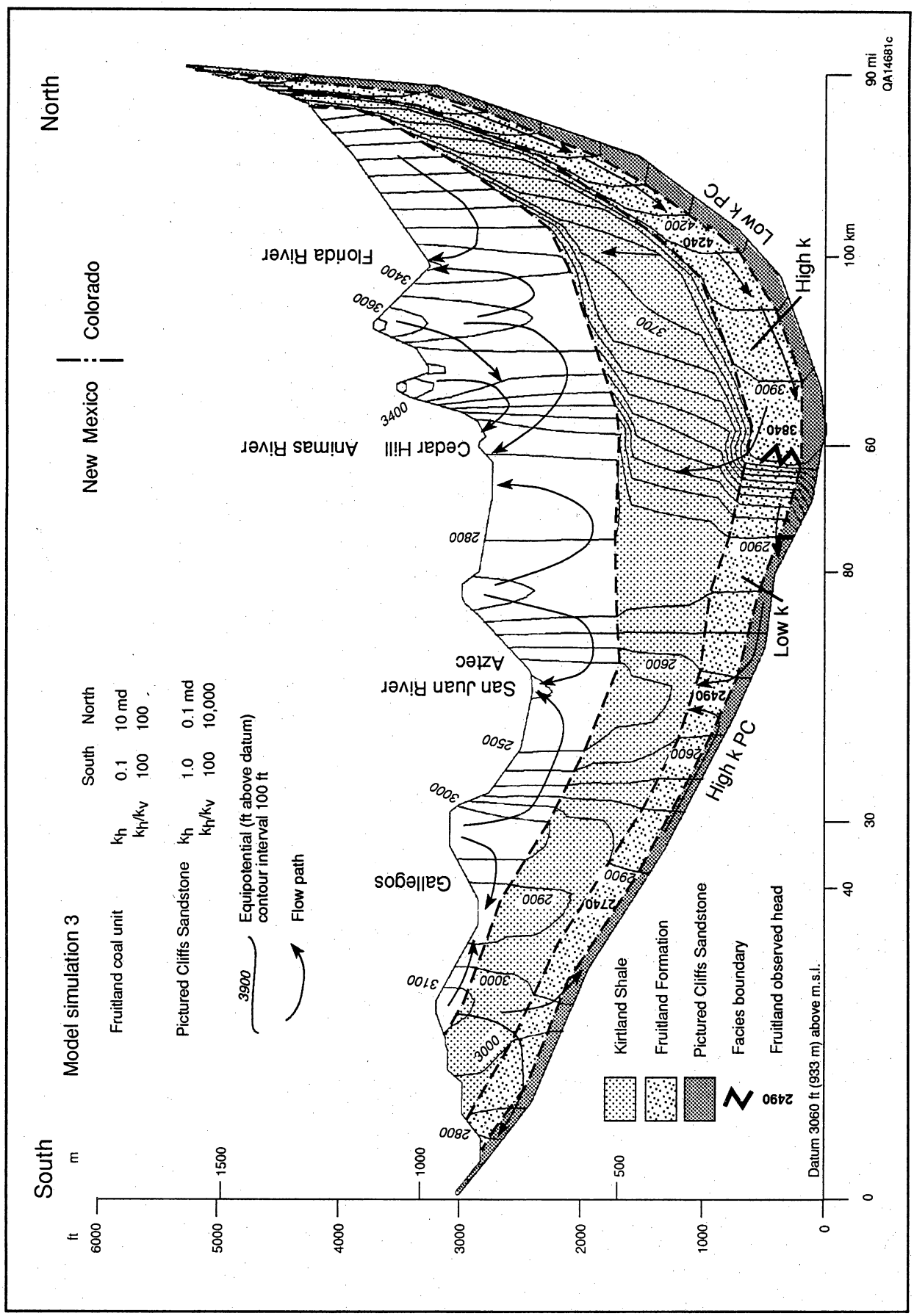

Figure 30. Equipotentials and generalized flow paths from Model Simulation 3, San Juan Basin. In the Cedar Hill area, a permeability barrier is imposed in the Fruitland Formation. Consequently, the hydraulic gradient is steep. Flow in the northern coal unit turns steeply upward at this point. South of the transition, flow is mainly in the basal Fruitland coal and Pictured Cliffs Sandstone. Note that the southern margin of the basin is a discharge area. Slight overpressuring is simulated in the San Juan River valley, consistent with observation. Pictured Cliffs overpressuring is simulated in the north, contrary to observation.

of the basin, recharge occurs by vertical leakage through Tertiary strata rather than by infiltration at the outcrop.

In the absence of a permeability barrier, hydraulic gradient in the Fruitland–Pictured Cliffs is uniform across the basin (fig. 29). When the barrier is imposed in the vicinity of Cedar Hill field, where thick, lower Fruitland aquifer coals pinch out, the model simulates flat and steep potentiometric surfaces, consistent with those mapped (fig. 1), and Fruitland hydraulic heads are close to the observed values (fig. 30). The steep hydraulic gradient reflects a modeled permeability contrast of two orders of magnitude between the northern and southern coal units across the permeability barrier (table 4). Ground-water flow turns steeply upward at this point and is mainly upward across the Kirtland Shale to the Animas River in the Cedar Hill area rather than to the San Juan River. Upward flow across the Kirtland to the San Juan River is negligible (Oldaker, 1990) and is a consequence of regional discharge to the river. Thus, the flattened potentiometric surface up hydraulic gradient of the barrier probably reflects higher permeability and diversion of lateral flow upward. Most flow in the lower section is concentrated in the northern coal unit, which has permeabilities that are orders of magnitude higher than those of the sandstone units (table 4).

Abnormal pressuring in the Fruitland Formation is simulated by modeling the permeability barrier as a regional facies boundary or fault zone. Assuming a facies change, the Fruitland is significantly overpressured in the north (Fruitland heads well above land surface). Overpressuring requires high permeability in the Fruitland Formation (10 md), confinement by the Kirtland Shale, and recharge at an elevated outcrop. In the southern part of the basin, regional underpressuring requires limited recharge at the basin's southern margin (it is actually a discharge area), low permeability in the Fruitland (0.1 to 1.0 md), poor hydraulic connection with the northern recharge area, and isolation from Tertiary water-table aquifers by the Kirtland Shale. The model simulates slightly underpressured, slightly overpressured, and normally pressured conditions in the south that require a permeability barrier in the Fruitland Formation at the basin's center to achieve hydraulic separation from northern recharge. Slight overpressure reflects convergent, upward flow under topographic lows such as to the San Juan River valley, whereas underpressure occurs under topographic highs. Normal pressure is expected where there is communication with Tertiary aquifers such as on the basin's southern margin.

The regional transition from overpressured to underpressured conditions may be wider than mapped; the modeled pressure transition is regionally in the correct position, but shifted somewhat southwest of the mapped transition (figs. 6 and 30). A few overpressured wells are present in the underpressured area. This may reflect interbedding of overpressured and underpressured coal seams, or seams connected and disconnected from the regional aquifer system, as expected in a transition zone. Discontinuity is also evident in the hydrochemistry of neighboring wells that have chemically disparate formation waters.

Faulting, through offset of aquifer coals, also may be a barrier to lateral flow (Ambrose and Ayers, this vol., their fig. 3). It was simulated by imposing in the Cedar Hill area a low-permeability barrier (0.1 to 0.01 md) of variable width (2.5 to 7.0 mi [4 to 11 km]) between the northern and southern coal units and increasing the permeability of the southern coal unit to 1.0 md. Permeability of the northern coal unit was not changed and its heads were unchanged in this simulation. In the south, underpressuring expanded under topographic highs to better fit observed conditions, whereas heads under the San Juan River valley were much higher than observed. The simulated hydraulic gradient was very steep within the barrier and gentler than observed to the south.

Abnormal pressuring is also simulated in the Farmington shale and sandstone unit on the basin's northern limb (fig. 30). Overpressuring has not been reported, and data are unavailable to assess that prediction. However, assuming sandstone interconnectedness, it is not an unreasonable prediction, given an elevated northern outcrop and confinement between shales.

The model shows overpressured Pictured Cliffs Sandstone in the northern part of the basin with only slightly lower heads than those in the overlying Fruitland Formation, contrary to observed conditions. Several factors may combine to explain this phenomenon. Nonattainment of static reservoir conditions during short-term well testing of low-permeability strata would result in apparent underpressuring. Thus, the main Pictured Cliffs Sandstone, although underpressured, may not be as underpressured as available pressure data indicate. Similarity of observed heads in the Fruitland Formation and upper Pictured Cliffs sandstone tongues indicates hydraulic communication between these units. Thus, the model is simply reflecting that the Fruitland Formation and Pictured Cliffs Sandstone were modeled in communication. The presence of a thin aquiclude between them is possible, but such a thin unit could not be modeled in a regional cross section.

In the central part of the basin, hydraulic gradient in the Pictured Cliffs Sandstone dramatically steepens at an imposed permeability facies boundary reported in the literature (Meissner, 1984) and inferred from head data and log analysis (Ayers and others, Bureau of Economic Geology unpublished spontaneous potential map). Here, simulated Pictured Cliffs heads are slightly

above Fruitland heads, contrary to observations. Perhaps transient conditions are reflected in the observed data because of extensive Pictured Cliffs hydrocarbon production in the area and present pressures are less than those modeled under steady-state conditions. If the facies boundary is moved northward, hydraulic gradient in the Fruitland Formation becomes less steep. Updip to the southwest of the facies boundary, heads drop and flow is focused in the higher permeability Pictured Cliffs Sandstone (table 4). Plots of velocity vectors and streamlines show that ground-water flow is slight and concentrated in the Pictured Cliffs Sandstone and basal Fruitland coal seams. For the most part, the Fruitland Formation is an aquitard in the southern part of the basin.

Clearly, Simulation 3 shows that permeability distribution is critical to describing ground-water flow in the San Juan Basin. Furthermore, modeling showed that flow is particularly sensitive to vertical permeability. Thus, well productivity may depend as much on vertical as on horizontal permeability. Vertical permeability is a critical parameter. For example, vertical-permeability values less than 0.1 md caused a dramatic decrease in simulated heads relative to observed heads in the northern coal unit, whereas at higher values there was only a minor increase in simulated heads. A vertical permeability in the Kirtland Shale of 0.0001 md was required to achieve confinement without a large increase or decrease of Fruitland heads relative to observed heads. In the southern part of the basin, a decrease in Kirtland permeability expanded the area of underpressure and caused higher heads under the San Juan River valley. An unrealistically low vertical permeability in the northern Pictured Cliffs Sandstone was required to simulate heads less than those in the Fruitland Formation. Finally, higher lateral permeabilities (>1.0 md) in the Pictured Cliffs Sandstone caused heads to decrease in the northern coal unit.

Recharge And Discharge

To further evaluate the cross-sectional model's approximation of observed data, recharge and discharge were calculated along its upper boundary at the constant potential nodes of the water table. FREESURF makes the calculations such that the amount of recharge to and discharge from the cross section is equal. Calculations were also made under prescribed flux boundaries. Recharge and discharge were calculated for the permeability distribution of Model Simulation 3.

Recharge rates in the San Juan Basin range from 1 to 4 percent of annual precipitation (Roybal and others, 1983; Mattick and others, 1987). A rate of approximately 1 percent was calculated from chloride mass balance in the arid Socorro and Las Cruces, New Mexico areas (Mattick and others, 1987), where annual precipitation is less than 9 inches/yr (23 cm/yr) and within the range (8 to 12 inches/yr [20 to 30 cm/yr]) reported for the southern part of the basin. Rates higher than 1 percent are predictable for the topographically higher and wetter northern part of the basin, which receives 20 to 30 inches/yr (51 to 76 cm/yr) precipitation. Phillips and Tansey (1984) postulated that most of the recharge in the San Juan Basin occurs at high elevations during the cool, wet, winter months of December through March.

In Simulation 3, most of the constant potential nodes were discharge points of less than 0.1 inch/yr (0.25 cm/yr) in topographic lows and on lower slopes of topographic highs. Highest discharge rates were from the outcrop of the Fruitland northern coal unit (>0.9 inch/yr [>2.3 cm/yr]) and where perennial rivers intersect the cross section (>0.1 inch/yr [>0.25 cm/yr]). Recharge nodes were located on topographic highs and on their upper slopes. Recharge rates over the highs ranged from 0.1 to 0.6 inch/yr (0.25 to 1.5 cm/yr), or 0.5 to 3 percent of an annual precipitation rate of 20 inches/yr (51 cm/yr) and 0.33 to 2.0 percent of a rate of 30 inches/yr (76 cm/yr). Recharge rates as high as 2.5 inches/yr (6.4 cm/yr) occur in the outcrop of the northern coal unit. When recharge and discharge rates in the northern coal unit were summed, the net recharge rate was 0.4 inch/yr (1.0 cm/yr), or 2 percent of a 20-inch (51-cm) annual precipitation.

Finally, simulations were made that varied recharge rates to evaluate their effect on the pressure regime. There was little effect on Fruitland hydraulic heads under conditions of constant head and no recharge to the Kirtland Shale and Pictured Cliffs Sandstone. Recharge rates as low as 0.05 inch/yr (0.13 cm/yr) (0.25 percent of 20 inches/yr [51 cm/yr]) simulated overpressuring, suggesting that overpressuring does not require extraordinary recharge rates. Even though no recharge was permitted to the Pictured Cliffs Sandstone, it was overpressured. The Fruitland Formation and Pictured Cliffs Sandstone were modeled in hydraulic communication. Consequently, the Fruitland Formation must be leaky to the Pictured Cliffs. It is possible that the Pictured Cliffs Sandstone is slightly overpressured or at least only slightly underpressured and that true reservoir pressures are obscured in short-term well testing by its low permeability.

Conclusions

1. In the Fruitland Formation, recharge is mainly from the northern margin of the basin, where coals crop out in the foothills of the San Juan Mountains; recharge is limited at the eastern, southern, and western margins because of low rainfall, a topographically low outcrop, and poor aquifer quality. The potentiometric surface is highest near the recharge area; in the north-central part

of the basin, the surface flattens nearly coincident with the distribution of thick Fruitland coal seams, the primary aquifer elements. Regionally, lateral ground-water flow converges from the northeast and southeast toward the San Juan River valley.

2. The Fruitland Formation is regionally overpressured (0.44 to 0.63 psi/ft) in the north-central part of the basin (BHP's 1,200 to 1,900 psi) and underpressured (0.30 to 0.40 psi/ft) in the remainder of the basin (BHP's 400 to 1,200 psi). Overpressuring is attributed to artesian conditions, which explains the need to dewater coalbed methane wells in the northern part of the basin. Underpressuring is due to basinal uplift, erosion, and cooling following the Oligocene thermal event. Underpressure endures in the southern part of the basin because discharge exceeds recharge and the two areas are hydraulically separated.

3. Fruitland waters are chemically diverse, reflecting their hydrologic setting rather than the producing lithology. Low-chloride, high-bicarbonate (Na-HCO_3) waters coincide with overpressure and high-chloride, saline (Na-Cl) waters coincide with underpressure. Consequently, hydrochemistry cannot be used to identify completion lithology. Northern waters are evolved meteoric waters rich in bacterially derived HCO_3^-, whereas southern waters are modified marine waters. Because of high bicarbonate contents in Fruitland waters, scaling by carbonate minerals during production and plugging of perforations and artificial permeability upon injection are expected.

4. In the northern San Juan Basin, the Fruitland Formation and upper Pictured Cliffs sandstone tongues form a hydrostratigraphic unit in which coal seams are the primary aquifer element. Fruitland coal beds and sandstones are in regional hydraulic communication. Local compartmentalization is indicated by large vertical and lateral pressure gradients. The Fruitland Formation and main Pictured Cliffs Sandstone are hydraulically separate. In the southern part of the basin, the basal Fruitland coal and Pictured Cliffs Sandstone form a hydrostratigraphic unit. For the most part the Fruitland is an aquitard in the south, accounting for water-free gas production in that part of the basin.

5. The cross-sectional model simulates hydraulic heads and gradients, potentiometric anomalies, abnormal pressure, and recharge rates observed in the Fruitland Formation. The cross-sectional model requires large ratios of horizontal to vertical permeability (k_h/k_v) to simulate observed heads and is very sensitive to this ratio. Vertical permeability is an important but overlooked flow parameter. Modeled potentiometric anomalies reflect regional permeability contrasts. Enhanced and reduced permeability can be inferred from gentle and steep hydraulic gradients, respectively. Barriers to lateral flow (facies changes and/or faults), rather than topography, are the most important causes of upward flow. Areas of upward flow correspond to potentiometric mounds. In the northern part of the basin, overpressure is simulated, affirming its hydrodynamic origin. The degree of underpressure in the southern part of the basin may be more apparent than real because of low permeability.

6. Hydrologic elements define an aquifer's ability to accept and transmit fluid; hence, they are indicators of permeability. Enhanced permeability in the Fruitland Formation is inferred from gentle hydraulic gradients, overpressure, and low-chloride formation waters. Permeability is inferred to be enhanced where the potentiometric surface is flat and reduced where it is steep. Overpressuring requires enhanced permeability and, because overpressure reduces effective stress, the permeability of coal is increased. Underpressure in the Fruitland is an indicator of low permeability and isolation from recharge; strata too tight to accept and transmit measurable recharge remain underpressured. In the north, the presence of low-chloride, meteoric waters is indicative of an active, dynamic flow system and of permeable pathways. In the south, the presence of modified marine water implies low permeability or limited recharge or both. The distributions of potential energy (head) and mass (dissolved solids) identify regional, ground-water flow paths and indicate permeability anisotropy.

Acknowledgments

John McCord collected DST data and static water levels, and A. H. Scanlon collected pressure data. R. K. Senger's assistance in the implementation of FREESURF was invaluable. We thank Amoco Production Company, Blackwood & Nichols Co., Ltd., and Giant Exploration & Production Company for allowing water sampling of their wells and the logistical support in collecting those samples. Discussions with R. S. Fisher, Y. K. Kharaka, and L. S. Land strengthened interpretation of the geochemical data. The manuscript was reviewed by R. W. Baumgardner, W. A. Ambrose, and W. B. Ayers, Jr. Their reviews tightened the presentation and improved the content.

Thermal Maturity of Fruitland Coal and Composition and Distribution of Fruitland Formation and Pictured Cliffs Sandstone Gases

Andrew R. Scott, W. R. Kaiser, and Walter B. Ayers, Jr.

Abstract

Fruitland coal rank largely reflects structural configuration of the basin. Coal rank and hydrodynamics control the composition and distribution of coalbed gases. Carbon dioxide content of coalbed gases ranges from less than 1 to more than 13 percent; C_1/C_{1-5} values range from less than 0.80 to 1.00. Gas composition alone will not distinguish among Fruitland coalbed, Fruitland sandstone, and Pictured Cliffs sandstone gases in all parts of the basin. Hydrogen-rich Fruitland coal produces chemically wet gases in the southern part of the basin. Gas compositional distributions and isotopic data suggest that some methane and carbon dioxide produced from coal beds in the northern basin have a mixed biogenic and thermogenic origin.

Introduction

The process of coalification encompasses the physical and chemical changes affecting peat and coal during burial and diagenesis. The degree of coalification, or coal rank, is often determined on the basis of vitrinite reflectance or volatile matter content of coals. With increasing thermal maturity and coal rank, vitrinite reflectance values increase and volatile matter content of the coal decreases. During coalification natural gases are generated from organic matter through biogenic, early thermogenic, and late thermogenic processes. Biogenic methane is produced at relatively low temperatures through the metabolic activity of methanogenic bacteria. Gases in the Fruitland Formation are thought to be mainly thermogenic in origin (Rice, 1983). Early thermogenic gases are formed before and during the main stage of liquid hydrocarbon generation, often referred to as the oil window. Dry thermogenic gases are formed by late thermogenic processes and/or are generated by cracking heavier hydrocarbons formed from sapropelic or hydrogen-rich organic matter during the oil-generating stage. Carbon dioxide and nitrogen are also released from organic matter during thermal maturation. Carbon dioxide is derived from the oxygen-bearing functional groups of the organic matter and is released during decarboxylation stages at relatively low levels of thermal maturity (Stach and others, 1975) before significant quantities of liquid hydrocarbons and thermogenic gases have been generated. At higher temperatures, decarboxylation of organic acids can generate both carbon dioxide and methane (Carothers and Kharaka, 1980). Molecular nitrogen in coalbed gas is probably derived from the participation of ammonia in redox reactions during coalification (Rohrback and others, 1983).

The thermal maturity of Fruitland coal beds in the San Juan Basin and the origin and migration pathways of natural gases produced from both the Pictured Cliffs Sandstone and the Fruitland Formation are important in evaluating gas reserves and in developing future exploration efforts. The distribution and compositional variations among Pictured Cliffs Sandstone and Fruitland sandstone and coalbed gases may prove useful in establishing gas migration pathways and in evaluating the environmental aspects of coalbed methane development in the San Juan Basin. Furthermore, nonhydrocarbon gas components may be corrosive (carbon dioxide) or inert gases (nitrogen and carbon dioxide), which significantly lower the BTU content of the gases. Recent papers that discussed the origin and composition of gases in both the Pictured Cliffs Sandstone and Fruitland sandstones and coal beds (Rice, 1983; Rice and others, 1988, 1989, and 1990) were based on the analysis of a limited number of samples obtained primarily from the thermally more mature northern San Juan Basin. This report, based on analyses of a significantly larger data base, evaluates differences in coalbed gas compositions between the overpressured and underpressured parts of the basin and integrates this data with coal rank and Fruitland hydrodynamics.

Objectives

The objectives of this study were to (1) map and evaluate coal rank in the Fruitland Formation, (2) determine if there are significant differences in composition

In Ayers, W. B., Jr., and others, 1991, Geologic and hydrologic controls on the occurrence and producibility of coalbed methane, Fruitland Formation, San Juan Basin: The University of Texas at Austin, Bureau of Economic Geology, topical report prepared for the Gas Research Institute under contract no. 5087-214-1544 (GRI-91/0072), p. 243–270.

among Fruitland coalbed, Fruitland sandstone, and Pictured Cliffs sandstone gases, (3) determine if minor variations in gas composition can be used to determine the origin and migration history of these gases, and (4) compare regional variations in Fruitland coalbed gas compositions with coal rank and basin hydrodynamics and evaluate factors controlling gas composition.

Methods

Proximate analyses and vitrinite reflectance data from 26 Fruitland coals, which ranged in rank from subbituminous to medium-volatile bituminous, were used to determine the relationship between volatile matter (dry, ash-free basis; VM_{daf}) and vitrinite reflectance values (Rm). Linear regression analyses, based on reflectance data points on either side of the coalification jump, were used to determine the equations for converting volatile matter content into calculated vitrinite reflectance values (Rc). Measured vitrinite reflectance values are from Kelso and Rushworth (1982), Rice (1983), Roybal and others (1985), Rice and others (1989), and this study. Approximately 142 measured and 72 calculated vitrinite reflectance values were used to map the rank of Fruitland coal.

Gas compositional data from more than 5,500 Pictured Cliffs sandstone wells and approximately 470 Fruitland wells were used in this study. These data were obtained from pipeline companies, published literature, and several Gas Research Institute cooperative wells. Gas samples were generally collected from the meter run downstream from production equipment or from the wellhead in nonproducing wells; the collection of gas samples directly from the meter reduces the possibility of air contamination. Samples were analyzed with a gas chromatograph using a silica column. Completion lithologies (sandstone and/or coal) for Fruitland wells were confirmed by the operator or identified from completion reports and geophysical logs. If logs were not available for a well, then equivalent perforation intervals on well logs from several adjacent wells were used to determine lithology. Wells whose producing zone and producing lithology could not be determined were designated as Basin Fruitland Coal completions on the basis of information provided by Dwight's Coal Bed Methane Report (1990a, b). Wells were omitted from the study if the gases were commingled, the producing lithology was uncertain, or if production could have been from both coal beds and sandstones. For Pictured Cliffs completions, only a limited number of wells were examined to verify that the perforation interval was actually in the Pictured Cliffs Formation.

Gas contents discussed in this report are given in mole percent. The ratio of methane (C_1) to total hydrocarbons (C_1 through C_5) can be used to determine a gas dryness index. Chemically very dry gases have C_1/C_{1-5} values greater than 0.99, dry gases have values ranging from 0.94 to 0.99, wet gases have values from 0.86 to 0.94, and very wet gases have C_1/C_{1-5} values less than 0.86.

Methane, carbon dioxide, and water isotopic data were collected from the literature. The $\delta^{13}C$ values for total dissolved carbonate species is from Kaiser, Swartz, and Hawkins (this vol.). Bicarbonate is the dominant species in Fruitland Formation water, and $\delta^{13}C$ values for the total dissolved carbonate species will be referred to as bicarbonate $\delta^{13}C$ values in this paper. All isotopic values are relative to the PDB standard unless otherwise designated.

Thermal Maturity of Fruitland Coal

Factors affecting the ability of a coal bed to generate and store natural gases include coal rank, ash content, and maceral composition. Coal rank and maceral composition, particularly the relative abundance of hydrogen-rich organic material, also control the types of gases produced from coal beds. Coal rank is often used to estimate gas reserves. In previous studies of the Fruitland Formation (Fassett and Hinds, 1971; Kelso and Rushworth, 1982; Rice, 1983; Meissner, 1984; Campbell, 1985; Roybal and others, 1985; Kelso and others, 1988; Fassett and Nuccio, 1990), vitrinite reflectance values or volatile matter were used to determine coal rank. In this study, volatile matter content data were converted to equivalent vitrinite reflectance values using equations determined from cross plots of vitrinite reflectance and volatile matter data from Fruitland coals; this approach provided a large regional data base of more than 200 measured and calculated values for mapping coal rank variations in the Fruitland Formation.

In cross plots of measured vitrinite values versus volatile matter content, two distinct linear trends are separated by an interval where Rm values increase rapidly with minor increases in VM_{daf} values (fig. 1). This sharp increase in vitrinite reflectance corresponds to the first coalification jump and reflects the generation of bitumen from the liptinitic components of the coal as the "oil window," or oil-generating stage, is reached during thermal maturation (Teichmüller, 1987). The percent volatile matter cutoff for using Equation 1 or Equation 2 to calculate vitrinite reflectance values was set at 47 percent volatile matter; this value represents the approximate intersection point of these two equations (fig. 1). Vitrinite reflectance values were determined using Equation 1 for samples containing more than 47 percent volatile matter (correlation coefficient of 0.787). Equation 2 (correlation coefficient of 0.972) was used to calculate vitrinite reflectance

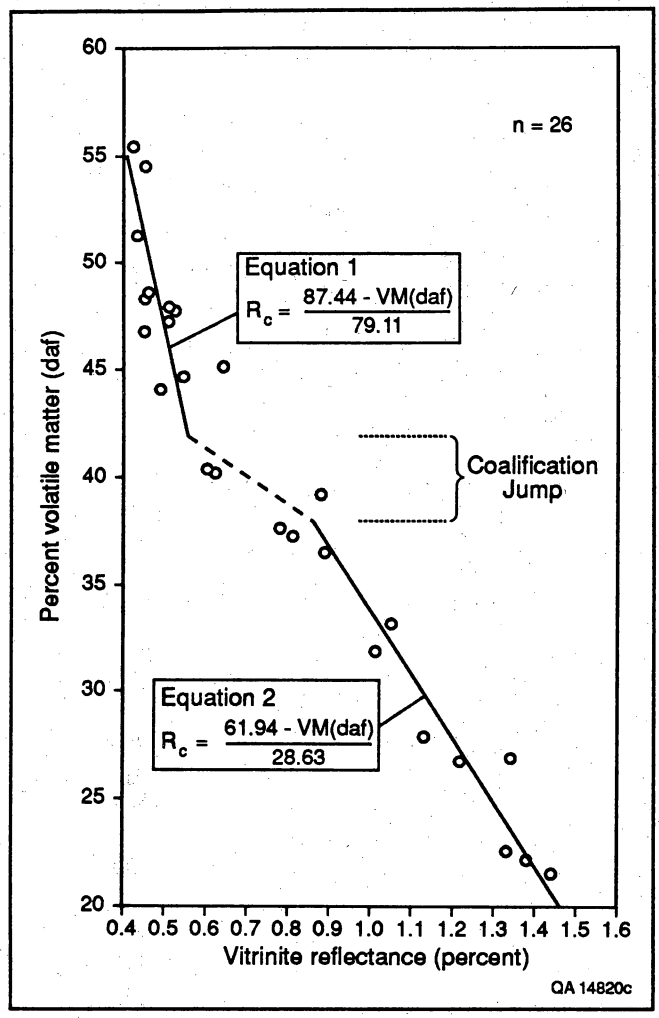

Figure 1. Relationship between vitrinite reflectance and volatile matter content of Fruitland coal. Two distinct linear trends are separated by an interval where vitrinite reflectance values increase abruptly with only a minor decrease in volatile matter (dry, ash-free basis). This is a coalification jump and reflects the generation of bitumen from the hydrogen-rich components of the coal.

values of samples with less than, or equal to, 47 percent volatile matter. The extension of Equation 2 to higher VM_{daf} values over the coalification jump range was necessary because (1) poor sample control over the coalification jump did not allow an equation to be calculated in this range, and (2) there was better correlation between measured and calculated vitrinite values over this volatile matter range. The excellent relationship (fig. 2; correlation coefficient of 0.986) between measured (Rm) vitrinite values and calculated (Rc) vitrinite values, determined from volatile matter content, provides the basis for using these equations to convert proximate data into equivalent vitrinite reflectance values. Over 75 percent of the calculated vitrinite values fall within 0.06 percent of the measured vitrinite values. Vitrinite values from lower rank Fruitland coals (Rm less than 1.0 percent) vary by as much as 0.08 percent over tens of feet (this study; Campbell, 1985), suggesting that Rc values generally fall within the normal range of variability for vitrinite reflectance values over short depth intervals within the Fruitland. This relatively large change in Rm values at low levels of thermal maturity, between or within individual coal beds, may be due to differences in maceral composition, hydrogen content, and/or differences in the degree of humification attained during the peat stage of diagenesis (Teichmüller, 1987).

More than 140 measured and 73 calculated vitrinite reflectance values were used to make the coal-rank map of the Fruitland Formation (fig. 3). Measured vitrinite values were selected over calculated values when both sets of data were available. Measured vitrinite reflectance values range from 0.42 to 1.51 percent and correspond to subbituminous to low-volatile bituminous coal ranks. Low-volatile bituminous Fruitland coal occurs within a northwest-trending band of medium-volatile bituminous coal in the northern third of the San Juan Basin. Coal rank decreases abruptly toward the northern margin of the basin along the Hogback Monocline (Ayers and others, this vol., their fig. 5) where high-volatile C to high-volatile A bituminous isorank lines parallel basin structure. This change in vitrinite reflectance values is most pronounced along the northwestern margin of the basin, where measured vitrinite values decrease from 1.45 percent to 0.8 percent in less than 6 mi (10 km) (fig. 3). Southward, vitrinite reflectance isorank lines generally parallel basin structural contours as coal rank gradually decreases to subbituminous in the southern third of the basin.

Overall, there appears to be a good correlation between the structural configuration of the San Juan Basin (Ayers and others, this vol., their fig. 5) and Fruitland coal rank (fig. 3). The anomalously low vitrinite reflectance values along the Ignacio Anticline and the Hogback Monocline indicate that development of these structures began before or during the main stage of coalification. North of the Bondad Anticline, coal rank does not follow present-day structure. High-rank Fruitland coals are structurally higher than adjacent low-rank coals. In this area, the elevation of the Huerfanito Bentonite rises from 2,800 ft (853 m; datum mean sea level) to nearly 4,000 ft (1,219 m) over a distance of 7 mi (11 km) (Ayers and others, this vol., their fig. 5), with no significant change in Rm values within Fruitland coals. The presence of structurally higher coal adjacent to structurally lower coal of the same rank (Rm values of 1.45 percent) suggests that significant local, post-

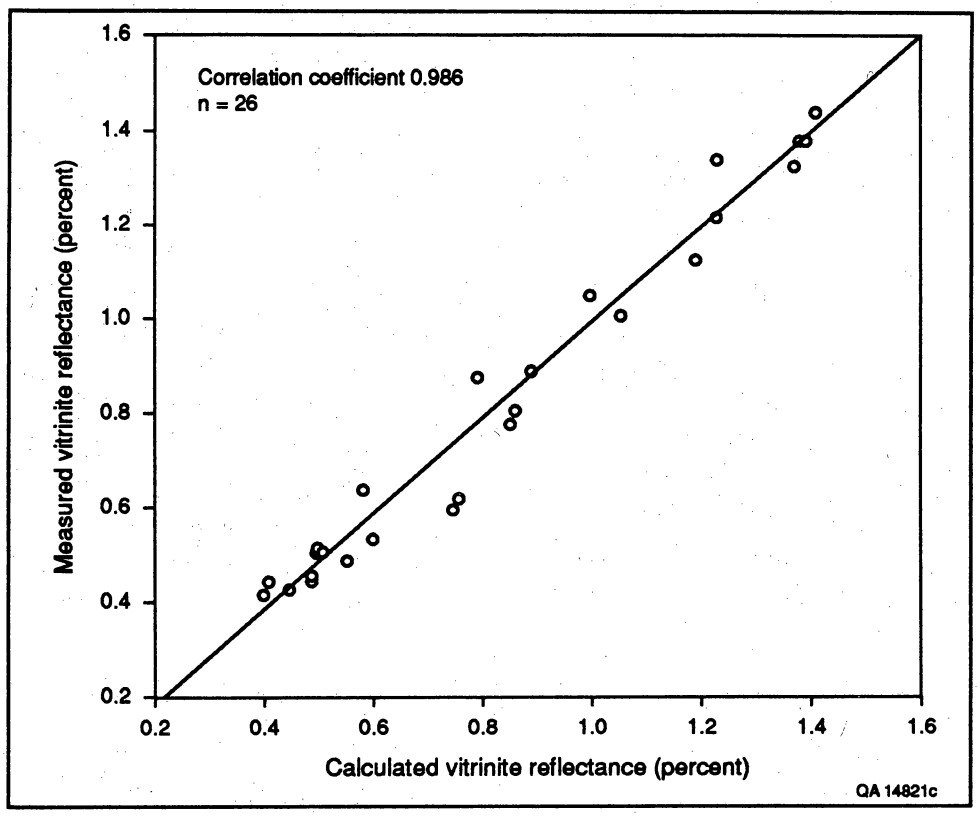

Figure 2. Calculated and measured vitrinite values. Vitrinite reflectance values calculated from volatile matter content using the equations in figure 1 show a very good correlation with measured vitrinite reflectance values.

coalification basin uplift and/or higher heat flux occurred in this area.

Anomalously high vitrinite reflectance values (Rm greater than 1.4 percent) in the northern San Juan Basin have been attributed to higher heat flux derived from the emplacement of the San Juan Batholith to the north (Rice, 1983; Bond, 1984), heat advection from groundwater movement (Clarkson and Reiter, 1987), or the presence of a localized, deeply buried heat source (Rice and others, 1989). Regional heat-flow studies of the San Juan Basin and surrounding areas (Reiter and Mansure, 1983; Clarkson and Reiter, 1987) indicate that heat flow increases from south to north in the San Juan Basin (fig. 4). According to Reiter and Mansure (1983), these trends are consistent with seismic, geomagnetic, and gravity data from the Colorado Plateau. The relatively large (10 by 40 mi [15 by 60 km]), eastward-trending gravimetric low (less than –250 mGal) in the northern San Juan Basin (fig. 4) may represent areas of higher heat flow. However, magnetic anomalies (Zietz and others, 1982) that would support a deep igneous heat source are absent, which suggests that the low gravity values may indicate increased thickness of lower density sedimentary rocks, regions of higher heat flow within the Colorado Plateau, vertical migration of fluids at depth as suggested by Law (1990b), and/or a combination of these factors.

The correlation between vitrinite reflectance and structure in the San Juan Basin suggests that burial depth and structural evolution of the basin were probably the major factors controlling the thermal maturity of Fruitland coals. The rather abrupt increase in vitrinite reflectance values greater than 0.70 percent in the northern basin coincides with a structural hingeline (Ayers and others, this vol., their fig. 5). Coal-rank trends and basin structure coincide with gravity trends in this area (figs. 3 and 4). Along the structural hingeline, closely spaced northwest-trending isogals may suggest the presence of a deep-seated structural feature. Ayers and others (this vol.) hypothesize that the structural hingeline is a northwest zone of normal faults with the downthrown side of the basement floor to the northeast. Significantly, offset of coal beds across the northwest-trending fault zone and the southwestward pinch-out of coal beds may have inhibited the southwestward migration of fluids derived from thermally more mature parts of the basin. This would explain the closely spaced isorank contours (Rm greater than 0.65 percent) in the northern basin as well as the southwest boundary of overpressuring.

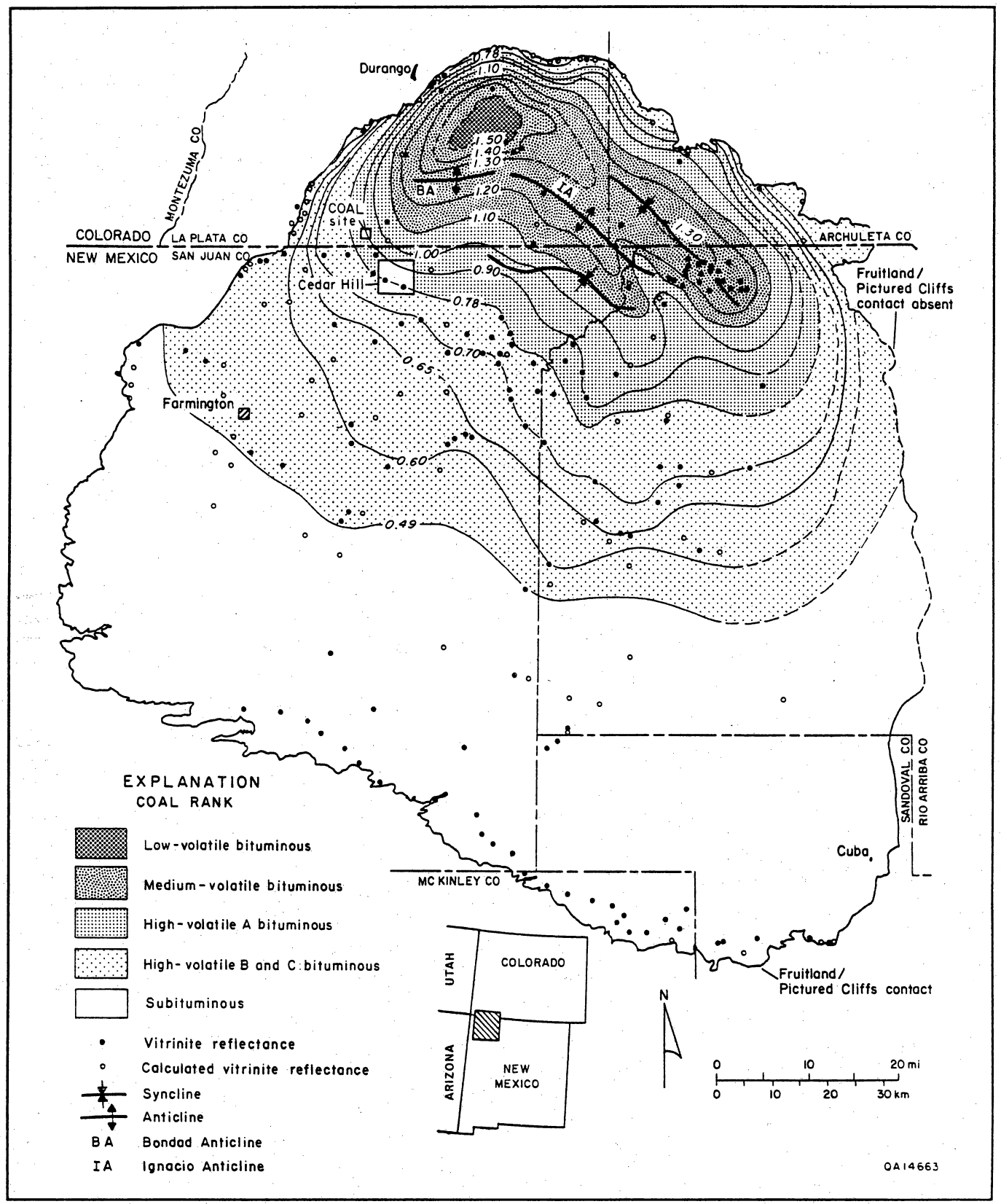

Figure 3. Fruitland Formation coal-rank map. The rank of coal generally reflects the structural configuration of the basin. Low vitrinite reflectance values over the Ignacio Anticline and along the Hogback Monocline suggest that these structural features were present during coalification. Structural axes are from the Huerfanito Bentonite datum (Ayers and others, this vol., their fig. 5).

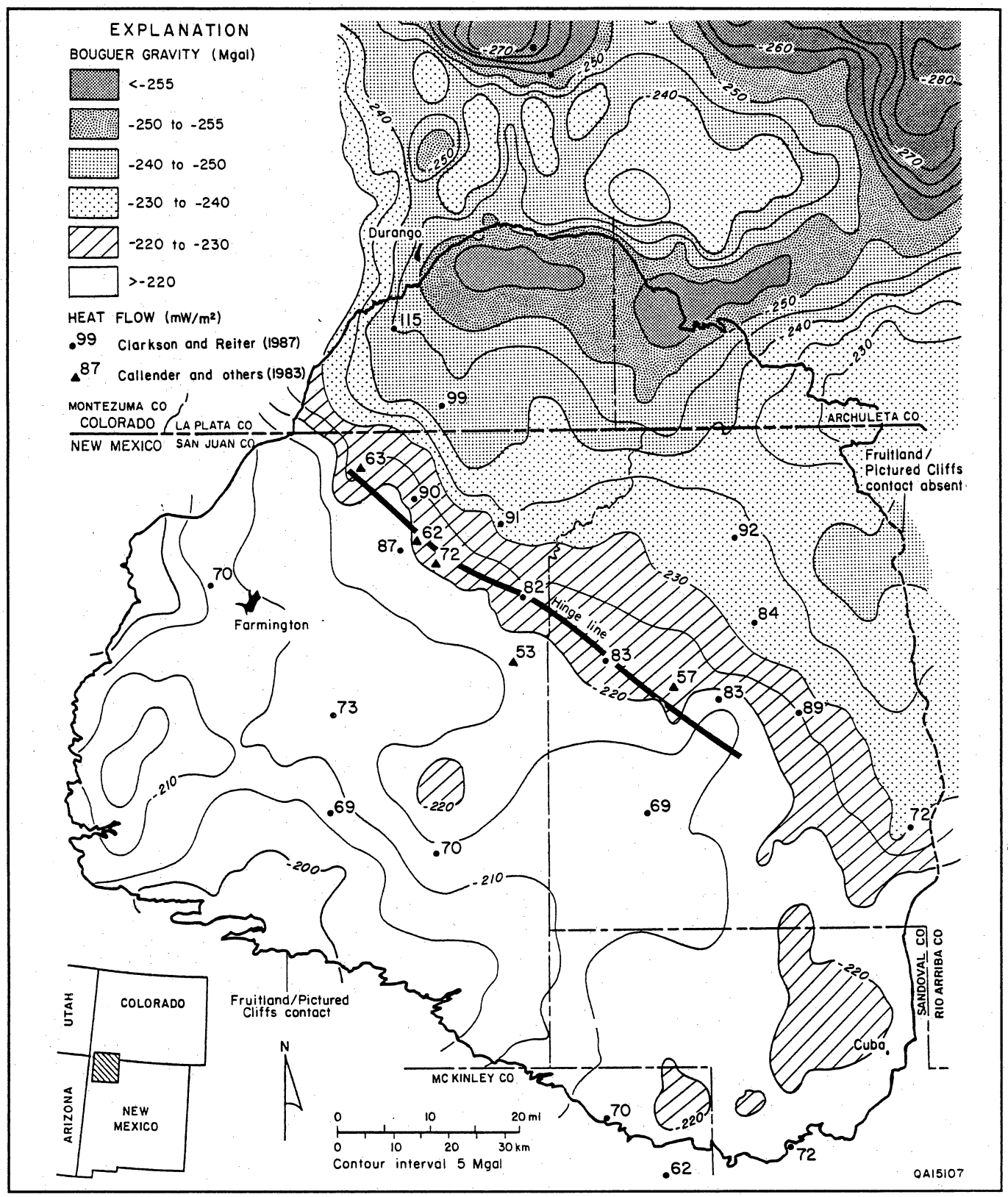

Figure 4. Bouguer gravity map and heat-flow data from the San Juan Basin. Bouguer gravity contour trends are northwest and highly spaced north of a structural hingeline, suggesting that there may be a change in the relative position of crustal blocks in this area. The negative gravity anomalies (less than –250 mGal) in the northern basin may be due to increased heat flux, vertical migration of fluids at depth, a thicker sequence of sedimentary rocks, or any combination of the above factors. Data are modified from Suits and Cordell (1981), Callender and others (1983), and Clarkson and Reiter (1987).

Composition and Distribution of Fruitland and Pictured Cliffs Gases

Both Fruitland and Pictured Cliffs reservoirs produce nonassociated gas and minor condensate. Fruitland coal alone is estimated to contain 43 Tcf to 49 Tcf of gas (Ayers and others, this vol.). Understanding the origin, migration, and compositional variability of these gases in the San Juan Basin is important for future exploration and production efforts. Previous studies have indicated that Fruitland coalbed gases are genetically distinct from Fruitland sandstone and Pictured Cliffs sandstone gases (Rice and others, 1988, 1989). However, these studies were based on relatively few samples and the extrapolation of these conclusions to all parts of the basin may be invalid.

Composition of gas produced from Fruitland coal beds does not appear to change significantly with time (Hale and Firth, 1988), indicating that the length of production should not be a major factor affecting gas compositional data and that gas compositional trends are probably valid. Carbon dioxide, ethane, and nitrogen were evaluated to characterize variations in gas compositions among Fruitland coal beds, Fruitland sandstones, and Pictured Cliffs sandstones. These three gas components rather than methane were used so that minor variations in gas compositions could be recognized. If methane had been used as an end member, gas compositional data points would have clustered at that corner of the ternary diagram. Furthermore, there appears to be a very good correlation between methane content and these three components (fig. 5) and between ethane and heavier gas components (C_3 through C_5 hydrocarbons). Coalbed gases from the overpressured parts of the basin follow gas compositional Trend A, which has a correlation coefficient of 0.990 (fig. 5a). These gases are composed predominantly of methane and carbon dioxide with very minor amounts of other hydrocarbon gases. Gases from underpressured Fruitland coal beds and sandstones generally follow Trend B (correlation coefficient of 0.907; fig. 5b). Both underpressured coalbed and sandstone gases follow Trend B, suggesting that there may be communication between sandstones and coals in the southern part of the basin. Overpressured sandstone and coalbed gases follow different trends (fig. 5). However, hydrochemical data indicate that sandstones and coal beds in overpressured parts of the basin are in regional hydraulic communication (Kaiser, Swartz, and Hawkins, this vol.). Therefore, differences between sandstone and coalbed gas compositional trends in the northern basin probably reflect the way gases are stored in and released from these reservoirs rather than noncommunication between reservoirs.

Fruitland Formation Gases

Previous studies indicate that Fruitland coalbed gas composition is distinctly different from the composition of Fruitland sandstone gases (Rice and others, 1988, 1989). Differences in gas composition were attributed to different organic source materials; chemically dry gases were derived from coal beds and chemically wet gases were generated from dispersed Type III kerogen found in adjacent carbonaceous shales. The presence of wet gases produced from Fruitland coal beds was attributed to unspecified completion practices rather than production directly from the coal. However, this study indicates that Fruitland coals are the source of wet coalbed gases. Furthermore, coalbed and sandstone gas compositions are very similar in the southern part of the basin, indicating that gas composition alone cannot always determine gas origin.

Fruitland Sandstone Gases

Gases produced from Fruitland sandstones have C_1/C_{1-5} values ranging from 0.80 to 1.00, with a mean of 0.90 (table 1). Underpressured sandstone gases are wetter than overpressured sandstone gases (mean C_1/C_{1-5} values of 0.90, and 0.94, respectively). Low C_1/C_{1-5} values (less than 0.91) in Fruitland sandstone gases occur in a southeast-trending band in the central part of the basin (fig. 6). This area generally falls between vitrinite reflectance values of 0.49 and 0.70 percent, which corresponds to the oil-generating stage of the organic matter. The ethane content of sandstone gases ranges from less than 1 percent to nearly 11 percent, with gases from the underpressured region containing significantly more ethane than gases from the overpressured region. Overpressured and underpressured sandstone gases have similar ranges of carbon dioxide content (table 1). However, Fruitland sandstone gases in the northern part of the basin generally contain more than 1 percent carbon dioxide (fig. 7) and have a mean carbon dioxide content of 2.2 percent. Gases in the southern basin generally have less than 1 percent carbon dioxide (mean of 0.50 percent), but some wells may contain more carbon dioxide. Nitrogen content ranges from less than 1 percent to more than 9 percent. Overpressured sandstone gases have a higher mean nitrogen content (1.8 percent) than gases from underpressured sandstones (mean of 0.6 percent). However, high nitrogen content in gases produced from overpressured sandstones may reflect sample contamination by air rather than the actual nitrogen content of these gases.

Ternary diagrams also reflect the relatively high ethane content of Fruitland sandstone gases (fig. 8).

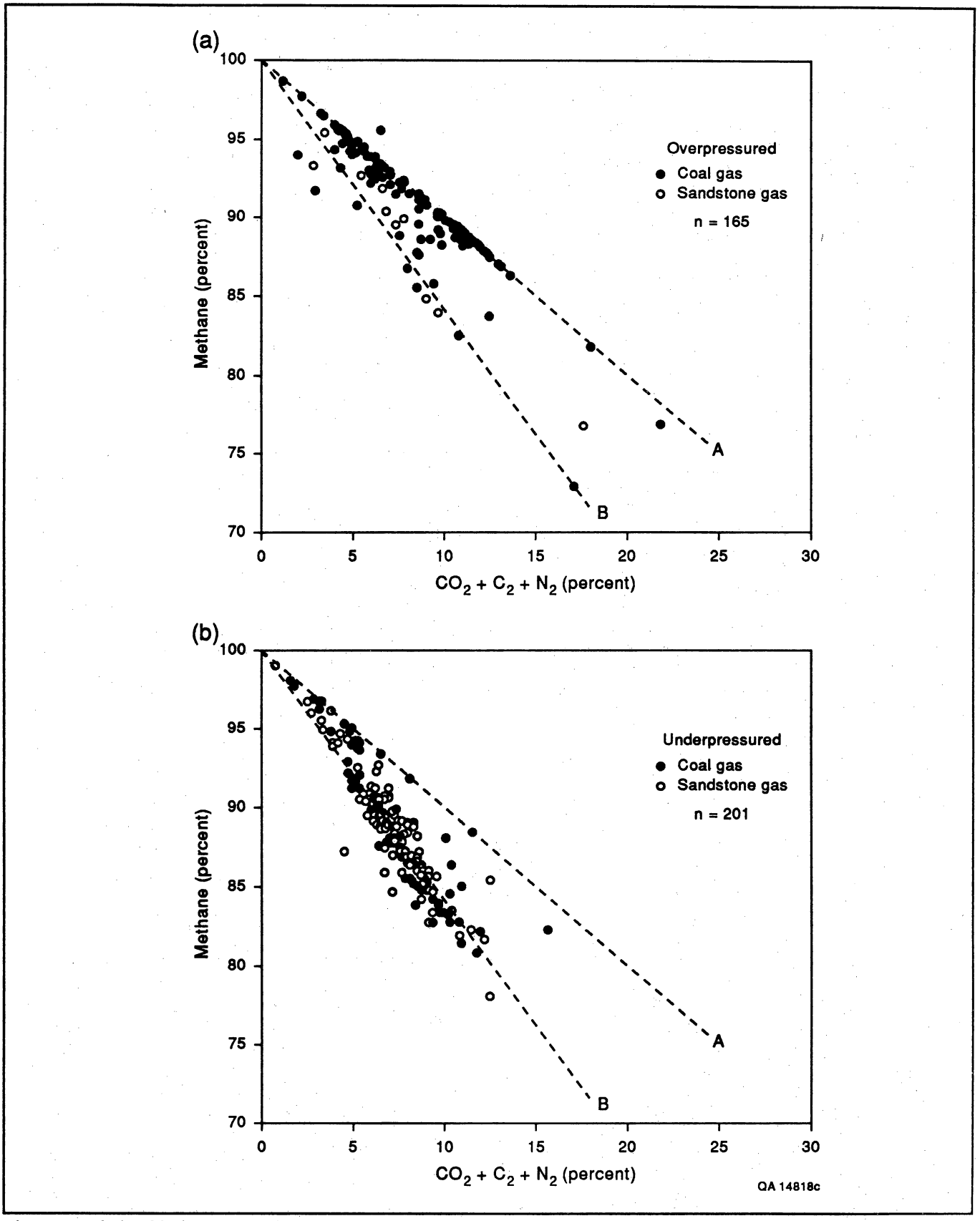

Figure 5. Relationship between major gas components in the (a) overpressured and (b) underpressured parts of the San Juan Basin. The correlation coefficients of Trends A and B are 0.990 and 0.907, respectively, indicating a good relationship between methane and other gas components.

Table 1. Composition ranges of Fruitland sandstone, Fruitland coalbed, and Pictured Cliffs sandstone gases.

		Fruitland sandstone gases			Fruitland coalbed gases			Pictured Cliffs sandstone gases
		All n = 101	UP n = 91	OP n = 10	All* n = 288	UP n = 111	OP n = 157	All n = 1,533
C_1/C_{1-5} value	$\bar{X}$	0.90	0.90	0.94	0.96	0.92	0.98	0.88
	S	0.04	0.03	0.04	0.05	0.04	0.03	0.04
	C	0.04	0.04	0.05	0.05	0.05	0.03	0.04
	Min.	0.80	0.80	0.86	0.77	0.83	0.85	0.75
	Max.	1.00	1.00	1.00	1.00	1.00	1.00	1.00
Ethane (percent)	$\bar{X}$	5.7	6.2	3.8	2.5	4.8	1.1	6.7
	S	2.0	1.86	2.00	2.69	2.35	1.70	1.83
	C	0.35	0.30	0.53	1.08	0.49	1.55	0.27
	Min.	0.3	0.3	0.6	0	<0.1	0	<0.5
	Max.	10.7	10.7	6.4	11.9	9.7	8.5	14.8
Carbon dioxide (percent)	$\bar{X}$	0.8	0.5	2.2	4.5	1.4	6.4	0.7
	S	0.73	1.86	0.87	3.90	1.54	3.71	0.64
	C	0.93	0.31	0.41	0.87	1.10	0.58	0.91
	Min.	0	0	<0.1	<0.1	<0.1	0.2	<0.1
	Max.	3.4	3.4	3.2	13.5	11.4	13.5	10.1
Nitrogen (percent)	$\bar{X}$	0.8	0.6	1.8	0.7	0.8	0.7	0.7
	S	1.28	0.90	2.95	1.56	1.32	1.79	0.52
	C	1.60	1.50	1.64	2.23	1.65	2.56	0.72
	Min.	0.1	0.1	0.3	0	0	0	0
	Max.	9.7	8.5	9.7	13.3	11.2	13.3	5.3

$\bar{X}$ = arithmetic mean
S = standard deviation
C = coefficient of variation
UP = underpressured parts of basin
OP = overpressured parts of basin
*Includes 20 samples from transition zone

Gases from overpressured sandstones and UP1 tongues have similar gas compositions and generally contain more carbon dioxide and less ethane than gases from underpressured Fruitland sandstones. Some Fruitland wells completed in sandstones have coal-decline production behavior, indicating that these sandstones are producing gases from adjacent coal beds (Kaiser, Ayers and others, this vol.). Some gases from these wells identified as having coal-decline production behavior have proportionally higher carbon dioxide and/or nitrogen contents (fig. 8), indicating that these sandstones may have derived at least some gas from adjacent coalbeds. However, other wells with coal-decline production behavior do not follow this trend and have gas compositions that are similar to other Fruitland sandstones; either the coalbed gas composition is similar to sandstone gas composition, the contribution of coalbed gases to the total production is relatively minor, or gas composition changed during migration from coal beds to sandstones.

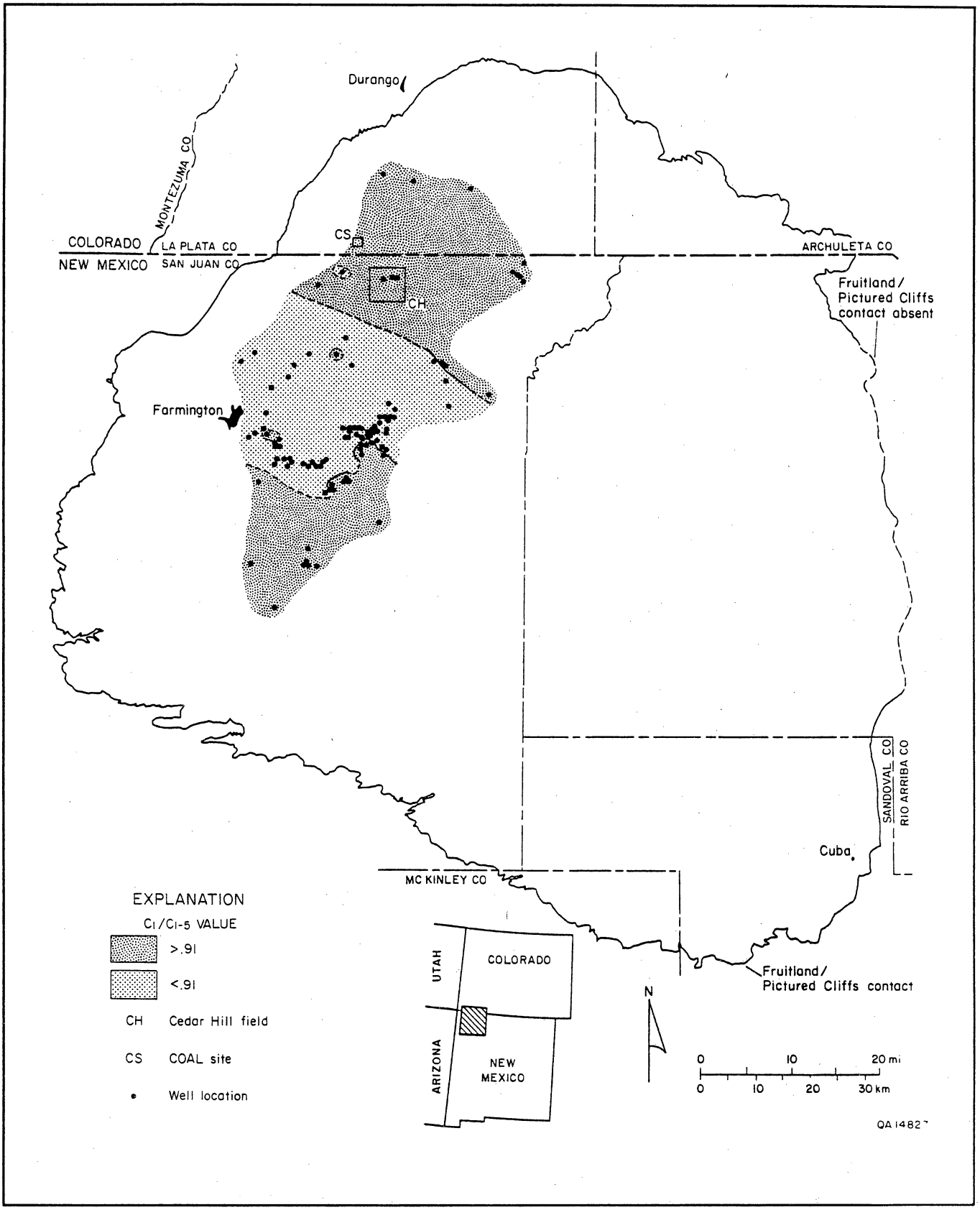

Figure 6. C_1/C_{1-5} values of Fruitland sandstone gases. Fruitland sandstone gases in the northern and southern parts of the basin are generally chemically drier than gases from the central basin. The wet gases coincide with vitrinite reflectance values between 0.50 and 0.70 percent and were probably derived from adjacent shales and/or coal beds.

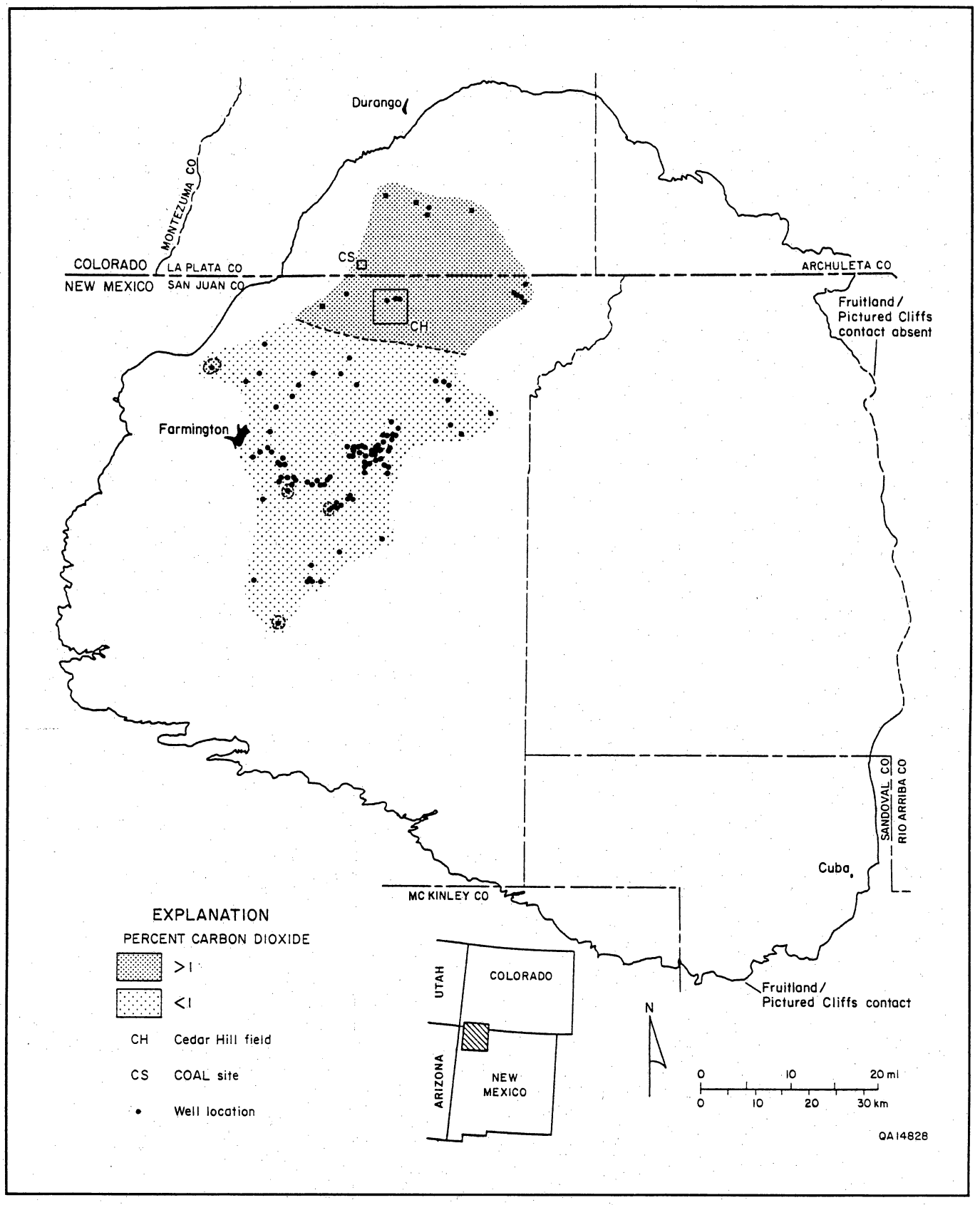

Figure 7. Carbon dioxide content of Fruitland sandstone gases. Fruitland sandstone gases in the northern basin contain slightly more carbon dioxide than do gases in the southern basin.

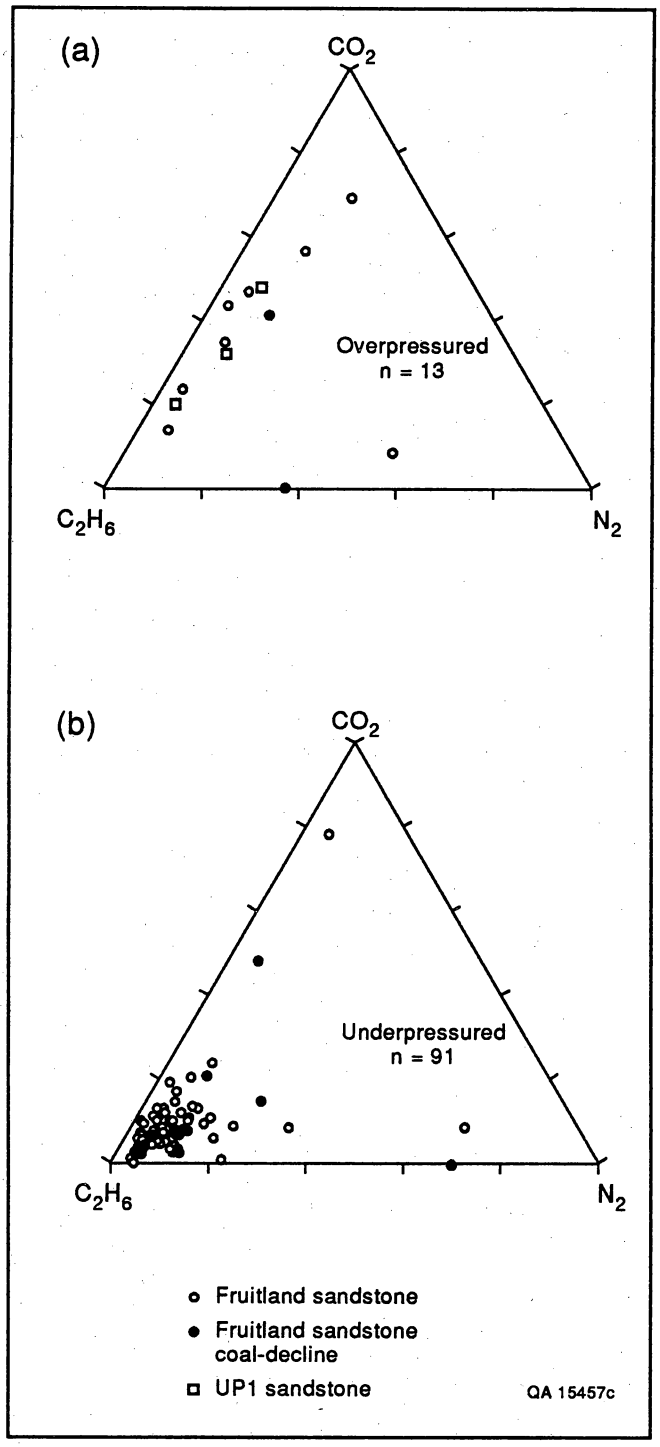

Figure 8. Ternary diagrams of gases produced from Fruitland sandstones. Overpressured sandstone gases (a) generally contain proportionally lower ethane and more carbon dioxide than underpressured sandstone gases. (b) Sandstones with known coal-decline behavior are believed to be in communication with coal beds; some, but not all, of these gases contain proportionally higher carbon dioxide and/or nitrogen, which suggests that the gases were derived from the coal. Gases produced from Upper Pictured Cliffs tongues have compositions similar to overpressured Fruitland sandstone gases.

Fruitland Coalbed Gases

Methane and other gases are generated from coal during coalification as temperatures increase with increasing burial depth. Coal rank, ash content, reservoir pressure, and maceral type, particularly the amount of hydrogen-rich components, all affect final gas composition. Analysis of Fruitland coalbed gases showed that although many coalbed gases are chemically dry, a significant number of gases were chemically wet. The range of C_1/C_{1-5} values of Fruitland coalbed gases (0.77 to 1.00) is similar to that of Fruitland sandstone gases (table 1). Chemically dry to very dry coalbed gases, located in both the overpressured, northern part and the underpressured, southern part of the basin, are separated by a west-northwest-trending band of relatively wet coalbed gases (fig. 9). Overpressured coalbed gases are chemically drier (mean C_1/C_{1-5} value of 0.98) than underpressured gases, which have a mean C_1/C_{1-5} value of 0.92. However, underpressured coalbed and sandstone gases have similar mean C_1/C_{1-5} values (0.92 and 0.90, respectively). Ethane content of Fruitland coalbed gases ranges from zero to more than 11 percent (table 1). The wet gases from underpressured coal beds have a significantly higher mean ethane content (4.8 percent) than do gases from overpressured coal beds (mean of 1.1 percent). Underpressured coalbed and sandstone gases have similar mean ethane values (table 1).

Carbon dioxide content in Fruitland coalbed gases ranges from less than 1 percent to more than 13 percent (table 1). Coalbed gases with the highest carbon dioxide content (greater than 10 percent) are from the north-central part of the basin. This area is characterized by very dry gases (C_1/C_{1-5} values of 1.00) and highly productive coalbed methane wells. From this area, carbon dioxide content of coalbed gases decreases gradually northwestward and very abruptly southward. Carbon dioxide content of Fruitland coalbed gases is generally less than 1 percent in the southern part of the basin (fig. 10). The ranges of carbon dioxide values for underpressured and overpressured coalbed gases are similar (table 1); however, the mean carbon dioxide of overpressured coalbed gases (6.4 percent) is significantly higher than underpressured coalbed gases (1.4 percent). Coalbed gases generally contain more carbon dioxide than underpressured and overpressured sandstone gases (table 1).

Underpressured and overpressured coalbed gases have similar ranges of nitrogen content. Nitrogen content in Fruitland coalbed gases is generally low (mean of 0.7), and more than 95 percent of the samples contain less than 3 percent nitrogen, indicating that contamination of the gas samples by air was not a major problem. Most of the data on gas samples with elevated nitrogen contents were obtained from published sources,

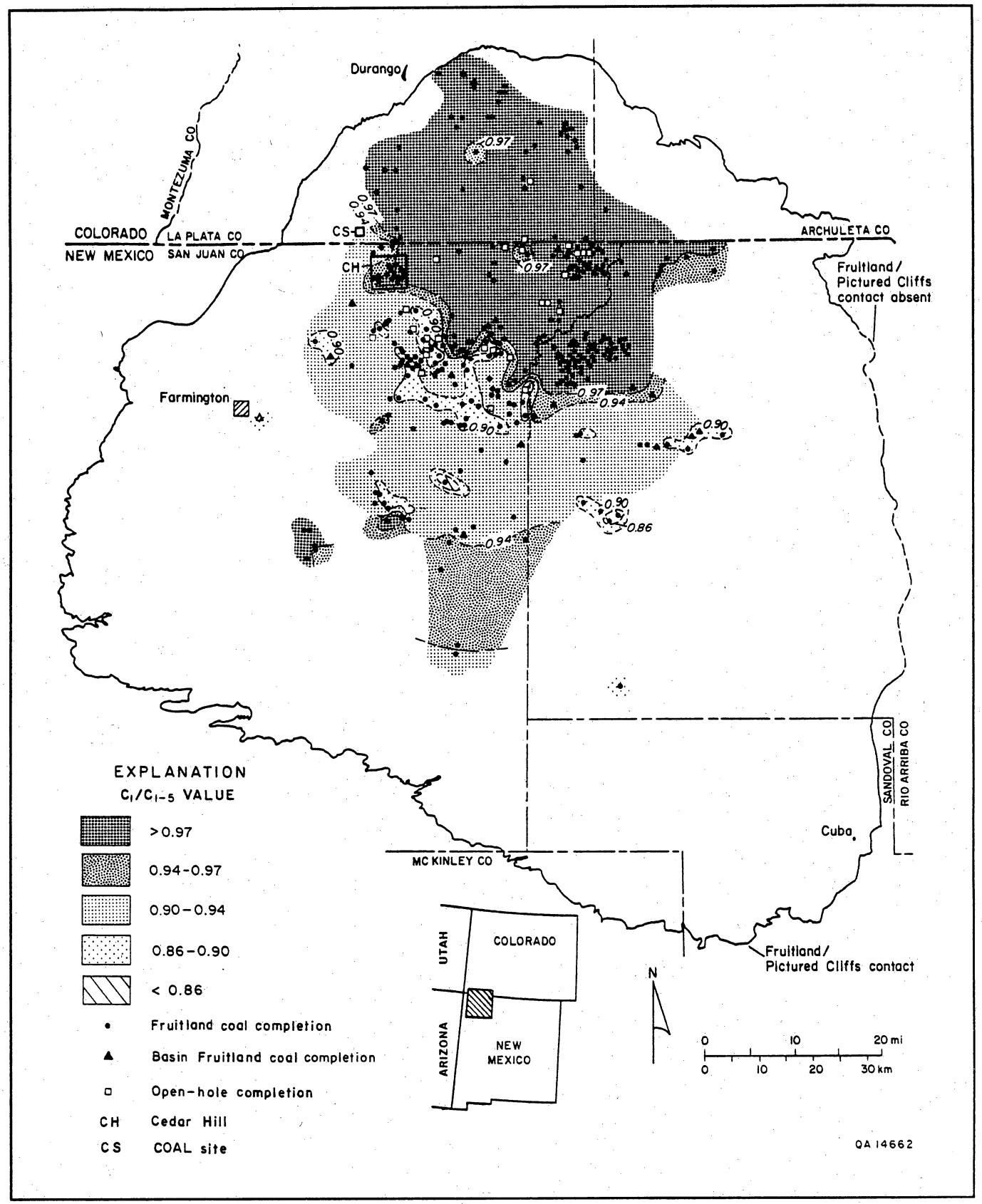

Figure 9. C_1/C_{1-5} values of Fruitland coalbed gases. Gases derived from higher rank coals (Rm >0.8 percent) in the overpressured area generally have C_1/C_{1-5} values greater than 0.97. Isotopic data and the abrupt transition from very dry to wet gases suggest that dry gases in the northern basin are derived from both thermogenic and biogenic sources.

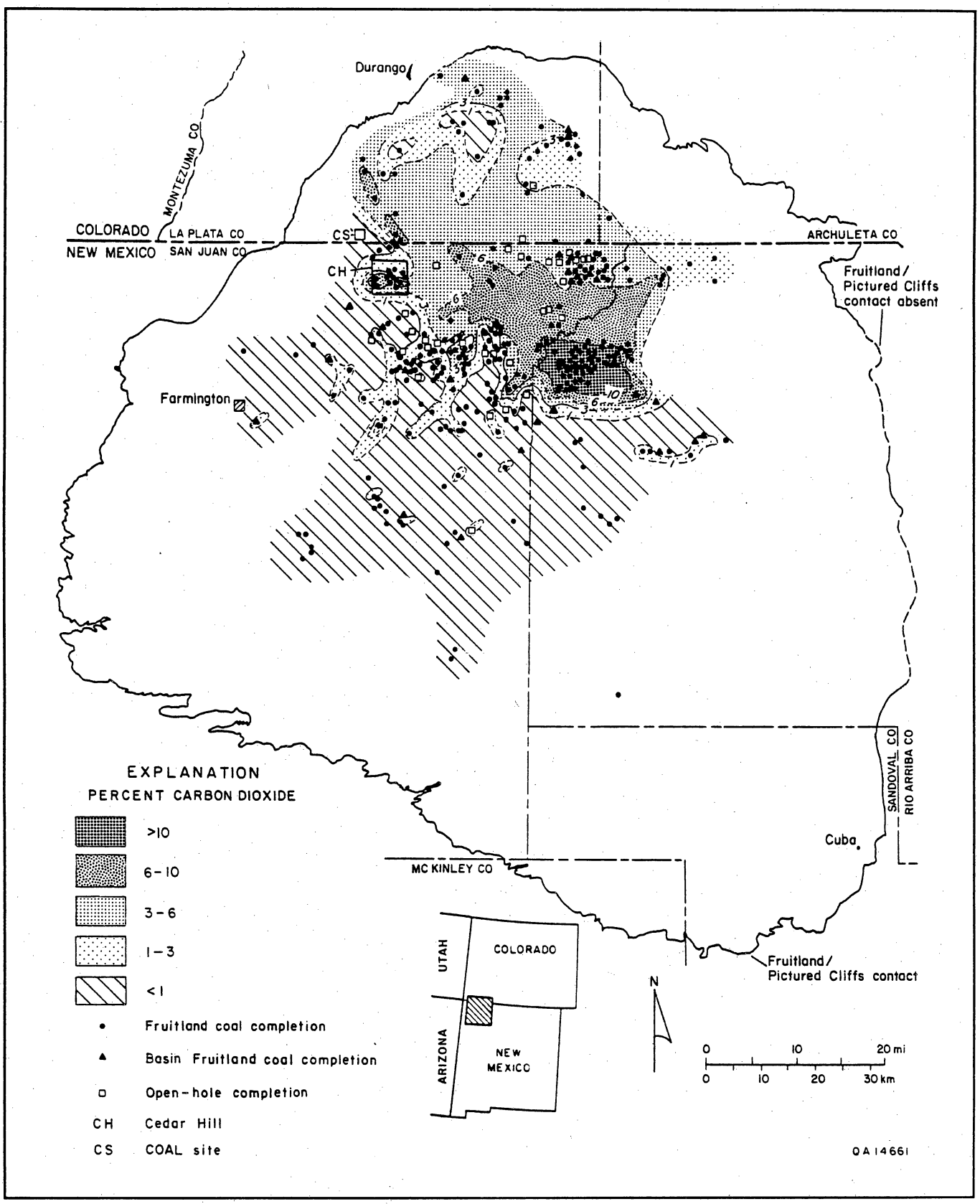

Figure 10. Carbon dioxide content of Fruitland coalbed gases. Gases containing relatively large amounts of carbon dioxide occur in the north-central basin. Highest carbon dioxide content (greater than 6 percent) coincides with highest bottom-hole pressures (greater than 1,600 psi) (Kaiser, Swartz, and Hawkins, this vol., their fig. 7).

and the nitrogen reported in these samples may represent air contamination. Nitrogen contents of sandstone and coalbed gases are similar, with sandstone gases containing slightly more nitrogen than coalbed gases (table 1).

There are major differences between overpressured and underpressured Fruitland coalbed gases (fig. 11). Gases from overpressured coal beds are generally drier and have significantly more carbon dioxide than gases from underpressured coal beds, which are characterized by a higher proportion of ethane (C_2H_6). Coalbed gases from the transition zone, located between overpressured and underpressured areas, have composition ranges that are similar to both pressure regimes (fig. 11). Underpressured coalbed gases generally have C_1/C_{1-5} values of less than 0.94 and carbon dioxide content of less than 2 percent (fig. 12). Gases from overpressured coal beds are significantly drier (C_1/C_{1-5} values generally greater than 0.97) and have more carbon dioxide (greater than 3 percent) than gases produced from underpressured coal beds. The anomalously high carbon dioxide content of Meridian 400 coalbed gases (greater than 10 percent) is reflected in the bimodal distribution of carbon dioxide values (fig. 12). The compositions of gases produced from underpressured coalbed and sandstone reservoirs are similar. Gases produced from these reservoirs have relatively high ethane and generally minor carbon dioxide and nitrogen contents (figs. 8b and 11c). Histograms of C_1/C_{1-5} values and carbon dioxide content of gases from underpressured coalbeds and sandstones show that both sandstones and coalbed gases are chemically wet to very wet and contain only minor carbon dioxide (fig. 13).

Pictured Cliffs Sandstone Gases

Gases produced from Pictured Cliffs sandstones are very similar to gases produced from Fruitland sandstones and underpressured Fruitland coal beds (figs. 11, 14, and 15). Pictured Cliffs gases show a normal distribution of C_1/C_{1-5} values that range from 0.72 to 1.00 (mean of 0.88); they may contain nearly 15 percent ethane (table 1). The ranges of carbon dioxide and nitrogen contents of these gases are also similar to those ranges found in Fruitland sandstone gases. However, Fruitland coalbed gases are generally chemically drier and contain more carbon dioxide than Pictured Cliffs sandstone gases (table 1). The mean nitrogen content of Pictured Cliffs gases (0.7 percent) is similar to the mean nitrogen content of Fruitland gases. The higher nitrogen content in some Pictured Cliffs gases may be related to the presence of sapropelic organic material (which contains nitrogen-rich proteins) in the underlying Lewis Shale relative to terrestrial organic matter. The highest nitrogen contents occur in the southeastern part of the basin.

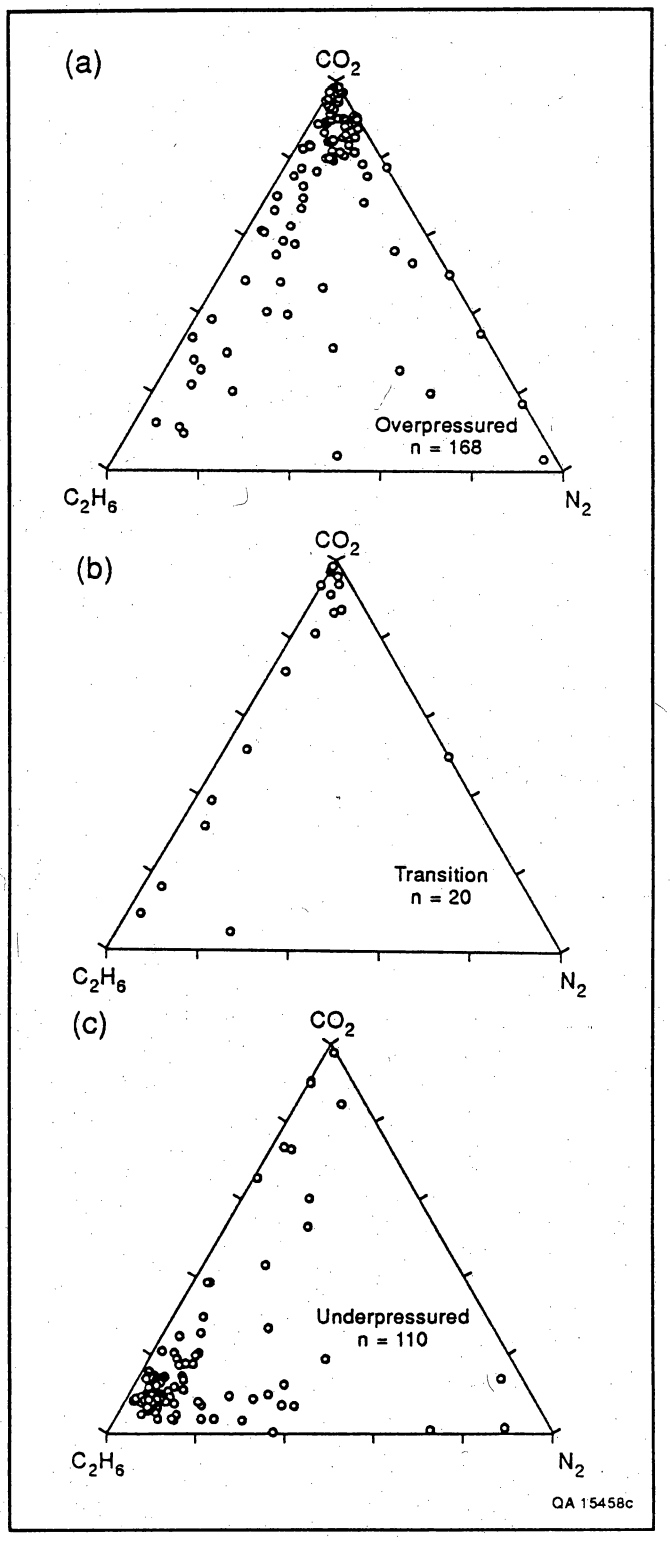

Figure 11. Ternary diagrams of Fruitland coalbed gases. (a) Overpressured coalbed gases generally contain significant amounts of carbon dioxide and minor ethane. (b) Coalbed gases from the transition zone between overpressuring and underpressuring contain variable amounts of carbon dioxide and ethane and relatively little nitrogen. (c) Underpressured coalbed gases contain higher amounts of ethane and variable amounts of carbon dioxide and nitrogen.

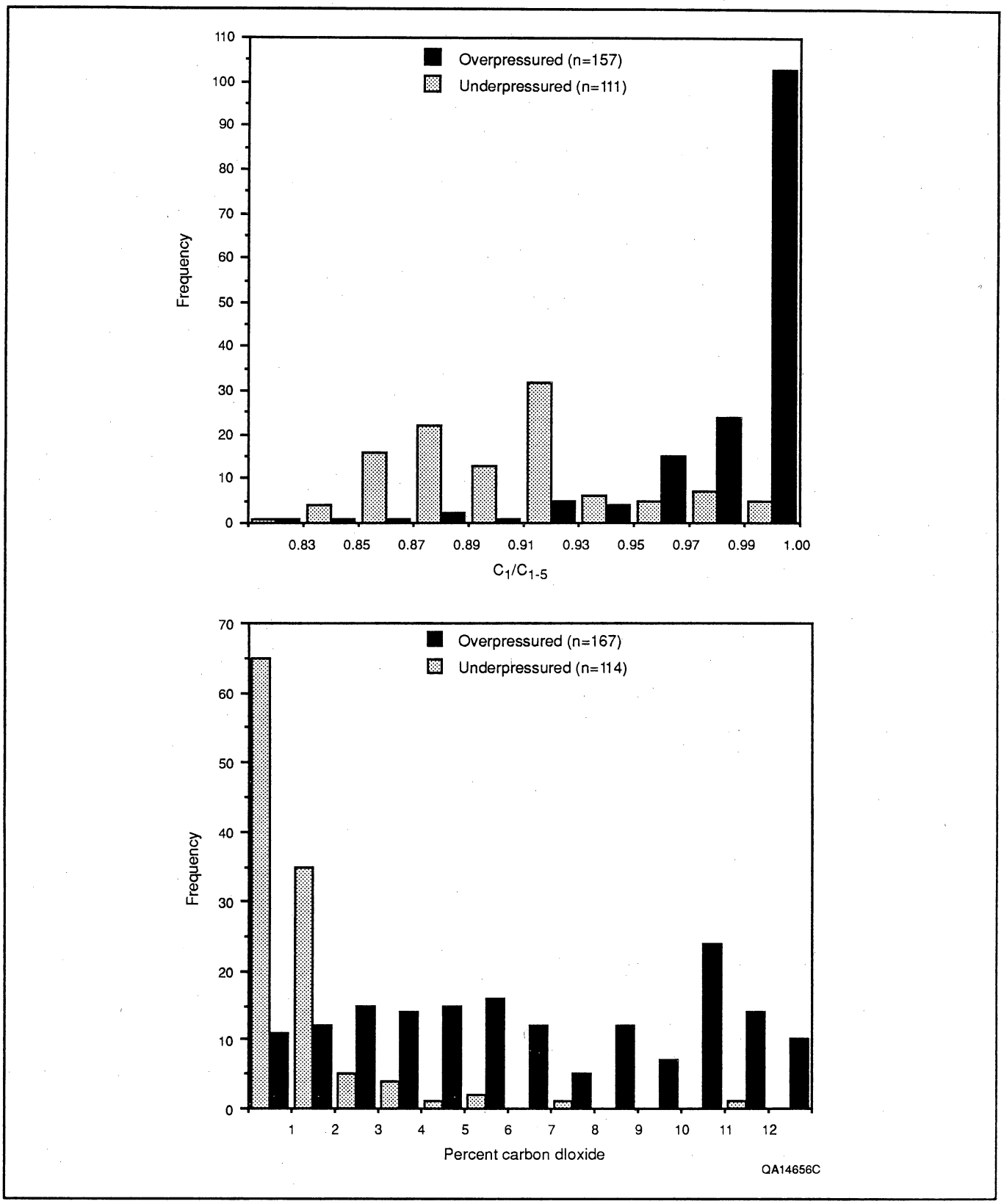

Figure 12. Histograms of C_1/C_{1-5} values and carbon dioxide content of gases from underpressured and overpressured Fruitland coal. Gases from the overpressured, thermally more mature coal in the northern basin are significantly drier than coalbed gases from the underpressured parts of the basin. Gases from underpressured coal beds generally contain less than 2 percent carbon dioxide, whereas gases from overpressured coal beds commonly contain more than 2 percent carbon dioxide. The bimodal distribution of carbon dioxide in the overpressured gases primarily reflects samples from the Meridian 400 area.

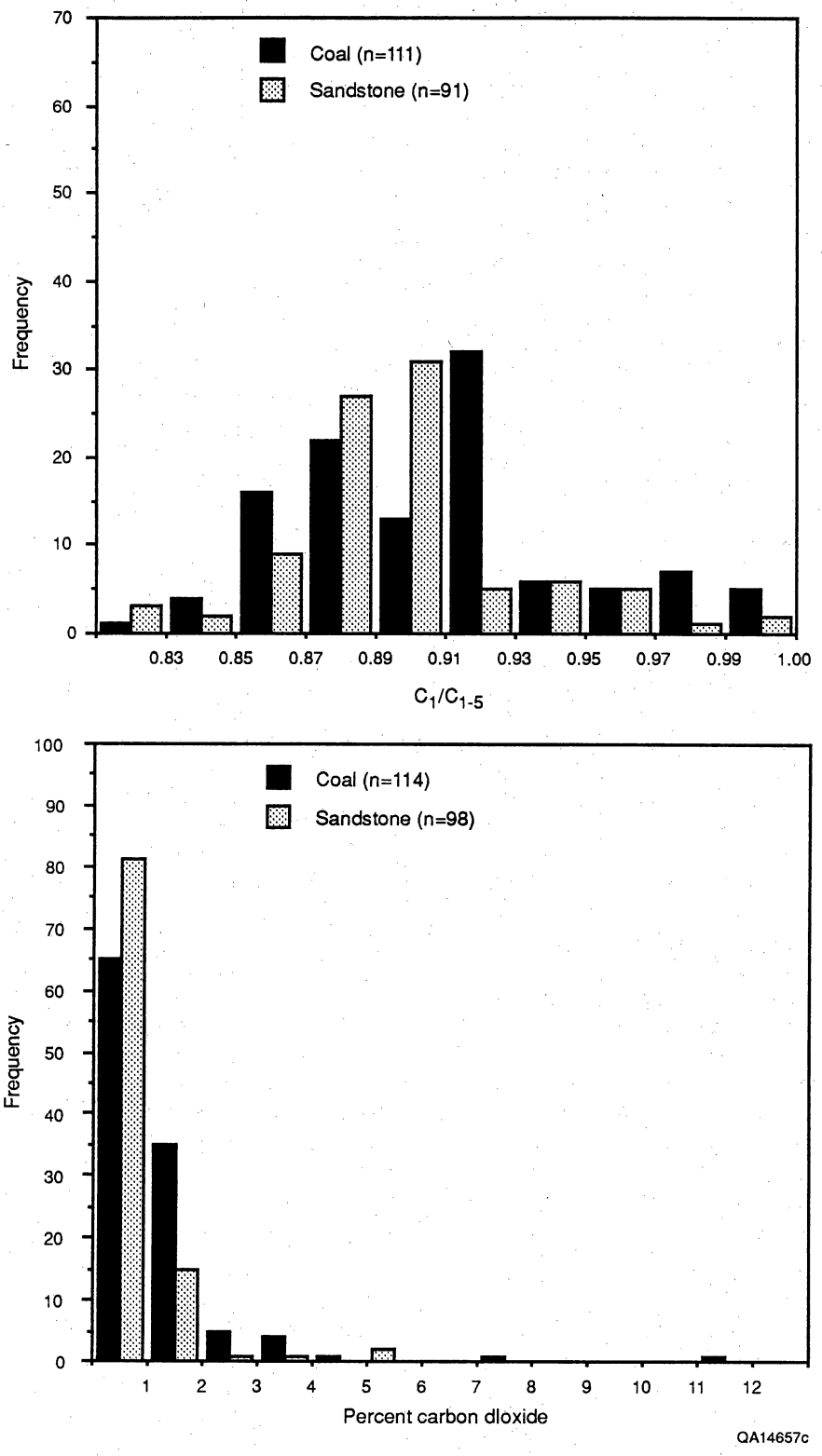

Figure 13. Histograms of C_1/C_{1-5} values and carbon dioxide content of gases from underpressured Fruitland coal beds and sandstones. Both coal and sandstone gases usually contain less than 2 percent carbon dioxide and have C_1/C_{1-5} values between 0.85 and 0.93.

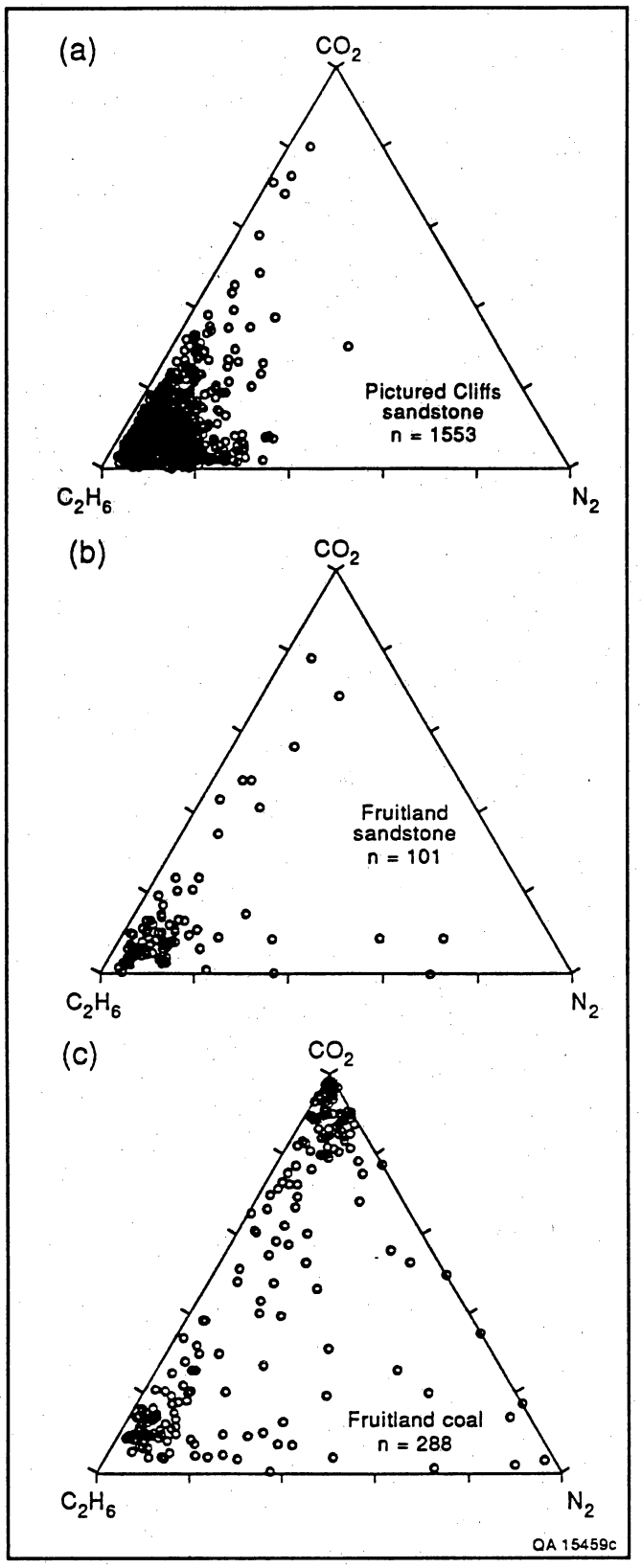

Figure 14. Ternary diagrams of Pictured Cliffs and Fruitland gases. The proportion of carbon dioxide, ethane, and nitrogen cannot be used to confidently differentiate among gases derived from Fruitland coal beds, Fruitland sandstones, and Pictured Cliffs sandstones.

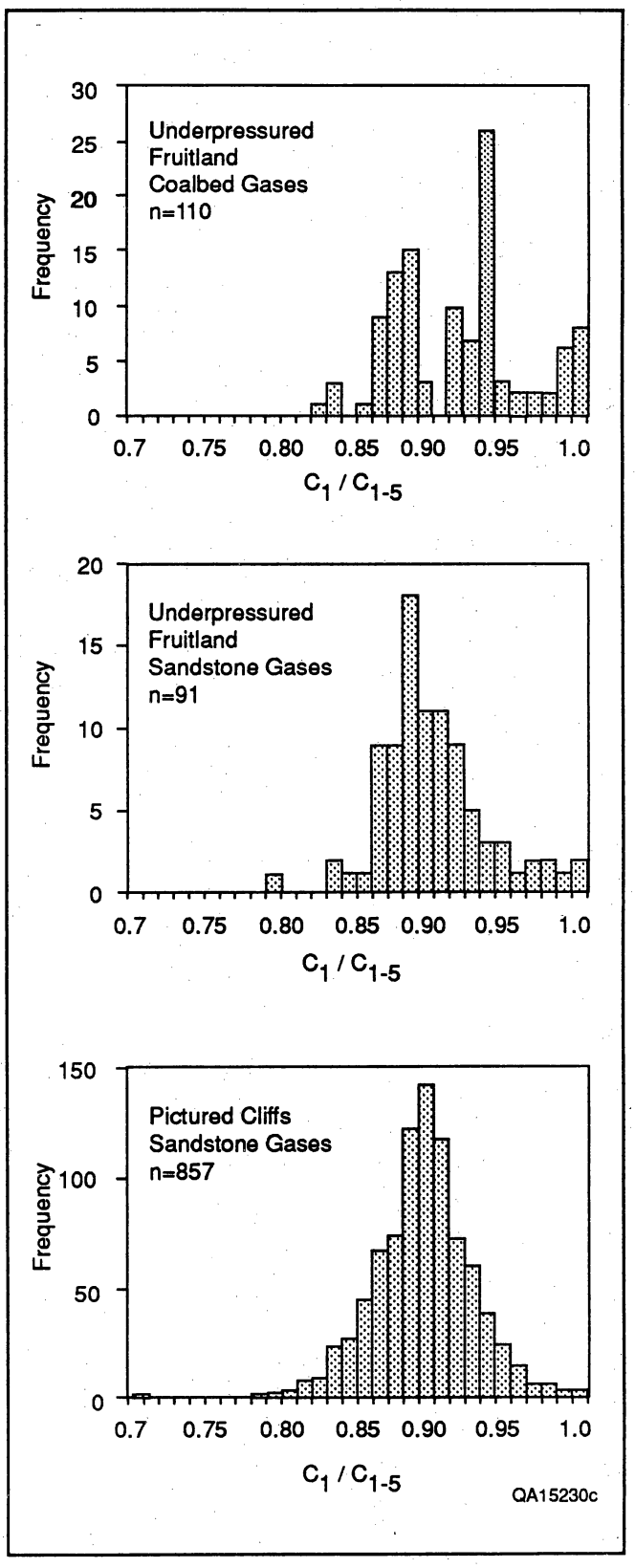

Figure 15. Histograms of gases from underpressured Fruitland coal bed, Fruitland sandstone, and Pictured Cliffs sandstones. Pictured Cliffs gas data used in this histogram are from the same part of the basin as Fruitland gas data.

The wettest Pictured Cliffs gases also occur in the southeastern part of the basin (fig. 16). The wetter gases in this area may reflect lower levels of thermal maturity and/or differences in kerogen type. Elongate trends of relatively dry gas (C_1/C_{1-5} values greater than 0.85) parallel depositional strike in the southeastern corner of the basin, suggesting that localized variations of gas composition may be due to (1) migration effects across shale/sandstone contacts that would enrich the gases in methane relative to the other components (Leythaeuser and others, 1979), or (2) migration of dry gas through more permeable sandstones. Although significant volumes of Pictured Cliffs gases were probably derived from the underlying Lewis Shale, some of these gases could have migrated from overlying Fruitland coal beds, and mixing of gases from these two sources is possible. Choate and others (1984) suggested that Pictured Cliffs reservoirs are sourced by Fruitland coal beds where pressure differences between the two formations result in the downward migration of chemically drier coalbed gases. Relatively dry (C_1/C_{1-5} values >0.88) sandstone gases occur in the northwestern part of the basin, where thick basal coal beds lie directly on top of Pictured Cliffs sandstones. The dip-elongate bands of coal are not found in the southeastern corner of the basin (Ayers and others, this vol., their fig. 23). The driest Pictured Cliffs gases (C_1/C_{1-5} values >0.91), which occur in a dip-elongate band in eastern San Juan County, may result from completion practices (dual completion in Fruitland coal beds and Pictured Cliffs sandstones) or downward migration from adjacent Fruitland coal beds. This trend of dry gases coincides with dip-elongate bands of basal Fruitland coal beds that may be in excess of 20 ft (6 m) thick (Ayers and others, this vol., their fig. 23). The C_1/C_{1-5} values of coalbed gases in western Rio Arriba County are similar to C_1/C_{1-5} values of gases from underlying Pictured Cliffs sandstone gases, which also suggests communication between these two reservoirs. The similarity of underpressured Fruitland coalbed and Pictured Cliffs sandstone C_1/C_{1-5} values and gas composition distributions (figs. 9 and 16) indicates that gas composition alone will not necessarily distinguish coalbed from sandstone gases in parts of the southern basin. More detailed analytical methods, including hydrogen and carbon isotopic analyses of both Fruitland and Pictured Cliffs gases on a basinwide scale, are probably required to establish the origin and migration pathways of these gases.

Carbon dioxide content of Pictured Cliffs sandstone gases is generally less than one percent (fig. 17). The highest carbon dioxide values of Pictured Cliffs sandstone gas occur in the northwestern part of the basin in the Cedar Hill area (figs. 10 and 17); gases from the southwestern part of the basin are chemically drier and contain more carbon dioxide (figs. 16 and 17). These areas of higher carbon dioxide content may represent communication between Fruitland coal beds and/or result from dual completions in Fruitland coal beds and Pictured Cliffs sandstones.

Relation of Gas Composition to Thermal Maturity and Pressure Regime

Previous interpretations of gas origin and composition in the Fruitland Formation and Pictured Cliffs sandstones were based upon the assumption that coal rank and burial history controlled gas composition. Furthermore, overpressuring in the Fruitland was thought to be caused by fossil geopressuring associated with basin subsidence and thermal maturation rather than by basin hydrodynamics (Decker and others, 1987). However, this study suggests that compositional variations in Fruitland coalbed gases and the regional distribution of these gases result from thermal maturity and basin hydrology. The Fruitland Formation is a regional aquifer, with recharge occurring in the northern basin where thick northwest-trending coal beds crop out along the Hogback Monocline (Kaiser, Swartz, and Hawkins, this vol.). Upon confinement and basinward pinch-out of coal beds and/or localized faulting (Ayers and others, this vol.), regional overpressuring is developed in the Fruitland (Kaiser, Swartz, and Hawkins, this vol.). Rice and others (1988 and 1989) suggested that Fruitland coalbed gases are chemically very dry (C_1/C_{1-5} values greater than 0.99) and that Fruitland coalbed gases with lower C_1/C_{1-5} values are a result of unspecified completion practices. But in the ensuing discussions, Rice and others (1989) cited geochemical evidence that Fruitland coal is hydrogen rich and may be the source of condensate produced from the coals. However, they did not explain why hydrogen-rich coals would produce only very dry gases. According to Hanson (1990), although desorbed coalbed gases are commonly dry to very dry, some gases may be wet to very wet, with gas wetness depending on coal rank and maceral composition. Furthermore, coalbed gas composition may vary between individual coal beds and laterally within a given coal bed if maceral content is highly variable.

Thermogenic gases become chemically drier with increasing thermal maturity. Predictably, coalbed gases from the thermally more mature northern part of the basin are chemically dry to very dry. However, the regional distribution of these gases (fig. 9) suggests that coal rank is not the only factor controlling the chemical composition of the gas. The eastern boundary of chemically dry coalbed gases does not coincide with

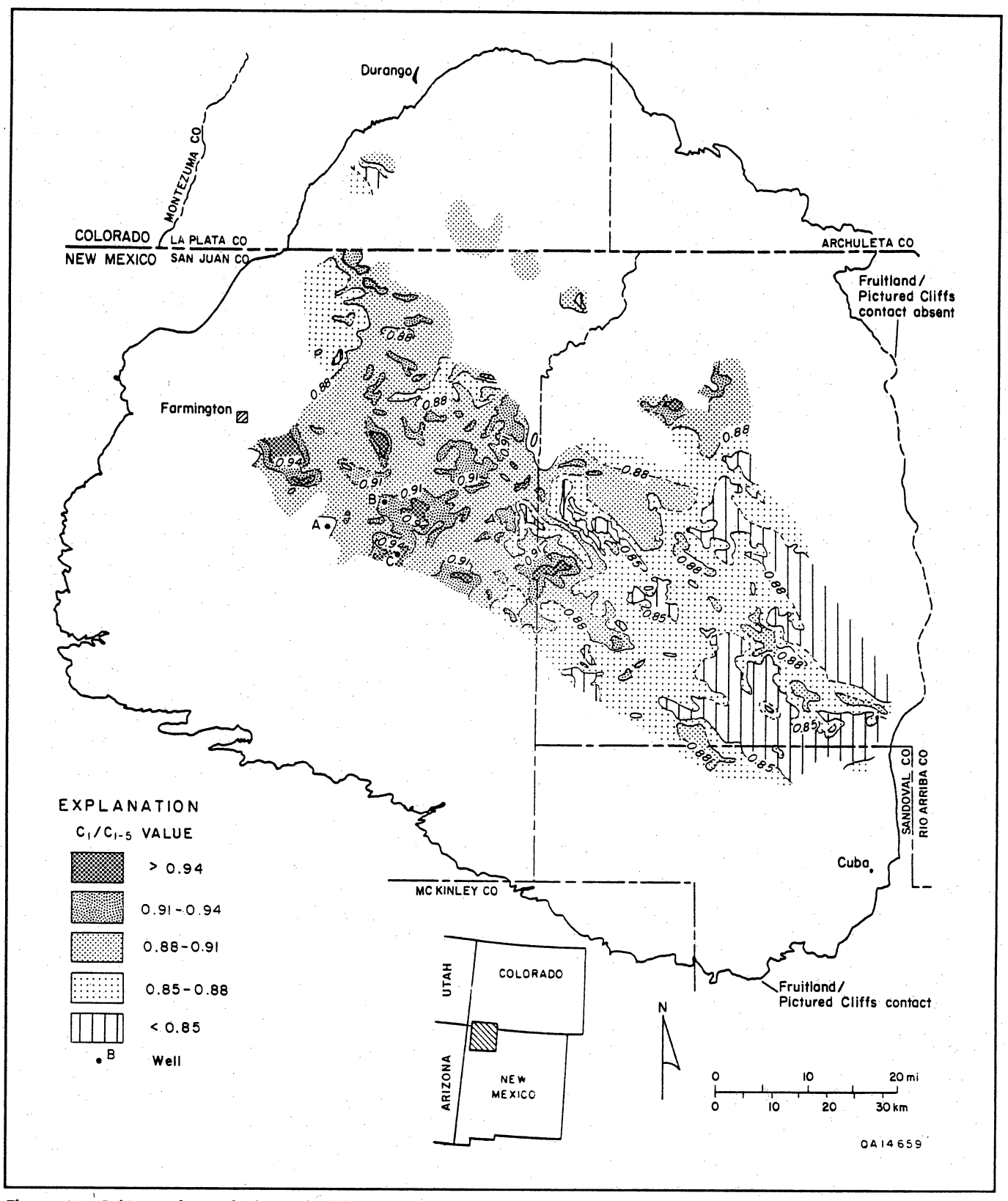

Figure 16. C_1/C_{1-5} values of Pictured Cliffs sandstone gases. Pictured Cliffs gases in the southeastern part of the basin are chemically wetter than gases produced from the northwestern part of the basin. The northeast-trending area of drier gases (C_1/C_{1-5} values greater than 0.88) coincides with an area where thicker Fruitland coal beds overlie the sandstones, suggesting that coalbed gases may have migrated downward. Gas compositions from more than 5,500 wells were used to construct this map.

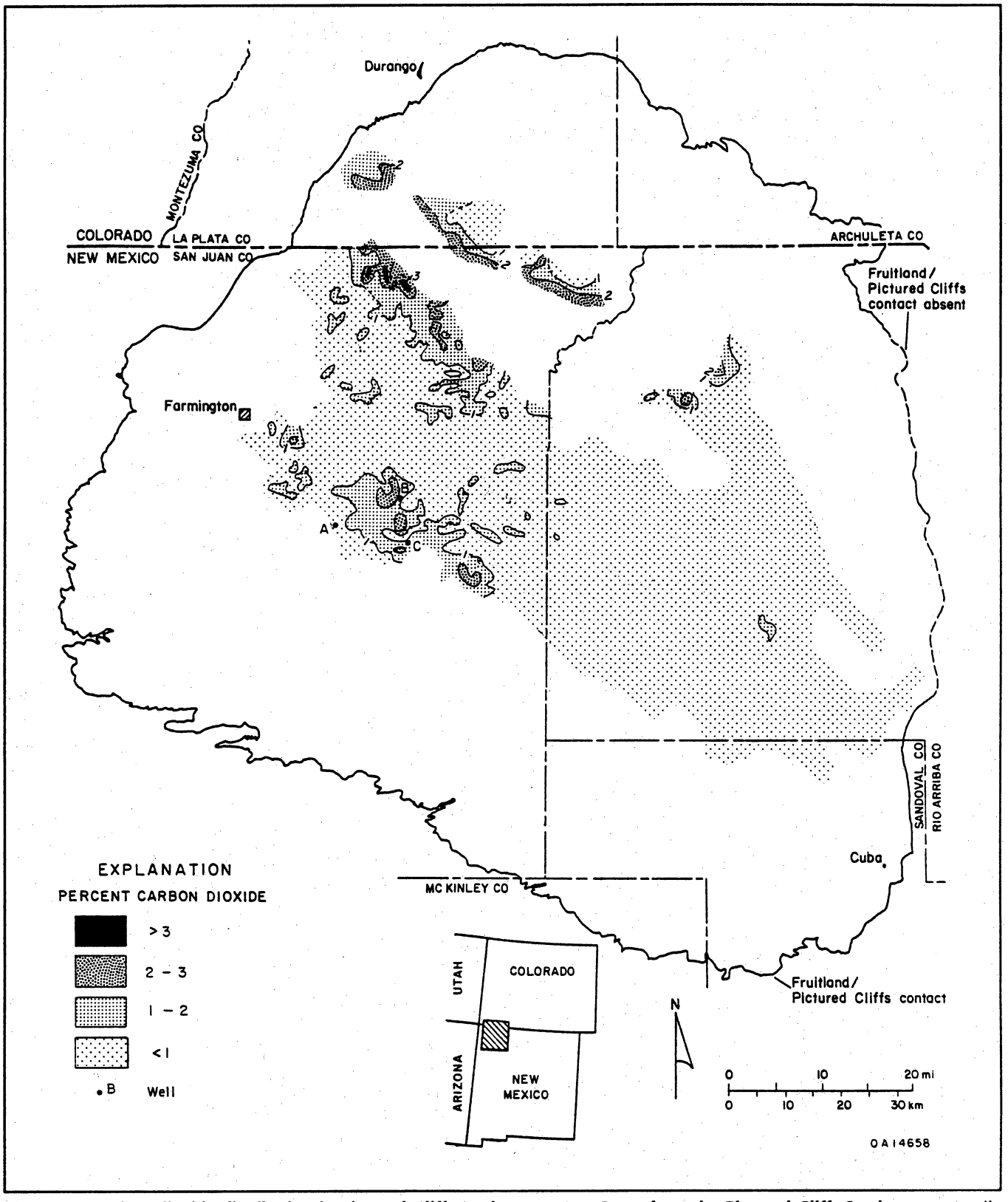

Figure 17. Carbon dioxide distribution in Pictured Cliffs sandstone gases. Gases from the Pictured Cliffs Sandstone generally have less than 1 percent carbon dioxide. Those with higher carbon dioxide content may be completed in or immediately below the basal Fruitland coal beds. Gas compositions from more than 5,500 wells were used to construct this map.

coal-rank trends (fig. 3). Furthermore, a gradational contact between very dry and wet coal gases paralleling vitrinite reflectance trends would be expected if coal rank alone controlled gas composition. Instead, there is an abrupt transition from very dry (C_1/C_{1-5} value of 1.00) to wet (C_1/C_{1-5} value of 0.87) coalbed gases over distances of less than 1.5 mi (2 km) along some parts of the overpressured/underpressured boundary. In fact, gas composition coincides with pressured conditions in the Fruitland Formation (Kaiser, Swartz, and Hawkins, this vol.) more than with coal rank. Therefore, basin hydrology is thought to be a major factor controlling coalbed gas composition. The origin of these gases will be discussed in the following section.

Previous studies have suggested that coalbed carbon dioxide content decreases with increasing coal rank (Rice and others, 1988, 1989; Rice and others, 1990). However, Fruitland coalbed gases with the highest carbon dioxide content occur in the northern part of the basin where coal rank is high-volatile A bituminous (fig. 10). Gases from low- and medium-volatile bituminous coals from the northern basin generally have lower carbon dioxide content (less than 3 percent) than some lower rank coals. Carbon dioxide content of gases from high-volatile A bituminous coal varies from less than 1 percent to more than 10 percent, indicating that coal rank is not the only factor controlling carbon dioxide content. High carbon dioxide content in coalbed gases coincides with the overpressured part of the basin and with highest bottom-hole pressures (fig. 10; Kaiser, Swartz, and Hawkins, this vol., their figs. 1 and 7) indicating that the carbon dioxide content is partly controlled by basin hydrology and regional overpressure. Dip-elongate bands of slightly higher carbon dioxide content in the southern basin represent diffusion of carbon dioxide and/or flow of dissolved bicarbonate from the overpressured part of the basin southwestward through coal beds that were offset by the northwest-trending fracture zone along the structural hingeline (Ayers and others, this vol.). These higher carbon dioxide content trends parallel dip-elongate coal beds, hydraulic gradients, and northeast-trending productivity trends (Ayers and others, this vol.; Kaiser and others; this vol.; Kaiser, Swartz, and Hawkins, this vol.). The relatively high carbon dioxide content bands terminate near the San Juan River valley in northern San Juan County, which acts as a regional flow boundary (Kaiser, Swartz, and Hawkins, this vol.).

Chemically dry gases with low carbon dioxide contents are associated with higher rank coal in the northern part of the basin, whereas chemically wet, low carbon dioxide content coalbed gases occur in the underpressured, southern region. Coalbed gases in high-volatile A bituminous coal are characterized by variable C_1/C_{1-5} values and carbon dioxide contents. The coincidence between regional overpressuring and the distribution of chemically dry to very dry, carbon dioxide-rich gases, and the abrupt transition between these gases and wetter gases with low carbon dioxide contents in the underpressured, southern part of the basin indicate that coalbed gas composition is related to basin hydrology in addition to coal rank.

Origin of Fruitland Coalbed Gases

Previous studies using gas wetness and carbon isotopic values of methane have suggested that most of the gases produced from the Fruitland Formation are thermogenic in origin; only a few gas samples in the southern basin were believed to have a possible biogenic origin (Rice, and others, 1988, 1989). The wet gases produced from Fruitland coal beds have been attributed to unspecified completion practices (Rice and others, 1988, 1990). However, the distribution of carbon dioxide content and C_1/C_{1-5} values for Fruitland coalbed gases do not necessarily support these conclusions. The distribution of wet gases in the Fruitland Formation and previous geochemical studies (Rice and others, 1989; Law and others, 1990) suggest that these gases are indigenous to the coal. Although the majority of gases produced from Fruitland coal beds probably have a thermogenic origin, mixing of thermogenic and biogenic gases can better explain gas compositional distributions and the $\delta^{13}C$ isotopic signatures of methane, total dissolved carbonate, and carbon dioxide found in the Fruitland Formation.

Wet coalbed gases (C_1/C_{1-5} values less than 0.94) occur between vitrinite reflectance values of 0.49 and 0.75 percent in the high-volatile C and B bituminous coal range (figs. 3 and 9). This range of vitrinite reflectance values corresponds to the early stages of oil generation; vitrinite reflectance values for the principal zone of oil generation, or oil window, range from approximately 0.5 to 1.3 percent (Tissot and Welte, 1978). This relationship between the distribution of chemically wet coalbed gases and vitrinite reflectance values suggests that wet coalbed gases in the Fruitland may be a direct result of the thermal maturation of organic matter and not a result of completion practices.

Coal has been traditionally thought of as a major source of dry gas having little potential for generating liquid hydrocarbons. However, hydrogen-rich coal is capable of generating liquid hydrocarbons (Khorasani, 1987). Furthermore, coals composed predominantly of vitrinite may contain submicroscopic particles of hydrogen-rich organic matter in the vitrinite; these particles would not be identified during microscopic studies of the kerogen resulting in interpretation of coal composed predominantly of vitrinite (Bertrand and others, 1986, and references therein).

Rock-Eval pyrolysis analyses of Fruitland coals (Rice and others, 1989; Law and others, 1990) indicate that these coals are hydrogen rich and have a moderate potential for generating liquid hydrocarbons (fig. 18a). Fruitland coals have hydrogen indices similar to oil-prone coals from Australia (Khorasani, 1987). However, these analyses suggest that Fruitland coals are composed of Type I and II kerogen rather than Type III kerogen, which is characteristic of terrestrial organic matter (Law and others, 1990). The relatively high hydrogen indices of Fruitland coal are probably related to the early generation of bitumen (probably the exsudatinite reported by Rice and others, 1989) during coalification. Bitumen released during the early stages of oil generation or bitumen migration into the source rock can adversely affect hydrogen indices (Clementz, 1979) and make it difficult to correctly identify kerogen type on the basis of Rock-Eval data alone. Most of the hydrogen-rich material found in Fruitland coals is presumably indigenous and has not migrated from adjacent shales (Rice and others, 1989). Elemental analyses, in which the bitumen was extracted before analysis, indicate that Fruitland coals are composed of Type III kerogen (fig. 18b), which is consistent with conclusions from petrographic studies (Rice and others, 1989; Law and others, 1990). Law and others (1990) reported correlation between the amount of generated bitumen and increasing vitrinite reflectance values, which suggests that Fruitland coals are progressively generating more hydrocarbons with increasing coal rank. The range of thermogenic hydrocarbon generation (Rm values of 0.60 to 0.85 percent) reported by Law and others (1990) nearly coincides with areas in the basin where wet coal gases occur (vitrinite values between 0.49 and 0.75 percent). These observations suggest that Fruitland coal beds are capable of producing wet gases and that areas of wet coalbed gases in the southern basin are directly related to coal rank.

Saturated hydrocarbon distributions on gas chromatograms of Fruitland coal and carbonaceous shale extracts are similar to condensates produced from Fruitland coal beds, indicating that the condensates originated from the coals (Rice and others, 1989). The similar compositional range of Fruitland sandstone and coalbed gases and the similarity between coalbed gas condensates and coal and carbonaceous shale extracts (Rice and others, 1989) are consistent with the migration of wet gases derived from carbonaceous shales and coal beds to adjacent Fruitland sandstones. The compositional variation between underpressured Fruitland sandstone and coalbed gases would not be large if the gases were derived from similar types of organic matter at the same levels of thermal maturity. With increasing thermal maturation, differences in the amounts and types of compounds released from different kinds

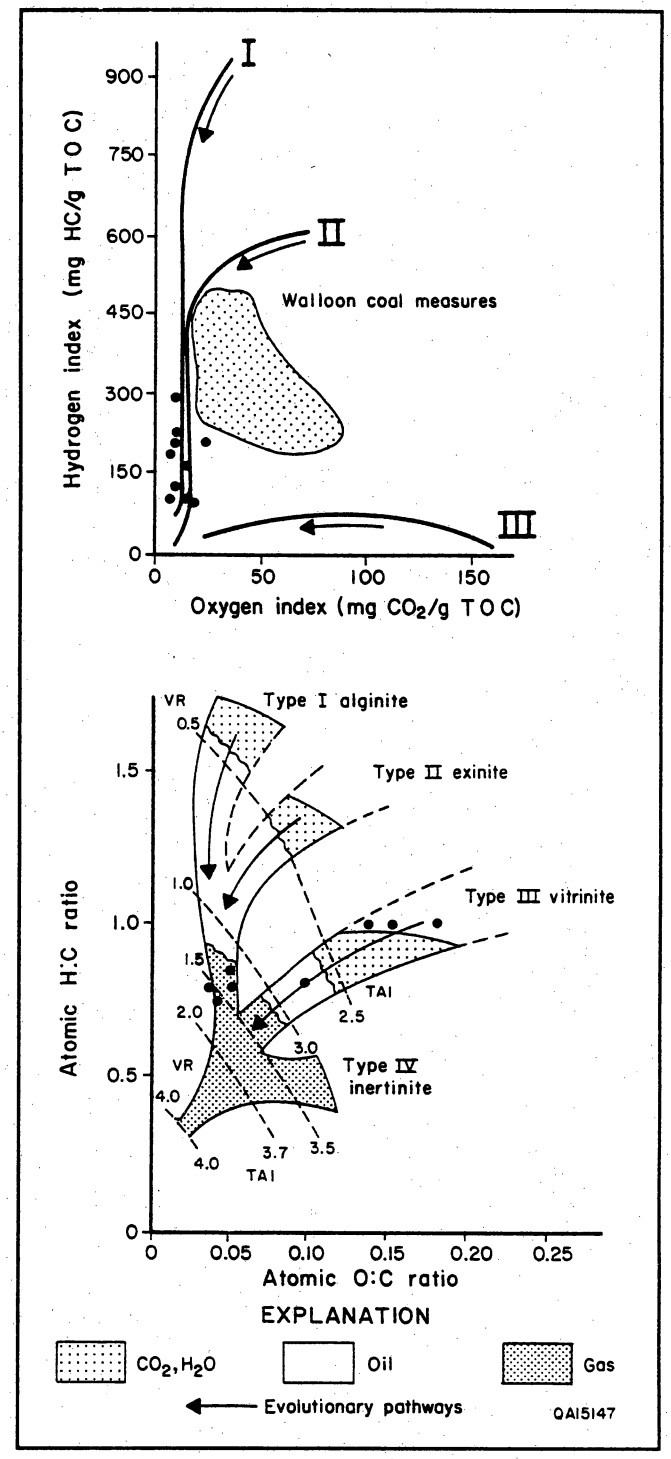

Figure 18. Geochemical characterization of Fruitland coal. Fruitland coals (solid circles) contain significant amounts of hydrogen-rich components and are capable of generating wet gases. (a) Rock-Eval pyrolysis of Fruitland coal indicates that the coal is hydrogen rich, but it incorrectly identifies the coal as Types I and II kerogen. (b) Elemental analyses correctly identify the Fruitland organic matter as Type III terrestrial kerogen. Figures modified from Espitalie and others (1977), North (1985), Khorasani (1987), and Rice and others (1989). VR = vitrinite reflectance (percent); TAI = thermal alteration index.

of organic matter would become more pronounced, and differences in gas compositions would become more readily apparent.

The generation of dry thermogenic gases from coal usually begins at vitrinite reflectance values of 0.7 percent (Meissner, 1987). This lower limit of thermogenic methane generation from coal beds coincides with the southwestern limit of dry coalbed gases (fig. 9), suggesting that the dry gases in the northern San Juan Basin are thermogenic in origin, as indicated previously (Rice and others, 1988, 1989). However, if Fruitland coalbed methane is entirely thermogenic, the $\delta^{13}C$ values of methane should become less negative (isotopically heavier) with increasing thermal maturation (thermogenic $\delta^{13}C$ values from –55 to –15‰; Jenden, 1985). Instead, the isotopic signature of methane from Fruitland coal beds is relatively consistent throughout the basin and does not vary significantly with coal rank (fig. 19). Either the process of thermogenic gas generation from coal is significantly different from gas generation from other types of organic matter, resulting in a relatively narrow range of $\delta^{13}C$ methane values, or Fruitland coalbed gases may represent a mixture of thermogenic and biogenic gases.

Biogenic methane $\delta^{13}C$ values range from less than –90‰ to –40‰ (Jenden, 1985), indicating that biogenic and thermogenic gases can have similar methane $\delta^{13}C$ isotopic values over the range of –55 to –40‰. Biogenic gases produced from carbonate reduction and/or acetate dissimilation can produce both chemically very dry gases (C_1/C_{1-5} values of 1.00) and isotopically heavy bicarbonate (Carothers and Kharaka, 1980). Furthermore, bacterial alteration of chemically wet gases can remove nearly all of the heavier gas components, producing chemically dry gases that resemble thermogenic gases (James and Burns, 1984). Therefore, the composition and distribution of coalbed gases and isotopic composition of bicarbonate from formation water must be considered in addition to methane $\delta^{13}C$ values to determine the origin of Fruitland coalbed methane.

Regional variations of carbon dioxide content and chemical composition (C_1/C_{1-5} values) of Fruitland coalbed gases coincide with regional overpressuring, indicating that there is a relationship between basin hydrology and gas composition. Waters from the overpressured, northern basin are dominantly Na-HCO_3 type and are characterized by high alkalinity and low chloride content (Kaiser, Swartz, and Hawkins, this vol.). Relatively minor amounts of organic acids are present in these waters, and alkalinity is predominantly inorganic (Kaiser, Swartz, and Hawkins, this vol., their table 3). The $\delta^{13}C$ values of the total dissolved carbonate species (predominantly composed of the bicarbonate ion) are isotopically heavy, ranging from +16.7 to +26.0‰ (Kaiser, Swartz, and Hawkins, this vol., their table 3). These values are consistent with those of Jones and others (1985), who reported $\delta^{13}C$ values of carbon dioxide produced from the Glover No. 1 well of +16.2 and +16.8‰. Isotopically heavy values such as these can be derived from bacterial activity and/or dissolution of isotopically heavy carbonate cement.

A combination of thermogenic and biogenic gases can explain both methane $\delta^{13}C$ values and the heavy isotopic signature of total dissolved carbonate species in Fruitland waters. Methanogenic degradation of short-chained organic acids through acetate fermentation would produce both positive $\delta^{13}C$ total dissolved carbonate values and methane that would be depleted in ^{13}C by 60 to 70‰ relative to the bicarbonate at present-day in situ formation temperatures of 30° to 60°C (Carothers and Kharaka, 1980). Furthermore, acetate dissimilation is probably the major source of biogenic gas in freshwater environments (Whiticar and others, 1986, and references therein). Biogenic carbonate reduction of carbon dioxide will also produce isotopically heavy bicarbonate and isotopically light methane. A mixture of 85 percent thermogenic methane ($\delta^{13}C$ of –42‰) and 15 percent biogenic methane ($\delta^{13}C$ of –48‰) would produce methane with an average isotopic value of –43‰. The $\delta^{13}C$ value of the corresponding bicarbonate would be +23‰, assuming a fractionation factor of 71‰ between the biogenic methane and bicarbonate. These isotopic values are similar to isotopic ranges seen in Fruitland coalbed gases and formation waters (fig. 19; Kaiser, Swartz, and Hawkins, this vol., their table 3). The less positive $\delta^{13}C$ values of total dissolved carbonate (+16.7 and +17.5‰) in the northwestern part of the basin (fig. 19) may indicate the dilution of isotopically heavy bicarbonate with fresh ground water containing isotopically light bicarbonate derived from atmospheric and/or soil sources.

Isotopically heavy bicarbonate can also be derived from the dissolution of isotopically heavy carbonate cements. Carbonates from the NEBU No. 403 well (T32N, R7W, sec. 9) in the overpressured part of the basin have a wide range of $\delta^{13}C$ values (table 2). Although the fracture-filling calcite is isotopically heavy ($\delta^{13}C$ of +17.2‰), the $\delta^{13}C$ isotopic values of authigenic carbonates from Fruitland sandstones and siltstones are negative ranging from –2 to –15.3‰ (table 2). Carbonate cement is also present in Fruitland coal cleats (Tremain and others, this vol., their table 3), but the coal and/or adjacent sandstones may not contain sufficient carbonate cement to account for the large quantities of carbon dioxide present in some coal beds. Furthermore, carbonate dissolution would have to be demonstrated; precipitation of isotopically heavy carbonate in the cleat system may have occurred rather than dissolution of isotopically heavy carbonate

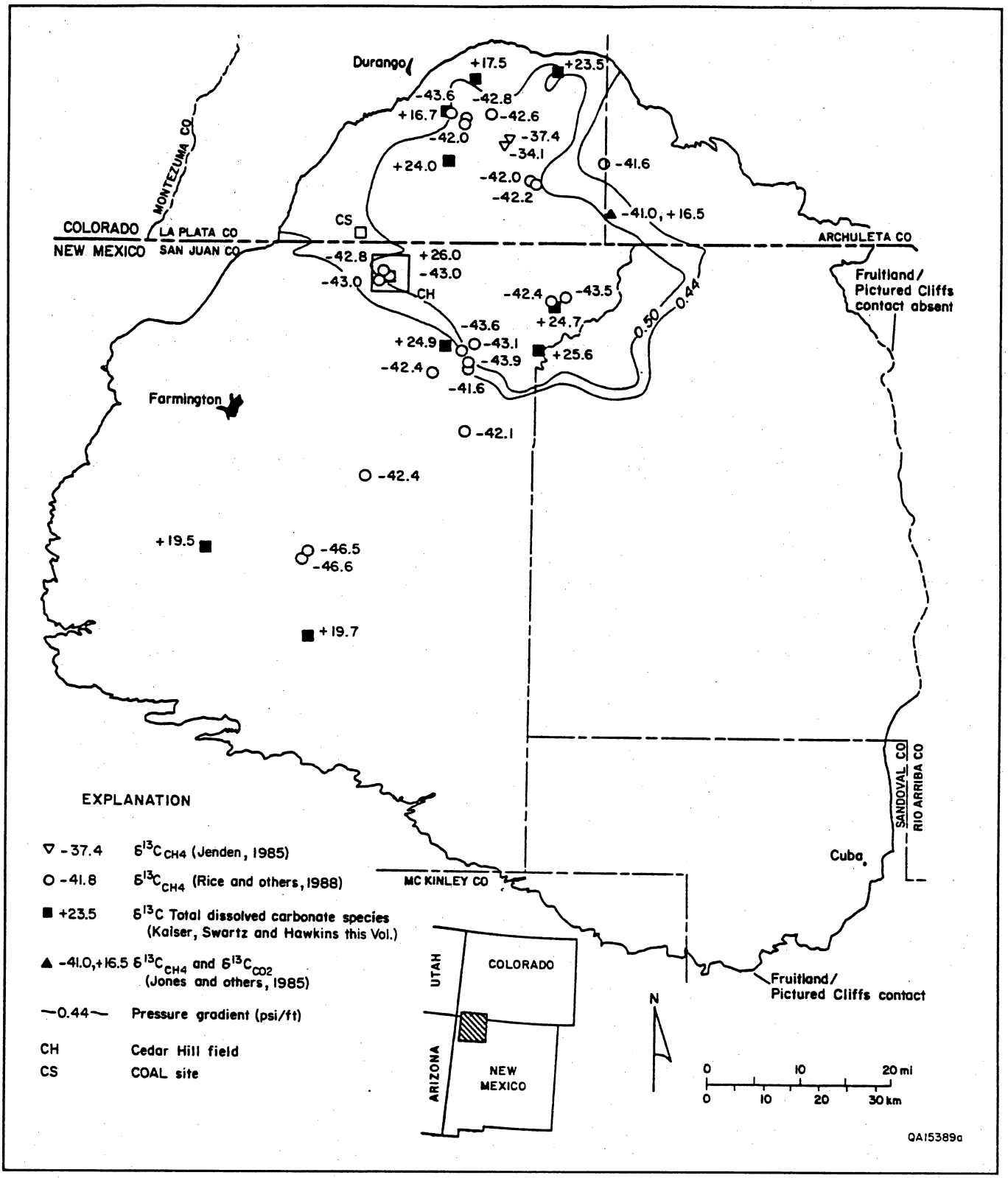

Figure 19. Distribution of $\delta^{13}C$ isotopic values of methane and carbon dioxide produced from Fruitland coal beds and $\delta^{13}C$ values of total dissolved carbonate species (predominantly bicarbonate) in Fruitland formation waters. The consistency of $\delta^{13}C$ methane values across the basin, light isotopic signature of methane associated with higher rank coals, isotopically heavy carbon dioxide from Fruitland coal beds, and isotopically heavy bicarbonate in Fruitland formation waters suggest that at least some coalbed gases in the overpressured, northern basin have a biogenic origin. Data from Jones and others (1985), Jenden (1985), Rice and others (1988), and Kaiser, Swartz, and Hawkins (this vol.).

Table 2. Isotopic composition of Fruitland Formation and Pictured Cliffs carbonates. Samples are from the NEBU No. 403 well in Rio Arriba County, New Mexico (T32N, R7W, Sec. 9) unless otherwise designated.

Formation	Depth (ft)	Carbonate	Comments	$\delta^{13}C_{PDB}$	$\delta^{18}O_{PDB}$
Fruitland	3086.5	calcite	fracture-filling	+17.2	–11.1
Fruitland	3093.2	dolomite	vfn sandstone	–15.3	–14.6
Fruitland	3097.3	siderite	concretion	–2.0	–12.5
Fruitland	3112.4	dolomite	siltstone	–9.6	–16.7
Pictured Cliffs	3131.8	dolomite	fn sandstone	–8.0	–15.2
Fruitland	outcrop	calcite	cone-in-cone*	–2.2	–13.7

*Sample from Ft. Lewis Mine, Colorado.

cement. Geochemical modeling indicates that Fruitland waters, under in situ conditions, are supersaturated with respect to all carbonate phases. Furthermore, the $\delta^{18}O$ isotopic value of the fracture-filling calcite suggests that the calcite precipitated at a temperature of approximately 33°C (91°F) (Friedman and others, 1977) assuming a $\delta^{18}O$ value of –7.4‰ for the formation water (Kaiser, Swartz, and Hawkins, this vol., their table 3, sample 5). This estimated precipitation temperature is similar to present-day formation temperatures.

Dissolution of large quantities of isotopically very heavy carbonate cement ($\delta^{13}C$ of +26‰) would be required to explain the $\delta^{13}C$ values of the total dissolved carbonate found in Fruitland Formation waters (up to +26.0‰). The absence of a relatively large isotopically heavy carbonate source in Fruitland coal beds indicates that the isotopically heavy $\delta^{13}C$ values of total dissolved carbonate found in Fruitland Formation waters are probably the result of bacterial activity rather than dissolution of carbonate cement. Bacterial degradation of organic acids and/or reduction of carbon dioxide by methanogenic bacteria may have produced both isotopically heavy carbon dioxide and bicarbonate, and biogenic methane in some parts of the basin.

Even with the mixing of thermogenic and biogenic gases, gases derived from higher rank coal in the northern part of the basin should have more positive isotopic values than those reported by Rice and others (1988), assuming that the proportion of biogenic methane in the system remains constant in the northern basin. Thermogenic gases become less negative with increasing maturation, and the mixing of thermogenic and biogenic gases would require a relatively higher proportion of biogenic methane to explain the reported $\delta^{13}C$ value of methane ($\delta^{13}C$ value of approximately –42‰) associated with gases from higher rank Fruitland coal. These isotopically light gases found in the overpressured part of the basin may represent biogenic methane present in the cleat system as free gas and on coal surfaces as adsorbed gas. Adsorption of methane onto coal surfaces is controlled by the amount of methane in the gas phase (Puri and Yee, 1990). Therefore, as the concentration of biogenic methane increases in the cleat system, the methane will be adsorbed onto coal surfaces. If the concentration of biogenic methane is insufficient for adsorption to occur, the methane would remain as a free gas phase in the cleat system or be removed from the system. Biogenic methane adsorbed onto coal surfaces would be released along with thermogenic methane as pressures drop during production.

During initial production, gases desorbed from coal surfaces would have a relatively large biogenic component (isotopically light methane), whereas subsequently desorbed gases would be progressively enriched in thermogenic methane (isotopically heavier). If this hypothesis is correct, $\delta^{13}C$ values of the produced methane should become less negative with time as the proportion of biogenic methane decreases and the amount of thermogenic gases desorbed from coal surfaces increases; with time the change in methane $\delta^{13}C$ values would be most pronounced in the northern basin, where coal is higher rank.

The presence of biogenic methane in coalbed gases is supported in part by studies involving the desorption of gases from Fruitland coal, which reported that desorbed methane from coal samples was isotopically heavier than the methane produced from nearby wells (Rice and Threlkeld [in press], quoted from Rice and others, 1988). This suggests that $\delta^{13}C$ values of produced gases could represent a mixture of biogenic

methane occurring as a free or dissolved gas in the cleat system and thermogenic methane desorbed from the coal surfaces. The presence of free gas in some wells may be indicated by a geometric mean for initial production (195 Mcf/d) that is significantly larger than that for maximum annual production (93 Mcf/d) (Kaiser, Ayers and others, this vol., their figs. 3 and 4).

Previous studies have suggested that dry coalbed gases in the southern basin may be biogenic in origin; the light isotopic signature of the methane ($\delta^{13}C$ values of –46.6 to –46.5‰) results from acetate dissimilation instead of carbonate reduction during methanogenesis (Rice and others, 1988, 1989). The $\delta^{13}C$ values of bicarbonate from Fruitland Formation water produced from two wells in this area are +19.5‰, supporting the conclusion that these gases are probably biogenic. The difference in $\delta^{13}C$ values between methane and bicarbonate from Fruitland Formation waters in this area is approximately 65‰, which is consistent with the fractionation between biogenic methane and bicarbonate reported by Carothers and Kharaka (1980) at low temperatures. Some relatively dry gases in the southwestern part of the basin may have an early thermogenic origin, as suggested by Rice and others (1989). Recent work (Galimov, 1988) on the origin of gases in the supergiant gas fields of western Siberia indicates that early thermogenic gases can be generated from terrestrial organic matter at low levels of thermal maturity (Rm from 0.4 to 0.5 percent). The isotopic signatures of these early thermogenic gases ($\delta^{13}C$ values of –50 to –46‰) are similar to those of Fruitland coalbed gases. The boundary between chemically dry and chemically wet gases in the southern basin is near the vitrinite reflectance isorank contour of 0.5 percent (figs. 3 and 9), which corresponds to the initial stage of liquid hydrocarbon generation. This boundary may represent the transition from predominantly biogenic and early thermogenic gases in the southwestern part of the basin to the predominantly wet gases associated with liquid hydrocarbon generation in the west-central part of the basin.

Some coalbed gases in the overpressured part of the basin contain significant amounts of carbon dioxide (fig. 10). These areas of higher carbon dioxide content (greater than 3 percent) coincide with regional overpressuring, lower rank coal (low-volatile A bituminous) and highest bottom-hole pressures, but do not follow regional productivity trends (Kaiser, Ayers, and others, this vol.). The high production rates and large quantities of carbon dioxide (greater than 10 percent) in gases produced from coal beds of the Northeast Blanco Unit (NEBU) and Meridian 400 areas may be a function of several factors, including (1) the presence of thick coal beds (which increases the resource) and folding (which increases fracture porosity and permeability in the coal) (Ayers and Zellers, this vol.); (2) coal rank, which may control the amount of carbon dioxide and organic acids in the system; (3) fluid movement, where a general southeastward movement of water transported organic compounds, bicarbonate, and methane southeastward to this area; (4) permeability controls restricting lateral flow in this area; (5) bacterial degradation of organic compounds to produce significant amounts of isotopically heavy carbon dioxide and isotopically light biogenic methane; and (6) a decrease in reservoir pressures during production, resulting in the release of carbon dioxide from the formation waters.

Lower rank coals contain more oxygen-bearing functional groups and are capable of generating larger amounts of carbon dioxide and organic acids than higher rank coals. Therefore, lower rank coal would contain significantly more organic compounds that could be utilized by bacteria as food sources. Microbial degradation of these compounds would produce chemically very dry methane with $\delta^{13}C$ isotopic values similar to methane isotopic values reported by Rice and others (1988) and would account for the isotopically heavy bicarbonate, low organic acid concentrations, and high alkalinities of formation waters in this area (Kaiser, Swartz, and Hawkins, this vol., their table 3).

Carbon dioxide is very soluble in water, and a significant portion of the isotopically heavy carbon dioxide produced from acetate dissimilation was probably dissolved in the formation water. Bicarbonate may have been transported southeastward (basinward) in Fruitland Formation waters. Because pressure increases basinward, progressively more carbon dioxide could be dissolved in the water, and total alkalinity would increase. As reservoir pressure is reduced during production, less carbon dioxide can remain dissolved in water, and carbon dioxide is released from the formation water to be produced along with coalbed gases. Desorption of biogenic carbon dioxide and methane from coal surfaces would also occur. The interpretation of exsolution of carbon dioxide from water is partly justified by the presence of isotopically heavy carbon dioxide ($\delta^{13}C$ values of +16.2 to +16.8‰) produced from coal beds at the Glover No. 1 well in southern Colorado (Jones and others, 1985). These isotopically heavy $\delta^{13}C$ values indicate a predominantly biogenic origin for this carbon dioxide because thermogenic carbon dioxide has negative $\delta^{13}C$ values (Jenden, 1985). Furthermore, bicarbonate from Fruitland waters is enriched in ^{13}C relative to coalbed carbon dioxide by 6 to 9‰, which is similar to the fractionation factor of the bicarbonate and carbon dioxide system (5 to 6‰ at 50°C) reported by Friedman and others (1977). However, the relatively large difference (greater than 6‰) between coalbed carbon dioxide $\delta^{13}C$ values

and some Fruitland water bicarbonate isotopic values suggests that at least some carbon dioxide from coalbed gases in the northern basin may be derived from the desorption of isotopically light (isotopically negative) thermogenic carbon dioxide from coal surfaces. A mixture of 95 percent biogenic carbon dioxide ($\delta^{13}C$ of +18‰) and 5 percent thermogenic carbon dioxide ($\delta^{13}C$ of –20‰) would produce a carbon dioxide with an average $\delta^{13}C$ value of 16.1‰, which is similar to Fruitland coalbed $\delta^{13}C$ carbon dioxide values.

Conclusions

1. Subbituminous and high-volatile C bituminous coals are found in the southern basin and along the Hogback Monocline. The low vitrinite reflectance values over the Ignacio Anticline and along the Hogback Monocline indicate that these structures formed before or during coalification. Northward of a structural hingeline, Fruitland coal rank increases abruptly reaching the low-volatile bituminous coal rank in the northern basin. The presence of structurally higher coals adjacent to structurally lower coal of the same rank in the northwestern corner of the basin suggests local, postcoalification uplift and/or higher heat flux.

2. Wet coalbed gases (C_1/C_{1-5} values less than 0.94) in the southern part of the basin are probably indigenous to the hydrogen-rich Fruitland coal and therefore would not result from completion practices and/or migration of gases from adjacent shales. Chemically dry to very dry coalbed gases in some parts of the southern basin are most likely biogenic in origin, although some early thermogenic methane may be present.

3. The similar composition of Pictured Cliffs sandstone, Fruitland sandstone, and underpressured Fruitland coalbed gases in the southern part of the basin makes determinations of gas origin, on the basis of gas composition alone, difficult or impossible. However, minor differences in carbon dioxide content and gas wetness between Fruitland coalbed and Pictured Cliffs and/or Fruitland sandstone gases in some parts of the southern basin may allow coalbed gases to be distinguished from sandstone gases locally.

4. The similarity between Fruitland coalbed and sandstone gases in some areas suggests that these two types of reservoirs are in communication and/or that the gases were derived from similar types of organic matter. Gas compositional data also suggest that there may be communication between basal Fruitland coal beds and Pictured Cliffs sandstones in the western part of the basin, where thick coal beds directly overlie Pictured Cliffs sandstones.

5. Basin hydrology and coal rank control Fruitland coalbed gas composition. The effect of basin hydrology on coalbed gas compositions is evidenced by the abrupt transition from carbon dioxide rich, chemically dry to very dry gases in the overpressured, northern part of the basin to carbon dioxide poor, chemically wet gases in the underpressured, southern part of the basin.

6. Bacterial degradation of organic acids by acetate dissimilation and/or the microbial reduction of carbon dioxide are required to produce the isotopically heavy bicarbonate ($\delta^{13}C$ ranges from +16.7 to +26‰) found in Fruitland coalbed waters. A mixture of 85 percent thermogenic methane ($\delta^{13}C$ of –42‰) and 15 percent biogenic methane ($\delta^{13}C$ of –48‰) would produce methane with an average isotopic value of –43‰. The $\delta^{13}C$ value of the corresponding bicarbonate would be +23‰, assuming a fractionation factor of 71‰ between the biogenic methane and bicarbonate. These isotopic values are similar to isotopic ranges reported for Fruitland coalbed gases and formation waters. Furthermore, the presence of free and dissolved biogenic methane in the cleat system of Fruitland coal and/or biogenic methane adsorbed onto coal surfaces would explain the relatively constant $\delta^{13}C$ methane values in the northern basin reported in earlier studies.

7. The large amounts of carbon dioxide in gases produced from coal beds in the Northeast Blanco Unit (NEBU) and Meridian 400 areas may result from a combination of factors. Isotopic data suggest that much of the carbon dioxide produced from Fruitland coal beds is biogenic in origin and that it may originate from the formation water. We suggest that bacterially generated carbon dioxide dissolved in formation waters and was transported basinward. As pressure is decreased during production, carbon dioxide exsolves from the formation water and mixes with carbon dioxide, methane, and other gases desorbed from coal surfaces.

Acknowledgments

We thank Jeff Peace and George Lippman of El Paso Natural Gas Company, Brent W. Hale of Northwest Pipeline Corporation, Tom Hemler of Jerome P. McHugh and Associates, and Ernie Busch of the New Mexico Oil and Gas Conservation Commission for providing the gas data used in this study. We also thank William B. Hanson of Amoco Production Research and Peter D. Jenden of Chevron Production Research for their valuable comments concerning coalbed gas chemistry. Finally, we thank Joseph Yeh for handling and digitizing the large gas data base and Tucker F. Hentz for reviewing the manuscript.

Integration of Geologic and Hydrologic Studies

Geologic and Hydrologic Characterization of Coalbed Methane Production, Fruitland Formation, San Juan Basin

W. R. Kaiser, W. B. Ayers, Jr., W. A. Ambrose, S. E. Laubach, A. R. Scott, and C. M. Tremain

Abstract

Production from Fruitland coalbed methane wells in the San Juan Basin ranges from 30 to more than 3,000 Mcf/d. Production varies markedly between wells, even where they are closely spaced; both regional and local controls on coalbed methane occurrence and production are identifiable. To determine geologic and hydrologic controls on occurrence and producibility of coalbed methane, we analyzed production of gas and water from Fruitland coal beds, mapped gas and water production, and compared production maps with geologic and hydrologic maps. Coalbed methane production is greatest where wells are completed in northwest-trending, thick coal deposits in the overpressured, northern part of the basin. Within these northwest-trending belts, highest production occurs in secondary, northeast-trending patterns, consistent with the depositional fabric. Although production is greatest from wells in the overpressured part of the basin, production values from the underpressured, southern part of the basin overlap those of the north. Because wells in the underpressured part of the basin are shallow, produce little or no water and low-carbon dioxide coalbed gas, they are inexpensive to drill and operate. On the basis of geology, hydrology, and production, the San Juan Basin was divided into three areas in which Fruitland coal beds have similar reservoir characteristics.

Introduction

The San Juan Basin is the largest producer of coalbed methane in the United States. Production increased from 3 Bcf in 1985 to 67 Bcf in 1989 and is predicted to exceed 130 Bcf in 1990. The number of completed coalbed methane wells in the Fruitland Formation also increased from fewer than 80 in 1985 to more than 500 in 1989. Production from coalbed methane wells varies locally and regionally. This increasingly large production data base affords an opportunity to compare production trends with geologic and hydrologic settings to determine geologic and hydrologic controls on the occurrence and producibility of coalbed methane.

For coalbed methane exploration to move into frontier areas, an exploration rationale must be developed. The objectives of this chapter are to (1) evaluate the production from Fruitland coalbed methane wells, (2) map gas and water production from coalbed methane wells, (3) clarify geologic and hydrologic controls on occurrence and producibility of coalbed methane by comparing these production maps with geologic and hydrologic maps, and (4) characterize the regional variations in Fruitland coalbed reservoirs.

In Ayers, W. B., Jr., and others, 1991, Geologic and hydrologic controls on the occurrence and producibility of coalbed methane, Fruitland Formation, San Juan Basin: The University of Texas at Austin, Bureau of Economic Geology, topical report prepared for the Gas Research Institute under contract no. 5087-214-1544 (GRI-91/0072), p. 273–301.

Gas and water production data from the Fruitland were plotted, and production statistics were analyzed. On the basis of the production statistics, contour intervals were selected, and gas and water production were mapped. Production maps were then compared with geologic and hydrologic maps to identify factors controlling the producibility of coalbed methane. Finally, potential for future coalbed methane production was evaluated in a basinwide characterization of reservoir parameters of Fruitland coal beds.

Production

Analysis of Fruitland production is based on (1) annual gas and water production data through 1987, collected by the Colorado Geological Survey, and (2) all reported Fruitland completions from Dwight's Oil and Gas Reports (Dwight's 1990a and b). Updated production and new wells through 1989 were obtained from Dwight's. We evaluated each well to confirm Fruitland completions and to determine the lithology of the producing interval. We identified approximately 780 coalbed completions and 225 sandstone completions in the Fruitland Formation as well as more than 100 coal and sandstone and 52 indeterminate (no log or poor log) but probable Fruitland completions through 1989. A review of completions listed as Fruitland/Pictured Cliffs showed that most are Pictured Cliffs completions. A few were completed in Fruitland coal seams and Pictured Cliffs sandstones; none were completed only in coal seams.

Because of recent orders by the New Mexico Oil Conservation Division (orders no. R-8768 and R-8769) designating all Fruitland coalbed methane wells as "Basin–Fruitland Coal Gas Pool," this report refers to productive areas in New Mexico by geographical area or by the name of the operator most active in an area. Order no. R-8768 established the Coal Gas Pool, and order no. R-8769 contracted the vertical limits of 26 existing Fruitland and Fruitland/Pictured Cliffs Gas Pools to include only the sandstone completions. In Colorado, Ignacio Blanco field is the only Fruitland field, and it includes production from both coal beds and sandstones.

Decline Behavior

Decline behavior was evaluated to establish a profile of coalbed methane performance and to compare performance of coalbed methane wells with that of Fruitland sandstone wells. We evaluated decline behavior by comparing production histories of coalbed and sandstone completions, using decline curves and Q plots. In the Q plot (REC, 1989a and b), first-year production (Q_1) divided by cumulative production to date (Q_{total}) is plotted against years of production. This technique can be used to analyze decline behavior of wells individually, by reservoir, and by stratigraphic interval. To facilitate analysis, type decline curves were generated for selected decline-rate factors of 5, 10, 20, 30, 50, and 75 percent per year, assuming exponential decline. With time, the curves asymptotically approach the selected rate factor.

Because long production histories are required to establish decline rates and there are many such sandstone wells, a basinwide plot of Fruitland sandstone production is used to introduce Q plots. Sandstones commonly show steep decline (20 to 50 percent) early in their production and typically less than 20 percent decline later, beyond 15 yr of production (fig. 1). Low decline rates are expected in the oldest wells because they should be little affected by depletion in offset wells. Newer wells (less than 15 yr production) showing steep decline probably are experiencing depletion because of production from older offset wells, whereas those with little decline (less than 10 percent) probably represent completions in new reservoirs. Scatter over the entire range of the Q plot reflects completions in a great number of different reservoirs. Such a plot for a single reservoir would indicate a highly compartmentalized reservoir.

Sandstone wells commonly have decline curves that cross the exponential-decline type curves in the early years (gently curved) and then flatten in the late years to parallel the type curves at decline rates of 10 to 20 percent per year (fig. 2). From the Q plots, we conclude that sandstones exhibit exponential decline late, as reported by operators, and hyperbolic decline early in their production. Sandstone Q plots by pressure regime show that overpressured wells have decline rates greater than 10 percent and little scatter, whereas underpressured wells show great scatter and have lower decline rates (less than 10 percent).

Although the Q plot was designed to evaluate sandstone reservoirs, it can be used to analyze coalbed reservoirs. Because many coalbed reservoirs show negative decline, or increased production with time in the early years, there will be an obvious effect on the Q plot, giving the well a decline rate in its late history much lower than that for sandstone. To compare coal and sandstone decline behavior we made Q plots for 40 selected wells—7 completed in coal beds and 33 in sandstones.

Q plots for coalbed wells show that production from coal beds declines exponentially at rates of less than 5 percent per yr (fig. 3). The San Juan 32-7 unit 6 well (Phillips 6-17) has a decline rate of 2.5 percent over 32 yr. Coal reservoirs in the Black Warrior Basin also display exponential decline (David Bolin, personal communication, 1989). Wells exhibiting classic negative decline (Cahn and Knauff wells) fall well below the exponential curve early (sharply curved), whereas others (Clay and Western Federal wells) exhibit no negative decline and closely follow the type curve. The latter two wells are in the underpressured, west-central part of the basin, and they produce little or no water.

Several wells in the underpressured, west-central part of the basin, carried as sandstone completions, have anomalously low decline rates of less than 10 percent per year (fig. 1). These wells display coal decline behavior (negative decline and very low decline rates) and probably are producing coalbed methane indirectly from adjacent coal seams (fig. 4). The Scott 21 is located in such a setting at Cedar Hill field. Sandstone wells that show greater decline (hyperbolic) early (gently curved Q plot) and exponential decline later (for example, Schultz Com F 11) may reflect initial production directly from a conventional sandstone reservoir and later production indirectly from coal seams (fig. 4). This may be the case for the San Juan 32-7 unit 6 well (fig. 3), which is completed open hole in interbedded sandstones and coal seams. Sandstone wells that show exponential decline throughout their productive histories may have been in early communication with coals.

In summary, three distinct Fruitland production Q plots, exhibiting decline behavior characteristic of production from coal seams, sandstone beds, and sandstone beds in communication with coal seams, are recognized (fig. 5). The representative coalbed Q plot drops quickly (sharply curved early) to exponential decline rates of less than 5 percent per yr, whereas the

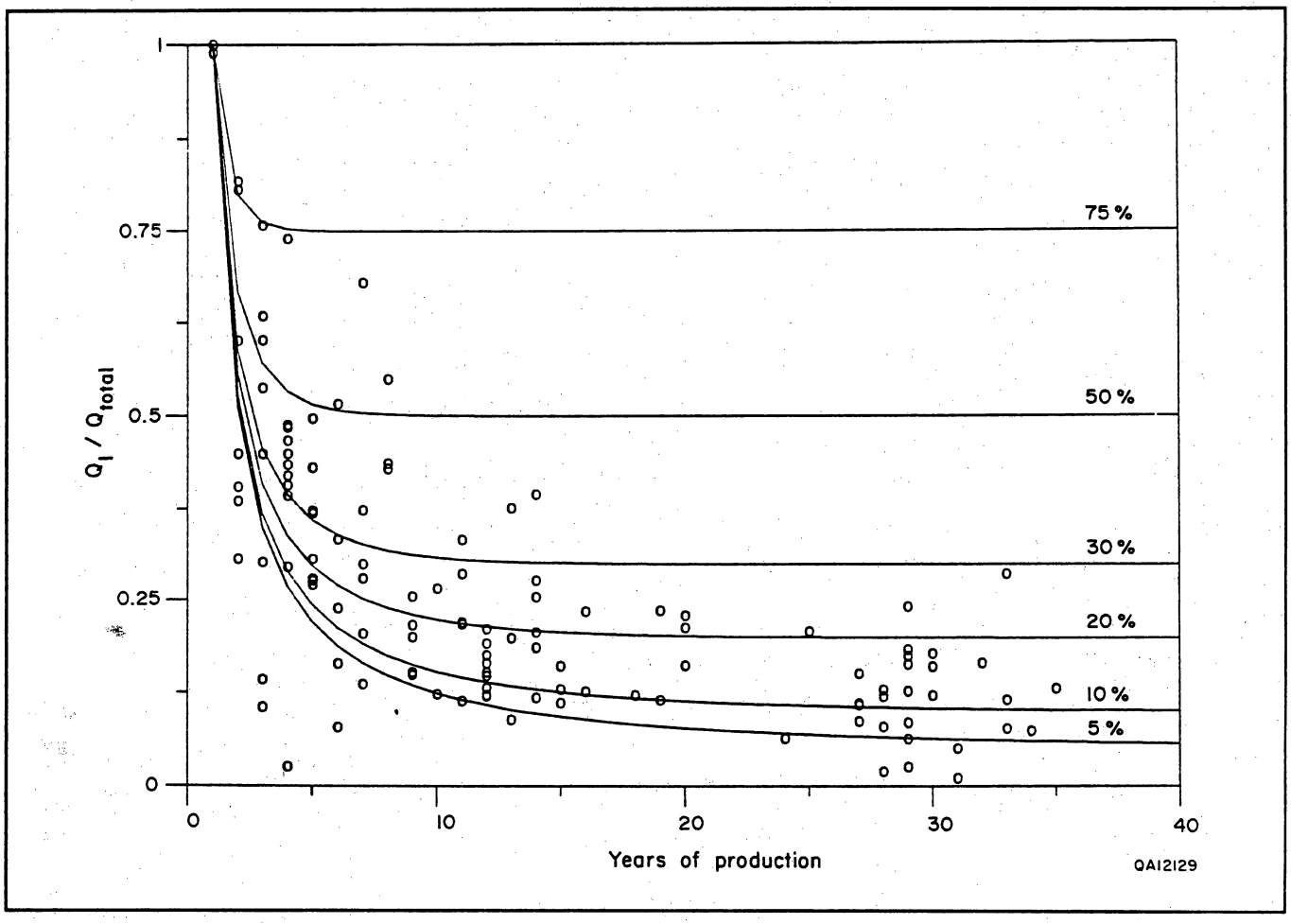

Figure 1. Q plot, Fruitland sandstone wells.

sandstone Q plot is gently curved early and exhibits decline rates of 10 to 20 percent. The Q plot of a sandstone completion inferred to be in contact with a coal bed (coalbed behavior) has features of both curves, gentle curvature early and low exponential decline (less than 5 percent) later in its production history. These decline-curve characteristics may allow Q plots to be used to distinguish wells producing from coal beds, sandstones, or both.

Production Statistics

We analyzed gas and water production from Fruitland coal beds in the overpressured and underpressured areas of the San Juan Basin to provide an overview of production statistics and to determine the contour interval to be used on production maps. Production statistics are subject to several pitfalls or limitations. Among these are (1) variations in completion techniques, (2) complications of negative decline, (3) limited production history, (4) incomplete reporting by operators, and (5) demand-related shut-ins. Despite these limitations, sufficient production of coalbed methane has occurred in the San Juan Basin to give an adequate database to begin developing a picture of geologic and hydrologic controls on coalbed methane.

To compare productivity among wells with long and short productive lives and to minimize the time variable inherent in cumulative production data, we evaluated initial potential (IP) and maximum annual production (MAP), where MAP is the average daily production of a well's most productive year. There was no adjustment to account for negative decline in the early productive years. Commonly, IP's were run for 3 hr on a 3/4-inch choke and were from both stimulated and unstimulated wells. There were more IP's available than MAP's because many completions are recent, and in dually completed wells, IP's usually are conducted separately for each formation, whereas production is commingled so that MAP cannot be evaluated.

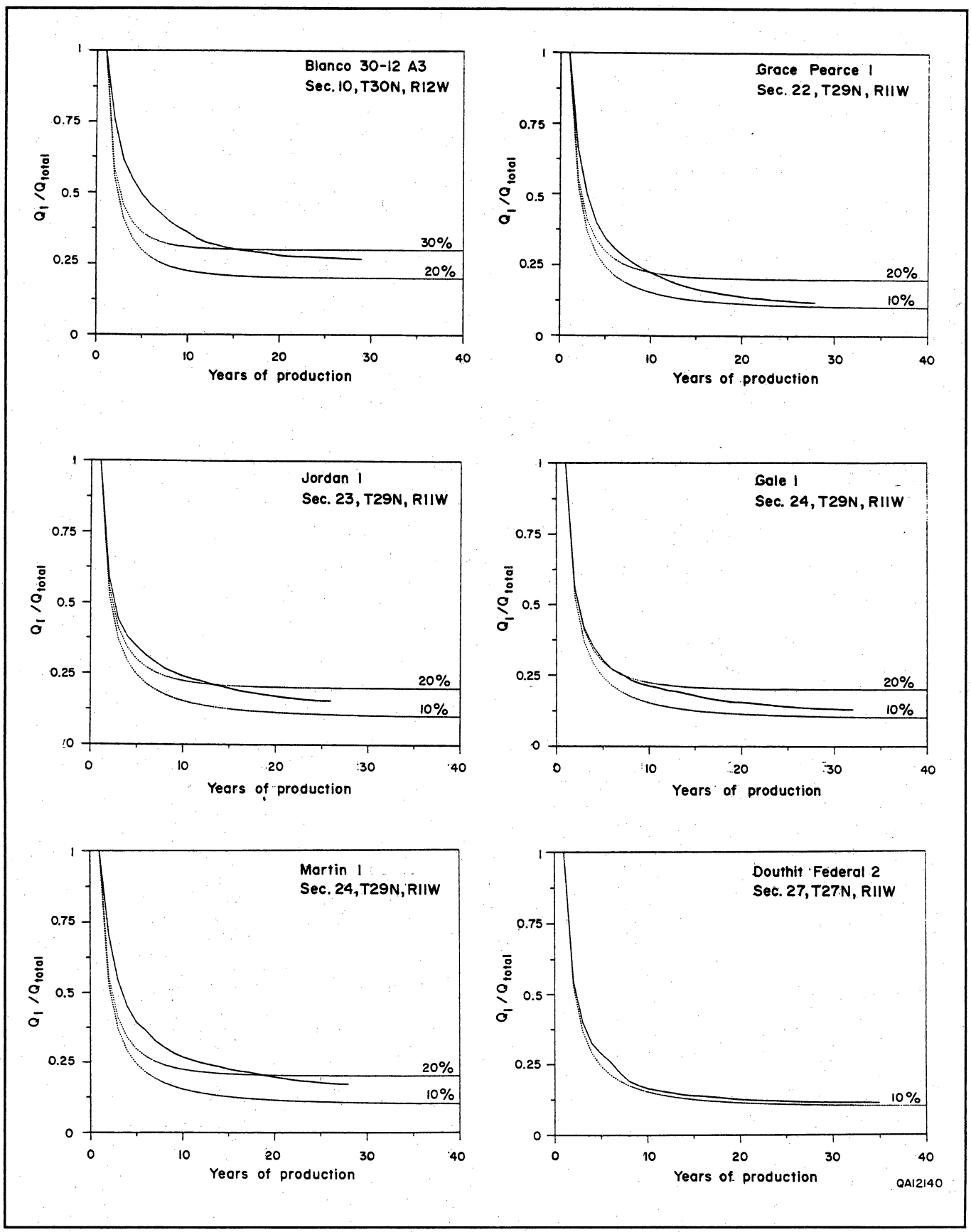

Figure 2. Q plots, individual Fruitland sandstone wells.

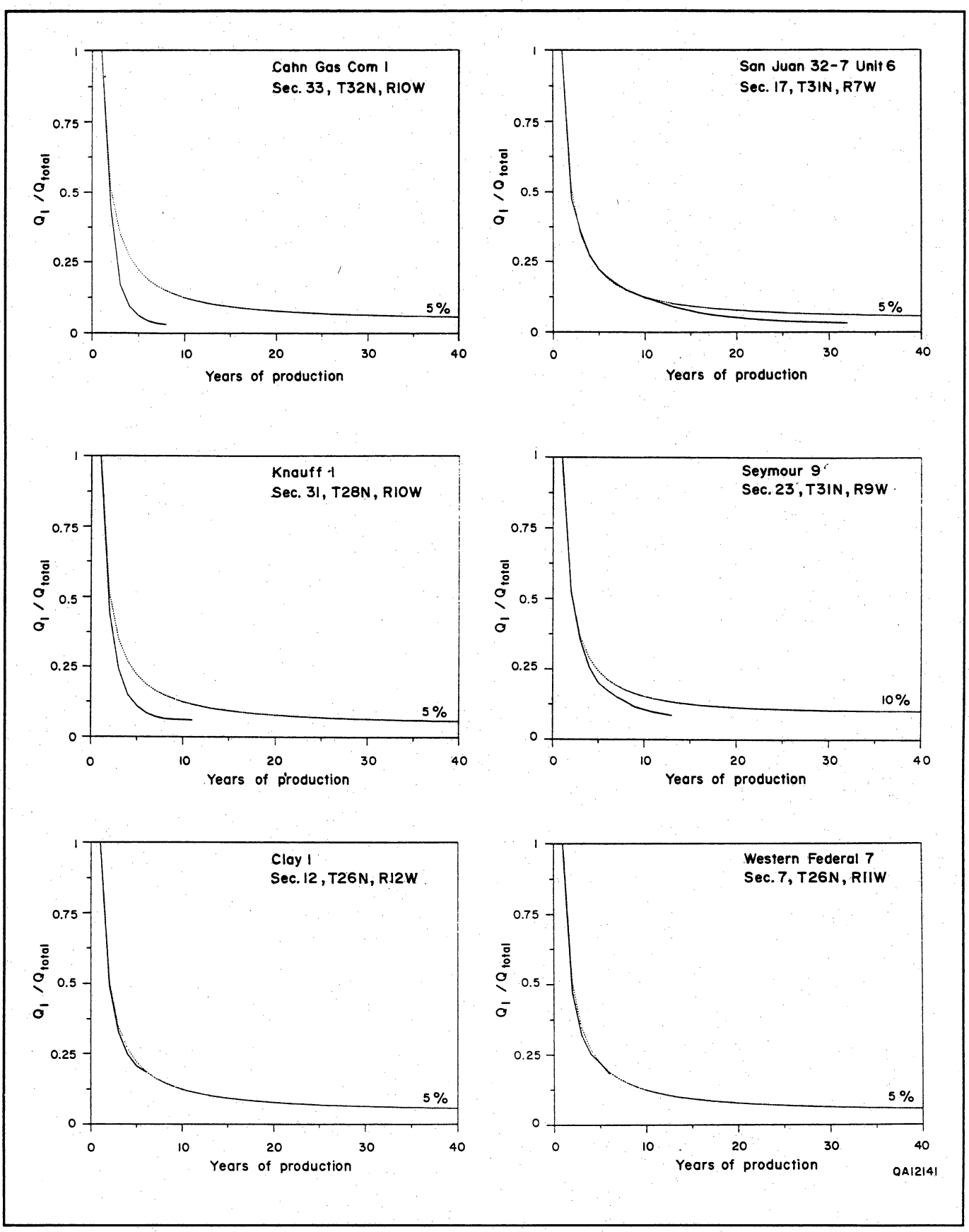

Figure 3. Q plots, individual Fruitland coal wells.

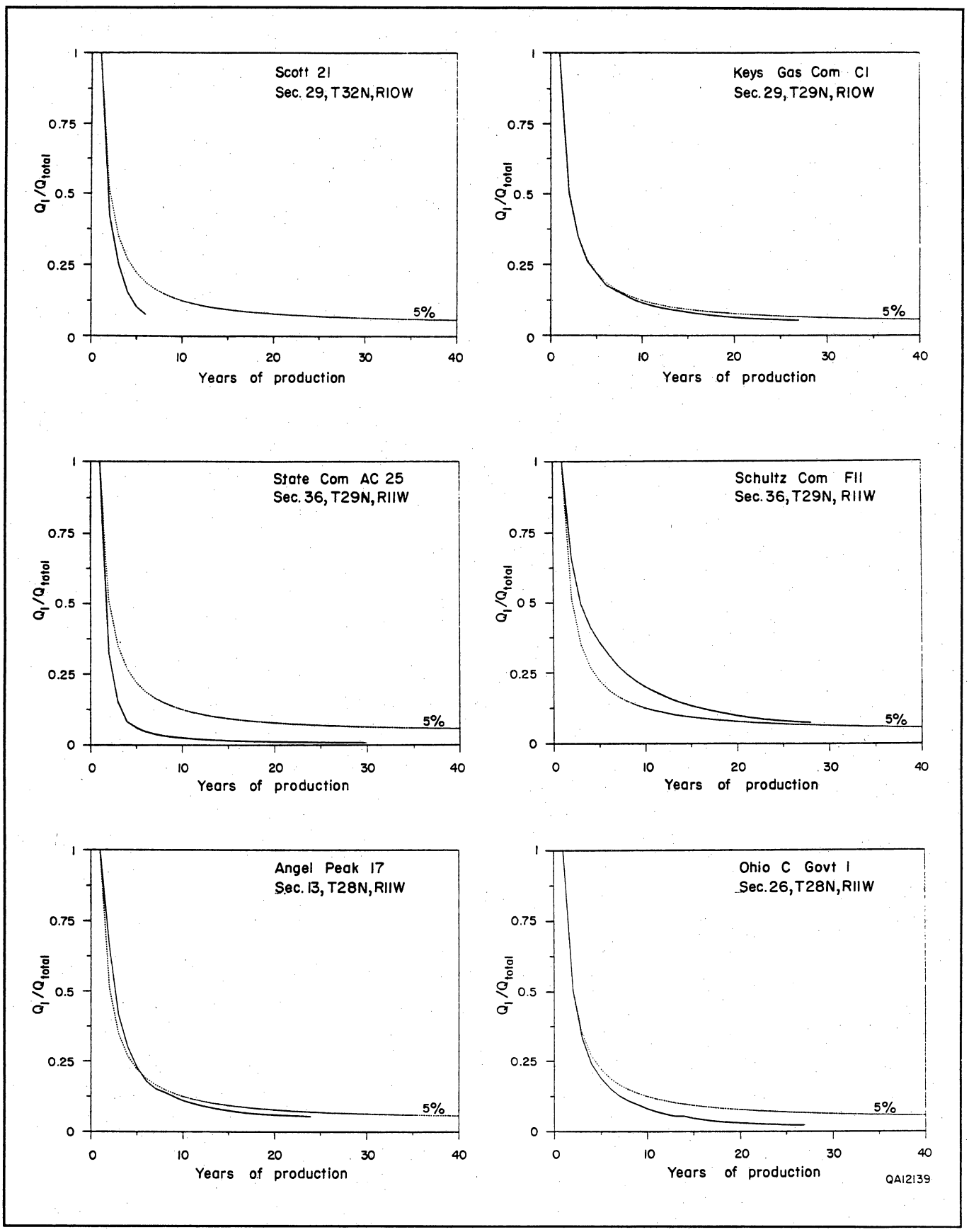

Figure 4. Q plots, individual Fruitland sandstone wells that exhibit coal-decline behavior.

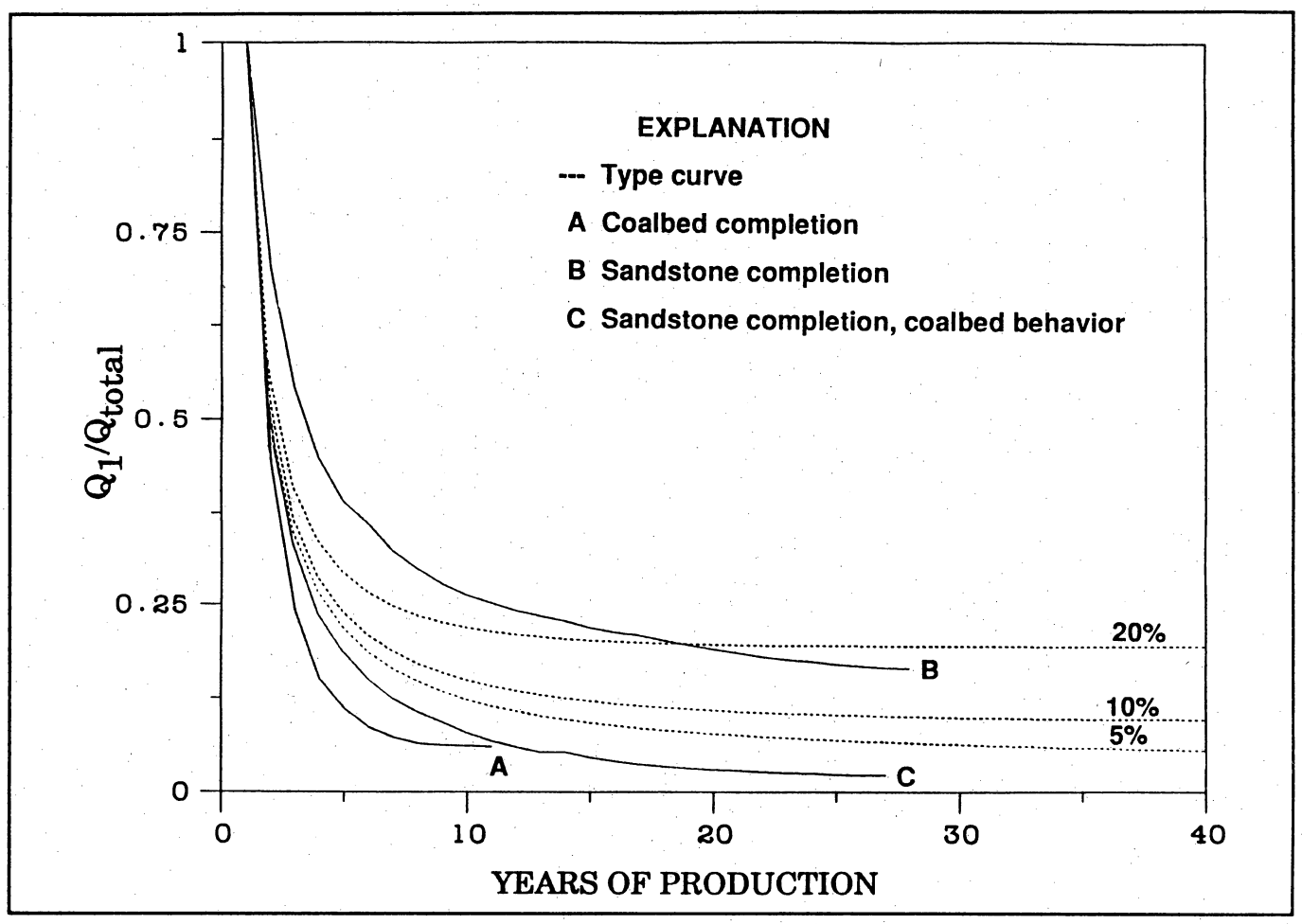

Figure 5. Q plots representative of gas production from coal beds, sandstones, and sandstones in communication with coal beds.

Maximum Annual Gas Production

Histograms of MAP for coalbed and sandstone completions show overlapping log-normal distributions (figs. 6 and 7), suggesting that coalbed reservoirs have production rates similar to sandstone reservoirs, after initial depressurization and the onset of desorption in coal beds. In other words, the two reservoir types have similar production rates at the end of negative decline. Moreover, on the basis of similar production rates, permeability of similar magnitude is inferred for coalbed and sandstone reservoirs. Basinwide, the geometric mean (GM) for MAP from coal beds is slightly larger than that for sandstones, whereas by pressure regime it is less than that for sandstones. In all cases, the mode for coal is less than that for sandstone (figs. 7 and 8). Lower GM's and modes for coal are not readily explained. Negative decline is the likely explanation in that many coalbed wells, because of short production histories, have not yet reached peak production. Few coalbed methane wells have produced for 5 or more years.

Initial Gas Potential

On initial potential (IP), the GM of coalbed wells (195 Mcf/d) is much less than that of sandstones (726 Mcf/d), which undoubtedly reflects the early production behavior of coalbed reservoirs, when fluid pressure and water saturation are high (negative decline characteristics). The central 68 percent of the distribution, or spread between 16 and 84 percent probability, is wider for coalbed than for sandstone completions, reflecting a large number of highly productive, overpressured coal wells. The probability of an overpressured coal well producing more than 1,000 Mcf/d is 10 percent (fig. 8). Overpressured coalbed wells are most productive, but production values from overpressured and underpressured wells overlap.

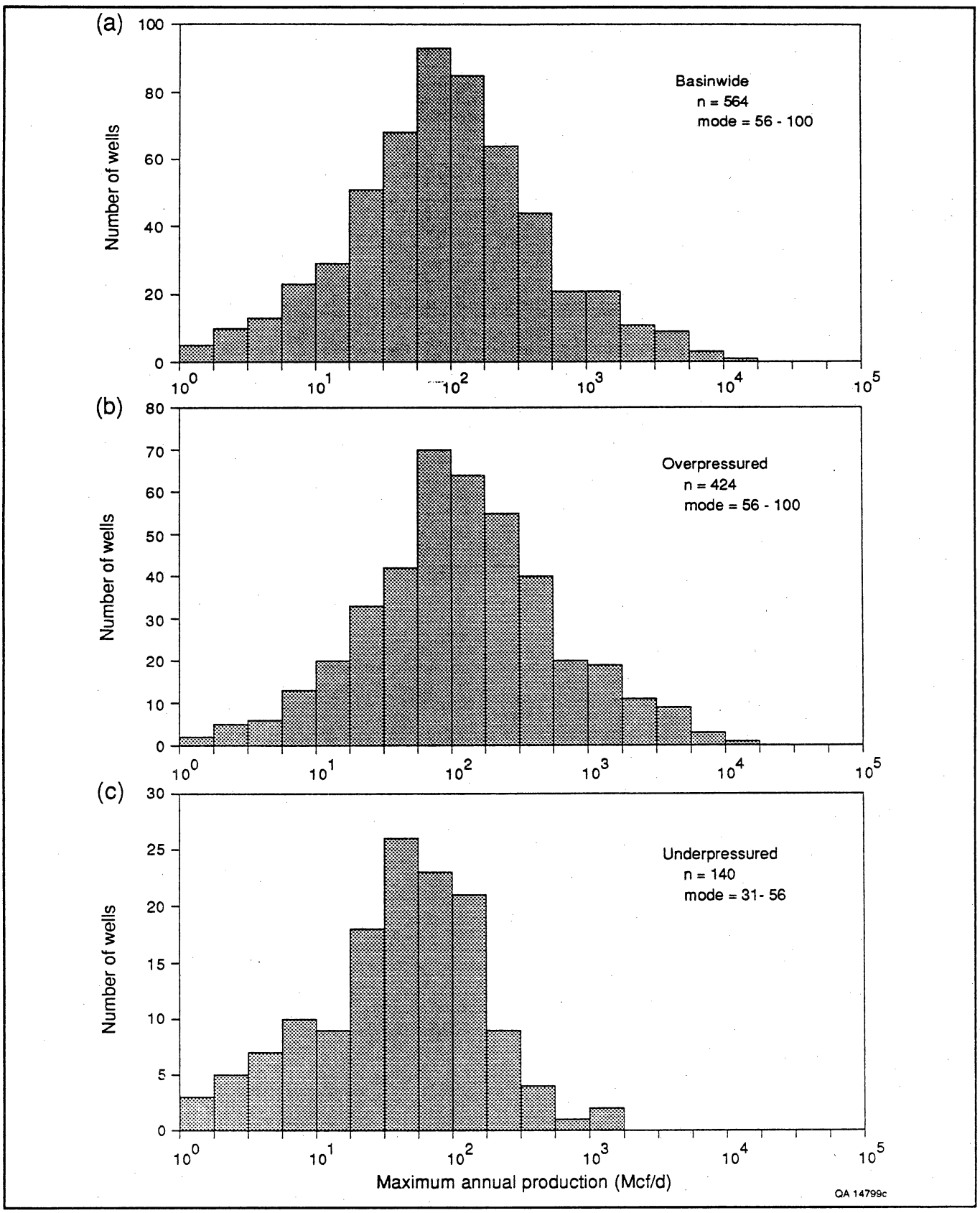

Figure 6. Histograms of maximum annual gas production from Fruitland coalbed wells, San Juan Basin. Maximum annual production is best productive year, normalized to daily production; it is plotted in 0.25-log units. Production is log-normally distributed.

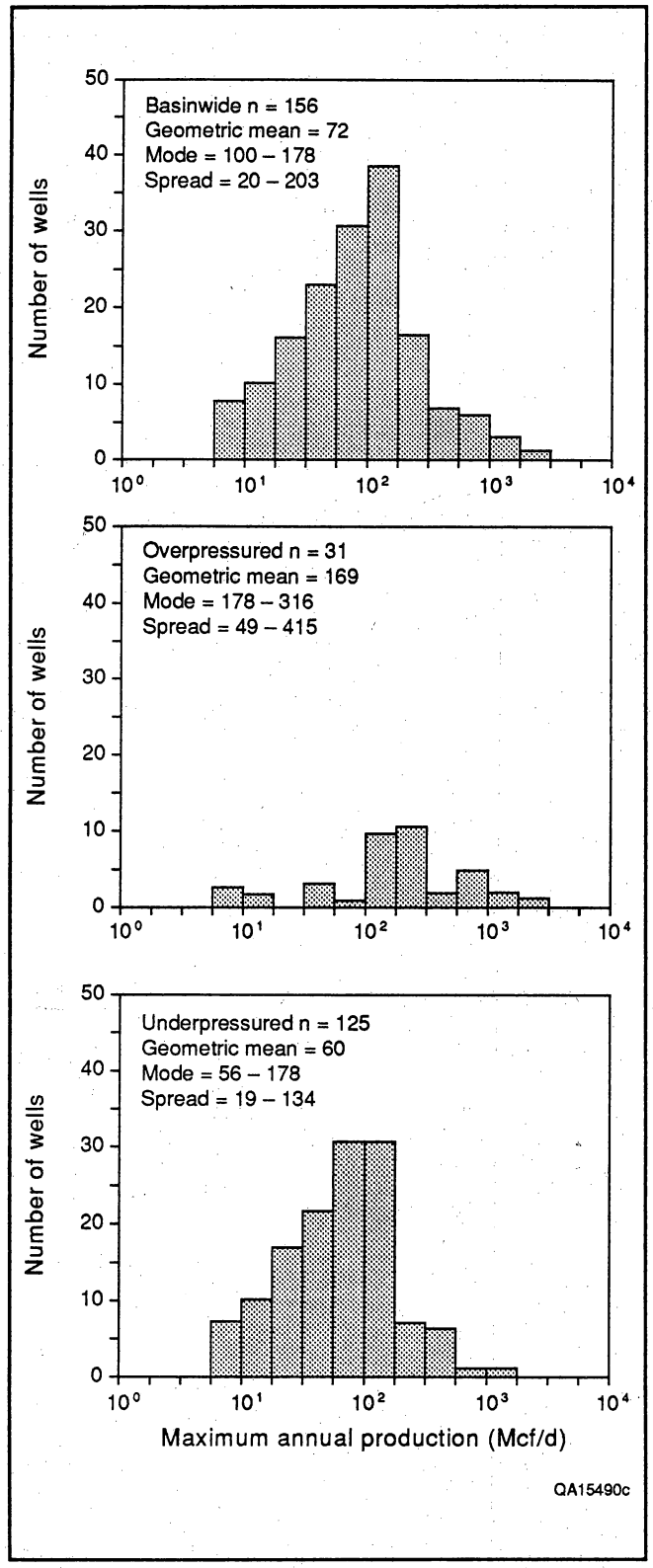

Figure 7. Histograms of maximum annual gas production from Fruitland sandstone wells, San Juan Basin.

High productivities from overpressured sandstones reflect better deliverabilities from high-pressure, conventional reservoirs. Maximum annual production (MAP) from underpressured coal seams and sandstones is skewed to lower values (fig. 6 and 7). Their distributions are similar, suggesting that underpressured coal seams contain free gas and possibly are below desorption pressure. Free gas in coal seams is also indicated by higher productivities upon initial testing than upon sustained production (figs. 8 and 9). Note that the GM's for IP are about twice those for MAP. On initial potential, coalbed production is bimodal (fig. 10). The high second mode (3,162 to 5,623 Mcf/d) reflects high IP's in the Meridian 400 area and is comparable to IP's from Fruitland sandstone reservoirs (562 to 5,623 Mcf/d). Here, the presence of free gas (significant fracture porosity) and/or fluid pressures close to desorption pressure, allowing gas to desorb upon only slight depressurization, are suspected.

Water Production

Initial water potential was also evaluated, because it has been shown to increase with permeability (Oldaker 1990). Water production, like gas production, is log-normal (fig. 11). Production is greatest from overpressured wells; GM of wells completed in overpressured coal beds is 211 barrels of water per day (bwpd). By water-well standards, most coalbed methane wells are low-yield wells (1 to 100 gallons per minute [gpm]). For example, 100 bwpd is equivalent to 3 gpm, which is well below a moderate-yield water well producing hundreds of gallons per minute (100 gpm = 3,420 bwpd). Wells testing water-free are most common in underpressured coal seams. Their anomalous occurrence in the overpressured region reflects low permeability, gas-saturated coals seams, or unreported water production; although operators are required to report water production, they do not always comply.

To identify predictors of productivity, we made scatter plots of IP and MAP. The only correlation seen was between IP and MAP for gas (fig. 12). In overpressured wells with IP's greater than 30 Mcf/d, IP is a predictor of long-term productivity, as indicated by MAP. Lack of correlation below 30 Mcf/d probably reflects high water yield during early production. Underpressured wells show a correlation over the entire range of IP's. A plot of MAP gas versus MAP water (fig. 13) shows a correlation at gas production rates of 10 to 500 Mcf/d and also that highly productive gas wells are not always prolific producers of water, suggesting the presence of free gas. A plot of IP water versus MAP gas showed no correlation (fig. 14), which was unexpected, because high water productivities (several 100 bwpd) are indicative of enhanced permeability.

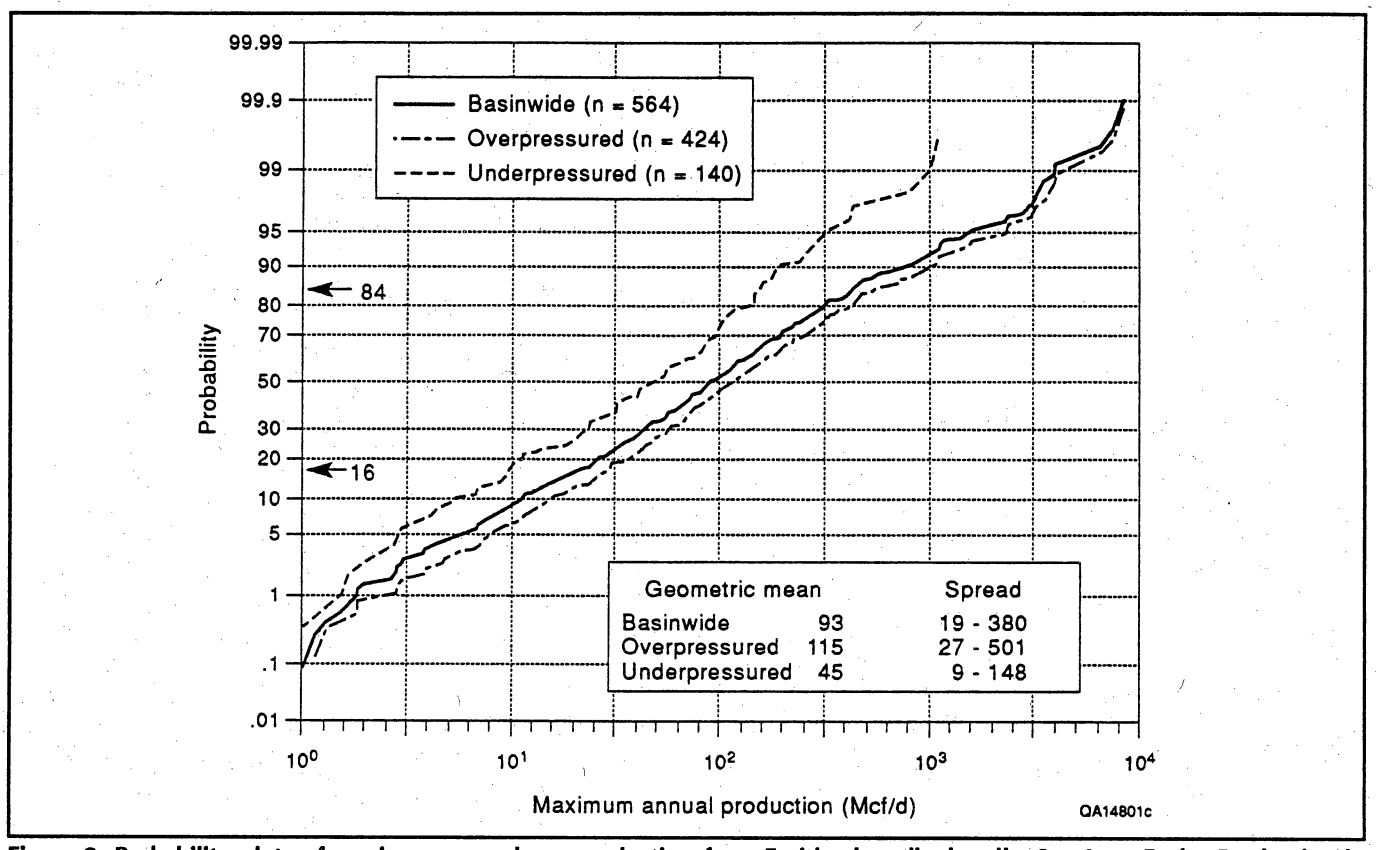

Figure 8. Probability plots of maximum annual gas production from Fruitland coalbed wells, San Juan Basin. Production is plotted in 0.1-log units.

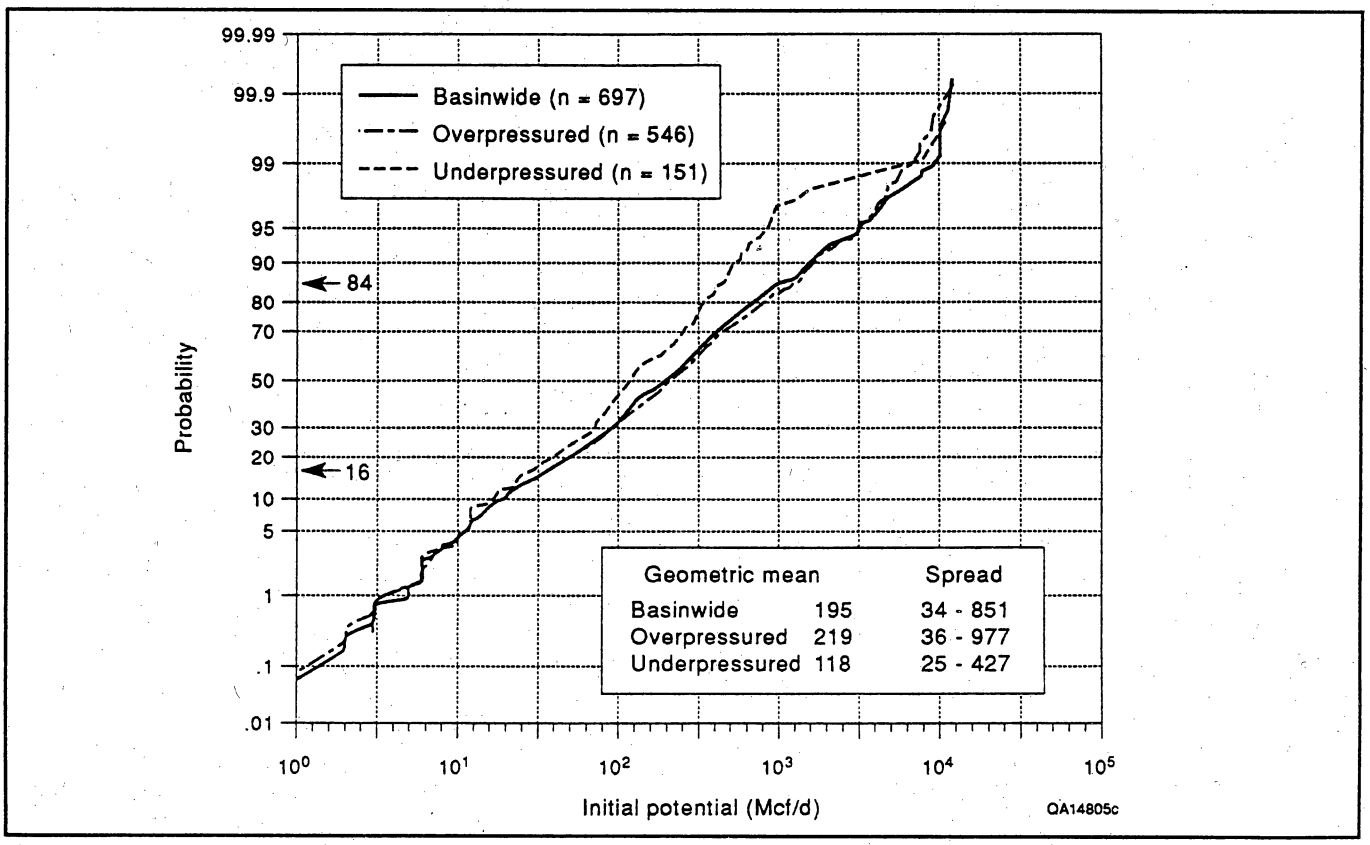

Figure 9. Probability plots of initial gas potential from Fruitland coalbed wells, San Juan Basin. Production is plotted in log units.

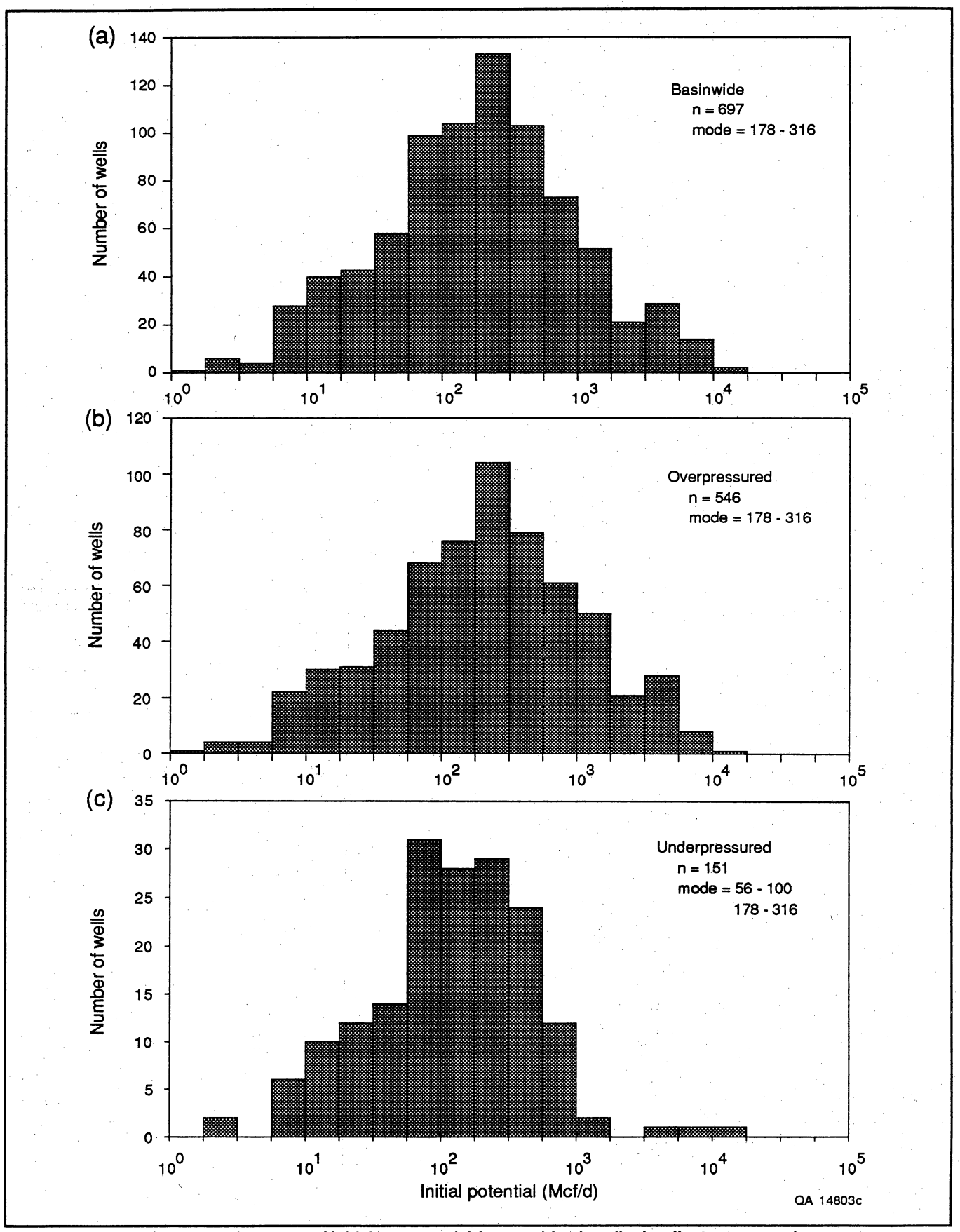

Figure 10. Histograms of initial gas potential from Fruitland coalbed wells, San Juan Basin.

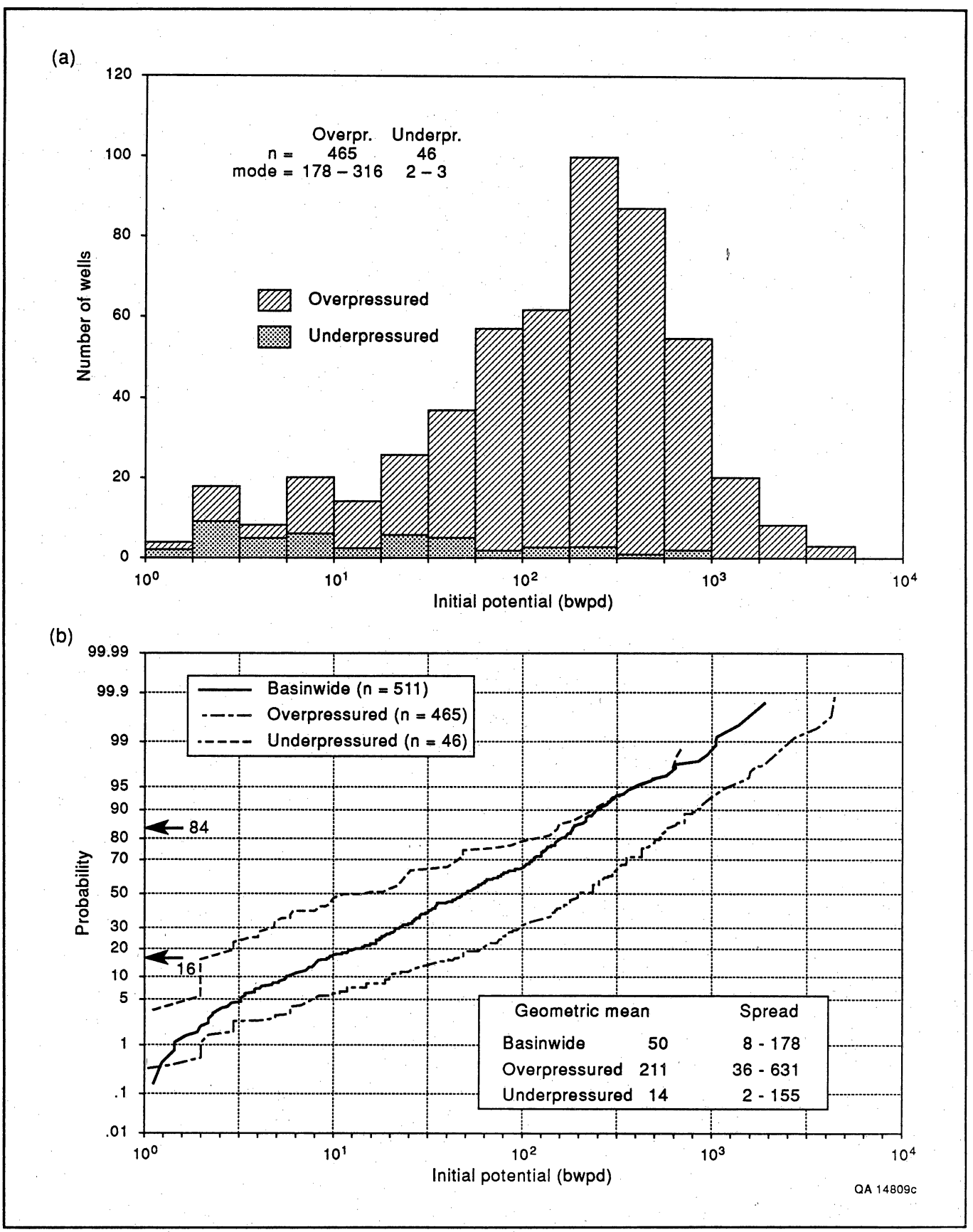

Figure 11. Stacked histograms and probability plots of initial water potential from Fruitland coalbed wells, San Juan Basin. Production, plotted in log units, correlates with pressure regime.

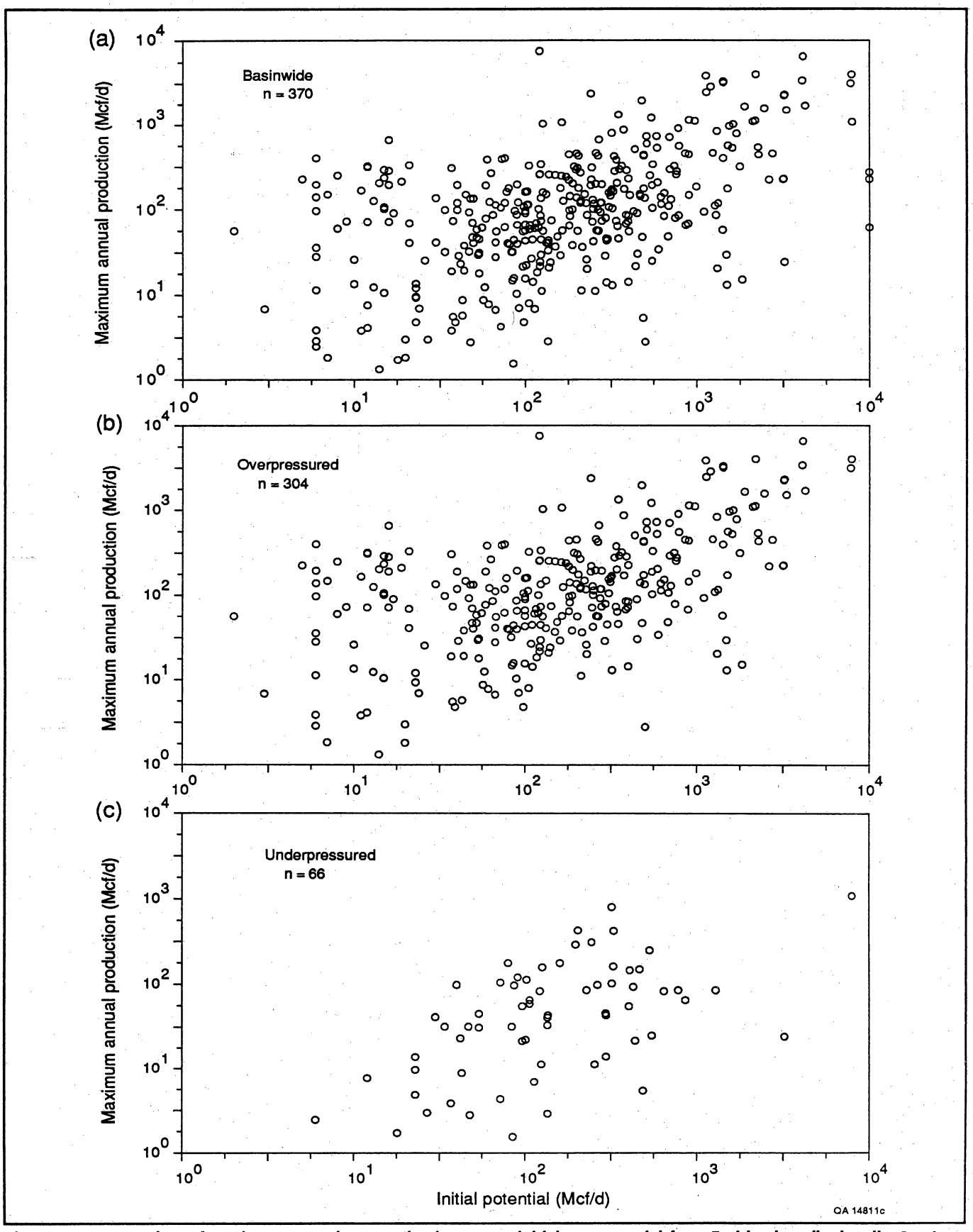

Figure 12. Scatter plots of maximum annual gas production versus initial gas potential from Fruitland coalbed wells, San Juan Basin. Annual and initial production show positive correlation above 30 Mcf/d (~$10^{1.5}$). Production is plotted in log units.

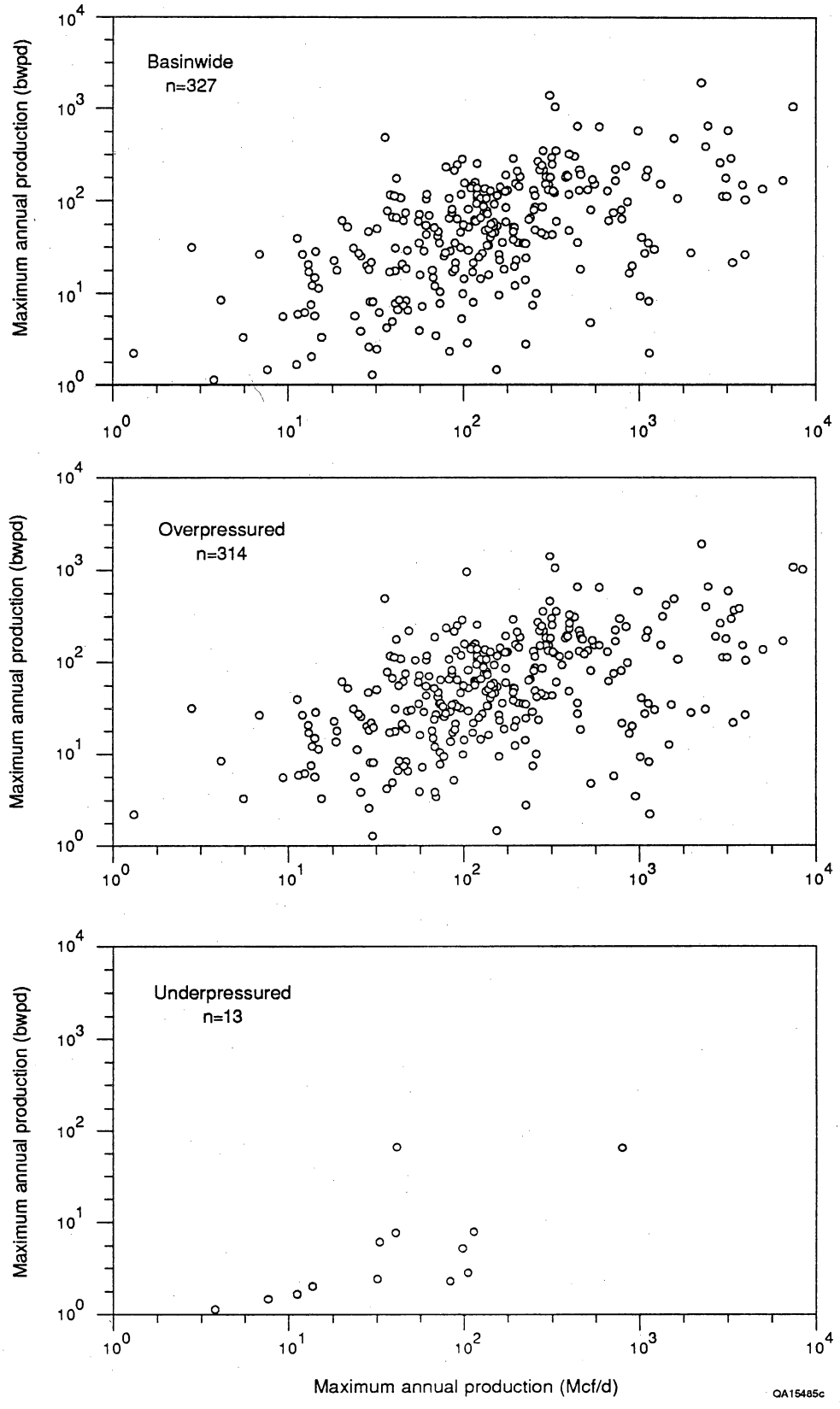

Figure 13. Scatter plots of maximum annual gas production versus maximum annual water production from Fruitland coalbed wells, San Juan Basin. A correlation is present between 10 and 500 Mcf/d (~$10^{2.75}$) but is absent above 500 Mcf/d.

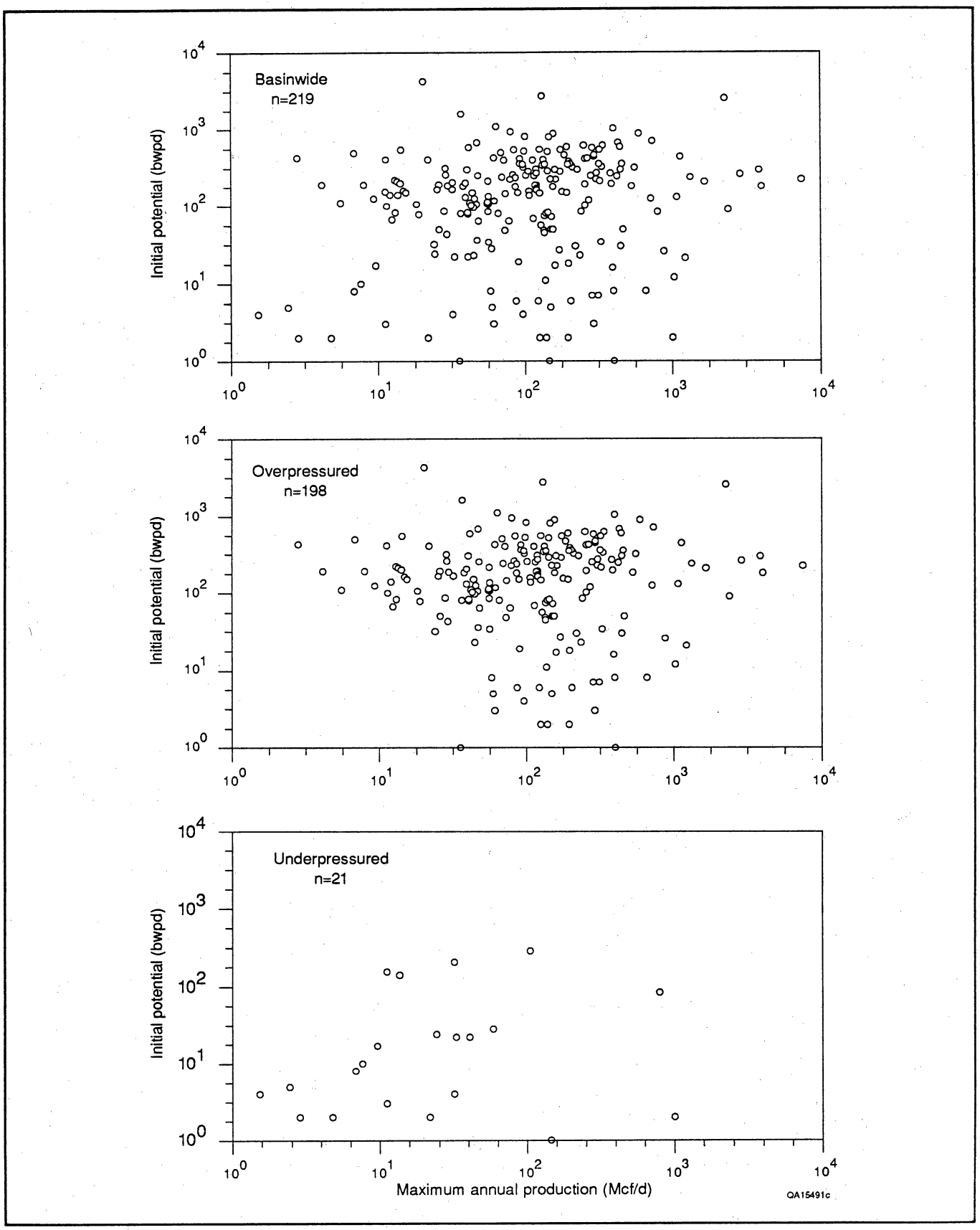

Figure 14. Scatter plots of maximum annual gas production versus initial water potential from Fruitland coalbed wells, San Juan Basin, showing no correlation.

Coalbed Methane Production History and Trends

In 1989, coalbed methane production from the Fruitland Formation in the San Juan Basin was 67 Bcf from more than 500 wells, a dramatic increase from the 20 Bcf produced from fewer than 250 wells in 1988. Most production is from the north-central part of the basin. The Meridian 400 area and Cedar Hill and Ignacio Blanco fields accounted for approximately 90 percent of the basinwide production in 1989. Prior to 1987, most coalbed methane activity was in the north-central part of the basin. However, in 1988 and 1989, there was considerable coalbed methane activity in the southern part, including new wells and old Pictured Cliffs wells recompleted in Fruitland coal seams. These new wells and recompletions are primarily in eastern San Juan County and secondarily in western Rio Arriba County, New Mexico, but they occur as far south as T24N and as far east as R2W. From maps of maximum annual gas production (MAP) and of initial gas and initial water production (figs. 15, 16, and 17), productivity trends were delineated. On all production maps, the boundary of regionally overpressured Fruitland strata, defined by the 0.44 psi/ft pressure-gradient contour (Kaiser, Swartz, and Hawkins, this vol., their fig. 6), is included for reference.

Two major trends—northwest and northeast—are evident on gas-production maps. The most productive coalbed methane wells occur in the overpressured, northern part of the basin (figs. 15 and 16), as was shown in production histograms (figs. 6 and 10). On the basis of the production histogram (fig. 6), highly productive wells were defined as those with MAP greater than the modal class of 100 Mcf/d. These highly productive wells occur in a northwest-trending belt (primary trend) in New Mexico, where MAP and IP for gas generally exceed 100 Mcf/d and locally are greater than 316 Mcf/d (figs. 15 and 16). This primary belt includes the Meridian 400 wells and Cedar Hill field. Two other less continuous, northwest-trending belts of highly productive wells occur in Colorado northeast of the primary belt. The first is defined on the map of maximum annual production, where it occurs southeast of Durango (fig. 15), and the second is apparent on the IP map, near the northern margin of the basin (fig. 16).

A secondary northeast trend is present on both gas-production maps (figs. 15 and 16) but is particularly evident on the map of maximum annual production (fig. 15). In New Mexico, in the northwest-trending primary belt of production greater than 100 Mcf/d (Meridian 400 to Cedar Hill areas), the most productive wells (300 to 3,000 Mcf/d) occur in secondary northeast-trending pods. Small northeast-trending pods of highly productive wells are present throughout the overpressured part of the basin. However, in the underpressured, southwestern part of the basin, highly productive wells occur in broad northeast-trending belts (figs. 15 and 16).

Most water-productive coalbed methane wells are in the overpressured, northern part of the basin (fig. 17), where initial water production from coalbed wells is greatest. Generally, areas of high water production coincide with this area of high gas production (compare figs. 15, 16, and 17). The dominant trend of high water production (defined as greater than 316 bbl/d, or $10^{2.5}$ [fig. 11]) is northeast, with secondary northwest and north trends present (fig. 17). Because of incomplete data, these trends may be as much an artifact of the reporting process as a reflection of the physical system. Note that the dominant water-production trend is a secondary trend for gas production. Water production in the underpressured, southwestern part of the basin is minimal.

Controls on Coalbed Methane Production

The reservoir, and hence production, characteristics of Fruitland coal beds vary across the San Juan Basin, reflecting their geologic and hydrologic settings, which were described in the preceding papers of this volume. These variable factors include coal and coal-gas resources, pressure regime, permeability, gas composition, and water production. By comparing geologic and hydrologic maps with production trends, controls on coalbed methane occurrence and producibility were identified. In this section, we first discuss physical controls on Fruitland coalbed methane occurrence and production, or reservoir characteristics: coalbed occurrence, thickness, and rank; formation pressure; and fracturing. We then describe two economic controls on coalbed methane production: gas composition and produced water.

Coal Occurrence, Trends, and Thickness

Coalbed thickness determines gas resources and affects production by influencing the size of the dewatered area, or cone of depression. Assuming equal permeability and overpressure, gas productivity will be greater in a thicker seam because a larger cone of depression is induced upon dewatering, freeing a larger volume of gas. Coal occurrence and thickness are controlled by depositional systems. The thickest coal seams occur in three northwest-trending belts landward (southwest) of the pinch-outs of upper Pictured Cliffs tongues and northeast of the southern hingeline of the basin floor (Ayers and others, this vol., their

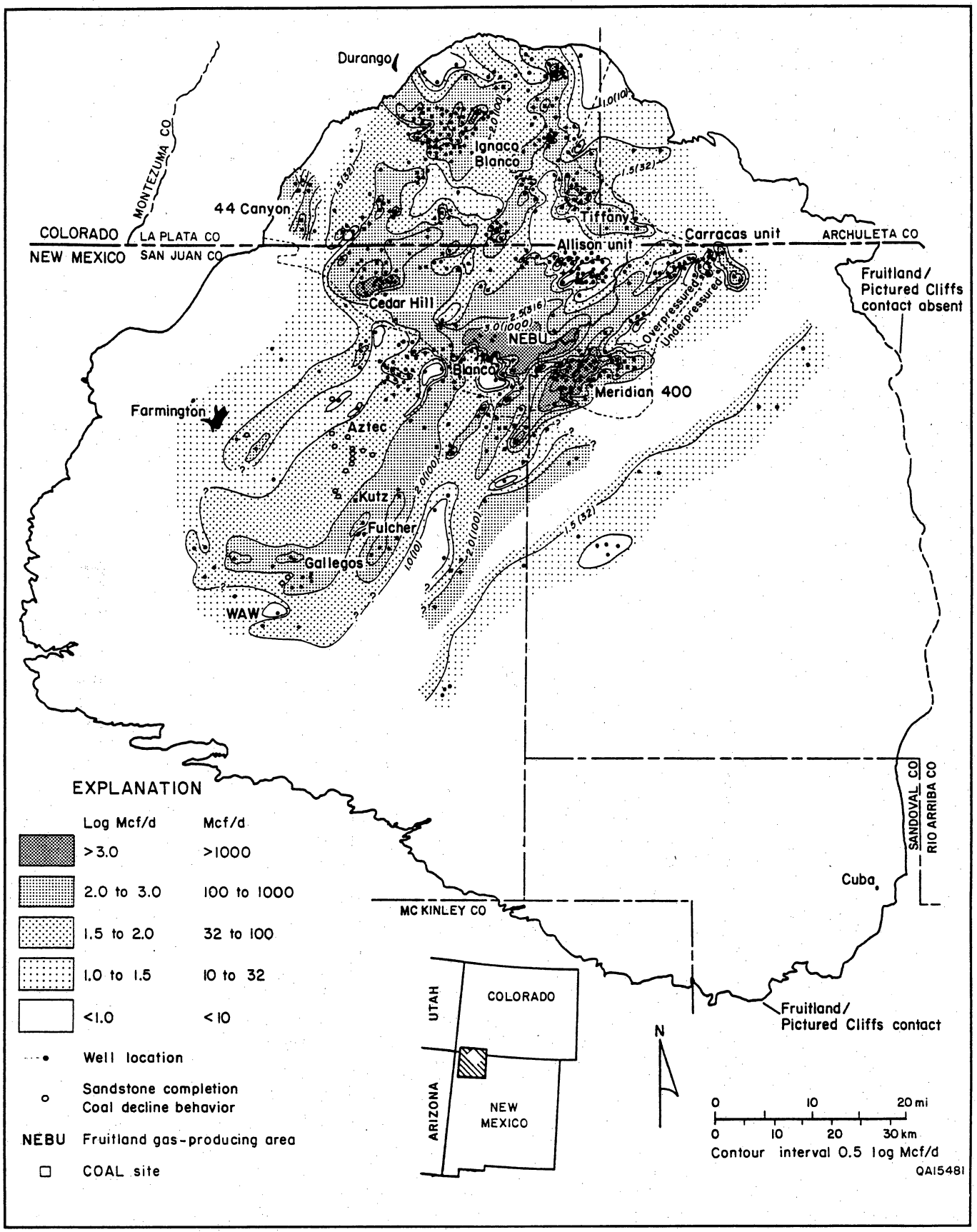

Figure 15. Map of maximum annual gas production from Fruitland coalbed wells, San Juan Basin. The dominant productivity trends are oriented northwest and northeast. Production is log-normally distributed; therefore, log of production was mapped.

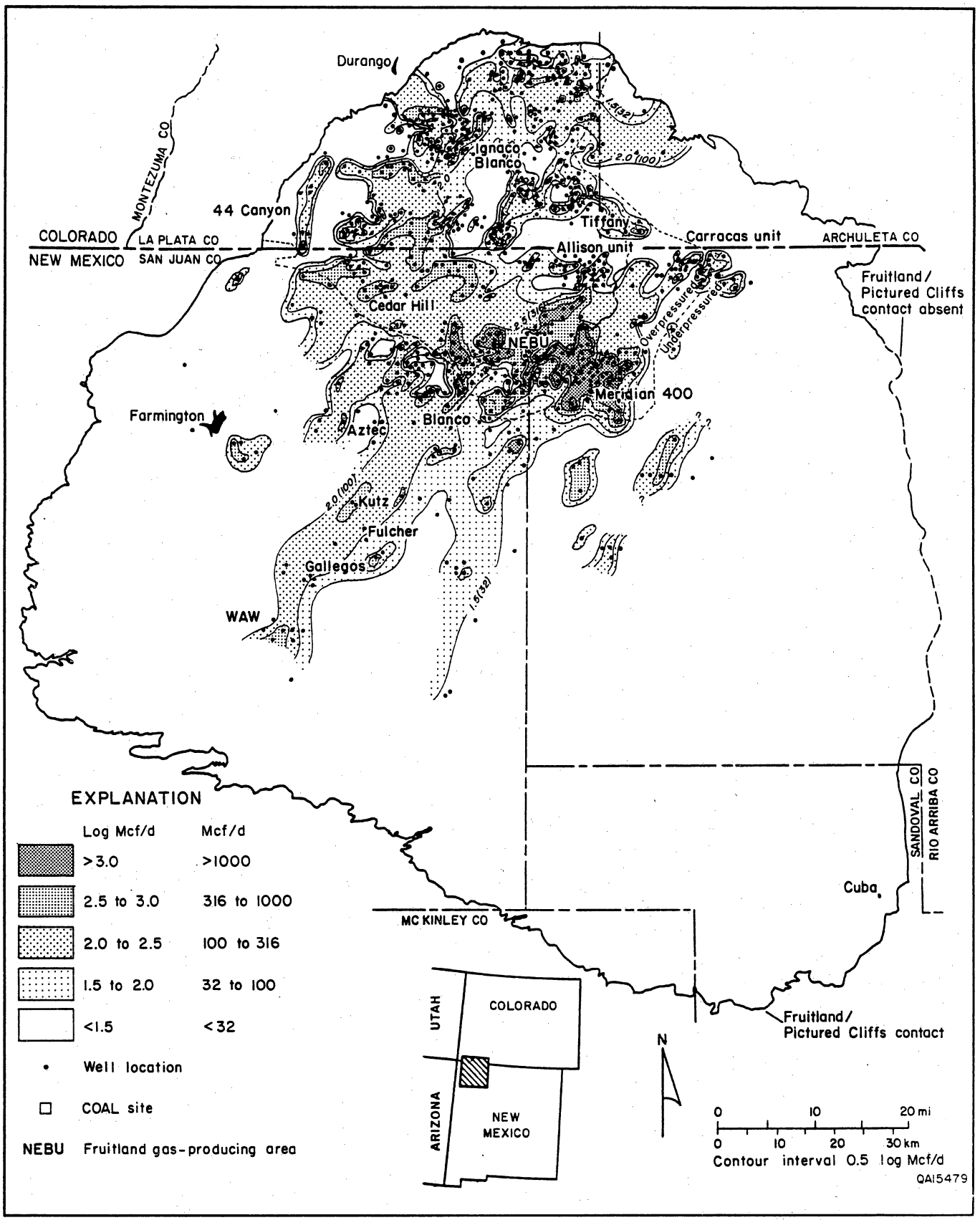

Figure 16. Map of initial gas potential from Fruitland coalbed wells, San Juan Basin. In northern New Mexico, areas of highest production trend east and north.

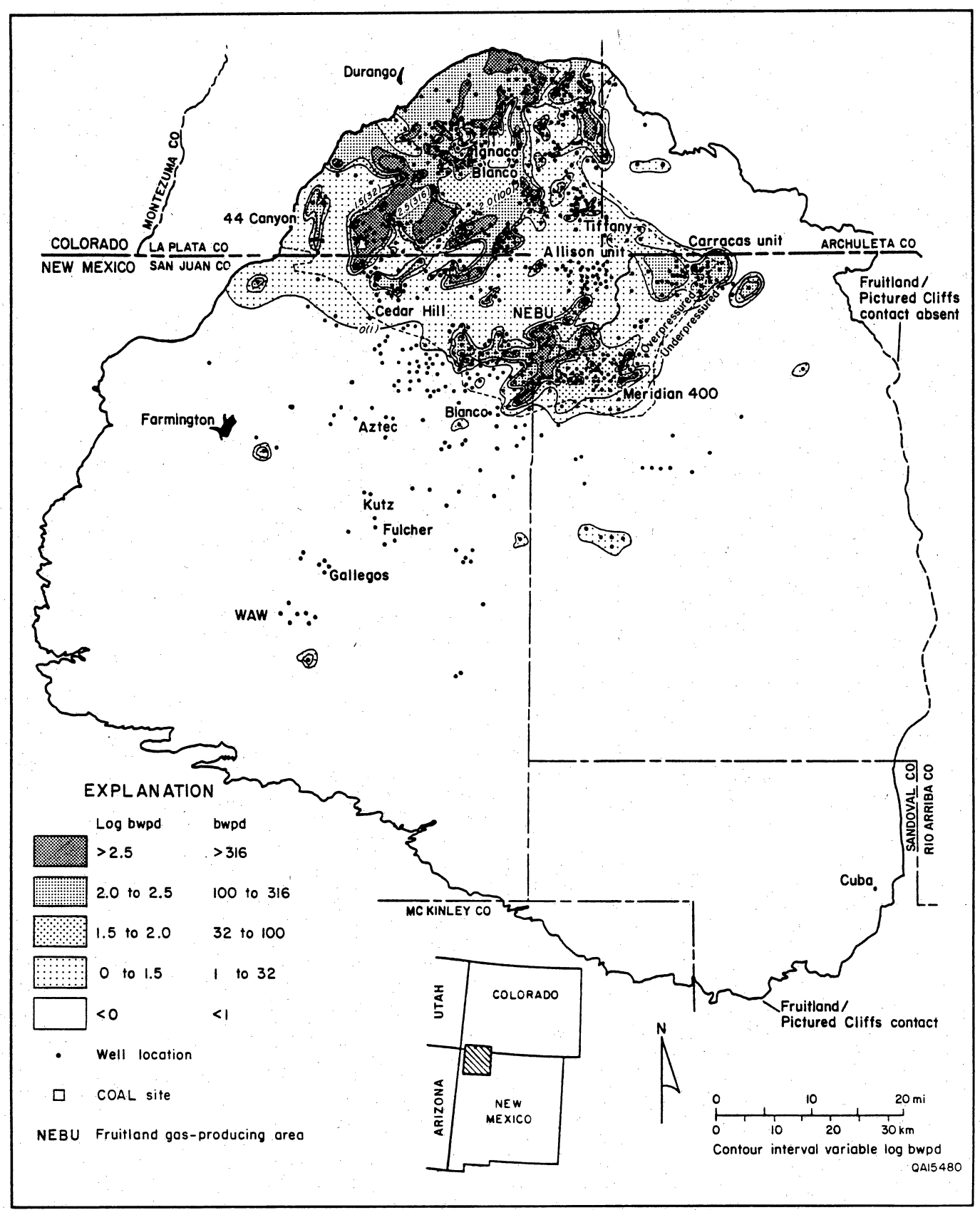

Figure 17. Map of initial water potential from Fruitland coalbed wells, San Juan Basin. Water-productive wells occur mainly in the overpressured area in the northwestern part of the basin (enclosed by the 0.44-psi/ft contour). Areas of low-water production shown within the overpressured area may reflect unreported water production.

fig. 21, belts E, F, and G; and their figs. 2 and 5). Southwest of the hingeline, coal deposits are thinner and are northeast-trending, lying between Fruitland channel-sandstone belts.

Depositional trends are reflected in the production maps. Production trends (figs. 15 and 16) parallel coal-thickness trends (Ayers and others, this vol., their figs. 22 and 25). Production is greatest from the northwest-trending coal deposits in the northern part of the basin; within these northwest-trending belts, secondary northeast production patterns are present. In this area, coalbed gas in place generally exceeds 15 Bcf/mi² and locally exceeds 35 Bcf/mi² (Ayers and others, this vol., their fig. 27). In the southwestern part of the basin, production patterns trend predominantly northeast and gas in place is commonly 5 to 15 Bcf/mi².

Coal Rank

The volume of gas generated in a coal bed and the coal's gas-storage capacity vary with coal rank. Fruitland coal rank is greatest in the northern San Juan Basin, where it is medium- to low-volatile bituminous. Coincidence of coal of high rank with the occurrence of thick coal beds and high reservoir pressure results in large coalbed methane resources in this part of the basin. The area encompassed by high-volatile A bituminous or higher rank coal (Scott and others, this vol., their fig. 3) makes up one-fourth of the basin, yet it contains more than one-half of the Fruitland coalbed methane resources. However, coal of lower rank does not preclude presence of economic coalbed methane resources; coalbed methane production is well-established in the southern San Juan Basin, where coal (subbituminous and high-volatile C bituminous rank) has not entered the thermogenic gas-generation window. Methane in the southern part of the basin may be biogenic methane or thermogenic methane that migrated either (1) upward along faults connected to older source rocks or (2) laterally (up the basin flank) from deeper, high-rank Fruitland coal beds.

Formation Pressure

The volume of gas stored in coal varies with formation pressure. In the Fruitland Formation, pressure is greatest in the overpressured, northern part of the basin, where it exceeds 1,600 psi (Kaiser, Swartz, and Hawkins, this vol., their figs. 6 and 7). The southwest boundary of overpressure is caused by pinch-out of aquifer coal seams (Kaiser, Swartz, and Hawkins, this vol.) and possibly by offset of seams by faults that occur along the basin's structural hingeline (Ayers and others, this vol.). The southeast boundary is thought to reflect (1) a major Fruitland channel sandstone belt that interrupts coal seam (aquifer) continuity and (2) minor normal faults that offset coal beds (Ayers and others, Bureau of Economic Geology, unpublished maps and cross sections).

Because more methane is adsorbed on coal at higher pressure, overpressure enhances gas content in coal beds. Moreover, because permeability in coal seams is stress dependent, it may be enhanced in the overpressured part of the basin (McKee and others, 1987). Wells in the overpressured area are the basin's most productive (figs. 6 and 8); highest MAP's correlate with high BHP's (fig. 18). In figure 18, two distinct populations are evident, reflecting the overpressured, north-central part of the basin and underpressured, west-central part of the basin. BHP's of coal wells in the west-central part of the basin are as low as 300 psi; yet some of these wells have MAP's comparable to coalbed wells in the north-central part of the basin that have BHP's of approximately 1,400 psi. Clearly, overpressuring is not a requirement for production of coalbed methane, because sustained production is evident from underpressured coal beds (figs. 6 and 18).

Because the desorption curve for many Fruitland coals flattens above 900 to 1,300 psi, pressure must be lowered considerably to release a small amount of gas; at reservoir pressures greater than 1,000 psi significant dewatering may be needed (Koenig and others, 1989). However, if reservoir pressure is too low, adsorbed gas volume may be small. Therefore, reservoir pressure that is either too high or too low is probably detrimental to the producibility of coalbed methane. Production of coalbed methane at low pressures requires subsequent compression, adding to the operating costs. The optimum reservoir pressure range is unknown but is thought to be large. Commercial production in the San Juan Basin has been established in coal seams having reservoir pressures as high as 1,900 psi and as low as 120 psi.

Tectonic Fractures and Cleats

Fractures are the primary control on coalbed permeability and include the regional cleat systems, formed during coalification, and local fractures of tectonic origin. Coalbed methane is produced from a variety of structural settings, including the flat central-basin floor, northern hogbacks and flexures, flanks of the structural axes, and southern monocline. Production from these varied settings suggests mainly unconventional trapping of methane and little direct control on methane occurrence by major structural elements. For example, few coalbed wells are completed on either the Ignacio or Bondad Anticlines, whereas some of the basin's most productive wells are located in a syncline at Cedar Hill field. The role of structural features is mainly generation of fracture-enhanced permeability.

For example, wells at the Carracas unit are associated with the plunging Ignacio Anticline, where permeability may be fracture enhanced in the anticlinal nose. Minor folds and faults not recognized on regional-scale maps may be more important to the production of coalbed methane than major structural elements, because these small structures may be sites of fracture-enhanced permeability and conventional traps. Small, northwest- and northeast-trending normal faults have been identified in the transition zone from overpressured to underpressured Fruitland strata and may account for abrupt pressure boundaries and offsets in productivity trends (fig. 15). A northwest-trending boundary, separating high and low production, extends from the Cedar Hill field southeastward to the Blanco area, parallel to the pressure transition, and may reflect faulting along the transition zone associated with the basin's structural hingeline (Ayers and others, this vol.). In the Blanco area, this boundary is offset to the northeast, coinciding with the northwestward projection of a prominent northwest-trending segment (lineament) of the San Juan River.

Regional studies have shown two principal face-cleat domains in Fruitland coal beds in the basin; a north-to-northeast domain is present in the southern part of the basin, whereas a northwest face cleat is prominent in the northern part (Tremain and others, this vol., their fig. 12). Primary cleat directions parallel the coalbed methane productivity trends (fig. 15). Coalbed permeability may be higher and success of the open-hole cavity method may be favored where the two fracture domains overlap; this concept can be investigated by describing cleats in cores from this area. Faults also trend northwest and may favor flow in that direction because present maximum horizontal stress direction is northwest (Tremain and others, this vol.). Southeast of Durango, productivity trends are orthogonally oriented (fig. 15), consistent with northwest-trending faults and the regional cleat system.

Gas Composition

The composition of coalbed gas is important because it affects production costs. The composition of Fruitland coalbed gases varies across the basin. Chemically dry to very dry gases occur in the overpressured, northern and underpressured, southern parts of the basin and are separated by a northwest-trending band of relatively wet gases (Scott and others, this vol., their fig. 9). Significantly, carbon dioxide content is highest (greater than 6 percent) in coalbed gases from the overpressured, north-central part of the basin. In the underpressured, southern part of the basin, coalbed gases commonly contain less than 1 percent carbon dioxide. Carbon dioxide is noncombustible and lowers the heating value of coalbed gas. Also, it is corrosive and must be stripped from the produced gas at a cost of $0.14/Mcf (Lon Mayhan, personal communication, 1990). Because pipeline companies prefer gas with a carbon dioxide content of 3 percent or less, coalbed methane produced from the overpressured part of the basin (high carbon dioxide) has a cost penalty relative to coalbed methane from the underpressured part of the basin (low carbon dioxide).

Produced Water

Water content of coal beds also significantly impacts operational costs. Both gas- and water-saturated coal beds occur in the San Juan Basin. Fruitland coal beds in the underpressured part of the basin produce little or no water. However, wells in the overpressured part of the basin, where coalbed methane production is highest, commonly are water productive in response to artesian overpressuring. Wells in the overpressured area that produce little or no water probably are located on structural highs or have been dewatered by nearby production.

The San Juan 32-7 unit 6 well (Phillips 6-17) has produced essentially water free since 1955 and is in pressure communication and is structurally high to a well 1/4 mi away (NEBU 218) that produces water at the rate of 50 bbl/d. A gas-saturated seam and structural trapping are implied for the San Juan 32-7 well. The Seymour 9 well has produced water free since 1978 and is located at Sedro Canyon; this well was drilled on an anticline mapped on the top of the Pictured Cliffs Sandstone. Likewise, the Ross 1 well (sec. 18, T32N, R5W), structurally high to the Glover 1 well, blew out and flowed gas during completion, whereas the Glover was water productive. Depletion by earlier production on the Ignacio Anticline is suspected as the cause of low water production in the Tiffany area and at Cedar Hill field, where 10 yr of production has reduced cumulative water production from Amoco's wells to less than 200 bbl/d.

Cost for disposal of Fruitland-produced waters ranges from $0.20 to $2.00/bbl, depending on disposal method. Water is disposed of in evaporation ponds or, more commonly, by injection into the Entrada, Morrison, and Mesaverde Formations. Water analyses (Kaiser, Swartz, and Hawkins, this vol., their table 3) and reports from operators suggest that scaling is a concern in parts of the San Juan Basin, which adds to operation costs in these areas. The fact that coalbed methane wells in the underpressured, southern part of the basin produce little or no water improves their economics relative to that of wells in the overpressured part of the basin, which produce more gas but require considerable dewatering (depressurizing) and subsequent disposal.

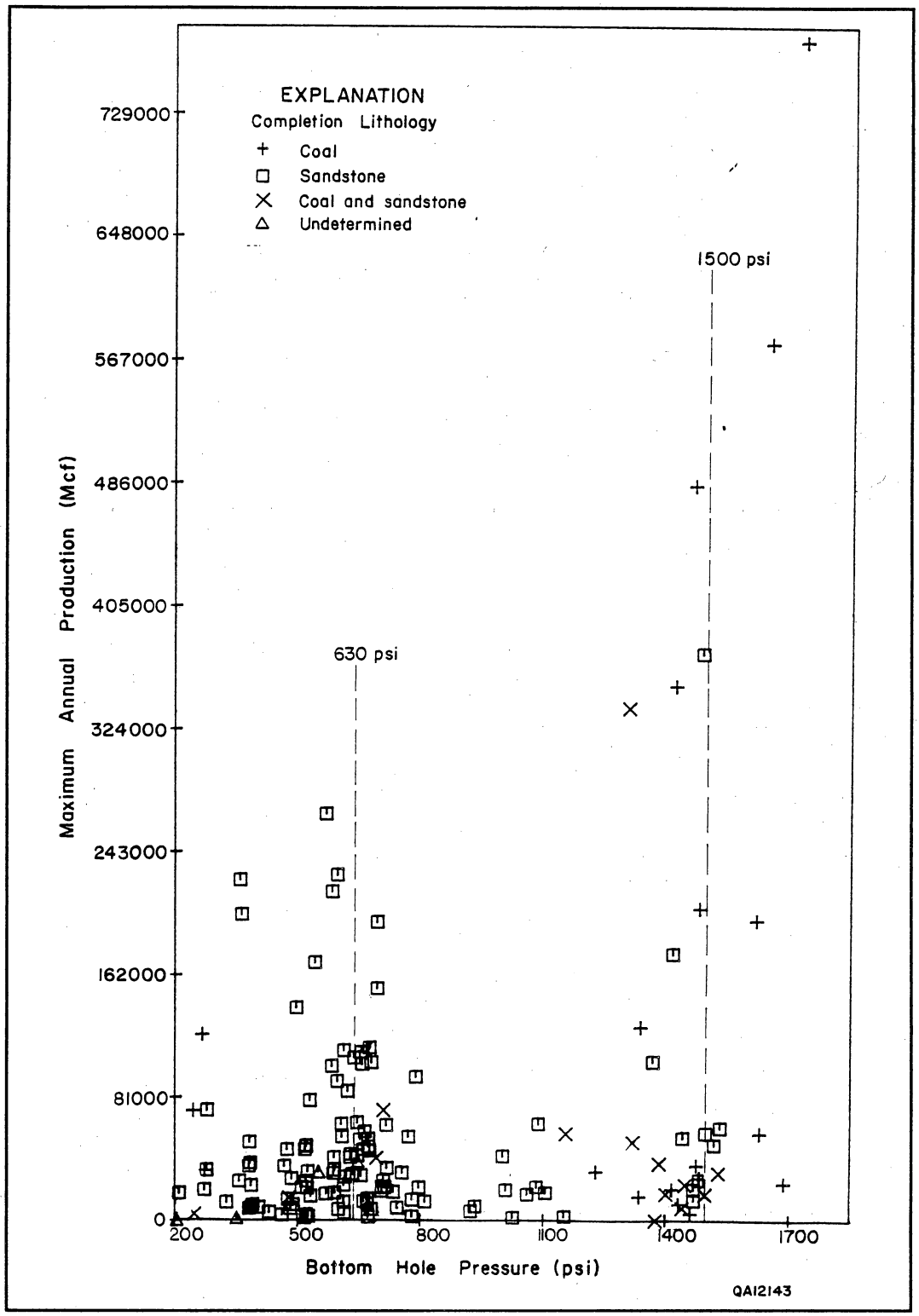

Figure 18. Cross plot of bottom-hole pressure versus maximum annual gas production by producing lithology (from Kaiser and others, 1990).

Regional Characterization of Fruitland Coalbed Reservoirs

On the basis of hydrodynamics and geology, the San Juan Basin was divided into three regions in which Fruitland coal beds have similar reservoir characteristics: Area 1, the regionally overpressured, north-central part of the basin; Area 2, the underpressured, regional discharge area in the west-central part of the basin; and Area 3, the underpressured, eastern part of the basin (fig. 19). In the following discussion, we summarize the salient characteristics of coalbed reservoirs in these areas and illustrate the effects of these characteristics using production histories of well-recognized coalbed methane wells. Fracture permeability is addressed only for the Hogback Monocline.

Area 1: Regionally Overpressured Area

Large coalbed methane resources in the north-central San Juan Basin result from occurrence of thick coal deposits, higher rank coal, and high formation pressures. The maximum coal is at least 10 ft (3 m) thick, and several northwest-trending and minor, northeast-trending belts of 20 ft (6 m) or more of maximum coal are developed in this area. Highly productive wells coincide with thick maximum coal (>20 ft) in several areas (fig. 15 and Ayers and others, this vol., their fig. 23). The correlation of maximum coal thickness with productivity trends is superior to that of average and net coal thickness. Within the regionally overpressured area, defined by simple pressure gradients of 0.50 to 0.60 psi/ft and BHP's greater than 1,200 psi, three subregions are identified (fig. 19). Area 1A has thick shoreline and alluvial coals (Ayers and others, this vol., their fig. 21) and exhibits high BHP's (locally greater than 1,800 psi), high-alkalinity waters (up to 20,000 mg/L), and high potential for upward flow (vertical pressure gradient ~0.80 psi/ft). The best production (Meridian 400 area and Cedar Hill field) lies up hydraulic gradient (northeast) from the area of marked steepening of the potentiometric surface and the transitions from overpressure to underpressure and from bicarbonate- to chloride-rich formation waters (Kaiser, Swartz, and Hawkins, this vol., their figs. 1, 6, and 16). This transition area is where ground-water flow turns steeply upward (Kaiser, Swartz, and Hawkins, this vol., their fig. 30). The steep potentiometric surface coincides with southwestward aquifer pinch-out and the structural hingeline (Ayers and others, this vol.). Low permeability is inferred from the steep surface. Consequently, wells in the Blanco area, which occur along this steep surface and the pressure transition, have low gas and water productivities (figs. 15 and 17). In the Blanco area (fig. 20), the hydraulic gradient is very steep (~0.045) (Kaiser, Swartz, and Hawkins, this vol., their figs. 1 and 6). Area 1B is an area of recharge along the northern and northwestern margins of the basin (Hogback Monocline). Productive wells occur in an area of downward flow close to the basin margin in association with a potentiometric high (fig. 15; Kaiser, Swartz, and Hawkins, this vol., their fig. 1). In this area, fracture permeability may be high because of tight folding. Production from the northwest (44 Canyon area) and northeast (Carracas unit) hogbacks (figs. 15 and 19) may be favored by fracturing associated with such tight folding. Likewise, wells clustered just southeast of Durango occur at a flexure, or abrupt change in dip, and fracture-enhanced permeability is inferred. Area 1C (fig. 19) is defined by a conspicuously flat potentiometric surface, which is thought to indicate enhanced permeability. Vertical flow is potentially downward in this area. To the east, wells in the Carracas unit, similar to those at Blanco, are in an area of steep potentiometric surface and are at the pressure transition. To date, Carracas wells, like those at Blanco, have not been highly productive (fig. 15).

In the north-central part of the basin, maximum annual gas production (MAP) ranges from less than 30 to greater than 3,000 Mcf/d (fig. 15). Productivities are less in Areas 1B and 1C than in Area 1A. Many water-productive coalbed methane wells had IP's of several hundred barrels of water per day (fig. 17). Their occurrence is predictable from artesian overpressuring, which extends to the northern and northwestern rims of the basin. Wells near that rim, or recharge area, may be difficult to dewater (depressurize). Nevertheless, some wells within 2 mi of the outcrop produce at high rates (greater than 300 Mcf/d) and apparently were successfully dewatered.

High water productivities indicate enhanced permeability (Oldaker, 1990). Good examples are the McKenzie Methane Southern Ute–Mobil 36-1 and ARCO's wells in south-central La Plata County, which lie in the area of flat potentiometric surface and inferred high permeability. Coal seams of the 36-1 well have natural permeabilities of approximately 50 md and when stimulated produced low-chloride water at rates greater than 2,000 bbl/d. Some ARCO wells produce gas at rates of 2,000 Mcf/d and water at rates of 1,000 bbl/d. Wells in the Meridian 400 area are also prolific producers of water (cumulative productions of several hundred thousand barrels).

Although most wells in Area 1 produce water, some produced little or no water on initial testing (fig. 17). Examples are clustered wells (for example, eastern La Plata County), isolated individual wells (for example, San Juan 32-7 unit 6 and Seymour 9), and individual wells within clusters of water producers (for example, San Juan 30-6 unit 402). The San Juan 32-7 and Seymour 9 are thought to be associated with structural anomalies.

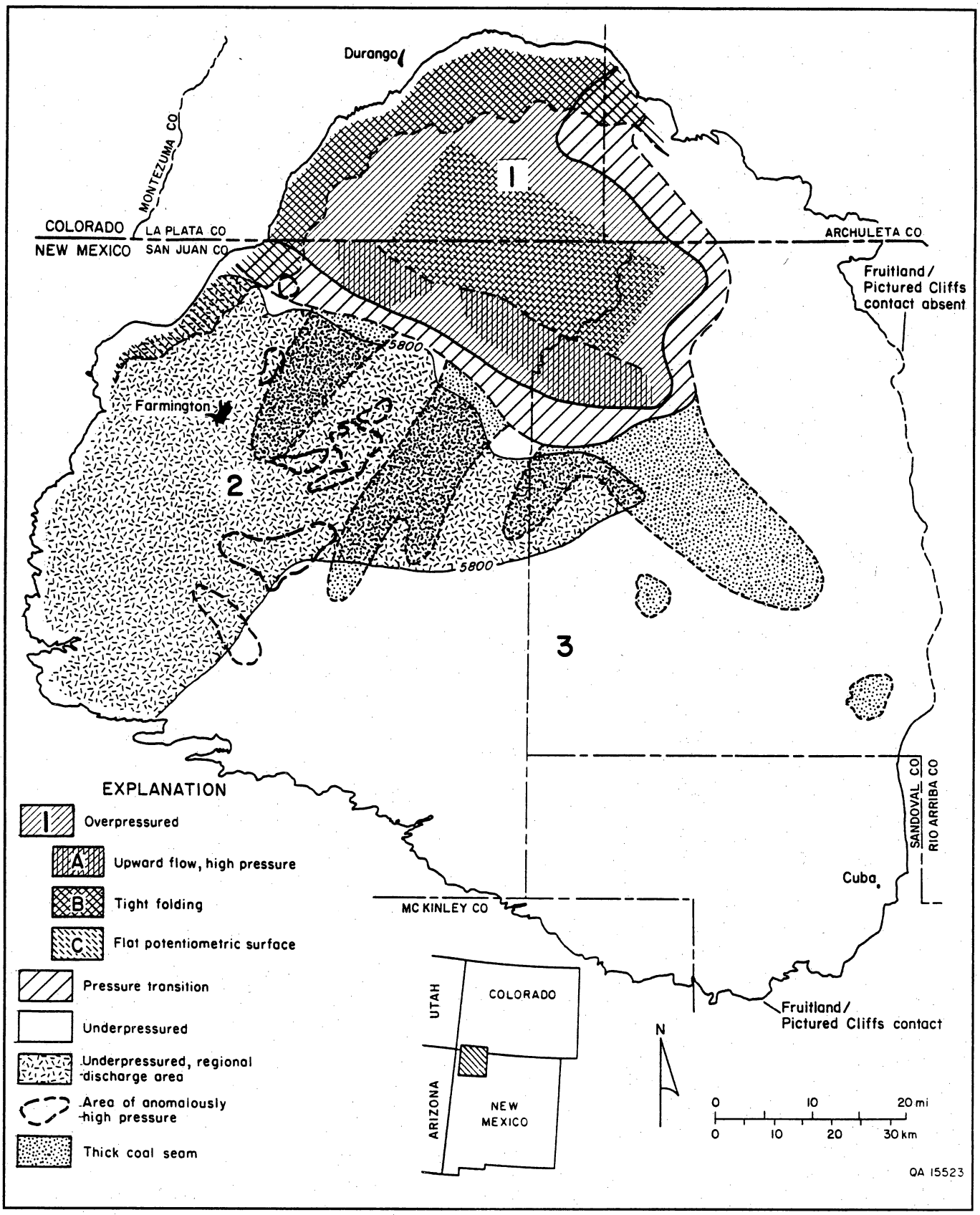

Figure 19. Hydrogeologic regions in the Fruitland Formation, San Juan Basin. Numbers refer to major regions and letters to subregions discussed in the text. Major regions are the (1) overpressured (north-central) area, (2) underpressured, regional discharge area, and (3) underpressured area, outside the regional discharge area (from Kaiser and others, 1990).

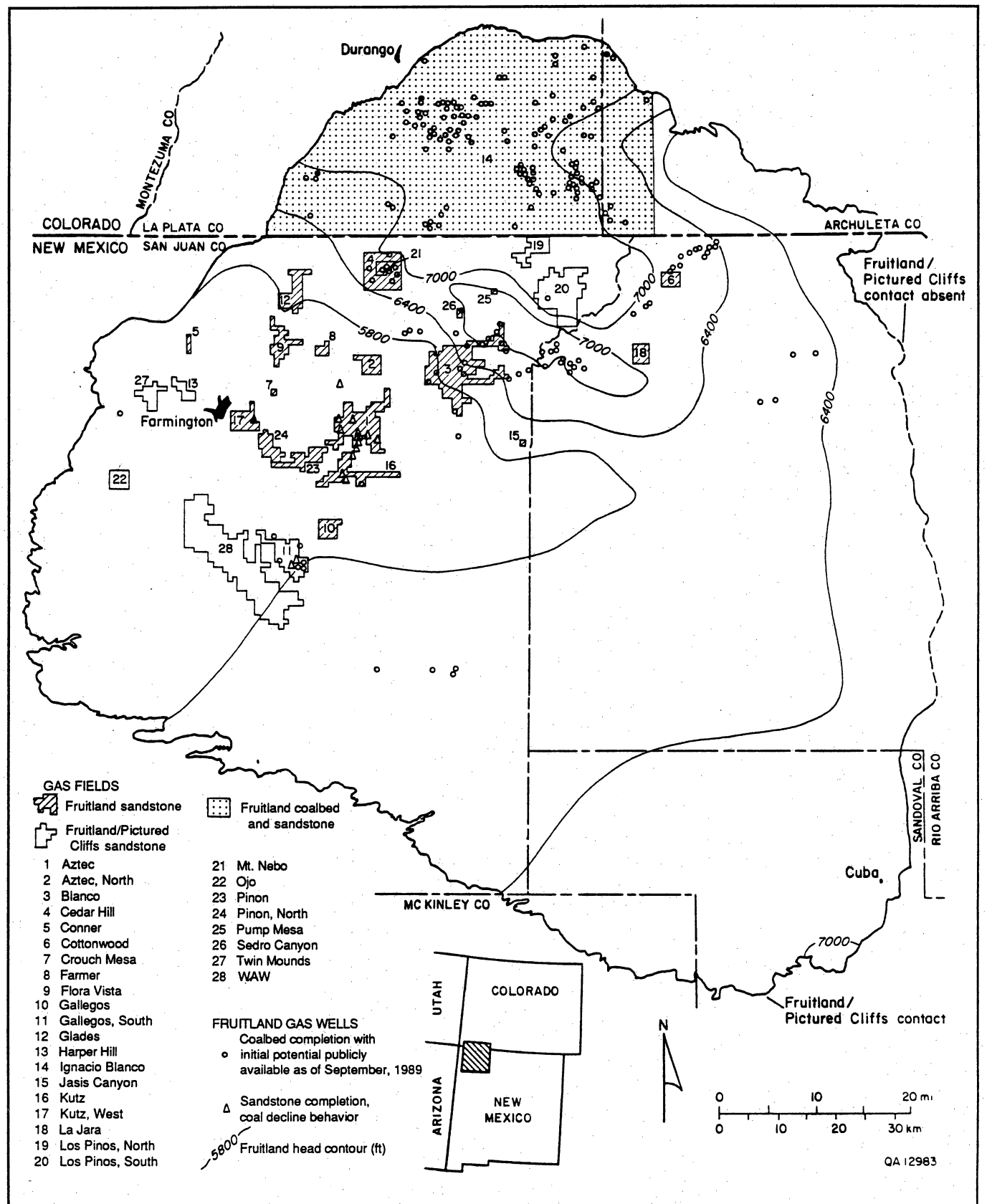

Figure 20. Fruitland potentiometric-surface map (fresh-water head, in ft) and the distribution of Fruitland and Fruitland/ Pictured Cliffs gas fields and tested Fruitland coalbed methane wells (from Kaiser and others, 1990).

Other wells at the northern and western margins of the basin may receive little direct recharge from the outcrop and/or have low permeability and thus have water-free production. For example, the Forty-four Canyon 22-2 (sec. 22, T33N, R11W) initially produced too little gas to gauge and no water. When stimulated, it produced 281 Mcf/d and 17.5 bwpd. The phenomenon of either isolated wells of low water (less than 30 bbl/d) or high water potential (hundreds of barrels of water per day) probably reflects a high degree of reservoir heterogeneity or compartmentalization in the coal seams. Reservoir characteristics of Fruitland coal beds in Area 1 are detailed in a discussion of the Meridian 400 area and Cedar Hill field; the Allison unit is included to show variable reservoir conditions in Area 1.

Meridian 400 Area

The Meridian 400 area is the basin's "sweet spot," where individual wells typically produce from 300 to over 3,000 Mcf/d (fig. 15) with considerable water. The area is overpressured, coincides with a conspicuous potentiometric mound, flanks the pressure-transition zone, and has thick coal seams. The mound reflects a pressure ridge and upward flow, which is indicated by a vertical pressure gradient of approximately 0.8 psi/ft (Kaiser, Swartz, and Hawkins, this vol., fig. 3). Southwestward and southeastward pinch-outs of coal seams cause a no-flow boundary and result in upward flow. Consequently, free gas is concentrated in conventional stratigraphic traps (Ayers and others, this vol., fig. 2; Ayers and Zellers, this vol., fig. 1). In other words, additional gas is inferred to be available for production beyond that predicted only from the sorption isotherm. Meridian 400 gases are carbon-dioxide rich (commonly greater than 10 percent), very dry (C_1/C_{1-5} values of 1.00), and reflect their hydrodynamic setting (Scott and others, this vol.). Wells are completed in northeast-trending coal deposits (Ayers and others, this vol., fig. 23) of high-volatile A bituminous rank (Scott and others, this vol., fig. 3). The Meridian 400 area lies at the edge of the basin floor and in an area of many minor structural features (Ayers and Zellers, this vol., figs. 16 and 19). The face cleat is oriented northeast (Tremain and others, this vol., fig. 12), parallel to the productivity trend, and permeability anisotropy is inferred across the area to favor flow in the northeast direction. This trend parallels a prominent northeast-trending segment of the San Juan River, a lineament that may reflect faulting or northeast-trending coal deposits (Ayers and others, this vol., fig. 23; Ayers and Zellers, this vol., fig. 10). The highly productive Meridian 400 area extends southeastward to the limits of overpressuring; this boundary is inferred to result from a major Fruitland channel-sandstone belt that interrupts coal seam (aquifer) continuity (Ayers and others, Bureau of Economic Geology, unpublished cross sections) to cause overpressuring and underpressuring, respectively, on either side of the channel belt. Minor faulting may also contribute to aquifer separation (Ayers and others, Bureau of Economic Geology, unpublished cross sections). Minor folds may contribute fracture permeability to the coal seams and form conventional structural traps (Ayers and Zellers, this vol., figs. 2 and 19). In the Meridian 400 area, many wells initially tested for little or no water but upon production yielded large volumes of water. For example, the Meridian San Juan 30-6 unit 402 produced no water upon initial testing but subsequently produced water at an average annual rate of 108,780 bbl. This behavior, coupled with a high gas IP (2,460 Mcf/d), suggests initial production of free gas and a coal seam with high fracture permeability (secondary porosity). Exceptional permeability and contribution from conventionally trapped gas are thought to explain high production in the Meridian 400 area.

Cedar Hill Field

At Cedar Hill field, production trends (fig. 15), face cleats (Tremain and others, this vol., their fig. 12), coal seams, and channel-sandstone belts are all oriented northeastward (Ambrose and Ayers, this vol., their figs. 6 and 10). Individual wells typically produce 300 to more than 1,000 Mcf/d (fig. 15). The field is overpressured, lies at the transition from a flat to steep potentiometric surface (Kaiser, Swartz, and Hawkins, this vol., their fig. 1), and has thick (some individual seams more than 20 ft) coal seams of high-volatile A and B bituminous rank (Scott and others, this vol., their fig. 3). Numerical modeling shows strong potential for upward flow of ground water at Cedar Hill field (Kaiser, Swartz, and Hawkins, this vol., their fig. 30). High productivity in this area is associated with a no-flow boundary (lateral flow restricted by southwestward pinch-out of aquifer coal seams and/or offset along faults) and probable upward flow, which favor concentration of free gas in conventional traps. Productivity at Cedar Hill field is also influenced by the structural setting and distribution of Fruitland coal seams. Cedar Hill field lies along the structural axis of the basin (Ayers and others, this vol., their fig. 5). The most productive wells (more than 1,800 Mcf/d) are on the southern flank of the synclinal axis in the eastern part of Cedar Hill field, where flexure along the syncline may have caused fracture-enhanced permeability. The map of maximum annual production (Yeh and others, this vol., their fig. 10) shows northeast-trending belts of high production (more than 1,000 Mcf/d) in the southwestern part of the field, coinciding with net coal

thickness of more than 30 ft in basal Fruitland coal seams (coal group A) (Ambrose and Ayers, this vol., their fig. 12). Production on the southern and southwestern flanks of the field may be limited by a zone of northwest-trending, normal faults (Ambrose and Ayers, this vol., their fig. 3) associated with the structural hingeline of the basin. A northwest-trending boundary separates high and low production (fig. 15) and continues southeastward to the Blanco area (fig. 15).

Allison Unit

The Allison unit (T32N, R6W and R7W) is an area of low production that is surrounded by higher production, is overpressured, and has a flat potentiometric surface in association with thick coal seams (fig. 15; Kaiser, Swartz, and Hawkins, this vol., their figs. 1 and 6; Ayers and others, this vol., their fig. 23). Over a short production history (1 to 2 yr), individual wells commonly have MAP rates of 30 to 100 Mcf/d (fig. 15) that have been disappointing and erratic, contrary to that expected from the hydrologic setting. Negative decline is only a partial explanation for low production, because several wells scattered throughout the unit produced at rates of 100 to 300 Mcf/d in early 1990. Production in the unit is erratic and probably reflects reservoir heterogeneity. Acceptable but unpredictable permeability is inferred from the area's gentle hydraulic gradient and associated water production of 50 to 200 bbl/d. The unit lies between an area of downward flow to the northwest and one of strong upward flow to the southeast. Consequently, in the absence of a no-flow boundary, there may be little or no potential for vertical flow in the Fruitland Formation and concentration of free gas. Coal thickness does not appear to be a limiting factor because the unit coincides in part or in whole with the thickest maximum, average, and net coal thickness. The unit is at the basin's structural floor and is bounded to the northeast by the plunging Ignacio Anticline (Ayers and others, this vol., their fig. 5). Free gas may have migrated up structure, possibly reducing gas content of coal beds. Structural and stratigraphic complexity locally may serve to compartmentalize the coal seams, contributing to reservoir heterogeneity. A minor, northwest-trending normal fault (~40 ft [~12 m] throw), which has been identified just to the southwest of the unit, occurs at the transition between high and low production (fig. 15). Coalbed continuity is uncertain and is complicated by coalbed termination, splitting, and overriding of UP2 sandstones (Ayers and others, this vol., their figs. 2 and 23). Currently, reservoir heterogeneity (because of highly variable permeability and minor faulting) and little contribution from conventionally trapped gas are thought to explain erratic production in the Allison unit.

Area 2: Underpressured, Regional Discharge Area

The west-central part of the basin is regionally underpressured (simple pressure gradients of 0.30 to 0.40 psi/ft and BHP's of less than 1,000 psi), except for local pressure anomalies, and is an area of regional convergence and discharge, as defined by the 5,800-ft head contour (fig. 19, Area 2). Hydrocarbon accumulation is favored in such an area (Tóth, 1980). Available chemical analyses show Na-Cl-type waters. Coal seams may be thicker than 10 ft (3 m) and occur in northeast-trending belts (Ayers and others, this vol., their figs. 21 and 23). A northeast-trending, dip-elongate belt of thick coal extends almost to the southwestern margin of the basin (Ayers and others, this vol., their figs. 23 and 25) and coincides with a similar trending belt of high production (greater than 100 Mcf/d) (fig. 15). This belt flanks a major northeast-trending Fruitland channel-sandstone belt (Ayers, Bureau of Economic Geology unpublished map) and includes productive wells (200 to 500 Mcf/d) in the Fulcher and WAW–Gallegos areas (fig. 15) completed in coal seams of subbituminous and high-volatile C bituminous rank (Scott and others, this vol., their fig. 3). Coal seams may have served as pathways for gas that migrated out of the north-central part of the basin, entrained or dissolved in ground water, or that diffused outward in response to the concentration gradient. This appears to be the case for carbon dioxide, because elongate areas of high carbon dioxide content trend updip (southwestward), coincident with the coal belts (Scott and others, this vol., their fig. 10), and terminate at the San Juan River valley, a regional no-flow boundary (Kaiser, Swartz, and Hawkins, this vol., their figs. 1 and 30). In the Aztec, Kutz, and Gallegos fields (fig. 20), sandstone completions predominate and occur in channel-sandstone belts (thin-coal areas) lying between northeast-trending belts of thick coal (Ayers and others, this vol., their fig. 21).

In the west-central part of the basin, the Fruitland Formation is mainly an aquitard and gas is produced water free (Kaiser, Swartz, and Hawkins, this vol.). Water-free production in this regional discharge area is explained in terms of the hydrostratigraphy, trapping mechanism, and coal wettability. Limited flow in the basal Fruitland coal and Pictured Cliffs Sandstone accounts for occasional water production in wells completed in the basal coal. Conventional trapping and low gas permeability relative to water are also important factors. Stratigraphic trapping is postulated to be more important than structural trapping on the basis of gentle, northeast monoclinal dip and associated updip (southwestward) pinch-out of reservoir coal seams (Ayers and others, this vol., their fig. 2). Coal seams in the southern part of the basin are lower rank (subbitumi-

nous to high-volatile C bituminous) and may be water wet; hence, in low-permeability strata such as these, water is less mobile than gas.

In the west-central part of the basin, underpressured Fruitland coalbed wells have MAP's ranging from 30 to 300 Mcf/d, similar to productivities of many overpressured wells in the north-central part of the basin (Ignacio Blanco field) in Areas 1B and 1C (fig. 19). Although cumulative productions reach 1 Bcf (for example, Clay 1, Gallegos area, more than 1 Bcf in 14 yr), most wells in the southwest have cumulative productions of a few hundred million Mcf, and some have produced small volumes of oil, 2 or 3 bbl/d. Numerous Fruitland sandstone gas fields dot the southwestern part of the basin (fig. 20). Several of them are associated with potentiometric mounds (Kaiser, Swartz, and Hawkins, this vol., their fig. 1). Analysis of production decline has shown that many wells identified as sandstone completions actually have coal-decline behavior and probably are producing coalbed methane indirectly from coal seams (fig. 4). In some cases, sandstone volumetrics require gas production from the associated coals. Operationally, it may be advantageous to complete in sandstones interbedded with coals, as is done in some western basins. Some wells are dually completed in Fruitland coal seams and Pictured Cliffs Sandstone or Mesaverde sandstones, and the production is commingled. Consequently, the contribution of Fruitland coalbed methane to total gas production in the west-central part of the basin is substantial but unquantifiable.

WAW–Gallegos Area

WAW–Gallegos is located in Area 2 in the southwestern corner of the basin (figs. 15 and 20), where individual wells produce at rates of 30 to more than 300 Mcf/d. Wells completed in 1990 average about 180 Mcf/d. Long-term productivity is demonstrated by the Clay 1 (sec. 12, T26N, R12W), which was completed as a coalbed well in 1976 and had an average production rate of 185 Mcf/d in 1989. The area is underpressured and lies mostly within the 5,800-ft head contour. Structural dip is homoclinal to the northeast at less than 1 degree (~80 ft/mi [~15 m/km]). Strike- and dip-elongate coal seams of subbituminous rank have maximum thicknesses of 10 to 20 ft (3 to 6 m) (Ayers and others, this vol., their fig. 23). Stratigraphic and hydrodynamic trapping may account for considerable gas volume beyond that adsorbed at reservoir pressures below or near hydrostatic pressure. Coal seams pinch out updip (southwestward), and ground water flows downdip (northeastward). Moreover, cross-sectional modeling suggests a local no-flow boundary in the WAW–Gallegos area (Kaiser, Swartz, and Hawkins, this vol., their fig. 30). Enhanced permeability is inferred for wells producing water from the basal Fruitland coal. Thus, the presence of significant free gas and enhanced permeability are thought to combine to explain relatively high gas productivities in the WAW–Gallegos area.

Area 3: Underpressured, Eastern Area

Little is known about the hydrogeology of the eastern part of the basin. Area 3 (fig. 19) is regionally underpressured, and because of limited data, it appears to be hydrologically featureless. Widely spaced head contours suggest sluggish ground-water flow (Kaiser, Swartz, and Hawkins, this vol., their fig. 1). Fruitland-produced waters are Na-Cl type that resemble seawater. Coal thickness exceeds 10 ft in a northwest-trending area in Rio Arriba County, parallel to depositional strike, corresponding to coals of belt E (Ayers and others, this vol., their fig. 21). There are a few producing Fruitland wells (coal and/or sandstone completions) in the area. After 1 or 2 yr of production, they have average annual productions of less than 1 to 3 MMcf, accompanied by little or no water.

Conclusions

1. Coalbed methane production in the Fruitland Formation is log-normally distributed. Statistical analysis suggests that coal beds having free gas may be common. Production from overpressured coal seams is greater than that from underpressured seams, although production from the two pressure regimes overlaps. Initial gas potential is a predictor of long-term productivity. Highly productive wells produce both gas and water, reflecting superior permeability. Decline curves of coalbed and sandstone reservoirs differ. Coalbed wells have negative decline early in their production history, followed by exponential decline at less than 5 percent per yr. Sandstone wells that exhibit coal-decline behavior probably are producing coalbed methane indirectly from adjacent coal seams.

2. Approximately 90 percent of the Fruitland coalbed methane production is from the Meridian 400 area and the Cedar Hill and Ignacio Blanco fields. In the overpressured part of the basin, wells in the Meridian 400 area are the most productive (more than 1,000 Mcf/d), and those in Ignacio Blanco field are the least productive (~30 to 300 Mcf/d). Coalbed wells in the west-central (underpressured) part of the basin, which produce little or no water, are as productive as those in the Ignacio Blanco field.

Acknowledgments

This research was funded by the Gas Research Institute under contract no. 5087-214-1544. During the course of the study, our ideas and concepts developed as we discussed research results with operators, other GRI contractors, and our GRI coalbed methane project managers, R. A. McBane and R. C. Klem. Additionally, several operators and pipeline companies supplied data that greatly enhanced the quality of the study; these contributions are gratefully acknowledged. We thank the Southern Ute Indian Tribe and other landowners for access to their properties and BHP–Utah International, Pueblo Coal, and Kaiser Steel Resources, Inc. for mine access. During this study, capable assistance was provided by J. D. Beckman, W. J. Garey, D. R. Grote, G. J. Hawkins, S. A. Jones, R. G. McMurry, Wahiduzzaman Mirza, M. M. Newton, P. S. Reiss, Ting-Ya Hsieh, T. E. Swartz, G. A. Warren, J. S. Yeh, and S. D. Zellers, all research assistants at The University of Texas at Austin.

This report benefited from reviews by B. C. Boyce, J. C. Close, and R. C. Klem. The computing staff of the Bureau of Economic Geology, managed by E. D. Orr, provided guidance in data processing and computer-assisted mapping. Drafting was by the cartographic staff of the Bureau under the direction of R. L. Dillon, chief cartographer. Word processing was by Melissa Snell, typesetting was by Susan Lloyd, design was by Margaret L. Evans, manuscript production was coordinated by Kitty Challstrom, and editing was by Bobby Duncan, under the direction of Susann Doenges, editor-in-charge.

Conversion Factors

Nonmetric unit		Conversion factor		Metric unit
feet (ft)	×	0.3048	=	meters (m)
inches (inch)	×	2.540	=	centimeters (cm)
miles (mi)	×	1.609	=	kilometers (km)
feet/mile (ft/mi)	×	0.1894	=	meters/kilometer (m/km)
square miles (mi2)	×	2.589	=	square kilometers (km2)
cubic feet (cf)	×	0.02832	=	cubic meters
short tons	×	0.9072	=	metric tons
pounds per square inch	×	6.895	=	kilopascals
psi/ft	×	22.62	=	kilopascals/meter

References

Aguilera, R., 1980, Naturally fractured reservoirs: Tulsa, OK, PennWell Books, 619 p.

Aldrich, M. J., Jr., Chapin, C. E., and Laughlin, A. W., 1986, Stress history and tectonic development of the Rio Grande Rift, New Mexico: Journal of Geophysical Research, v. 91, no. B6, p. 6199–6211.

Ammosov, I. I., and Eremin I. V., 1960, Fracturing in coal (translated from Russian), IZDAT Publishers, Moscow, available from the Office of Technical Services, Washington, D.C., 109 p.

Armstrong, R. L., 1968, Sevier orogenic belt in Nevada and Utah: Geological Society of America Bulletin, v. 79, p. 429–458.

Ayers, W. B., Jr., and Ambrose, W. A., 1990, Geologic controls on the occurrence of coalbed methane, Fruitland Formation, San Juan Basin, *in* Ayers, W. B., and others, Geologic evaluation of critical production parameters for coalbed methane resources, Part 1: San Juan Basin: Gas Research Institute, contract no. 5087-214-1544 (GRI-90/0014.1), p. 9–72.

Ayers, W. B., Jr., and Kaiser, W. R., 1984, Lacustrine interdeltaic coal in the Fort Union Formation (Palaeocene), Powder River Basin, Wyoming and Montana, U.S.A., *in* Rahmani, R. A., and Flores, R. M., eds., Sedimentology of coal and coal-bearing sequences: International Association of Sedimentologists Special Publication No. 7, p. 61–84.

Ayers, W. B., Jr., and Zellers, S. D., 1988, Sedimentologic and structural controls on the occurrence and producibility of coalbed methane, Fruitland Formation, northern San Juan and Rio Arriba Counties, New Mexico; *in* Ayers, W. B., Jr., and others, Geologic evaluation of critical production parameters for coalbed methane resources, Part 1, San Juan Basin: Gas Research Institute, contract no. 5087-214-1544 (GRI-88/0332.1), p. 3–59.

Bair, E. S., O'Donnell, T. P., and Picking, L. W., 1985, Potentiometric mapping from incomplete drill-stem test data: Palo Duro Basin area, Texas and New Mexico: Ground Water, v. 23, p. 198-211.

Baltz, E. H., 1967, Stratigraphy and regional tectonic implications of part of Upper Cretaceous and Tertiary rocks in east-central San Juan Basin, New Mexico: U.S. Geological Survey Professional Paper 552, 101 p.

Barnes, Harley, 1953, Geology of the Ignacio area, Ignacio and Pagosa Springs Quadrangles, La Plata and Archuleta Counties, Colorado: U.S. Geological Survey Oil and Gas Investigations Map OM-138, scale 1:63,360.

Barnes, Harley, Baltz, E. H., Jr., and Hayes, P. T., 1954, Geology and fuel resources of the Red Mesa area, La Plata and Montezuma Counties, Colorado: U.S. Geological Survey Oil and Gas Investigations Map OM-149, scale 1:62,500.

Barton, C. C., and Hsieh, P. A., 1989, Physical and hydrogeologic flow properties of fractures: Field trip guidebook T385, 28th International Geological Congress, 36 p.

Barton, C. C., and Larsen, E., 1985, Fractal geometry of two-dimensional fracture networks at Yucca Mountain, southwestern Nevada, *in* Fundamentals of Rock Joints: Proceedings of the International Symposium, Bjorkliden, Sweden, p. 77–84.

Barton, C. C., Larsen, Eric, Page, W. R., and Howard, T. M., 1987, Characterizing fractured rock for fluid-flow, geomechanical, and paleostress modeling: methods and preliminary results from Yucca Mountain, Nevada: United States Department of the Interior, USGS Open-File Report USGS-OFR-87.

Baumgardner, R. W., Jr., 1987, Landsat-based lineament analysis, East Texas Basin and Sabine Uplift area: The University of Texas at Austin, Bureau of Economic Geology Report of Investigations No. 167, 26 p.

Beach, L. J., and Jentgen, R. W., 1978, Coal test drilling for the San Juan Mine Extension, San Juan County, New Mexico: U.S. Geological Survey Open-File Report 78-960, 87 p.

Belitz, K., and Bredehoeft, J. D., 1988, Hydrodynamics of Denver Basin: explanation of subnormal fluid pressures: American Association of Petroleum Geologists Bulletin, v. 72, no. 11, p. 1334-1359.

Berry, F. A. F., 1959, Hydrodynamics and geochemistry of the Jurassic and Cretaceous systems in the San Juan Basin, northwestern New Mexico and southwestern Colorado: Stanford University, Ph.D. dissertation, 192 p.

Bertrand, Philippe, Behar, Francoise, and Durand, Bernard, 1986, Composition of potential oil from humic coals in relation to their petrographic nature: Organic Geochemistry, v. 10, p. 601–608.

Bond, W. A., 1984, Application of Lopatin's method to determine burial history, evolution of the geothermal gradient, and timing of hydrocarbon generation in Cretaceous source rocks in the San Juan Basin, northwestern New Mexico and southwestern Colorado, *in* Woodward, J., and others, eds., Hydrocarbon source rocks of the greater Rocky Mountain region: Denver, Rocky Mountain Association of Geologists, p. 433–447.

Brace, W. F., 1964, Brittle fracture of rocks, *in* Judd, W. R., ed., State of stress in the Earth's crust: New York, Elsevier, p. 111–180.

Bradley, J. S., 1975, Abnormal formation pressure: American Association of Petroleum Geologists Bulletin, v. 59, no. 6, p. 957-973.

Briscoe, F. H., Camp, B. S., Lottman, L. K., and Malone, P. G., 1988, A study of coal-bed methane production trends as related to geologic features, Warrior Basin, Alabama: Coal-bed methane, San Juan Basin, Rocky Mountain Association of Geologists, p. 237–246.

Britten, R. A., Smyth, M., Bennett, A. J. R., and Shibaoka, M., 1975, Environmental interpretations of Gondwana coal measure sequence in the Sydney Basin of New South Wales, *in* Campbell, K. S. W., ed., Gondwana Geology: Australian National University Press, Canberra, p. 233–247.

Burchfiel, B. C., and Davis, G. A., 1975, Nature and controls of Cordilleran orogenesis, western United States: Extensions of an earlier synthesis: American Journal of Science, v. 275 A, p. 363–396.

Callender, J. F., Seager, W. R., and Swanberg, C. A., 1983, Late Tertiary and Quaternary tectonics and volcanism: Geothermal Resources of New Mexico: Scientific Map Series, New Mexico State University Energy Institute; work performed under United States Department of Energy contract number AS07-781D01717, scale 1:500,000.

Campbell, F. W., 1985, Chemical characteristics of the coals, *in* Roybal, G. H., Campbell, F. W., Beaumont, E. C., Cohen, A. D., Kuellmer, F. J., and Kottlowski, F. E., Quality assessment of strippable coals in the San Juan Basin of northwestern New Mexico: New Mexico Bureau of Mines and Mineral Resources division of New Mexico Energy Research and Development Institute, Report No. 2-73-4304, 89 p.

Carothers, W. W., and Kharaka, Y. K., 1978, Aliphatic acid anions in oil field waters—implications for origin of natural gas: American Association of Petroleum Geologists Bulletin, v. 62, p. 2441–2453.

_____ 1980, Stable carbon isotopes of HCO_3^- in oil-field waters—implications for the origin of CO_2: Geochimica et Cosmochimica Acta, v. 44, p. 323–332.

Chapin, C. E., and Cather, S. M., 1981, Eocene tectonics and sedimentation in the Colorado Plateau-Rocky Mountain area, *in* Dickinson, W. R., and Payne, M. D., eds., Relations of tectonics to ore deposits in the southern Cordillera: Arizona Geological Society Digest, v. 14, p. 173–198; *also in* Lowell, J. D., ed., Rocky Mountain foreland basins and uplifts: Rocky Mountain Association of Geologists, Guidebook, 1983 Field Conference, p. 33–56.

Choate, Raoul, Lent, J., and Rightmire, C. T., 1984, Upper Cretaceous geology, coal, and the potential for methane recovery from coalbeds in San Juan Basin—Colorado and New Mexico, *in* Rightmire, C. T., Eddy, G. E., and Kirr, J. N., eds., Coalbed methane resources of the United States: American Association of Petroleum Geologists Studies in Geology Series No. 17, p. 185–222.

Choate, Raoul, and Rightmire, C. T., 1982, Influence of the San Juan Mountain geothermal anomaly and other Tertiary igneous events on the coalbed methane potential in the Piceance, San Juan and Raton Basins, Colorado and New Mexico: SPE 10805, *in* Proceedings of the Unconventional Gas Recovery Symposium, May 16–18, 1982, Pittsburgh, Pennsylvania, Society of Petroleum Engineers/U.S. Department of Energy, p. 151–164.

Clarkson, Gerry, and Reiter, Marshall, 1987, The thermal regime of the San Juan Basin since late Cretaceous times and its relationship to San Juan Mountain thermal sources: Journal of Volcanology and Geothermal Research, v. 31, p. 217–237.

_____ 1988, An overview of geothermal studies in the San Juan Basin, New Mexico and Colorado, *in* Fassett, J. E., ed., Geology and coal-bed methane resources of the northern San Juan Basin, Colorado and New Mexico: Rocky Mountain Association of Geologists, p. 285–291.

Claypool, G. E., and Kaplan, I. R., 1974, The origin and distribution of methane in marine sediments, *in* Kaplan, I. R., ed., Natural gases in marine sediments: New York, Plenum Press, p. 99–139.

Clementz, D. M., 1979, Effect of oil and bitumen saturation on source-rock pyrolysis: American Association of Petroleum Geologists Bulletin, v. 63, p. 2227–2232.

Collins, E. W., Laubach, S. E., and Vendeville, B. C., 1990, Faults and fractures in the Balcones Fault Zone, Central Texas: Austin Geological Society Guidebook 13, 34 p.

Colorado Geological Survey (CGS) files, various years, informal reports available from the Colorado Geological Survey, unpaginated.

Colorado Oil and Gas Conservation Commission (COGCC) well file, geological well data files Denver, Colorado.

Condon, S. M., 1988, Joint patterns on the northwest side of the San Juan Basin (Southern Ute Indian Reservation), southwest Colorado, *in* Fassett, J. E., ed., Geology and coal-bed methane resources of the San Juan Basin, Colorado and New Mexico: Rocky Mountain Association of Geologists, p. 61–68.

Cordell, Lindrith, and Grauch, V. J. S., 1985, Mapping basement magnetization zones from aeromagnetic data in the San Juan Basin, New Mexico, *in* Hinze, W. J., ed., The utility of regional gravity and magnetic anomaly maps: Society of Exploration Geophysicists, p. 181–197.

Cullender, M. H., and Smith, R. V., 1956, Practical solutions of gas-flow equation for wells and pipelines with large temperature gradients: Transactions, American Institute of Mining, Metallurgical, and Petroleum Engineers, v. 207, p. 281–287.

Cumella, S. P., 1981, Sedimentary history and diagenesis of the Pictured Cliffs Sandstone, San Juan Basin, New Mexico and Colorado: The University of Texas at Austin, Texas Petroleum Research Committee Report No. UT 81-1, 219 p.

_____ 1983, Relation of Upper Cretaceous regressive sandstone units of the San Juan Basin to source area tectonics, *in* Reynolds, M. W., and Dolly, E. D., eds., Mesozoic paleogeography of west-central United States: Denver, Colorado, Rocky Mountain Section, Society of Economic Paleontologists and Mineralogists, p. 189–199.

Dabbous, M. K., Reznik, A. A., Mody, B. G., Fulton, P. F., and Taber, J. J., 1976, Gas-water capillary pressure in coal at various overburden pressures: Society of Petroleum Engineers Journal, v. 16, no. 5, p. 261–268.

Dane, C. H., 1936, The La Ventana—Chacra Mesa coal field, pt. 3A, Geology and fuel resources of the southern part of the San Juan Basin, New Mexico: U.S. Geological Survey Bulletin 860-C, p. 81–161.

Davis, J. C., 1986, Statistics and data analysis in geology, 1st ed.: New York, John Wiley, 550 p.

Decker, A. D., Close, J. C., and McBane, R. A., 1989, The use of remote sensing, curvature analysis, and coal petrology as indicators of higher coal reservoir permeability, *in* Proceedings, 1989 Coalbed Methane Symposium: University of Alabama, Tuscaloosa, p. 325–340.

Decker, A. D., and Horner, D. M., 1987, Origin and production implications of abnormal coal reservoir pressure: Proceedings, 1987 Coalbed Methane Symposium, University of Alabama, School of Mines and Energy Development, p. 51–62.

Decker, A. D., Jeu, S. J., Cooper, J. D., and Wicks, D. E., 1988, Geology, geochemistry, reservoir engineering, and completion methods at the Cedar Hill field, San Juan County, New Mexico: A field study of classic coal degasification behavior, *in* Fassett, J. E., ed., Geology and coal-bed methane resources of the northern San Juan Basin, Colorado and New Mexico: Rocky Mountain Association of Geologists Guidebook, p. 221–235.

Decker, A. D., Klusman, R., and Horner, D. M., 1987, Geochemical techniques applied to the identification and disposal of connate coal water: The University of Alabama, School of Mines and Energy Development, Proceedings, The 1987 Coalbed Methane Symposium, p. 229-242.

Devine, P. E., 1980, Depositional patterns in the Point Lookout Sandstone, northwest San Juan Basin, New Mexico: The University of Texas at Austin, Master's thesis, 238 p.

Diamond, W. P., McCulloch, C. M., and Bench, B. M., 1976, Use of surface joint and photolinear data for predicting subsurface coal cleat orientation: United States Bureau of Mines Report of Investigations 8120, 13 p.

Dickinson, W. R., Klute, M. A., Hayes, M. J., Janecke, S. U., Lundin, E. R., McKittrick, M. A., and Olivares, M. D., 1988, Paleogeographic and paleotectonic setting of Laramide sedimentary basins in the central Rocky Mountain region: Geological Society of America Bulletin, v. 100, p. 1023–1039.

Dilworth, O. L., 1960, Upper Cretaceous Farmington Sandstone of northeastern San Juan County, New Mexico: New Mexico University, Master's thesis.

Dix, O. R., and Jackson, M. P. A., 1981, Statistical analysis of lineaments and their relation to fracturing, faulting, and halokinesis in the East Texas Basin: The University of Texas at Austin, Bureau of Economic Geology Report of Investigations No. 110, 30 p.

Dixon, J. M., and Jake, T., 1979, Coal cleat intensity, *in* Donaldson, A. C., Presley, M. W., and Renton, J. J., eds., Carboniferous coal guidebook: West Virginia Geological and Economic Survey Bulletin B-37-1, p. 38–46.

Dobrin, M. B., 1976, Introduction to geophysical prospecting, 3rd ed.: New York, McGraw-Hill, 630 p.

Dobrin, M. B., and Savit, C. H., 1988, Introduction to geophysical prospecting, 4th ed.: New York, McGraw-Hill, 867 p.

Donaldson, A. C., 1979, Origin of coal seam discontinuities, *in* Donaldson, A. C., Presley, M. W., and Renton, J. J., eds., Carboniferous coal guidebook: West Virginia Geological and Economic Survey Bulletin B-37-1, p. 102–132.

Donaldson, A. C., Presley, M. W., and Renton, J. J., eds., 1979, Carboniferous coal guidebook: West Virginia Geological and Economic Survey Bulletin B-37-1, 301 p.

DuChene, H. R., 1989, Fracture reservoirs in the San Juan Basin, Colorado and New Mexico," *in* Lorenz, J. C., and Lucas, S. G., eds., Energy frontiers in the Rockies, Albuquerque Geological Society, p. 101–109.

Dunne, W. M., and North, C. P., 1990, Orthogonal fracture systems at the limits of thrusting: an example from southwestern Wales: Journal of Structural Geology, v. 12, no. 2, p. 207–216.

Dwight's Oil and Gas Reports, 1990a, Natural gas well production histories: Colorado statewide coal bed methane report, v. 1, 373 p.

_____ 1990b, Natural gas well production histories: New Mexico statewide coal bed methane report, v. 1, 853 p.

El-Etr, H. A., 1976, Proposed terminology for natural linear features, *in* Hodgson, R. A., and others, eds., Proceedings, 1st International Conference on the New Basement Tectonics: Utah Geological Association Publication No. 5, p. 480–489.

Emmendorfer, Alan, 1989, Fracture orientation use in the dipmeter type fracture log: The Mountain Geologist, v. 26, p. 63–67.

Engelder, Terry, 1985, Loading paths to joint propagation during a tectonic cycle: an example from the Appalachian Plateau, U.S.A.: Journal of Structural Geology, v. 7, no. 3/4, p. 459–476.

Epis, R. C., and Chapin, C. E., 1975, Geomorphic and tectonic implications of the post-Laramide, late Eocene erosion surface in the southern Rocky Mountains, *in* Curtis, B. F., ed., Cenozoic history of the southern Rocky Mountains: Geological Society of America, Memoir 144, p. 45–74.

Erpenbeck, M. F., 1979, Stratigraphic relationships and depositional environments of the Upper Cretaceous Pictured Cliffs Sandstone and Fruitland Formation, southwestern San Juan Basin, New Mexico: Texas Tech University, Master's thesis, 78 p.

Espitalie, J., Laporte, J. L., Madec, M., Leplat, P., Paulet, J., Boutfeu, A., 1977, Methode rapide de caracterisation des roches meres, de leur potentiel petrolier et de leur degre d'evolution: Rev. Inst. Fr. Petr., v. 32, p. 23–42.

Ettinger, I., Chaplinsky, A., Lamba, E., Adomov, V., 1966, Natural factors influencing coal sorption properties III—comparative sorption of carbon dioxide and methane on coals: Fuel, v. 45, p. 351–356.

Fassett, J. E., 1967, Core description from GB-1 (Gasbuggy 1) in the northeastern part of the San Juan Basin, Rio Arriba County, New Mexico: U.S. Geological Survey Open-File Report, 37 p.

_____ 1985, Early Tertiary paleogeography and paleotectonics of the San Juan Basin area, New Mexico and Colorado, *in* Flores, R. M., and Kaplan, S. S., eds., Cenozoic paleogeography of the west-central United States: Society of Economic Paleontologists and Mineralogists, Rocky Mountain Section, Rocky Mountain Paleogeography Symposium 3, p. 317–334.

_____ 1986, The non-transferability of a Cretaceous coal model in the San Juan Basin of New Mexico and Colorado, *in* Lyons, P. C., and Rice, C. L., eds., Paleo-environmental and tectonic controls in coal-forming basins in the United States: Geological Society of America Special Paper 210, p. 155–171.

_____ 1987, Geometry and depositional environments of Fruitland Formation coalbeds, San Juan Basin, New Mexico and Colorado: Anatomy of a giant coal-bed methane deposit: University of Alabama, School of Mines and Energy Development, Proceedings, 1987 Coalbed Methane Symposium, p. 19–35.

_____ 1988, Second day—road log from Durango, Colorado around northeast rim of San Juan Basin via Bayfield, Chimney Rock, Arboles, Allison, and Ignacio, Colorado and back to Durango, *in* Geology and coalbed methane resources of the San Juan Basin, Colorado and New Mexico: Rocky Mountain Association of Geologists, p. 337–351.

Fassett, J. E., and Hinds, J. S., 1971, Geology and fuel resources of the Fruitland Formation and Kirtland Shale of the San Juan Basin, New Mexico and Colorado: U.S. Geological Survey Professional Paper 676, 76 p.

Fassett, J. E., and Nuccio, V. F., 1990, Vitrinite reflectance values of coals from drill-hole cuttings from the Fruitland and Menefee Formations, San Juan Basin, New Mexico: U.S. Geological Survey Open-File Report 90-290, 22 p.

Finley, R. F., Laubach, S. E., Holtz, M. H., and Tyler, Noel, 1990, Opportunities for horizontal drilling in Texas: The University of Texas at Austin, Bureau of Economic Geology Geological Circular 90-2, 32 p.

Fisher, W. L., Brown, L. F., Scott, A. J., and McGowen, J. H., 1969, Delta systems in the exploration for oil and gas: The University of Texas at Austin, Bureau of Economic Geology Research Colloquium, 212 p.

Flores, R. M., and Erpenbeck, M. F., 1981, Differentiation of delta front and barrier lithofacies of the Upper Cretaceous Pictured Cliffs Sandstone, southwestern San Juan Basin,

New Mexico: The Mountain Geologist, v. 18, no. 2, p. 23–34.

Fogg, G. E., and Senger, R. K., 1985, Automatic generation of flow nets with conventional ground-water modeling algorithms: Ground Water, v. 23, no. 3, p. 336–344.

Freeze, R. A., and Cherry, J. A., 1979, Groundwater: Englewood Cliffs, New Jersey, Prentice-Hall, 604 p.

Friedman, Irving, O'Neil, J. R., and Fleischer, Michael (technical editor), 1977, Compilation of stable carbon isotope fractionation factors of geochemical interest: U.S. Geological Survey Professional Paper 440-KK, 12 p.

Galimov, E. M., 1988, Sources and mechanisms of formation of gaseous hydrocarbons in sedimentary rocks: Chemical Geology, v. 71, p. 77–95.

Garven, G., 1986, The role of regional fluid flow in the genesis of the Pine Point deposit, western Canada sedimentary basin—a reply: Economic Geology, v. 81, p. 1015–1020.

Gorham, F. D., Jr., Woodward, L. A., Callender, J. F., and Greer, A. R., 1979, Fractures in Cretaceous rocks from selected areas of San Juan Basin, New Mexico—exploration implications: American Association of Petroleum Geologists Bulletin, v. 63, p. 598–607.

Grossman, E. L., Coffman, B. K., Fritz, S. J., and Wada, W., 1989, Bacterial production of methane and its influence on ground-water chemistry in east-central Texas aquifers: Geology, v. 17, no. 6, p. 495–499.

Grout, M. A., and Verbeek, E. R., 1985, Fracture history of the Plateau Creek and adjacent Colorado River valleys, southern Piceance Basin: implications for predicting joint patterns at depth: U.S. Geological Survey Open-File Report 85-744, 17 p.

Haimson, B. C., 1978, Near surface and deeper hydrofracturing stress measurements in the Waterloo Quartzite (abs.): American Geophysical Union Transactions, v. 59, p. 327–328.

———— 1979, New hydrofracturing measurements in the Sierra Nevada Mountains and the relationship between shallow stresses and surface topography: 20th U.S. Symposium on Rock Mechanics, Austin, Texas, p. 675–682.

Hale, B. W., and Firth, C. H., 1988, Production history of the San Juan Unit No. 6 well, northern San Juan basin, New Mexico, *in* Fassett J. E., ed., Geology and coal-bed methane resources of the northern San Juan Basin Colorado and New Mexico: Rocky Mountain Association of Geologists, p. 199–204.

Hall, K. R., and Yarborough, L., 1973, A new equation of state for Z-factor calculations: Oil and Gas Journal, v. 71, no. 25, p. 82–92.

Hamilton, Warren, 1978, Mesozoic tectonics of the western United States, *in* Howell, D. G., and others, eds., Mesozoic paleogeography of the western United States: Society of Economic Paleontologists and Mineralogists, Pacific Coast Paleogeography Symposium No. 2, p. 33–70.

Hancock P. L., and Bevan, T. G., 1987, Brittle modes of foreland extension, *in* Coward, M. P., Dewey, J. F., and Hancock, P. L., eds., Continental Extensional Tectonics, Geological Society of London Special Publications N. 28, p. 127–138.

Hanson, W. B., 1990, Chemistry of western interior USA coal-bed gases based upon desorption of subsurface coal samples (abs.): American Association of Petroleum Geologists Bulletin, v. 74, p. 1326.

Hattin, D. E., 1965, Stratigraphy of the Graneros Shale (Upper Cretaceous) in central Kansas: Kansas Geological Survey, Bulletin 178, 83 p.

Heller, P. L., Bowdler, S. S., Chambers, H. P., Coogan, J. C., Hagen, E. S., Shuster, M. W., and Winslow, N. S., 1986, Time of initial thrusting in the Sevier orogenic belt, Idaho-Wyoming and Utah: Geology, v. 14, p. 388–391.

Henckle, W. R., Jr., Muhm, J. R., and DeBuyl, M. H. F., 1977, Cleat orientation in some subbituminous coals of the Powder River and Hanna Basins, Wyoming, *in* Proceedings of the Second Symposium on the Geology of Rocky Mountain Coal–1977: Colorado Geological Survey Resource Series No. 4, p. 129–141.

Henderson, R. G., 1960, A comprehensive system of automatic computation in magnetic and gravity interpretation: Geophysics, v. 25, p. 569–585.

Hickman, S. H., Healy, J. H., and Zoback, M. D., 1985, In situ stress, natural fracture distribution, and borehole elongation in the Auburn geothermal well, Auburn, New York: Journal of Geophysical Research, v. 90, no. B7, p. 5497–5512.

Hobbs, W. H., 1904, Lineaments of the Atlantic border region: Geological Society of America Bulletin, v. 15, p. 483–506.

Horne, J. C., Ferm, J. C., Caruccio, F. T., and Baganz, B. P., 1978, Depositional models in coal exploration and mine planning in Appalachian region: American Association of Petroleum Geologists Bulletin, v. 62, p. 2379–2411.

Houseknecht, D. W., and Iannacchione, A. T., 1982, Anticipating facies-related coal mining problems in Hartshorne Formation, Arkoma Basin: American Association of Petroleum Geologists Bulletin, v. 66, no. 7, p. 923–946.

Hucka, B. P., 1989, Analysis of cleats in Utah coal seams: Utah Geological and Mineral Survey Open-File Report 154, 156 p.

Huffman, A. C., and Taylor, D. J., in press, Basement fault control on the occurrence and development of San Juan Basin energy resources: Geological Society of America Abstracts with Programs.

Irving, E., 1979, Paleopoles and paleolatitudes of North America and speculations about displacement terrains: Canadian Journal Earth Sciences, v. 16, p. 669–694.

Jaeger, J. C., and Cook, N. G. W., 1979, Fundamentals of rock mechanics: London, Methuen, 593 p.

James, T. A., and Burns, B. J., 1984, Microbial alteration of subsurface natural gas accumulations: American Association of Petroleum Geologists Bulletin, v. 68, p. 957–960.

Jenden, P. D., 1985, Analysis of gases in the earth's crust: Gas Research Institute, contract no. 5081-360-0533 (GRI-85/0106), 110 p.

Jones, A. H., 1985, Methane production characteristics of deeply buried coalbed reservoirs, Final Report (February 1982–December 1984): Gas Research Institute, GRI-85/0033, NTIS PB85-223386, 144 p.

Jones, A. H., Kelkar, S., Bush, D., Hanson, J., Rakop, K., Ahmed, U., Holland, M., Tibbitts, G., Owen, L. B., and Bowman, K. C., 1985, Methane production characteristics of deeply buried coalbed reservoirs: Gas Research Institute, contract no. 5081-214-0577 (GRI-85/0033), 176 p.

Jordan, T. E., 1981, Thrust loads and foreland basin evolution, Cretaceous, western United States: American Association of Petroleum Geologists Bulletin, v. 65, p. 2506–2520.

Kaiser, W. R., Johnston, J. E., and Bach, W. N., 1978, Sand-body geometry and the occurrence of lignite in the Eocene

of Texas: The University of Texas at Austin, Bureau of Economic Geology Circular 78-4, 19 p.

Kaiser, W. R., and Swartz, T. E., 1988, Hydrology of the Fruitland Formation and coalbed methane producibility, *in* Ayers, W. B., Jr., and others, Geologic evaluation of critical production parameters for coalbed methane resources, Part 1: San Juan Basin: Gas Research Institute, contract no. 5087-214-1544 (GRI-88/0332.1), p. 61–81.

———— 1989, Fruitland Formation hydrology and producibility of coalbed methane in the San Juan Basin, New Mexico and Colorado: University of Alabama, School of Mines and Energy Development, Proceedings of the 1989 Coalbed Methane Symposium, p. 87–97.

———— 1990, Hydrodynamics of the Fruitland Formation, *in* Ayers, W. B., Jr., and others, Geologic evaluation of critical production parameters for coalbed methane resources, Part 1: San Juan Basin: Gas Research Institute, contract no. 5087-214-1544 (GRI-90/0014.1), p. 99–126.

Kaiser, W. R., Swartz, T. E., Ambrose, W. A., and Ayers, W. B., Jr., 1990, Hydrogeologic parameters for the producibility of coalbed methane, *in* Ayers, W. B., Jr., and others, Geologic evaluation of critical production parameters for coalbed methane resources, Part 1: San Juan Basin: Gas Research Institute, contract no. 5087-214-1544 (GRI-90/0014.1), p. 127–155.

Kauffman, E. G., 1977, Geological and biological overview—Western Interior Cretaceous basin, *in* Kauffman, E. G., ed., Cretaceous facies, faunas, and paleoenvironments across the Western Interior basin: The Mountain Geologist, v. 6, p. 227–245.

Kelley, V. C., 1951, Tectonics of the San Juan Basin: New Mexico Geological Society Guidebook of the south and west sides of the San Juan Basin, New Mexico and Arizona, Second Field Conference, p. 124–131.

———— 1955, Regional tectonics of the Colorado Plateau and relationship to the origin and distribution of uranium: University of New Mexico Publications in Geology, no. 5, 120 p.

Kelley, V. C., and Clinton, N. J., 1960, Fracture systems and tectonic elements of the Colorado Plateau: University of New Mexico Publications in Geology, no. 6, 104 p.

Kelso, B. S., Decker, A. D., Wicks, D. E., and Horner, D. M., 1987, GRI geologic and economic appraisal of coalbed methane in the San Juan Basin: University of Alabama, School of Mines and Energy Development, Proceedings, 1987 Coalbed Methane Symposium, p. 119–125.

Kelso, B. S., Goolsby, S. M., and Tremain, C. M., 1980, Deep coalbed methane potential of the San Juan River coal region, southwestern Colorado: Colorado Geological Survey Open-File Report 80-2, 56 p.

Kelso, B. S., and Rushworth, Peter, 1982, Southern Ute/Department of Energy coalbed methane test wells: Colorado Geological Survey Open File Report 82-4, 21 p.

Kelso, B. S., Wicks, D. E., and Kuuskraa, V. A., 1988, A geologic assessment of natural gas from coal seams in the Fruitland Formation, San Juan Basin: Chicago, Gas Research Institute Topical Report GRI 88/034, 56 p.

Kendall, P. F., and Briggs, H., 1933, The formation of rock joints and the cleat of coal, *in* Proceedings, Royal Society of Edinburgh, v. 53, p. 164–187.

Keystone, 1986, 1986 Keystone coal industry manual: Colorado—description of seams, p. 431–452; New Mexico—description of seams, p. 514–523, New York, McGraw-Hill.

Kharaka, Y. K., Hull, R. W., and Carothers, W. W., 1985, Water-rock interactions in sedimentary basins, *in* Gautier, D. L., and others, eds., Relationship of organic matter and mineral diagenesis: Society of Economic Paleontologists and Mineralogists, SEPM Short Course No. 17, p. 79–176.

Kharaka, Y. K., Law, L. M., Carothers, W. W., and Goerlitz, D. F., 1986, Role of organic species dissolved in formation waters from sedimentary basins in mineral diagenesis, *in* Gautier, D. L., ed., Roles of organic matter in sedimentary diagenesis: Society of Economic Paleontologists and Mineralogists, Special Publication No. 38, p. 111–122.

Khorasani, G. K., 1987, Oil-prone coals of the Walloon Coal Measures, Surat Basin, Australia, *in* Scott, A. C., ed., Coal and coal-bearing strata: Recent advances: Blackwell Scientific Publications, Geological Society Publication No. 32, p. 303–310.

Kluth, C. F., and Coney, P. J., 1981, Plate tectonics of the Ancestral Rocky Mountains: Geology, v. 9, p. 10–15.

Knepper, D. H., Jr., 1982, Lineaments derived from analysis of linear features mapped from Landsat images of the Four Corners region of the southwestern United States: U.S. Geological Survey Open-File Report 82-849, 79 p.

Koenig, R. A., Bumb, A. C., McKee, C. R., Murphy, C. L., Ramesh, M. S., Reverand, J. M., and Way, S. C., 1989, Application of hydrology to evaluation of coalbed methane reservoirs: Gas Research Institute, contract no. 5087-214-1489 (GRI-89/0031), 114 p.

Komar, C. A., Overbey, W. K., Jr., Rough, R. L., and Lambert, W. G., 1971, Factors that predict fracture orientation in a gas storage reservoir: Journal of Petroleum Technology, v. 23, May, p. 546–550.

Kulander, B. R. and Dean, S. L., 1980, Fracture trends in the Allegheny Plateau of West Virginia: West Virginia Geologic and Economic Survey Map WV-11.

Ladeira, F. L., and Price, N. J., 1981, Relationship between fracture spacing and bed thickness: Journal of Structural Geology, v. 3, p. 179–183.

LaPointe, P. R., 1988, A method to characterize fracture density and connectivity through fractal geometry: International Journal of Rock Mechanics and Geomechanics Abstracts, v. 25, no. 6, p. 421–429.

LaPointe, P. R., and Hudson, J. A., 1985, Characterization and interpretation of rock mass joint patterns: Geological Society of America Special Paper 199, 37 p.

Laubach, S. E., 1991, Fracture patterns in low-permeability-sandstone gas reservoir rocks in the Rocky Mountain region: Proceedings, Society of Petroleum Engineers Joint Rocky Mountain Regional Meeting and Low-Permeability Reservoirs Symposium, SPE Paper 21853.

Laubach, S. E., and Marshak, Stephen, 1987, Fault patterns generated during the extension of crystalline basement, NW Scotland, *in* Coward, M. P., Dewey, J. F., and Hancock, P. L., eds., Continental Extensional Tectonics, Geological Society of London Special Publication No. 28, p. 495–499.

Laubach, S. E., Reynolds, S. J., Spencer, J. E., and Marshak, Stephen, 1989, Progressive deformation and superposed fabrics related to Cretaceous crustal underthrusting in western Arizona, U.S.A.: Journal of Structural Geology. v. 11, no. 6, p. 735–749.

Laubach, S. E., Tremain, C. M., Whitehead, N. H., and Baumgardner, R. W., 1990, Fracture-trace maps of Upper Cretaceous Pictured Cliffs Sandstone pavements, San Juan Basin, Colorado: Implications for coalbed methane

exploration (abs.): Geological Society of America Abstracts with Programs, v. 22, no. 7, p. A202.

Law B. E., 1990a, Thermal evolution of the Upper Cretaceous Fruitland Formation, San Juan Basin, Colorado and New Mexico, *in* Sixth V. E. McKelvey Forum on Mineral and Energy Resources: U.S. Geological Survey Circular 1060, p. 49–50.

———— 1990b, Thermal Evolution of the Upper Cretaceous Fruitland Formation, San Juan Basin, Colorado and New Mexico, *in* Carter, L. M. H., ed., U.S. Geological Survey Research on Energy Resources, 1990, Programs and Abstracts, p. 49–50.

Law, B. E., Anders, D. E., and Michael, G. E., 1990, Use of Rock-Eval pyrolysis and vitrinite reflectance data in characterizing type and maturity of organic matter in coal, Upper Cretaceous Fruitland Formation, San Juan Basin, New Mexico and Colorado (abs.): American Association of Petroleum Geologists Bulletin, v. 74, p. 1333.

Leckie, D. A., Singh, Chaitanya, Goodarzi, Fariborz, and Wall, J. H., 1990, Organic-rich, radioactive marine shale: A case study of a shallow-water condensed section, Cretaceous Shaftesbury Formation, Alberta, Canada: Journal of Sedimentary Petrography, v. 60, no. 1, p. 101–117.

Levey, R. A., 1985, Depositional model for understanding geometry of Cretaceous coals: major coal seams, Rock Springs Formation, Green River Basin, Wyoming: American Association of Petroleum Geologists Bulletin, v. 69, no. 9, p. 1359–1380.

Leythaeuser, D., Schaefer, R. G., Cornford, C., and Weiner, B., 1979, Generation and migration of light hydrocarbons (C_2-C_7) in sedimentary basins: Organic Geochemistry, v. 1, p. 191–204.

Lindenlaub, J. C., 1976, The physical basis of remote sensing: fundamentals of remote sensing: Purdue University Minicourse Series, 13 p.

Lipman, P. W., Doe, B. R., Hedge, C. E., and Steven, T. A., 1978, Petrologic evolution of the San Juan volcanic field, southwestern Colorado Pb and Sr isotope evidence: Geological Society of America Bulletin, v. 89, p. 59–82.

Logan, T. L., 1989, Coalbed methane-6, western basins dictate varied operations: Oil & Gas Journal, Dec. 4, 1989, p. 35–39.

Long, J. C. S., and Billaux, D. A., 1987, From field data to fracture network modeling: an example incorporating spatial structure: Water Resources Research, v. 23, p. 1201–1216.

Long, J. C. S., and Witherspoon, P. A., 1985, The relationship of the degree of interconnection to permeability in fracture networks: Journal of Geophysical Research, v. 90, no. B4, p. 3087–3099.

Lorenz, J. C., Teufel, L. W., and Warpinski, N. R., in press, Regional fractures I: A mechanism for the formation of regional fractures in flat-lying reservoirs: American Association of Petroleum Geologists Bulletin.

Lundegard, P. D., and Land, L. S., 1986, Carbon dioxide and organic acids: their origin and role in diagenesis, the Texas Gulf Coast Tertiary, *in* Gautier, D. L., ed., Roles of organic matter in sedimentary diagenesis: Society of Economic Paleontologists and Mineralogists, Special Publication No. 38, p. 129–146.

Manfrino, Carrie, 1984, Stratigraphy and palynology of the upper Lewis Shale, Pictured Cliffs Sandstone, and lower Fruitland Formation (Upper Cretaceous) near Durango, Colorado: The Mountain Geologist, v. 21, no. 4, p. 115–132.

Manley, Kim, Scott, G. R., and Wobus, R. A. (compilers), 1987, Geologic map of the Aztec 1° × 2° quadrangle, northwestern New Mexico and southern Colorado: U.S. Geological Survey, Miscellaneous Investigations Series, Map I-1730.

Matthews, J. L., Emanuel, A. S., and Edwards, K. A., 1989, Fractal methods improve Mitsue miscible predictions, Journal of Petroleum Technology, v. 41, no. 11, p. 1136–1145.

Mattick, J. L., Duval, T. A., and Phillips, F. M., 1987, Quantification of groundwater recharge rates in New Mexico using bomb-36Cl, bomb-3H, and chloride as soil-water tracers: Las Cruces, New Mexico, New Mexico State University, New Mexico Water Resources Research Institute, WRRI Report No. 220, 184 p.

Mavor, M. J., and Close, J. C., 1989a, Western Cretaceous coal seam project, evaluation of the cooperative research area Northeast Blanco Unit operated by Blackwood & Nichols Co., Ltd.: Gas Research Institute Topical Report GRI-90/0041, variously paginated.

———— 1989b, Western Cretaceous coal seam project, evaluation of the cooperative research well Southern Ute-Mobil 36-1 operated by McKenzie Methane Cooperation: Gas Research Institute Topical Report GRI-90/0042, variously paginated.

———— 1989c, Western Cretaceous coal seam project, evaluation of the cooperative research well Colorado 32-7 #9 operated by Mobil Oil Corporation: Gas Research Institute Topical Report GRI-90/0043, variously paginated.

———— 1989d, Western Cretaceous coal seam project, evaluation of the cooperative research well Hamilton #3 operated by Mesa Operating Limited Partnership: Gas Research I Institute Topical Report GRI-90/0040, variously paginated.

McCord, J. P., 1988, Hydrogeology of a Fruitland Formation aquifer, San Juan Basin—New Mexico and Colorado, with emphasis on using temperature distribution data to estimate lateral groundwater velocity: New Mexico Institute of Mining and Technology, Master's thesis, 121 p.

McCulloch, C. M., Deul, Maurice, and Jeran, P. W., 1974, Cleat in bituminous coalbeds: United States Bureau of Mines Report of Investigations No. 7910, 23 p.

McCulloch, C. M., Diamond, W. P., Bench, B. M., and Deul, Maurice, 1975, Selected geological factors affecting mining of the Pittsburgh Coalbed, RI 8093, U.S. Bureau of Mines, 72 p.

McGowen, J. H., 1968, Utilization of depositional models in exploration from nonmetallic minerals, *in* Brown, L. F., Jr., ed., Proceedings, Fourth forum on geology of industrial minerals: The University of Texas at Austin, Bureau of Economic Geology, p. 157–174.

McKee, C. R., Bumb, A. C., and Koenig, R. A., 1987, Stress-dependent permeability and porosity in coal: University of Alabama, School of Mines and Energy Development, Proceedings, 1987 Coalbed Methane Symposium, p. 183–193.

Meissner, F. F., 1984, Cretaceous and Lower Tertiary coals as sources for gas accumulations in the Rocky Mountain area, *in* Woodward, J., Meissner, F. F., and Clayton, J. L., eds., Hydrocarbon source rocks of the greater Rocky Mountain region: Rocky Mountain Association of Geologists, p. 401–431.

———— 1987, Mechanisms and patterns of gas generation and expulsion-migration and accumulation associated with coal measures, Green River and San Juan Basins Rocky Mountain region, USA, *in* Doligez, Brigitte, ed., Migration of hydrocarbons in sedimentary basins: Editions Technip, Paris, p. 79–112.

Merewether, E. A., and Cobban, W. A., 1986, Biostratigraphic units and tectonism in the Mid-Cretaceous foreland of Wyoming, Colorado, and adjoining areas, *in* Peterson, J. A., ed., Paleotectonics and sedimentation in the Rocky Mountain region, United States: American Association of Petroleum Geologists, Memoir 41, p. 443–468.

Molenaar, C. M., and Baird, J. K., 1989, North-south stratigraphic cross-sections of Upper Cretaceous rocks, northern San Juan Basin, Colorado: U.S. Geological Survey Miscellaneous Field Studies Map MF-2068, 3 sheets.

Morton, R. A., and Land, L. S., 1987, Regional variations in formation water chemistry, Frio Formation (Oligocene), Texas Gulf Coast: American Association of Petroleum Geologists Bulletin, v. 71, no. 2, p. 191–206.

Muñoz-Espinoza, R. E., 1968, Fracture finding by structural curvature mapping: The University of Texas at Austin, unpublished Master's thesis, 44 p.

Murray, G. H., 1968, Quantitative fracture study — Sanish pool, McKenzie County, North Dakota: American Association of Petroleum Geologists Bulletin, v. 52, p. 57–65.

Mytton, J. W., and Schneider, G. B., 1987, Interpretive geology of the Chaco area, northwestern New Mexico: U.S. Geological Survey, Miscellaneous Investigation Series, Map I-1777, scale 1:24,000.

Nelson, R. A., Lenox, L. C., and Ward, B. J., 1987, Oriented core: its use, error, and uncertainty: American Association of Petroleum Geologists, v. 71, p. 357–368.

Neuman, S. P., and Witherspoon, P. A., 1970, Finite element method of analyzing steady seepage with a free surface: Water Resources Research, v. 6, no. 3, p. 889–897.

Newman, K. R., and McCord, J. P., 1980, Detailed site investigation, northern San Juan Basin: unpublished report to TRW for U.S. DOE, available for inspection at the Colorado Geological Survey, Denver, Colorado, variously paginated.

North, F. K., 1985, Petroleum Geology: Allen & Unwin, Boston, 607 p.

Novak, S. A., and Eckstein, Y., 1988, Hydrochemical characterization of brines and identification of brine contamination in aquifers: Ground Water, v. 26, no. 3, p. 317–324.

Nur, Amos, 1982, The origin of tensile fracture lineaments: Journal of Structural Geology, v. 4, p. 31–40.

Oldaker, P. R., 1990, Hydrogeology of the Fruitland Formation, San Juan Basin, Colorado and New Mexico: paper presented at The Coalbed Methane Forum, Lakewood, Colorado, February 22, 1990, unpaginated.

O'Leary, D. W., Friedman, J. D., and Pohn, H. A., 1976, Lineament and linear, a terminological reappraisal, *in* Podwysocki, M. H., and Earle, J. L., eds., Proceedings, 2nd International Conference on Basement Tectonics: Denver, Basement Tectonics Committee, p. 571–577.

Olson, Jon, and Pollard, D. D., 1989, Inferring paleostresses from natural fracture patterns: a new method: Geology, v. 17, no. 4, p. 345–347.

O'Sullivan, R. O., and Beikman, H. M. (compilers), 1963, Geology, structure and uranium deposits of the Shiprock quadrangle, New Mexico and Arizona: U.S. Geological Survey, Miscellaneous Geologic Investigations, Map I-345.

Palmer, J. J., and Scott, A. J., 1984, Stacked shoreline and shelf sandstone of La Ventana Tongue (Campanian), northwestern New Mexico: American Association of Petroleum Geologists Bulletin, v. 68, no. 1, p. 74–91.

Paul, G. W., 1990, Coalbed methane simulation: Quarterly Review of Methane from Coal Seams Technology, v. 7, no. 4, p. 14–16.

Peffer, J. W., 1985, An improved method for calculating bottom-hole pressures in gas wells: The University of Texas at Austin, Master's thesis, 138 p.

Peffer, J. W., Miller, M. A., and Hill, A. D., 1986, An improved method for calculating bottom-hole pressures in flowing gas wells with liquid present: Richardson, Texas, Society of Petroleum Engineers, SPE 15655, 6 p.

Petzet, G. A., 1990, Devon pressing Fruitland coal seam program: Oil and Gas Journal, v. 88, no. 45, p. 28–30.

Phillips, F. M., Peeters, L. A., Tansey, M. K., and Davis, S. N., 1986, Paleoclimatic inferences from an isotopic investigation of groundwater in the central San Juan Basin, New Mexico: Quaternary Research, v. 26, p. 179–193.

Phillips, F. M., and Tansey, M. K., 1984, An integrated isotopic/physical approach to a numerical model of groundwater flow in the San Juan Basin: Las Cruces, New Mexico, New Mexico State University, New Mexico Water Resources Research Institute, WRRI Report No. 197, 146 p.

Phillips, F. M., Tansey, M. K., Peeters, L. A., Cheng, S., and Long, A., 1989, An isotopic investigation of groundwater in the central San Juan Basin, New Mexico carbon 14 dating as a basis for numerical flow modeling: Water Resources Research, v. 25, no. 10, p. 2259–2273.

Pirson, S. J., 1977, Geologic well log analysis: Houston, Gulf Publishing Co., 370 p.

Pollard, D. D., and Aydin, A., 1988, Progress in understanding jointing over the past century: Geological Society of America Bulletin, v. 100, no. 8, p. 1181–1204.

Puri, R., and Yee, D., 1990, Enhanced coalbed methane recovery: Society of Petroleum Engineer Paper No. 20732, *in* 1990 SPE Annual Technical Conference and Exhibition, September 23-26, 1990, New Orleans, Louisiana, p. 193–202.

Raistrick, A., and Marshall, C. E., 1939, The nature and origin of coal and coal seams: London, The English Universities Press LTD., p. 42–45.

REC, 1989a, Stratton field, preliminary engineering assessment: Englewood, Colorado, Research & Engineering Consultants, Inc., prepared for the Bureau of Economic Geology, The University of Texas at Austin, report no. REC-SGR 89.1, 31 p.

———— 1989b, McAllen Ranch field, preliminary engineering assessment: Englewood, Colorado, Research & Engineering Consultants, Inc., prepared for the Bureau of Economic Geology, The University of Texas at Austin, report no. REC-SGR 89.2, 65 p.

Reiter, Marshall, and Mansure, A. J., 1983, Geothermal studies in the San Juan Basin and the four corners area of the Colorado Plateau I. Terrestrial heat-flow measurements: Tectonophysics, v. 91, p. 233–251.

Rice, D. D., 1983, Relation of natural gas composition to thermal maturity and source-rock type in San Juan Basin, northwestern New Mexico and southeastern Colorado: American Association of Petroleum Geologists Bulletin, v. 67, no. 8, p. 1199–1218.

Rice, D. D., Clayton, J. L., and Pawlewicz, M. J., 1989, Characterization of coal-derived hydrocarbons and source-rock potential of coal beds, San Juan Basin, New Mexico and Colorado, U.S.A.: International Journal of Coal Geology, v. 13, p. 597–626.

Rice, D. D., Threlkeld, C. N., Vuletich, A. K., and Pawlewicz, M. J., 1988, Identification and significance of coal-bed gas, San Juan Basin, northwestern New Mexico and southwestern Colorado, *in* Fassett, J. E., ed., Geology and coal-bed methane resources of the northern San Juan Basin, Colorado and New Mexico: Denver, Rocky Mountain Association of Geologists, p. 51–59.

———— 1990, Nonassociated gas potential of San Juan Basin considerable: Oil & Gas Journal, v. 88, August 13, 1990, p. 60–61.

Ridgley, J. L., and Huffman, A. C., Jr., 1990, Basin analysis study of the San Juan Basin, Colorado and New Mexico, in the Sixth V. E. McKelvey Forum on Mineral and Energy Resources: U.S. Geological Survey Circular 1060, p. 68–69.

Roberts, L. N. R., 1989, Results of 1988 coal exploratory drilling in the Fruitland Formation, western part of the Southern Ute Indian Reservation, La Plata County, Colorado: U.S. Geological Survey Open-file Report 89-487, 221 p.

Roberts, L. N. R., and Uptegrove, Jane, 1991, Coal geology and preliminary coal zone correlations in the Fruitland Formation, western part of the Southern Ute Indian Reservation, La Plata County, Colorado: U.S. Geological Survey Coal Investigations Map, C-138, scale 1:24,000.

Rohrback, B. G., Peters, K. E., Sweeney, R. E., and Kaplan, I. R., 1983, Ammonia formation in laboratory simulated thermal maturation: Implications related to the origin of nitrogen in natural gas; *in* Bjoroy, M., ed., Advances in Organic Geochemistry, 1981: New York, John Wiley, p. 819–823.

Ross, C. A., and Ross, J. R. P., 1986, Paleozoic paleotectonics and sedimentation in Arizona and New Mexico, *in* Peterson, J. A., ed., Paleotectonics and sedimentation in the Rocky Mountain region: American Association of Petroleum Geologists Memoir 41, p. 653–668.

Roybal, F. E., and others, 1983, Hydrology of area 60, northern Great Plains, and Rocky Mountain coal provinces, New Mexico, Colorado, Utah, and Arizona: U.S. Geological Survey, Water Resources Investigations Open-file Report 83-203, 80 p.

Roybal, G. H., Campbell, F. W., Beaumont, E. C., Cohen, A. D., Kuellmer, F. J., and Kottlowski, F. E., 1985, Quality assessment of strippable coals in New Mexico, Phase I, Fruitland and Cleary coals in the San Juan Basin of northwestern New Mexico: New Mexico Energy Research and Development Institute Report No. 2-73-4304, 89 p.

Royse, F., Jr., Warner, M. A., and Reese, D. L., 1975, Thrust belt structural geometry and related stratigraphic problems, Wyoming-Idaho-northern Utah, *in* Bolyard, D. W., ed., Deep drilling frontiers of the central Rocky Mountains: Rocky Mountain Association of Geologists, p. 41–54.

Ryer, T. A., and Langer, A. W., 1980, Thickness change involved in the peat-to-coal transformation for a bituminous coal of Cretaceous age in central Utah: Journal of Sedimentary Petrology, v. 50, no. 3, p. 987–992.

Sandberg, D. T., 1988, Coal resources and coal-bed geometry, Fruitland Formation, Southern Ute Indian Reservation, Archuleta and La Plata Counties, Colorado, *in* Fassett, J. E., ed., Geology and coal-bed methane resources of the northern San Juan Basin, Colorado and New Mexico: Rocky Mountain Association of Geologists, p. 39–50.

Scruton, P. C., 1961, Rocky Mountain Cretaceous stratigraphy and regressive sandstones: Wyoming Geological Association Guidebook, 16th Annual Field Conference, p. 242–249.

Sears, J. D., Hunt, C. B., and Hendricks, T. A., 1941, Transgressive and regressive Cretaceous deposits in southern San Juan Basin, New Mexico: U.S. Geological Survey Professional Paper 193-F, p. 101–121.

Senger, R. K., 1989, Hydrodynamics of gravity-driven flow systems in sedimentary basins: example of the Palo Duro Basin, Texas: The University of Texas at Austin, Ph.D. dissertation, 191 p.

———— 1990, Regional characterization of variable-density fluid flow in sedimentary basins: implications on model interpretation: paper presented at the Fifth Annual Canadian/American Conference on Hydrogeology: Parameter Identification and Estimation for Aquifer and Reservoir Characterization, Calgary, Alberta, Canada, September 18–20, 1990.

Senger, R. K., Fogg, G. E., and Kreitler, C. W., 1987, Effects of hydrostratigraphy and basin development on hydrodynamics of the Palo Duro Basin, Texas: The University of Texas at Austin, Bureau of Economic Geology Report of Investigations No. 165, 48 p.

Shoemaker, E. M., Squires, R. L., and Abrams, M. J., 1974, The Bright Angel and Mesa Butte fault systems of northern Arizona, *in* Geology of northern Arizona with notes on archaeology and paleoclimate, pt. 1: Geological Society of America, Rocky Mountain Section, p. 355–391.

Siegel, Sidney, 1956, Nonparametric statistics of the behavioral sciences: New York, McGraw-Hill, 312 p.

Sikkink, P. G. L., 1987, Lithofacies relationships and depositional environment of the Tertiary Ojo Alamo Sandstone and related strata, San Juan Basin, New Mexico and Colorado, *in* Fassett, J. E., and Rigby, J. K., Jr., eds., The Cretaceous-Tertiary boundary in the San Juan and Raton Basins, New Mexico and Colorado: Geological Society of America Special Publication 209, p. 81–104.

Silver, Caswell, 1951, Cretaceous stratigraphy of the San Juan Basin: New Mexico Geological Society, Guidebook of the south and west sides of the San Juan Basin, New Mexico and Arizona, Second Field Conference, p. 104–118.

———— 1957, Relation of coastal and submarine topography to Cretaceous stratigraphy (New Mexico): Four Corners Geological Society Guidebook, Geology of southwestern San Juan Basin, Second Field Conference, p. 128–137.

Spears, D. A., and Caswell, S. A., 1986, Mineral matter in coals: cleat minerals and their origin in some coals from the English Midlands: International Journal of Coal Geology, v. 6, p. 107–125.

Spencer, C. W., 1987, Hydrocarbon generation as a mechanism for overpressuring in Rocky Mountain region: American Association of Petroleum Geologists Bulletin, v. 71, no. 4, p. 368-388.

Stach, E., Mackowsky, M.-Th., Teichmüller, M., Taylor, G. H., Chandra, D., and Teichmüller, R., 1975, Stach's Textbook of Coal Petrology, 2nd edition: Gebrüder Borntraeger, Berlin, Stuttgart, 428 p.

Stearns, D. W., and Friedman, M., 1972, Reservoirs in fractured rock: American Association of Petroleum Geologists Memoir 16, Stratigraphic oil and gas fields, p. 82–106.

Steven, T. A., 1975, Middle Tertiary volcanic field in the southern Rocky Mountains, *in* Curtis, B. F., ed., Cenozoic history of the southern Rocky Mountains: Geological Society of America, Memoir 144, p. 75–94.

Steven, T. A., Lipman, P. W., Hail, W. J., Jr., Barker, Fred, and Luedke, R. G. (compilers), 1974, Geologic map of the Durango quadrangle, southwestern Colorado: U.S. Geological Survey, Miscellaneous Investigations Series, Map I-764.

Stone, W. J., Lyford, F. P., Frenzel, P. F., Mizell, N. H., and Padgett, E. T., 1983, Hydrogeology and water resources of San Juan Basin, New Mexico: Socorro, New Mexico, New Mexico Bureau of Mines and Mineral Resources, Hydrologic Report 6, 70 p.

Suits, V. J., and Cordell, Lindrith, 1981, Bouger gravity map of the San Juan Basin area, Colorado and New Mexico: U.S. Geological Survey Open-File Report No. 81-0657.

Taylor, D. J., and Huffman, A. C., 1988, Overthrusting in the northwestern San Juan Basin, New Mexico—A new interpretation of the Hogback Monocline (abs.): U.S. Geological Survey Circular 1025, V. E., McKelvey Forum on Mineral and Energy Resources, p. 60.

Teichmüller, Marlies, 1987, Recent advances in coalification studies and their application to geology, *in* Scott, A. C., ed., 1987, Coal and coal-bearing strata: recent advances: London, Blackwell Scientific Publications, Geological Society Publication No. 32, p. 127–169.

TerraTek, 1990, Preliminary cleat and fracture data, Resource Enterprises, Inc. well: Southern Ute Tribal H#1, 5 p.

Thompson, G. A., and Zoback, M. L., 1979, Regional geophysics of the Colorado Plateau: Tectonophysics, v. 61, p. 149–181.

Ting, F. T. C., 1977, Origin and spacing of cleats in coal beds: Journal of Pressure Vessel Technology, v. 99, p. 624–626.

Tissot, B., and Welte, D., 1978, Petroleum formation and occurrence: Berlin, Springer-Verlag, 521 p.

Tóth, J., 1978, Gravity-induced cross-formational flow of formation fluids, Red Earth region, Alberta, Canada: analysis, patterns, and evolution: Water Resources Research, v. 14, no. 5, p. 805–843.

Tóth, J., 1980, Cross-formational gravity-flow of ground water; a mechanism of the transport and accumulation of petroleum; the generalized hydraulic theory of petroleum migration, *in* Roberts, W. H., III, and Cordell, R. J., eds., Problems of petroleum migration: Tulsa, American Association of Petroleum Geologists, Studies in Geology No. 10, p. 121–167.

Tremain, C. M. and Whitehead, N. H., III, 1990, Natural fracture (cleat and joint) characteristics and patterns in Upper Cretaceous and Tertiary rocks of the San Juan Basin, New Mexico and Colorado, *in* Ayers, W. B., Jr., and others, Geologic evaluation of critical production parameters for coalbed methane resources: Part I, San Juan Basin, Annual Report prepared for Gas Research Institute, contract no. 5087-214-1544, p. 73–98.

TRW, 1978, Preliminary well test report on Western Coal Co., P-07, San Juan County, New Mexico, on file at Colorado Geological Survey.

Turcotte, D. L., and Schubert, G., 1982, Geodynamics applications of continuum physics to geological problems: New York, John Wiley, 450 p.

Velde, B., Dubois, J., Touchard, G., and Badri, A., 1990, Fractal analysis of fractures in rocks: the Cantor's Dust method: Tectonophysics, v. 179, p. 345–352.

Ver Steeg, K., 1942, Jointing in the coal beds of Ohio, *in* Economic Geology, v. 37, Economic Publishing Co., p. 503–509.

Vistelius, A. B., 1966, Structural diagrams: New York, Pergamon, 178 p.

Wandrey, C. J., 1989, Lineament map of part of the Southern Ute Reservation, San Juan Basin, Southwestern Colorado: U.S. Geological Survey Open-File Report No. 89-112, scale 1:100,000.

Way, S. C., Bumb, A. C., Koenig, R. A., McKee, C. R., and Reverand, J. M., 1985, Hydrologic characterization of coal seams for methane recovery, activities 5 and 7 progress report: review of single-phase hydrologic testing in coalbeds and development of unsaturated-flow well test procedures: Chicago, Gas Research Institute Topical Report GRI 85/0046, 79 p.

Weimer, R. J., 1986, Relationship of unconformities, tectonics, and sea level changes in the Cretaceous of the Western Interior, United States, *in* Peterson, J. A., ed., Paleotectonics and sedimentation in the Rocky Mountain region, United States: American Association of Petroleum Geologists, Memoir 41, p. 397–422.

Welhan, J. A., 1987, Stable isotope hydrology, *in* Kyser, T. K., ed., Stable isotope geochemistry of low temperature processes: Mineralogical Society of Canada Short Course Handbook v. 13, p. 129–161.

Whiticar, M. J., Faber, E., and Schoell, Martin, 1986, Biogenic methane formation in marine and freshwater environments: CO_2 reduction vs. acetate fermentation—isotope evidence: Geochimica et Cosmochimica Acta, v. 50, p. 693–709.

Williams, G. D., and Stelck, C. R., 1975, Speculations on the Cretaceous paleogeography of North America, *in* Caldwell, W. G. E., ed., The Cretaceous system in the Western Interior of North America: Geological Association of Canada Special Paper 13, p. 1–20.

Williams, R. S., Jr., 1983, Geological applications, *in* Colwell, R. N., ed., Manual of remote sensing (2d ed.): American Society of Photogrammetry, v. 2, *in* Estes, J. E., ed., Interpretation and applications, p. 1667–1953.

Wilson, R. W., and Jentgen, R. W., 1980, Coal test drilling for the De-Na-Zin Bisti Area, San Juan County, New Mexico: U.S. Geological Survey Open-File Report 80-1289, 111 p.

Wong, I. G., and Humphrey, J. R., 1989, Contemporary seismicity, faulting, and the state of stress in the Colorado Plateau: Geological Society of America Bulletin, v. 101, p. 1127–1146.

Wood, G. H., Jr., Johnson, R. B., and Dixon, G. H., 1948, Geology of the southern part of Archuleta County, Colorado: U.S. Geological Survey Oil and Gas Investigation Preliminary Map 81, scale 1:63,360.

Woodruff, C. M., Jr., and Caran, S. C., 1984, Lineaments of Texas—possible surface expressions of deep-seated phenomena: The University of Texas at Austin, Bureau of Economic Geology, final report prepared for U.S. Department of Energy, Division of Geothermal Energy, under contract no. DE-AS07-79ID12057, Geothermal resource assessment for the State of Texas, 68 p.

Woodward, L. A., and Callender, J. F., 1977, Tectonic framework of the San Juan Basin, *in* San Juan Basin III:

New Mexico Geological Society, 28th Guidebook, p. 209–212.

Wright, Robyn, 1986, Cycle stratigraphy as a paleogeographic tool: Point Lookout Sandstone, southeastern San Juan Basin, New Mexico: Geological Society of America Bulletin, v. 96, p. 661–673.

Yamaguchi, Yasushi, 1985, Image-scale and look-direction effects on the detectability of lineaments in radar images: Remote Sensing of Environment, v. 17, no. 2, p. 117–127.

Yarborough, L., and Hall, K. R., 1974, How to solve equation of state for Z-factors: Oil and Gas Journal, v. 72, no. 7, p. 86-88.

Yurtsever, Y., and Gat, J. R., 1981, Atmospheric waters, *in* Gat, J. R., and Gonfiantini, R., eds., Stable isotope hydrology: deuterium and oxygen-18 in the water cycle: International Atomic Energy Agency Technical Report Series No. 210, p. 103–142.

Zapp, A. D., 1949, Geology and coal resources of the Durango area, La Plata and Montezuma Counties, Colorado: U.S. Geological Survey Oil and Gas Investigation Preliminary Map 109, scale 1:31,680.

Zietz, Isidore (compiler) and others, 1982, Composite magnetic anomaly map of the United States, Part A: Conterminous United States: U.S. Geological Survey Geophysical Investigation Map, GP-0954-A, 1:250,000.

Zoback, M. D., Tsukahara, Hiroaki, and Hickman, Stephen, 1980, Stress measurements at depth in the vicinity of the San Andreas Fault: implications for the magnitude of shear stress at depth: Journal of Geophysical Research, v. 85, no. B11, p. 6157–6173.

Zoback, M. L., and Zoback, Mark, 1989, Tectonic stress field of the continental United States, *in* Pakiser, L. C., and Mooney, W. D., eds., Geophysical framework of the continental United States: Geological Society of America Memoir 172, p. 523–539.

Zoback, M. L., and Zoback, M. D., 1980, State of stress in the conterminous United States: Journal of Geophysical Research, v. 85, p. 6113–6156.

Zoback, M. L., and Zoback, M. D., 1990, Tectonic stress field of the continental United States, *in* Pakiser, L. C., and Mooney, W. D., eds., Geohphysical framework of the continental United States: Geological Society of America Memoir 172, p. 523–540.